Shining Light on Mechanochemistry through Real-time Spectroscopy and Diffraction

Patrick A. Julien

Department of Chemistry, McGill University, Montreal, QC

A Thesis submitted to McGill University in partial fulfillment of the requirements of the degree of Doctor of Philosophy (Ph.D.)

Table of Contents

Abstract

The desire to develop sustainable and efficient methods for chemical synthesis has driven recent developments in mechanochemistry, where chemical reactions are driven by mechanical energy, as an alternative to solution methodologies. Ball milling reactions are a broadly applicable, sustainable, and cost-effective method of chemical synthesis due to fast reaction times, high conversions, and reduction of solvent cost and waste. Despite the increasing popularity of mechanochemical methods, instrumental techniques capable of providing real-time data for milling reactions remain limited. Real-time monitoring of milling reactions has enormous potential for optimizing and providing mechanistic insights into mechanochemical processes. This Thesis focuses on development of novel mechanochemical syntheses as well as the creation and application of methods for bench-top monitoring of milling reactions. Advances herein include instrumental setups which expand the scope of Raman reaction monitoring, which is rapidly emerging as the leading methodology for monitoring of milling reactions without the need for a synchrotron radiation source. In addition, the first ever use of fluorescence spectroscopy to monitor mechanochemical reactions is presented. These real-time techniques provide complementary information to X-ray powder diffraction studies to better understand a wide variety of mechanochemical syntheses including organic transformations, coordination chemistry, and materials such as metal organic frameworks. The analysis of *in situ* data provides fundamental insights into reaction rates, kinetics, and reaction optimization of potentially industry relevant materials ranging from agrochemicals to pharmaceuticals. Advances in real-time monitoring of mechanochemical reactions enabled the discovery of novel and potentially isolatable intermediates and aided in the elucidation of the kinetics and fundamental mechanisms involved in milling reactions.

Résumé

Le désir de développer des méthodes plus durables et efficaces de synthèses chimiques ont motivé des récents progrès de la mécanochimie, où les réactions

chimiques sont effectuées par l'énergie mécanique, comme alternative aux méthodologies en solution. Les réactions de broyage à billes sont une méthode de synthèse chimique durable et rentable, qui peuvent être appliquées de manière générale et efficace en raison de la rapidité de leurs réactions et de la réduction du coût des solvants et des déchets. Malgré la popularité des méthodes mécanochimiques, les méthodes instrumentales capables de fournir des informations en temps réel pour les réactions de broyage restent limitées, bien qu'elles aient un potentiel considérable pour fournir des connaissances mécanistiques. Cette Thèse se concentre sur le développement de nouvelles synthèses mécanochimiques, et sur la création et l'application de méthodes de surveillance des réactions de broyage. Les avancées dans les configurations instrumentales ont élargi la portée de l'observation des réactions par spectroscopie Raman, qui deviendra rapidement la principale méthode de surveillance des réactions de broyage sans nécessiter une source de rayonnement synchrotron. Également, la première utilisation de la spectroscopie à fluorescence pour surveiller les réactions mécanochimiques est reportée. Ces techniques fournissent des informations complémentaires aux études sur la diffraction des poudres aux rayons-X afin mieux comprendre une grande variété de synthèses mécanochimiques, notamment les transformations organiques, la chimie de coordination et des matériaux tels que les réseaux métallo-organiques. L'analyse des mesures *in situ* fournit des informations fondamentales sur les vitesses de réaction, la cinétique, et l'optimisation de la synthèse de matériaux potentiellement pertinents pour l'industrie, aussi bien agrochimique que pharmaceutique. Les avancées dans la surveillance en temps réel des réactions mécanochimiques ont permis la découverte de nouveaux intermédiaires potentiellement isolables et ont contribué à élucider la cinétique et les mécanismes fondamentaux impliqués dans les réactions de broyage.

Acknowledgements

If I have seen further it is by standing on the shoulders of giants.

-Isaac Newton

Context is key for understanding any story or body of work, and I must acknowledge all the people without whom this Thesis would not exist. I must first thank my parents for their continuous help, guidance, and support over the years, who taught me the value of education and provided the opportunity to freely pursue it. I must also thank Isabelle for standing by me all these years.

I owe thanks to many people during my education at McGill, which set the stage for everything in this Thesis. This Thesis would likely not exist if my high school science teacher Mr. Jensen had not inspired a lasting interest in chemistry. I must thank Dr. Matthew Haley for teaching me how to perform organic synthesis in the lab, I still use these techniques on a daily basis. I wish to thank Mitch Huot and Dr. Sam Sewall who continuously helped me both at the undergraduate and graduate level, as they have done for so many other students. I highly appreciate the efforts of a number of professors at McGill in providing excellent undergraduate and graduate level courses, including Dr. Power who first taught me MATLAB, and Dr. Arndtsen for use of the Raman instrument throughout this Thesis. Finally, I would like to thank all of my friends, Tim, Chris, Jan, Laura, Ryan, Ted, and many others who made what was often a challenging experience enjoyable. I am also entirely convinced that a large part of my success is due to many of my friends who shone light on what was to come a few years down the road. Thank you Jev, Michelle, Graeme, Laure, Mary, Monika, Nick, and so many others who made my graduate and undergraduate experience so much more enjoyable.

I must acknowledge the vast amount of help and guidance provided by my lab mates and collaborators over the years. I must thank Davin, Jose, Cristina, Neil, Thanassis, Fabien, Dayaker, Mihails, Hatem, Ghada, Blaine and Louis for all their work in building the lab to what it is today, help on my projects, and for being great lab mates, colleagues, and friends over the years. To Luzia, Jan, Chris, Filip, Sandra and Igor thanks for all the help and the good times. To the many friends in the department I have made, my experience here would have been far less enjoyable and productive without you. Finally, I must thank my many collaborators, Luzia, Tristan, Kruno, Vjeko, Viktorija, Ivan, Dominic, and Ivani for all their help and discussions critical for the success of much of this work.

Finally, I would like to thank my supervisor Dr. Tomislav Friščić for everything the has done over the years. It is no exaggeration to say that without his help, I would not have continued my studies and McGill, and his unwavering support has been critical throughout the many bumps in the course of a PhD.

Contribution to Original Knowledge

The contribution to original knowledge found this Thesis is the advancement in understanding mechanochemical reactions through the development and application of *in situ* methodologies. Specifically, monitoring mechanochemical reactions through fluorescence spectroscopy has been achieved for the first time, and the use of sapphire jars has extended the scope of real-time reaction monitoring of milling reactions using Raman spectroscopy. The application of these techniques has enabled monitoring a wide variety of mechanochemical reactions, including an organic condensation reaction, where the role of temperature is shown to be critical for modulating reaction kinetics through increased mobility at higher temperature. A novel approach of decoupling thermal effects from the physical mixing and grinding effects of milling was developed by utilizing hot-stage Raman spectroscopy to analyze milled reaction mixtures. Subsequently, the synthesis of metal-organic frameworks (MOFs) was explored, revealing step-wise transformation mechanisms, and the ability to synthesize unknown metastable intermediate structures. For the case of europium-based frameworks, fluorescence spectroscopy is demonstrated as an accessible and reliable means of monitoring

mechanochemical reactions, while providing the first real-time monitoring for the mechanochemical synthesis of lanthanide based frameworks. In addition, the mechanochemical synthesis of co-crystals has been explored, revealing the first direct evidence of an autocatalytic mechanochemical reaction kinetics driven by water generated over the course of the reaction. Finally, fluorescence emission spectroscopy is presented as a novel means of monitoring mechanochemical reactions including co-crystallization and amorphization of pharmaceutically relevant materials.

Declaration of Conflicts of Interest

Tomislav Friščić is a founder of Form-Tech Scientific.

Contribution of Authors

All sections of the Thesis not explicitly stated below have been written by Patrick A. Julien and edited by Tomislav Friščić.

Chapters 1&2: Introduction and Literature Review

These chapters have been written in their entirety by P. A. Julien. and edited by T. Friščić. The text contains excerpts from the following article: P. A. Julien, C. Mottillo and T. Friščić, *Green Chemistry*, 2017, **19**, 2729-2747, which was written by P. A. Julien and T. Friščić, with C. Mottillo contributing figures and editing. Parts of this chapter are being reworked into a review article to be published.

Chapter 3: Methodology

All work and writing in this chapter was conducted by P. A. Julien and edited by T. Friščić.

Chapter 4: The effect of milling frequency on a mechanochemical organic reaction monitored by in situ Raman spectroscopy.

This chapter consists of the manuscript: P. A. Julien, I. Malvestiti and T. Friščić, *Beilstein Journal of Organic Chemistry*, 2017, **13**, 2160-2168. All work and writing in this chapter conducted by P.J., data was collected with the assistance of Ivani Malvestiti, and the manuscript edited by both I. Malvestiti and T. Friščić.

Chapter 5: In-situ monitoring of mechanochemical and thermochemical reactions reveals kinetics modulated by thermal induced changes in mobility in an organic transformation.

This chapter was written by P. A. Julien and edited by T. Friščić. Real-time hot-stage Raman data was acquired with the help of T. Borchers, and synchrotron data was acquired with L. S. Germann and M. Etter who integrated the 2D diffraction data. All further analysis was performed by P. Julien. This chapter will be reformatted for submission to the *Journal of Physical Chemistry Letters.*

Chapter 6: In situ monitoring and mechanism of the mechanochemical formation of a microporous MOF-74 framework.

This chapter consists of the manuscript: P. A. Julien, K. Užarević, A. D. Katsenis, S. A. J. Kimber, T. Wang, O. K. Farha, Y. Zhang, J. Casaban, L. S. Germann, M. Etter, R. E. Dinnebier, S. L. James, I. Halasz and T. Friščić, *Journal of the American Chemical Society*, 2016, **138**, 2929-2932.

The syntheses used in this work were developed by P. A. Julien Synchrotron diffraction data was measured principally by P. A. Julien along with the assistance of other team members, including: K. Užarević, A. D. Katsenis, S. A. J. Kimber, L. S. Germann, M. Etter, R. E. Dinnebier, and I. Halasz. Surface area and electron microscopy characterization were conducted by T. Wang and O. K. Farha, Northwestern University. Supplementary characterization of the reaction products and Rietveld analysis was conducted by K. Užarević, A. D. Katsenis, and I. Halasz. P. A. Julien and T. Friščić were the principal contributors to the preparation of the manuscript.

Chapter 7: Tandem Monitoring Mechanochemical Reactivity of Lanthanides in Real-time using Fluorescence Spectroscopy and Powder Diffraction.

This chapter consists of an article is being prepared for submission in Journal of Materials Chemistry C with the following authors: Patrick A. Julien, Luzia Germann, Martin Etter, Ivani Malvestiti, Stipe Lukin, Krunoslav Užarević, and Tomislav Friščić. The reactions used in this work were screened by P. A. Julien and I. Malvestiti. Synchrotron diffraction

data was collected by P. A. Julien, L. S. Germann, M. Etter, S. Lukin, and K. Užarević. The manuscript was written by P. A. Julien and edited by T. Friščić.

Chapter 8: In situ monitoring of mechanochemical synthesis of calcium urea phosphate fertilizer co-crystal reveals highly effective water-based autocatalysis.

This chapter consists of a manuscript currently submitted: Patrick A. Julien, Luzia S. Germann, Hatem M. Titi, Martin Etter, Robert E. Dinnebier, Lohit Sharma, Jonas Baltrusaitis, and Tomislav Friščić *Chemical Science (submitted)*.

Synchrotron data was collected by P. A. Julien, L. S. Germann, H. Titi, M. Etter, and R. Dinnebier. DVS studies were conducted by, L. Sharma and J. Baltrusaitis. All other data was collected by P. A. Julien. The manuscript was written by P. A. Julien with editing from T. Friščić and other authors.

Chapter 9: Expanding the Toolbox: Monitoring the Mechanochemical Co-crystallization of Pharmaceuticals in Real-time using Fluorescence Spectroscopy.

Data in this chapter was collected by P. A. Julien with synchrotron diffraction data was collected and analyzed by P. A. Julien and L. S. Germann. The manuscript was written by P. A. Julien and edited by T. Friščić.

Chapter 10: Discussion and Conclusion

This chapter was written by P. A. Julien and edited by T. Friščić.

Appendix 3: Investigation of BINOL-3,3'-dicarboxylate as a ligand for the formation of extended coordination-based structures.

This appendix consists of the published manuscript: Patrick A. Julien, Jan-Constantin Christopherson, Hatem M. Titi, Robin D. Rogers, Tomislav Friščić. *Supramolecular Chemistry,* 2018, **30**, 488-503.

All reported compounds were synthesized and characterized by P. A. Julien. Crystallographic data collection was performed by P. A. Julien and Hatem Titi. Crystallographic structure determination and subsequent analysis was performed by Hatem Titi and T. Friščić.

List of Abbreviations

AB - amidoboranes

APIs - active pharmaceutical ingredients

apyH$^+$ - aminopyridinium cations

arPLS - asymmetrically reweighted penalized least squares

AsLS - asymmetric least squares

AZB - azobenzene

barb - barbituric acid

BET - Brunnauer-Emmet-Teller

BINOL - 1,1′-binaphthol

CCD - Charge Coupled Device

CCDC - Cambridge Crystallographic Data Centre

CLS - classical least-squares

COFs - covalent organic frameworks

CP-MAS SSNMR - cross-polarized magic-angle spinning solid-state nuclear magnetic resonance

CSD - Cambridge Structural Database

dabco - 1,4-diazabicyclo[2.2.2]octane

DESY - Deutsches Elektronen-Synchrotron

DFT - density functional theory calculations

DMF - *N*,*N*-Dimethylformamide

DSC – Differential scanning calorimetry

DVS - dynamic vapour sorption

EDS - energy- dispersive X-ray spectroscopy

ESRF - European Synchrotron Radiation Facility

FTIR-ATR - Fourier-transform infrared attenuated total reflectance

GC-FID - gas chromatography with a flame ionization detector

GUI - graphical user interface

H_2BDC - benzene-1,4-dicarboxylic acid

H_3BTC -Trimesic acid

H_4bna - 1,1′-bi-2-naphthol-3,3′-dicarboxylic acid

H_4dhta - 2,5-dihydroxyterephthalic acid

HPLC - high-pressure liquid chromatography

HS - hardened steel

ILAG - ion-and liquid-assisted grinding

IPF - instrumental profile function

LAG - liquid-assisted grinding

LCA - Life-Cycle Assessment

LEDs - light emitting diodes

LOESS - locally estimated scatterplot smoothing

MCR-ALS - Multivariate Curve Resolution Alternating Least Squares

MeIm - 2-methylimidazole

MOFs - metal organic frameworks

MSC - multiplicative scatter correction

MSR - mechanically induced self-propagating reactions

na - nicotinamide

NMF - non-negative matrix factorization (Projected Gradient Approach)

NMR - nuclear magnetic resonance

NNLS - non-negative least squares

NNMF - non-negative matrix factorization (Alternating Least Squares approach)

NNSVD – non-negative double singular value decomposition

PMMA - polymethyl-methacrylate

PTFE – polytetrafluoroethylene (Teflon)

PXRD - powder X-ray diffraction

RH - relative humidity

Rpm – rotations per minute

SDBS - Spectral Database for Organic Compounds

SEM - Scanning electron microscopy

SNV - standard normal variate

SS - stainless steel

sub - suberic

TD-DFT - time-dependent density functional theory

TGA - thermogravimetric analysis

UHS - unhardened steel

UV - ultraviolet

van - vanillin

VT-XRPD - variable temperature X-ray powder diffraction

XRPD - X-ray powder diffraction

ZIF - zeolitic imidazolate framework

List of Tables

List of Figures

1. Introduction

Mechanochemistry, where a chemical reaction is induced by mechanical energy, has rapidly gained popularity as a sustainable and efficient means of chemical synthesis, due to the elimination of bulk solvents which often are responsible for much of the waste, cost, and negative environmental consequences of solution based chemical processes. Mechanochemistry has evolved rapidly from manual grinding of powders in a mortar and pestle (Figure 1a) to a variety of automated ball mills such as vibratory ball mills (Figure 1b) and even continuous processing methods such as twin screw extrusion (Figure 1d)[1]. Despite the popularity of using ball milling as a means of mechanochemical synthesis, these reactions remain poorly understood. This is at least in part due to challenges associated with obtaining accurate analyses of milling reactions in real-time without disrupting milling. Relatively recently, real-time methods for monitoring milling reactions have emerged, providing a unique opportunity to gain insights into mechanochemical reactions. The development and application of mechanochemistry as a potentially more sustainable synthetic methodology is reviewed in the literature review section of this chapter, along with the rise of *in situ* monitoring (Figure 1c) of milling reactions as a leading methodology for investigating the mechanisms underlying mechanochemical reactions. The body of this Thesis focuses on understanding mechanochemical syntheses of a variety of supramolecular materials utilizing *in situ* reaction monitoring. Analysis of real-time reaction monitoring data provides unique insights into the kinetic behavior of mechanochemical reactions, including thermal and autocatalytic effects, and reveals reaction mechanisms which can be applied in hopes of optimizing, tuning, and ultimately reducing the cost and increasing the sustainability of the synthesis of supramolecular materials.

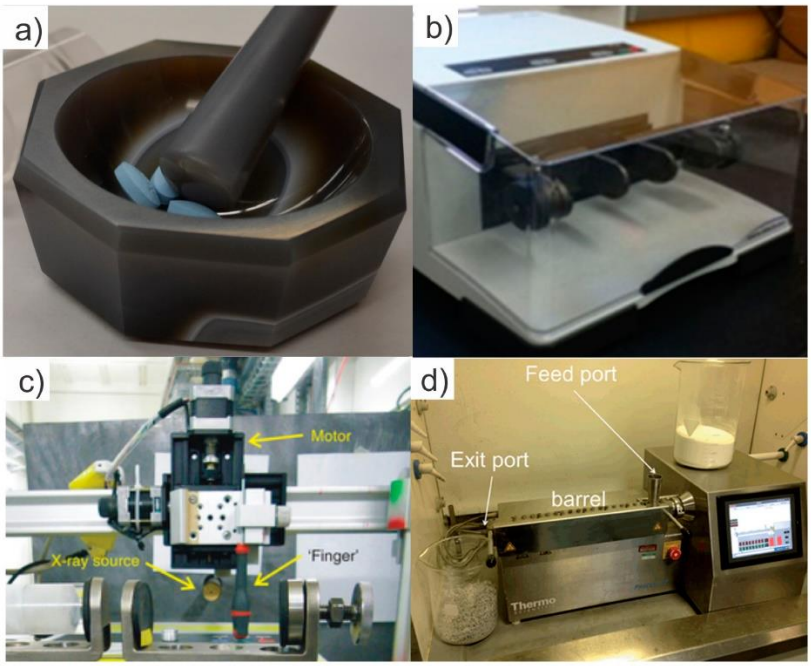

Figure 1. a) Traditional mortar and pestle grinding, b) a laboratory-scale vibratory ball mill, c) a setup for in situ monitoring of ball milling reactions using synchrotron X-ray powder diffraction. d) Continuous mechanochemical synthesis using twin-screw extrusion. Reproduced from ref. [1].

Given the overarching goal of better understanding the milling synthesis of supramolecular materials, a two-step approach was chosen which consisted of: 1) expanding the currently under-developed instrumental methods for monitoring milling reactions, and 2) the application of these methods to a diverse set of supramolecular materials. This Thesis examines mechanochemical reactions involving a covalent bond forming condensation reaction, the formation of coordination bonds in metal organic frameworks (MOFs) and, finally, supramolecular non-covalent interactions *via* the synthesis of ionic and organic co-crystals. The diversity in applications highlights the versatility and utility of real-time monitoring of milling reactions and novel mechanistic insights.

Having hopefully familiarized the reader with the literature on the emergence of real-time monitoring of milling reactions in the second chapter of this Thesis, the third chapter compiles the variety of methodological advances developed throughout this Thesis. Improvements in the capability of monitoring milling reaction includes the development of a novel monitoring method, namely, fluorescence emission spectroscopy, as well as

improvements to previously reported monitoring techniques, such as Raman spectroscopy, *via* the development of more optically transparent milling jars. The challenge of monitoring a reaction where the sample is inherently moving required the development of a customized data analysis approach capable of efficiently processing the hundreds of thousands of spectra and diffraction patterns acquired during this Thesis. While a detailed discussion on the processing of *in situ* data is beyond the scope of this Thesis, this chapter concludes with an overview of the data processing approach utilized throughout this Thesis.

The fourth chapter of this Thesis utilizes *in situ* techniques to explore the effect of milling frequency on the kinetics of a condensation reaction between benzil and *o*-phenylenediamine, as a model system for forming covalent bonds in organic synthesis. The temperature increase associated with milling at higher frequency is demonstrated to play a crucial role in modulating the kinetics of the reaction. Chapter five extends this work using hot-stage Raman microscopy as a means of decoupling thermal and mechanical effects during milling, suggesting the presence of a transient eutectic phase although large-scale melting is not observed during the course of the reaction.

The sixth chapter explores monitoring coordination chemistry in the context of the milling synthesis of metal organic frameworks. Here synchrotron X-ray powder diffraction studies revealed the stepwise formation of Zn-MOF-74 from a coordination polymer. In addition, novel intermediate phases were identified and characterized, and real-time diffraction data enabled the optimization of the milling synthesis. In the seventh chapter, tandem synchrotron and fluorescence measurements are applied towards the milling synthesis of europium lanthanide organic frameworks from carbonates. The accessibility and utility of fluorescence measurements is highlighted for both the development of novel milling syntheses and for understanding the behavior of these reactions.

The final two chapters of the Thesis return to monitoring mechanochemistry, namely, the formation of co-crystals. In this case, mechanochemically induced changes in non-covalent interactions and the supramolecular environment modify the spectral, physical, and chemical properties of a material which enable monitoring in real-time. First, the synthesis of an ionic calcium urea phosphate co-crystal with potential applications as a

fertilizer is explored providing the first direct evidence of water-based autocatalysis in a milling reaction using Raman spectroscopy and synchrotron powder X-ray diffraction in chapter nine. Next, in chapter ten, the formation of a pharmaceutical co-crystal is explored using Raman and fluorescence spectroscopies, providing a means to monitor the synthesis of pharmaceutical solid forms involved in tableting.

The Thesis concludes with a very brief chapter on the use of *in situ* techniques as a way of both rapidly optimizing mechanochemical syntheses and gaining insights into the fundamental behavior of mechanochemical reactions which remain poorly understood.

The appendix contains the supplementary information for published chapters as well as a manuscript published during this Thesis which deviates from the rest of the work in this Thesis. It presents the design and synthesis of various 1,1'-binaphthol based coordination polymers using solution methods, with the ultimate goal of synthesizing porous and optically active materials with potential chirality. The primary purpose of this project was to extend our experience in MOFs from making known structures towards the discovery of novel materials, with properties of general interest which are also amenable towards in situ monitoring of their milling syntheses.

As a whole, the work herein represents an effort to develop more sustainable processes which produce functional materials while minimizing environmental impact and costs, yet remain suitable for industrial scale manufacture with rapid reaction times, high yields, and high purity. Combining materials discovery with novel approaches to chemical reactivity and improved instrumental analysis methods represents a promising approach towards mitigating some of the environmental impact of chemical processes while maintaining the ability to produce valuable functional materials on a large scale.

2. Literature Review

2.01 The Impact of Chemistry

Advances in chemistry and materials science have contributed to a modern world with previously unknown levels of prosperity, security, and health for much of the world's population. The economic impact of catalysis is estimated to be roughly 30% of the gross

domestic product of developed economies, and 80% of manufactured products involve catalysis at some step,[2] demonstrating both the scale and importance of materials production. However, this has come at the cost of increasingly dire environmental consequences. Accordingly, considerable research is underway in order to improve materials so that they retain their function while minimizing environmental consequences.

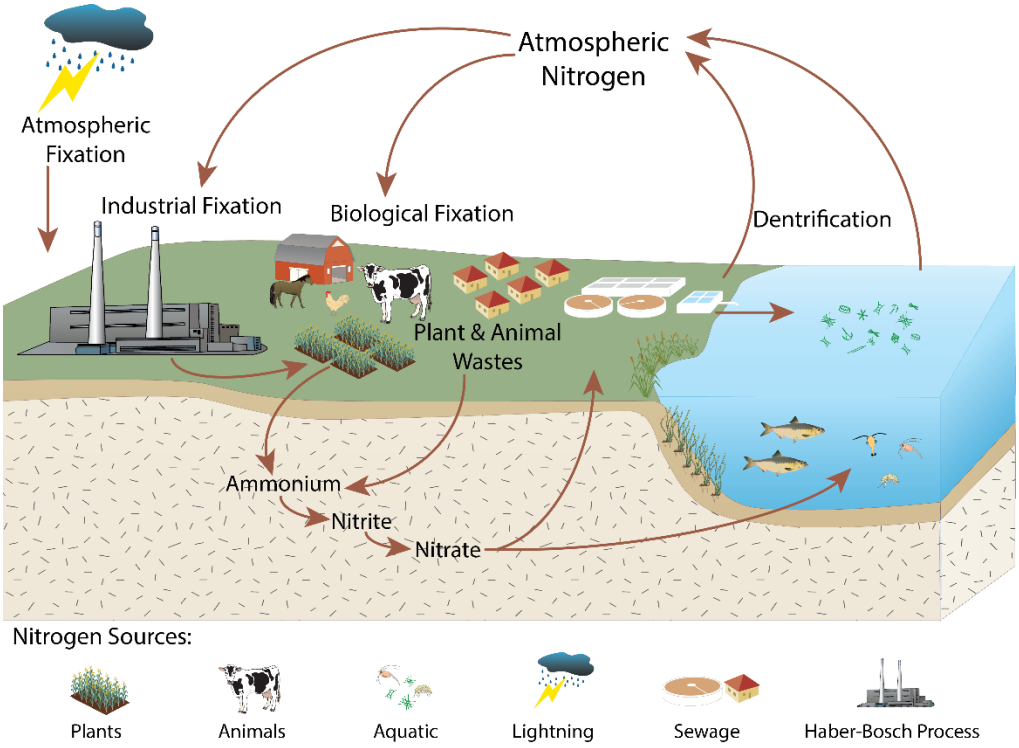

Figure 2. Influence of the Haber-Bosch process on the nitrogen cycle. Image attribution: Catherine Ward, Integration and Application Network, University of Maryland Center for Environmental Science (ian.umces.edu/imagelibrary/).

An emblematic example of both the importance and consequences of industrial chemical processes is the Haber-Bosch process of transforming atmospheric nitrogen into ammonia (Figure 2). This process underlies fertilizer production which has fed billions of people and is currently estimated to sustain nearly 50% of the human population.[3] Despite the potential to end food insecurity, current estimates suggest 821 million people (2017 estimate) remain undernourished.[4] It has also resulted in significant ecological consequences with only 17Tg of the 100Tg of nitrogen produced to be consumed by humans, an estimated waste of nearly 1 percent of primary global energy supply.[3] Much of this lost nitrogen is estimated to remain in reactive forms[5] which disturb the balance of

greenhouse gases, affects ozone levels, result in soil acidification, and, for coastal ecosystems, cause algal blooms and loss of biodiversity[3]. Critically, the efficiency of nitrogen use for the production of cereals, representing over 60% of human food[6], has declined from nearly 80% to 30% in 2000, suggesting a pressing need for scalable technological innovation for greater efficiency. The chemical industry has contributed significantly to greenhouse gas emissions at nearly 10% of global total final energy consumption and 7% of 'greenhouse gas' emissions[7] which has significant negative effects on both the physical and biological systems of the planet.[8] Reducing the energy demand of chemical processes is critical for minimizing the economic, health, and environmental consequences associated with global warming and the associated concerns of environmental and health pollution.

In addition to the adverse impact from disturbing biogeochemical cycles, the sustainability and long-term fate of materials are of growing concern. Plastic materials have been produced at a massive scale of approximately 8.3 billion metric tons of which 4.9 billion metric tons currently lies in landfills or in the environment[9] and is highly resistant to environmental degradation.[10] Similarly, health concerns related to persistent organic pollutants, such as flame-retardants,[11] perfluorinated compounds,[12] and poly-chlorinated biphenyls, have warranted international treaties such as the Stockholm Convention to eliminate their use and release.[13] Persistent organic pollutants have been detected in most environments on earth[14] and are of considerable health concern due to their toxicity which are of special concern as many pollutants bioaccumulate and bioamplify in the food chain.[15]

The rather stark reality of the consequences of global industrialization has driven demand for sustainable technologies through the development of novel materials and processes that can deliver improved performance whilst minimising environmental, societal, and economic cost.[16] This led to increased scrutiny of chemical processes with regards to energy efficiency, safety, and environmental impact, steering researchers' attention towards "green" methodologies and materials.[17, 18]

2.02 Emergence of Green Chemistry

Widespread public concern over pollution and resource depletion drove the formation of the environmental movement after the publication of “Silent Spring” by Rachel Carson, leading to the formation of the US EPA in 1970.[19] Throughout a number of international conferences such as the Stockholm Conference, the concept of sustainable development was established which the so-called “Brundtland Report” defined as development that meets the needs of the current generation without compromising the future generation,[20] a definition which provides the foundation for the current UN sustainable development goals.[21] In response to public concerns, the chemical industry has attempted efforts towards self-regulation in order to minimize pollution and improve the health and safety of the manufacture and transport of chemicals, with the U.S. Chemical Manufacturers Association creating the Responsible Care program.[22] Aligned government and industry interest in the development of more sustainable chemistry drove the evolution of the modern field of green chemistry, with programs such as the ACS Green Chemistry Institute and the Presidential Green Chemistry Challenge, journals such as Green Chemistry and ACS Sustainable Chemistry and Engineering, and numerous conferences. The philosophy or definition of green chemistry were formalized by Anastas as the use of chemical skills and knowledge to reduce or eliminate the use or generation of hazardous substances during the planning, manufacturing, and application of chemicals in order to minimize threats to the health of operators and the environment.[23] This was expanded into the 12 principles of Green Chemistry (Table 1), which currently provides the basis for the field.[24]

Table 1. 12 principles of Green Chemistry with a basic description.

Number	Name	Description
1	Prevention	Waste prevention is better than treatment.
2	Atom Economy	Syntheses should maximize incorporation of materials used in the process into desired products.

3	Safer Chemical Synthesis	Syntheses should minimize their impact on human health and the environment.
4	Safer Chemicals Design	Products should minimize toxicity while retaining function.
5	Use of Safer Solvents and Auxiliaries	Solvents and auxiliaries should either be eliminated or be as benign as possible.
6	Design for Energy Efficiency	For economic and environmental reasons, energy use should be minimized.
7	Use of Renewable Raw Materials	Renewable resources are preferable to those which will be depleted.
8	Reduction of Derivatives	Unnecessary derivatization (such as protecting groups) should be avoided if possible.
9	Catalysis	Catalytic Reagents are preferable to stoichiometric ones.
10	Degradation Products Design	Chemical products should degrade and not persist in the environment.
11	Real-time Analysis for Pollution Prevention	Methodologies for real-time process monitoring and control to detect the formation of hazardous substances.
12	Accidents Prevention	Processes should minimize the risk of accidents such as releases, fires, or explosions.

The development of Green Chemistry has significantly impacted academic research. There is no single solution or approach for applying the principles of Green Chemistry to chemical syntheses, resulting in diverse approaches towards lowering the impact of chemical reactions. Consequently, different fields of chemistry have adopted different approaches towards “greener” chemistry.

In organic chemistry, a field often associated with relatively lengthy synthetic methods, environmental and sustainability challenges have driven the emergence of green metrics

for chemical synthesis, such as the E-factor[25] and atom efficiency,[25] as well as the adoption of more comprehensive methodologies such as life-cycle assessment.[26] Metrics provide critical insights into the relative benefits and disadvantages of different syntheses, but must be critically evaluated. Only rarely is there a synthetic innovation which clearly outperforms alternative syntheses in every aspect, generally resulting in analyses focused on understanding trade-offs between, cost, toxicity, safety, and environmental impact. The availability of such metrics has facilitated the development and discovery of cleaner, more efficient chemical transformations.

In contrast, the Green Chemistry of materials, especially in regard to inorganic or metal-organic materials, is often evaluated by the ability to design[27] advanced materials for green applications (*e.g.* energy storage,[28] light harvesting,[29] or catalysis[30]) rather than the environmental impact and sustainability of methods for their preparation. Environmentally-mindful synthetic procedures are increasingly important for commercialisation of inorganic and metal-organic materials, driving the development of sustainable, scalable, and cost-effective approaches to coordination bonds.[31] There is, however, a difficulty - while many concepts of Green Chemistry are well established in organic chemistry, such “green” concepts and methods have only recently emerged to address the unique challenges of assembling structures composed of inorganic and organic components.[32-35]

2.03 Engineering Solid Materials: Crystal Engineering and Supramolecular Chemistry

Solid-state materials are often highly desirable for many applications due to their general stability and handling relative to solution, liquid, and gaseous forms. Solid forms of materials dominate numerous industrial applications such as catalysis and pharmaceuticals, with solid heterogenous catalysts being responsible for ca. 90% of global chemical production by volume[36] and approximately 80% of marketed drugs in solid form.[37] Importantly, structurally different solid forms (e.g. polymorphs) of a material can have considerable differences in properties, including optical properties, solubility, stabilities, and even chemical reactivity. Molecular crystalline materials, solids with long range order where molecules are arranged periodically, are of particular interest as the

environment of molecules is uniform with the exception of defects and surface chemistry. Advances in crystallography have made solving the structure of crystalline materials based on X-ray or electron diffraction routine. Consequently, the structure of a material can be readily determined and used to try and understand the properties of the material. This structure-property relationship has driven the field of Crystal Engineering, which seeks to control and design the arrangement of molecules within crystalline lattices in order to achieve or modify properties of the resulting materials.[38] There are two principle classes of interactions utilized in Crystal Engineering for the formation of three-dimensional (3-D) crystalline materials. Either supramolecular non-covalent interactions or covalent bonding can be used to create structures that exhibit periodicity in any direction. Assembly using only supramolecular interactions typically results in discrete molecules arranged into a periodic structure, whereas the use of only covalent interactions results in a framework where the entire single crystal can be considered a single molecule, as shown in Figure 3. Obviously, for the assembly of crystals in three dimensions such approaches can be combined where covalent interactions can be used to connect either one or two dimensions resulting in one-dimensional (1-D) or two-dimensional (2-D) polymers which can be assembled using supramolecular interactions into a 3-D periodic structure.

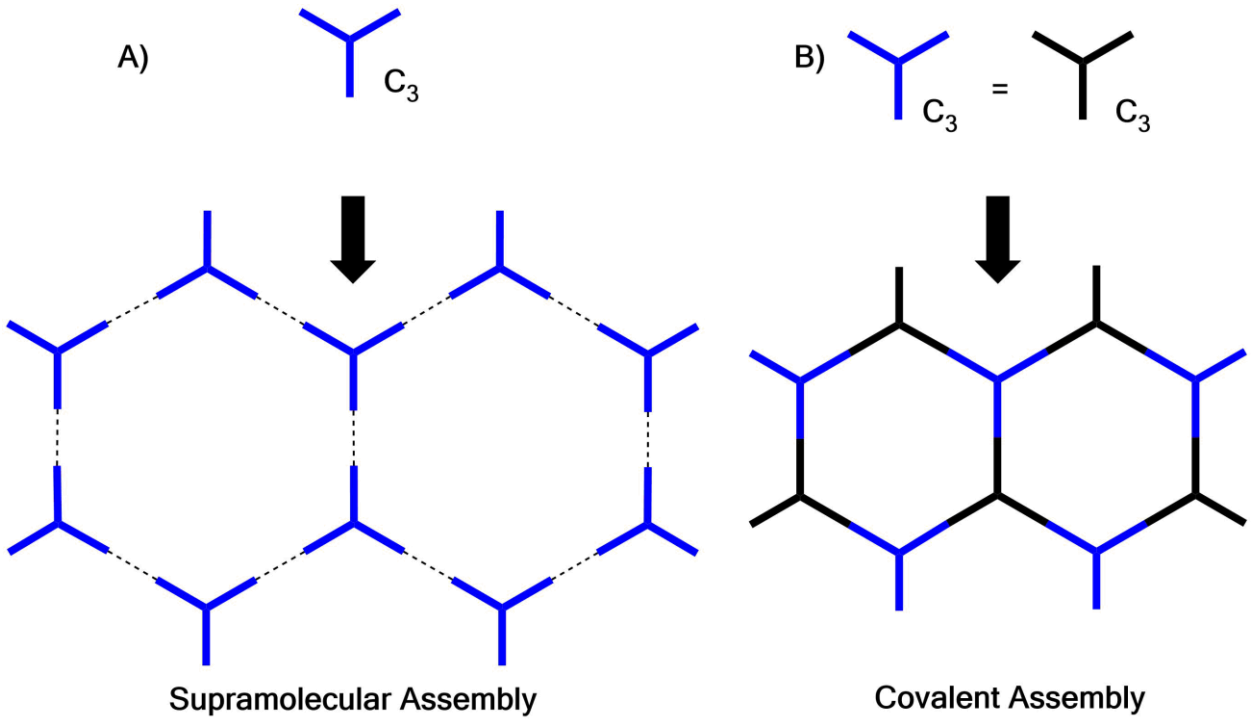

Figure 3: Representation of two-dimensional assembly of components with 3-fold symmetry into a hexagonal lattice using a) discrete molecules assembled by supramolecular interactions vs. b) the same components covalently bound together with alternating equivalent units differently colored for clarity.

(a) Supramolecular Crystal Engineering and Co-crystals

Considerable parts of Crystal Engineering and this Thesis focus on the assembly of discrete molecules into various solid-state structures, specifically solid forms. Much of the research in the crystallization of organic molecules has been driven by developing solid forms of active pharmaceutical ingredients (APIs) where the different chemical, physical, and biopharmaceutical properties of various solid forms of the same API have considerable impact on the properties and cost of the final drug.[37] Screening for solid forms is a key step in drug development, especially for improving the poor solubility of APIs. Solids where molecules are arranged in a more or less random fashion, called amorphous phases or glasses, are in general higher in free energy than crystalline states and thus molecules prefer to form crystalline solid states if possible. A single molecule can have multiple crystalline solid states, called polymorphs, or it can crystallize in a manner which includes solvent molecules to form solvates, or for the specific case of

water, hydrates. Alternatively, neutral molecules can often be converted to salts *via* either protonation or deprotonation reactions. It is also possible to form a crystal with multiple components that is not an ionic salt, often two neutral components can be combined to form a neutral co-crystal. For the case of hydrogen-bonded co-crystals, the proton is shared between the hydrogen bond donor and acceptor, whereas proton transfer from the hydrogen bond donor to the acceptor results in the formation of a salt. Schematics of different types of crystalline forms are highlighted in Figure 4.

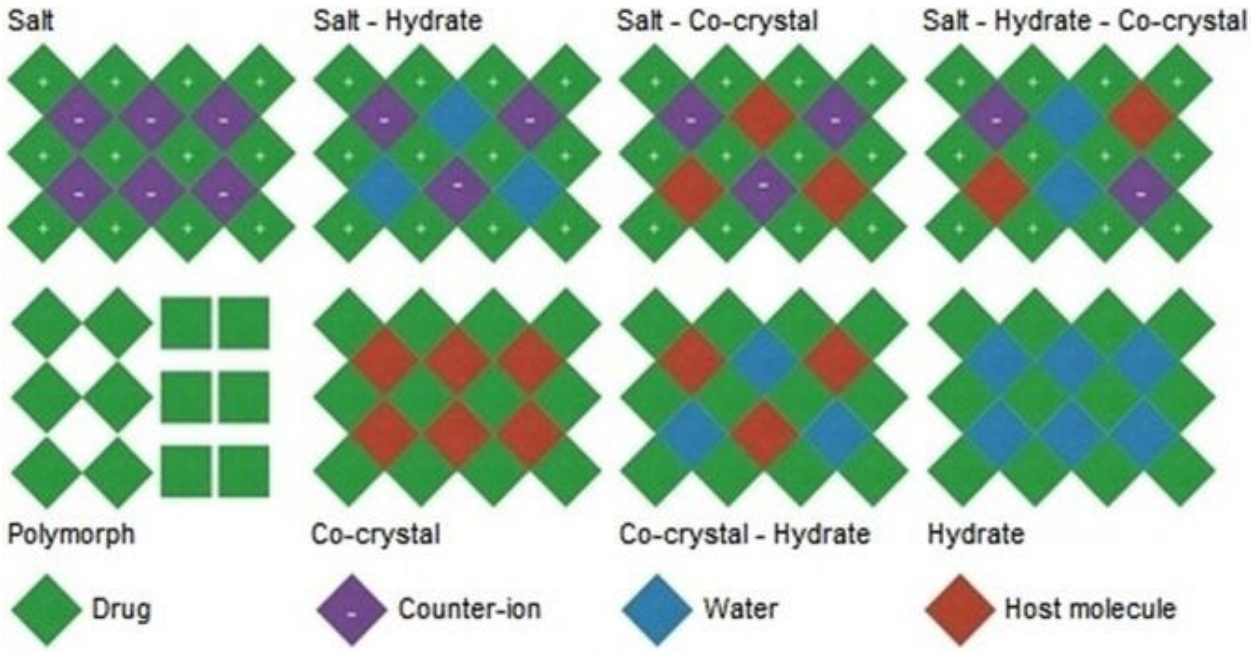

Figure 4. Different types of solid forms of a drug which can be used to modulate various properties of the final solid material, reproduced from ref. [37].

(b) Covalent Crystal Engineering

In contrast to the supramolecular approach to Crystal Engineering, crystalline materials can be constructed using covalent bonds, where discrete molecules react to form a covalently linked extended and highly symmetrical molecular structure. The most prominent classes of such materials are inorganic frameworks, metal organic frameworks (MOFs), and covalent organic frameworks (COFs). As implied in the name, inorganic frameworks consist of frameworks constructed using only inorganic units, such as zeolites (porous silicates)[39] or polyoxometalates, whereas MOFs are a combination of metals ions and organic molecules, and COFs[40] which only contain organic components. While

considerable research effort has been devoted to engineering both inorganic frameworks and COFs, these materials are beyond the scope of this Thesis. It should be noted that the methodologies developed herein may be of use in improving existing mechanochemical methods for making both COFs[41] and inorganic materials.[42] However, in the context of covalent assemblies, this Thesis exclusively explores MOFs.

(c) Metal Organic Frameworks

Metal Organic Frameworks (MOFs) are a diverse family of compounds that have recently received significant attention from chemists and materials scientists due to their modular nature and ease of geometric design. This class of recently commercialised materials† has considerable potential in a wide variety of technologies, due to their crystallinity, structural diversity, and record-breaking porosities combined with ease of chemical functionalization.[43] MOFs can largely be designed using a wide variety of metal ligand interactions to form one, two, or three-dimensional structures which self-assemble by coordinating nodes of metal ions with various organic linkers with the appropriate symmetry elements, or for the case of so called inverted MOFs, organic nodes with metal ion linkers (Figure 5).

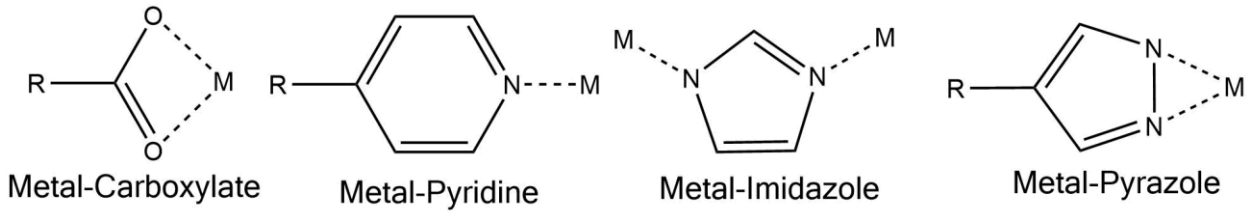

Figure 5: Common metal-linker interactions in MOFs

These periodic structures range from closed packed to highly porous. Potentially tunable nanometer sized pores have attracted commercial interest in MOF use for gas separation and storage.[44] The well-defined crystalline nature of these materials coupled with their rational design and tunability make MOFs a compelling platform for researchers to develop high performance materials as alternative to both carbon and inorganic based

† Current reports on the commercial status MOFs are limited. The first examples of commercial applications are all based on gas storage such as hazardous gases for the semiconductor industry and slow release of a gas which inhibits fruit ripening and have recently been discussed in *Nature Chem.* **2016, *8*,** 987.

porous materials.[44] The last decade has seen impressive advances resulting from the continued exploration of novel frameworks and a continuing effort to understand, tune, and even predict properties of MOFs *via* experiments and theoretical modelling.[45, 46] Such developments have driven research in MOFs aimed for a wide variety of uses,[35] such as energy storage,[47-49] carbon sequestration,[50] light harvesting,[29, 51] gas storage[52] and separation,[53] heterogeneous[54] and asymmetric[55] catalysts, drug delivery,[56, 57] and sensing.[58, 59] Prime examples of gas separation utilizing MOFs are the efficient separation of CO_2 from natural gas by MOF-74,[60] or the separation of CO_2 and nitrogen using PCN-26[61] (Figure 6). Beyond gas storage and separation, MOFs have also demonstrated a wide range of heterogeneous catalytic activity that include coupling catalysis to separations and substrate size selective catalysis,[54] such as the selective oligomerization of propene in Ni-MOF-74.[62] This makes them candidates for industrial scale homogenous catalysis due to product selectivity, facile separation, and compatibility with flow cell reactors. In addition, MOFs are currently being investigated as potential drug carriers due to their high drug loadings, biodegradability, and versatile functionality.[56]

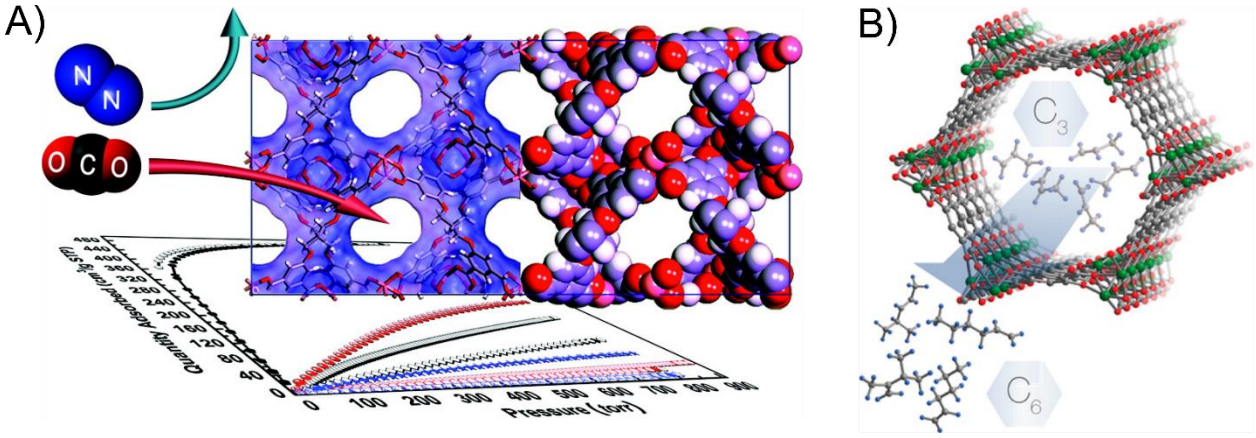

Figure 6: a) Schematic of gas separation of CO_2 and N_2 in a metal organic framework reproduced from ref. [61], and b) Graphical representation of propene oligomerization in Ni-MOF-74 reproduced from ref. [62] Copyright (2012) American Chemical Society.

2.04 Sustainable Approaches in Crystal Engineering

The large-scale commercialisation of supramolecular materials such as metal organic frameworks and co-crystals mandates the creation of new, innovative, and sustainable approaches toward their synthesis. For example, industry has highlighted the revision of

current synthetic methods as a prerequisite for MOF commercialisation and their use in prospective industrial applications.[63] The large-scale production, raw material costs, toxicity of reagents and solvents, availability/purity of chemicals, and safety have all been outlined as evaluative criteria for MOF commercialisation by the BASF team that pioneered their industrial manufacture.[31] Even when these criteria[64] have been successfully applied in individual examples of industrial-scale MOF synthesis, as illustrated by the water-based ton-scale production of Basolite A520®,[31] manufacture of each MOF must be analysed and re-developed on a case-by-case basis (Figure 7). Given the diversity of MOF structures and compositions it is clear that finding a "one size fits all" manufacturing process is unlikely, if not impossible.

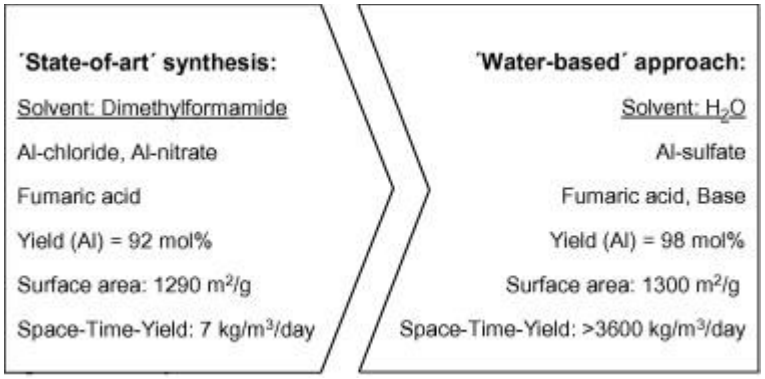

Figure 7. Redesign of the synthesis of Basolite A520® for industrial scale production.[31]

Consequently, new, scalable, and sustainable synthetic strategies must become a significant part of supramolecular chemistry and Crystal Engineering. An additional benefit of integrating the principles of Green Chemistry with synthetic criteria[64] for industrial manufacture are synthetic innovations that can accelerate the adoption of technologies based on Crystal Engineering.

While cost currently appears to be the dominant factor in commercialization†, environmental impact and safety are emerging as significant concerns for industrial scale synthesis. Indeed, reducing the environmental impact of a synthesis is often associated with lower production costs. While Life-Cycle Assessment (LCA) is generally considered

† As MOFs are not currently produced on large industrial scales, discussions of the cost of a MOF synthesis must be projected and is highly dependent on the method of synthesis, due to solvent and estimated process costs, and the overall scale of production.[91]

the best method for evaluating the impact and shortfalls of a synthetic process, it is often time-consuming, costly, and requires a truly detailed understanding of every process step.[26] As such, its utility in reaction and materials development and early process design is limited.[65] In contrast, the 12 principles of Green Chemistry[66] provide a useful guide for the development of novel synthetic methods and novel crystalline materials while considering environmental and health concerns not inherently present in cost analysis (Figure 8).

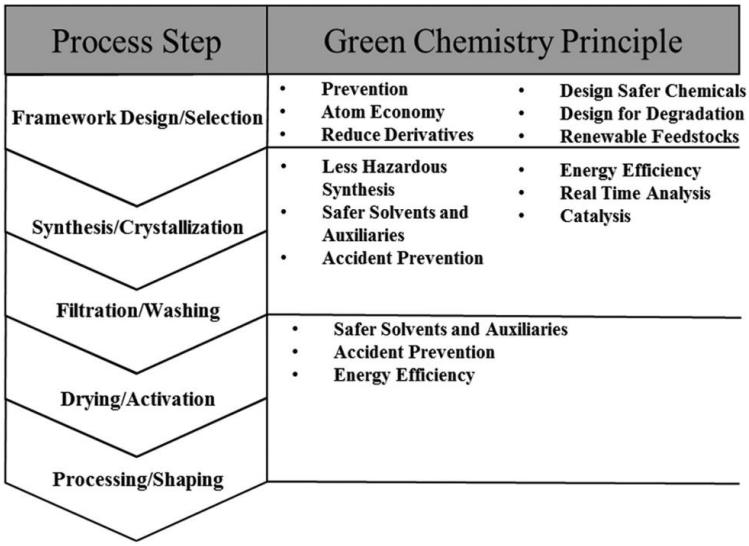

Figure 8. The application of 12 principles of Green Chemistry to MOF synthesis steps.[67]

Indeed, combining these principles with the previously described process step analyses is a useful tool to simultaneously mitigate the economic, and environmental costs of production of crystalline materials such as MOFs and co-crystals. Consideration of all the principles of Green Chemistry should aid in the design of crystalline materials which are not only greener, but also more cost-effective and thereby more likely to reach the market.

(a) Synthesis of co-crystals

The development and evaluation of novel synthetic methods for co-crystal formation remains an active area of research. Solution methods such as slow evaporation remain popular for producing single crystals suitable for structure solution *via* X-ray diffraction. However, due to the relatively low yields of solvent evaporation and anti-solvent precipitation, solid-state methodologies have increasingly been employed for the large

scale synthesis of co-crystal materials.[68] Efforts to increase yields, avoid solvent waste and excessive energy input for solvent removal have led to a variety of techniques which utilize supercritical solvents, mainly supercritical carbon dioxide, as a greener and more efficient method for co-crystal synthesis.[68] Research into further reducing solvent volumes led to slurry and sonochemical reactions and drove the development of mechanochemical methods for co-crystal synthesis. While so-called neat grinding (i.e. grinding without any additives) can be effective for certain systems, it often suffers from low conversions, prolonged reaction times, and generally produces an amorphous product which is undesirable for co-crystal formation. The addition of small amounts of liquid, so called liquid-assisted grinding, is a fast and highly selective method for polymorph or co-crystal discovery, and large scale preparation.[69] With respect to efficient scalable processes suited for large scale manufacturing, continuous methods such as mechanochemical twin screw extrusion,[70] hot-melt extrusion techniques, and spray drying are being explored.[69]

(b) Synthesis of metal organic frameworks

The synthetic methods for MOFs have recently been reviewed,[71] as were greener approaches to their production.[67] Selection of a synthetic method for a particular material will largely depend on the desired material properties such as purity, crystallite size, and overall morphology (*e.g.* thin film *vs.* powder). However, the overall energy consumption during material synthesis and processing is an important factor in both the cost and environmental analysis of any synthetic process.

The variety of MOF synthetic approaches can be classified according to type of energy input: 1) conventional solvothermal, 2) microwave-assisted, 3) electrochemical, 4) sonochemical, and 5) mechanochemical (Figure 9.).[35] Conventional MOF synthesis is generally conducted solvothermally, by using a high-boiling solvent (*e.g. N*,*N*-Dimethylformamide (DMF)), often at high temperatures and pressures achieved in autoclaves. Alternatively, certain MOFs can be efficiently obtained by room temperature reactivity, or with the use of water under hydrothermal conditions.[35] Such syntheses are highly popular in research, as they can be done with standard equipment, either in batch reactors or in high-throughput setups suitable for MOF discovery and optimizing of their

crystallisation.[72,73] Solvothermal protocols are particularly valuable as they can yield crystals suitable for single crystal X-ray diffraction, which is a major advantage for discovery and structure elucidation of new materials. Considerable effort has recently been put into understanding and optimising solvothermal MOF crystallisation through *in situ* methods,[74, 75] and has been recently reviewed.[35]

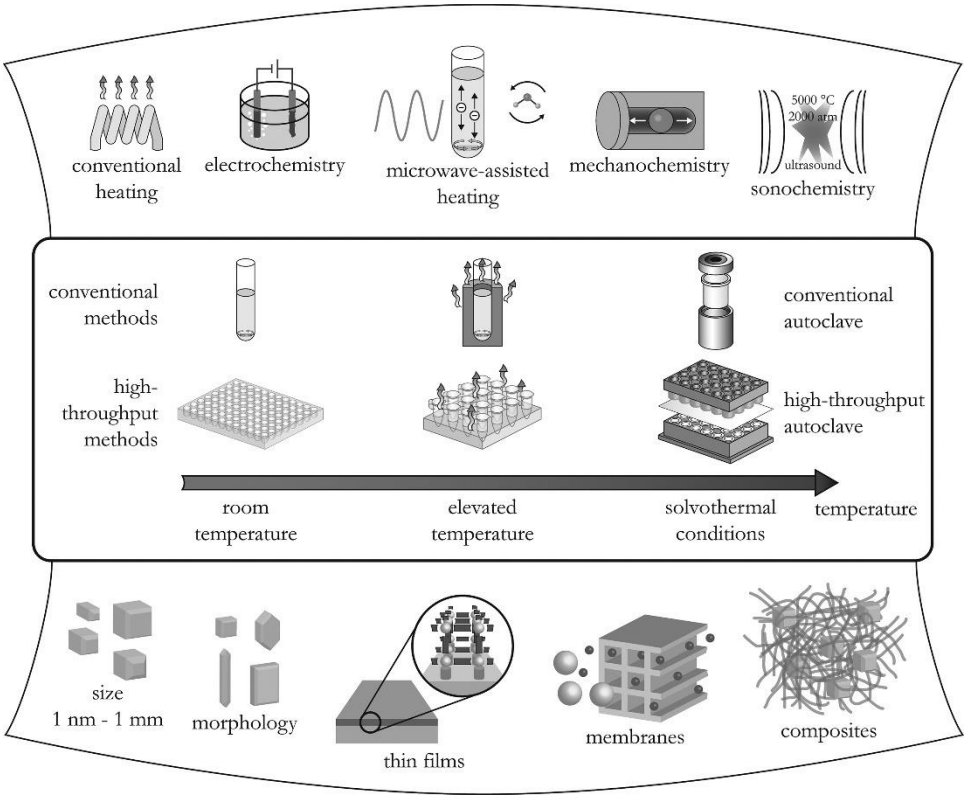

Figure 9. Synthetic methods, reaction temperatures, and MOF products. Reproduced from ref. [35] Copyright (2012) American Chemical Society.

Solvothermal processes tend to be energy-intensive due to long reaction times at high temperatures and pressures, presenting a considerable hurdle for large-scale production. Therefore, commercialisation of such syntheses requires extensive optimisation for short reaction times, and/or near-ambient temperatures and pressures.

Thermochemical synthesis protocols, where reactions are conducted in the melt phase of the linker with no additional solvent, have been developed to minimize issues of energy input and solvent stability associated with maintaining reactions at high temperatures and pressures for long periods of time.[76] Examples of such "solvent-free" thermochemical syntheses utilise imidazole or trimesic acid linkers at temperatures in excess of >160°C

or >120°C, respectively.[76-78] As a result, these procedures are highly dependent on the properties of the linker molecules, and are potentially energy intensive.

One approach to reducing the energy demand of MOF syntheses is *via* microwave heating, which is considerably more efficient than conventional heating by virtue of shorter reaction times and focusing power input on the reaction mixture itself.[79] The combined use of flow reactors with microwave heating has been reported for numerous MOF syntheses, including for the formation of HKUST-1 where it was determined to be the most rapid synthetic method for rapidly producing highly porous and crystalline material.[80] Flow reactors enable continuous production at lower energy inputs relative to alternative batch methods (Figure 10).[81] Microwave heating has also been applied to solvent-free melt phase reactions, leading to more efficient energy use due to shorter reaction times whilst maintaining yields and MOF surface areas comparable to those of materials obtained by conventional heating.[77]

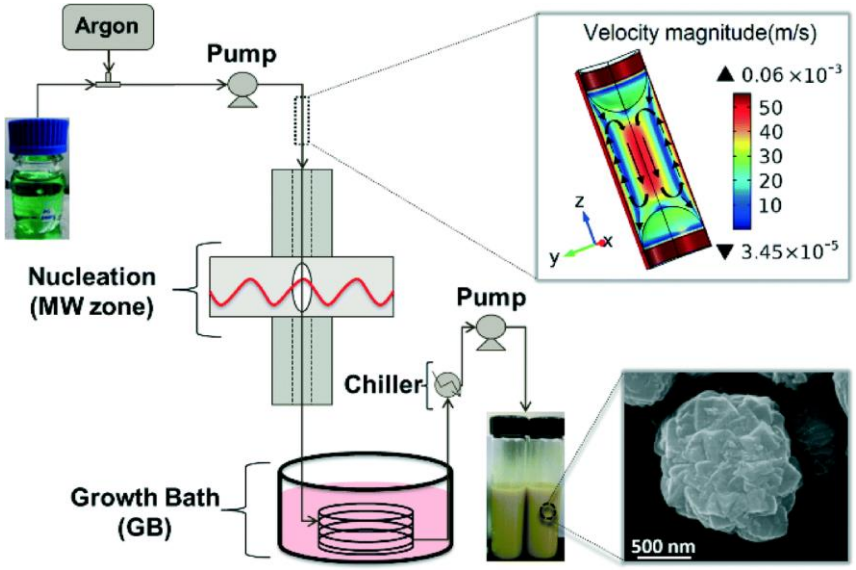

Figure 10. Continuous microwave synthesis of MOFs. Reproduced from ref. [81].

Synthesis of MOFs can also be driven directly using electrical energy. Such electrochemical syntheses have the advantage of proceeding rapidly, at ambient pressures and temperatures and, as already mentioned, can avoid hazards associated with anions by generating metal cations through direct anodic oxidation of a bulk metal.[82] For example, BASF reported the electrochemical bulk synthesis of the copper(II)

trimesate framework[83] HKUST-1 through electrochemical oxidation of copper metal. Recently, chemical oxidation has emerged as a methodology for conversion of zinc, manganese, or copper metals into coordination complexes and polymers.[84] High Faraday efficiencies and quantitative conversions have been reported for electrochemical MOF syntheses, although the dissolution of linkers often calls for organic solvents which have higher resistivity than aqueous solutions and may require electrolyte additives. While the anodic processes in these organic solutions are poorly understood, the production of hazardous hydrogen gas is also probable.[82] Electrochemical methods have been noted as particularly promising for producing high-quality MOF films for specialised optoelectronic and sensing applications.[82]

Sonochemical syntheses of MOFs such as MOF-5[85] have also been reported, where high-energy ultrasonic irradiation generates alternating areas of high and low pressure in a solvent. Interestingly, changing the power level appears to allow control over interpenetration (where two or more individual frameworks are interlocked with each other) for certain systems such as copper 4,4′,4″-s-triazine-2,4,6-triyltribenzoate (CuTATB).[86] The associated cavitation processes produce “hot spots”:[35] highly localised environments of extreme temperature and pressure. High-yielding sonochemical MOF syntheses, operating under mild conditions or at room temperature, have been reported to yield crystallites in the nanometer to micrometer size range.[35]

The elimination of bulk solvent using solvent-free reactions is an appealing approach towards MOF synthesis. Currently, there are three principal solvent-free routes for the synthesis of porous MOFs: thermochemical, mechanochemical, and diffusion-controlled solid-state "accelerated aging". Solvent-free routes to coordination polymers and MOFs were recently reviewed.[1]

The principal difference between the above listed methods is the way energy is introduced into the reaction. Thermochemical reactions proceed *via* a complete or partial melt phase, as illustrated by the synthesis of the microporous zeolitic imidazolate framework ZIF-8 (or MAF-4, sold commercially as Basolite Z1200®) from ZnO and molten 2-methylimidazole.[78] Thermochemical syntheses avoid external solvents, can give quantitative conversions and also show potential for synthesizing shaped objects.[76-78]

However, such reactions also require linkers to be stable at or above melting temperatures, potentially constraining their utility. Furthermore, using high-melting linkers is likely to associate thermochemical techniques with considerable energy demands. Recently, the Chen group demonstrated the thermochemical synthesis of MOFs, which enabled the conversion of metal oxides and hydroxides into azolate frameworks including ZIF-8, as well as triazolate-based MAF-27 and MAF-28.[78]

Another route to transform metal oxides into MOFs is "accelerated aging",[87] wherein exposing a static mixture of the oxide reactant and the organic linker precursor to controlled atmosphere and mild temperatures leads to spontaneous assembly into a metal-organic structure (Figure 11). The reactivity is readily facilitated by small, catalytic amounts of salt additives. Detailed analysis of the assembly of ZIFs *via* accelerated aging with catalytic ammonium salt additives provided strong evidence of a proton-transfer catalytic mechanism,[87, 88] mediated through a highly active imidazolium species. This enabled the systematic design and screening of alternative catalytic additives, resulting in a simple and rapid methodology for the quantitative, scalable assembly of ZIF-8,[88] as well as gram-scale syntheses of other azolate frameworks that have previously been accessible only in milligram amounts, such as RHO-topology structure based on zinc and 2-ethylimidazolate ions.

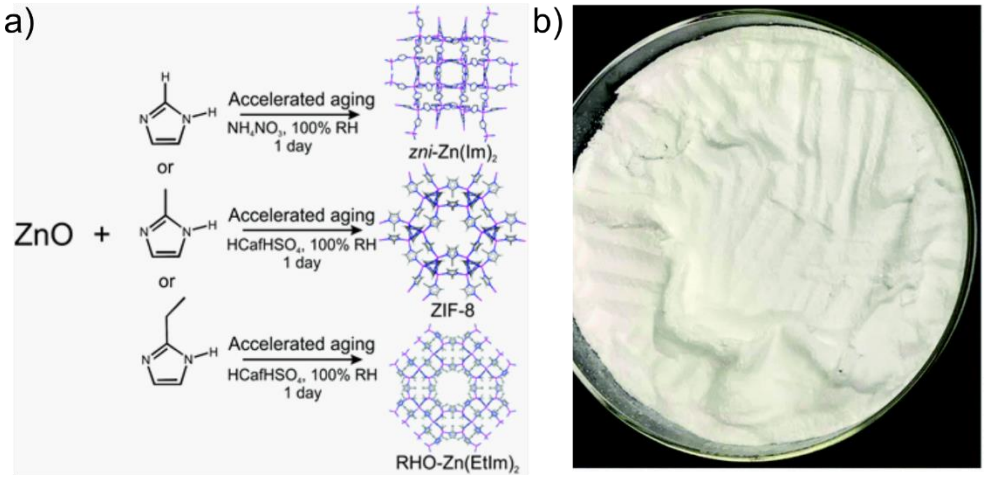

Figure 11. a) Accelerated aging syntheses of porous zeolitic imidazolate frameworks without agitation, high heat, or solvent. b) Accelerated aging synthesis of ZIF-8 at the 10g scale. Modified from ref. [67].

Finally, the synthesis of MOFs aided by mechanical agitation (grinding, milling, or shearing), known as mechanochemical synthesis, has been reported and appears highly promising in the context of overall efficiency and environmental impact. Mechanochemical reactions generally proceed at nominally ambient temperature and can be optimised for quantitative conversion within considerably less time (minutes or hours) than conventional solvothermal syntheses (days).[89, 90] Given the speed of these reactions and the low energy input needed, such reactions are being considered as leading candidates for low-cost and scalable synthesis of crystalline MOF powders.[91]

2.05 Mechanochemistry: green, rapid, scalable, and cost effective

Mechanochemistry has gained considerable interest as a valuable synthetic methodology due to its potential as a sustainable and cost-effective technique and its unique combination of chemical reactivity and supramolecular arrangements. Mechanochemical reactions are defined by IUPAC as a "chemical reaction that is induced by the direct absorption of mechanical energy".[92] Conducting reactions in ball mills has emerged as the leading methodology in mechanochemistry due to accessibility, operational simplicity, scalability, and ability to deliver reproducible and tunable mixing and impact force on solid samples. Characteristic advantages of ball milling reactions include rapid reaction times, high efficiency, and elimination of bulk solvent, and have driven the development of the technique as a promising area of Green Chemistry. Milling has been reported for bond-forming reactions in organic, organometallic, coordination chemistry. Surprisingly, ball milling has been shown to be highly amenable towards the formation of extended and/or crystalline supramolecular structures such as metal organic frameworks and pharmaceutical co-crystals.[93] These developments have garnered considerable attention and have recently been extensively reviewed.[94]

(a) Ball milling

The simplest way to conduct a mechanochemical reaction is manual grinding using a mortar and pestle. However, manual grinding is generally slow and suffers from problems of reproducibility due to variation in how the operator conducts the milling and ambient conditions such as temperature and humidity.[95, 96] Both temperature and humidity have been shown to strongly influence reactivity in certain systems.[97] In response to these

concerns, a multitude of different automated mills have been developed, including a variety of ball mills including shaker, planetary, and tumbler mills, which vary in the type of the motion applied to a sealed vessel, often called a milling jar (Figure 12).

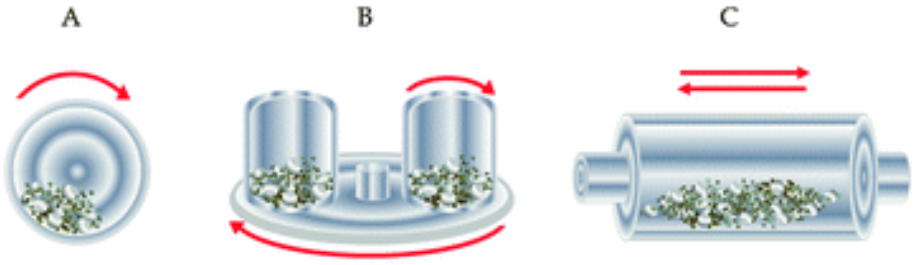

Figure 12. Types of ball mills: A) a tumbler ball mill, B) planetary ball mill and C) a vibratory ball mill. Modified from ref. [98].

While it should be noted that devices other than ball mills have been used for mechanochemistry such as twin-screw extruders[70] or specially designed setups capable of applying precise amounts of force and impact,[99] the work in this Thesis and the majority of chemical research is currently focused on ball milling. Most importantly, ball milling is performed by use of a programmable electric motor capable of applying a tunable and consistent agitation to the reaction vessel containing milling media which are generally balls of hard materials such as stainless steel or zirconia (ZrO_2). Such ball milling setups are highly tunable, as the reaction time and mill oscillation frequency can be easily and reproducibly modified. Milling vessels and grinding media are commonly available in different sizes of materials such as polytetrafluoroethylene, stainless steel, zirconia, or tungsten carbide, allowing for the easy control of properties such as hardness and chemical inertness. By modifying the number, type, size of milling balls as well as the amount of sample relative to the size of milling jar, impact forces and friction can be tuned, with smaller numbers of larger balls favoring impact forces and many smaller balls favoring friction. Typically, denser and harder materials such as tungsten carbide are expected to provide stronger impact than lower density ones such as polytetrafluoroethylene. A powerful modification of the grinding is the addition of a small amount (< 1uL/mg of material)[100] of liquid, generally water or petroleum-based solvents, called liquid-assisted grinding (LAG). This approach has a strong effect on both reactivity and selectivity and has vastly increased the scope milling reactionsf. LAG strategies are particularly amenable when reactions exhibit strong solvent effects on reactivity and

selectivity, or where problems related to poor or incongruent solubility arise in solution. For this Thesis, a vibratory ball mill with transparent milling jars was utilized due to its minimal area of motion and ability to maintain high impact forces and mixing for small sample sizes, making it particularly amenable for laboratory scale research and *in situ* monitoring experiments (Figure 13).

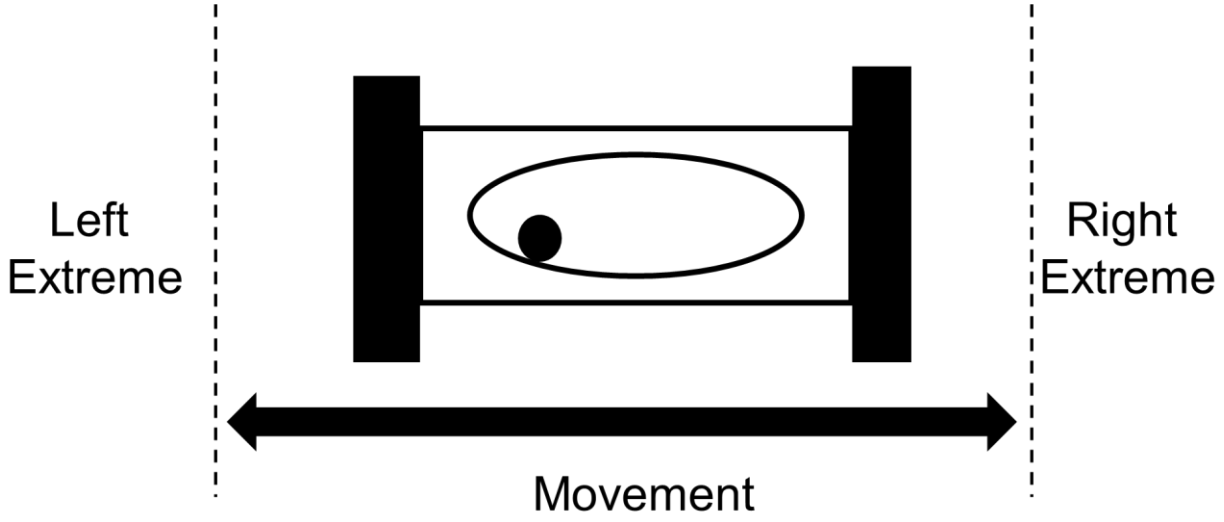

Figure 13. Schematic of the movement of the shaker mills used in this Thesis.

2.06 Mechanochemical Co-crystal Synthesis

Mechanochemistry has emerged as a leading methodology for the synthesis of co-crystals, due to the absence of bulk solvent which affects yields *via* solubility and requires considerable time and energy to remove. The application of mechanochemistry for a wide variety of co-crystals, including pharmaceutical, halogen-bonded, ionic, and even organic-organometallic co-crystals has recently been reviewed.[101] Early reports by Tanaka and Toda demonstrated that host-guest complexes not accessible in solution could be formed mechanochemically (Figure 14a).[102] The formation of a hydrogen bonded co-crystal of 9-methyladenine, ground with solid 1-methylthymine, provided the first evidence that compounds with high melting points can self organize[103] (Figure 14b). The observation of hydrogen-bonded Hoogsteen base pairs in the co-crystal suggested that formation of assemblies based on supramolecular interactions can proceed *via* grinding. Indeed, halogen bonded co-crystals, complexes of metal ions, and macrocyclic

crown ethers, and many other supramolecular materials have subsequently been synthesized mechanochemically.[104]

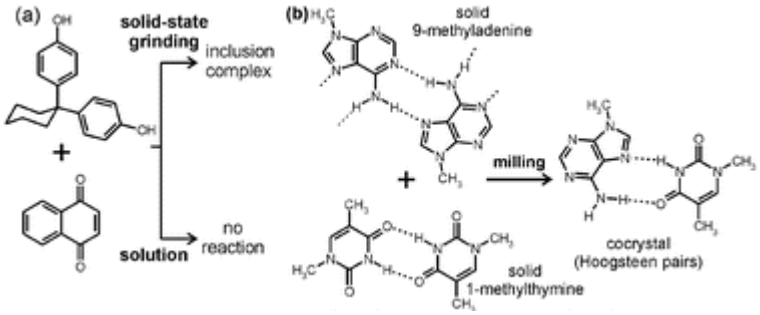

Figure 14. a) Mechanochemical synthesis of host-guest inclusion compound not accessible in solution. b) Mechanochemical formation of a Hoogsteen-bonded co-crystal of 9-methyladenine and 1-methylthymine. Modified from ref. [104].

Driven by the discovery that milling could access to previously unknown solid forms of materials, the formation of co-crystals of pharmaceutical molecules was investigated. For such systems, LAG was shown to provide quantitative yields of co-crystals inaccessible by neat grinding with much shorter reaction times and greater crystallinity.[105] In order to compare neat grinding, LAG, and other methods of co-crystal synthesis such as slurry and solution, the eta parameter (η) was introduced and defined as the ratio of the volume of the liquid phase to the weight of co-crystal components[100] (Figure 15). It was demonstrated that co-crystallization at low η values was not affected by the solubilities of individual components while slurry and solution reactions with high η values typically precipitate the least soluble co-crystal component in the case of very different solubilities of the components.[100]

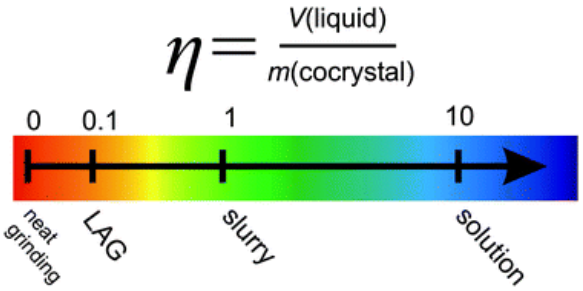

Figure 15. Definition of the η parameter and its values for typical syntheses of co-crystals by different methods. Reproduced from ref. [100].

The speed and efficiency of the LAG method coupled with its ability to avoid solubility issues and potentially produce solid forms unobservable from solution have solidified mechanochemistry as a leading and more sustainable methodology for the development of pharmaceutical solid forms and other co-crystal systems.[106-108]

2.07 Mechanochemical Metal Organic Framework Synthesis

One of the most promising applications of mechanochemistry is in the field of MOFs. Early synthesis of coordination polymers *via* mechanochemistry emerged from mechanochemical coordination chemistry,[109] with protocols largely mimicking solution based synthetic methods where soluble metal salts such as acetates, nitrates, and chlorides were ground with nitrogen based ligands. For example, metal chlorides were reacted with 4,4'-bipyridines to give one and two dimensional coordination polymers by elimination of hydrochloric acid.[110] Similar reactivity was observed between Zn(II), Co(II), and Cu(II) chlorides and pyrazole and imidazole ligands, resulting in both discrete complexes and 1-D coordination polymer chains.[111]

The first report of a mechanochemical synthesis of a porous MOF was published by the James group in 2006.[112] This archetypal mechanochemical synthesis of a MOF yielded desolvated copper(II) isonicotinate framework by 10 minutes of grinding of copper(II) acetate dihydrate with isonicotinic acid.[112] The broad applicability of mechanochemistry for the synthesis of MOFs was demonstrated when an array of various metal sources such as acetates, nitrates, and sulfates, were ground for 15 minutes at 30 Hz in a vibrating mill with five bridging ligands including carboxylic acids and pyridines.[113] Of the sixty possible reactions, forty gave detectable reactions, thirty-eight of which were crystalline, and twenty-nine appeared quantitative by powder X-ray diffraction (PXRD). Products included known highly porous frameworks such as HKUST-1, non-porous 3-D coordination polymers, 1-D coordination polymers, as well as previously unreported phases. Interestingly, milling of copper(II) acetate monohydrate and trimesic acid showed complete conversion to HKUST-1 after 5 minutes[114] and subsequent washing with ethanol and subsequent evacuation gave surface area values of up to 1364 m^2/g, which is consistent with conventional solvothermally prepared samples.

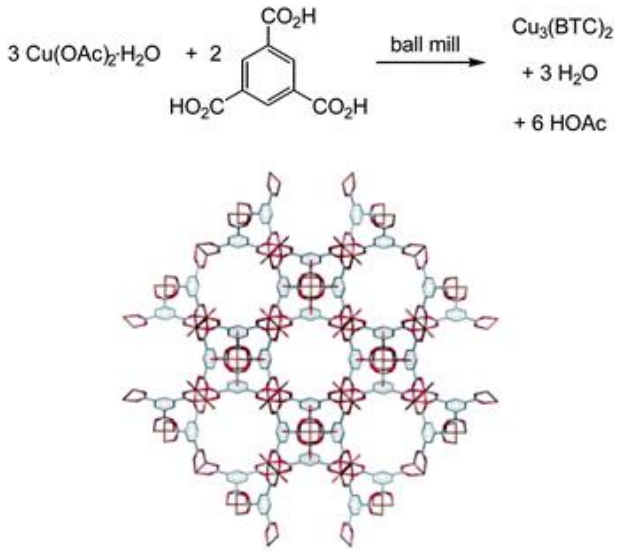

Figure 16. Mechanochemical synthesis of HKUST-1. Reproduced from ref. [114].

Since then, milling reactions have been used to rapidly synthesize MOFs from a wide range of ligand precursors in high yield and purity, while minimizing or eliminating the use of expensive and toxic solvents used in traditional solvothermal synthesis such as N,N-dimethylformamide (DMF). While neat grinding of solid chemical reactants has given promising results for some early systems, more recent mechanochemical MOF synthesis has emerged out of the development of liquid-assisted grinding (LAG). Small amounts (< 1ml per gram) of water or organic solvents can impart mobility, facilitate proton transfer reactions, and improve the crystallinity of the final product.[115] In certain cases, solvents can act as a template to help steer reactions towards a certain product.[116] Some mechanochemical reactions can be catalysed by salts, which are also capable of acting as templates. Such strategies are called ion and liquid-assisted grinding (ILAG). The development of these techniques has enabled the synthesis of a wide variety of frameworks from various metal sources including poorly soluble oxides and carbonates which avoid some of the toxicity and corrosion concerns of soluble nitrates, chlorides, and perchlorates.[117]

One of the most important synthetic advantages of mechanochemistry is that reactants with low solubility, which are often unsuitable for solution synthesis, can be utilized in mechanochemical reactions. Metal oxides and carbonates are appealing metal sources for MOF synthesis, as they are inexpensive, readily available, and produce safer by-

products. In contrast, the use of metal salts as reactants produces either acid by-products which must be neutralized, or waste salts which must be removed by washing. Metal oxide and carbonate reactants form water, or water and CO_2, respectively, as the only by-products, neither of which needs extra steps to be removed. The first report of using metal oxides to form metal organic frameworks utilized LAG to synthesize a variety of 1-D, 2-D, and 3-D zinc fumarate coordination polymers.[118] It was noted that in general neat grinding works poorly for MOF formation from oxides and carbonates, however LAG has emerged as a selective and versatile technique.[118] Contrary to solution synthesis, these mechanochemical reactions gave quantitative conversion after a 30 minute one-pot procedure. This one-pot synthesis method also worked for the synthesis of porous 3-component MOFs consisting of zinc ions, fumarate, and bipyridyl based linkers. It was subsequently shown that the use of ILAG improves the reaction rate and selectivity of the synthesis of paddlewheel MOFs from zinc oxide, terephthalic acid, and 1,4-diazabicyclo[2.2.2]octane (dabco).[117] The use of metal oxides is not limited to frameworks based on carboxylic acid linkers. The synthesis of various topologically different porous and non-porous zeolitic imidazolate frameworks (ZIFs) from zinc oxide and various imidazoles using both LAG and ILAG with ammonium salt additives has been reported in quantitative conversion at room temperature.[119] Beyond transition metals, lanthanide carbonates have shown reactivity under LAG conditions to form porous frameworks, including mixed lanthanide frameworks.[120]

(a) Selectivity and Control in Mechanochemical MOF Synthesis

One of the advantages of using mechanochemistry for the synthesis of metal-organic materials is the selective formation of various polymorphs, solvates, and porous structures. An early example of selective control between 1-D, 2-D, and 3-D coordination polymers formed by mechanochemistry was observed in the reactivity of zinc oxide and fumaric acid, reported in 2009 (Figure 17).[118] High selectivity was achieved by only changing the LAG additive. It was subsequently shown that this selectivity is dependent on the mole fraction and activity of the liquid additive.[121]

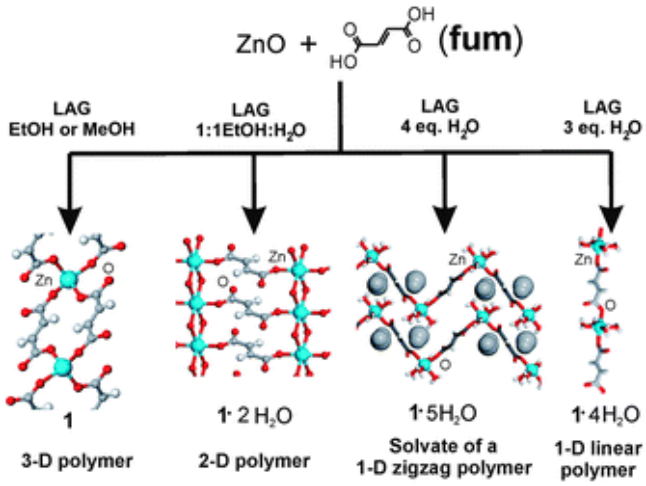

Figure 17. Reaction of zinc oxide with fumaric acid to provide a variety of coordination polymers. Modified from ref. [118].

An important extension of LAG is milling with the addition of salts which can serve as catalysts and templates via anion incorporation. This ILAG method was shown to be useful in directing the synthesis of pillared MOFs of zinc, terephthalic acid, and 1,4-diazabicyclo-[2.2.2]octane (dabco). Zinc sulfate salts formed a hexagonal structure while zinc nitrate salts yielded a tetragonal structure.[117] Similar selectivity was observed in the synthesis of ZIFs from 2-ethylimidazole and zinc oxide. In this case, the addition of $(NH_4)_2SO_4$ leads to a RHO topology, while NH_4NO_3 additive leads to a previously unreported crystalline material with a hexagonal close-packed *qtz* topology.[119] Whereas previous reports of ion templating were focused on anion templating in porous structures, the subsequent work on ZIFs shows that this method of synthesis can be applied to non-porous materials, and that the ammonium cations appear to act as protic catalysts. Given the high reactivity of materials under grinding conditions, the ability to direct the synthesis of desired structures using catalysts and templating agents will likely be key to maintaining selectivity control in complex reactions.

Mechanochemistry is beginning to be applied to reactions which are challenging for solution methods. Traditional solvent-based syntheses often struggle in producing materials with multiple components or in directly adding a component. Examples in the emerging MOF science literature include metal-organic materials which contain multiple metals within one single crystalline phase.[122] For example, neat grinding of metal halides with bases and basic linkers was shown to be capable of generating mixed metal-di-

halide-bipyridine coordination polymers.[123] The sensitivity and selectivity of metal organic materials to LAG solvent can not only be used to synthesize but also interconvert between different metal organic materials.[124] It was shown that it is possible to convert between different 1-D, 2-D, and 3-D metal-organic coordination polymers of zinc terephthalate by milling with different LAG additives. The lability of MOFs under LAG conditions can be used to regenerate materials which have lost their crystallinity or bridging ligands such as dabco to generate multi-component frameworks. The LAG method was capable of synthesizing 3-component frameworks not accessible from either solution synthesis or one-pot mechanosynthesis.[124] The use of mechanochemistry to synthesize multi-component materials either directly or by interconversion and ligand addition is still in its infancy, but represents an area where mechanochemical techniques may outperform solution synthesis.

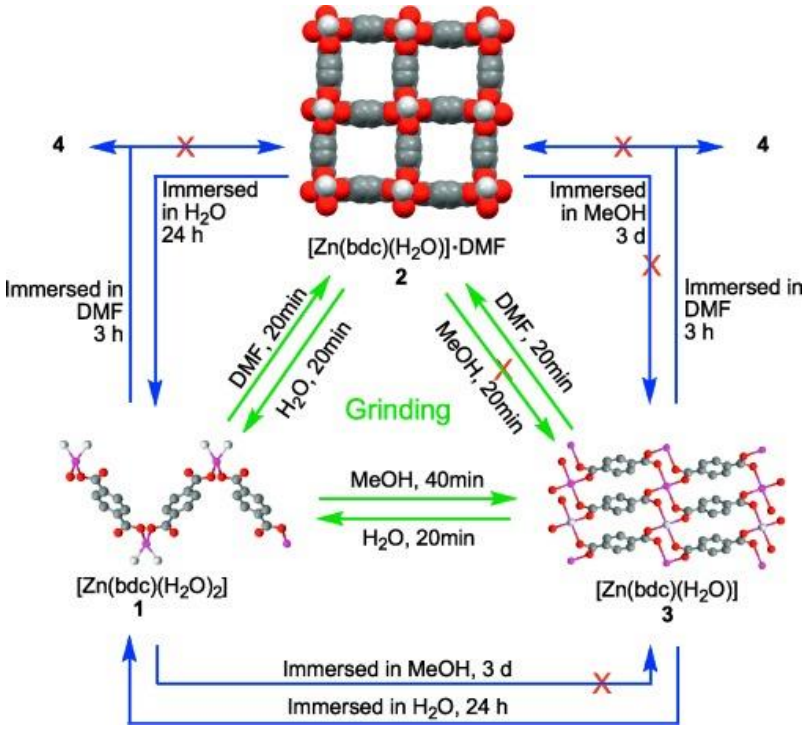

Figure 18. Mechanochemical interconversion between zinc-terephthalate coordination polymers. Reproduced from ref. [124].

Mechanochemical approaches to MOF synthesis were recently shown to be scalable. Twin and single screw extruders are capable of producing metal complexes and commercially relevant MOFs such as ZIF-8 and HKUST-1 in near quantitative

conversions with space-time yields orders of magnitude higher than those obtained using other methods.[125] Importantly, the surface areas and pore volumes of these MOF materials were equivalent to those prepared by conventional solvent-based methods.

2.08 Characterization of Mechanochemical Reactions

Mechanochemical reactions almost exclusively produce powdered solids which can be analyzed utilizing a wide variety of methods. This Thesis focuses primarily on diffraction-based measurements, as well as fluorescence and Raman spectroscopy. Accordingly, the theory behind these three techniques will be briefly summarized followed by an overview of their application in understanding mechanochemical milling reactions.

(a) Raman Spectroscopy

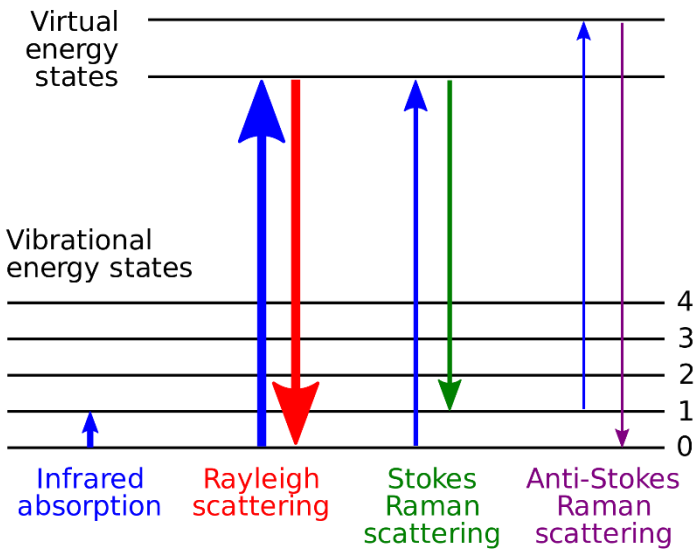

Figure 19: Energy levels of Rayleigh and Raman scattering, reproduced from ref. [126].

Matter has the ability to scatter photons of light in two principle ways: either elastically where the energy is conserved such as in Rayleigh scattering or inelastically where the energy of the incident light changes (Figure 19). Raman spectroscopy utilizes this inelastic interaction between molecular vibrations or other phonons which provides characteristic shifts in energy to elucidate vibrational modes in the system. The vibrational modes of a molecule provide characteristic information which can be used to monitor chemical reactions and can provide insights into the environment of the molecules, which

is of relevance for crystalline materials as changes in crystal packing can often be detected with Raman spectroscopy.

(b) X-ray Diffraction

X-ray diffraction is based on elastic scattering of X-rays by electrons in crystalline lattices. Periodic arrays of electron density scatter light which interfere destructively except for a few specific directions where constructive interference occurs as defined by Bragg's law, where θ is the scattering angle, *d* is the distance between scatterers, *n* is an integer, and λ is the wavelength of the incident light:

$$2d\ sin\ \theta = n\lambda \qquad (1)$$

The wavelength (λ) of light satisfying the Bragg condition for the case of periodic atomic structures is in the X-ray regime. For the case of a single crystal, this will lead to characteristic diffraction spots corresponding to the angle and intensity of the diffracted beam. These patterns can be used to calculate the distribution of electron density within the crystal, providing information on the average positions of the atoms as well as chemical information such as bond lengths and angles. For the case of powdered samples, where the sample consists of a collection of randomly oriented crystallites, diffraction produces Debye-Scherrer rings, which possess unique spacing and intensity values for each crystal structure.

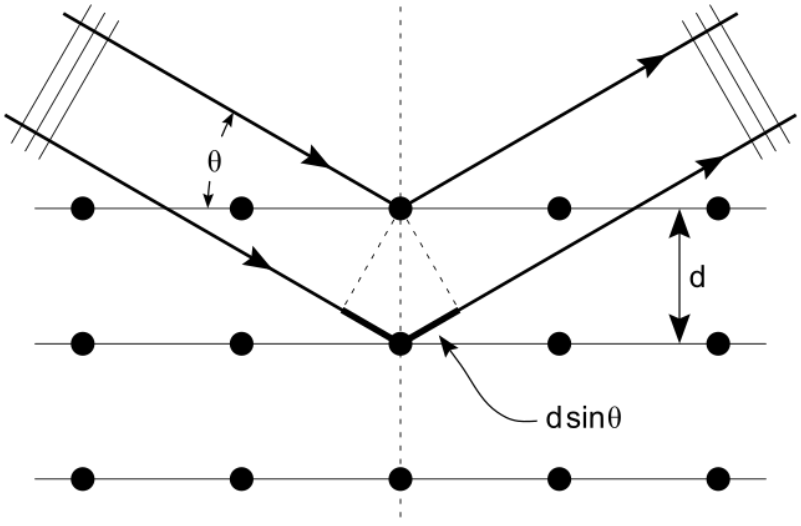

Figure 20: Bragg diffraction of a periodic lattice, reproduced from ref. [127].

(c) Fluorescence Spectroscopy

In contrast to the previous techniques, fluorescence is not a scattering-based technique, instead it relies on the absorption of a photon which promotes the molecule into an electronic excited state, followed by non-radiative decays to a lower energy excited state which subsequently emits a photon at lower energy than the incident photon (Figure 21.). While fluorescence spectroscopy is obviously limited to molecular species which emit, it can provide considerable information into the electronic states of the molecule, and the emission is often sensitive to both chemical changes as well as supramolecular interactions.

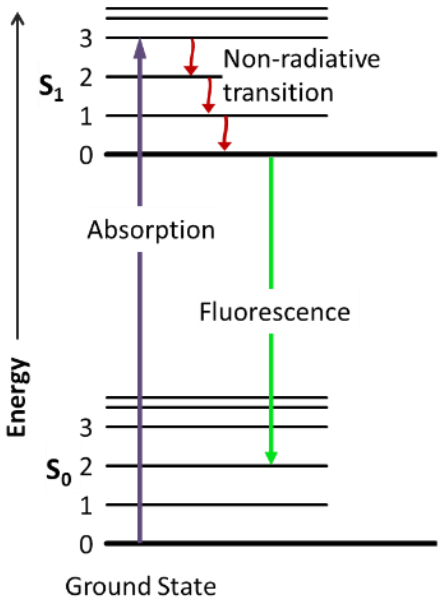

Figure 21: Jablonski diagram demonstrating the absorption, non-radiative decay, and fluorescence emission of a molecule. Reproduced from ref. [128].

2.09 Monitoring Milling Reactions

The ability of mechanochemistry to synthesize solid materials with defined supramolecular arrangements has revealed unique reaction pathways, with molecules and phases which are not known to be accessible under solution conditions and are presumably stabilized by their arrangement in crystal structures. These discoveries have driven considerable interest and research into understanding the fundamental behavior

of mechanochemical reactions by both the chemistry community. The discoveries of novel reactions, pathways, and accelerated kinetics have driven interest in monitoring and understanding the behavior of mechanochemical reactions. Monitoring milling reactions differs significantly from reaction monitoring in solution in terms of experimental setups, the type of sample being analyzed, and kinetic behavior. The unique challenges associated with mechanochemical reaction monitoring, require the development of novel instrumental setups and approaches, which may in turn prove useful for researchers interested in other types of reaction monitoring.

(a) Combining reactivity with supramolecular arrangements

Traditionally, reactions are conducted in solution or gas phase where molecules have considerable freedom in terms of movement and collisions. In contrast, the fields of supramolecular chemistry and specifically crystal engineering look at the importance of the arrangement and interactions of molecules in crystalline solids. A relatively unique feature of milling reactions is the presence of both reactants and products as potentially crystalline solid phases throughout the reaction. Accordingly, milling reactions provide an opportunity to understand the supramolecular arrangement of molecules as a reaction occurs. This approach has enabled the reaction of solid or crystalline phases otherwise considered inert such as metal oxides,[67] and led to unique insights into the relationship between supramolecular arrangements and chemical reactivity, such as when a reaction occurs *via* a co-crystal intermediate, as demonstrated in the Knoevenagel condensation of barbituric acid and vanillin.[129]

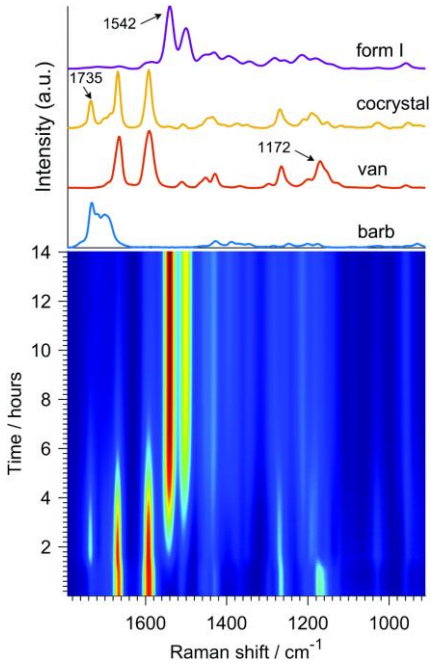

Figure 22. (top) Raman spectra of barbituric acid (barb), vanillin (van), the reported barb-van co-crystal, and the form 1 (product of the Knoevenagel condensation). (bottom) Real-time Raman monitoring of the mechanochemical reaction reveals a co-crystal intermediate. Reproduced from ref. [129].

In addition to the practical advantages of mechanochemistry, the combination of the well controlled supramolecular environment of the crystalline solid-state with chemical reactivity is of fundamental interest for synthetic chemists. The desire to use crystal engineering to help control reactivity has driven much of the research into better instrumental and experimental techniques for monitoring mechanochemical reactions. Accordingly, it provides a basis for understanding the challenges in the field of monitoring milling reactions.

(b) Challenges in monitoring milling reactions

Monitoring milling reactions has unique challenges relative to solution protocols, as the products formed in mechanochemical reactions are crystalline or amorphous solids held together through coordination or non-covalent interactions. In contrast to solution methods, obtaining a sample of the reaction without disturbing the milling process is a challenge, and preserving the supramolecular structure prohibits sample dissolution which is required for many analytic and instrumental techniques such as high-pressure liquid chromatography (HPLC). Additionally, while the solid-state environment provides

novel approaches to monitor reactivity, it can have significant impacts on the choice and interpretation of the results of spectroscopic techniques.

Obtaining samples of the reaction mixture without interfering or stopping the reaction remains a largely unsolved problem in mechanochemistry. Ball milling is almost always conducted in sealed containers which are in constant motion and experience a constant barrage of impacts by milling media. As such, milling must in most cases be stopped and the sealed milling vessel opened so that part of the sample can be removed, which inherently slows or stops the reaction, and disrupts the environment in the milling jar. For example, stopping the mill has a cooling effect on the entire milling setup, and opening the jar allows for the loss of gas phase reactants, and may result in exposure to moisture or CO_2. The development of effective sampling methods is further complicated by the fact that the majority of probes cannot withstand the motions and impacts associated with milling, and ports tend to clog with sample. Consequently, either care must be taken that sampling does not influence the results, or *in situ* methods which do not perturb the milling vessel should be utilized to avoid sampling.

Monitoring of reactions which proceed *via* solid powders enables unique measurements but also carries considerable implications for spectroscopic techniques. A final consideration in the analysis of solid samples is that neighboring molecules in the solid-state environment can significantly influence many spectroscopic techniques such as UV-vis, IR, Raman, and fluorescence spectroscopies. Another example is the case of solid-state nuclear magnetic resonance (NMR) where interpretation of many nuclei remains more challenging than in solution due to anisotropic and orientation dependent interactions. Significant improvements in modelling of solid samples, such as structure solution from powder diffraction data, or periodic density functional theory calculations (DFT) provide significant insight for the interpretation of diffraction and spectroscopic data.

As such, the challenge of effectively sampling and analyzing milling reactions is so fundamental it has largely shaped approaches towards mechanochemical reaction monitoring. It has principally been addressed either by repeating a reaction and stopping the reaction at various time points to sample and analyze the reaction mixture, so called

ex situ analysis and compiling a dataset, or by *in situ* reaction monitoring techniques, where the reaction in monitored through the walls of the milling vessel under operation.

2.10 Ex situ monitoring of milling reactions

The most prevalent and flexible method of monitoring mechanochemical reactions remains *ex situ* analysis of milled products, where the milling is stopped, and the sample is removed and analysed. The principle advantage of this approach is that nearly any type of analysis of the powdered sample can be acquired, and assuming sample permitting, a variety of both solid and solution measurements can be collected.

(a) Monitoring reactions at a fixed timepoint

As laboratory mills typically operate on timers, the most prevalent approach for analyzing the influence of various factors such as temperature, milling speed, milling media and material is to stop the reaction at a uniform time point and analyze the resulting mixture. This straightforward approach enables the quick comparison of a wide variety of parameters which can affect milling reactions, however, a single time point provides little insight into the reaction profile and changes to this profile. Nor is this approach particularly well suited for revealing reaction intermediates. Accordingly, this approach is most suited to aid in the elucidation of reaction mechanisms by varying reaction parameters. It is extensively used in reaction screening and optimization due to its speed and versatility.

The ability to rapidly screen and optimize conditions is of importance for the development of highly selective and efficient organic and inorganic reactions. Due to the prevalence of this approach, a comprehensive review of its use is beyond the scope of this work, however we wish to highlight some pertinent examples. Optimizing reaction conditions using a single time point has been extensively applied towards catalyst screening and reaction scope screening for reactions such as the “A3” coupling reaction between an amine, aldehyde, and acetylene (Figure 23).[130] It was also extensively employed in the development of a mechanochemical olefin metathesis reaction, as well as the solvent free oxidation of palladium and gold metals into salts and coordination complexes.[131, 132] In both cases, reagent/catalysts and loadings, as well as both liquid and

solid additives were screened, enabling the discovery of high yielding and robust reaction conditions.

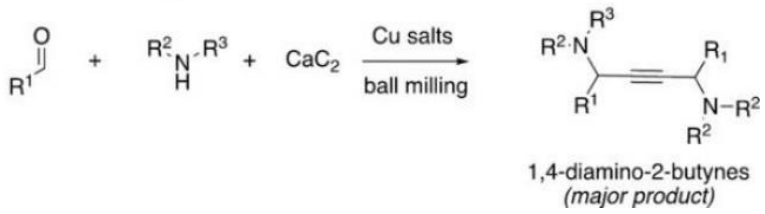

Figure 23. Mechanochemical "A3" coupling. Modified from ref. [130].

Beyond simple optimization, such screening can be used to gain valuable insights into mechanochemical processes. For example, monitoring the milling frequency at a constant reaction time and determining the yield of selected neat Diels-Alder reactions revealed an exponential relationship between frequency and reaction yields for milling.[133] The observed increase in reaction rate was associated with higher temperatures of the milling vessel as determined with a thermocouple. This showed a correlation between calculated activation energies and reaction yields rooted in the Arrhenius equation. Decoupling temperature and mill oscillation frequency can be achieved by cooling the mill. Diastereomeric excess was determined for the reaction of 4-tert-butylcylohexanone with sodium borohydride at a constant time point. Varying frequency and temperature suggested sub-ambient temperatures resulted in higher selectivity than analogous solution reactions.[134] However, increased milling frequency resulted in lower selectivity but higher yields at an equivalent temperature. Both studies provide strong examples of how changing fundamental parameters for milling reactions at a defined reaction timepoint can reveal the principles which underlie mechanochemical reactions.

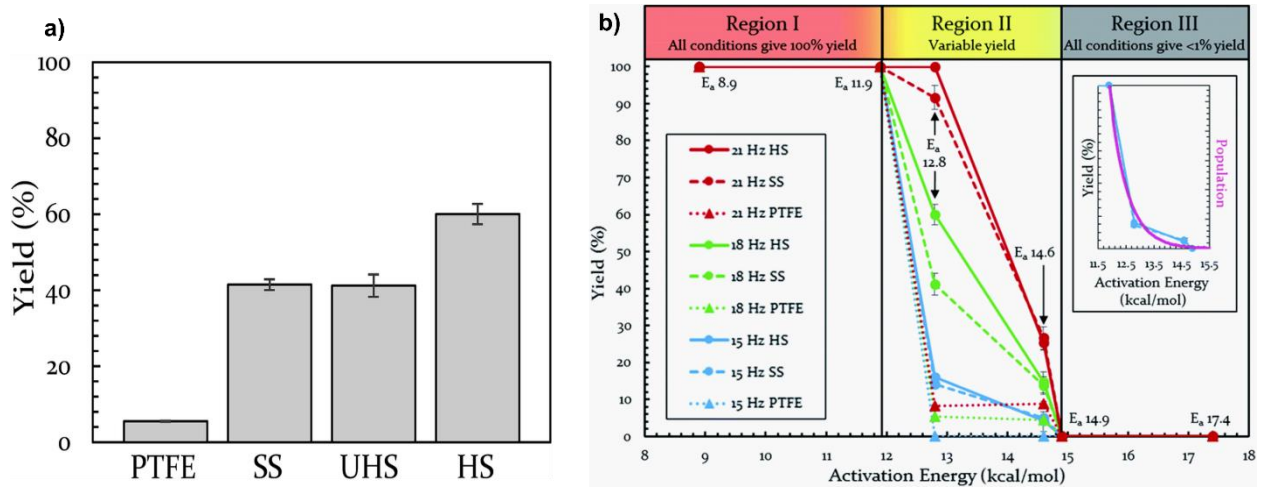

Figure 24. a) Reaction yields when using different milling vial materials: Teflon (PTFE), unhardened steel (UHS), stainless steel (SS), and hardened steel (HS). b) Yields of mechanochemical reactions under different conditions and associated activation energies. Modified from ref. [133].

Screening reactions at a constant time point enables observation of the relative effects of liquid, other additives, or catalysts. However, understanding the kinetic behavior of milling reactions is still a critical challenge for mechanochemists which requires sampling at multiple time points. Research which combines single time point reaction screening and *in situ* or *ex situ* monitoring studies is becoming increasingly prevalent and highlights how both approaches provide important and complementary insights into reaction conditions and profiles.

(b) Ex situ analysis at multiple time points (stepwise analysis)

Gaining insights into the kinetic behavior and profiles of reactions requires the analysis at multiple time points. Early examples of mechanochemical reaction monitoring utilizing this approach include the determination of the equilibration of calcite and aragonite phases under ball milling conditions by *ex situ* X-ray powder diffraction.[135] In cases where *in situ* setups are unavailable or unsuitable, the most common approach is sampling and analyzing the reaction at multiple time points. However, this requires stopping and opening the milling jar, removing the powdered sample and subsequent analysis, all of which can affect the reaction. When milling is paused, sample grinding and mixing stop, the reaction mixture cools as frictional heating stops, and opening the sealed reaction vessel allows gases and vapours to exchange with the external environment. These

effects limit the ability to accurately sample a reaction at different time points without interference. For these reasons, it is generally recommended to run replicate reactions and sample each reaction at a different time point to obtain realistic kinetics, reaction profiles, and intermediates. While this approach is time and resource intensive, it has the advantage that any quantitative analysis techniques suitable for the sample can be utilized with little or no modifications including chromatographic methods such as gas chromatography with a flame ionization detector (GC-FID),[136] nuclear magnetic resonance (NMR)[137] analyses, X-ray powder diffraction,[138] Raman,[139] and even terahertz (THz) spectroscopy.[140] For this reason, this approach remains common for optimization as well as kinetic and other fundamental studies based on instrumental analysis techniques for which *in situ* setups are unavailable.

Monitoring reaction progress at certain timepoints is especially useful for optimization of reaction times. For example, appropriate catalyst loading for a given time frame or conversion target can be determined. This is of special interest as one of the advantages of mechanochemistry is shorter reaction times, with potentially lower catalyst loadings. This was demonstrated in the Au(I) catalyzed C-H alkynylation of indoles where analyzing the reaction mixture at different time points demonstrated much faster reactivity with lower catalyst loading relative to the analogous reported solution reaction.[141] Similarly, the bromination of mesitylene using NaBr and Oxone was analysed at different time points to determine the affect of milling time on yield and degree of bromination. This revealed longer reaction times resulting in higher conversions without a significant change in the degree of bromination (Figure 25).[136] These examples demonstrate reaction optimization is possible with only a few time points and without special setups making *ex situ* analysis especially useful for tuning reactions.

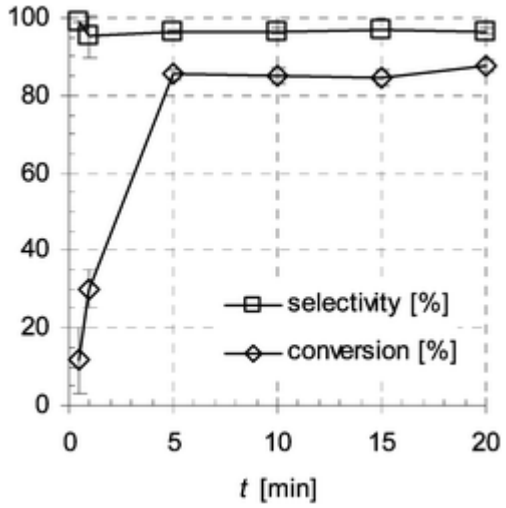

Figure 25. Influence of milling time on reaction conversion and selectivity for the bromination of mesitylene using NaBr and Oxone. Reproduced from ref. [136].

Beyond optimization, considerable fundamental work on understanding the mechanisms involved in mechanochemical reactions utilized *ex situ* monitoring at multiple timepoints. An early example studied the mechanochemical formation of co-crystals of various carboxylic acids with nicotinamide in various stoichiometries.[138] X-ray powder diffraction patterns of the co-crystallization of suberic (sub) and nicotinamide (na) were analyzed at various time points and revealed formation of the $(na)_2{\cdot}(sub)$ co-crystal *via* the (na)·(sub) co-crystal intermediate. This is one of the first examples of the characteristic stepwise transformation behavior often observed in milling reactions. Quantitative *ex situ* Raman monitoring of the synthesis of the zeolitic imidazolate framework ZIF-6 from zinc oxide, imidazole, and N,N-dimethylformamide revealed milling frequency dependent pseudo-second order kinetics.[139] A strong dependence on milling frequency was observed without any change in reaction rate over time despite considerable increases in both reaction temperature and moisture content during milling. This was explained using a 'pseudo-fluid' model where the reaction rate is determined by mixing and attrition.

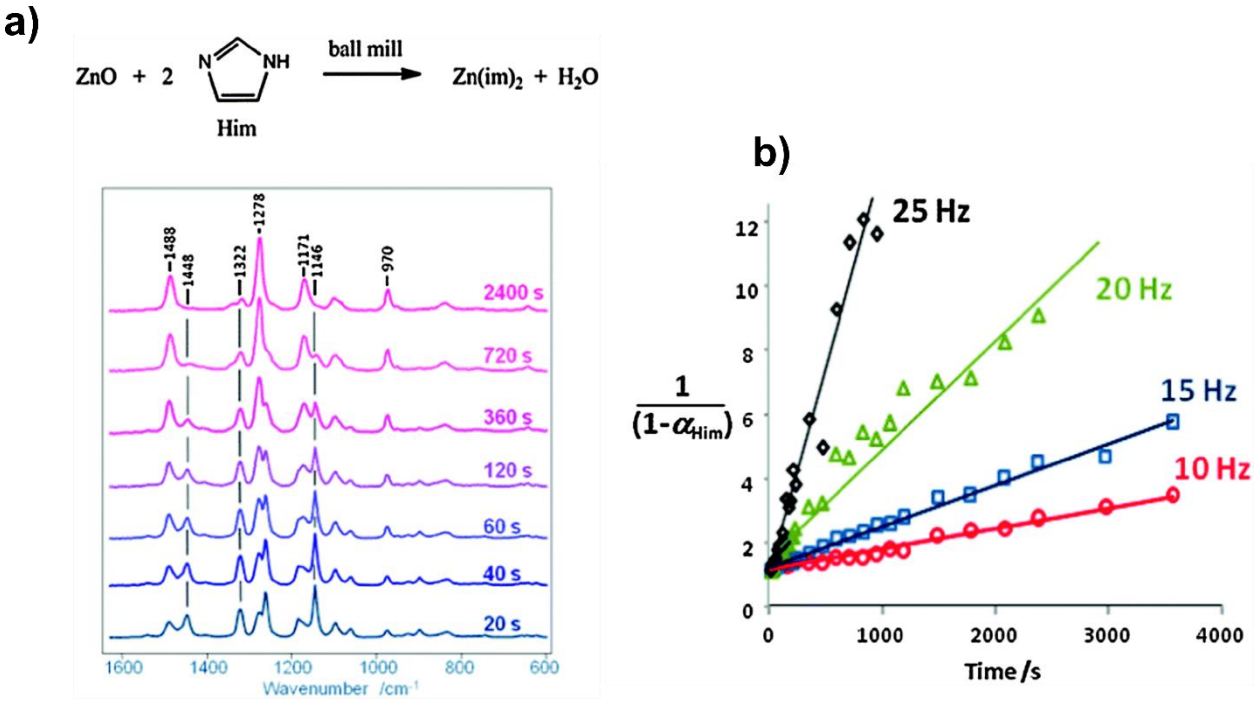

Figure 26. a) Mechanochemical formation of ZIF-6 monitored by ex situ Raman spectroscopy. b) Pseudo 2nd order integrated plot of the kinetic data. Reproduced from ref.[139].

In contrast, monitoring the mechanochemical Knoevenagel condensation *via ex situ* NMR revealed sigmoidal reaction kinetics which contrast to the equivalent solution reaction.[137]

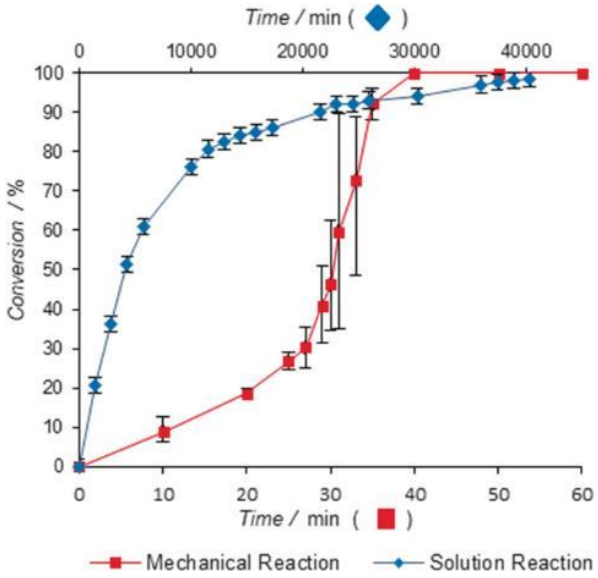

Figure 27. Solution and milling kinetics for the Knovenagel condensation reaction. Reproduced from ref. [137].

Here the effect of temperature, reaction by-product (water), and particle size reduction were all examined. However, the observed feedback kinetics were explained by changes in sample rheology from a free-flowing powder to more cohesive rubber-like state. These examples highlight how mechanistic insights can be gained for different systems *via ex situ* monitoring of milling reactions at multiple timepoints using a variety of instrumental techniques. *Ex situ* techniques continue to yield important mechanistic insights due to their broad applicability, however, they are highly resource intensive due to the number of replicates required. The desire to rapidly acquire a large number of timepoints without stopping or disturbing the milling reaction provided the foundation for *in situ* methods.

2.11 *In situ* monitoring of milling reactions

In order to gain deeper understanding into the behavior of milling reactions, the reaction mixture should be analyzed in real-time without stopping or perturbing the system. Due to challenges with extracting the sample from the milling jars, the current approach revolves around measurements conducted through the milling vessel itself. The continuous acquisition of data provides important insights into the reaction mixture composition and kinetics simultaneously, enabling rapid optimization of a synthesis using a single experiment. The use of *in situ* data for the development of novel mechanochemical syntheses has demonstrated applications in coordination chemistry, metal organic frameworks,[142] organometallic chemistry,[129] organic synthesis,[5] and pharmaceuticals.[150] *In situ* monitoring of milling reactions facilitates the discovery of novel intermediates and provides a convenient approach for exploring mechanisms and kinetics which underlie mechanochemical syntheses. There have been two general approaches towards *in situ* monitoring of mechanochemical reactions, (1) attaching sensors to the milling jar for measuring temperature and pressure, or (2) using milling jars which are sufficiently transparent towards either light or X-rays for spectroscopy and diffraction techniques.

(a) *In situ* measurements of physical properties: temperature and pressure

The earliest examples of *in situ* monitoring of milling reactions were based on monitoring pressure of gas during solid-gas milling reactions. These high-speed ball milling reactions focused on the synthesis of inorganic materials such as nitrides and were

conducted under relatively harsh conditions which often induced combustion with large and readily observed temperature and pressure increases. For example, the pressure of a sealed planetary milling jar was monitored with a Bourdon-tube chart recorder connected to a glycerine filled rotary joint during the reaction of zirconium metal in an ammonia atmosphere (Figure 28).[143] A decrease in pressure was observed for the first 35 hours of milling before rising and saturating at a pressure considerably higher than the starting ammonia gas pressure. The decrease in pressure was explained *via* the formation of a ZrH_2 intermediate observed *via ex situ* XRPD. The intermediate hydride phase subsequently converts to ZrN over the course of the next 75 hours, liberating H_2 gas resulting in an overall pressure increase. Similarly, the pressure of high energy ball milling of titanium powder in a nitrogen atmosphere was monitored and revealed autocatalytic formation of TiN[144].

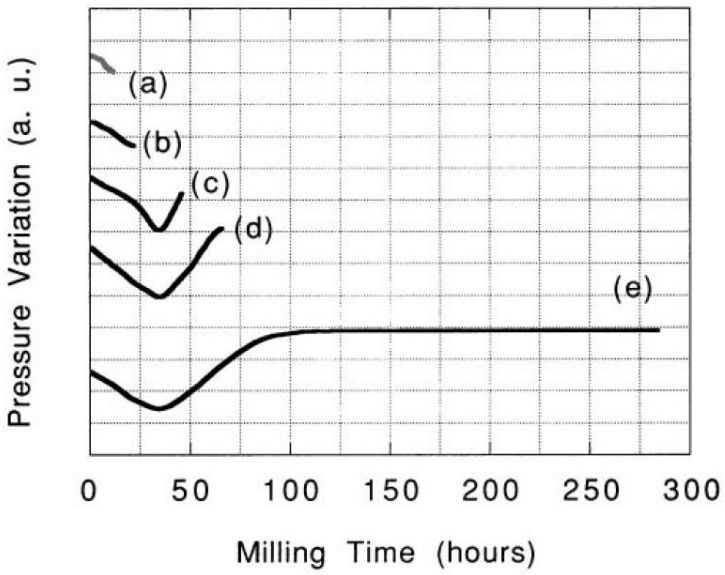

Figure 28. Variation in pressure during the milling of Zr for a)12 hours, b) 22 hours, c) 46 hours, d) 66 hours, and e) 288 hours. Reproduced from ref. [143].

Under milder milling conditions with smaller ball sizes and lower nitrogen pressures, a smooth sigmoidal pressure profile was observed, while under harsher conditions, a self-catalytic combustion reaction takes place where nearly all the nitrogen in the reaction vial was consumed rapidly with a rapid temperature increase of around 40°C and evidence of melting *via* SEM (Figure 29). It was determined that a large surface area associated with

small titanium particles and a minimum ball weight/impact energy were required to ignite the combustion reaction.

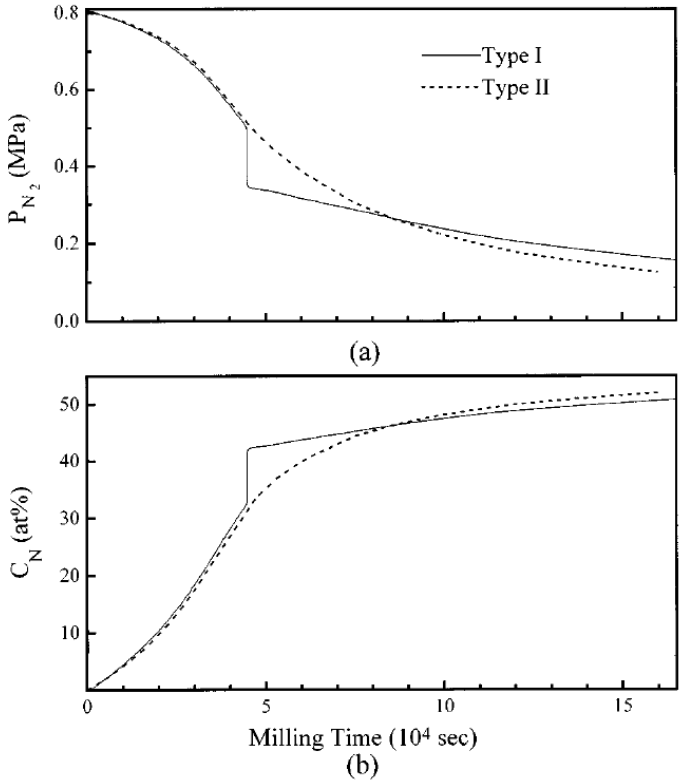

Figure 29. Kinetics of the nitridation of titanium powder. Type I profile is associated with the combustion reaction, while no combustion is seen in type II. Reproduced from ref. [144].

Similarly, the first reports of thermal monitoring of mechanochemical reactions were focused on highly exothermic mechanically induced self-propagating reactions (MSR) between two solids. Fortunately, the development of these reactions and associated thermal monitoring has been thoroughly reviewed by Takacs.[145] A prominent example is the monitoring of the mechanochemical reduction of Fe_3O_4 with Zr in a SPEX Mixer Mill using a K-type thermocouple (Figure 30).

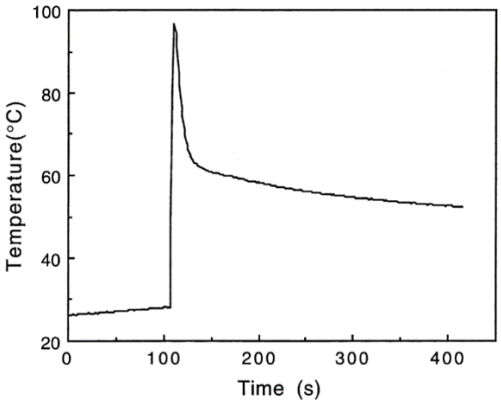

Figure 30. Thermal monitoring of the mechanochemical reaction of Fe_3O_4 with Zr. Reproduced from ref. [145].

A slow and mild temperature increase is observed for the first 100 seconds of the reaction, before a near instant increase of nearly 70°C followed by rapid cooling to equilibrate near 60°C after 400 seconds. Here the use of thermal monitoring was especially important to understand which conditions led to self-propagating reactions. The instrumental and experimental design utilized in these experiments demonstrated the ability to monitor reactivity and provided important insights into the temperature variation at different points on the milling jar. This work provided the foundation for monitoring the thermal behavior of milling reaction coupled with simultaneous diffraction or spectroscopic measurements.

(b) The development of *in situ* diffraction and spectroscopic measurements

Techniques to monitor reactions through the walls of the milling vessel during milling include X-ray powder diffraction to identify crystalline materials, and spectroscopic approaches conducted through the wall of a transparent milling vessel such as Raman and fluorescence spectroscopies.. Despite being reviewed relatively recently,[146] the rapid pace of research in this area warrants continued attention.

(c) In situ X-ray diffraction

In 2013, a breakthrough occurred in monitoring milling reactions using highly penetrating synchrotron X-rays to measure the diffraction of crystalline samples inside of a milling jar during milling.[147] This was achieved by modifying a conventional Retsch mixer mill so that the sample holders were above the mill and the X-ray beam penetrated the

milling jar while it oscillated sideways. Analysis of the resulting *in situ* powder diffraction data using Rietveld refinement enabled comparison of reaction profiles and kinetics under different conditions and Pawley refinement provided estimates of crystallite size.

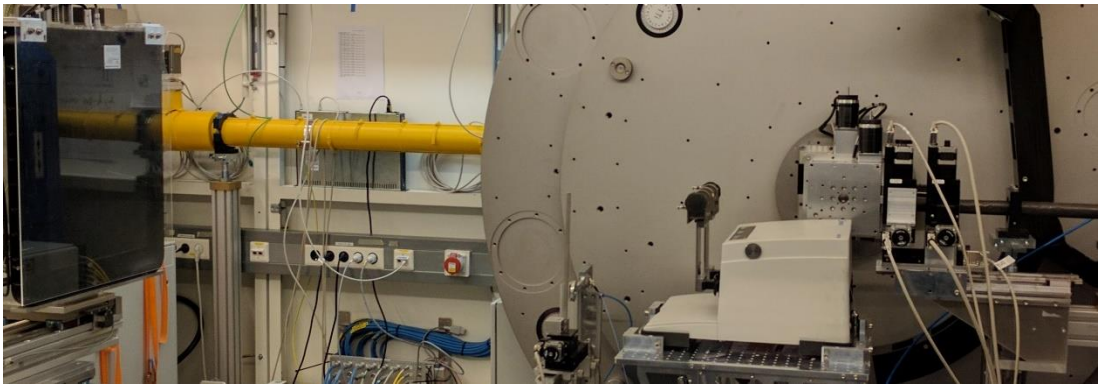

The utility of this setup was first demonstrated for the mechanochemical synthesis of zeolitic imidazole frameworks (ZIFs) from zinc oxide and imidazole ligands. Real-time reaction monitoring revealed reaction kinetics, intermediates, and interconversion between different ZIF topologies.[148] It was shown that catalytic amounts (3-5 mol%) of ammonium salts dramatically increase the reaction rate and provided direct evidence of stepwise formation of products in mechanochemical reactions, with reactions of ethyl-imidazole and zinc oxide proceeding through three distinct topological phases: RHO → ANA → qtz (Figure 31). When only small amounts of N,N-dimethylformamide (DMF) were added the intermediate ANA phase was no longer detected, suggesting reaction mechanisms of milling reactions are dependent on the presence and quantity of liquid additives. Direct transformation between crystalline phases can readily be detected and quantified, however amorphous phases require the addition of a crystalline silicon diffraction standard for quantification. Considerable amorphous weight fractions were discovered in the synthesis of ZIFs as well as the softer co-crystal materials, and suggests amorphous phases play a crucial role in the milling transformations with up to 35% by weight amorphous content for both LAG and ILAG reactions.[149]

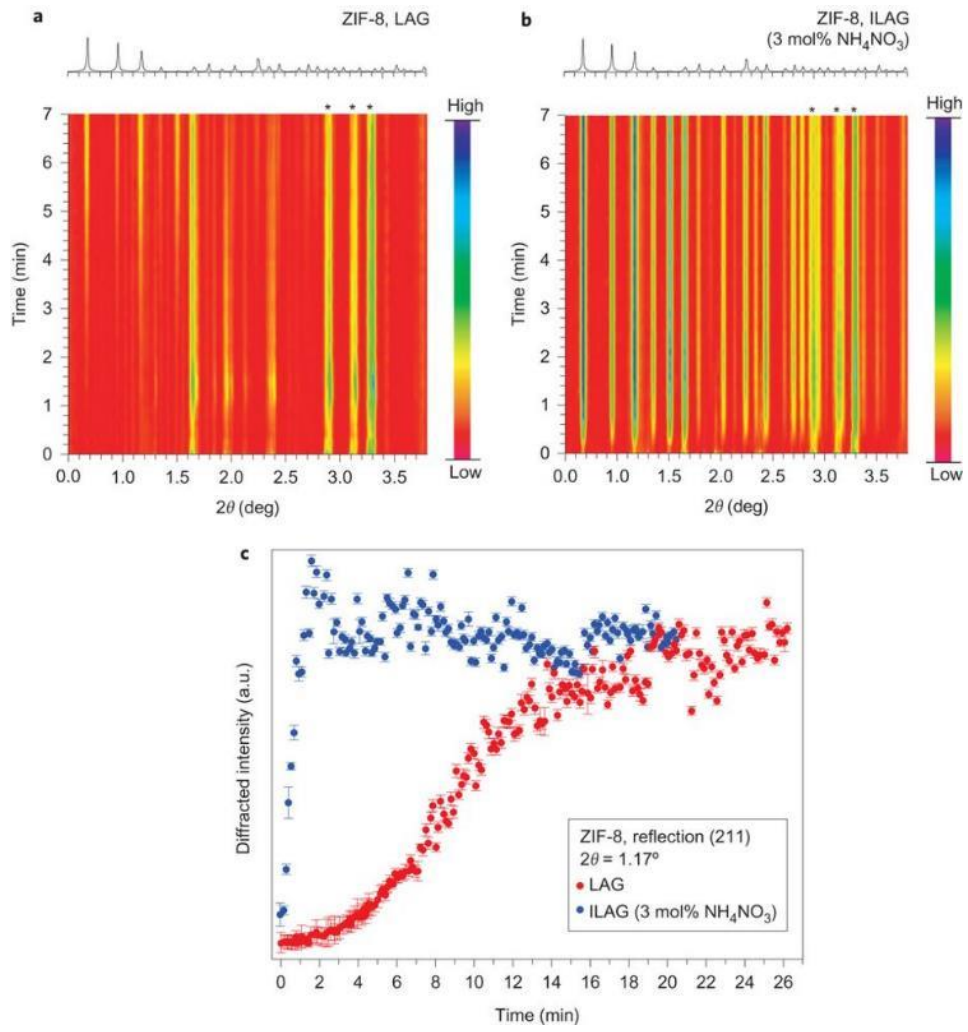

Figure 31. Time-resolved diffractogram for the a) LAG reaction of ZnO and HMeIm and b) analogous ILAG reaction. c) Time-resolved intensity of the strongest reflection for the ZIF-8 product. Reproduced from ref. [148].

In situ monitoring by diffraction has been applied towards understanding the mechanochemical synthesis of pharmaceutical co-crystals, which are important in drug tableting and formulations, and provides insights into the reactivity of crystalline organic solids *via* milling.[150] The rapid kinetics of the molecular assembly of carbamazepine and saccharin under liquid-assisted grinding with acetonitrile were determined *via* Rietveld refinement of the *in situ* X-ray data. Similarly, the formation of the 2:1 co-crystal of nicotinamide and suberic acid proceeds *via* the formation of the known 1:1 co-crystal. This demonstrated the utility of diffraction based *in situ* techniques for studying transformations of soft materials under milling conditions.

The application of *in situ* X-ray diffraction methods extends beyond known phases and is a powerful tool for the discovery of novel structures and phases in systems. One of the most prominent examples of this was the unexpected synthesis of amorphous ZIF-8 from the LAG reaction of ZnO and 2-methylimidazole in the presence of aqueous acetic acid.[151] Rapid formation of crystalline ZIF-8 was observed before further grinding yielded an amorphous phase which surprisingly retained the ZIF-8 network as confirmed by cross-polarized magic angle spinning ^{13}C solid-state NMR. Continued milling led to the nucleation of *dia*-Zn(MeIm)$_2$, a dense packed structure with diamondoid topology, while a previously unknown metastable intermediate phase was observed in roughly half of reactions. Structure solution from powder diffraction data revealed a previously unknown porous framework with a novel topology which was named *katsenite (kat).* This apparently stochastic and spontaneous recrystallization demonstrates the structural lability of the framework under mildly acidic conditions and supported the hypothesis that the order of phases follows Ostwald's rule of stages, where the system evolves through the formation of increasingly stable solid phases. This provided the foundation of subsequent work on the theoretical periodic DFT calculations and experimental solution calorimetry measurements on the thermodynamic properties of ZIFs, which confirmed the relative increasing stability of observed phases in mechanochemical reactions[152] (Figure 32).

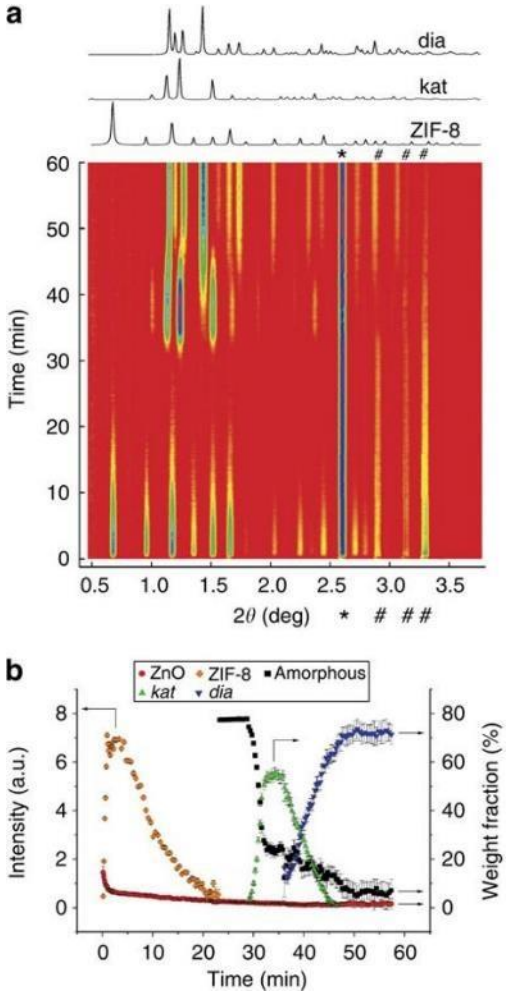

Figure 32. a) Time resolved diffraction patterns of the evolution of the reaction of ZnO and 2-methylimidazole. b) Quantification of each phase via Rietveld analysis. Modified from ref. [151].

Uniquely for the case of LAG with DMF, a novel and isolatable metastable phase was obtained with spectral properties between that of the 1-D coordination polymer and Zn-MOF-74. Unfortunately, in this case, attempts at structure solution from powder diffraction data or crystallization from solution were not successful. Similarly, formation of HKUST-1 from trimesic acid and Cu(II) acetate monohydrate proceeds *via* direct transformation utilizing LAG with solvents such as DMSO, methanol, acetone, or acetonitrile.[153] Use of solvents with longer alkyl chains results in the presence of a mononuclear copper complex as an intermediate phase, once again demonstrating a stepwise transformation mediated by the liquid additive. Interestingly, interruption of milling and opening the reaction vessel resulted in the reaction mixture forming a different mononuclear copper

species regardless of which liquid additive was used. This is a particularly informative example of the advantage of *in situ* techniques over *ex situ* analyses.

Beyond just optimizing liquid additives, *in situ* diffraction measurements revealed the importance of the structure of zirconium cluster precursors for the formation of highly porous zirconium frameworks such as UiO-67 and NU-901, which are both based on hexanuclear zirconium nodes and carboxylic acid linkers.[154] The pivotal finding was the use of a dodecanuclear zirconium acetate cluster as a precursor for the mechanochemical synthesis. *In situ* X-ray diffraction analysis of the reaction mixture from the common Zr_6 methacrylate precursor led to poor crystallinity and porosity, due to formation of a novel 16-coordinated Zr_6 cluster formed with DMF, which impedes the formation of both NU-901 and UiO-67. In contrast, direct conversion to NU-901 and UiO-67 is observed with dodecanuclear zirconium acetate cluster resulting in pure product with much higher crystallinity and porosity values. These studies suggest that for the mechanochemical synthesis of MOFs, stepwise evolution of phases is highly sensitive to liquid additives and the environment of the sealed reaction vessel. Preliminary thermodynamic work suggests the observed phases obey Ostwald's rule of stages where progressively more stable structures emerge.

(d) *In situ* Raman spectroscopy

A key disadvantage of the diffraction method for real-time monitoring of mechanochemical reactions is the need for synchrotron radiation, which severely limits the accessibility of the technique. The desire for a readily accessible laboratory technique led to the development of *in situ* Raman monitoring of milling reactions utilizing optically transparent polymethyl-methacrylate (PMMA) milling jars.[155] Despite the considerable Raman activity of the PMMA jar, it was demonstrated that characteristic Raman shifts of the previously mentioned nicotinamide and suberic acid co-crystallization could be observed without interference of the jar material. The overall co-crystallization kinetics were observed. However, due to the similarity between the spectra of the 2:1 and 1:1 co-crystals (Figure 33), it was not possible to definitively identify the 1:1 co-crystal intermediate *via* Raman spectroscopy unlike in X-ray studies. *In situ* Raman spectroscopy was used to examine for the formation of coordination polymers consisting of the reaction

between cadmium chloride and cyanoguanidine. Both a 1:1 $CdCl_2$:cyanoguanidine 3-D coordination polymer and a 1:2 $CdCl_2$:cyanoguanidine 1-D coordination polymer form *via* neat grinding. The 1:1 stoichiometry 3-D coordination polymer was detected as an intermediate in the synthesis of the 1:2 1-D coordination polymer when milled with a milling ball of 2.9 grams. However, increasing the ball weight to 4 grams resulted in the direct formation of the 1:2 stoichiometry coordination polymer. In addition, for both systems rapid reactions involving liquid-assisted grinding were successfully monitored, suggesting a highly versatile method of investigating mechanochemical reactions in standard research laboratories, capable of providing insights complementary to diffraction-based studies into milling reactions.

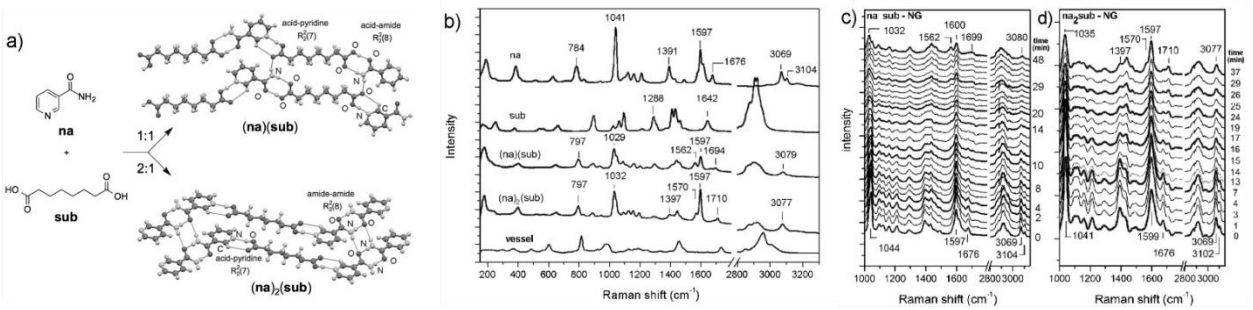

Figure 33. a) Formation of stoichiometrically different co-crystals from nicotinamide and suberic acid. b) Raman spectra of the pure reaction components. c, d) In situ Raman spectra of neat-grinding reactions with a 1:1 (c) and 2:1 (d) nicotinamide : suberic acid reactant ratio. Reproduced from ref. [155].

The use of *in situ* Raman spectroscopy is of importance in monitoring covalent bond forming reactions, as organic systems often have limited crystallinity but characteristic changes in vibrational spectra. The first reported direct mechanochemical C-H insertion into an asymmetrical azobenezene where palladium(II) acetate inserts to form both dimeric mono- and di-cyclopalladated complexes, depending on the equivalents of $Pd(OAc)_2$ using acetic acid.[156]

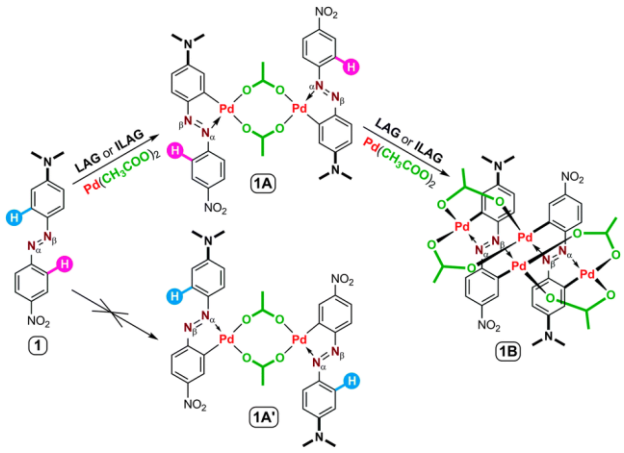

Figure 34. Mechanochemical C-H insertion of palladium into an azobenzene. Reproduced from ref. [156].

Once again, the 1:1 mono-cyclopalladated insertion product was found to be an intermediate for the di-cyclopalladated product *via in situ* spectroscopy. Reaction rates were consistent with those observed in solution, and interpretation of Raman spectra was facilitated by DFT simulations enabling the correlation of vibrational spectra with structural changes of the respective complexes. This work was expanded upon to examine the relative rates and mechanisms of common palladium(II) catalysts for C-H activation, as well as how the acid/base properties of different liquid and solid additives effect the reaction mechanism.[157] For polymeric palladium(II) chloride based precursors, a three step reaction is observed. First, the formation of the palladium-azobenzene adduct, where one azo-nitrogen is bound to the palladium, was observed before subsequent C-H insertion forms a mono-palladated complex, followed by a second insertion to form the di-palladated species, as observed by *in situ* Raman spectroscopy. It was found that the presence of acetonitrile results in slower reaction rates due to formation of $PdCl_2(MeCN)_2$, whereas addition of water and DMF accelerates the reaction, most likely due to basicity which facilitates proton elimination for the rate-determining step of C-H bond cleavage (Figure 35). Solid additives with mild basicity such as sodium acetate were key for achieving reactivity and served to neutralize the detrimental acid by-product of the reaction. Changing palladium precursor has a significant effect on the reaction with $[Pd(MeCN)_4][BF_4]_2$ resulting in rapid formation of monomeric product with minor adduct impurity observed *via in situ* Raman, while the use of $Pd(OAc)_2$ results in much slower transformation to a di-palladated species. In contrast to the palladium(II) chloride system,

the second palladation using $Pd(OAc)_2$ is considerably slower than the first palladation. Adduct formation was not observed suggesting that breaking the $[Pd(OAc)_2]_3$ trimer is rate determining. This analysis demonstrates the power of *in situ* Raman to for elucidating reaction mechanisms and optimizing reaction conditions for mechanochemical reactions.

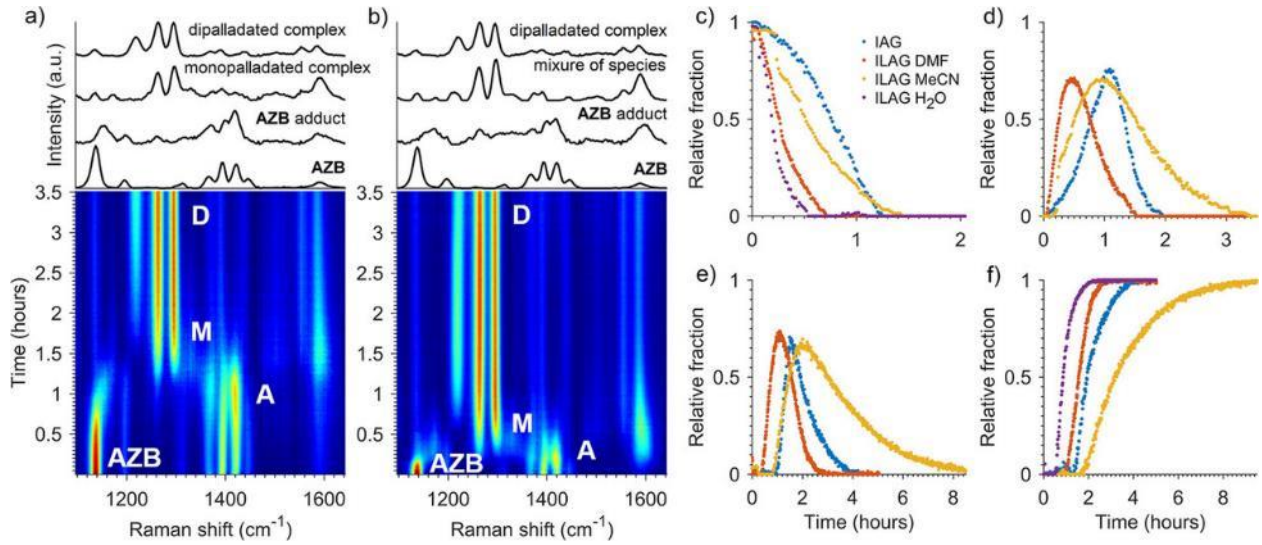

Figure 35. Raman monitoring of the ion-assisted grinding a) and ion-and liquid-assisted grinding b) cyclopalladation of azobenzene (AZB), displaying the adduct (A), monopalladated species (M), and dipalladated complex (D). Reaction profiles estimated for c) AZB, d) the adduct, e) the monopalladated species and f) the dipalladated species. Reproduced from ref. [157].

Real-time reaction monitoring of mechanochemical reactions enables exploration of the fundamental parameters of milling in organic chemistry. The influence of LAG effects on organic reactions inspired a fundamental study monitoring mechanochemical nucleophilic substitution reactions using the reaction of 4-nitrobenzoyl azide and 1,4-diaminobenzene to yield N-(4-aminophenyl)-4-nitrobenzamide.[158] The reaction proceeds using a variety of liquid additives with a strong correlation between the basicity of the liquid additive and reaction rate. The addition of various mild solid bases under LAG conditions also supported a correlation between basicity and reaction rate. This suggests a base catalyzed mechanism where proton abstraction is at least partially rate limiting. Beyond mechanistic interpretation, fundamental experimental parameters of milling reactions can also be investigated in real-time.

Real-time Raman reaction monitoring of milling reactions is not limited to organic systems, and has provided information on inorganic materials such as the synthesis of metal amidoboranes (AB), which have potential application in hydrogen storage and fuel cells.[160] A two-step reaction pathway is revealed, where LiH or NaH first react with AB, giving an intermediate M(AB)·AB species which subsequently reacts with MgH_2, giving the desired bimetallic amidoboranes product. *In situ* measurements revealed that this second reaction competes with a side-reaction leading to oligomeric M($BH_3NH_2BH_2NH_2BH_3$) phases, irrespective of reaction conditions. This preliminary work suggests considerable promise for the use of Raman reaction monitoring for inorganic materials.

The sapphire jars designed in this Thesis enabled monitoring the formation of the first ever reported halogen-bonds with phosphorus, arsenic, and antimony based acceptors[161] (Figure 36).

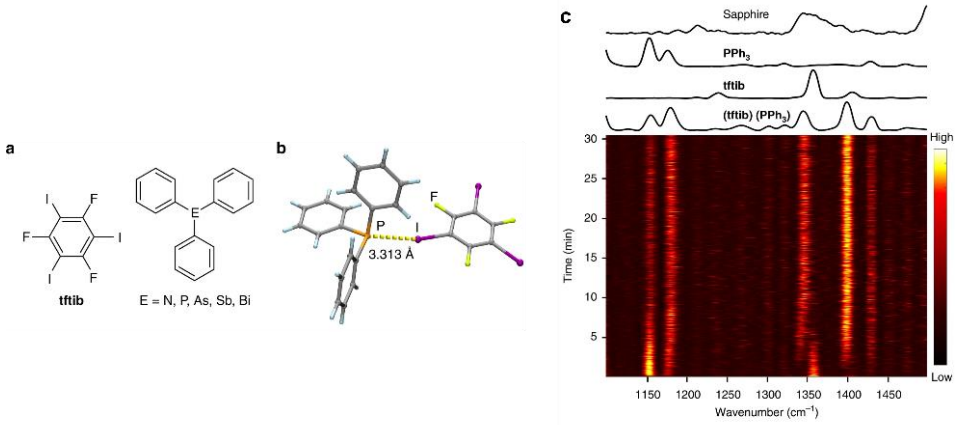

Figure 36. a) tftib and triphenylphosphine forming b) a halogen-bonded co-crystal monitored by c) in situ Raman monitoring. Reproduced from ref. [161] under CC license.

Changes in relatively weak supramolecular interactions often corresponds with small changes in low intensity Raman bands. Improvements in Raman monitoring setups enable detection of subtle changes in supramolecular arrangements that previously required synchrotron radiation for analysis. Due to accessibility, cost, and sensitivity, Raman spectroscopy is rapidly emerging as the *de facto* standard reaction monitoring approach for milling reactions in different areas of chemistry.

(e) Tandem in situ spectroscopy and diffraction:

The development of *in situ* spectroscopic, diffraction, pressure, and temperature measurements provide an opportunity for simultaneous acquisition of multiple types of spectroscopic data. The first realization of a tandem approach was the simultaneous utilization of a Raman probe during synchrotron X-ray diffraction measurements utilizing a custom poly-methyl-methacrylate (PMMA) milling vessel. A variety of distinct syntheses were evaluated including the formation of the metal organic framework ZIF-8, a metal phosphonate $CoPhPO_3 \cdot H_2O$, and the 1:1 co-crystal theophylline:benzoic acid.[162] Both spectroscopic and diffraction measurements yielded consistent kinetics and insights into the molecular and crystalline behavior of reactants and products. Raman spectroscopy provided important insights into the protonation states of imidazole and phenylphosphonate species which are unobservable in diffraction methods.

A quantitative method for the analysis and comparison of *in situ* Raman and X-ray diffraction data was developed and demonstrated on the co-crystallization of benzoic acid with nicotinamide as a model system[163] (Figure 37). Various co-crystal polymorphs were revealed during the stepwise kinetic transformation of the reaction which was dependent on the liquid additive. Quantitative analysis comparing the profile of a classical least-squares output of the Multivariate Curve Resolution Alternating Least Squares (MCR-ALS) for Raman spectroscopy and Rietveld refinement of diffraction data revealed very similar reaction profiles for the 1:1 reaction of benzoic acid with nicotinamide using water. Changing the LAG additive to methanol revealed that both reactant consumption and product formation followed roughly first order kinetics, suggesting that at least in some cases LAG reactions can mimic solution behavior.

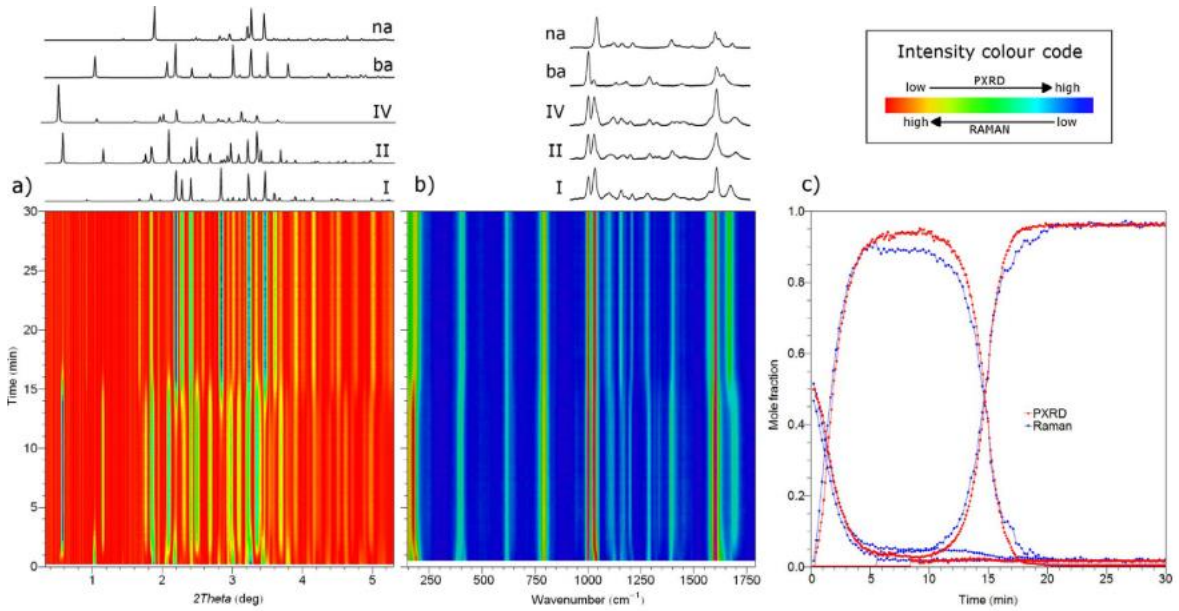

Figure 37. Tandem in situ monitoring by (a) PXRD and (b) Raman spectroscopy of the LAG reaction of benzoic acid with nicotinamide revealing similar reaction profiles derived from each method (c). Reproduced from ref. [163].

This tandem reaction monitoring approach was applied to better understand a classical organic reaction in the solid state: the Knoevenagel condensation of vanillin and barbituric acid.[129] While both *in situ* Raman and X-ray diffraction were applied, X-ray diffraction measurements exhibited weak diffraction signals and the reaction product remained X-ray amorphous. However, Raman spectroscopy clearly revealed the formation of a 1:1 co-crystal of barbituric acid to vanillin, which was later solved from *ex situ* powder diffraction data, as the intermediate phase. Reaction rate acceleration with the addition of N,N-diisopropylethylamine, a non-nucleophilic base, circumvented the formation of the co-crystal. This work demonstrated the importance of supramolecular arrangements in solid-state reactivity and provides a concrete example of the limitations of X-ray diffraction work on soft materials which amorphize. Tandem *in situ* reaction monitoring and the structure solution from *ex situ* diffraction data were shown to be highly complementary.

In order to better understand the dynamics involved in mechanochemical reactions, isotopically labeled solids were monitored *via* tandem Raman and diffraction studies. Rapid hydrogen/deuterium exchange was observed for liquid assisted grinding of benzoic acid with D_2O as well as during the formation of a 2-Pyridone:benzoic acid co-crystal.[164] This suggests milling overcomes slow solid-state diffusion to equilibrate at a distribution

of hydrogen to deuterium. This insight enabled the development of a highly efficient deuterium labeling protocol requiring 60 times less labelled solvent and opens the door towards fundamental kinetic isotope effect studies in milling reactions which provide critical mechanistic insights into organic reactions.

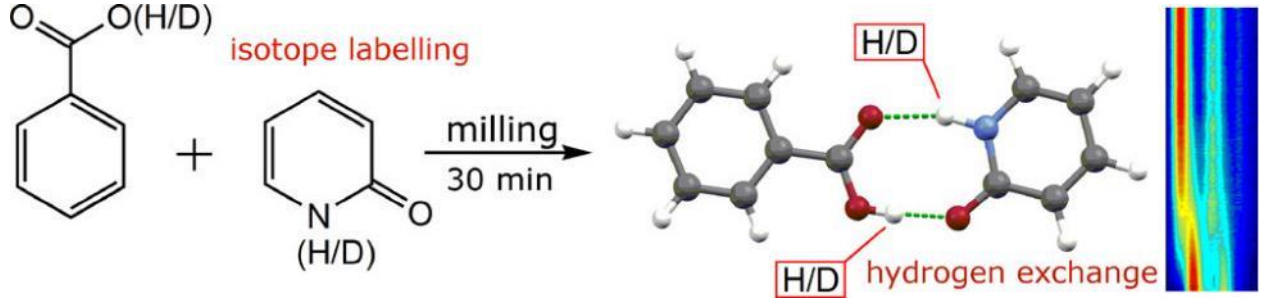

Figure 38. Real-time monitoring of the hydrogen/deuterium exchange during milling. Reproduced from ref. [164].

(f) Separate in situ spectroscopy and diffraction

Due to limited access to synchrotron sources, increasingly chemical systems are being explored using separate diffraction and Raman experiments under identical milling conditions. An example of this type of analysis is the scalable milling synthesis of a co-crystal of ascorbic acid and nicotinamide.[165] Both X-ray and Raman datasets revealed the presence of an intermediate phase. Different LAG additives influenced polymorph selectivity and resulted in the discovery of a new polymorph by structure solution from *ex situ* PXRD data. Understanding the role of the liquid additive is critical for reaction optimization for large scale synthesis *via* planetary ball milling or twin-screw extrusion. This demonstrates the applicability of *in situ* datasets towards understanding and optimizing scalable mechanochemical processes.

(g) Combining real-time thermal measurements with diffraction and spectroscopic techniques

Temperature is fundamental to understanding chemical reactions, and monitoring the temperature of the milling vessel along with the reaction profile enable fundamental kinetic studies of milling reactions. The combination of real-time spectroscopic and diffraction measurements with thermal monitoring is a critical advance for the field. The first reported example of this approach combined X-ray diffraction and Raman

spectroscopy with thermography for three prototypical mechanochemical reactions: the co-crystallization of theobromine with oxalic acid, a Knoevenagel condensation, and the formation of a manganese phosphonate framework.[166] Thermography determined the temperature distribution of the external surface of the milling jar, and suggested that neither the Raman laser nor the synchrotron radiation had a measurable effect on reaction temperature. For the condensation reaction, melting is observed both in the thermography and diffraction data. Formation of the crystalline product is accompanied by a corresponding increase in temperature, which stabilizes and returns to the previous equilibrium temperature after crystallization is completed. For MOF formation, the release of liquid by-products briefly reduces the jar temperature before the temperature returns to a steady equilibrium after crystallization.

In order to better understand the nature of thermal effects in milling, another study examined the formation of the metal organic framework ZIF-8 *via* synchrotron diffraction using a thermocouple temperature sensor embedded into the wall of the jar. In this case, the thermocouple is in contact with the sample through a highly thermally conductive aluminum plug, enabling the detection of small changes in sample temperature with little time delay (Figure 39).[167] The elevated steady-state temperature observed during milling results from frictional heating from inelastic collisions between the milling media, vessel walls, and sample, balanced against the heat loss through the jar to the cooler surroundings. The thermal behavior of milling reactions was described using three main parameters (1) heat input *via* friction, (2) heat change from reaction enthalpy, and (3) heat loss to the surroundings. In cases where no chemical reaction is present, it was shown that the efficiency of the conversion of kinetic energy to heat *via* collisions in the mill determine the temperature of a milling vessel. Parameters such as amount and nature of the sample and the softness of the milling media change the efficiency of this conversion of kinetic energy to heat. As the temperature increases, so does heat loss to the environment resulting in thermal equilibration. Different phases of ZIF-8 yielded different thermal equilibrium temperatures enabling detection of phases *via* thermal profiles. Simulation of heat flow suggests that changes in the frictional properties of materials dominate the contribution of slightly exothermic reactions, as evidenced by a loss in temperature for the formation of ZIF-8. This suggests interpreting thermal milling data

goes beyond reaction enthalpies and opens the door to thermal monitoring of reaction even with small changes in enthalpy.

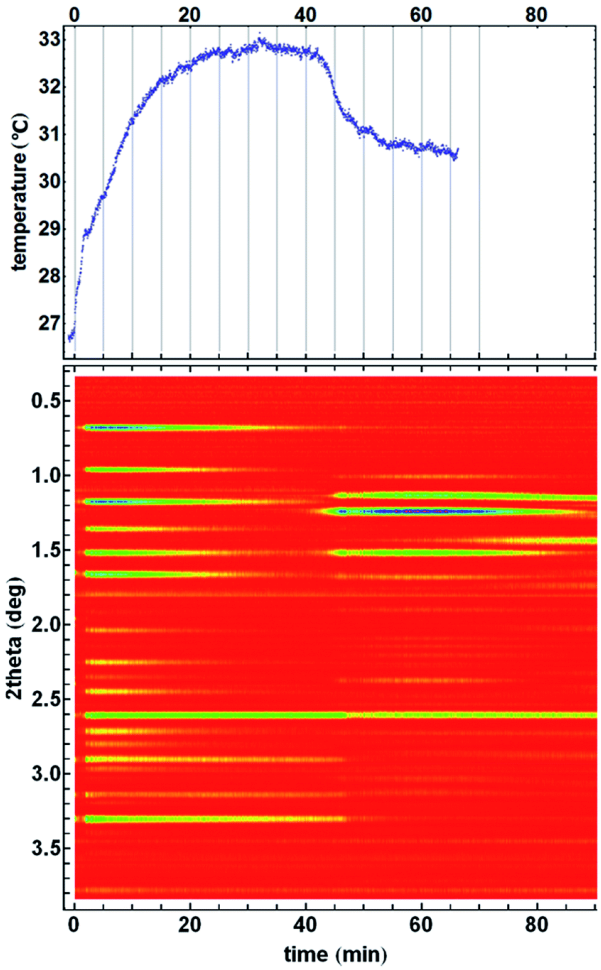

Figure 39. Tandem real-time thermal and diffraction monitoring of the formation of the kat-polymorph of ZIF-8. Reproduced from ref. [167].

2.12 Conclusions:

The desire to discover new solid forms and modulate the structure and properties of materials has driven the development of crystal engineering and supramolecular chemistry. At the same time, the pressing need for improved sustainability has fostered research into alternative synthetic methods. For the case of crystalline solids, mechanochemistry has emerged at the confluence of these research areas, providing a rapid and efficient method for synthesizing both known and novel solid forms not accessible through solution methods. Mechanochemistry has shown considerable

promise in enhancing sustainability by minimizing solvent cost, waste, and environmental impact while potentially minimizing energy input. A key challenge limiting the development of mechanochemistry remains a poor mechanistic understanding of milling reactions. Recently, considerable progress has been made in both real-time *ex situ* and *in situ* methods for monitoring mechanochemical reactions. These methods have provided the basis for mechanochemical reaction kinetics, mechanisms, and identified intermediates present in milling reactions. Despite this progress, the ability to monitor milling reactions is still highly limited when compared to solution reactions. As the diversity and prevalence of mechanochemical syntheses increase, the need for and importance of monitoring milling reactions will likely increase. As such, novel approaches capable of directly analyzing the solid samples produced by milling reactions are required.

This Thesis provides several advances improving the instrumental methods available for monitoring milling reactions, and applies these improvements to better understand the mechanochemical synthesis of a wide variety of crystalline materials, including an organic condensation reaction, co-crystals, and MOFs with the hope that improved mechanistic understanding will further the development and adoption of more sustainable chemical syntheses for solid materials.

2.13 References:

1. Mottillo, C.; Friščić, T.; *Molecules* **2017,** *22*, (1), 144.
2. Catlow, C.R.; Davidson, M.; Hardacre, C.; Hutchings, G.J.; *Philosophical Transactions of the Royal Society A: Mathematical, Physical and Engineering Sciences* **2016,** *374*, (2061), 20150089.
3. Erisman, J.W.; Sutton, M.A.; Galloway, J.; Klimont, Z.; Winiwarter, W.; *Nature Geoscience* **2008,** *1*, 636.
4. FAO, I., UNICEF, WFP and WHO *The State of Food Security and Nutrition in the World 2018. Building climate resilience for food security and nutrition.*; FAO: Rome, 2018.
5. Galloway, J.N.; Dentener, F.J.; Capone, D.G.; Boyer, E.W.; Howarth, R.W.; Seitzinger, S.P.; Asner, G.P.; Cleveland, C.C.; Green, P.A.; Holland, E.A., et al.; *Biogeochemistry* **2004,** *70*, (2), 153-226.
6. Tilman, D.; Cassman, K.G.; Matson, P.A.; Naylor, R.; Polasky, S.; *Nature* **2002,** *418*, (6898), 671.

7. Griffin, P.W.; Hammond, G.P.; Norman, J.B.; *Applied Energy* **2018,** *227*, 587-602.
8. Rosenzweig, C.; Karoly, D.; Vicarelli, M.; Neofotis, P.; Wu, Q.; Casassa, G.; Menzel, A.; Root, T.L.; Estrella, N.; Seguin, B., et al.; *Nature* **2008,** *453*, 353.
9. Geyer, R.; Jambeck, J.R.; Law, K.L.; *Science Advances* **2017,** *3*, (7), e1700782.
10. Schmidt, C.; Krauth, T.; Wagner, S.; *Environmental Science & Technology* **2017,** *51*, (21), 12246-12253.
11. Segev, O.; Kushmaro, A.; Brenner, A.; *International journal of environmental research and public health* **2009,** *6*, (2), 478-491.
12. Suja, F.; Pramanik, B.K.; Zain, S.M.; *Water Science and Technology* **2009,** *60*, (6), 1533-1544.
13. Tang, H.P.-o.; *Trends in Analytical Chemistry* **2013,** *45*, 48-66.
14. Beyer, A.; Biziuk, M., Environmental Fate and Global Distribution of Polychlorinated Biphenyls. In *Reviews of Environmental Contamination and Toxicology Vol 201*; Whitacre, D.M., Ed. Springer US: Boston, MA, 2009; pp 137-158.
15. Safe, S.H.; *Critical Reviews in Toxicology* **1994,** *24*, (2), 87-149.
16. Dewulf, J.; Van Langenhove, H.; Muys, B.; Bruers, S.; Bakshi, B.R.; Grubb, G.F.; Paulus, D.M.; Sciubba, E.; *Environmental Science & Technology* **2008,** *42*, (7), 2221-2232.
17. Dunn, P.J.; *Chemical Society Reviews* **2012,** *41*, (4), 1452-1461.
18. Izatt, R.M.; Izatt, S.R.; Bruening, R.L.; Izatt, N.E.; Moyer, B.A.; *Chemical Society Reviews* **2014,** *43*, (8), 2451-2475.
19. Lewis, J.; *EPA J.* **1985,** *11*, 6.
20. Brundtland, G.H.; *Environmental policy and law* **1985,** *14*, (1), 26-30.
21. Griggs, D.; Stafford-Smith, M.; Gaffney, O.; Rockström, J.; Öhman, M.C.; Shyamsundar, P.; Steffen, W.; Glaser, G.; Kanie, N.; Noble, I.; *Nature* **2013,** *495*, 305.
22. King, A.A.; Lenox, M.J.; *Academy of Management Journal* **2000,** *43*, (4), 698-716.
23. Anastas, P.T.; *Critical Reviews in Analytical Chemistry* **1999,** *29*, (3), 167-175.
24. Anastas, P.T.; Warner, J.; *Frontiers* **1998**.
25. Sheldon, R.A.; *Chemical Society Reviews* **2012,** *41*, (4), 1437-1451.
26. Finnveden, G.; Hauschild, M.Z.; Ekvall, T.; Guinée, J.; Heijungs, R.; Hellweg, S.; Koehler, A.; Pennington, D.; Suh, S.; *Journal of Environmental Management* **2009,** *91*, (1), 1-21.
27. Cook, T.R.; Zheng, Y.-R.; Stang, P.J.; *Chemical Reviews* **2013,** *113*, (1), 734-777.

28. Yang, Z.; Zhang, J.; Kintner-Meyer, M.C.W.; Lu, X.; Choi, D.; Lemmon, J.P.; Liu, J.; *Chemical Reviews* **2011,** *111*, (5), 3577-3613.

29. Lee, C.Y.; Farha, O.K.; Hong, B.J.; Sarjeant, A.A.; Nguyen, S.T.; Hupp, J.T.; *Journal of the American Chemical Society* **2011,** *133*, (40), 15858-15861.

30. Sheldon, R.A.; Arends, I.; Hanefeld, U., *Green chemistry and catalysis*; John Wiley & Sons: 2007.

31. Gaab, M.; Trukhan, N.; Maurer, S.; Gummaraju, R.; Müller, U.; *Microporous and Mesoporous Materials* **2012,** *157*, 131-136.

32. Friščić, T.; Halasz, I.; Štrukil, V.; Eckert-Maksić, M.; Dinnebier, R.E.; *Croatica Chemica Acta* **2012,** *85*, (3), 367-378.

33. Ibarra, I.A.; Bayliss, P.A.; Perez, E.; Yang, S.; Blake, A.J.; Nowell, H.; Allan, D.R.; Poliakoff, M.; Schroder, M.; *Green Chemistry* **2012,** *14*, (1), 117-122.

34. Sarawade, P.; Tan, H.; Polshettiwar, V.; *ACS Sustainable Chemistry & Engineering* **2013,** *1*, (1), 66-74.

35. Stock, N.; Biswas, S.; *Chemical Reviews* **2012,** *112*, (2), 933-969.

36. Rothenberg, G., *Catalysis: concepts and green applications*;John Wiley & Sons: 2017.

37. Couillaud, B.M.; Espeau, P.; Mignet, N.; Corvis, Y.; *ChemMedChem* **2019,** *14*, (1), 8-23.

38. Soldatov, D.V.; Terekhova, I.S.; *Journal of Structural Chemistry* **2005,** *46*, (1), S1-S8.

39. ALOthman, Z.A.; *Materials* **2012,** *5*, (12), 2874-2902.

40. Feng, X.; Ding, X.; Jiang, D.; *Chemical Society Reviews* **2012,** *41*, (18), 6010-6022.

41. Das, G.; Balaji Shinde, D.; Kandambeth, S.; Biswal, B.P.; Banerjee, R.; *Chemical Communications* **2014,** *50*, (84), 12615-12618.

42. Majano, G.; Borchardt, L.; Mitchell, S.; Valtchev, V.; Pérez-Ramírez, J.; *Microporous and Mesoporous Materials* **2014,** *194*, 106-114.

43. Farha, O.K.; Eryazici, I.; Jeong, N.C.; Hauser, B.G.; Wilmer, C.E.; Sarjeant, A.A.; Snurr, R.Q.; Nguyen, S.T.; Yazaydın, A.Ö.; Hupp, J.T.; *Journal of the American Chemical Society* **2012,** *134*, (36), 15016-15021.

44. Kitagawa, S.; Kitaura, R.; Noro, S.; *Angewandte Chemie International Edition* **2004,** *43*, (18), 2334-2375.

45. Chung, Y.G.; Camp, J.; Haranczyk, M.; Sikora, B.J.; Bury, W.; Krungleviciute, V.; Yildirim, T.; Farha, O.K.; Sholl, D.S.; Snurr, R.Q.; *Chemistry of Materials* **2014,** *26*, (21), 6185-6192.

46. Zhao, D.; Timmons, D.J.; Yuan, D.; Zhou, H.-C.; *Accounts of Chemical Research* **2011,** *44*, (2), 123-133.

47. Peng, Y.; Krungleviciute, V.; Eryazici, I.; Hupp, J.T.; Farha, O.K.; Yildirim, T.; *Journal of the American Chemical Society* **2013,** *135*, (32), 11887-11894.

48. Pang, J.; Jiang, F.; Wu, M.; Liu, C.; Su, K.; Lu, W.; Yuan, D.; Hong, M.; *Nature Communications* **2015,** *6*, 7575.

49. Rosi, N.L.; Eckert, J.; Eddaoudi, M.; Vodak, D.T.; Kim, J.; O'Keeffe, M.; Yaghi, O.M.; *Science* **2003,** *300*, (5622), 1127-1129.

50. Nandi, S.; De Luna, P.; Daff, T.D.; Rother, J.; Liu, M.; Buchanan, W.; Hawari, A.I.; Woo, T.K.; Vaidhyanathan, R.; *Science Advances* **2015,** *1*, (11).

51. Jin, S.; Son, H.-J.; Farha, O.K.; Wiederrecht, G.P.; Hupp, J.T.; *Journal of the American Chemical Society* **2013,** *135*, (3), 955-958.

52. He, Y.; Zhou, W.; Qian, G.; Chen, B.; *Chemical Society Reviews* **2014,** *43*, (16), 5657-5678.

53. Li, J.-R.; Kuppler, R.J.; Zhou, H.-C.; *Chemical Society Reviews* **2009,** *38*, (5), 1477-1504.

54. Lee, J.; Farha, O.K.; Roberts, J.; Scheidt, K.A.; Nguyen, S.T.; Hupp, J.T.; *Chemical Society Reviews* **2009,** *38*, (5), 1450-1459.

55. Ma, L.; Abney, C.; Lin, W.; *Chemical Society Reviews* **2009,** *38*, (5), 1248-1256.

56. Huxford, R.C.; Della Rocca, J.; Lin, W.; *Current Opinion in Chemical Biology* **2010,** *14*, (2), 262-268.

57. Horcajada, P.; Serre, C.; Maurin, G.; Ramsahye, N.A.; Balas, F.; Vallet-Regí, M.; Sebban, M.; Taulelle, F.; Férey, G.; *Journal of the American Chemical Society* **2008,** *130*, (21), 6774-6780.

58. Kuppler, R.J.; Timmons, D.J.; Fang, Q.-R.; Li, J.-R.; Makal, T.A.; Young, M.D.; Yuan, D.; Zhao, D.; Zhuang, W.; Zhou, H.-C.; *Coordination Chemistry Reviews* **2009,** *253*, (23–24), 3042-3066.

59. Kuppler, R.J.; Timmons, D.J.; Fang, Q.-R.; Li, J.-R.; Makal, T.A.; Young, M.D.; Yuan, D.; Zhao, D.; Zhuang, W.; Zhou, H.-C.; *Coordination Chemistry Reviews* **2009,** *253*, (23), 3042-3066.

60. Britt, D.; Furukawa, H.; Wang, B.; Glover, T.G.; Yaghi, O.M.; *Proceedings of the National Academy of Sciences* **2009,** *106*, (49), 20637-20640.

61. Zhuang, W.; Yuan, D.; Liu, D.; Zhong, C.; Li, J.-R.; Zhou, H.-C.; *Chemistry of Materials* **2012,** *24*, (1), 18-25.

62. Mlinar, A.N.; Keitz, B.K.; Gygi, D.; Bloch, E.D.; Long, J.R.; Bell, A.T.; *ACS Catalysis* **2014,** *4*, (3), 717-721.

63. Mueller, U.; Schubert, M.; Teich, F.; Puetter, H.; Schierle-Arndt, K.; Pastre, J.; *Journal of Materials Chemistry* **2006,** *16*, (7), 626-636.

64. Czaja, A.; Leung, E.; Trukhan, N.; Müller, U., Industrial MOF Synthesis. In *Metal-Organic Frameworks*; Wiley-VCH Verlag GmbH & Co. KGaA: 2011; pp 337-352.

65. Millet, D.; Bistagnino, L.; Lanzavecchia, C.; Camous, R.; Poldma, T.; *Journal of Cleaner Production* **2007,** *15*, (4), 335-346.

66. Anastas, P.T.; Warner, J.C.; *Green chemistry: Theory and practice* **1998**, 29-56.

67. Julien, P.A.; Mottillo, C.; Friščić, T.; *Green Chemistry* **2017,** *19*, (12), 2729-2747.

68. Douroumis, D.; Ross, S.A.; Nokhodchi, A.; *Advanced Drug Delivery Reviews* **2017,** *117*, 178-195.

69. Weyna, D.R.; Shattock, T.; Vishweshwar, P.; Zaworotko, M.J.; *Crystal Growth & Design* **2009,** *9*, (2), 1106-1123.

70. Crawford, D.E.; Miskimmin, C.K.G.; Albadarin, A.B.; Walker, G.; James, S.L.; *Green Chemistry* **2017,** *19*, (6), 1507-1518.

71. Lee, Y.-R.; Kim, J.; Ahn, W.-S.; *Korean Journal of Chemical Engineering* **2013,** *30*, (9), 1667-1680.

72. Banerjee, R.; Phan, A.; Wang, B.; Knobler, C.; Furukawa, H.; O'Keeffe, M.; Yaghi, O.M.; *Science* **2008,** *319*, (5865), 939-943.

73. Stock, N.; *Microporous and Mesoporous Materials* **2010,** *129*, (3), 287-295.

74. Ahnfeldt, T.; Moellmer, J.; Guillerm, V.; Staudt, R.; Serre, C.; Stock, N.; *Chemistry – A European Journal* **2011,** *17*, (23), 6462-6468.

75. Millange, F.; Medina, M.I.; Guillou, N.; Férey, G.; Golden, K.M.; Walton, R.I.; *Angewandte Chemie International Edition* **2010,** *49*, (4), 763-766.

76. Lanchas, M.; Vallejo-Sanchez, D.; Beobide, G.; Castillo, O.; Aguayo, A.T.; Luque, A.; Roman, P.; *Chemical Communications* **2012,** *48*, (79), 9930-9932.

77. Lanchas, M.; Arcediano, S.; Aguayo, A.T.; Beobide, G.; Castillo, O.; Cepeda, J.; Vallejo-Sanchez, D.; Luque, A.; *RSC Advances* **2014,** *4*, (104), 60409-60412.

78. Lin, J.-B.; Lin, R.-B.; Cheng, X.-N.; Zhang, J.-P.; Chen, X.-M.; *Chemical Communications* **2011,** *47*, (32), 9185-9187.

79. Klinowski, J.; Almeida Paz, F.A.; Silva, P.; Rocha, J.; *Dalton Transactions* **2011,** *40*, (2), 321-330.

80. Schlesinger, M.; Schulze, S.; Hietschold, M.; Mehring, M.; *Microporous and Mesoporous Materials* **2010,** *132*, (1), 121-127.

81. Albuquerque, G.H.; Fitzmorris, R.C.; Ahmadi, M.; Wannenmacher, N.; Thallapally, P.K.; McGrail, B.P.; Herman, G.S.; *CrystEngComm* **2015,** *17*, (29), 5502-5510.

82. Martinez Joaristi, A.; Juan-Alcañiz, J.; Serra-Crespo, P.; Kapteijn, F.; Gascon, J.; *Crystal Growth & Design* **2012,** *12*, (7), 3489-3498.

83. Czaja, A.U.; Trukhan, N.; Muller, U.; *Chemical Society Reviews* **2009,** *38*, (5), 1284-1293.

84. Glavinovic, M.; Qi, F.; Katsenis, A.D.; Friscic, T.; Lumb, J.-P.; *Chemical Science* **2016,** *7*, (1), 707-712.

85. Son, W.-J.; Kim, J.; Kim, J.; Ahn, W.-S.; *Chemical Communications* **2008**, (47), 6336-6338.

86. Kim, J.; Yang, S.-T.; Choi, S.B.; Sim, J.; Kim, J.; Ahn, W.-S.; *Journal of Materials Chemistry* **2011,** *21*, (9), 3070-3076.

87. Cliffe, M.J.; Mottillo, C.; Stein, R.S.; Bucar, D.-K.; Friscic, T.; *Chemical Science* **2012,** *3*, (8), 2495-2500.

88. Mottillo, C.; Lu, Y.; Pham, M.-H.; Cliffe, M.J.; Do, T.-O.; Friscic, T.; *Green Chemistry* **2013,** *15*, (8), 2121-2131.

89. Friščić, T.; Reid, D.G.; Halasz, I.; Stein, R.S.; Dinnebier, R.E.; Duer, M.J.; *Angewandte Chemie* **2010,** *122*, (4), 724-727.

90. Klimakow, M.; Klobes, P.; Thünemann, A.F.; Rademann, K.; Emmerling, F.; *Chemistry of Materials* **2010,** *22*, (18), 5216-5221.

91. DeSantis, D.; Mason, J.A.; James, B.D.; Houchins, C.; Long, J.R.; Veenstra, M.; *Energy & Fuels* **2017,** *31*, (2), 2024-2032.

92. Jones, W.; Eddleston, M.D.; *Faraday Discussions* **2014,** *170*, (0), 9-34.

93. James, S.L.; Friščić, T.; *Chemical Society Reviews* **2013,** *42*, (18), 7494-7496.

94. Do, J.-L.; Friščić, T.; *ACS Central Science* **2017,** *3*, (1), 13-19.

95. Scholz, G.; Feist, M.; Kemnitz, E.; *Solid State Sciences* **2008,** *10*, (11), 1640-1650.

96. Huskić, I.; Christopherson, J.-C.; Užarević, K.; Friščić, T.; *Chemical Communications* **2016,** *52*, (29), 5120-5123.

97. Takacs, L.; *Chemical Society Reviews* **2013,** *42*, (18), 7649-7659.

98. Baláž, P.; Achimovičová, M.; Baláž, M.; Billik, P.; Cherkezova-Zheleva, Z.; Criado, J.M.; Delogu, F.; Dutková, E.; Gaffet, E.; Gotor, F.J., et al.; *Chemical Society Reviews* **2013,** *42*, (18), 7571-7637.

99. Tumanov, I.A.; Achkasov, A.F.; Boldyreva, E.V.; Boldyrev, V.V.; *CrystEngComm* **2011,** *13*, (7), 2213-2216.

100. Friščić, T.; Childs, S.L.; Rizvi, S.A.A.; Jones, W.; *CrystEngComm* **2009,** *11*, (3), 418-426.

101. Braga, D.; Maini, L.; Grepioni, F.; *Chemical Society Reviews* **2013,** *42*, (18), 7638-7648.

102. Toda, F.; Tanaka, K.; Sekikawa, A.; *Journal of the Chemical Society, Chemical Communications* **1987**, (4), 279-280.

103. Etter, M.C.; Reutzel, S.M.; Choo, C.G.; *Journal of the American Chemical Society* **1993,** *115*, (10), 4411-4412.

104. Friščić, T.; *Chemical Society Reviews* **2012,** *41*, (9), 3493-3510.

105. Caira, M.R.; Nassimbeni, L.R.; Wildervanck, A.F.; *Journal of the Chemical Society, Perkin Transactions 2* **1995**, (12), 2213-2216.

106. Delori, A.; Friščić, T.; Jones, W.; *CrystEngComm* **2012,** *14*, (7), 2350-2362.

107. Hasa, D.; Jones, W.; *Advanced Drug Delivery Reviews* **2017,** *117*, 147-161.

108. Karimi-Jafari, M.; Padrela, L.; Walker, G.M.; Croker, D.M.; *Crystal Growth & Design* **2018,** *18*, (10), 6370-6387.

109. Garay, A.L.; Pichon, A.; James, S.L.; *Chemical Society Reviews* **2007,** *36*, (6), 846-855.

110. Adams, C.J.; Haddow, M.F.; Lusi, M.; Orpen, A.G.; *Proceedings of the National Academy of Sciences* **2010,** *107*, (37), 16033-16038.

111. Adams, C.J.; Kurawa, M.A.; Orpen, A.G.; *Inorganic Chemistry* **2010,** *49*, (22), 10475-10485.

112. Pichon, A.; Lazuen-Garay, A.; James, S.L.; *CrystEngComm* **2006,** *8*, (3), 211-214.

113. Pichon, A.; James, S.L.; *CrystEngComm* **2008,** *10*, (12), 1839-1847.

114. Yuan, W.; Garay, A.L.; Pichon, A.; Clowes, R.; Wood, C.D.; Cooper, A.I.; James, S.L.; *CrystEngComm* **2010,** *12*, (12), 4063-4065.

115. Friscic, T.; *Journal of Materials Chemistry* **2010,** *20*, (36), 7599-7605.

116. Adams, C.J.; Colquhoun, H.M.; Crawford, P.C.; Lusi, M.; Orpen, A.G.; *Angewandte Chemie International Edition* **2007,** *46*, (7), 1124-1128.

117. Friščić, T.; Reid, D.G.; Halasz, I.; Stein, R.S.; Dinnebier, R.E.; Duer, M.J.; *Angewandte Chemie International Edition* **2010,** *49*, (4), 712-715.

118. Friscic, T.; Fabian, L.; *CrystEngComm* **2009,** *11*, (5), 743-745.

119. Beldon, P.J.; Fábián, L.; Stein, R.S.; Thirumurugan, A.; Cheetham, A.K.; Friščić, T.; *Angewandte Chemie International Edition* **2010,** *49*, (50), 9640-9643.

120. Yuan, W.; O'Connor, J.; James*, S.L.; *CrystEngComm* **2010,** *12*, (11), 3515-3517.

121. Strobridge, F.C.; Judas, N.; Friscic, T.; *CrystEngComm* **2010,** *12*, (8), 2409-2418.

122. Wang, L.J.; Deng, H.; Furukawa, H.; Gándara, F.; Cordova, K.E.; Peri, D.; Yaghi, O.M.; *Inorganic Chemistry* **2014,** *53*, (12), 5881-5883.

123. Adams, C.J.; Gillon, A.L.; Lusi, M.; Orpen, A.G.; *CrystEngComm* **2010,** *12*, (12), 4403-4409.

124. Yuan, W.; Friščić, T.; Apperley, D.; James, S.L.; *Angewandte Chemie International Edition* **2010,** *49*, (23), 3916-3919.

125. Crawford, D.; Casaban, J.; Haydon, R.; Giri, N.; McNally, T.; James, S.L.; *Chemical Science* **2015,** *6*, (3), 1645-1649.

126. Commons, W. File:Raman energy levels.svg. https://commons.wikimedia.org/w/index.php?title=File:Raman_energy_levels.svg&oldid=194552951 (June 25th 2019),

127. contributors, W.C. File: Bragg diffraction 2.svg. https://commons.wikimedia.org/w/index.php?title=File:Bragg_diffraction_2.svg&oldid=219002913 (June 25th 2019),

128. contributors, W.C. File: Jablonski Diagram of Fluorescence Only.png. https://commons.wikimedia.org/w/index.php?title=File:Jablonski_Diagram_of_Fluorescence_Only.png&oldid=237484813 (June 25th 2019),

129. Lukin, S.; Tireli, M.; Lončarić, I.; Barišić, D.; Šket, P.; Vrsaljko, D.; di Michiel, M.; Plavec, J.; Užarević, K.; Halasz, I.; *Chemical Communications* **2018,** *54*, (94), 13216-13219.

130. Turberg, M.; Ardila-Fierro, K.J.; Bolm, C.; Hernández, J.G.; *Angewandte Chemie International Edition* **2018,** *57*, (33), 10718-10722.

131. Do, J.-L.; Mottillo, C.; Tan, D.; Štrukil, V.; Friščić, T.; *Journal of the American Chemical Society* **2015,** *137*, (7), 2476-2479.

132. Do, J.L.; Tan, D.; Friscic, T.; *Angewandte Chemie International Edition* **2018,** *57*, (10), 2667-2671.

133. Andersen, J.M.; Mack, J.; *Chemical Science* **2017,** *8*, (8), 5447-5453.

134. Andersen, J.; Mack, J.; *Angewandte Chemie International Edition* **2018,** *57*, (40), 13062-13065.

135. Schrader, R.; Hoffmann, B.; *Zeitschrift für anorganische und allgemeine Chemie* **1969,** *369*, (1-2), 41-47.

136. Schmidt, R.; Stolle, A.; Ondruschka, B.; *Green Chemistry* **2012,** *14*, (6), 1673-1679.

137. Hutchings, B.P.; Crawford, D.E.; Gao, L.; Hu, P.; James, S.L.; *Angewandte Chemie International Edition* **2017,** *56*, (48), 15252-15256.

138. Karki, S.; Friščić, T.; Jones, W.; *CrystEngComm* **2009,** *11*, (3), 470-481.

139. Ma, X.; Yuan, W.; Bell, S.E.J.; James, S.L.; *Chemical Communications* **2014,** *50*, (13), 1585-1587.

140. Lien Nguyen, K.; Friščić, T.; Day, G.M.; Gladden, L.F.; Jones, W.; *Nature Materials* **2007,** *6*, 206.

141. Hermann, G.N.; Unruh, M.T.; Jung, S.H.; Krings, M.; Bolm, C.; *Angewandte Chemie International Edition* **2018,** *57*, (33), 10723-10727.

142. Julien, P.A.; Užarević, K.; Katsenis, A.D.; Kimber, S.A.J.; Wang, T.; Farha, O.K.; Zhang, Y.; Casaban, J.; Germann, L.S.; Etter, M., et al.; *Journal of the American Chemical Society* **2016,** *138*, (9), 2929-2932.

143. Chen, Y.; Williams, J.S.; *Journal of Materials Research* **1996,** *11*, (6), 1500-1506.

144. Chin, Z.H.; Perng, T.P.; *Applied Physics Letters* **1997,** *70*, (18), 2380-2382.

145. Takacs, L.; *Progress in Materials Science* **2002,** *47*, (4), 355-414.

146. Užarević, K.; Halasz, I.; Friščić, T.; *The Journal of Physical Chemistry Letters* **2015,** *6*, (20), 4129-4140.

147. Halasz, I.; Kimber, S.A.J.; Beldon, P.J.; Belenguer, A.M.; Adams, F.; Honkimäki, V.; Nightingale, R.C.; Dinnebier, R.E.; Friščić, T.; *Nature Protocols* **2013,** *8*, 1718.

148. Friščić, T.; Halasz, I.; Beldon, P.J.; Belenguer, A.M.; Adams, F.; Kimber, S.A.J.; Honkimäki, V.; Dinnebier, R.E.; *Nature Chemistry* **2012,** *5*, 66.

149. Halasz, I.; Friščić, T.; Kimber, S.A.J.; Užarević, K.; Puškarić, A.; Mottillo, C.; Julien, P.; Štrukil, V.; Honkimäki, V.; Dinnebier, R.E.; *Faraday Discussions* **2014,** *170*, (0), 203-221.

150. Halasz, I.; Puskaric, A.; Kimber, S.A.; Beldon, P.J.; Belenguer, A.M.; Adams, F.; Honkimaki, V.; Dinnebier, R.E.; Patel, B.; Jones, W., et al.; *Angewandte Chemie International Edition* **2013,** *52*, (44), 11538-11541.

151. Katsenis, A.D.; Puškarić, A.; Štrukil, V.; Mottillo, C.; Julien, P.A.; Užarević, K.; Pham, M.-H.; Do, T.-O.; Kimber, S.A.J.; Lazić, P., et al.; *Nature Communications* **2015,** *6*, 6662.

152. Akimbekov, Z.; Katsenis, A.D.; Nagabhushana, G.P.; Ayoub, G.; Arhangelskis, M.; Morris, A.J.; Friščić, T.; Navrotsky, A.; *Journal of the American Chemical Society* **2017,** *139*, (23), 7952-7957.

153. Stolar, T.; Batzdorf, L.; Lukin, S.; Žilić, D.; Motillo, C.; Friščić, T.; Emmerling, F.; Halasz, I.; Užarević, K.; *Inorganic Chemistry* **2017,** *56*, (11), 6599-6608.

154. Fidelli, A.M.; Karadeniz, B.; Howarth, A.J.; Huskić, I.; Germann, L.S.; Halasz, I.; Etter, M.; Moon, S.-Y.; Dinnebier, R.E.; Stilinović, V., et al.; *Chemical Communications* **2018,** *54*, (51), 6999-7002.

155. Gracin, D.; Strukil, V.; Friscic, T.; Halasz, I.; Uzarevic, K.; *Angewandte Chemie International Edition* **2014,** *53*, (24), 6193-6197.

156. Juribašić, M.; Užarević, K.; Gracin, D.; Ćurić, M.; *Chemical Communications* **2014,** *50*, (71), 10287-10290.

157. Bjelopetrović, A.; Lukin, S.; Halasz, I.; Užarević, K.; Đilović, I.; Barišić, D.; Budimir, A.; Juribašić Kulcsár, M.; Ćurić, M.; *Chemistry- A European Journal* **2018,** *24*, (42), 10672-10682.

158. Tireli, M.; Juribašić Kulcsár, M.; Cindro, N.; Gracin, D.; Biliškov, N.; Borovina, M.; Ćurić, M.; Halasz, I.; Užarević, K.; *Chemical Communications* **2015,** *51*, (38), 8058-8061.

159. Julien, P.A.; Malvestiti, I.; Friščić, T.; *Beilstein Journal of Organic Chemistry* **2017,** *13*, 2160-2168.

160. Biliškov, N.; Borgschulte, A.; Užarević, K.; Halasz, I.; Lukin, S.; Milošević, S.; Milanović, I.; Novaković, J.G.; *Chemistry- A European Journal* **2017,** *23*, (64), 16274-16282.

161. Lisac, K.; Topić, F.; Arhangelskis, M.; Cepić, S.; Julien, P.A.; Nickels, C.W.; Morris, A.J.; Friščić, T.; Cinčić, D.; *Nature Communications* **2019,** *10*, (1), 61.

162. Batzdorf, L.; Fischer, F.; Wilke, M.; Wenzel, K.-J.; Emmerling, F.; *Angewandte Chemie International Edition* **2015,** *54*, (6), 1799-1802.

163. Lukin, S.; Stolar, T.; Tireli, M.; Blanco, M.V.; Babic, D.; Friscic, T.; Uzarevic, K.; Halasz, I.; *Chemistry- A European Journal* **2017,** *23*, (56), 13941-13949.

164. Lukin, S.; Tireli, M.; Stolar, T.; Barišić, D.; Blanco, M.V.; di Michiel, M.; Užarević, K.; Halasz, I.; *Journal of the American Chemical Society* **2019,** *141*, (3), 1212-1216.

165. Stolar, T.; Lukin, S.; Tireli, M.; Sović, I.; Karadeniz, B.; Kereković, I.; Matijašić, G.; Gretić, M.; Katančić, Z.; Dejanovic, I., et al.; *ACS Sustainable Chemistry & Engineering* **2019**.

166. Kulla, H.; Haferkamp, S.; Akhmetova, I.; Rollig, M.; Maierhofer, C.; Rademann, K.; Emmerling, F.; *Angewandte Chemie International Edition* **2018,** *57*, (20), 5930-5933.

167. Užarević, K.; Ferdelji, N.; Mrla, T.; Julien, P.A.; Halasz, B.; Friščić, T.; Halasz, I.; *Chemical Science* **2018,** *9*, (9), 2525-2532.

3. Methodology Development

3.01 Introduction and Chapter Summary

This chapter highlights the advances in both instrumentation and data processing which were developed throughout this Thesis. As these advances are distributed throughout the experimental sections and supplementary information sections of various manuscripts and chapters which constitute the rest of the Thesis, this chapter serves to highlight the key methodological advancements which enabled much of the work in this Thesis. Monitoring mechanochemistry has recently garnered considerable attention by the synthetic chemical research community as a means of better understanding mechanochemical reactions. If mechanochemistry is to be broadly applied and understood, accessible methods capable of producing high quality real-time data for a wide variety of chemical systems are critical. This chapter is designed to provide an overview and discussion focused on improvements in instrumental setups and data processing and highlight novel contributions of this Thesis.

Efforts in this Thesis towards improving real-time monitoring of milling reactions were focused on 1) acquiring novel types of *in situ* data on mechanochemical reactions, 2) improvements in applicability and data quality for existing setups and 3) finding effective methods for processing this data. Several advancements developed in this Thesis are significant enough to warrant highlighting as they have the potential to significantly aid in the understanding of mechanochemical reactions, such as the application of *in situ* fluorescence emission spectroscopy. The development of novel jars from optical grade sapphire capable of withstanding prolonged milling possess excellent optical properties enabled *in situ* Raman monitoring of previously unobservable reactions. Finally, the need to efficiently process large volumes of data drove the development of a data processing approach implemented in MATLAB.[1]

3.02 Development of Fluorescence

Fluorescence spectroscopy is an appealing candidate for monitoring mechanochemical reactions, which is highly complementary to existing techniques.

Fluorescence is generally much more sensitive relative to Raman spectroscopy,[2] has few interference issues, requires a relatively simple and low-cost setup, and in contrast to diffraction and Raman approaches does not require a focused beam, which can minimize the effect of sample movement.

The optically transparent jars developed in this Thesis and utilized for Raman spectroscopy enable other types of spectroscopy in the visible region. As transmission-based measurements are often challenging due to the motion of the milling vessel and varying sample distribution, fluorescence was chosen as a promising candidate for monitoring milling reactions due to its strong signal and flexible instrumental geometry. Building a setup for fluorescence monitoring of milling reactions fundamentally consists of three parts: (1) an excitation source, (2) an optically transparent jar capable of withstanding milling and transmitting both excitation and emission wavelengths, and (3) collection and analysis of the light by a spectrometer.

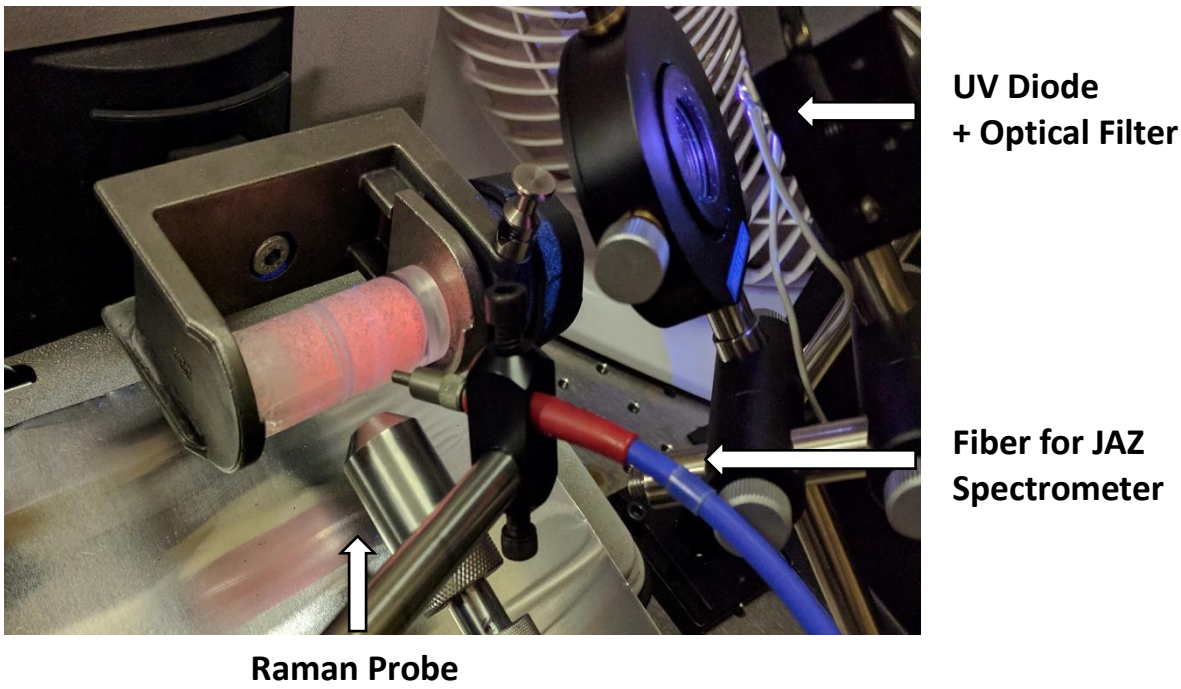

Figure 40. Setup for combined fluorescence and Raman monitoring of milling reactions.

(a) Excitation Source

In order to validate the fluorescence measurements and ensure compatibility with Raman spectroscopy, fluorescent systems with an excitation wavelength in the ultraviolet

(UV) range and a visible emission below 700nm were selected to enable the use of the 785nm excitation laser for Raman spectroscopy without interference. UV excitation centered at 365nm was chosen due to the prevalence of relatively inexpensive UV light emitting diodes (LEDs) (LED Engin LZ4-04UV00-0000) at this wavelength, which provide considerably more excitation power at a far lower cost than excitation sources such as xenon arc or deuterium lamps.[3] In order to ensure that red-shifted light originates from fluorescence and is not produced by the excitation diode, a 400nm short-pass optical filter is used between the excitation source and the milling jar. In certain cases, the broad band excitation from diodes complicates the interpretation of fluorescence data, so a 375nm laser (Coherent® OBIS™ 1185045 | 375nm LX 16mW Laser) has been utilized, which has one of the lowest wavelengths currently commercially available at relatively low cost with a narrow line shape and high intensity. As shown in Figure 40, an advantage of utilizing an excitation diode is the ability to illuminate the entire sample jar, which averages out the distribution of material being measured, the laser beam was dispersed to minimize variations in fluorescence intensity due to stochastic variations of material moving in the jar while milling. The developed approach is compatible with other light sources, as nearly any light source can be integrated into the current setup using fiber optics. As the prevalence of low-cost UV light sources continues to expand,[3] this setup can easily be modified to monitor a wide variety of reactions assuming suitable excitation sources and jar material.

(b) Optically Transparent Milling Jars

Measuring *in situ* fluorescence for milling reactions requires an appropriate transparency of the milling jar. In this Thesis, excitation has been limited to the UV-A range (315-400nm), however, even shorter wavelengths UV-B (280–315nm) and UV-C (100–280nm) would be desirable for monitoring reactions, as this expands the number of molecules that can be monitored *via* fluorescence. For molecules excited in the UV-A range, polymer-based milling vessels previously employed in the literature on *in situ* techniques[4-7] can be used. These milling jars are readily available, low cost, and tolerant of milling conditions, however, PMMA and other transparent polymers exhibit considerable absorption below 350nm. For molecules which require excitation in the UV-B or UV-C range, we have developed sapphire milling jars due to their strength, hardness,

and optical transparency from 200nm to 6µm, enabling a wide variety of measurements from the deep UV to the mid-infrared while surviving the impact forces of milling. While all the projects in this Thesis focus on the 375nm excitation range and emission under 700nm, the developed approach can readily be extended to the entire range from UV-C to mid-IR provided appropriate sources and detectors are available.

(c) Collecting and Analyzing the Fluorescence

The final part of the fluorescence setup is collecting and analyzing the fluorescence emission spectrum. For the sake of simplicity, a fiber optic coupled spectrometer was chosen to measure the fluorescence emission, with the fiber optic pointing at the fluorescent jar. Modern portable spectrometers such as the Ocean Optics QE65000 used in this work rely on silicon based Charge Coupled Device (CCD) detectors which enable the rapid acquisition of the entire visible spectrum of the emission without the need for scanning monochromators.[8, 9] Fortunately, fluorescence sensitivity is nearly ten orders of magnitude stronger than non-resonant Raman scattering,[2] meaning spectra can potentially be collected at much faster time resolution than other current *in situ* techniques such as powder X-ray diffraction and Raman spectroscopy. Given the desire to monitor reactions in real-time, a rapid acquisition rate is critical for understanding reactivity for rapid reactions and differentiating kinetic models which may have similar profiles.

Despite these notable advantages, interpretation of fluorescence data poses a challenge, as the emission is generally broad and may be difficult to interpret, as demonstrated by the similarity of the spectra of indometacin and the co-crystal of indometacin-saccharin in Figure 41. In contrast, diffraction and vibrational spectroscopy provide well-defined and separated peaks. Changes in chemical or supramolecular structure can result in subtle shifts in shape of the emission profile or changes in intensity. Computational methods such as DFT provide a means of correlating structural changes with shifts in the fluorescence emission of molecules utilizing time-dependent density functional theory (TD-DFT).[10] The case of monitoring mechanochemistry through the fluorescence emission of solids is further complicated by the influence of the solid-state environment, which requires more computationally intensive periodic calculations to model and understand fluorescence emission and Raman spectra.[10, 11]

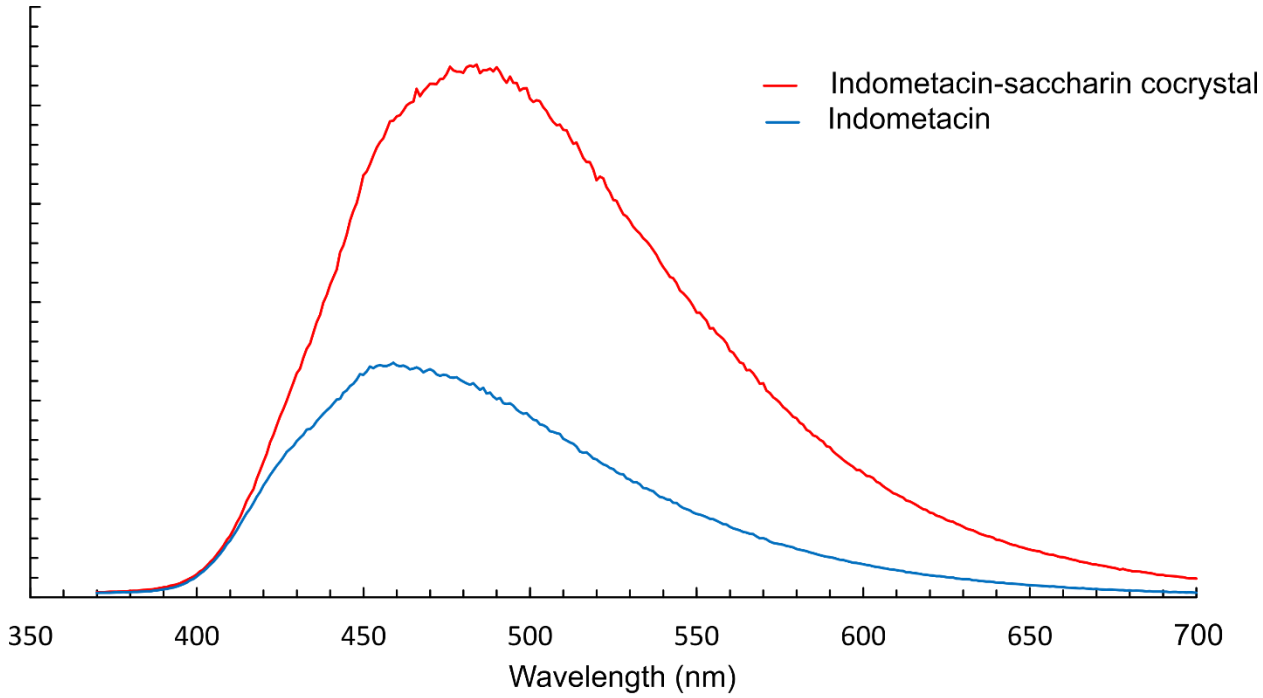

Figure 41. Fluorescence emission of indometacin and the indometacin-saccharin co-crystal, recorded using Biotek Synergy 2 multi-mode microplate reader using a transparent polystyrene plate.

Certain lanthanide elements exhibit well-defined fluorescence emission lines corresponding to *d-f* and *f-f* transitions,[12] although for efficient luminescence they often require a ligand which acts as an "antenna" which absorbs incoming UV photons and transfers the energy to the lanthanide ion which emits (Figure 42). The narrow and well-defined emission lines of lanthanides are particularly useful for real-time reaction monitoring, as these emission lines can be easily distinguished from instrumental background. Europium(III) is particularly appealing as the relative intensity of emission bands change as a function of the coordination environment,[13] enabling monitoring changes in the lanthanide ion coordination environment in a wide variety of materials. This provides a responsive probe for the chemistry of lanthanide elements allowing the detection of different coordination species and reaction kinetics. However, understanding the structural information contained in this luminescence remains a challenge as

theoretical methods for interpreting and predicting lanthanide luminescence remains an active area of research.[14]

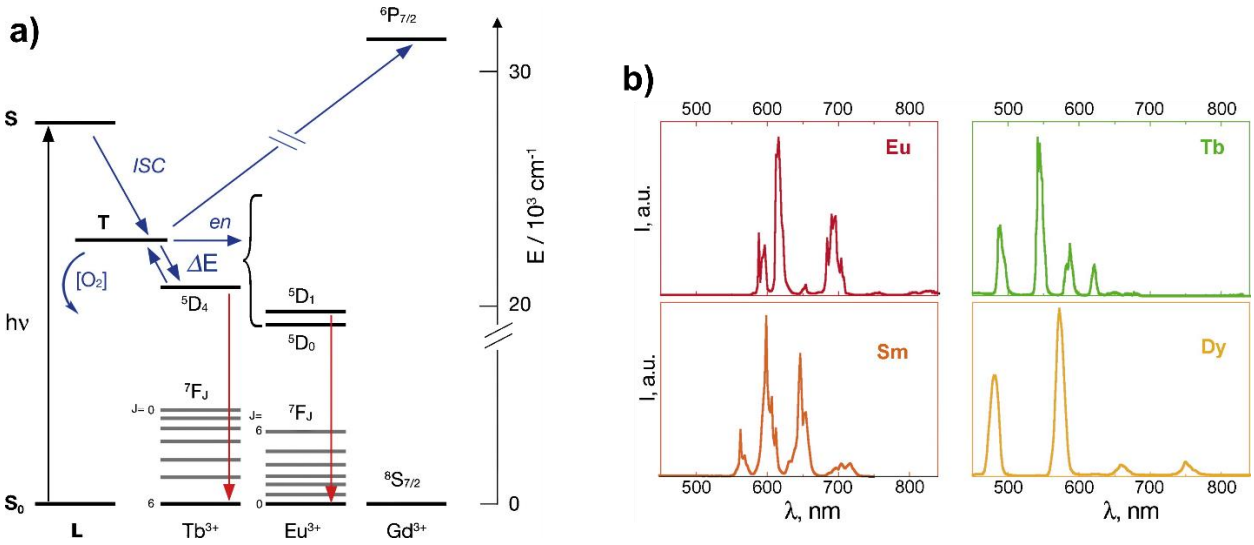

Figure 42. a) The antenna effect of ligand (L) transferring energy non-radiatively (blue arrows) for radiative emission by lanthanide ions. b) Fluorescence emission spectra of lanthanide emitters: Eu, Tb, Sm, and Dy with the same ligand. Reproduced with modification from [12].

3.03 Sapphire Milling Jars

Conducting *in situ* Raman monitoring through PMMA milling jars revealed the inherent challenge of monitoring chemical reactions of organic molecules through a material which possesses similar Raman active bands. This along with the desire to access the UV-B and UV-C regions for fluorescence excitation, motivated a search for alternative jar materials with superior optical properties and potential to survive milling. The most promising candidate identified was sapphire which is both extremely hard (~9 on the Mohs scale, Young's Modulus: ~370 GPa[15]) and exhibits exceptional optical transmission throughout the UV to mid-IR range and exhibits few Raman bands at relatively low wavenumbers, avoiding overlap with most systems so far studied *via in situ* Raman.

(a) Design and Stability

As sapphire is grown as single crystals which are subsequently carved into shape, the following design principles were followed: 1) minimize the complexity of the sapphire piece, and 2) maximize the uninterrupted length of sapphire for measurement. In contrast to previous PMMA designs, the sapphire final design was the use of a standard tube of optical grade sapphire lowering custom design costs purchased from Rayotek Scientific Inc., which is capped at both ends with polytetrafluoroethylene (PTFE) caps designed and manufactured by FormTechScientific as shown in Figure 43.

Figure 43. a) Sapphire milling jar with a pen for scale b) standard design of the PMMA milling jar from FormTechScientific.

While the hardness of sapphire enables it to withstand milling, the precise design of both the jar and milling media utilized were designed to avoid catastrophic failure of the jar. Milling produces impacts capable of shattering sapphire due to its brittle nature, evidenced in the failure of a jar prototype. However, the extreme hardness of sapphire destroyed most rigid materials considerably softer than itself such as stainless-steel milling media upon impact, resulting in contaminated samples. As such, either materials with similar hardness such as zirconia (~8 Mohs scale, Young's Modulus: ~144 GPa[15]) or soft non-brittle materials such as polymers were used. Maintaining strong impact forces is critical for many reactions in mechanochemistry, favoring the use of hard milling media. The narrower design of the sapphire jar enabled lower sample loadings and minimizes the ability for the zirconia ball to impact perpendicular to the sapphire. It was speculated

that maximizing the parallel force vector between the ball and the sapphire coupled with the flexible PTFE end caps which tend to bounce the ball from one end to another enables the jar to survive the significant impact force of milling at 30Hz for prolonged periods of time, while maintaining impacts on the sample. However, this places limitations on the milling media, as loading more than one milling ball resulted in small cracks in the jar and is therefore not recommended. The jar has so far withstood well over 50 hours of milling without failure. The main drawback of the current design is the lack of curvature at the ends of the jar which result in accumulation of sample in the corner of the jar. Future redesign of the PTFE endcaps has the potential to mitigate this disadvantage.

(b) Optical Properties

The principal benefit of utilizing sapphire vessels for real-time measurements is the improved optical properties in fluorescence and Raman spectroscopy studies. While the improved optical transmission into the deep UV has not yet been tested, due to a lack of appropriate sources, a dramatic improvement in Raman spectroscopy measurements was observed in terms of background spectrum. The polymer jar exhibits numerous Raman bands throughout the spectrum, while sapphire displays 5 large bands all under 1000 cm^{-1}, as shown in Figure 44.

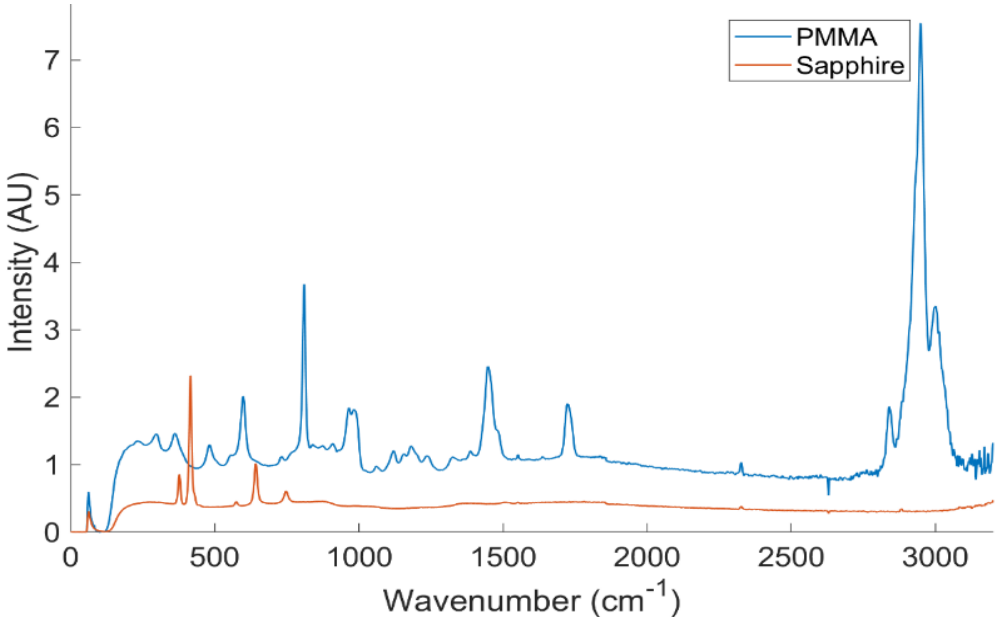

Figure 44. Comparison of uncorrected Raman spectra of PMMA and sapphire milling jar.

The use of sapphire minimizes the interference of the Raman signals of the milling jar with those from the reaction and allows for the detection of signals difficult to measure with polymer jars such as the reaction between calcium carbonate, urea, and urea phosphate shown in Figure 45. In contrast to many measurements in PMMA jars, the jar signal intensity of sapphire is often comparable to the sample intensity. Interestingly, despite much higher sensitivity and much lower interference from the jar, it was observed that sapphire jars generally exhibit lower Raman spectral intensity than polymer jars under the same conditions. This lower intensity may be due to more efficient optical transmission and the high refractive index of sapphire (~1.77) which may result in less light being collected by the backscattering probe.

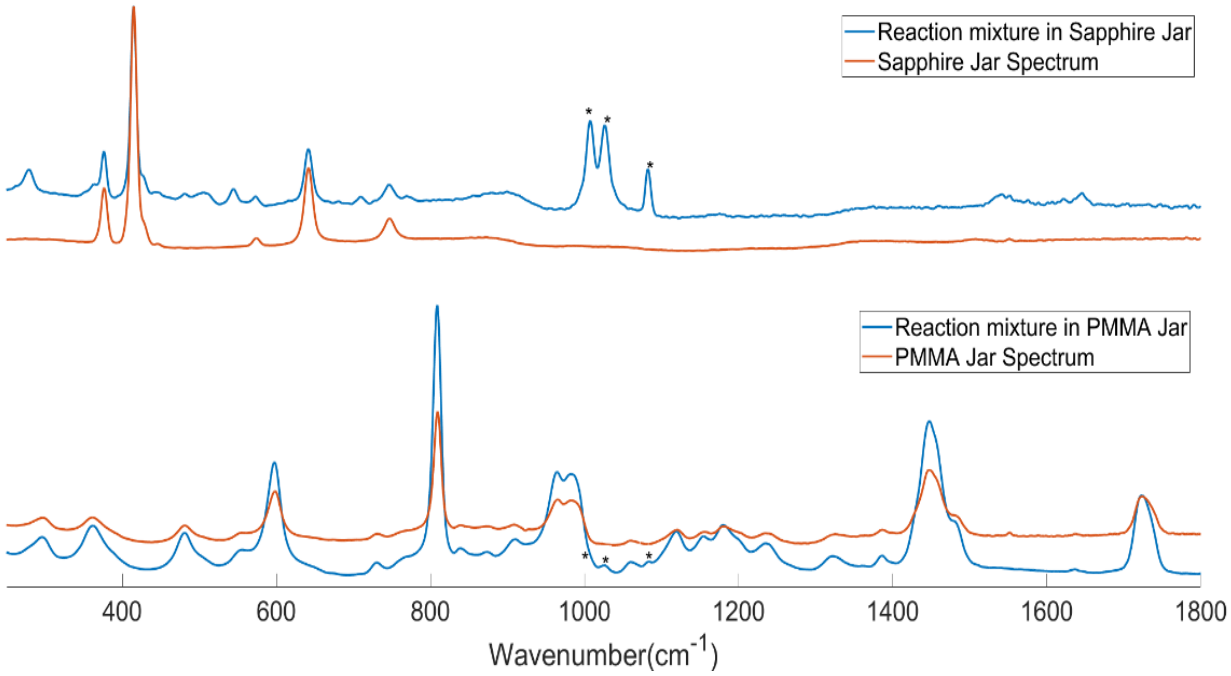

*Figure 45. Normalized in situ Raman spectra for the reaction of calcium carbonate with urea and urea phosphate in sapphire (top) and PMMA (bottom) jars. * denote the most prominent peaks of the reaction.*

The improved optical performance of the sapphire jars was pivotal in the execution of the work on calcium urea phosphate co-crystals (Chapter 9) where Raman monitoring was only possible using sapphire.

(c) Diffraction Properties of Sapphire Milling Jar

Evaluation of sapphire milling jars for use in real-time synchrotron X-ray diffraction measurements was conducted at the PETRA III beamline P02.1 at Deutsches Elektronen-Synchrotron (DESY), with λ = 0.207 Å, using a setup analogous to previous reports.[4] Sapphire jars are produced from a single crystal, so diffraction spots (averaged over the motion of the mill) are observed in contrast to the broad diffraction from polymer jars as shown in Figure 46a and b. The high crystallinity of sapphire results in intense diffraction at a few spots, which are highly dependent on the orientation of the jar. Fortunately, despite detector oversaturation no change in detector response was observed at these pixels, suggesting that measurements can be conducted with similar integration and exposure times to polymer jars. As powder diffraction patterns are generated from these detector images *via* radial diffraction, the monocrystalline diffraction spots can be masked without eliminating powder diffraction peaks at this 2-theta value, assuming a fixed jar orientation. Such masking is not possible for PMMA as the diffraction pattern exists as Debye-Scherrer rings which cannot be masked without information loss for the corresponding diffraction angle. Efficient masking results in the powder diffraction spectrum with virtually no background, which may be of particular importance when examining reactions with poor crystallinity or considerable amorphous content which may be difficult to differentiate from the broad amorphous diffraction of PMMA, as shown in radial integration of the diffraction images in Figure 46c.

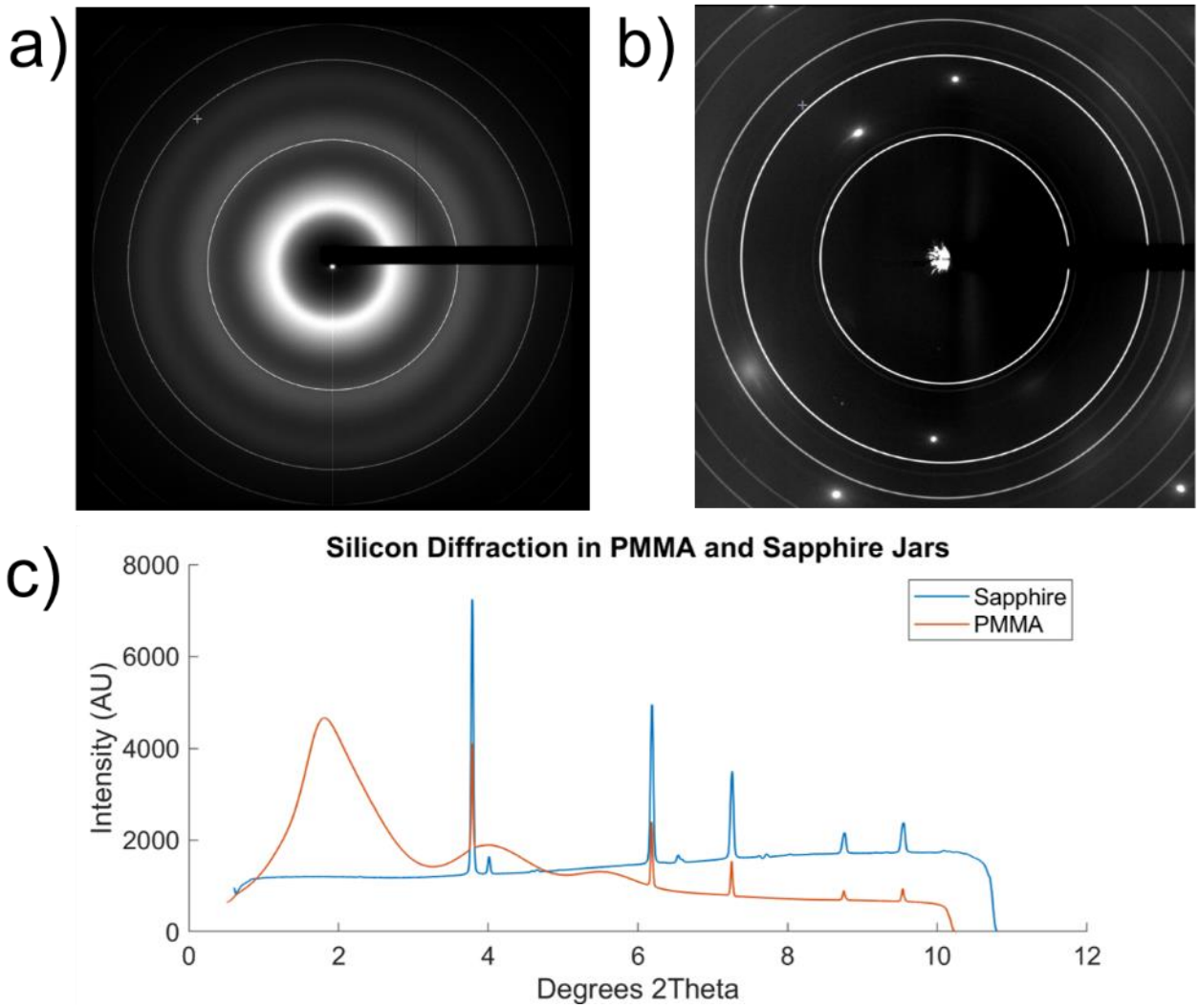

Figure 46. a) Synchrotron diffraction of crystalline silicon in a PMMA milling jar with broad background profile. Lighter color denotes higher intensity. b) synchrotron X-ray diffraction of Si in the sapphire milling jar with single crystal diffraction spots. c) Integrated diffraction of Si in a sapphire jar (masked) and a PMMA jar. Extra peaks of silicon in the sapphire jar are due to poor positioning of the sapphire jar as preliminary measurements of the sapphire jar were conducted under conditions optimized for PMMA, resulting in diffraction from sample on the front and back walls of the milling jar.

Experimental setups designed to account for jar orientation and data processing methods capable of differentiating single diffraction spots versus Debye-Scherrer rings may enable the measurement of *in situ* powder diffraction data on milling reactions with

little to no background contribution of the milling jar, which may be particularly informative for cases with amorphous phases or total scattering analysis.

3.04 Data Processing

Real-time monitoring of a mechanochemical reaction generates large volumes of data (typically between 180-1000 spectra or diffraction patterns per reaction), which must be processed in an efficient, rapid, and user-friendly manner if such techniques are to become widespread and applied to diverse mechanochemical processes. Unfortunately, existing software packages which efficiently process large volumes of spectra are limited, especially with respect to the challenges associated with milling data, such as constant fluctuation in amount of sample measured. In order to address the challenge of efficiently analyzing *in situ* Raman, diffraction, and fluorescence data simultaneously, we have developed a customizable approach to data processing implemented in MATLAB (Figure 47.) designed to complement specialized programs such as TOPAS-academic, which conducts Rietveld refinement and structure solution of diffraction data.

(a) Data Processing Design

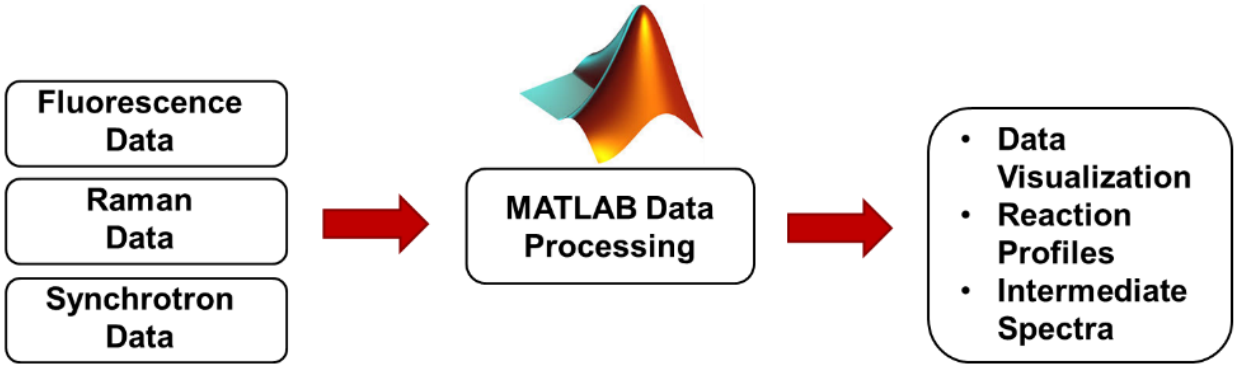

Figure 47. MATLAB data processing design

In this context, the following principles guided the development of the data processing approach:

1. Generalizable
    a. Designed to process a wide variety of data.
2. Flexible

a. Numerical approaches which do not require an *a-priori* model.
b. Modular structure which can be easily rearranged.
c. Flexible options: allow user to quickly choose and use different processing methods.

3. Rapid and Unified Workflow

a. Process entire dataset in a continuous run.
b. Analyze multiple datasets (same or different) in a unified way.

Data processing methods, especially for extracting reaction component and profiles from an *in-situ* dataset, remain an active area of research and are highly dependent on both the specifics of a measurement, the quality and nature of the data, and on preprocessing methods. As a full discussion of approaches and their relative advantages and disadvantages is beyond the scope of this Thesis, so a summary of implemented methods will be presented.

The goals of a generalizable, flexible, and unified workflow guided the decision to make a single flexible data processing routine instead of developing separate routines for different types of data (Raman, fluorescence, and diffraction in this case). All data is processed through a main routine, with the user specifying the desired processing method. This facilitates exploratory analysis of data by cross-applying algorithms originally developed for different types of data and simplifies comparing datasets as they are handled in a consistent manner. The limitation of this approach is that only general numerical approaches, which do not rely on some sort of structural or instrumental model, can be used within the main routine. The freedom and modularity of the data processing structure must also be used with some caution as inappropriate manipulations can substantially distort the data.

(b) Data Processing Overview

All options included in the main processing routine are summarized in Figure 48, with the routine having five main stages: (*i*) Loading the data into the data structure, (*ii*) preprocessing, (*iii*) correcting the data, (*iv*) fitting the data, and finally (*v*) plotting and exporting the data.

(i) Loading the data into the data structure

In order to facilitate the loading of large amounts of data, with multiple processing steps, we have designed the following interface. The user selects the desired processing options and provides the appropriate parameters for the various algorithms in a single script with text inputs, and subsequently loads the dataset and pure components (optional) *via* a graphical user interface (GUI) from a folder full of individual data files of spectra or diffraction patterns. The user specified parameters can be applied to a user specified spectrum, and subsequently modified, until satisfactory results are achieved. At this point, the data has been assembled into the overall data structure. This is an important point in the data processing, as all required information has been provided and formatted, and represents the minimum amount of data which can be saved from which nominally identical results will be obtained. Past this point, the routine runs without further input until completion, as the routine retains a copy of the matrix of spectra after each modification, for analysis and further processing, the data volume rapidly expands.

(ii) Preprocessing the data

Depending on the nature and quality of the data, several key preprocessing steps were identified in the literature, which were subsequently implemented in a sequential manner. These are 1) smoothing, 2) baseline correction, 3) cutting the dataset, and 4) normalization/scaling. Smoothing is useful as a means of reducing noise in a dataset and can be especially useful when working with large noise or low signal. Default MATLAB implementations for Savitsky-Golay[16] and locally weighted regression (locally estimated scatterplot smoothing (LOESS))[17] are included in the workflow as well as some more recent adaptations such as an iterative Savitsky-Golay algorithm,[18] and the Whittaker smoother based on penalized least squares.[19] Baseline correction is a critical step for many milling datasets due to strong background from the milling jar or fluorescence and scattering in Raman spectroscopy. The Sonneveld-Visser algorithm[20] originally developed for X-ray diffraction data provides a robust method for consistent baseline estimation, while asymmetric least squares (AsLS)[21] and recent extension using asymmetrically reweighted penalized least squares (arPLS)[22] are reported to result in a more accurate baseline correction, but are more sensitive to the input parameter in our

experience. After the calculated baseline is subtracted, the dataset can be cut to either a region of interest, or to remove regions with various interferences such as excitation sources and the edges of the detector which have distortions. The final part of the preprocessing routine is normalization or scaling. For this step, the data can be scaled according to the intensity at a specific X value (wavelength, wavenumber, etc.) or be scaled *via* vector normalization, in this case the Euclidean norm. Alternatively, the data can be normalized so that the data fits a normal (gaussian) distribution *via* standard normal variate (SNV)[23] or multiplicative scatter correction (MSC).[24]

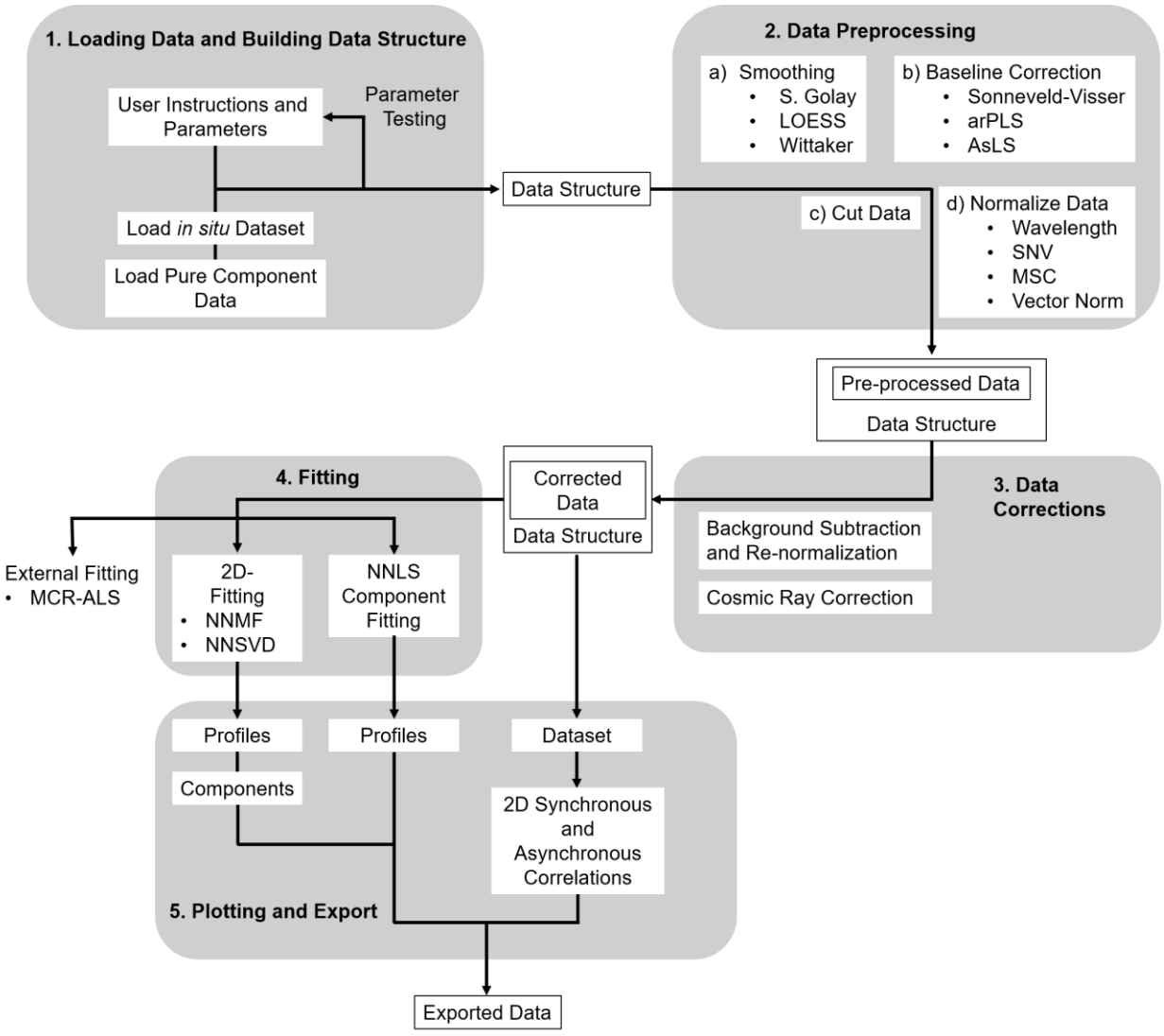

Figure 48. Summary of main data processing routine.

(iii) Correcting the data

The results of each step of the data pre-processing are stored within the data structure and the final pre-processed data is utilized for the third data correction stage. Here, we implemented two important corrections, 1) cosmic ray removal for Raman spectra, and 2) background subtraction of the milling jar. Random intensity spikes in Raman spectra due to cosmic rays can be removed using a polynomial based cosmic ray removal method.[25] Additionally, at this stage the spectrum of the milling jar can be subtracted from each *in situ* spectrum by applying the pre-processing sequence to the spectrum of an empty milling jar, and subsequently subtracting the non-negative least squares fit of the background spectrum to each experimental spectrum.[26] As the background intensity often dominates the sample intensity, the option to rescale or renormalize the data after background subtraction is included.

(iv) Fitting the data

There are two approaches currently implemented for fitting the data, depending on whether the spectra of pure components are known or unknown. If it is possible to collect spectra (or diffraction patterns) of pure components (starting materials, intermediates, and products of the reaction), a user-defined region of each *in situ* spectrum can be fit with a linear combination of pure components using a non-negative least squares regression.[26] This method relies on all signals being assigned to known pure components. For the case where the components of the *in situ* data are not known, methods which simultaneously estimate both components and profiles are required. There are inherent limitations to this approach, as species which appear simultaneously can often not be resolved (such as two reactants which appear or disappear in unison), and resolving overlapping peaks is very challenging. As Raman active vibrations cannot exhibit negative intensity, nor can there be a negative quantity of a substance, algorithms with non-negativity constraints have been applied for simultaneous component and profile estimation. This family of algorithms is known as non-negative matrix factorization (NNMF),[27] the implemented variants include projected gradient methods to accelerate convergence[28] and non-negative double singular value decomposition (NNSVD) which uses singular value decomposition to improve initialization of a NNMF algorithm.[29]

Alternatively, data can be assigned to external packages such as multivariate curve resolution-alternating least squares (MCR-ALS)[30] for curve fitting utilizing non-negative and other constraints.

(v) Plotting and export

The original, intermediate, and final *in situ* datasets can be plotted after various preprocessing steps and corrections as three-dimensional surface plots. Both components and reaction profiles can be plotted in addition to the fitting residuals of the dataset. The two-dimensional synchronous and asynchronous correlation matrices can be plotted to visualize correlations in the data over time.[31] Finally, all of the datasets and calculated profiles and components can be exported in a variety of formats such as .txt, .xy, or .xye files for further processing by other programs.

The entire main data processing routine can be run either sequentially to process multiple datasets or overwrite itself to optimize parameters. This enables the user to rapidly correct and fit data and compare results from different parameters or datasets. Given the speed with which *in situ* data can be acquired, and the amount of corrections often required for milling datasets, developing a user-friendly and efficient processing method capable of extracting vital information from the data and visualizing this data is critical for the utility of real-time reaction monitoring for milling reactions as a field.

3.05 Conclusions and Outlook

Expanding the utility and scope of monitoring milling reactions required the development of novel methods, improving the quality of existing setups, and improving data processing methods. We have developed fluorescence spectroscopy to provide insights into changes in the electronic structure of fluorescent materials under milling reaction conditions and demonstrate how relatively simple and low-cost setups can enable new types of real-time measurements. This setup coupled with europium as a fluorescent probe represents an important advance in lanthanide mechanochemistry. To our knowledge, this Thesis is the first instance of *in situ* monitoring of lanthanide mechanochemistry. Sapphire milling jars greatly expand the scope and utility of Raman measurements to systems previously considered impossible to measure. Finally, given

the inherent challenges associated with processing milling data, such as variations in sample amounts and significant background contribution of milling jars, we created a suite of data processing scripts capable of facilitating the analysis of large numbers of *in situ* datasets. In the future, simulating datasets may provide an important approach to the currently unmet challenge of evaluating different data processing approaches and validate emerging approaches in machine learning for estimating reaction profiles and components. Our hope is that the data processing methods assembled in this Thesis can be expanded upon and be made freely available to the public as they may also prove useful for reaction monitoring beyond mechanochemistry.

3.06 References

1. *MATLAB*, version 9.6 (R2019a); The MathWorks Inc.: Natick, Massachusetts, 2019.
2. Asher, S.A.; *Handbook of vibrational spectroscopy* **2002**, 557-571.
3. Muramoto, Y.; Kimura, M.; Nouda, S.; *Semiconductor Science and Technology* **2014,** *29*, (8), 084004.
4. Halasz, I.; Kimber, S.A.J.; Beldon, P.J.; Belenguer, A.M.; Adams, F.; Honkimäki, V.; Nightingale, R.C.; Dinnebier, R.E.; Friščić, T.; *Nature Protocols* **2013,** *8*, 1718.
5. Batzdorf, L.; Fischer, F.; Wilke, M.; Wenzel, K.-J.; Emmerling, F.; *Angewandte Chemie International Edition* **2015,** *54*, (6), 1799-1802.
6. Gracin, D.; Strukil, V.; Friscic, T.; Halasz, I.; Uzarevic, K.; *Angewandte Chemie International Edition* **2014,** *53*, (24), 6193-6197.
7. Tireli, M.; Juribašić Kulcsár, M.; Cindro, N.; Gracin, D.; Biliškov, N.; Borovina, M.; Ćurić, M.; Halasz, I.; Užarević, K.; *Chemical Communications* **2015,** *51*, (38), 8058-8061.
8. Neece, G.A., *Microspectrometers: an industry and instrumentation overview*; Optical Engineering + ApplicationsSPIE: 2008; Vol. 7086.
9. *QE65000 Data Sheet*, Ocean Optics: 830 Douglas Ave, Dunedin, FL.
10. Arhangelskis, M.; Jochym, D.B.; Bernasconi, L.; Friščić, T.; Morris, A.J.; Jones, W.; *The Journal of Physical Chemistry A* **2018,** *122*, (37), 7514-7521.
11. Milman, V.; Refson, K.; Clark, S.J.; Pickard, C.J.; Yates, J.R.; Gao, S.P.; Hasnip, P.J.; Probert, M.I.J.; Perlov, A.; Segall, M.D.; *Journal of Molecular Structure: THEOCHEM* **2010,** *954*, (1), 22-35.
12. Armelao, L.; Quici, S.; Barigelletti, F.; Accorsi, G.; Bottaro, G.; Cavazzini, M.; Tondello, E.; *Coordination Chemistry Reviews* **2010,** *254*, (5), 487-505.

13. Ozaki, T.; Arisaka, M.; Kimura, T.; Francis, A.; Yoshida, Z.; *Analytical and Bioanalytical Chemistry* **2002,** *374*, (6), 1101-1104.

14. Dutra, J.D.L.; Lima, N.B.; Freire, R.O.; Simas, A.M.; *Scientific reports* **2015,** *5*, 13695.

15. Wachtman J.R., J.B.; Lam J.R., D.G.; *Journal of the American Ceramic Society* **1959,** *42*, (5), 254-260.

16. Savitzky, A.; Golay, M.J.E.; *Analytical Chemistry* **1964,** *36*, (8), 1627-1639.

17. Cleveland, W.S.; Devlin, S.J.; *Journal of the American Statistical Association* **1988,** *83*, (403), 596-610.

18. Schulze, H.G.; Foist, R.B.; Ivanov, A.; Turner, R.F.B.; *Applied Spectroscopy* **2008,** *62*, (10), 1160-1166.

19. Eilers, P.H.C.; *Analytical Chemistry* **2003,** *75*, (14), 3631-3636.

20. Sonneveld, E.J.; Visser, J.W.; *Journal of Applied Crystallography* **1975,** *8*, (1), 1-7.

21. Eilers, P.H.; Boelens, H.F.; *Leiden University Medical Centre Report* **2005,** *1*, (1), 5.

22. Baek, S.-J.; Park, A.; Ahn, Y.-J.; Choo, J.; *Analyst* **2015,** *140*, (1), 250-257.

23. Barnes, R.J.; Dhanoa, M.S.; Lister, S.J.; *Applied Spectroscopy* **1989,** *43*, (5), 772-777.

24. Geladi, P.; MacDougall, D.; Martens, H.; *Applied Spectroscopy* **1985,** *39*, (3), 491-500.

25. Schulze, H.G.; Turner, R.F.B.; *Applied Spectroscopy* **2013,** *67*, (4), 457-462.

26. Lawson, C.L.; Hanson, R.J., *Solving least squares problems*; Siam: 1995; Vol. 15.

27. Berry, M.W.; Browne, M.; Langville, A.N.; Pauca, V.P.; Plemmons, R.J.; *Computational statistics & data analysis* **2007,** *52*, (1), 155-173.

28. Lin, C.-J.; *Neural computation* **2007,** *19*, (10), 2756-2779.

29. Boutsidis, C.; Gallopoulos, E.; *Pattern Recognition* **2008,** *41*, (4), 1350-1362.

30. Jaumot, J.; de Juan, A.; Tauler, R.; *Chemometrics and Intelligent Laboratory Systems* **2015,** *140*, 1-12.

31. Noda, I.; Dowrey, A.E.; Marcoli, C.; Story, G.M.; Ozaki, Y.; *Applied Spectroscopy* **2000,** *54*, (7), 236A-248A.

4. The effect of milling frequency on a mechanochemical organic reaction monitored by *in situ* Raman spectroscopy

4.01 Preface

Milling frequency is a fundamental parameter in all ball milling reactions, with substantial influence on the rates of conversion of mechanochemical reactions, yet the relationship between milling frequency and reaction kinetics remains poorly understood. We postulated that milling frequency would have an especially profound effect on so called neat grinding reactions, where two crystalline solids are ground together without the addition of a liquid phase which imparts mobility to the reaction mixture. These reactions are of particular interest from a fundamental perspective, as it is not immediately obvious why certain reactions proceed without the need for liquid additives, whereas others require LAG conditions. The synthesis of 2,3-diphenylquinoxaline from benzil and *o*-phenylenediamine proceeds in high yield and without reported intermediates, was identified as a neat grinding reaction amenable to *in situ* monitoring *via* Raman spectroscopy. The following chapter explores the effect of milling frequency on this condensation reaction, and has been published as P. A. Julien, I. Malvestiti and T. Friščić, *Beilstein Journal of Organic Chemistry*, 2017, **13**, 2160-2168. All experimental work was conducted by P. A. Julien with the assistance of I. Malvestiti. All data processing and writing was done by P. A. Julien. The manuscript was edited by T. Friščić. This work is expanded upon in the following chapter.

4.02 Abstract

We provide the first *in situ* and real-time study of the effect of milling frequency on the course of a mechanochemical organic reaction conducted using a vibratory shaker (mixer) ball mill. The use of *in situ* Raman spectroscopy for real-time monitoring of the mechanochemical synthesis of a 2,3-diphenylquinoxaline derivative revealed a pronounced dependence of chemical reactivity on small variations in milling frequency.

In particular, *in situ* measurements revealed the establishment of two different regimes of reaction kinetics at different frequencies, providing tentative insight into processes of mechanical activation in organic mechano-chemical synthesis.

4.03 Introduction

Over the past decade, mechanochemical reactions,[1-4] i.e., chemical transformations induced or sustained through the application of mechanical force in the form of grinding, milling and shearing, have emerged as a highly versatile and general route to conduct chemical reactions in the absence of bulk solvents.[2] Indeed, the demonstrated versatility in organic,[5-8] organometallic,[9,10] pharmaceutical,[11,12] supramolecular,[13] metal-organic,[14,15] and materials synthesis[16] has rendered mechanochemical reactions by ball milling or grinding as viable, highly environmentally-friendly alternatives to solution-based chemistry. Importantly, mechanochemistry provides not only a means to conduct chemical transformations of poorly soluble reagents,[17] but also enables access to reactions that are difficult or even impossible to achieve in solution,[18-20] and allows the synthesis of molecular targets that have so far been considered impossible to synthesize[21] or isolate[22].

However, in contrast to rapid expansion of applications of mechanochemistry, the mechanistic understanding of the underlying physicochemical process remains poor. It was only recently that significant effort was invested in understanding how fundamental environmental parameters, such as temperature, milling frequency, or sample-to-volume ratio[23-26] affect the course of organic mechanochemical reactions. A significant recent advance in mechanistic studies of mechanochemical reaction mechanisms was the introduction of techniques for *in situ*, real-time monitoring of ball milling processes,[27] first through synchrotron X-ray powder diffraction (XRPD),[28,29] and later by Raman spectroscopy[30] or by a tandem technique combining these two techniques.[31] Whereas valuable mechanistic information on the course of a milling reaction can be obtained through stepwise, ex situ monitoring[32] based on periodically interrupting the milling process followed by sample extraction and analysis[33,34] such techniques can also lead to misleading results due to the sample either relaxing rapidly after milling[35] or reacting with surrounding atmosphere during preparation for analysis[36]. Such problems are additionally

exacerbated in mechanochemistry of organic or metal-organic materials, readily activated through milling into transient, reactive amorphous phases. In contrast, real-time monitoring provides the opportunity to investigate the reaction course with time resolution in seconds, and without disrupting the milling process[31]. So far, the majority of real-time monitoring studies have focused on reactions of inorganic substances converting into metal-organic frameworks[17,28,37] or supramolecular reactions of co-crystallization.[38] Real-time monitoring of an organic mechanochemical reaction was only recently reported by Tireli and co-workers, who utilized Raman spectroscopy to investigate how the choice of base influences the course of a base-catalysed nucleophilic substitution reaction.[39]

Raman spectroscopy is particularly well-suited for monitoring and tracking organic reactions. It is a generally accessible and inexpensive, with an output based on changes to molecular structure rather than its crystallinity, offering a powerful tool for *in situ* studies of mechanochemical organic reactions that often proceed through amorphous or eutectic intermediates. We now report a Raman spectroscopy study of the effect of ball milling frequency on the course of a model organic transformation, the previously reported mechanochemical condensation of a diketone and a diamine to form an *N*-heteroacene.[40] We have utilized an in-house built setup for real-time Raman spectroscopy monitoring of the synthesis of 2,3-diphenylquinoxaline from benzil and *o*-phenylenediamine (Figure 49). As the Raman signals of both reactants and the quinoxaline product can readily be distinguished, and the product can be obtained in high yield and purity by brief milling (less than an hour), we found this model system to be particularly appealing for mechanistic studies.

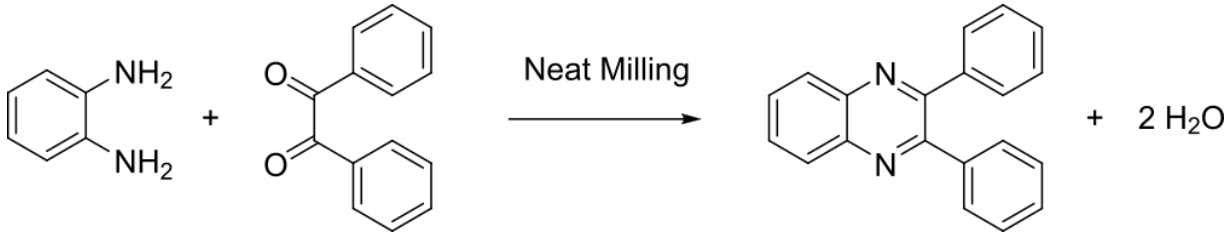

Figure 49. Milling synthesis of 2,3-diphenylquinoxaline from benzil and ortho-phenylenediamine.

The milling frequency is one of the fundamental parameters of mechanochemical reactions conducted by ball milling, and for a vibratory shaker (mixer) ball mill it represents

the number of full oscillations of the milling vessel (milling jar) per unit time along a curved path (Figure 50). It is often used as a simple, primary assessment of the intensity of the milling process, and it affects the overall impact force, number and rate of impacts of milling media, as well as associated frictional heating.

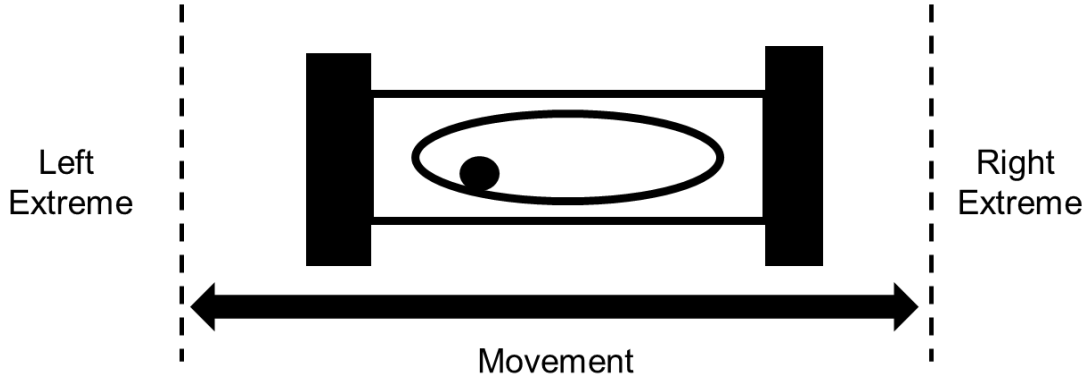

Figure 50. Movement of the milling jar and sample holder under milling conditions.

Raman spectroscopy was recently utilized for a stepwise, ex situ assessment of the effect of milling frequency on the mechanochemical synthesis of a MOF from ZnO and imidazole in the presence of a small amount of *N*,*N*-dimethylformamide.[41] This study revealed reaction kinetics consistent with a 2nd order reaction rate law, rationalized through a “pseudo-fluid” reaction model in which the rate-determining factor is the frequency of reactive encounters between the particles. In contrast, ex situ gas chromatography studies of the Knoevenagel condensation between vanillin and barbituric acid in a planetary mill revealed a sigmoidal dependence of reaction yield with time.[22] Similarly, sigmoidal dynamics were detected by *in situ* XRPD monitoring of the formation of glycinium oxalate salts from γ-glycine and oxalic acid dihydrate.[42] Other examples of explorations of the effect of milling frequency on mechanochemical reactivity include aromatic substitution reactions[43] and the synthesis of nitrogen-doped titania,[44] which have all revealed a non-linear relationship between milling frequency and reaction conversion.

4.04 Results and Discussion

(a) *In situ* monitoring of the model condensation reaction

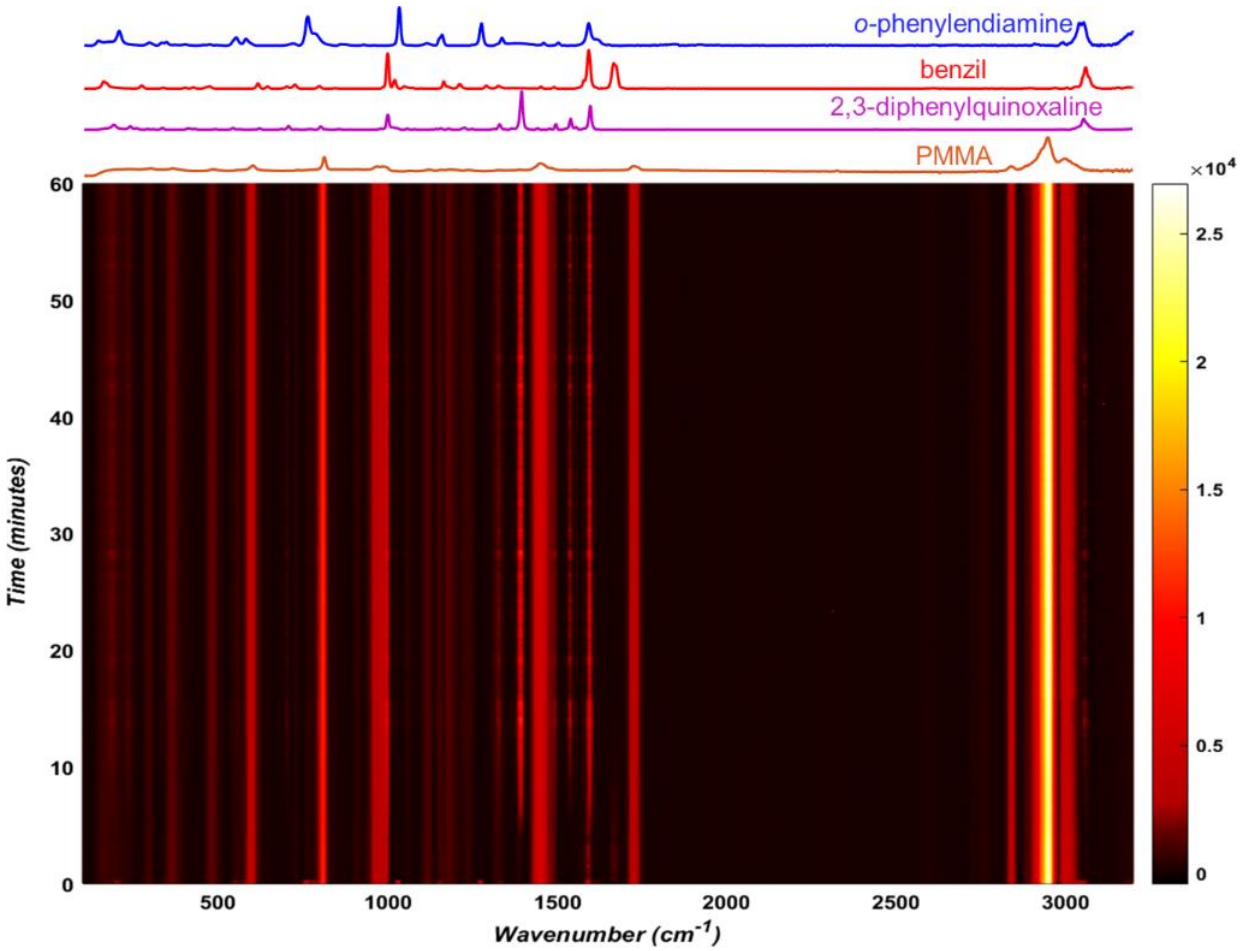

Figure 51. Time-resolved Raman spectrum for the double condensation of o-*phenylenediamine and benzil to form 2,3-diphenylquinoxaline by milling at 30 Hz, with relevant spectra of reaction components and the PMMA milling jar shown above.*

A preliminary investigation of the model condensation reaction was conducted by milling of *o*-phenylenediamine (108 mg, 1.0 mmol) with benzil (210 mg, 1.0 mmol) using a Retsch MM400 mixer mill operating at 30 Hz. The reaction mixture was placed in a 15 mL volume optically transparent PMMA jar, along with one zirconia ball of 10 mm diameter (ca. 3 grams weight). After 30 minutes milling, the analysis of the crude reaction product by ^{1}H nuclear magnetic resonance spectroscopy (see Appendix 1) suggested quantitative conversion, with the presence of only trace impurities. Importantly, as the melting points

of the starting materials and the product are considerably above room temperature (benzil: 94–96 °C; *o*-phenylenediamine: 100–102 °C; 2,3-diphenylquinoxaline: 125–127 °C) and no melting was observed upon grinding together of the two reactants, the formation of 2,3-diphenylquinoxaline is a good example of a solid-state reaction. Moreover, XRPD analysis of the crude reaction mixture after milling indicated that the product was crystalline (see Appendix 1). Monitoring of the reaction *in situ* by Raman spectroscopy revealed the clear disappearance of reactant signals, as well as the emergence of strong signals of the product (Figure 51). Complete disappearance of reactant signals was observed *in situ* after ≈20 minutes milling, a timescale that is well suited for our study. Due to the significant scattering associated with collecting data through the 3 mm thick PMMA jar wall, all data were baseline corrected as described in the experimental section.

(b) Circumventing PMMA interference

The milling jar wall produces a strong PMMA Raman signal which creates a strong background and interferes with *in situ* measurements of our reaction components. To minimize this effect, we focused our study on the spectral region between 1510 cm^{-1} and 1710 cm^{-1}, where both starting materials and the product exhibit characteristic signals, and the PMMA spectrum is featureless (Figure 52).

(c) Fitting the dataset

A principal challenge associated with *in situ* monitoring of a milling reaction is the variation of the amount of sample in the beam due to the motion of the milling assembly. The resulting variations in the Raman signals of the sample and the scattering background affect the ability to monitor reaction progress, leading us to estimate the ratio of each component within the reaction mixture by a direct classical least-squares (CLS) approach based on experimentally obtained spectra of all scattering materials.[45] As the PMMA signal in the characteristic region between 1510–1700 cm^{-1} is sufficiently low to be neglected, this was limited to the spectra of the two starting materials, *o*-phenylenediamine and benzil, as well as the product 2,3-diphenylquinoxaline (Figure 52, top). The critical assumption in this approach is that all components are known and all spectral signals can be assigned to either the product or any of the reactants. Therefore,

the calculated spectrum (C) can be described as a sum of pure component spectra x_nA_n, where x_n is the contribution of each spectrum and A_n is the spectrum of each pure component, with all components being known (Equation 1).

$$C = \sum_n x_n A_n = x_1 A_1 + x_2 A_2 + x_3 A_3 \qquad (1)$$

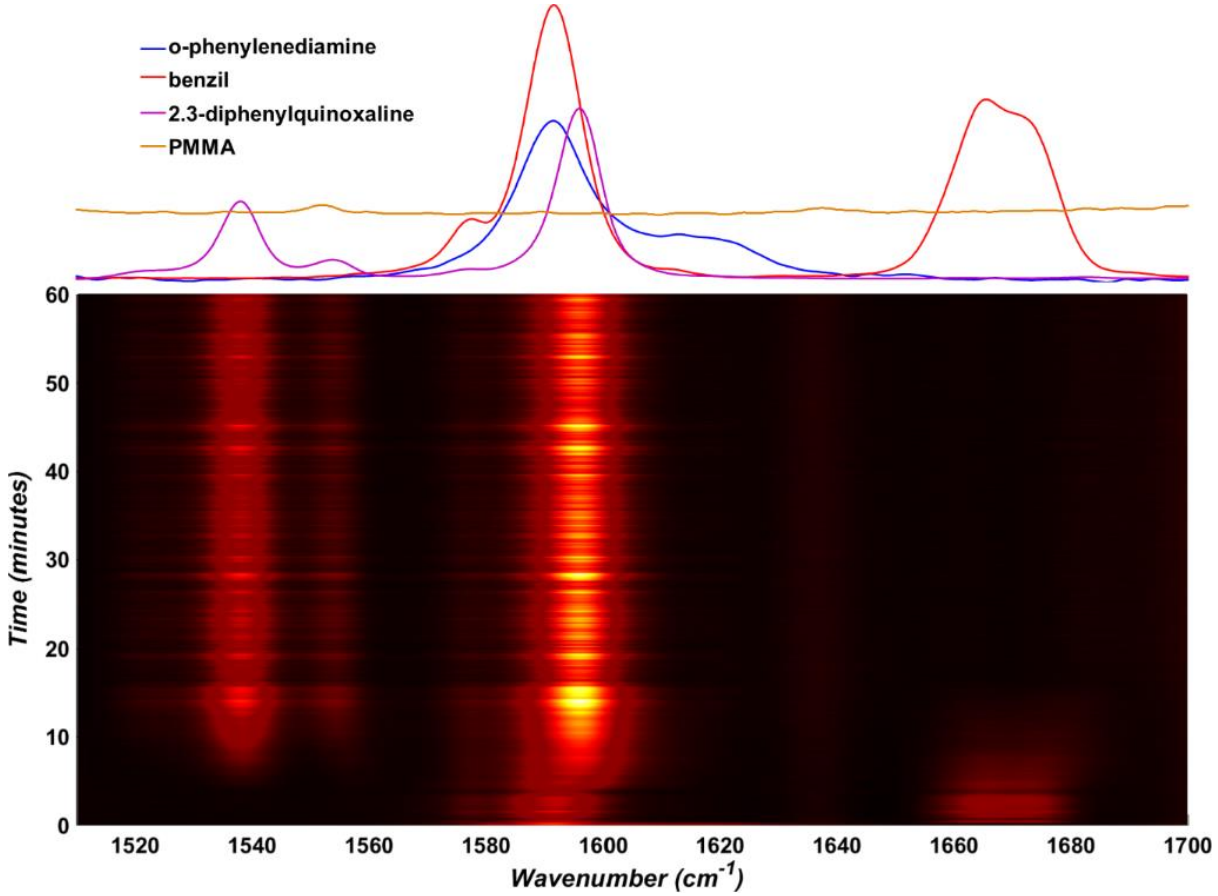

Figure 52. Section of the time-resolved Raman spectrum for the model mechanochemical reaction conducted at 30 Hz, that was selected for least-squares fitting. Normalized and baseline-corrected spectra for pure o-phenylenediamine (blue), benzil (red), 2,3-diphenylquinoxaline (purple) and an empty PMMA milling jar (yellow, offset for clarity) are shown above the time-resolved plot.

At the same time, the total sum of spectral contributions of all three reaction components must be equal to one, enabling the ratio of components to be calculated for each spectrum (Equation 2).

$$\sum_n x_n = x_1 + x_2 + x_3 = 1 \qquad (2)$$

Variations in background scattering between all *in situ* collected spectra and the spectra of individual reaction components were accounted for by using the Sonneveld–Visser baseline correction algorithm.[46] *In situ* collected spectra were fitted as a sum of the normalized component spectra using a non-negative linear least squares algorithm ("lsqnonneg" in Matlab) which solves the fitting problem[47] of Equation 3:

$$\min_x \| A * x - E \|_2^2 \qquad (3)$$

where *A* is a matrix containing the pure components spectra, E is the *in situ* obtained experimental spectrum, and *x* is a matrix of the mole fraction of each component, which satisfies $x \geq 0$. Solving equation 3 provides the best values of *x* that minimize the difference between *A* * *x* and *E*.

The described linear least-squares fitting procedure was applied to every spectrum in the *in situ* dataset and, following Equation 1 and Equation 2, enabled us to evaluate the relative spectral contribution of each reaction component x_n (Figure 53).

It is important to note that the herein presented approach to data analysis assumes that the Raman spectra of individual reactants or products are not significantly affected by the degree of crystallinity or changes in the composition of the reaction mixture. While Raman scattering is expected to be directly proportional to the concentration of a particular molecular species,[45] which suggests that the spectral contribution of a reaction component should also be directly proportional to its mole fraction, we have not yet calibrated this relationship. Accurate quantitative methods for analysing *in situ* Raman milling reactions are currently under development in our laboratory.

(d) The effect of milling frequency on the model reactions

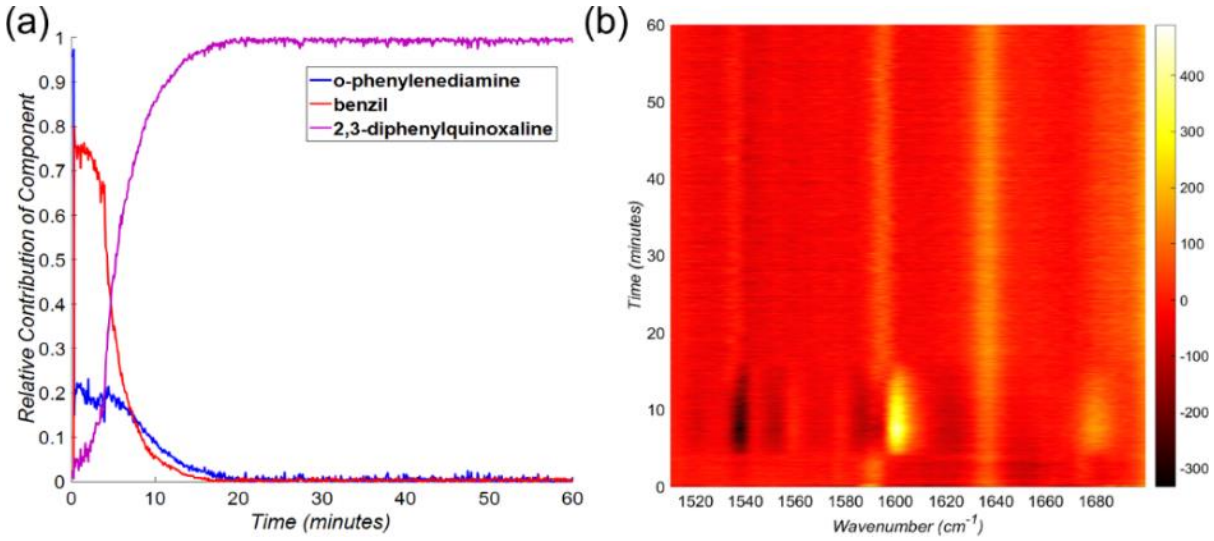

Figure 53. (Left) Estimated contribution of each component for each Raman spectrum over time of the synthesis of 2,3-diphenylquinoxaline at 30 Hz. (Right) Residual plot of the difference between experimental and estimated Raman spectra. In this case, this plot suggests an overestimation of 2,3-diphenylquinoxaline and an underestimation of o-phenylenediamine between ~5 and ~15 minutes. More information on the fitting can be found in Appendix 1.

Having identified a suitable model reaction and an approach for the analysis of *in situ* reaction data, we were able to systematically explore the effect of milling frequency on the reaction rate. The systematic studies were conducted by measuring Raman spectra for chemical reactions that were, to the best of our ability, identical in all respects except the choice of milling frequency, i.e., the choice of milling media, the jar volume and material, the ball-to-sample weight ratio, and reactant batches were all kept constant. Specifically, we investigated the reaction behavior upon milling at 20 Hz, 22.5 Hz, 25 Hz, 27.5 Hz, and 30 Hz. For each of the frequencies, the measurements were performed in triplicate, and on the same day, in order to maximize reproducibility and minimize the variations in the reaction behaviour due to daily variation of ambient temperature or humidity. The final conversion for each experiment was verified by ^{1}H NMR spectroscopy in solution (see Table S1 in Appendix 1) and was found to be consistent with the *in situ* Raman spectroscopy data. Averaging the triplicate measurements of the time-dependent variation of product spectral contribution for each frequency (Figure 54) reveals remarkable sensitivity of the reaction rate on small changes in milling frequency.

The *in situ* monitoring data indicates that the reaction progress adopts a sigmoidal profile at milling frequencies higher than 25 Hz, which is consistent with the results of earlier ex situ studies of a Knoevenagel condensation reaction.[22] At milling frequencies below 25 Hz, however, the reaction appears to exhibits linear behavior. Further insight into the frequency-dependent behavior of our model reaction is obtained from the consistency of measurements within each set of triplicate *in situ* Raman scattering datasets for a given milling frequency (Figure 55). The individual datasets before averaging reveal that all measurements for a particular frequency are mutually consistent when milling at 30 Hz, 27.5 Hz, 22.5 Hz and 20 Hz.

At 25 Hz, however, the behavior of the reaction for each of the triplicate measurements was highly erratic and generally irreproducible. Overall, there is a clear difference in the kinetics of product formation when ball milling at 27.5 Hz and 30 Hz, compared to milling at frequencies of 20 Hz and 22.5 Hz, while milling at an intermediate frequency

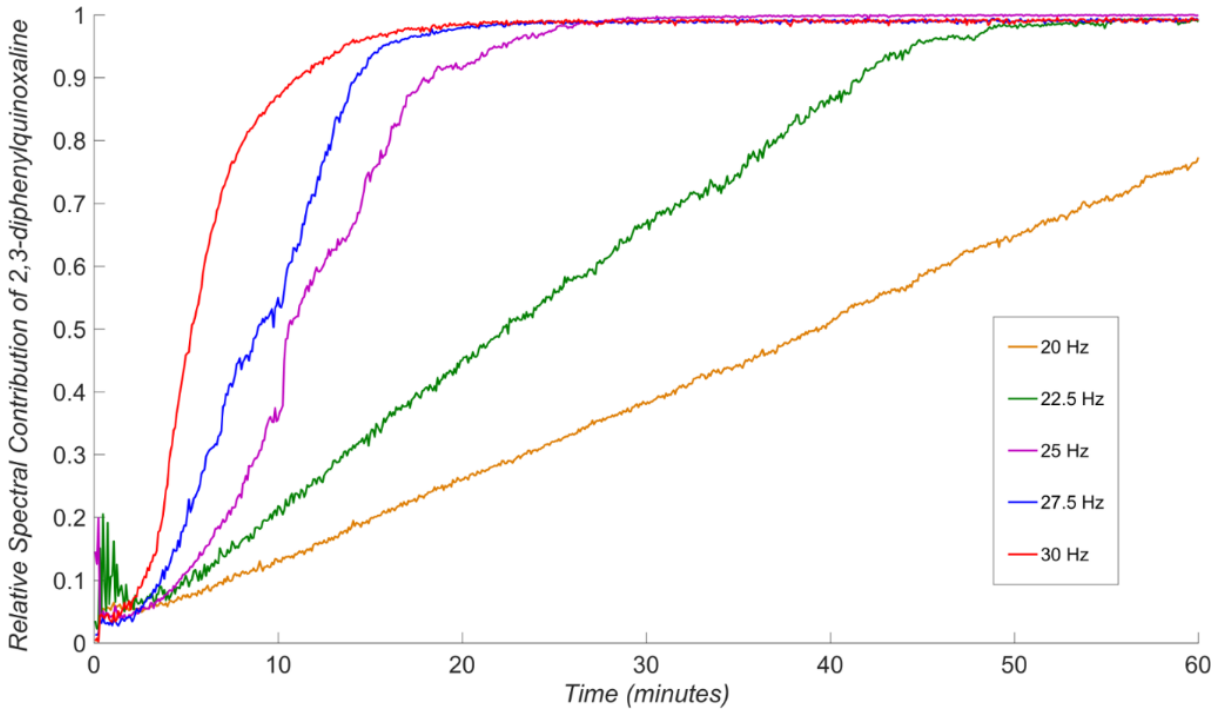

Figure 54. The effect of milling frequency on the milling condensation of benzil and o-phenylenediamine to form 2,3-diphenylquinoxaline, with data for each milling frequency averaged from a set of triplicate measurements. Variation close to the onset of milling may be due to poor initial homogeneity of the sample.

of 25 Hz led to irreproducible behavior. Tentatively, we interpret such switching between reactivity profiles by adopting the assumption that mechanochemical reactions proceed through the introduction of mechanically activated sites at which the reactions are

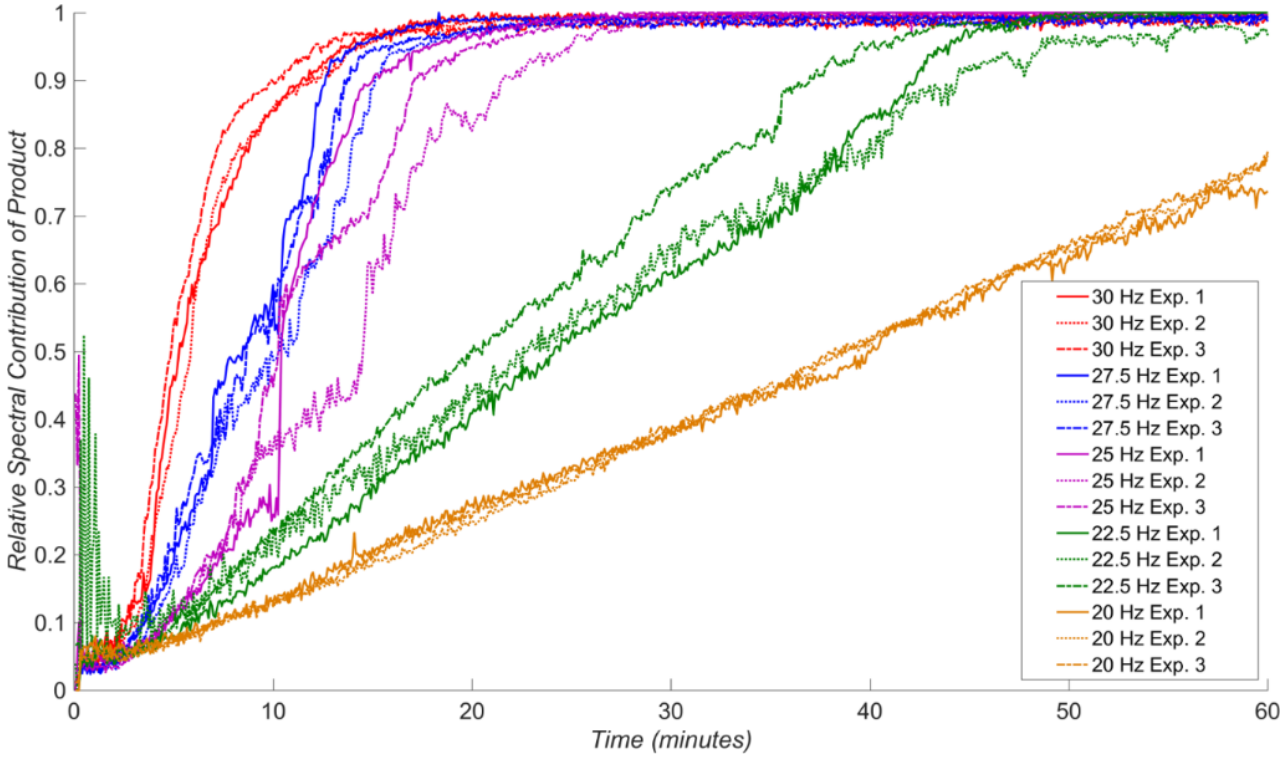

Figure 55. The reproducibility of varying milling frequency on the neat mechanochemical condensation of benzil and o*-phenylenediamine, as measured by triplicate experiments.*

facilitated, such as stacking faults and structural defects in general.[48] In such a scenario, different frequencies of milling are expected to lead to different levels of mechanical activation: at lower frequencies (i.e., 20 Hz or 22.5 Hz), the extent of mechanical activation is expected to be lower and product formation can progress at a similar rate to creation of novel activated sites. In contrast, at higher milling frequencies the rate of mechanical activation is much higher and product formation takes place in a highly activated environment, leading to a sigmoidal dependence of product formation with time. The above tentative explanation of our observations suggests that real-time Raman spectroscopy studies could offer an opportunity to directly probe the nature of mechanical activation underlying mechanochemical reactivity. Importantly, the proposed explanation is also consistent with different modes of ball motion during milling, as lower frequencies

are known to favor rolling and shearing motion, whereas higher ones should lead to a greater number of more energetic mechanical impacts.[25,49]

Milling frequency vs temperature

One of the challenges in exploring the effects of milling frequency on mechanochemical reactivity is the increase in temperature of milling jars due to frictional heating.[50,51] Due to such heating effects, an increase in milling frequency should lead not only to greater mechanical activation, e.g., through impact and structure deformation, but also to an increase in reaction rate.[52] In order to evaluate the thermal effect associated with each

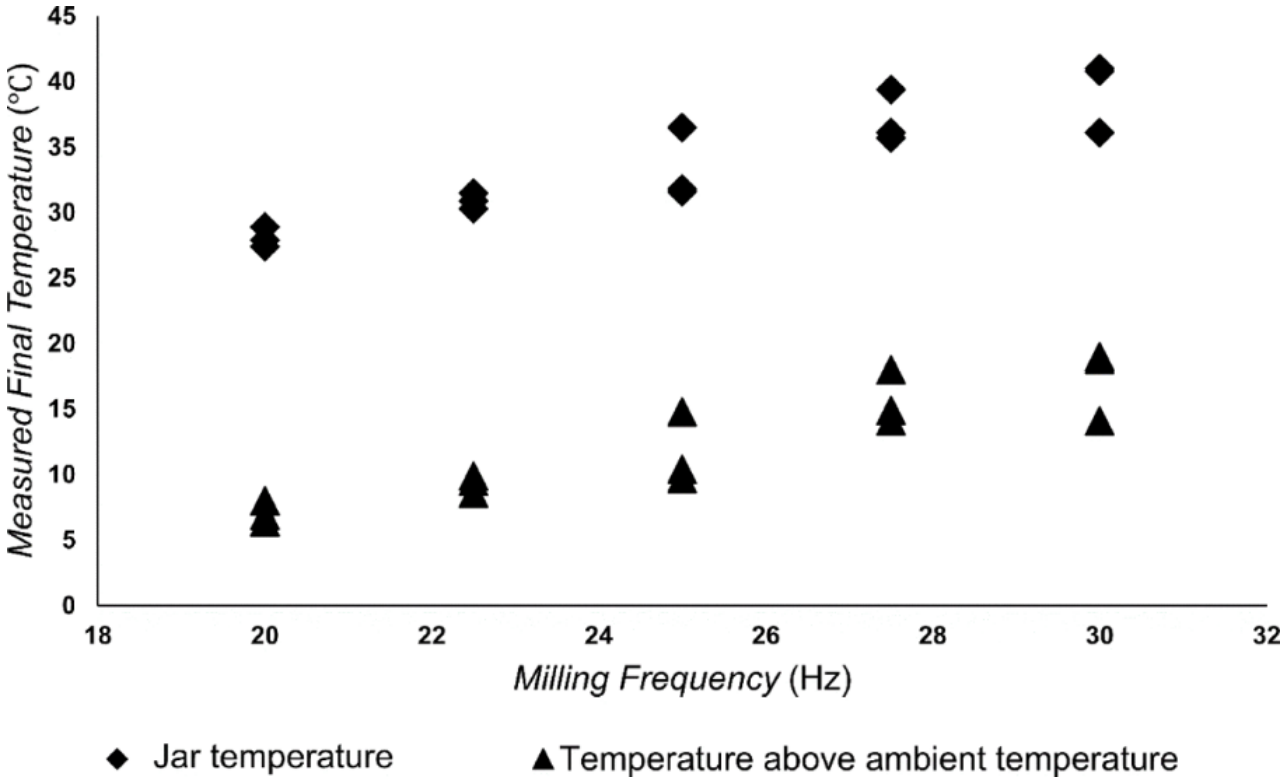

Figure 56. The effect of milling frequency on the internal jar temperature measured immediately after reaction completion.

of herein explored ball milling frequencies, we have also measured the temperature of the internal jar wall immediately after milling, revealing a potentially linear relationship between milling frequency and jar temperature (Figure 56). Importantly, the measured temperature never exceeded 45 °C, and was never higher than 19 °C above the ambient temperature. Although the observed temperature increases are generally not very large, they might be relevant for the observed variation of reaction kinetics with milling

frequency, especially as a recent variable-temperature *in situ* PXRD study has demonstrated that mechanochemical reaction rates can be highly sensitive to temperature.[52]

4.05 Conclusion

In conclusion, we have utilized an in-house Raman spectroscopy setup to conduct real-time, *in situ* monitoring of the progress of a model mechanochemical organic reaction at different ball milling frequencies. The methodologies for real-time monitoring of mechanochemistry by ball milling have only recently been introduced and have so far been employed largely in studies of metal-organic or organic materials (e.g., model pharmaceutical co-crystals). The herein presented proof-of-principle study is the first to investigate in real-time how the milling frequency, which is one of the fundamental parameters of mechanochemical reactivity, affects an organic transformation. Our results reveal high sensitivity of a carefully selected model mechanochemical reaction to the milling frequency, and establishment of clearly different regimes of reaction kinetics depending on the frequency. At lower frequencies, the model reaction exhibits a largely linear profile, resembling pseudo-zero order reaction kinetics, whereas increasing the frequency lead to a switch to apparently sigmoidal behavior. While these observations can tentatively be rationalized by different levels of mechanical activation of the reaction mixture at different frequencies, validating such an explanation requires further and quantitative studies. Nevertheless, we believe that the apparent ability of a mechanochemical reaction to switch between different regimes of chemical kinetics in response to minor changes in milling frequency is an important observation not only in the context of organic mechanochemistry and may even be of importance in reconciling differences in recently reported *in situ* and ex situ studies of mechanochemical reactivity.[22,41,42,53]

4.06 Experimental

(a) Chemicals

Benzil (98%) was purchased from Aldrich Chemical. *o*-Phenylenediamine (98%) was purchased from Alfa Aesar. Both were used without further purification.

(b) Milling reactions and characterization

The double condensation was conducted by milling 210 mg of benzil (1.0 mmol) and 108 mg of *o*-phenylenediamine (1.0 mmol) with a single zirconia ball of 10 mm diameter (ca. 3 grams weight) in a 15 mL PMMA optically transparent milling jar, using a Retsch® MM400 mixer mill. For all real-time reaction monitoring, reactions were monitored using a RamanRxn1™ analyzer by Kaiser Optical Systems Inc. every 5 seconds using a 785 nm laser. Spectra were dark and intensity corrected using the Holograms® software package before being processed. The products of these reactions were analyzed without purification. The identity of the final product was confirmed through ^{1}H and ^{13}C NMR in $CDCl_3$ using a 500 MHz AVIIIHD 500 Bruker spectrometer.

Infrared spectra were collected on a Bruker Vertex 70 FT-IR Platinum ATR, while X-ray powder diffraction patterns were collected on a Proto Manufacturing AXRD Benchtop Powder Diffractometer using Ni-filtered Cu K_α radiation. The conversion for each solid-state reaction was evaluated after milling using ^{1}H NMR spectroscopy conducted in $CDCl_3$ on a 300 MHz Varian Mercury spectrometer. The ambient temperature was measured using a digital thermometer by VWR and the internal jar temperature was acquired immediately after milling finished using a Mastercraft Temperature Reader with Digital Display and Laser Pointer (accuracy ±2 °C).

4.07 Supporting Information

Product characterization and the full *in situ* Raman datasets are provided in Appendix 1.

4.08 Acknowledgements

We would like to thank Prof. B. A. Arndtsen for use of the Raman system and Dr. S. L. Sewall for advice. We acknowledge the financial support of the NSERC PGS-D program (P.A.J.), the NSERC Discovery Grant program (grant RGPIN 418592-12) and NSERC E. W. R. Steacie Memorial Fellowship (T.F.), and CNPq for the Post-Doctoral fellowship (201474/2015-8) (I.M.).

4.09 References

1. Hernández, J. G.; Friščić, T. *Tetrahedron Lett.* **2015,** *56,* 4253–4265.

2. James, S. L.; Adams, C. J.; Bolm, C.; Braga, D.; Collier, P.; Friščić, T.; Grepioni, F.; Harris, K. D. M.; Hyett, G.; Jones, W.; Krebs, A.; Mack, J.; Maini, L.; Orpen, A. G.; Parkin, I. P.; Shearouse, W. C.; Steed, J. W.; Waddell, D. C. *Chem. Soc. Rev.* **2012,** *41,* 413–447.

3. Ostwald, W. *The fundamental principles of chemistry: an introduction to all text-books of chemistry;* Longmans, Green, and Company: New York, 1909.

4. Takacs, L. *Chem. Soc. Rev.* **2013,** *42,* 7649–7659.

5. Wang, G.-W. *Chem. Soc. Rev.* **2013,** *42,* 7668–7700.

6. Stolle, A.; Szuppa, T.; Leonhardt, S. E. S.; Ondruschka, B. *Chem. Soc. Rev.* **2011,** *40,* 2317–2329.

7. Rodríguez, B.; Bruckmann, A.; Rantanen, T.; Bolm, C. *Adv. Synth. Catal.* **2007,** *349,* 2213–2233.

8. Stolle, A.; Ondruschka, B. *Pure Appl. Chem.* **2011,** *83,* 1343–1349.

9. Juribašić, M.; Užarević, K.; Gracin, D.; Ćurić, M. *Chem. Commun.* **2014,** *50,* 10287–10290.

10. Rightmire, N. R.; Hanusa, T. P. *Dalton Trans.* **2016,** *45,* 2352–2362.

11. Tan, D.; Loots, L.; Friščić, T. *Chem. Commun.* **2016,** *52,* 7760–7781.

12. Delori, A.; Friščić, T.; Jones, W. *CrystEngComm* **2012,** *14,* 2350–2362.

13. Friščić, T. *Chem. Soc. Rev.* **2012,** *41,* 3493–3510.

14. Friščić, T. *J. Mater. Chem.* **2010,** *20,* 7599–7605.

15. Braga, D.; Giaffreda, S. L.; Grepioni, F.; Pettersen, A.; Maini, L.; Curzi, M.; Polito, M. *Dalton Trans.* **2006,** 1249–1263.

16. Ralphs, K.; Hardacre, C.; James, S. L. *Chem. Soc. Rev.* **2013,** *42,* 7701–7718.

17. Julien, P. A.; Užarević, K.; Katsenis, A. D.; Kimber, S. A. J.; Wang, T.; Farha, O. K.; Zhang, Y.; Casaban, J.; Germann, L. S.; Etter, M.; Dinnebier, R. E.; James, S. L.; Halasz, I.; Friščić, T. *J. Am. Chem. Soc.* **2016,** *138,* 2929–2932.

18. Tan, D.; Mottillo, C.; Katsenis, A. D.; Štrukil, V.; Friščić, T. *Angew. Chem., Int. Ed.* **2014,** *53,* 9321–9324.

19. Wang, G.-W.; Komatsu, K.; Murata, Y.; Shiro, M. *Nature* **1997,** *387,* 583–586.

20. Hernández, J. G.; Bolm, C. *J. Org. Chem.* **2017,** *82,* 4007–4019.

21. Shi, Y. X.; Xu, K.; Clegg, J. K.; Ganguly, R.; Hirao, H.; Friščić, T.; García, F. *Angew. Chem., Int. Ed.* **2016,** *55,* 12736–12740.

22. Štrukil, V.; Gracin, D.; Magdysyuk, O. V.; Dinnebier, R. E.; Friščić, T. *Angew. Chem., Int. Ed.* **2015,** *54,* 8440–8443.

23. Stolle, A.; Schmidt, R.; Jacob, K. *Faraday Discuss.* **2014,** *170,* 267–286.

24. Schmidt, R.; Burmeister, C. F.; Baláž, M.; Kwade, A.; Stolle, A. *Org. Process Res. Dev.* **2015,** *19,* 427–436.

25. McKissic, K. S.; Caruso, J. T.; Blair, R. G.; Mack, J. *Green Chem.* **2014,** *16,* 1628–1632.

26. Michalchuk, A. A. L.; Tumanov, I. A.; Drebushchak, V. A.; Boldyreva, E. V. *Faraday Discuss.* **2014,** *170,* 311–335.

27. Užarević, K.; Halasz, I.; Friščić, T. *J. Phys. Chem. Lett.* **2015,** *6,*4129–4140.

28. Halasz, I.; Kimber, S. A. J.; Beldon, P. J.; Belenguer, A. M.; Adams, F.; Honkimäki, V.; Nightingale, R. C.; Dinnebier, R. E.; Friščić, T. *Nat. Protoc.* **2013,** *8,* 1718–1729.

29. Friščić, T.; Halasz, I.; Beldon, P. J.; Belenguer, A. M.; Adams, F.; Kimber, S. A. J.; Honkimäki, V.; Dinnebier, R. E. *Nat. Chem.* **2013,** *5,* 66–73.

30. Gracin, D.; Štrukil, V.; Friščić, T.; Halasz, I.; Užarević, K. *Angew. Chem., Int. Ed.* **2014,** *53,* 6193–6197.

31. Batzdorf, L.; Fischer, F.; Wilke, M.; Wenzel, K.-J.; Emmerling, F. *Angew. Chem., Int. Ed.* **2015,** *54,* 1799–1802.

32. Tumanov, I. A.; Achkasov, A. F.; Boldyreva, E. V.; Boldyrev, V. V. *CrystEngComm* **2011,** *13,* 2213–2216.

33. Cinčić, D.; Friščić, T.; Jones, W. *J. Am. Chem. Soc.* **2008,** *130,* 7524–7525.

34. Karki, S.; Friščić, T.; Jones, W. *CrystEngComm* **2009,** *11,* 470–481.

35. Štrukil, V.; Fábián, L.; Reid, D. G.; Duer, M. J.; Jackson, G. J.; Eckert-Maksić, M.; Friščić, T. *Chem. Commun.* **2010,** *46,* 9191–9193.

36. Braga, D.; Giaffreda, S. L.; Grepioni, F.; Polito, M. *CrystEngComm* **2004,** *6,* 459–462.

37. Katsenis, A. D.; Puškarić, A.; Štrukil, V.; Mottillo, C.; Julien, P. A.; Užarević, K.; Pham, M.-H.; Do, T.-O.; Kimber, S. A. J.; Lazić, P.; Magdysyuk, O.; Dinnebier, R. E.; Halasz, I.; Friščić, T. *Nat. Commun.* **2015,** *6,* No. 6662. https://doi.org/10.1038%2Fncomms7662

38. Halasz, I.; Puškarić, A.; Kimber, S. A. J.; Beldon, P. J.; Belenguer, A. M.; Adams, F.; Honkimäki, V.; Dinnebier, R. E.; Patel, B.; Jones, W.; Štrukil, V.; Friščić, T. *Angew. Chem., Int. Ed.* **2013,** *52,* 11538–11541.

39. Tireli, M.; Juribašić Kulcsar, M.; Cindro, N.; Gracin, D.; Biliškov, N.; Borovina, M.; Ćurić, M.; Halasz, I.; Užarević, K. *Chem. Commun.* **2015,** *51,* 8058–8061.

40. Sahoo, P. K.; Giri, C.; Haldar, T. S.; Puttreddy, R.; Rissanen, K.; Mal, P. *Eur. J. Org. Chem.* **2016,** 1283–1291.

41. Ma, X.; Yuan, W.; Bell, S. E. J.; James, S. L. *Chem. Commun.* **2014,** *50,* 1585–1587.

42. Michalchuk, A. A. L.; Tumanov, I. A.; Konar, S.; Kimber, S. A. J.; Pulham, C. R.; Boldyreva, E. V. *Adv. Sci.* **2017,** *4,* 1700132.

43. Schmidt, R.; Stolle, A.; Ondruschka, B. *Green Chem.* **2012,** *14,* 1673–1679.

44. Yin, S.; Yamaki, H.; Komatsu, M.; Zhang, Q.; Wang, J.; Tang, Q.; Saito, F.; Sato, T. *J. Mater. Chem.* **2003,** *13,* 2996–3001.

45. Strachan, C. J.; Rades, T.; Gordon, K. C.; Rantanen, J. *J. Pharm. Pharmacol.* **2007,** *59,* 179–192.

46. Sonneveld, E. J.; Visser, J. W. *J. Appl. Crystallogr.* **1975,** *8,* 1–7. https://doi.org/10.1107%2FS0021889875009417

47. Lawson, C.; Hanson, R. *Solving Least Squares Problems;* Prentice-Hall: Upper Saddle River, New Jersey, 1974; pp 161.

48. Baláž, P.; Achimovičová, M.; Baláž, M.; Billik, P.; Cherkezova-Zheleva, Z.; Criado, J. M.; Delogu, F.; Dutková, E.; Gaffet, E.; Gotor, F. J.; Kumar, R.; Mitov, I.; Rojac, T.; Senna, M.; Streletskii, A.; Wieczorek-Ciurowa, K. *Chem. Soc. Rev.* **2013,** *42,* 7571–7637.

49. Michalchuk, A. A. L.; Tumanov, I. A.; Boldyreva, E. V. *CrystEngComm* **2013,** *15,* 6403–6412.

50. Kulla, H.; Wilke, M.; Fischer, F.; Röllig, M.; Maierhofer, C.; Emmerling, F. *Chem. Commun.* **2017,** *53,* 1664–1667.

51. Fang, Y.; Salamé, N.; Woo, S.; Bohle, D. S.; Friščić, T.; Cuccia, L. A. *CrystEngComm* **2014,** *16,* 7180–7185.

52. Užarević, K.; Štrukil, V.; Mottillo, C.; Julien, P. A.; Puškarić, A.; Friščić, T.; Halasz, I. *Cryst. Growth Des.* **2016,** *16,* 2342–2347.

53. Halasz, I.; Friščić, T.; Kimber, S. A. J.; Užarević, K.; Puškarić, A.; Mottillo, C.; Julien, P.; Štrukil, V.; Honkimäki, V.; Dinnebier, R. E. *Faraday Discuss.* **2014,** *170,* 203–221.

5. *In situ* monitoring of mechanochemical and thermochemical reactions reveals kinetics modulated by thermal induced changes in mobility in an organic transformation

5.01 Preface

The variable reaction kinetics observed upon milling in the previous chapter warranted further investigation. The observation of increased reaction temperature at higher milling frequency drove our investigation towards the influence of temperature in these transformations. Decoupling impact forces and mixing from thermal effects remains a challenge in the field of mechanochemistry. This challenge was herein addressed *via* variable temperature measurements of pre-milled reaction mixtures. This represents a new approach towards understanding mechanochemical reactions and reveals that for the reaction of *o*-phenylenediamine and benzil, thermal effects dominate the kinetics of the reactions. However, lower conversions for thermal reactions, presumably due to sublimation provide a justification for the use of milling for these thermally controlled reactions. This chapter will be reformatted for submission as Patrick A. Julien*, Tristan H. Borchers, Hatem Titi, Luzia S. Germann, Martin Etter, Christopher J. Barrett, Robert Dinnebier, Tomislav Friščić* aimed towards the *Journal of Physical Chemistry Letters.* All experimental work was conducted by P. A. Julien, with T. H. Borchers assisting with the hot-stage Raman microscopy measurements, H. Titi assisting with variable temperature XRPD, and L.S. Germann, M. Etter, assisting with synchrotron data collection and processing. The text was written by P. A. Julien and edited by T. Friščić.

5.02 Introduction

A major challenge in understanding the kinetics and mechanism of mechanochemical milling reactions is the difficulty in decoupling of the effect of mixing and impact forces from thermal friction-related effects in milling. Understanding thermal behavior of mechanochemical reactions has been a longstanding interest of research into

mechanochemistry.[1] Recent interest in mechanochemistry is due to its potential as a rapid, cost-effective, and scalable methodology for improving the sustainability and reducing the environmental impact of a wide variety of chemical and materials syntheses.[2-4] This has driven advances in understanding the effects of temperature on mechanochemical reactions and significant advances in mechanochemical reaction monitoring.[5] Recent efforts have focused on modulating the temperature of a mechanochemical synthesis by either heating or cooling the milling vessel to understand the thermal effects on reaction yields[6] and selectivities[7] of organic reactions. Alternatively, thermal measurements have been conducted in real-time and combined with other types of *in situ* diffraction[8] or spectroscopic[9] reaction monitoring methods. Recent thermal monitoring of milling reactions has revealed significant frictional heating effects during milling,[8] suggesting that the reaction temperature is highly dependent on both the milling conditions and the frictional properties of reaction mixture itself. Equilibration between frictional heating and heat loss to the environment can vary throughout the course of a reaction resulting in temperature variations significant enough to enable *in situ* observation of new phases. Temperature changes complicate the interpretation of reaction profiles and make it difficult to decouple thermal effects in milling reactions with those from mixing and impact forces.

Mechanochemical condensation reactions to form N-heteroacenes[10] are useful model systems for the understanding of mechanochemical reactions, due to their rapid conversions and high yields. The mechanochemical reaction of *ortho*-phenylenediamine with benzil to form 2,3-diphenylquinoxaline has been utilized in multiple mechanistic studies and has been monitored *via* ^{13}C CP-MAS NMR,[11] HPLC,[12] and Raman spectroscopy.[13] Reaction kinetics vary from linear product formation at lower milling frequency (20 Hz) to sigmoidal profiles at higher milling speeds (30 Hz)[13] as observed by Raman spectroscopy. Measuring the temperature of the reaction mixture at the end of the reaction suggested a linear relationship between milling frequency and temperature, suggesting the change in reaction kinetics may be due to thermal effects. Similarly, when the reaction temperature was modified *via* external heating/cooling, the Arrhenius plot revealed the potential existence of two separate linear regions, suggesting a change in activation energy and reaction mechanism.[12] Hot-stage microscopy measurements

revealed eutectic melting of the powder was likely responsible for the observed non-linearity of the Arrhenius plot. Specifically, this suggested that a eutectic melt may play a key role in the observed change in reaction kinetics at different milling frequencies from linear to sigmoidal profiles. Similar thermal effects have been observed in room temperature and cryo-grinding polymorphs of chlorpropamide which suggested that increased molecular mobility under high temperatures is critical in the kinetics of grinding reactions and thermal reactions of pre-ground mixtures.[14] In order to better understand whether the observed variation in kinetics at different milling frequencies is driven by changes in mechanical impact, shearing, and mixing or if it is largely a thermal effect, we attempted a separate study in order to try and decouple the thermal and mechanical effects of milling on this chemical reaction. Due to the difficulty in controlling temperature during milling reactions, we have chosen to completely eliminate mechanical agitation and examine the behavior of milled reaction mixtures upon heating, using a hot-stage Raman microscope.

5.03 Results and Discussion

To generate a homogeneous mixture of solid reactants while minimizing the conversion to final product, a 1:1 stoichiometric mixture of *ortho*-phenylenediamine and benzil was milled at 20 Hz using a Retsch MM200 for 1 minute as shown in Figure 57.

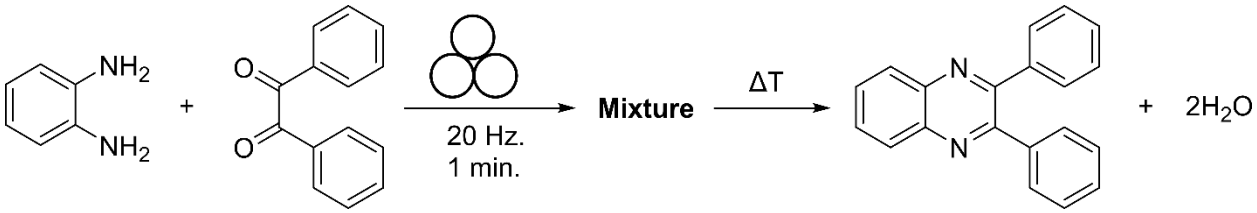

Figure 57. Brief milling of o-phenylenediamine with benzil to form a mixture of solid reactants with minor presence of product, and subsequent heating to form 2,3-diphenylquinoxaline.

(a) Hot-Stage Raman Microscopy Measurements

In order to ensure the homogeneity and measure the conversion of the milled mixture, we acquired the Raman spectrum of a 25x25 square grid of points spaced 40µm apart, yielding a total of 625 Raman spectra. Processing of this data using the non-negative

least squares approach described in our previous work[13] (Figure 58), reveals good sample homogeneity and relatively low product conversion (< 10 mol%).

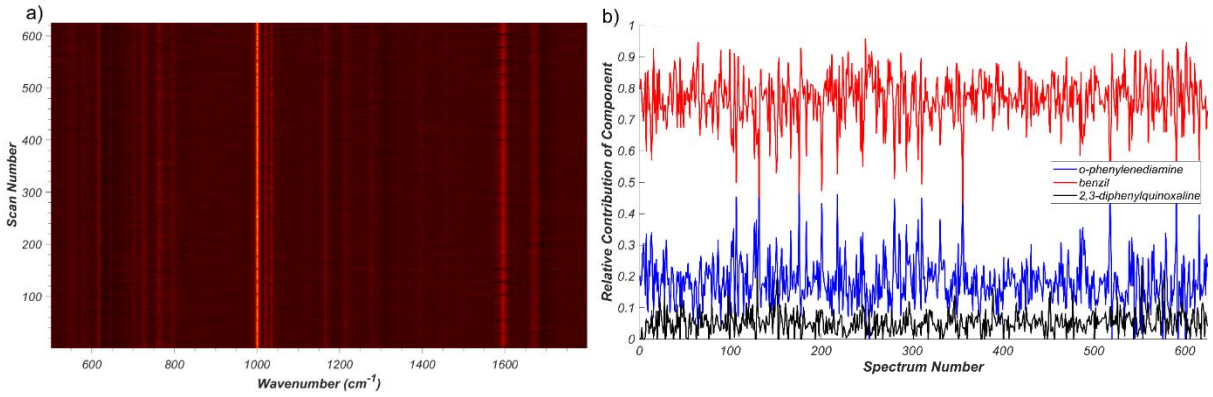

Figure 58. a) Raman spectra of 625 different spots of the pre-milled mixture before heating to assess homogeneity (brighter color denotes higher intensity), b) estimated spectra contributions from the non-negative least square fitting procedure.

After establishing that sampling of a single spot of the reaction mixture would result in a representative dataset, we applied a slow temperature ramp of 0.1°C/min to the reaction mixture and observed approximately linear evolution of product. These observations are similar to those reported for milling at low frequency[13] (Figure 59.). Interestingly, this suggests that the continuous application of mechanical force may not be the driving factor in the observed linear kinetics of the reaction, and that the increase in temperature while milling may account for the linear reaction rate.

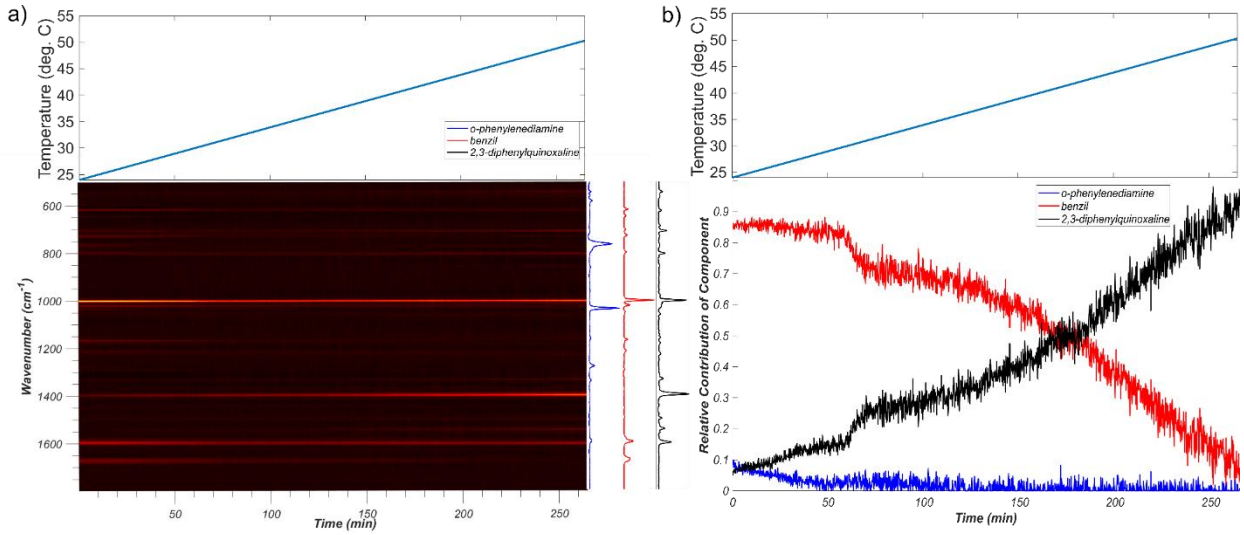

Figure 59. a) Real-time Raman monitoring of the reaction mixture (brighter color denotes higher intensity) and the 0.1°C/min temperature profile, b) estimated spectra contributions from non-negative least square fitting procedure.

As the reaction had largely reached completion by the time the mixture had reached the temperature of the reported deep eutectic near 50°C[12] (melting point of benzil is ~95°C, while the melting point of *ortho*-phenylenediamine is ~103°C) the reaction profile appeared to be nearly linear and proceed to high conversion. In an effort to observe a potential eutectic phase and change in reaction kinetics, a faster heating rate of 1°C/min was applied to a similarly pre-milled reaction mixture (Figure 60.). In this case, the sigmoidal reaction profile characteristic of higher frequency milling was observed near 50°C, which is consistent with published literature.[12] This suggests that the observed changes in kinetic behavior of different milling frequencies are likely the result of higher temperatures, due to increased frictional heating. It appears that pre-milling and homogenization is, at least for the case of this reaction, sufficient to induce subsequent reactivity at elevated temperatures.

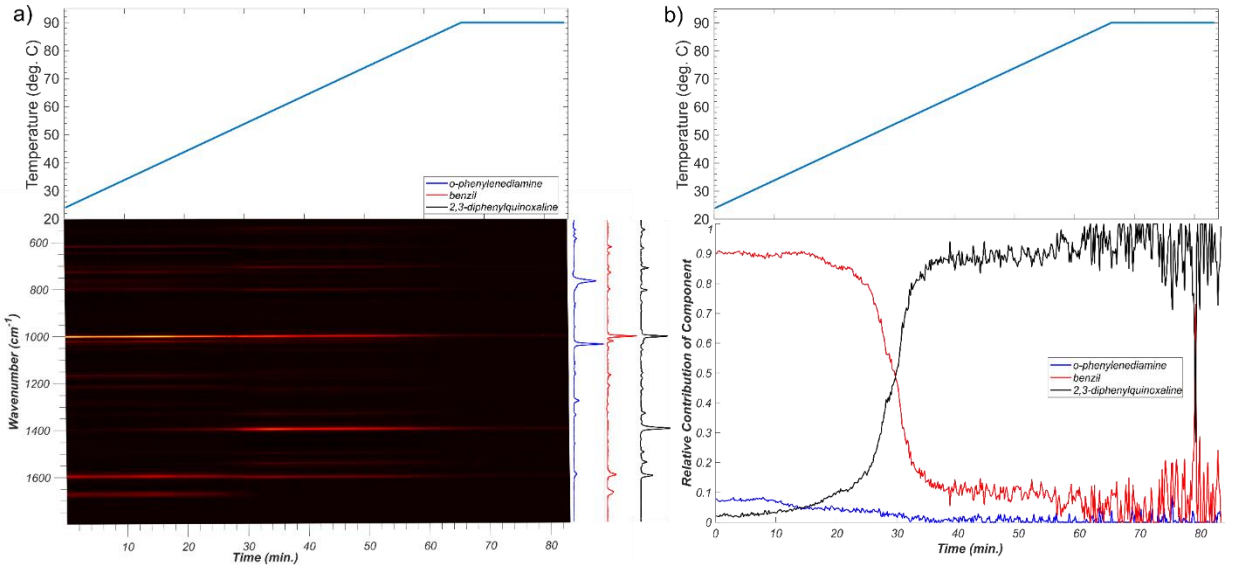

Figure 60. a) (bottom) Real-time Raman monitoring of the reaction mixture (brighter color denotes higher intensity) and (top) the 1°C/min temperature profile, b) (bottom) estimated spectra contributions from non-negative least square fitting procedure.

Microscopy imaging of the sample homogeneity before and after the heating rate of 1°C/min revealed minor changes in sample (Figure 61a,b), and applying same 25x25 sampling grid of Raman spectra, good agreement between all the spectra was observed (Figure 61c), although the relatively low signal to noise resulted in variation in the non-negative least squares fitting(Figure 61d). Despite what appears to be a relatively homogenous mixture consisting of mostly 2,3-diphenylquinoxaline, no evidence of large-scale melting was observed from the microscopy images.

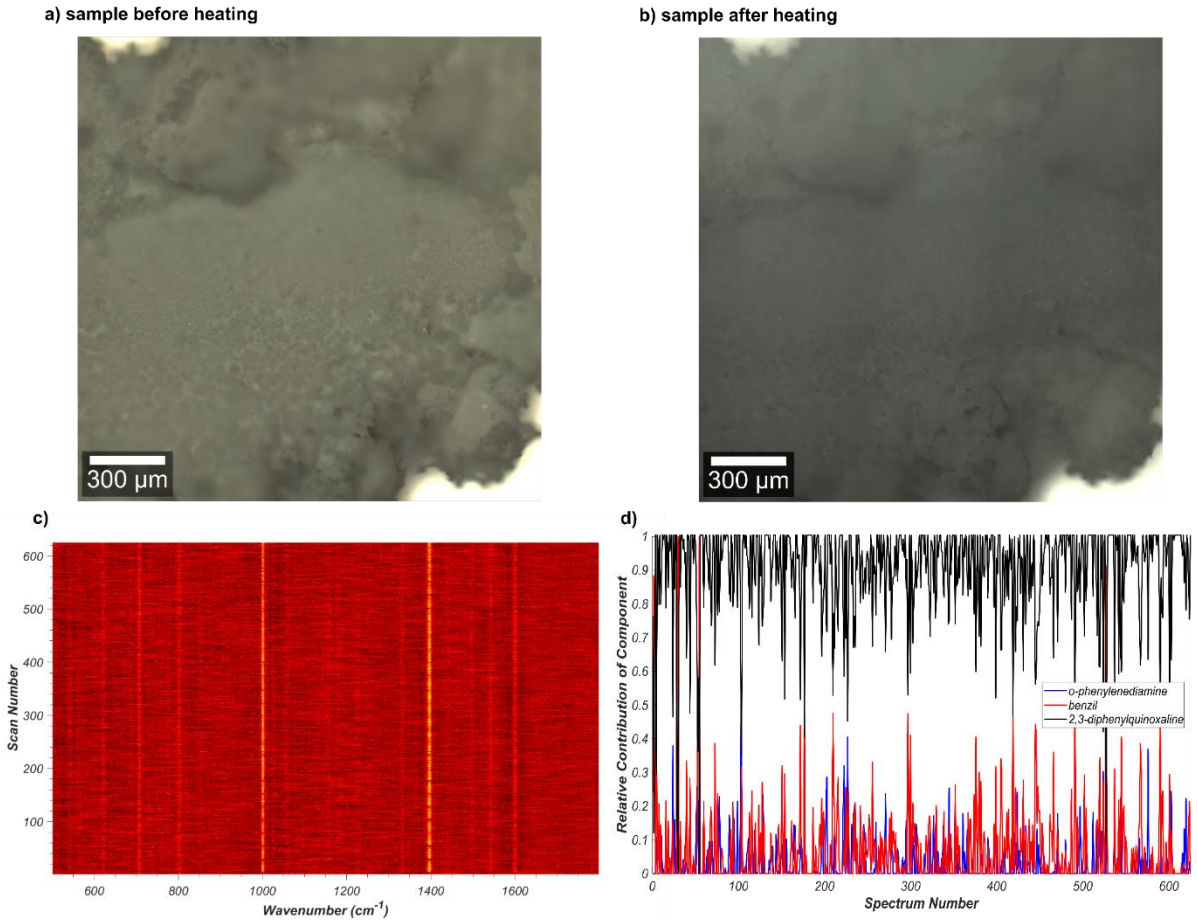

Figure 61. a) Sample mixture before heating at 1°C/min and b) the same sample after heating (image has been brightened and contrast enhanced due to low brightness). c) Raman spectra investigating the homogeneity of the milled mixture (brighter color denotes higher intensity), d) estimated spectra contributions from the non-negative least square fitting procedure.

(b) *In situ* synchrotron X-ray powder diffraction

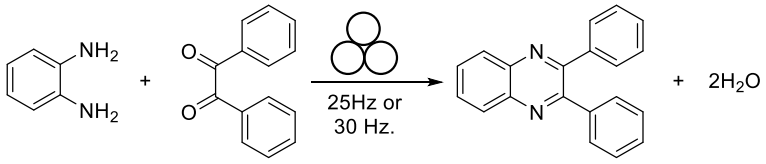

Figure 62. Milling reaction of benzil with o-phenylenediamine.

In order to detect eutectic melting, the milling reaction was monitored at various milling frequencies using *in situ* synchrotron X-ray diffraction (Figure 62). Monitoring by synchrotron X-ray diffraction was conducted using a previously reported design[15] at the PETRA III beamline P02.1 at Deutsches Elektronen-Synchrotron, with λ = 0.207 Å, in PMMA milling jars. All 2D XRPD patterns were integrated using Dioptas[16] and

background PMMA signal was subtracted with the Sonneveld-Visser algorithm[17] and cut to the relevant region between 0.5° and 5° 2θ.

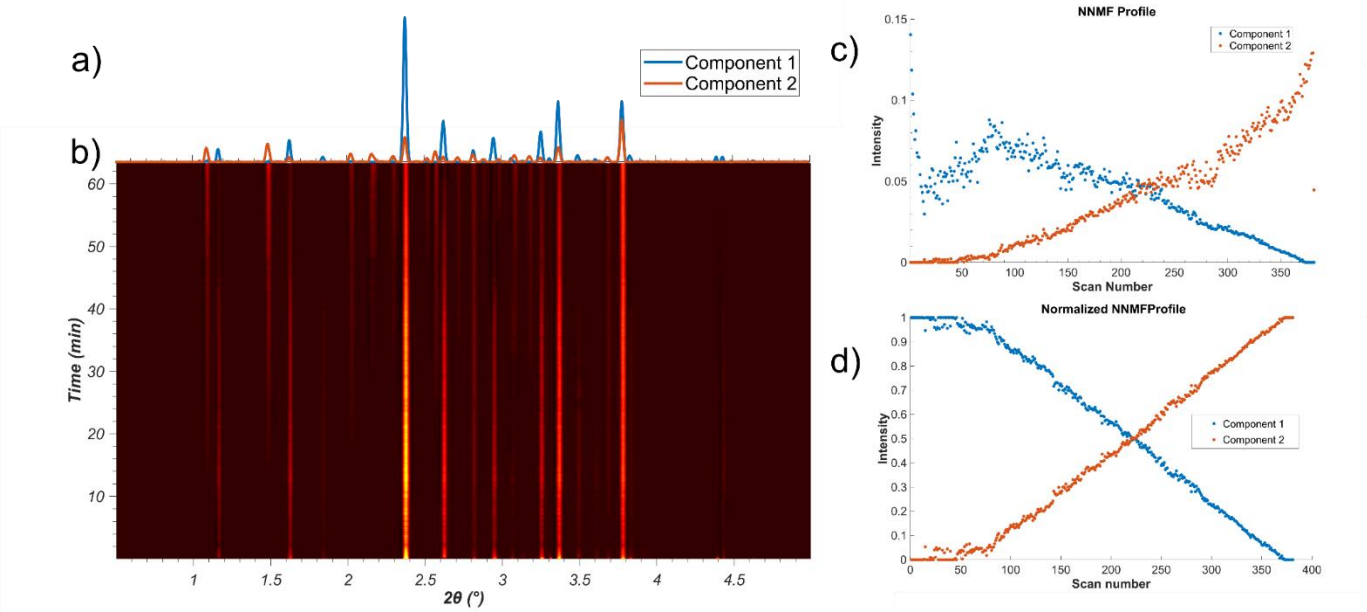

Figure 63. Milling reaction of benzil with o-phenylenediamine at 25Hz. a) Components estimates obtained from NNMF, component 1 primarily consists of the diffraction signal of the two starting materials, while component 2 primarily corresponds to the diffraction signal of the product, with some diffraction contribution of the starting materials as the reaction did not reach completion. b) Sequential in situ diffraction measurements, a brighter color denotes higher intensity. c) Reaction profile as estimated by NNMF processing. d) Normalization of the reaction profile obtained from NNMF (Figure 6c).

For a reaction undergoing rate acceleration due to eutectic melting, we expected to observe a loss in signal corresponding to a melt phase. However, the presence of starting materials and the emergence of product is readily observed with no major loss in diffraction signal over the course of the reaction at either milling frequency (Figure 63b &Figure 65b.). Despite clear formation of 2,3-diphenylquinoxaline as observed by solution ^{1}H NMR, X-ray powder diffraction pattern (XRPD) of the product is not consistent with the previously reported structure. Attempts at structure solution for this newly discovered product were so far not successful, which precludes the use of Rietveld refinement and fitting to determine the reaction profile (Figure 64).

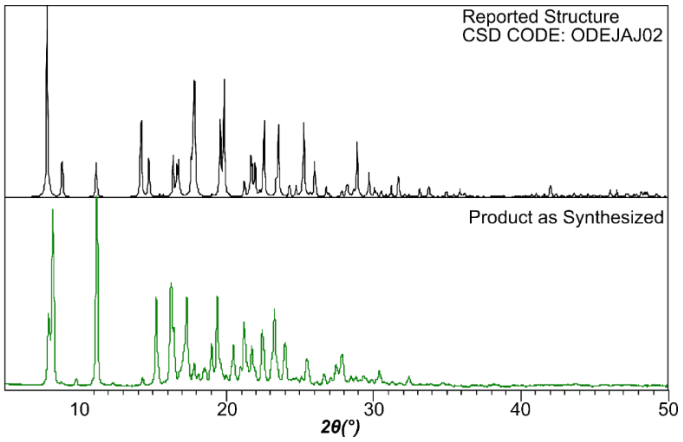

Figure 64. X-ray powder diffraction patterns of 2,3-diphenylquinoxaline: as synthesized (bottom) compared to the simulated pattern for the reported crystal structure (top).

In order to obtain the reaction profile, non-negative matrix factorization was applied to estimate the components of the reaction and their associated reaction profile over time, due to the inherent non-negative property of the data.[18] In this case, a two-component system was chosen, which approximates the contributions of 1) the mixture of the two starting materials and 2) the contribution of the product. The two components obtained for both datasets are largely consistent with this assumption (Figure 63a & Figure 65a). As NNMF seeks to approximate the intensity over the course of the reaction, the profile obtained from NNMF is sensitive to stochastic variations in intensity caused by the sample moving in out of the beam path during milling (Figure 63c & Figure 65c). Importantly, no diffuse or unknown signal is observed nor is a drop in signal intensity, indicating that large scale melting of the reaction mixture is not observed at either milling frequency.[19] Following our assumption of a two-component system, the stochastic variations in intensity can be removed by normalizing the sum of both components to 1.0 (Figure 63d &Figure 65d).

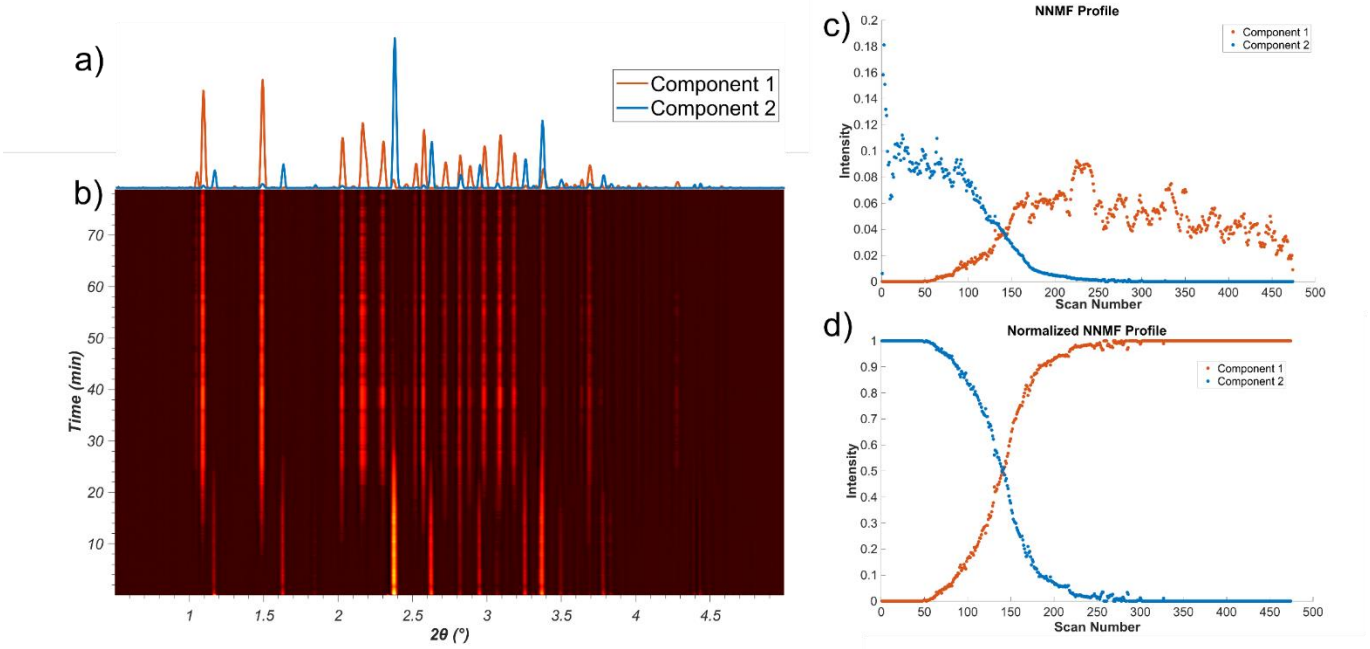

Figure 65. Milling reaction of benzil with o-phenylenediamine at 30Hz. a) Components estimates obtained from NNMF, component 1 is primarily the diffraction signal of the product, while component 2 primarily corresponds to the two starting materials. b) Sequential in situ diffraction measurements, a brighter color denotes higher intensity. c) Reaction profile as estimated by NNMF processing. d) Normalization of the reaction profile obtained from NNMF (Figure 7c).

Normalization of the *in situ* corrected spectra clearly indicates linear product formation at 25Hz (Figure 63d) and a sigmoidal reaction profile at 30Hz (Figure 65d) consistent with our previous measurements *via* Raman spectroscopy[13] for milling and the thermal measurements described in this study. This suggests that the variation in reaction kinetics observed proceeds is not the result of large-scale eutectic melting often observed in organic "solid-solid" reactions.[20] Both diffraction and Raman spectroscopic measurements suggest a transient or "hidden" eutectic phase.[21] This implies that diffusion or mobility in the solid state is a critical factor for understanding mechanochemical reaction kinetics. In this case, the often used "pseudo-fluid" model[22] for mechanochemical reactions, which yields sigmoidal kinetics[23] is applicable only above a critical temperature near 50°C where reaction mobility dramatically increases.

(c) Variable temperature X-ray powder diffraction (VT-XRPD)

In order to verify the influence of thermal effects on the *in situ* synchrotron X-ray diffraction studies, variable temperature X-ray powder diffraction (VT-XRPD) measurements were conducted. A temperature ramp from 27°C to 70°C was applied at an increment of 1°C per scan (~7minutes per scan). The observed transformation is remarkably similar to that observed *via* milling. Below 47 °C, the reported eutectic temperature for *o*-phenylenediamine and benzil,[12] the normalized reaction profile obtained from NNMF demonstrates linear reaction kinetics similar to those observed milling at 20 Hz. A rapid acceleration in reaction rate, consistent with the sigmoidal profile, is observed above 47 °C and is similar to milling reactions conducted at 30 Hz. This further supports that the variations in mechanochemical kinetics are thermally driven, although large-scale melting is not observed *via* VT-XRPD.

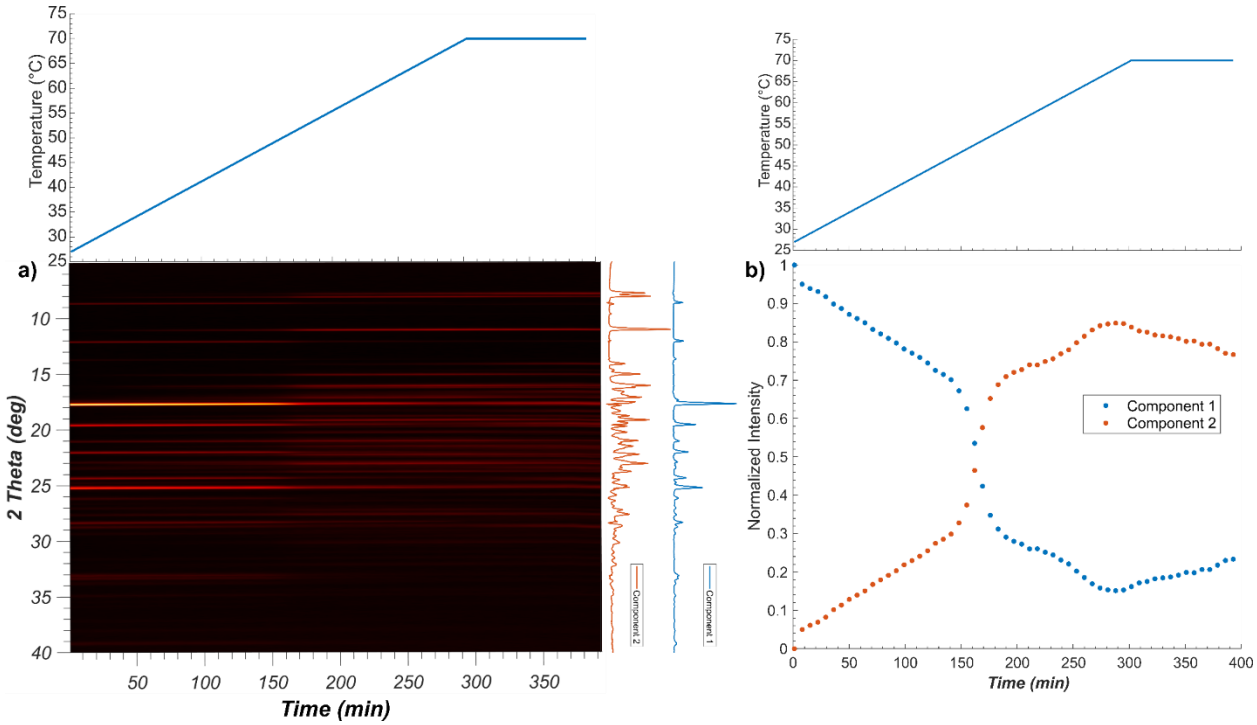

Figure 66. a) (bottom)Variable temperature X-ray powder diffraction patterns for a mixture of benzil with o-phenylenediamine, with the associated temperature (top). Brighter color denotes higher intensity. b) (bottom) Normalized reaction profile obtained from NNMF analysis with the associated temperature (top). The estimated components from NNMF are shown between the diffraction patterns and the estimated reaction profile.

In order to better quantify and understand the effects of heating the reaction mixture, solution ^{1}H nuclear magnetic resonance spectroscopy was performed on the milled reaction mixture both before and after the VT-XRPD study (Figure 67), confirming the identity of the product. Even after only brief milling integration of the ^{1}H NMR spectrum suggests a conversion of ~11% of the product, which increases to nearly 82% after VT-XRPD. This contrasts with previous reported milling reactions which proceed to quantitative conversion.[13] This low conversion is likely due to the sublimation of *o*-phenylenediamine, which is no longer detected in the final reaction mixture, despite the presence of remaining benzil, providing a synthetic advantage of milling with respect to heating solid reactants.

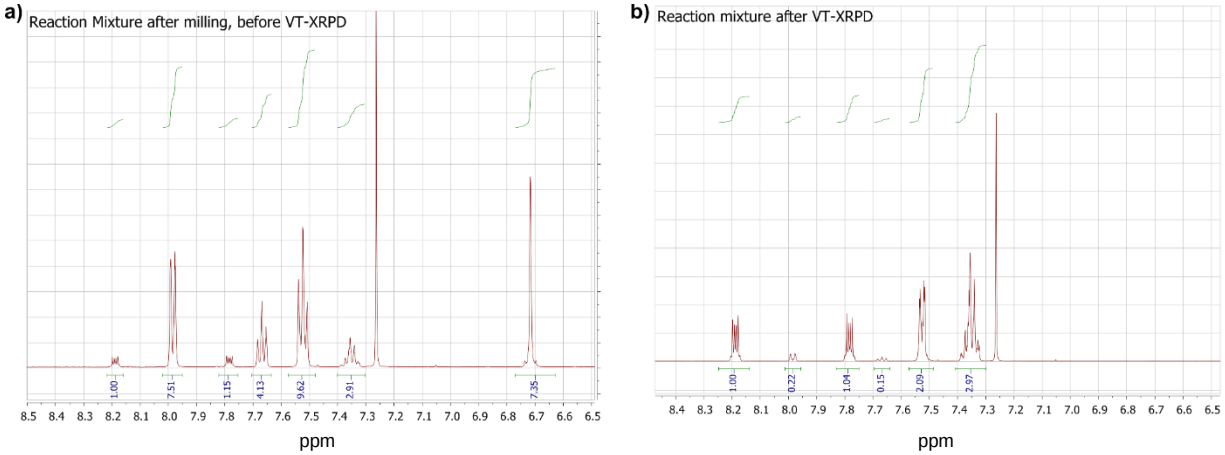

Figure 67. ^{1}H NMR in $CDCl_3$ spectra of the reaction mixture before (a) and after (b) the VT-XRPD study. The o-phenylene diamine peak at ~6.7ppm is no longer detected after VT-XRPD despite the presence of excess benzil.

5.04 Conclusions

Given the challenges of accurately measuring and controlling temperature during mechanochemical reactions, we have demonstrated an alternative method to isolate thermal and mechanical effects, where brief milling and homogenization is followed by hot-stage measurements, in this case Raman spectroscopy, to better understand the thermal behavior of mechanochemically homogenized reaction mixtures. Given the prevalence and diversity of types of variable temperature setups, including X-ray powder diffraction, and Raman spectroscopy, this presents an accessible method which is highly complementary to *in situ* milling measurements. In this case, hot stage measurements suggest the kinetic behavior observed in the condensation reaction between benzil and

o-phenylenediamine is highly sensitive to temperature consistent with a eutectic phase. *In situ* synchrotron X-ray powder diffraction measurements while milling reveal that this behavior is not due to large scale melting of the material, suggesting that the reaction proceeds through a transient or hidden eutectic or dynamic solid phase consistent with proposed 'pseudo-fluid' model. This work suggests that temperature can be a critical factor in explaining mechanochemical kinetics not only due to its effect on chemical reaction rates, but the diffusion properties of the reaction mixture.

5.05 Experimental

Benzil was purchased from Sigma-Aldrich and *o*-phenylenediamine was purchased from Alfa Aesar. All reagents were used without further purification. Milling reactions were conducted in a ~15mL poly-methyl-methacrylate milling jar at a frequency of 20Hz for 1 minute using 4g zirconia ball in a Retsch MM200 mill.

(a) Raman Spectroscopy

Raman spectra were collected on a WITec alpha300 R Confocal Raman Imaging system using ra 10x objective and a 785nm laser operating at 70mW equipped with a Linkam hot-stage and programmable controller. All spectra were analyzed using a previously described fitting procedure implemented in MATLAB.[13]

(b) Synchrotron X-ray Powder Diffraction

Milling reactions were conducted using the above mentioned conditions in a modified Retsch® MM400 mixer mill operating at a frequency of 30 Hz. Experiments were performed at the high-resolution powder diffraction beamline PETRA III (P02.1, λ = 0.207 Å (59.9 keV)) beamline at DESY with acquisition every 10 seconds utilizing a PerkinElmer 2D area detector. All 2D XRPD patterns were integrated using Dioptas.[16] Subsequent processing of the data was conducted in MATLAB,[24] and consisted of background subtraction using the Sonneveld-Visser algorithm.[17] NNMF was applied using the default *nnmf* function[25] in MATLAB.[24]

(c) Ex situ XRPD and VT-XRPD

All *ex situ* and variable temperature powder X-ray diffraction measurements were conducted using a Bruker D8 Advance equipped with a Ni-filtered Cu*K*α radiation source and a Lynxeye linear position sensitive detector (Bruker AXS, Madison, WI). Variable temperature measurements were conducted using an Anton Paar CHC Cryo & Humidity Chamber with a heating rate of 1°C per scan with a scan time of 427 seconds per increment for a range between 27 to 70°C before holding at 70°C for the remainder the measurements.

(d) Solution NMR

All NMR spectra were recorded using a Varian VNMRS 500 MHz NMR Spectrometer, in $CDCl_3$. The product matches the reported spectrum of the Spectral Database for Organic Compounds (SDBS), SDBS No. 32951CDS-10-500.

5.06 Acknowledgements

The authors thank Dr. Matthew Harrington for use of the confocal Raman imaging system.

5.07 References

1. Takacs, L.; *Progress in Materials Science* **2002,** *47*, (4), 355-414.
2. Andersen, J.; Mack, J.; *Green Chemistry* **2018,** *20*, (7), 1435-1443.
3. Do, J.-L.; Friščić, T.; *ACS Central Science* **2017,** *3*, (1), 13-19.
4. James, S.L.; Adams, C.J.; Bolm, C.; Braga, D.; Collier, P.; Friščić, T.; Grepioni, F.; Harris, K.D.M.; Hyett, G.; Jones, W., et al.; *Chemical Society Reviews* **2012,** *41*, (1), 413-447.
5. Užarević, K.; Halasz, I.; Friščić, T.; *The Journal of Physical Chemistry Letters* **2015,** *6*, (20), 4129-4140.
6. Andersen, J.M.; Mack, J.; *Chemical Science* **2017,** *8*, (8), 5447-5453.
7. Andersen, J.; Mack, J.; *Angewandte Chemie International Edition* **2018,** *57*, (40), 13062-13065.
8. Užarević, K.; Ferdelji, N.; Mrla, T.; Julien, P.A.; Halasz, B.; Friščić, T.; Halasz, I.; *Chemical Science* **2018,** *9*, (9), 2525-2532.
9. Kulla, H.; Haferkamp, S.; Akhmetova, I.; Röllig, M.; Maierhofer, C.; Rademann, K.; Emmerling, F.; *Angewandte Chemie International Edition* **2018,** *57*, (20), 5930-5933.

10. Sahoo, P.K.; Giri, C.; Haldar, T.S.; Puttreddy, R.; Rissanen, K.; Mal, P.; *European Journal of Organic Chemistry* **2016,** *2016*, (7), 1283-1291.

11. Oliveira, P.F.M.; Haruta, N.; Chamayou, A.; Guidetti, B.; Baltas, M.; Tanaka, K.; Sato, T.; Baron, M.; *Tetrahedron* **2017,** *73*, (16), 2305-2310.

12. Oliveira , P.F.M.; Baron, M.; Chamayou, A.; Baltas, M.; Guidetti, B.; Haruta, N.; Tanaka, K.; Sato , T.; *ChemistrySelect* **2016,** *1*, (5), 984-988.

13. Julien, P.A.; Malvestiti, I.; Friščić, T.; *Beilstein Journal of Organic Chemistry* **2017,** *13*, 2160-2168.

14. Drebushchak, T.N.; Ogienko, A.A.; Boldyreva, E.V.; *CrystEngComm* **2011,** *13*, (13), 4405-4410.

15. Halasz, I.; Kimber, S.A.J.; Beldon, P.J.; Belenguer, A.M.; Adams, F.; Honkimäki, V.; Nightingale, R.C.; Dinnebier, R.E.; Friščić, T.; *Nature Protocols* **2013,** *8*, 1718.

16. Prescher, C.; Prakapenka, V.B.; *High Pressure Research* **2015,** *35*, (3), 223-230.

17. Sonneveld, E.J.; Visser, J.W.; *Journal of Applied Crystallography* **1975,** *8*, (1), 1-7.

18. Stanev, V.; Vesselinov, V.V.; Kusne, A.G.; Antoszewski, G.; Takeuchi, I.; Alexandrov, B.S.; *npj Computational Materials* **2018,** *4*, (1), 43.

19. Andrault, D.; Morard, G.; Bolfan-Casanova, N.; Ohtaka, O.; Fukui, H.; Arima, H.; Guignot, N.; Funakoshi, K.; Lazor, P.; Mezouar, M.; *High Pressure Research* **2006,** *26*, (3), 267-276.

20. Rothenberg, G.; Downie, A.P.; Raston, C.L.; Scott, J.L.; *Journal of the American Chemical Society* **2001,** *123*, (36), 8701-8708.

21. Dolotko, O.; Wiench, J.W.; Dennis, K.W.; Pecharsky, V.K.; Balema, V.P.; *New Journal of Chemistry* **2010,** *34*, (1), 25-28.

22. Ma, X.; Yuan, W.; Bell, S.E.J.; James, S.L.; *Chemical Communications* **2014,** *50*, (13), 1585-1587.

23. Hutchings, B.P.; Crawford, D.E.; Gao, L.; Hu, P.; James, S.L.; *Angewandte Chemie* **2017,** *129*, (48), 15454-15458.

24. *MATLAB*, version 9.6 (R2019a); The MathWorks Inc.: Natick, Massachusetts, 2019.

25. Berry, M.W.; Browne, M.; Langville, A.N.; Pauca, V.P.; Plemmons, R.J.; *Computational Statistics & Data Analysis* **2007,** *52*, (1), 155-173.

6. *In situ* monitoring and mechanism of the mechanochemical formation of a microporous MOF-74 framework.

6.01 Preface

In contrast to previous chapters which focused on organic reactions and “soft” materials, we also explored the potential of real-time reaction monitoring methods for coordination chemistry and the synthesis of hybrid organic-inorganic materials. Metal organic frameworks were studied as they combine both coordination chemistry and crystal engineering as they self-assemble into periodic 3-D assemblies. The mechanochemical synthesis of MOFs from insoluble precursors such as metal oxides and carbonates has been developed as a greener method of MOF synthesis as it minimizes the solvent cost, waste, and produces relatively benign by-products such as CO_2 and water. In this chapter the mechanochemical synthesis of a highly porous metal-organic framework, Zn-MOF-74, from zinc oxide was developed and monitored utilizing synchrotron X-ray powder diffraction, which was published as the following article: Patrick A. Julien, Krunoslav Užarević, Athanassios D. Katsenis, Simon A. J. Kimber, Timothy Wang, Omar K. Farha, Yuancheng Zhang, José Casaban, Luzia S. Germann, Martin Etter, Robert E. Dinnebier, Stuart L. James, Ivan Halasz, and Tomislav Friščić. *Journal of the American Chemical Society* **2016** ,138, 2929-2932. The syntheses used in this work were developed by P. A. Julien. Synchrotron diffraction data was measured principally by P. A. Julien along with the assistance of other team members, including: K. Užarević, A. D. Katsenis, S. A. J. Kimber, L. S. Germann, M. Etter, R. E. Dinnebier, and I. Halasz. Surface area and electron microscopy characterization were conducted by T. Wang and O. K. Farha at Northwestern University. Supplementary characterization of reaction products and Rietveld analysis was conducted by K. Užarević, A. D. Katsenis, and I. Halasz. P. A. Julien and T. Friščić were the principal contributors to the preparation of the manuscript. The supplementary material for this manuscript can be found in Appendix 2.

6.02 Abstract

Mechanochemistry provides a rapid, efficient approach to the metal-organic framework Zn-MOF-74 directly from a metal oxide and without bulk solvent. *In situ* reaction monitoring using synchrotron X-ray diffraction revealed two new phases and an unusual stepwise reaction in which a close-packed intermediate reacts to form the open framework. The reaction can be performed on a gram scale to yield highly porous materials after standard activation.

6.03 Introduction

Metal-organic frameworks (MOFs)[1] are advanced materials with potential applications ranging from storage and separation of fuel gases,[2] CO_2 sequestration[3] and degradation of nerve gases,[4] to fuel cells,[5] catalysis,[6] drug delivery[7] and light harvesting.[8] Commercialization of MOFs has highlighted unique challenges of safety and efficiency associated with metal-organic synthesis.[9] Conventional synthetic procedures often involve solvothermal conditions and require soluble reagents, such as metal nitrates or chlorides which, while common in a laboratory, are intractable in large-scale manufacturing due to issues of cost, toxicity, and explosive (nitrates) or corrosive (chlorides) nature.[9,10] It was recently demonstrated that liquid-catalyzed mechanochemistry,[11] *e.g.* liquid-assisted grinding (LAG) permits facile, room-temperature transformation of safer metal oxides, carbonates or hydroxides, into MOFs, resulting in a cleaner and more atom-efficient process that avoids the need for external bases and production of mineral acids or their salts as byproducts.[12,13] Indeed, MOFs can now be manufactured mechanochemically on a large scale by extrusion.[14] However, the scope of mechanochemistry for making currently relevant MOFs remains modest, limited to HKUST-1 and ZIF-8.[15]

6.04 Results and Discussion

We now present mechanosynthesis of Zn-MOF-74,[16] a representative of M-MOF-74 (also CPO-27) materials,[17-21] from stoichiometric ZnO and 2,5-dihydroxyterephthalic acid (H_4**dhta**) (Figure 68). We provide mechanistic insight into this transformation by real-time,

in situ X-ray powder diffraction (XRPD) monitoring, conducted at the Deutsches Elektronen-Synchroton (DESY) beamline P02.1 and the European Synchrotron Radiation Facility (ESRF) beamline ID15B, using radiation of wavelengths 0.207 Å and 0.142 Å, respectively.[22,23]

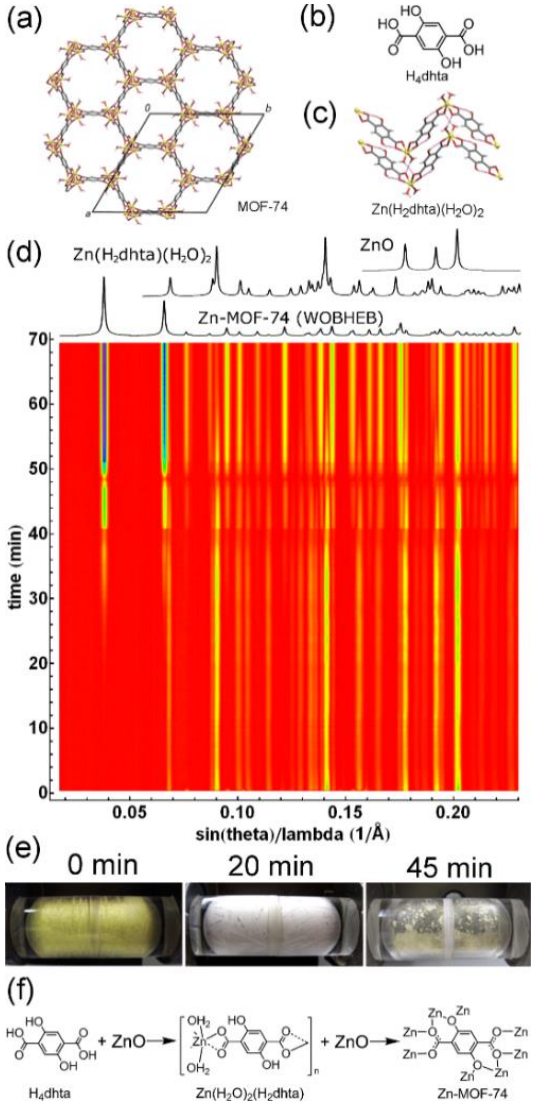

*Figure 68. Structures of: (a) Zn-MOF-74 (CCDC WOBHEB); (b) H_4**dhta**; (c) $Zn(H_2O)_2(H_2$**dhta**$)$ (CCDC ODIPOH). (d) Time-resolved in situ X-ray powder diffractogram for LAG of ZnO and H_4**dhta** (stoichiometric ratio 2:1) with water, (η=0.625 µL/mg, λ= 0.207 Å). Signal losses at 40 min and 48 min are artefacts of time-dependent sample distribution inside the jar during milling; (e) reaction mixture at different milling times and (f) stepwise formation of Zn-MOF-74.*

Without guests occupying the pores, Zn-MOF-74 has the composition $Zn_2(H_2O)_2$(**dhta**), consisting of Zn^{2+} ions coordinated by H_4**dhta** anions and water. We attempted the synthesis of Zn-MOF-74 on 1.1 mmol scale (ca. 400 mg, see SI) by milling ZnO and H_4**dhta** in 2:1 stoichiometric ratio, using 250 μL of water as the grinding liquid. The liquid-to-solid ratio (η)[24] of 0.625 μL/mg was selected based on our previous experience in LAG mechanosynthesis of open MOFs. Milling was conducted using a modified Retsch MM200 mill operating at 30 Hz, in a 14 mL poly(methyl)methacrylate[22,23] jar containing a single 3.5 g stainless steel ball. *In situ* monitoring reveals almost instantaneous (40 s) disappearance of crystalline H_4**dhta**, most likely due to chemical reactions as well as amorphization.[25] Disappearance of H_4**dhta** reflections is followed by formation of the non-porous $Zn(H_2O)_2(H_2$**dhta**) (CCDC ODIPOH) and concomitant drop in intensity of ZnO reflections (Figure 68d, S2b).[26] After 25 min, reflections of residual ZnO and $Zn(H_2O)_2(H_2$**dhta**) begin to vanish, simultaneously with the appearance of Zn-MOF-74 (CCDC WOBHEB).[27] The final product is a free-flowing Zn-MOF-74 powder, characterized by XRPD, Fourier-transform infrared attenuated total reflectance (FTIR-ATR) spectroscopy, ^{13}C cross-polarized magic-angle spinning solid-state nuclear magnetic resonance (CP-MAS SSNMR) spectroscopy and thermogravimetric analysis (TGA).

The observed reaction sequence is confirmed by Rietveld analysis of *in situ* data, which reveals little change in the contents of residual ZnO and initially formed $Zn(H_2O)_2(H_2$**dhta**) until ca. 25 min milling, when both disappear at a comparable rate, concomitantly with the appearance of Zn-MOF-74 (Figure S2c). Rietveld analysis of the final PXRD pattern revealed no other phases except Zn-MOF-74, indicating complete conversion (Figure S2d). The reaction sequence was also verified *ex situ* by XRPD and FTIR-ATR (Figures S3, S4). The same mechanism is observed by *in situ* PXRD monitoring under milder conditions, by using a one 2.9 g stainless steel ball, but formation of Zn-MOF-74 was not quantitative within 70 min (Figure S5).

The stepwise process is also observable visually, as the milled sample, initially canary yellow due to H_4**dhta**, turns white due to transformation into colourless $Zn(H_2O)_2(H_2$**dhta**), and finally takes on the yellow hue of Zn-MOF-74 (Figure 68e,f). The sequence contrasts previous studies of mechanosynthesis of coordination polymers and MOFs, which

revealed initial formation of either highly solvated or open structures that later transform into dense, less solvated products.[28] Course of Zn-MOF-74 formation may be explained by rapid reaction of carboxylic acid groups on H_4**dhta**, leading to formation of $Zn(H_2O)_2(H_2$**dhta**). On further milling, less acidic phenol groups react with residual ZnO, giving Zn-MOF-74. Such mechanism is supported by milling the pre-made $Zn(H_2O)_2(H_2$**dhta**) with one equivalent of ZnO, which gave complete conversion into Zn-MOF-74 (Figure S6).[29]

Mechanosynthesis of Zn-MOF-74 becomes more complex if the milling liquid contains *N*,*N*-dimethylformamide (DMF), a solvent often used in MOF synthesis. We first explored milling with a 4:1 (*v*/*v*) mixture of DMF and water, using a 2.9 gram stainless steel ball. *In situ* monitoring (λ=0.142 Å, Figure 69a) revealed the initial formation of $Zn(H_2O)_2(H_2$**dhta**), followed after ca. 20 min by a new short-lived phase (**1**), which is quickly replaced by another new phase (**2**). Reflections of Zn-MOF-74 appear at ca. 45 min.[17] XRPD patterns of **1** and **2** do not match any structures involving divalent metal ions and H_4**dhta** anions in the Cambridge Structural Database.[30]

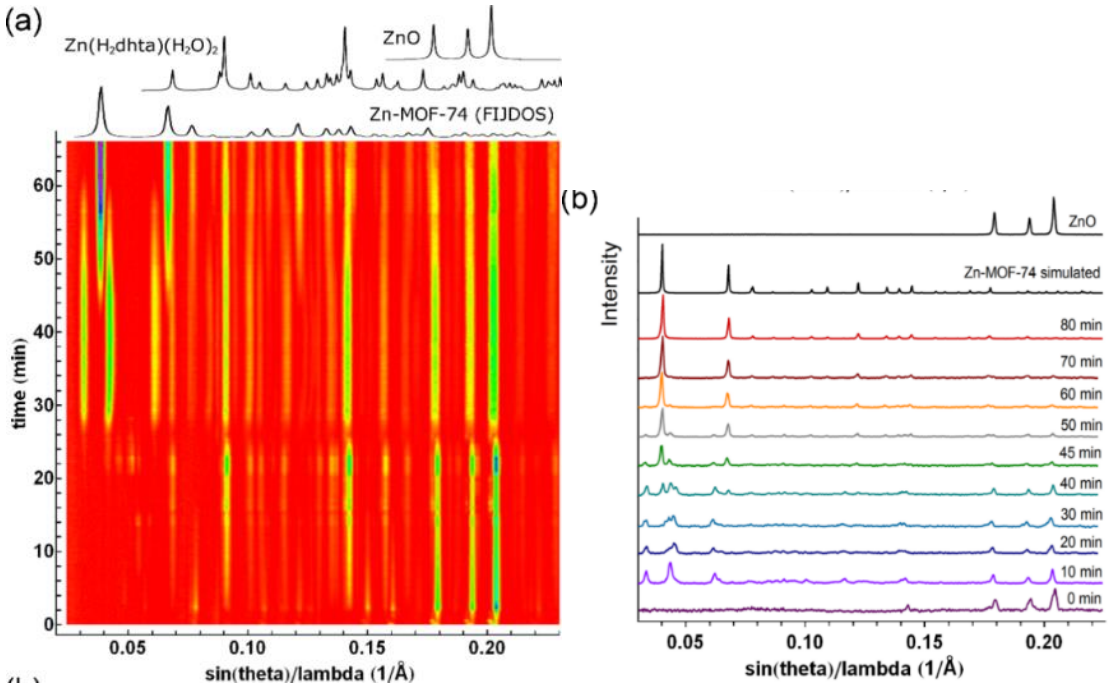

*Figure 69. (a) Time-resolved XRPD data for LAG of ZnO and H_4**dhta** (stoichiometric ratio 2:1) with a DMF:water mixture (4:1 v/v, η=0.625 μL/mg, λ=0.142 Å), using a 2.9 gram ball. Rectangles at 20-25 min and 25-45 min highlight reflections of **1** and **2**, respectively.*

Disappearance of the scattering signal around 26 min is an artefact of time-dependent sample distribution inside the reaction jar during milling.[22] (b) Laboratory XRPD patterns for reaction conducted with a heavier, 3.5 gram milling ball.

Repeating the reaction under harsher conditions, by using a 3.5 gram ball, enabled complete conversion into Zn-MOF-74 in 70 min. Reaction analysis *ex situ*, by recording XRPD patterns of the extracted reaction mixture every 5-10 min, broadly agrees with *in situ* monitoring (Figure 69b). However, using a 3.5 gram ball led to faster appearance of **2** (in 10 min) and Zn-MOF-74 (after 40 min), and to faster disappearance of $Zn(H_2O)_2(H_2$**dhta**), which was less prominent and no longer noticeable after 40 min. Intermediate **1** was not observed by *ex situ* monitoring, which may be attributed to its brief existence during milling, and is consistent with limitations of *ex situ* analysis in analyzing mechanochemical reactions. The LAG reaction using only DMF was slower, requiring almost 3 hours for complete conversion into Zn-MOF-74 and, based on *ex situ* analysis, also involved the intermediate **2** (Figure S9).

As milling with water, DMF, or a mixture of both, gave Zn-MOF-74, we conclude that the organic liquid is not critical for the mechanochemical assembly of the MOF-74 structure. However, **1** and **2** show that DMF, in comparison to water, makes accessible additional assembly motifs in this system. While **1** was too short-lived for isolation, we succeeded in preparing **2** as an almost pure phase, with only traces of ZnO evident in the XRPD pattern, by milling ZnO and H_4**dhta** in a 1.4:1 stoichiometric ratio. However, **2** is not stable and over time undergoes structural changes that are manifested in its XRPD pattern, most notably the shifting and broadening of the X-ray reflection at 2θ=7.40° (Figure S15). This is also evident during milling, as *ex situ* and *in situ* monitoring reveal broadening and splitting of this reflection (Figure 69). While poor stability has so far prevented us from acquiring XRPD data suitable for structure characterization, **2** has been characterized by CP-MAS ^{13}C SSNMR, TGA and FTIR-ATR (Figures S16-18, S20).

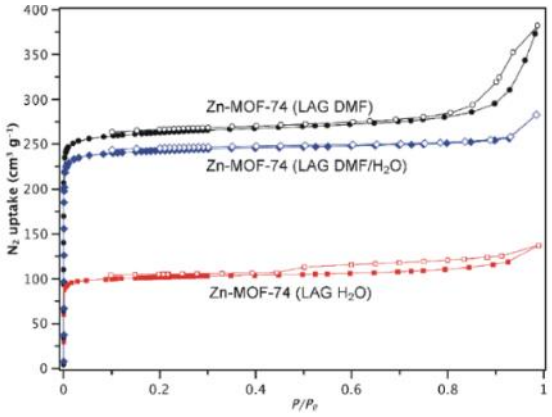

Figure 70. Nitrogen sorption curves for activated samples of Zn-MOF-74 made by LAG with water (red), 4:1 DMF:H2O (v/v) (blue) and DMF (black).

After activation, nitrogen sorption analysis at 77 K (Figure 70) of Zn-MOF-74 obtained by LAG with water revealed a Brunnauer-Emmet-Teller (BET) surface area of 416 $m^2\ g^{-1}$ and a distribution (8.0 Å-11.8 Å) of pore widths. However, samples made by LAG with DMF or with a water:DMF mixture exhibited respective BET areas of 1081 $m^2\ g^{-1}$ and 1006 $m^2\ g^{-1}$, which exceeds most reported values,[18,31] and a pore width of 10.0 Å, consistent with the MOF-74 structure. We speculate that lower microporosity of Zn-MOF-74 obtained by LAG with only water might be due to difficulty of removing all guest water molecules.[32]

Mechanosynthesis of Zn-MOF-74 is also effective on a gram scale: milling H_4**dhta** (1.1 g, 5.5 mmol) with ZnO (0.9 g, 11 mmol) with 1 mL of water in a Retsch PM-100 planetary mill (525 rpm, ball-to-sample weight ratio 4.5:1) gave 2.7 g of unactivated Zn-MOF-74 after 2 h (Figure S6). Mechanosynthesis is not limited only to oxides as inorganic precursors: preliminary results show that the framework can also be synthesized by LAG from basic zinc carbonate, with >830 $m^2\ g^{-1}$ BET surface area.

In summary, we demonstrated fast and efficient gram-scale mechanosynthesis of Zn-MOF-74 directly from the metal oxide and without using bulk solvents. Real-time and *in situ* reaction monitoring revealed two new, metastable phases in this system, one of which was isolated by systematic variation of reaction parameters. It also revealed an unexpected stepwise reaction mechanism in which an open structure is generated from a close-packed reaction intermediate. Mechanosynthesis is accelerated by water, and the

presence of DMF leads to BET surface areas that match highest reported ones.[18,31-33] We are now expanding this methodology to MOF-74 materials based on metals other than zinc.

6.05 Supporting Information

Description of *in situ* studies, selected XRPD, TGA, FTIR-ATR and SSNMR data, scanning electron microscopy images and nitrogen sorption isotherms. This material is available in Appendix 2.

6.06 Acknowledgment

We thank Canadian Foundation for Innovation (CFI), NSERC Discovery Grant, FRQNT Nouveaux Chercheurs grant and McGill University. We thank Ruđer Bošković Institute and Center of Excellence for Advanced Materials and Sensors, Croatia for financial support. KU is supported by the European Commission and the Croatian Ministry of Science, Education and Sports Marie Curie FP7-PEOPLE-2011-COFUND program NEWFELPRO (Grant Agreement No. 62). OKF acknowledges the Army Research Office (project no. W911NF-13-1-0229).

6.07 References

1. a) Deng, H.; Grunder, S.; Cordova, K. E.; Valente, C.; Furukawa, H.; Hmadeh, M.; Gándara, F.; Whalley, A. C.; Liu, Z.; Asahina, S.; Kazumori, H.; O'Keeffe, M.; Terasaki, O.; Stoddart, J. F.; Yaghi, O. M. *Science* **2012**, *336*, 1018; b) Moulton, B.; Zaworotko, M. J. *Chem. Rev.* **2001**, *101*, 1629; c) Batten, S. R.; Champness, N. R.; Chen, X.-M.; Garcia-Martinez, J.; Kitagawa, S.; Öhrström, L.; O'Keeffe, M.; Suh, M. P.; Reedijk, J. *Pure Appl. Chem.* **2013**, *85*, 1715; f) Farha, O. K.; Hupp, J. T. *Acc. Chem. Res.* **2010**, *43*, 1166; g) Kitagawa S.; Kitaura, R.; Noro, S.-i. *Angew. Chem. Int. Ed.* **2004**, *43*, 2334; h) Zhang, J.-P.; Zhang, Y.-B.; Lin, J.-B.; Chen, X.-M. *Chem. Rev.* **2012**, *112*, 1001.

2. a) Getman, R. B.; Bae, Y.-S.; Wilmer, C. E.; Snurr, R. Q. *Chem. Rev*. **2012**, *112*, 703; b) Suh, M. P.; Park, H. J.; Prasad, T. K.; Lim, D.-W. *Chem. Rev*. **2012**, *112*, 782; c) Herm, Z. R.; Bloch, E. D.; Long, J. R. *Chem. Mater.* **2014**, *26*, 323.

3. a) Xiang, S.; He, Y.; Zhang, Z.; Wu, H.; Zhou, W.; Krishna, R.; Chen, B. *Nature Comm.* **2012**, *3*, 954; b) Sumida, K.; Rogow, D. L.; Mason, J. A.; McDonald, T. M.; Bloch, E. D.; Herm, Z. R.; Bae, T.-H.; Long, J. R. *Chem. Rev*. **2012**, *112*, 724; c) D'Alessandro,

D. M.; Smit, B.; Long, J. R. *Angew. Chem. Int. Ed.* **2010**, *49*, 6058; d) McDonald, T. M.; Lee, W. R.; Mason, J. A.; Wiers, B. M.; Hong, C. S.; Long. J. R. *J. Am. Chem. Soc.* **2012**, *134*, 7056.

4. a) Katz, M. J.; Mondloch, J. E.; Totten, R. K.; Park, J. K.; Nguyen, S. T.; Farha, O. K.; Hupp, J. T. *Angew. Chem. Int. Ed*. **2013**, *53*, 497; b) Mondloch, J. E.; Katz, M. J.; Isley, W. C.; Ghosh, P.; Liao, P.; Bury, W.; Wagner, G. W.; Hall, M. G.; DeCoste, J. B.; Peterson, G. W.; Snurr, R. Q.; Cramer, C. J.; Hupp, J. T.; Farha, O. K. *Nature Mater.* **2015**, *14*, 512.

5. Hurd, J. A.; Vaidhyanathan, R.; Thangadurai, V.; Ratcliffe, C. I.; Moudrakovski, I. L.; Shimizu, G. K. H. *Nature. Chem*. **2009**, *1*, 705.

6. a) Fujita, M.; Kwon, Y. J.; Washizu, S.; Ogura, K. *J. Am. Chem. Soc*. **1994**, *116*, 1151; b) Lee, J.; Farha, O. K.; Roberts, J.; Sheidt, K. A.; Nguyen, S. T.; Hupp, J. T. *Chem. Soc. Rev.* **2009**, *38*, 1450; c) Hasegawa, S.; Horike, S.; Matsuda, R.; Furukawa, S.; Mochizuki, K.; Kinoshita, Y.; Kitagawa, S. *J. Am. Chem. Soc*. **2007**, *129*, 2607; d) Corma, A.; Garcia, H.; Llabres, F. X.; Xamena, I.*Chem. Rev.* **2010**, *110*, 4606; e) Yoon, M.; Srirambalaji, R.; Kim, K.*Chem. Rev*. **2012**, *112*, 1196.

7. a) Vallet-Regi, M.; Balas, F.; Arcos, D. *Angew. Chem. Int. Ed.* **2007**, *46*, 7548; b) Horcajada, P.; Serre, C.; Maurin, G.; Ramsahye, N. A.; Balas, F.; Vallet-Regi, M.; Sebban, M.; Taulelle, F.; Ferey, G. *J. Am. Chem. Soc*. **2008**, *130*, 6774.

8. a) Lee, C. Y.; Farha, O. K.; Hong, B. J.; Sarjeant, A. A.; Nguyen, S. T.; Hupp, J. T. *J. Am. Chem. Soc*. **2011**, *133*, 15858; b) Son, H.-J.; Jin, S.; Patwardhan, S.; Wezenberg, S. J.; Jeong, N. C.; So, M.; Wilmer, C. E.; Sarjeant, A. A.; Schatz, G. C.; Snurr, R. Q.; Farha, O. K.; Wiederrecht, G. P.; Hupp, J. T. *J. Am. Chem. Soc*., **2013**, 135, 862: c) Fateeva, A.; Chater, P. A.; Ireland, C. P.; Tahir, A. A.; Khimyak, Y. Z.; Wiper, P. V.; Darwent, J. R.; Rosseinsky, M. J. *Angew. Chem. Int. Ed.* **2012**, *51*, 7440; d) Wang, J. L.; Wang, C.; Lin, W. B. *ACS Catal.* **2012**, 2, 2630; e) Foster, M. E.; Azoulay, J. D.; Wong, B. M.; Allendorf, M. D. *Chem. Sci.* **2014**, *5*, 2081.

9. a) Czaja, A.; Leung, E.; Trukhan, N.; Müller, U. *Industrial MOF Synthesis* in: *Metal-Organic Frameworks: Applications from Catalysis to Gas Storage,* 1st Edition, Ed. D. Farrusseng, Wiley-VCH (2011); b) Czaja, A. U.; Trukhan, N.; Müller, U. *Chem. Soc. Rev.* **2009**, *38*, 1284.

10. a) Yilmaz, B.; Trukhan, N.; Müller, U. *Chin. J. Catal.* **2012**, *33*, 3; b) Gaab, M.; Trukhan, N.; Maurer, S.; Gummaraju, R.; Müller, U. *Micropor. Mesopor. Mater.* **2012**, *157*, 131; b) Stock, N.; Biswas, S. *Chem. Rev.* **2012**, *112*, 933; c) Zhang, Z.; Zaworotko, M. J. *Chem. Soc. Rev.* **2014**, *43*, 5444.

11. a) James, S. L.; Adams, C. J.; Bolm, C.; Braga, D.; Collier, P.; Friščić, T.; Grepioni, F.; Harris, K. D. M.; Hyett, G.; Jones, W.; Krebs, A.; Mack, J.; Maini, L.; Orpen, A. G.; Parkin, I. P.; Shearouse, W. C.; Steed, J. W.; Waddell, D. C. *Angew. Chem. Int. Ed.* **2012**, *41*, 413; b) Braga, D.; Maini, L.; Grepioni, F. *Chem. Soc. Rev.* **2013**, *42*, 7638.

12. Friščić, T.; Jones. W. *Cryst. Growth Des.* **2009**, *9*, 1621.

13. a) Friščić, T.; Reid, D. G.; Halasz, I.; Stein, R. S.; Dinnebier, R. E.; Duer, M. J. *Angew. Chem. Int. Ed.* **2010**, *49*, 712; b) Adams, C. J.; Kurawa, M. A.; Lusi, M.; Orpen, A. G. *CrystEngComm* **2008**, *10*, 1790.

14. Crawford, D.; Casaban, J.; Haydon, R.; Giri, N.; McNally, T.; James, S. L. *Chem. Sci.* **2015**, *6*, 1645.

15. a) Beldon, P. J.; Fabian, L.; Stein, R. S.; Thirumurugan, A.; Cheetam, A. K.; Friščić, T. *Angew. Chem. Int. Ed.* **2010**, *49*, 9640; b) Yuan, W.; Lazuen Garay, A.; Pichon, A.; Clowes, R.; Wood, C. D.; Cooper, A. I.; James, S. L. *CrystEngComm* **2010**, *12*, 4063.

16. Rosi, N. L.; Kim, J.; Eddaoudi, M.; Chen, B.; O'Keeffe, M.; Yaghi, O. M. *J. Am. Chem. Soc.* **2005**, *127*, 1504.

17. a) Dietzel, P. D. C.; Panella, B.; Hirscher, M.; Blom, R.; Fjellvag, H. *Chem. Commun*., **2006**, 959; b) Dietzel, P. D. C.; Blom, R.; Fjellvag, H. *Eur. J. Inorg. Chem*. **2008**, 3624; c) Rowsell, J. L. C.; Yaghi, O. M. *J. Am. Chem. Soc.* **2006**, *128*, 1304.

18. Schoenecker, P. M.;Carson, C. G.; Jasuja, H.; Flemming, C. J. J.; Walton, K. S. *Ind. Eng. Chem. Res*, **2012**, *51*, 6513.

19. a) Caskey, S. R.; Wong-Foy, A. G. ; Matzger, A. J. *J. Am. Chem. Soc*. **2008**, *130*, 10870; b) Millward, A. R.; Yaghi, O. M. *J. Am. Chem. Soc.* **2005**, *127*, 17998.

20. a) Yang, D.-A.; Cho, H.-Y.; Kim, J.; Yang, S.-T.; Ahn, W.-S. *Energy Environ. Sci.*, **2012**, *5*, 6465; b) Cho, H.-Y.; Yang, D.-A.; Kim, J.; Yeong, S.-Y.; Ahn, W.-S. *Catal Today*, **2012**, *185*, 35; c) Calleja, G.; Sanz, R.; Orcajo, G.; Briones, D.; Leo, P.; Martinez, F. *Catal. Today*, **2014**, *227*, 130.

21. a) Bae, T.-H.; Long, J. R. *Energy Environ. Sci.* **2013**, *6*, 3565; b) Britt, D.; Furukawa, H.; Wang, B.; Grant Glover, T.; Yaghi, O. M.; *Proc. Natl. Acad. Sci*, *U S A* **2009**, *106*, 20637; c) Britt, D.; Tranchemontagne, D.; Yaghi., O. M. *Proc. Natl. Acad. Sci. U.S.A.* **2008**, *105*, 11623.

22. a) Halasz, I.; Kimber, S. A. J.; Beldon, P. J.; Belenguer, A. M.; Adams, F.; Honkimäki, V.; Nightingale, R. C.; Dinnebier, R. E.; Friščić. T. *Nature Protocols* **2013**, 8, 1718; b) Katsenis, A. D.; Puškarić, A.; Štrukil, V.; Mottillo, C.; Julien, P. A.; Užarević, K.; Pham, M.-H.; Do, T.-O.; Kimber, S. A. J.; Lazić, P.; Magdysyuk, O.; Dinnebier, R. E.; Halasz, I.; Friščić, T. *Nature Commun.* **2015**, *6*, 6662; c) Halasz, I.; Friščić, T.; Kimber, S. A. J.; Užarević, K.; Puškarić, A.; Mottillo, C.; Julien, P.; Štrukil, V.; Honkimäki, V.; Dinnebier, R. E. *Faraday Discuss.* **2014**, *170*, 203.

23. Užarević, K.; Halasz, I.; Friščić, T. *J. Phys. Chem. Lett.* **2015**, *6*, 4129.

24. Friščić, T.; Childs, S. L.; Rizvi, S. A. A.; Jones, W. *CrystEngComm* **2009**, *11*, 418.

25. Halasz, I.; Friščić, T.; Kimber, S. A. J.; Užarević, K.; Puškarić, A.; Mottillo, C.; Julien, P.; Štrukil, V.; Honkimäki, V.; Dinnebier, R. E. *Faraday Discuss.* **2014**, *170*, 203.

26. Ghermani, N. E.; Morgant, G.; d'Angelo, J.; Desmaele, D.; Fraisse, B. Bonhomme, F.; Dichi, E.; Sgahier, M. *Polyhedron* **2007**, *26*, 2880.

27. Dietzel, P. D. C.; Johnsen, R. E.; Blom, R.; Fjellvag, H. *Chem. Eur.J.* **2008**, *14*, 2389.

28. a) Friščić, T.; Halasz, I.; Beldon, P. J.; Belenguer, A. M.; Adams, F.; Kimber, S. A. J.; Honkimäki, V.; Dinnebier, R. E. *Nature Chem.* **2013**, *5*, 66; b) Strobridge, F. C.; Judaš, N.; Friščić, T. *CrystEngComm* **2010**, *12*, 2409; c) Tumanov, I. A.; Achkasov, A. F.; Boldyreva, E. V.; Boldyrev, V. V. *Russ. J. Phys. Chem. A* **2012**, *86*, 1014; d) Ma, X.; Yuan, W.; Bell, S. E. J.; James, S. L. *Chem. Commun.* **2014**, *50*, 1585.

29. Stepwise reactivity dictated by the presence of two distinct functionalities on a reactant is known in co-crystal mechanosynthesis: a) Halasz, I.; Puškarić, A.; Kimber, S. A. J.; Beldon, P. J.; Belenguer, A. M.; Adams, F.; Honkimäki, V.; Dinnebier, R. E.; Patel, B.; Jones, W.; Štrukil, V.; Friščić, T. *Angew. Chem. Int. Ed.* **2013**, *52*, 11538; b) Cinčić, D.; Friščić, T.; Jones, W. *J. Am. Chem. Soc.* **2008**, *130*, 7524.

30. Cambridge Structural Database (v. 5.36, update Nov 2014) search was done for a general **dhta** fragment and any metal without a defined coordination mode, yielding 129 structures whose simulated XRPD patterns were compared to our experimental data.

31. a) Sánchez-Sánchez, M.; Getachew, N.; Díaz, K.; Díaz -García, M.; Chebude, Y.; Díaz**,** I. *Green. Chem.* **2015**, *17*, 1500; b) Díaz-García, M.; Mayoral, Á.; Díaz, I.; Sánchez-Sánchez, M. *Cryst. Growth Des*., **2014**, *14*, 2479; c) Liu, Y.; Kabbour, H.; Brown, C. M.; Neumann, D. A.; Ahn, C. C. *Langmuir*, **2008**, *24*, 4772; d) Botas, J. A.; Calleja, G.; Sánchez-Sánchez, M.; Orcajo, M. G. *Int. J. Hydrogen Energy*, **2011**, *36*, 10834; e) Srinivas, G.; Krungleviciute, V.; Guo, Z.; Yildirim, T. *Energy Environ. Sci.* **2014**, *7*, 335.

32. a) Tan, K.; Zuluaga, S.; Gong, Q.; Canepa, P.; Wang, H.; Li, J.; Chabal, Y. J.; Thonhauser, T. *Chem. Mater*. **2014**, *26*, 6886; b) Kumar, A.; Madden, D. G.; Lusi, M.; Chen, K.-J.; Daniels, E. A.; Curtin, T.; Perri IV, J. J.; Zaworotko, M. J. *Angew. Chem. Int. Ed.* **2015**, *54*, 1.

33. Schlesinger, M.; Schulze, S.; Hietschold, M.; Mehring, M. *Micropor. Mesopor. Mater.* **2010**, *132*, 121.

7. Tandem Monitoring Mechanochemical Reactivity of Lanthanides in Real-time using Fluorescence Spectroscopy and Powder Diffraction

7.01 Preface

Having demonstrated the utility of *in situ* powder diffraction for optimizing the synthesis of Zn-MOF-74 and elucidating the stepwise mechanism of its formation by milling, we centered subsequent work on investigating the synthesis of lanthanide organic frameworks. Despite considerable interest in their unique topological, optical, magnetic, and catalytic properties, to the best of our knowledge, the mechanochemical syntheses of lanthanide organic frameworks have not yet been explored using *in situ* methods.[1] The unique luminescence of lanthanides provided an opportunity for the development of *in situ* monitoring using the fluorescence of europium ions. Accordingly, this chapter of the Thesis represents an application of the developed fluorescence methodology and represents the first real-time measurements of the mechanochemical synthesis of lanthanide organic frameworks. In addition, the use of *in situ* measurements to assist in the development of the previously unreported mechanochemical syntheses of europium terephthalate frameworks are described.

The work herein is being prepared for submission in *Journal of Materials Chemistry C* with the following authors: Patrick A. Julien, Luzia Germann, Martin Etter, Ivani Malvestiti, Stipe Lukin, Krunoslav Užarević and Tomislav Friščić.

7.02 Abstract:

We report the first use of fluorescence emission spectroscopy for real-time reaction monitoring of mechanochemical lanthanide-based reactions. Tandem *in situ* fluorescence and X-ray diffraction have for the first time been applied to monitor the milling synthesis of lanthanide-based materials, namely, a variety of europium containing metal organic frameworks. Comparison of real-time fluorescence emission and synchrotron X-ray diffraction suggests fluorescence emission spectroscopy as novel low-cost approach to mechanochemical reaction monitoring. Reaction profiles estimated from fluorescence are largely consistent with diffraction based measurements. Utilizing the fluorescence

emission of lanthanides provides a unique spectroscopic handle to study the coordination environment of lanthanide ions during mechanochemical reactions. It has significant potential to improve the fundamental understanding of lanthanide mechanochemistry and enables the rapid development of solid-state reactivity of lanthanide-based materials.

7.03 Introduction

The desire for safer and more sustainable functional materials has driven interest in lanthanides due to their low toxicity coupled with their unique magnetic, optical, and catalytic properties. At the same time, mechanochemistry has risen to prominence in the field of green chemistry as an environmentally sustainable, cost effective, and scalable methodology of chemical synthesis. The green synthesis of functional lanthanide materials, such as lanthanide-based metal organic frameworks (MOFs), is a topic of considerable interest, with the milling synthesis of lanthanide-based frameworks from rare earth carbonates being well established.[2] To date, studies on the milling syntheses of lanthanide based MOFs remain limited to frameworks consisting of lanthanide frameworks based on trimesic acid[3,4] or 2,3-pyrazinedicarboxylic acid.[5] Real-time monitoring of milling reactions is critical for optimizing synthetic conditions and gaining insights into mechanochemical reaction behavior and remains unreported for lanthanide based mechanosynthesis. Currently reported techniques for monitoring mechanochemical reactions are limited to X-ray powder diffraction,[6] Raman spectroscopy,[7, 8] and thermal[8, 9] or pressure measurements.[10] The well-defined emission of lanthanides, provides a unique opportunity to monitor the milling synthesis of inorganic or metal-organic materials *via* the lanthanide coordination center. Europium in particular exhibits characteristic emission from *d-f* and *f-f* transitions with narrow emission bands sensitive to the symmetry of the europium species.[11] Monitoring the fluorescence emission during a mechanochemical synthesis of a europium-based metal organic framework provides a unique opportunity to monitor the coordination environment of the europium ion throughout the formation of different crystalline phases. Coupling fluorescence spectroscopy with the established X-ray powder diffraction (PXRD) monitoring method facilitates the discovery of intermediate phases and novel structures. This dual monitoring approach represents a novel method for contrasting reaction and crystallization kinetics of the stepwise transformation for metal organic materials.

To monitor reactions using fluorescence emission spectroscopy, we have developed a simple setup consisting of a UV diode as an excitation source, a transparent jar, and fiber optically coupled spectrometer. This simple and portable setup enabled simultaneous measurements with other established monitoring techniques, including *in situ* synchrotron X-ray diffraction.[12] Given the novelty of *in situ* fluorescence measurements, a quantitative method for analyzing these data sets has not yet been firmly established. Additionally, the frequent presence of unknown phases prohibits or greatly complicates the use of Rietveld refinement in our data.[13] To facilitate the analysis and comparison of real-time data from both diffraction and fluorescence measurements, we have applied non-negative matrix factorization (NMF) in order to estimate both components (i.e. estimated spectra or diffraction pattern) and the profile (i.e. estimated relative amount) of phases emerging in the reaction. NMF data processing was chosen due to the inherent parts-based representation emerging from the non-negativity constraints of the algorithm, along with the inherent non-negative properties of our data.[14] NMF seeks to approximate the data matrix V as a product of the matrices W and H (Equation 1) by minimizing Equation 2 subject to non-negativity constraints on W and H (Equation 3). In this case, we have utilized the projected gradient method for factorization, with a pre-specified number of components, determined from visual inspection of the data set to provide estimates for spectra or diffraction patterns and profiles.[14]

$$V \approx \mathrm{WH} \qquad (1)$$

$$\min_{W,H} \qquad f(W,H) = \frac{1}{2}\sum_{i=1}^{n}\sum_{j=1}^{m}(V_{ij} - (WH)_{ij})^2 \qquad (2)$$

$$\text{subject to } W_{ia} \geq 0, H_{bj} \geq 0, \forall \mathrm{i,a,b,j}. \qquad (3)$$

The tandem fluorescence emission and X-ray diffraction methodology is broadly applicable to a variety of europium based lanthanide based organic frameworks. Many MOF linkers consist of rigid and conjugated organic molecules capable of acting as lanthanide “antennas”, where the linker is excited and subsequently transfers energy to excite the lanthanide ion which subsequently emits. The high crystallinity of MOF materials and the “antenna effect” make them an ideal system for tandem *in situ* fluorescence emission and X-ray powder diffraction measurements. In this work, for the

first time, we have applied this tandem technique towards monitoring the mechanochemical synthesis of a few prominent lanthanide organic frameworks.

7.04 Results and Discussion

(a) Europium Trimesate Frameworks

We began our studies with the previously reported liquid-assisted grinding (LAG) of europium carbonate with trimesic acid (H_3BTC) using either N,N-dimethylformamide (DMF) or a mixture of DMF and water to form both porous and close-packed frameworks (Figure 71).[2]

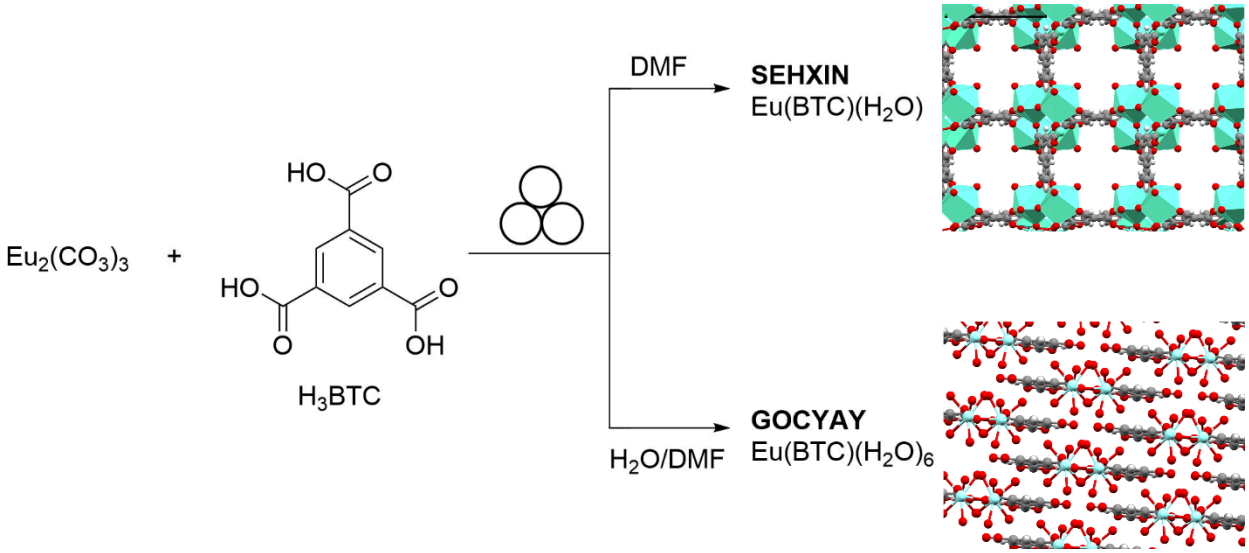

Figure 71. Previously reported liquid-assisted grinding reaction of europium(III) carbonate with trimesic acid (H_3BTC) to form a porous framework (CSD code: SEHXIN) when DMF is used, while the addition of water to DMF results in the formation of a hydrated coordination polymer isostructural to a previously reported structure (CSD code: GOCYAY).[2]

Tandem *in situ* synchrotron diffraction and fluorescence monitoring of LAG with 50µL of DMF confirms the formation of a porous europium trimesate framework $Eu(BTC)(H_2O)$ (CSD code: SEHXIN) after approximately an hour of milling, although several unidentified reflections are present in the final product (Figure 72). The reaction proceeds through a weakly diffracting intermediate phase, which we are unable to clearly identify. Both the formation of the unidentified intermediate phase and the known MOF

structure can be clearly observed in the fluorescence emission of the reaction. Crystallization of the final MOF phase appears to precede significant changes in fluorescence, suggesting that substantial amounts of europium remain in coordination environments different from that of the crystalline MOF, such as an amorphous phase. This hypothesis is supported by the observed increase in diffraction intensity near the end of the reaction suggesting crystallization from amorphous phases. This suggests that europium fluorescence may provide insights into amorphous phases of a reaction.

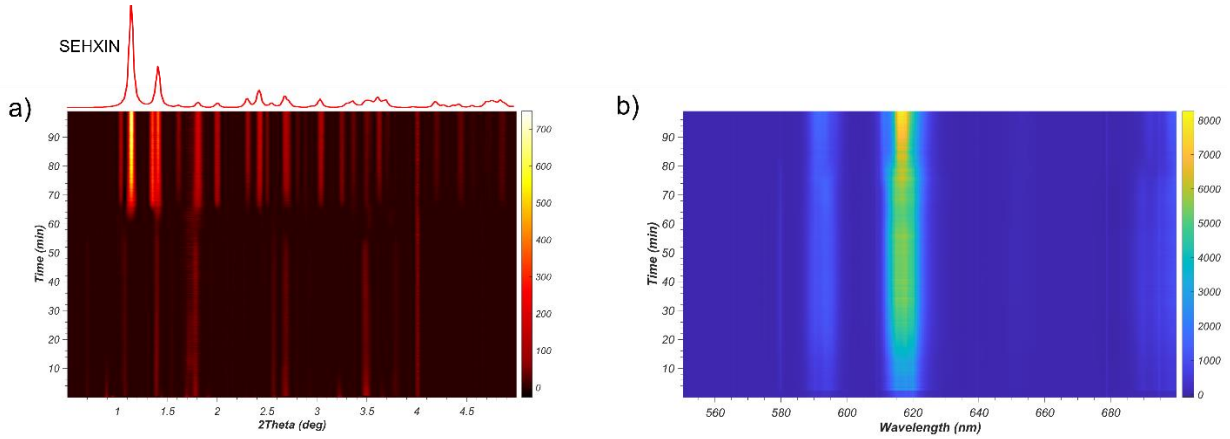

Figure 72. Tandem in situ monitoring of the reaction of europium(III) carbonate with trimesic acid and DMF using a) diffraction and b) fluorescence, showing the formation of the porous Eu(BTC)(H_2O) (CSD code: SEHXIN) structure.

In contrast to the relatively slow formation of the porous europium(III) trimesate under DMF, the presence of 20µL water with 30µL of DMF results in the rapid (under 5 minutes) formation of a hydrated coordination polymer Eu(BTC)(H_2O)$_6$ (CSD code: GOCYAY) as previously reported in the literature, along with recrystallized trimesic acid (Figure 73). This suggests that the presence of water greatly accelerates the reaction kinetics, but also plays a key role in reaction selectivity, favoring the formation of dense-packed phases.

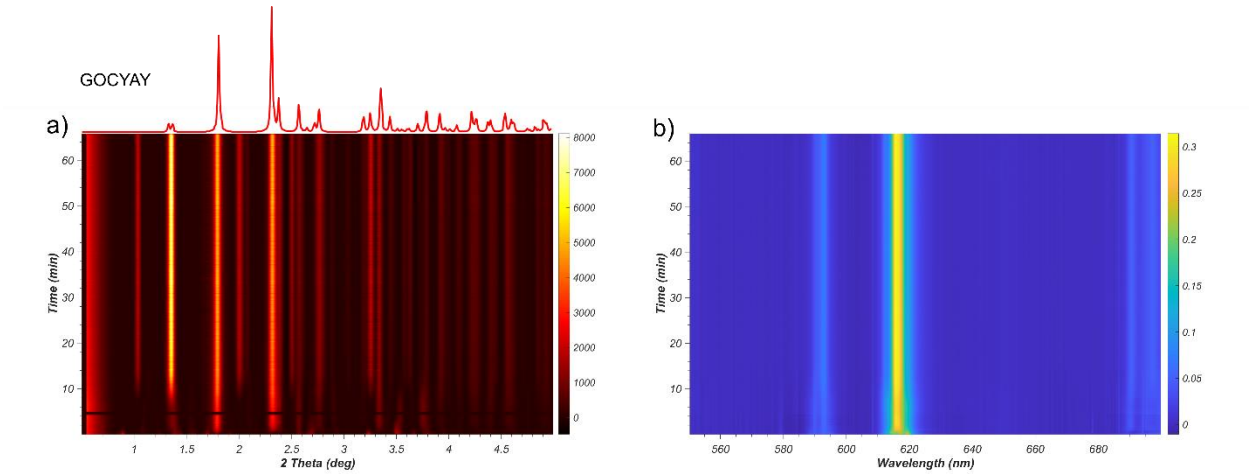

Figure 73. Tandem a) in situ diffraction and b) fluorescence emission monitoring of the formation of the GOCYAY hydrate phase.

(b) Europium *Benzene-1,4-Dicarboxylate Frameworks*

In order to demonstrate the utility of *in situ* fluorescence measurements for developing and understanding novel mechanochemical syntheses, we chose to develop a novel mechanochemical synthesis of a known lanthanide organic framework. Lanthanide organic frameworks based on benzene-1,4-dicarboxylic acid (H_2BDC) were chosen due to the popularity of this linker, with a Cambridge Structural Database V. 5.40 (CSD) search of $[BDC]^{-2}$ combined with a lanthanide ion leading to 331 reported structures. Potential reaction conditions were screened with less expensive and more readily available samarium(III) carbonate, which generally forms frameworks isostructural to europium. When three equivalents of H_2BDC were ground with two equivalents of samarium(III) carbonate (Figure 74), the formation of an interpenetrated samarium(III) framework which isostructural to a reported europium framework: $Eu_2(BDC)_3(DMF)_2(H_2O)_2$ (CSD code: WECSAZ), was observed.

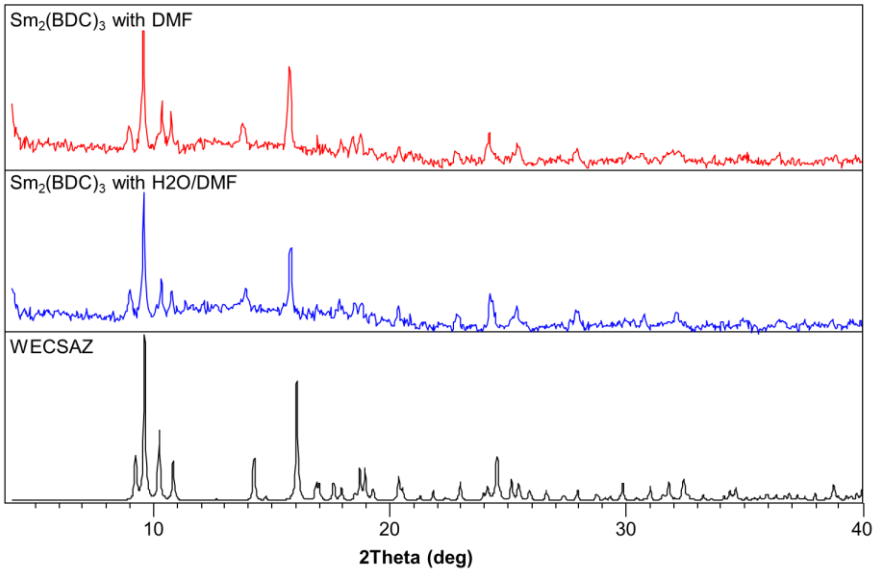

Figure 74. XRPD patterns of the product phase (WECSAZ) using samarium(III) carbonate collected using CuKα.

Unlike in the trimesic acid system, similar reactivity was observed for LAG with DMF as well as a mixture of H_2O and DMF. The analogous reaction of europium(III) carbonate with H_2BDC was monitored *in situ* using fluorescence emission (Figure 75) which was deconvoluted using a 3-component NMF, suggesting the emergence of the product after approximately 50 minutes of grinding, with fluorescence emission suggesting the presence of an intermediate phase at 30-40 minutes (Figure 75c).

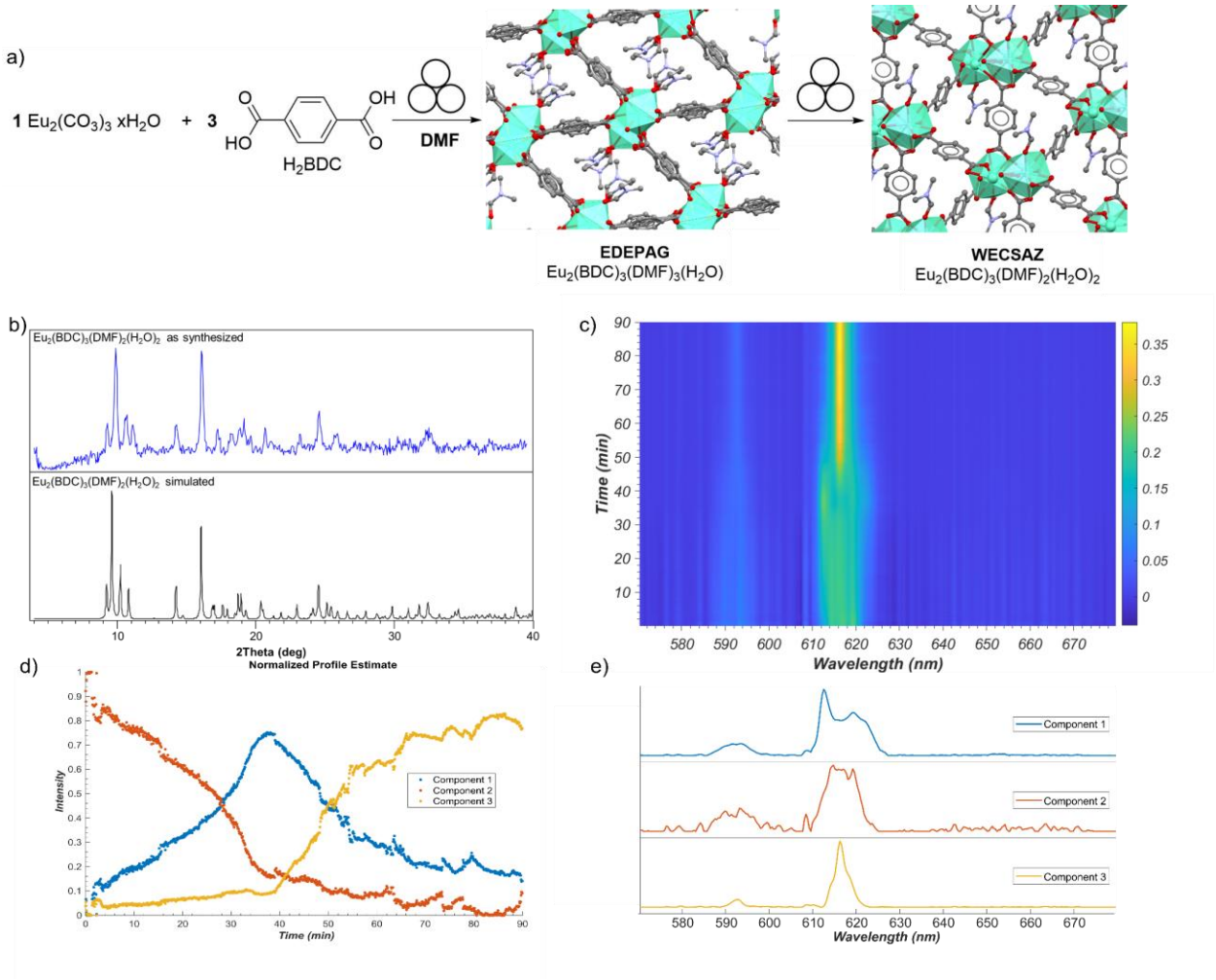

Figure 75. a) Mechanochemical synthesis of $Eu_2(BDC)_3(DMF)_2(H_2O)_2$ (CSD code: WECSAZ) as monitored by b) X-ray powder diffractogram collected using CuKα and c) in situ normalized fluorescence suggesting the presence of an intermediate phase later identified as $Eu_2(BDC)_3(DMF)_3(H_2O)$ (CSD Code: EDEPAG) before the formation of WECSAZ. d) Normalized profile estimate corresponding with e) component spectra of obtained from NMF analysis.

The intermediate fluorescence emission (Figure 75d, component 1) is very similar to the fluorescence emission of $Eu_2(BDC)_3(DMF)_3(H_2O)$ (CSD code: EDEPAG), as determined in subsequent *in situ* synchrotron X-ray diffraction experiments (Figure 78d, component 1), suggesting the transformation from a porous to a denser interpenetrated framework. Emergence of the final product may be due to higher density or the accumulation of water formed as a by-product of the reaction. In contrast, when the LAG

is conducted with water, formation of the dense packed $Eu_2(BDC)_3(H_2O)_4$ (CSD code: QACTUJ) occurs within 10 minutes without the detection of intermediates *via* fluorescence (Figure 76). Modification of the liquid additives in the reaction has significant impacts on product selectivity and reaction rates. In both cases, fluorescence spectroscopy enabled the identification of intermediate phases and reaction profiles.

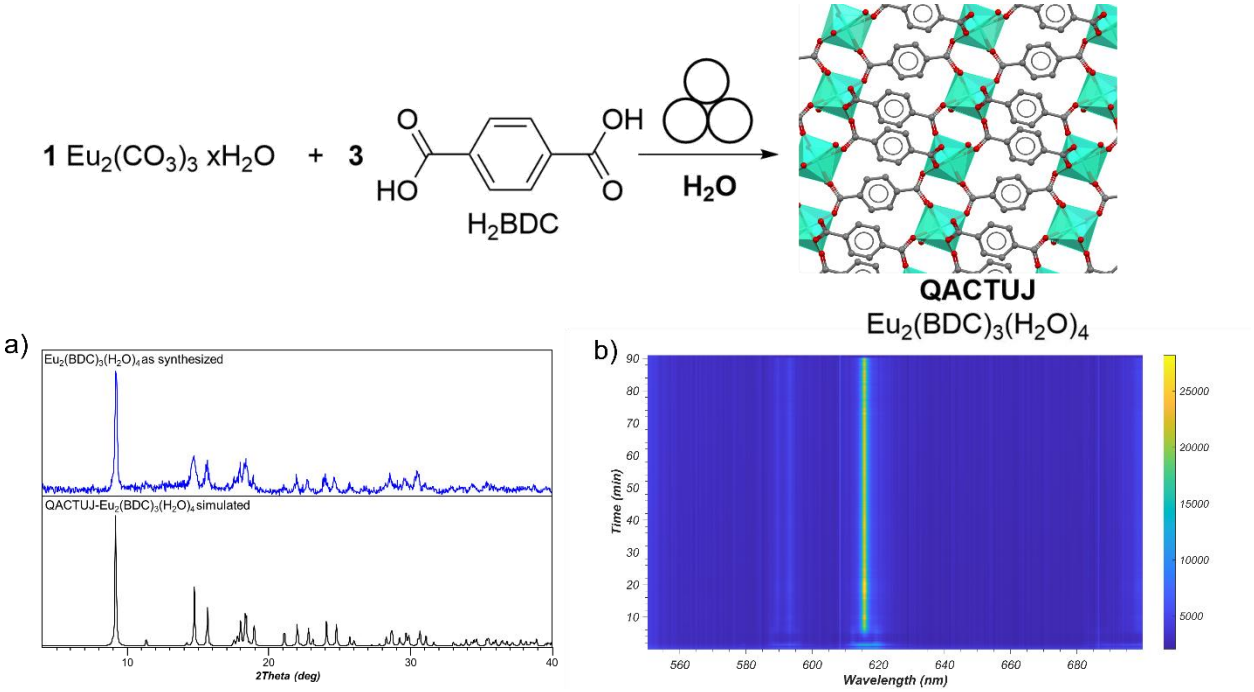

Figure 76. Synthesis of $Eu_2(BDC)_3(H_2O)_4$ (CSD Code: QACTUJ) as confirmed by a) X-ray powder diffractogram collected using CuKα and b) in situ fluorescence revealing the rapid formation of the dense-packed framework in under 10 minutes.

Having explored the solvent selectivity, we chose to examine the effect of modifying the stoichiometry of the reaction. The addition of an extra equivalent of H_2BDC did not appear to affect the final product of the reaction, as observed by XRPD (Figure 77).

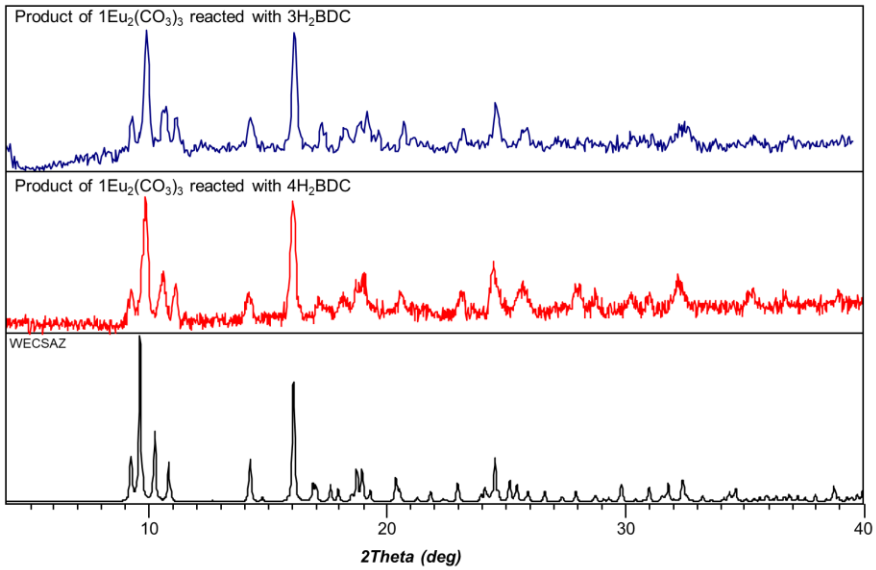

Figure 77. XRPD patterns of the product WECSAZ using europium carbonate in the correct stoichiometry and with excess H_2BDC collected using CuKα.

However, increasing the relative amount of europium(III) carbonate to H_2BDC to a 1:1 stoichiometric ratio leads to a different observed reaction mechanism. A stepwise transformation is observed where the end-product appears to be a mixture of materials containing a crystalline phase $Eu_2(BDC)_3(DMF)_2(H_2O)_2$ (CSD code: WECSAZ) along with a so far unidentified phase (Compound **1**, which largely corresponds to component 4 in Figure 78e). In order to explore the identity of intermediate phases, we conducted tandem *in situ* monitoring *via* both X-ray diffraction and fluorescence emission spectroscopy (Figure 78a&b). Components and profiles for both diffraction and fluorescence data sets were approximated using a 4 component NMF. The reaction profiles obtained from NMF were normalized so that the relative amounts of components for each spectrum must sum to 1.0, revealing consistent reaction profile estimates (Figure 78e&f). The NMF approximation for the diffraction data set yields components with remarkable similarity to the simulated diffraction pattern of reported phases $Eu_2(BDC)_3(DMF)_2(H_2O)_2$ (CSD code: WECSAZ) and $Eu_2(BDC)_3(DMF)_3(H_2O)$ (CSD code: EDEPAG). The reaction appears to proceed stepwise through a series of phases, with the first being isostructural to $Eu_2(BDC)_3(DMF)_3(H_2O)$ (CSD code: EDEPAG) framework, followed by a mixture of phases isostructural to $Eu_2(BDC)_3(DMF)_2(H_2O)_2$ (CSD code: WECSAZ) and Compound **1** by the end of the reaction. A notable difference between the estimated fluorescence

and diffraction profiles are the amount of component 2 at the beginning of both data sets, which represents starting materials along with background, likely due to the low signal of the starting materials in both data sets. Additionally, the ratios of components 3 and 4 differ between the data sets, which may be due to the much stronger fluorescence of component 3 relative to component 4, which can distort the fitting, or it may suggest that the fluorescence emission is not entirely due to crystalline phases.

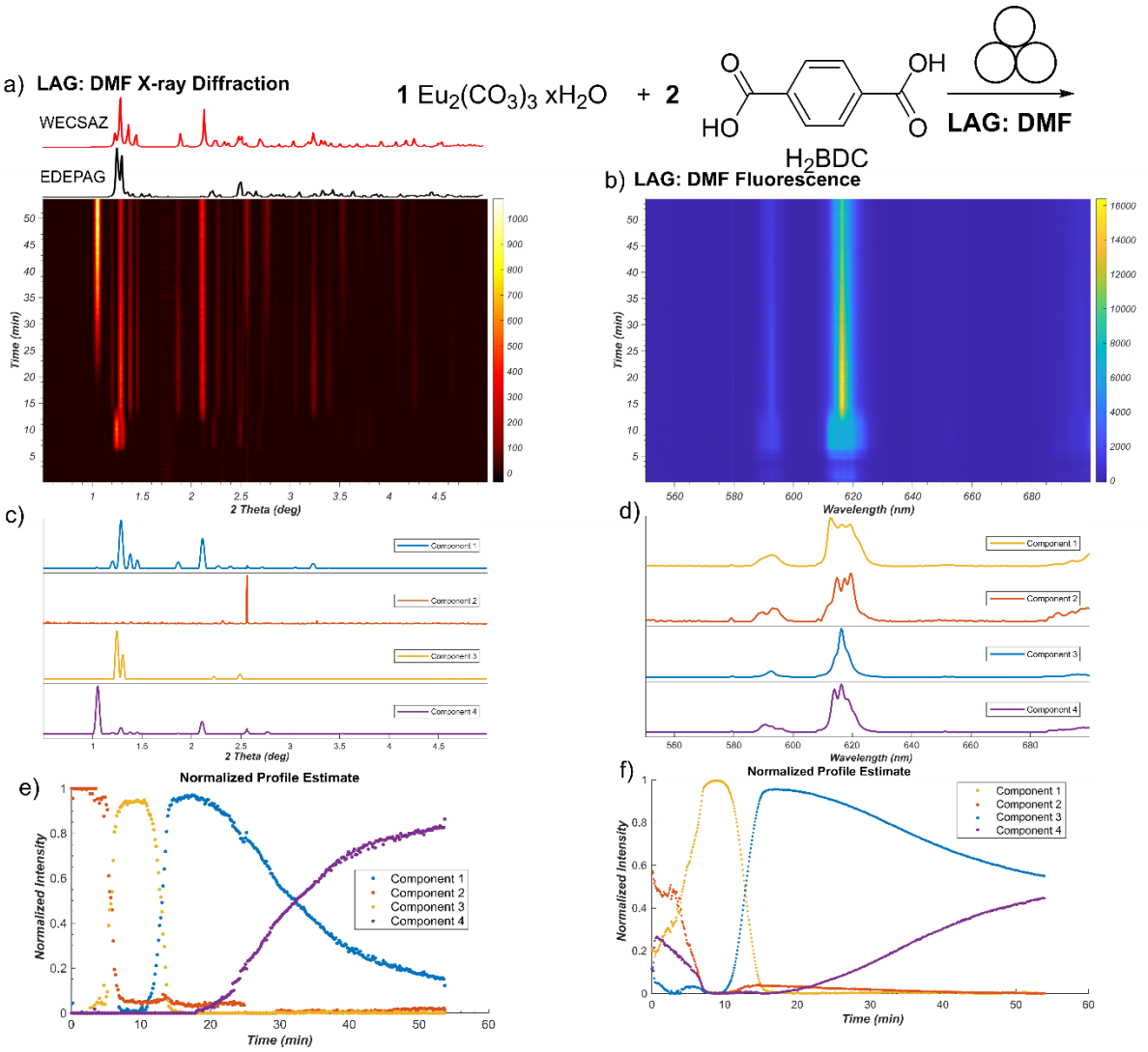

Figure 78. Reactions of one equivalent of europium(III) carbonate with two of H_2BDC under LAG conditions with DMF. a) Tandem real-time monitoring of X-ray powder diffraction. b) Tandem real-time monitoring of the fluorescence emission in a LAG reaction using DMF. c) Estimated components for the diffraction data set and d) estimated components of the fluorescence data set obtained from NMF. These components correspond with the e) normalized profile estimate for the diffraction data set and f) the normalized profile estimate for the fluorescence data set obtained from NMF. Associated components have been assigned the same colors.

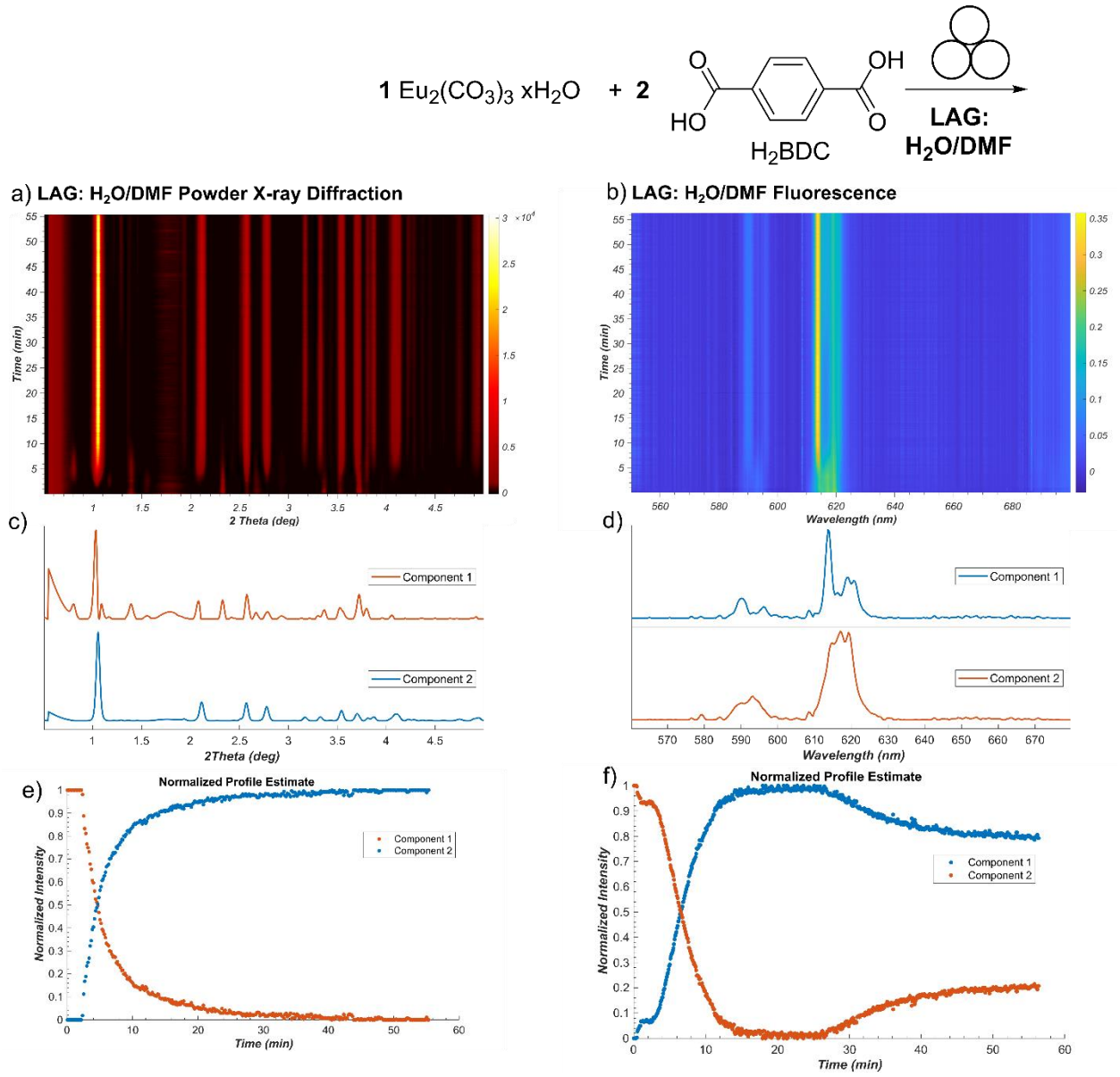

*Figure 79. Reactions of one equivalent of europium(III) carbonate with two of H_2BDC under LAG conditions with DMF and water. a) Tandem real-time monitoring of X-ray powder diffraction reveals rapid formation of Compound **1**. b) Tandem real-time monitoring of the fluorescence emission of LAG using DMF. c) Estimated components for the diffraction data set and d) estimated components of the fluorescence data set obtained from NMF. These components correspond with the e) normalized profile estimate for the diffraction data set and f) the normalized profile estimate for the fluorescence data set obtained from NMF. Associated components have been assigned the same colors.*

Tandem *in situ* measurements reveal that the reaction course is strongly affected by substitution of pure DMF with a 1:1 mixture of water and DMF as the composition of the liquid phase (Figure 79). In this case, the formation of Compound **1** was promoted and occurs within 10 minutes of milling, along with the presence of an unidentified transient phase, with a reflection at ~0.5° and ~1.3° 2θ. Due to the difficulty in modeling minor changes in diffraction and fluorescence, a two component NMF approximation was chosen (Figure 79c-f). The resulting normalized reaction profiles appear similar for the first 30 minutes of the data set before a small amount of $Eu_2(BDC)_3(DMF)_2(H_2O)_2$ (CSD code: WECSAZ) begins to appear. The diffraction signal of this phase is too weak for the applied NMF model, however, the emergence of a fluorescence signal at ~617nm is observed. The NMF model detects this phase, but due to the similarity of the fluorescence emission of the combination of Compound **1** and $Eu_2(BDC)_3(DMF)_2(H_2O)_2$ (CSD code: WECSAZ) with the starting material of the reaction, it is modelled a re-emergence of component 2. Interestingly, this suggests that despite the different reaction profiles, both LAG with DMF and LAG with H_2O & DMF ultimately yield a similar mixture of products, as confirmed by *ex situ* X-ray powder diffraction (Figure 80). Attempts to synthesize a pure sample of the unknown phase for structure solution from powder diffraction data have so far been unsuccessful.

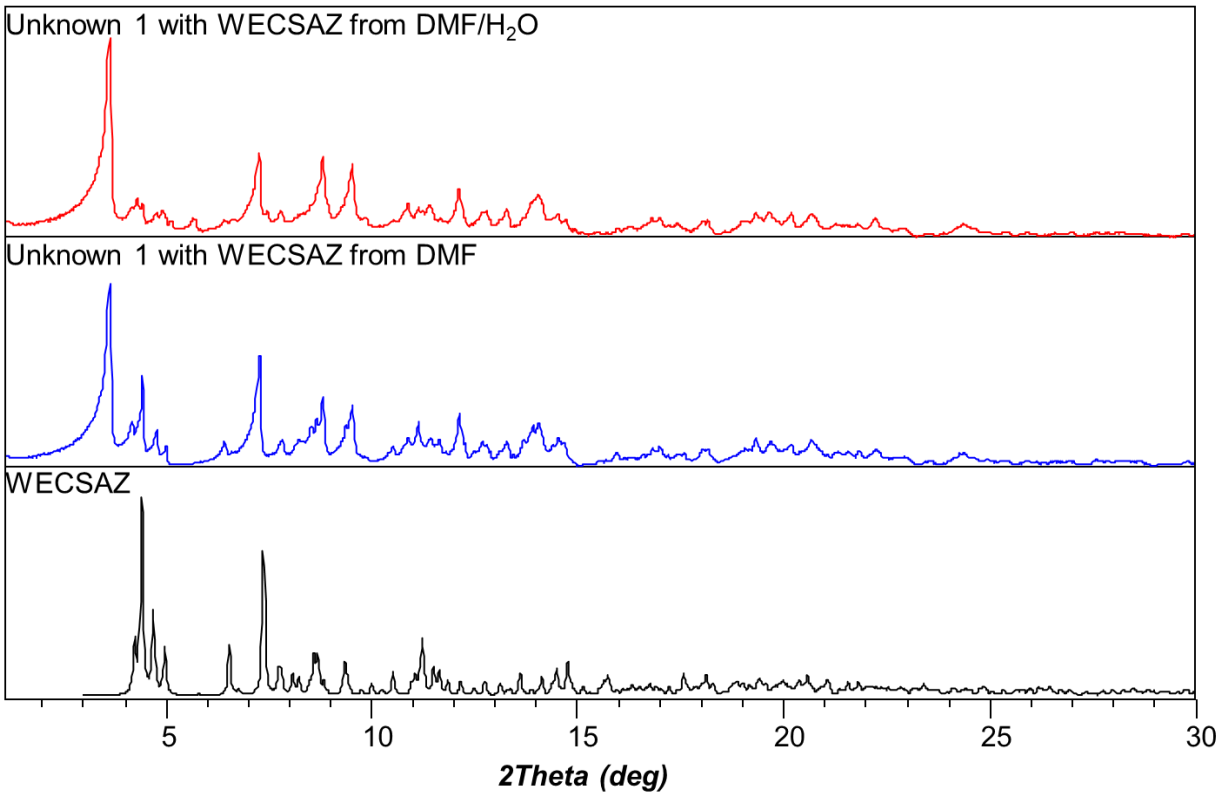

*Figure 80. PXRD patterns of the final mixtures containing both $Eu_2(BDC)_3(DMF)_2(H_2O)_2$ (CSD code: WECSAZ) and Compound **1** from a 1:1 mixture of europium(III) carbonate to H_2BDC, collected using MoKα.*

7.05 Conclusions:

Real-time monitoring of the emission of europium(III) ions provides a powerful and low cost method for monitoring mechanochemical reactions of lanthanide based materials such as lanthanide organic frameworks. We have, for the first time, applied *in situ* fluorescence and diffraction techniques to analyze the mechanochemical syntheses of lanthanide based frameworks in real time. The utility of *in situ* techniques in the development and optimization of novel mechanochemical syntheses of europium BDC frameworks was clearly demonstrated. Both fluorescence emission and X-ray diffraction measurements reveal stepwise reactivity sensitive to the liquid additive used and the stoichiometry of the reaction mixture. Tandem reaction monitoring *via* lanthanide emission and X-ray powder diffraction enables rapid phase identification, assists in

identifying novel structures, and suggests considerable potential in elucidating the mechanisms involved in the mechanochemical syntheses of lanthanide based materials.

7.06 Experimental:

All lanthanide carbonate hydrates were purchased from STREM chemicals. H_3BTC, H_2BDC, and DMF were purchased from Sigma-Aldrich and used without further purification. All mechanochemical reactions were conducted in transparent polymethyl-methacrylate (PMMA) jars using a 4 g stainless steel ball in a RETSCH MM400 mixer mill operating at 30 Hz.

(a) *Ex situ* Diffraction Measurements:

The diffraction patterns of final products were collected using a Bruker D2 Phaser diffractometer using CuKα radiation. Diffraction patterns using molybdenum were collected using a Stoe Stadi-P machine (Mo $K\alpha_1$ radiation, λ = 0.7093 Å), equipped with a MYTHEN 1K detector and a Johann Ge(111) monochromator in Debye Scherrer geometry.

(b) *In situ* Diffraction Measurements:

All real-time diffraction measurements were performed at the Petra III P02.1 beamline at Deutsches Elektronen-Synchrotron (DESY) using an X-ray wavelength of 60 keV (λ ~ 0.207 Å) and a modified RETSCH MM400 or an In Solido Technologies IST500 mill. Integration of diffraction images was performed using DAWN. Datasets were subsequently corrected, truncated, and plotted using custom scripts in MATLAB R2018a with PMMA background subtraction performed using the Sonneveld and Visser algorithm[15] and normalization performed using vector normalization (L2 norm). NMF was performed using the MATLAB implementation reported by C.J. Lin with a tolerance of $1x10^{-8}$.[14] Normalized profile estimates were calculated by setting the sum of all components in each spectrum to unity.

(c) In situ Fluorescence Measurements:

Fluorescence measurement were conducted using a 365 nm UV LED (LZ1-00UV00) from LED Engin excitation source and fiber-optically coupled QE65000 spectrometer from Ocean Optics. Datasets were smoothed slightly using a Savitsky-Golay filter (*sgolayfilt* command) in MATLAB2018a.[16] The baseline was corrected using the Sonneveld and

Visser algorithm,[15] truncated to the limits shown in the data sets, and normalized using vector normalization (L2 norm). NMF was performed using the MATLAB implementation reported by C.J. Lin with a tolerance of $1x10^{-8}$.[14] Normalized profile estimates were calculated by setting the sum of all components in each spectrum to one.

(d) Mechanochemical synthesis of Eu(BTC)(H_2O) (SEHXIN):

121 mg of $Eu_2(CO_3)_3$ xH_2O and 105 mg of trimesic acid were milled with 50 µL of DMF.

(e) Mechanochemical synthesis of Eu(BTC)(H_2O)$_6$ (GOCYAY):

121 mg of $Eu_2(CO_3)_3$ xH_2O and 105 mg of trimesic acid were milled with 30 µL of DMF and 20 µL of distilled H_2O.

(f) Mechanochemical synthesis of $Eu_2(BDC)_3(DMF)_2(H_2O)_2$ (WECSAZ):

98 mg of $Eu_2(CO_3)_3$ xH_2O and 102 mg of H_2BDC were milled with 50 µL of DMF.

(g) Mechanochemical Synthesis of $Eu_2(BDC)_3(H_2O)_4$ (QACTUJ):

98 mg of $Eu_2(CO_3)_3$ xH_2O and 102 mg of H_2BDC were milled with 70 µL of distilled H_2O.

(h) Mechanochemical synthesis of $Eu_2(BDC)_3$ mixture with excess Eu:

148 mg of $Eu_2(CO_3)_3$ xH_2O and 101 mg of H_2BDC were milled with either 30 µL DMF and 30 µL distilled H_2O or 60 µL of DMF.

7.07 Acknowledgements:

The authors would like to acknowledge Dr. Sam Sewall for the use of QE65000 spectrometer and In Solido Technologies for the use of their mill. The authors also thank DESY for providing beamtime.

7.08 References:

1. Cui, Y.; Chen, B.; Qian, G.; *Coordination Chemistry Reviews* **2014,** *273-274*, 76-86.
2. Yuan, W.; O'Connor, J.; James, S.L.; *CrystEngComm* **2010,** *12*, (11), 3515-3517.
3. Alammar, T.; Hlova, I.Z.; Gupta, S.; Balema, V.; Pecharsky, V.K.; Mudring, A.-V.; *Dalton Transactions* **2018,** *47*, (22), 7594-7601.
4. Singh, N.K.; Gupta, S.; Pecharsky, V.K.; Balema, V.P.; *Journal of Alloys and Compounds* **2017,** *696*, 118-122.
5. Derakhshandeh, P.G.; Soleimannejad, J.; Janczak, J.; Kaczmarek, A.M.; Van Hecke, K.; Van Deun, R.; *CrystEngComm* **2016,** *18*, (35), 6738-6747.

6. Friščić, T.; Halasz, I.; Beldon, P.J.; Belenguer, A.M.; Adams, F.; Kimber, S.A.J.; Honkimäki, V.; Dinnebier, R.E.; *Nature Chemistry* **2012,** *5*, 66.

7. Gracin, D.; Štrukil, V.; Friščić, T.; Halasz, I.; Užarević, K.; *Angewandte Chemie International Edition* **2014,** *53*, (24), 6193-6197.

8. Batzdorf, L.; Fischer, F.; Wilke, M.; Wenzel, K.-J.; Emmerling, F.; *Angewandte Chemie International Edition* **2015,** *54*, (6), 1799-1802.

9. Užarević, K.; Ferdelji, N.; Mrla, T.; Julien, P.A.; Halasz, B.; Friščić, T.; Halasz, I.; *Chemical Science* **2018,** *9*, (9), 2525-2532.

10. Chen, Y.; Williams, J.S.; *Journal of Materials Research* **1996,** *11*, (6), 1500-1506.

11. Vicentini, G.; Zinner, L.B.; Zukerman-Schpector, J.; Zinner, K.; *Coordination Chemistry Reviews* **2000,** *196*, (1), 353-382.

12. Halasz, I.; Kimber, S.A.J.; Beldon, P.J.; Belenguer, A.M.; Adams, F.; Honkimäki, V.; Nightingale, R.C.; Dinnebier, R.E.; Friščić, T.; *Nature Protocols* **2013,** *8*, 1718.

13. Rietveld, H.; *Journal of Applied Crystallography* **1969,** *2*, (2), 65-71.

14. Lin, C.-J.; *Neural Computation* **2007,** *19*, (10), 2756-2779.

15. Sonneveld, E.J.; Visser, J.W.; *Journal of Applied Crystallography* **1975,** *8*, (1), 1-7.

16. Press, W.H.; Teukolsky, S.A.; Vetterling, W.T.; Flannery, B.P.; *The art of scientific computing* **1992,** *2*, 1002.

8. *In situ* monitoring of mechanochemical synthesis of calcium urea phosphate fertilizer co-crystal reveals highly effective water-based autocatalysis

8.01 Preface

Mechanochemical solid-state acid-base reactions are of fundamental interest in solid-state chemistry. This project focused on the synthesis of an agrichemical co-crystal of interest, namely calcium-urea-phosphate. The development of sapphire jars enabled the real-time monitoring of the reaction of insoluble calcium carbonate and hydroxide with urea-phosphate utilizing Raman spectroscopy, revealing the first direct evidence of the autocatalytic role of water in mechanochemical reactions.

This chapter consists of a manuscript currently submitted: Patrick A. Julien, Luzia S. Germann, Hatem M. Titi, Martin Etter, Robert E. Dinnebier, Lohit Sharma, Jonas Baltrusaitis, and Tomislav Friščić submitted to *Chemical Science*. Synchrotron data was collected by P.A. Julien, L. S. Germann, H. Titi, M. Etter, and R. Dinnebier. Dynamic vapor sorption (DVS) studies were conducted by, L. Sharma and J. Baltrusaitis. All other data was collected by P. A. Julien. The manuscript was written by P. A. Julien with editing from T. Friščić and other authors.

8.02 Abstract

Using the mechanosynthesis of the calcium phosphate and urea fertilizer co-crystal as a model, we provide a quantitative investigation of chemical autocatalysis in a mechanochemical reaction. The application of *in situ* Raman spectroscopy and synchrotron X-ray powder diffraction to monitor the reaction of urea phosphate and either calcium hydroxide or carbonate enabled the first quantitative and *in situ* study of a mechanochemical system in which one of the products of a chemical reaction (water) mediates the rate of transformation and underpins positive feedback kinetics. The herein observed autocatalysis by water generated in the reaction enables reaction acceleration

at amounts that are up to 3 orders of magnitude smaller than in a typical liquid-assisted mechanochemical reaction.

8.03 Introduction

The need for more sustainable agriculture and agrochemicals has driven the search for novel and efficient fertilizers, which minimize the negative environmental impacts of runoff and eutrophication.[1, 2] Recently, co-crystallization has emerged as a powerful approach to develop new solid forms of fertilizers, which could maximize absorption by crops while minimizing runoff, which negatively impacts the environment and human health *via* eutrophication.[3-5] Urea phosphate is one of the most prevalent fertilizer components for the delivery of critical plant nutrients nitrogen and phosphorus, with the added benefit of reducing ammonia losses by enzymatic degradation.[6] The loss of ammonia from urea fertilizers is further reduced by the presence of calcium, another key nutrient for plants, leading to improved formulations for simultaneous delivery of nitrogen, phosphorus and calcium.[7-9] An example is calcium urea phosphate $Ca[CO(NH_2)_2]_4(H_2PO_4)_2$ (**1**), an example of an agrochemical ionic co-crystal.[10,11] The co-crystal **1** is highly desirable as a fertilizer due to its stability, reduction in ammonia loss, while providing three critical nutrients and good moisture stability. Mechanochemical reactions, conducted by milling, grinding or extrusion, have emerged as an efficient and rapid route to synthesize a wide range of molecules and materials, from pharmaceutical co-crystals to metal-organic frameworks.[12] Mechanochemistry has been shown to enable synthesis independent of the relative solubilities of reactants, providing an excellent opportunity to form agrochemical co-crystals that are typically based on inexpensive but poorly soluble ionic starting materials.[12] Mechanochemistry enables rapid reactions, such as the green synthesis of calcium urea phosphate, from very poorly soluble inorganic precursors, such as calcium carbonate or calcium hydroxide,[4, 13,14] producing innocuous by-products of water and CO_2 (Figure 81).

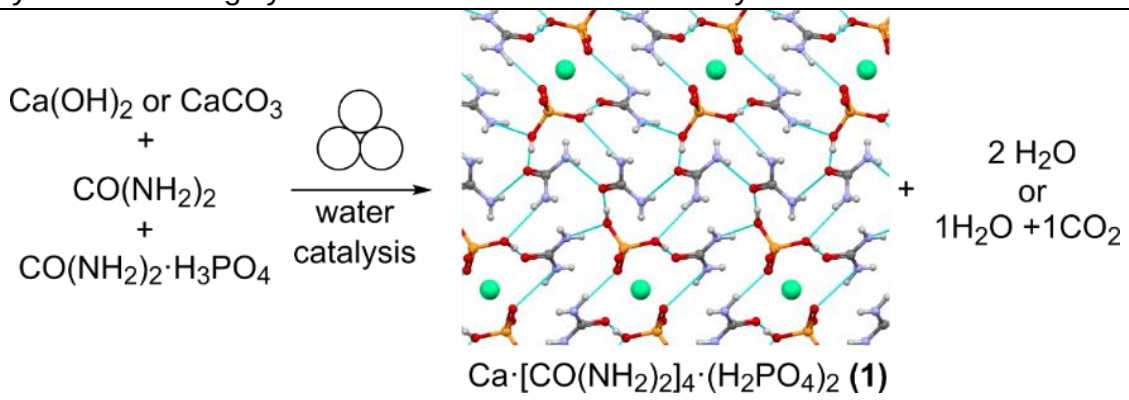

*Figure 81. Mechanochemical synthesis of the agrochemical co-crystal 1 from urea, urea phosphate and either calcium hydroxide or carbonate. Calcium ions are shown in green, and hydrogen bonding interactions are displayed in light blue for **1** (CSD code URECAP).*

Here, we investigate and compare the mechanisms of mechanochemical formation of the agrochemical co-crystal **1** by a neutralization reaction from either $Ca(OH)_2$ or $CaCO_3$, using the recently developed techniques for monitoring mechanochemical reactions in real-time using Raman spectroscopy and synchrotron X-ray powder diffraction (XRPD).[15,16] The *in situ* measurements reveal the appearance of sigmoidal reaction kinetics, which is herein shown to result from an autocatalytic feedback mechanism[17] involving water released in the reaction. These results provide the first insight into factors controlling the mechanochemical formation of agrochemical co-crystals and, to the best of our knowledge, they also represent the first quantitative and *in situ* analysis of chemical autocatalysis caused by a product of a mechanochemical reaction.

Real-time monitoring by synchrotron X-ray diffraction was conducted using a previously reported design[16] at the PETRA III beamline P02.1 at Deutsches Elektronen-Synchrotron (DESY), with λ = 0.207 Å, in polymethyl-methacrylate (PMMA) milling jars. Real-time Raman spectroscopy monitoring[18] was done in jars made of sapphire, as the signal from PMMA jars significantly obscured the signal for the formation of **1** (see Appendix 4). Milder conditions employed for synchrotron studies (smaller balls, PMMA plastic jar) resulted in a slower reaction.

Real-time Raman spectroscopy monitoring (Figure 82) of the reaction involving $CaCO_3$, urea, and urea phosphate in 1:2:2 respective stoichiometric ratios revealed the appearance of **1** after ca. 5 minutes milling. Despite considerable overlap of Raman bands of reactants and product, formation of **1** was clearly observable by the appearance

of the characteristic band at 1083 cm^{-1}. The reaction achieves quantitative conversion to **1** within 30 minutes, as determined by XRPD, Fourier-transform infrared attenuated total reflectance (FTIR-ATR) measurements and thermogravimetric analysis (TGA) after milling.

In contrast, using $Ca(OH)_2$ instead of $CaCO_3$ revealed a dramatic acceleration in reaction rate, with near-quantitative conversion achieved in 5 minutes (see Appendix 4 SI-9). The results of *in situ* Raman spectroscopy monitoring were validated by monitoring the reaction progress using *in situ* synchrotron XRPD, which again revealed much faster progress for the reaction involving $Ca(OH)_2$ (Figure 83).

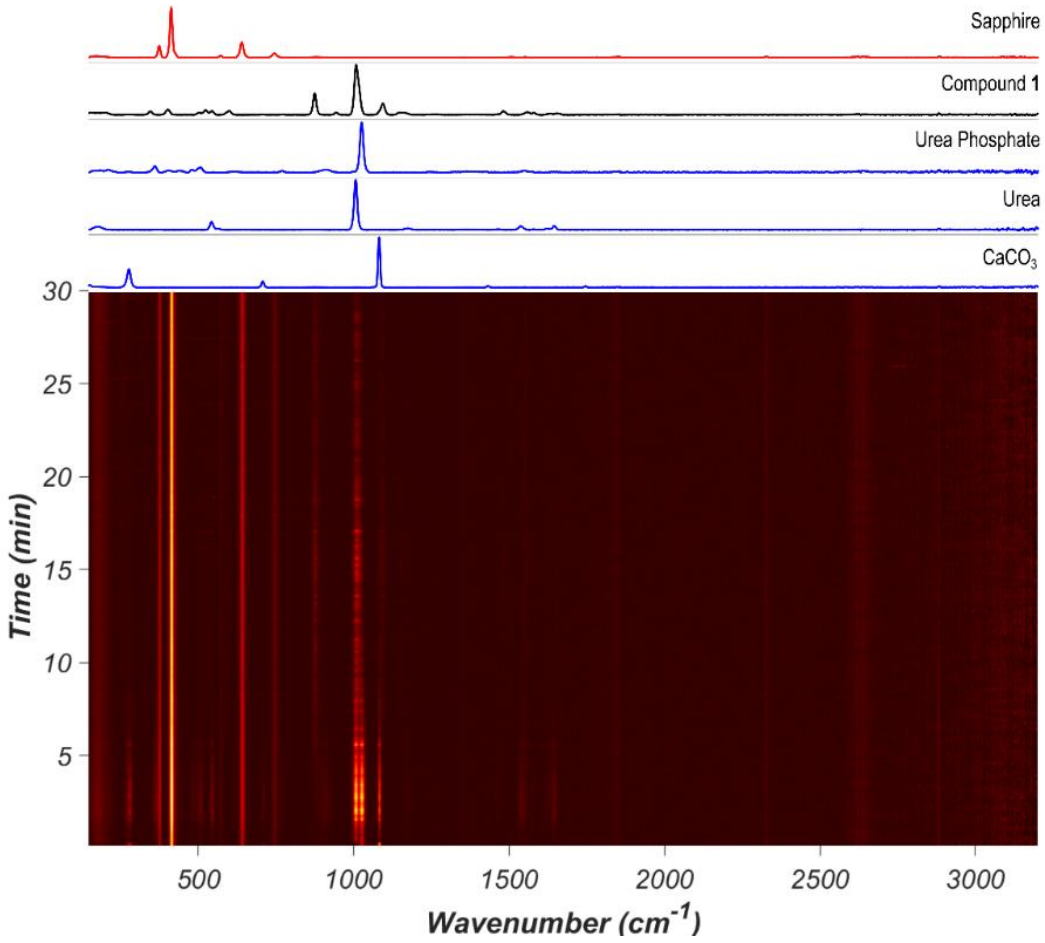

Figure 82. (Bottom) In situ Raman spectra of the neat milling reaction between $CaCO_3$, urea, and urea phosphate. Brighter colour denotes higher intensity. (Top) Raman spectra of reactants (blue), the product (black), and background from the sapphire milling jar (red) with individual spectra of reactants and product above the 2D plot.

8. In situ monitoring of mechanochemical synthesis of calcium urea phosphate fertilizer co-crystal reveals highly effective water-based autocatalysis

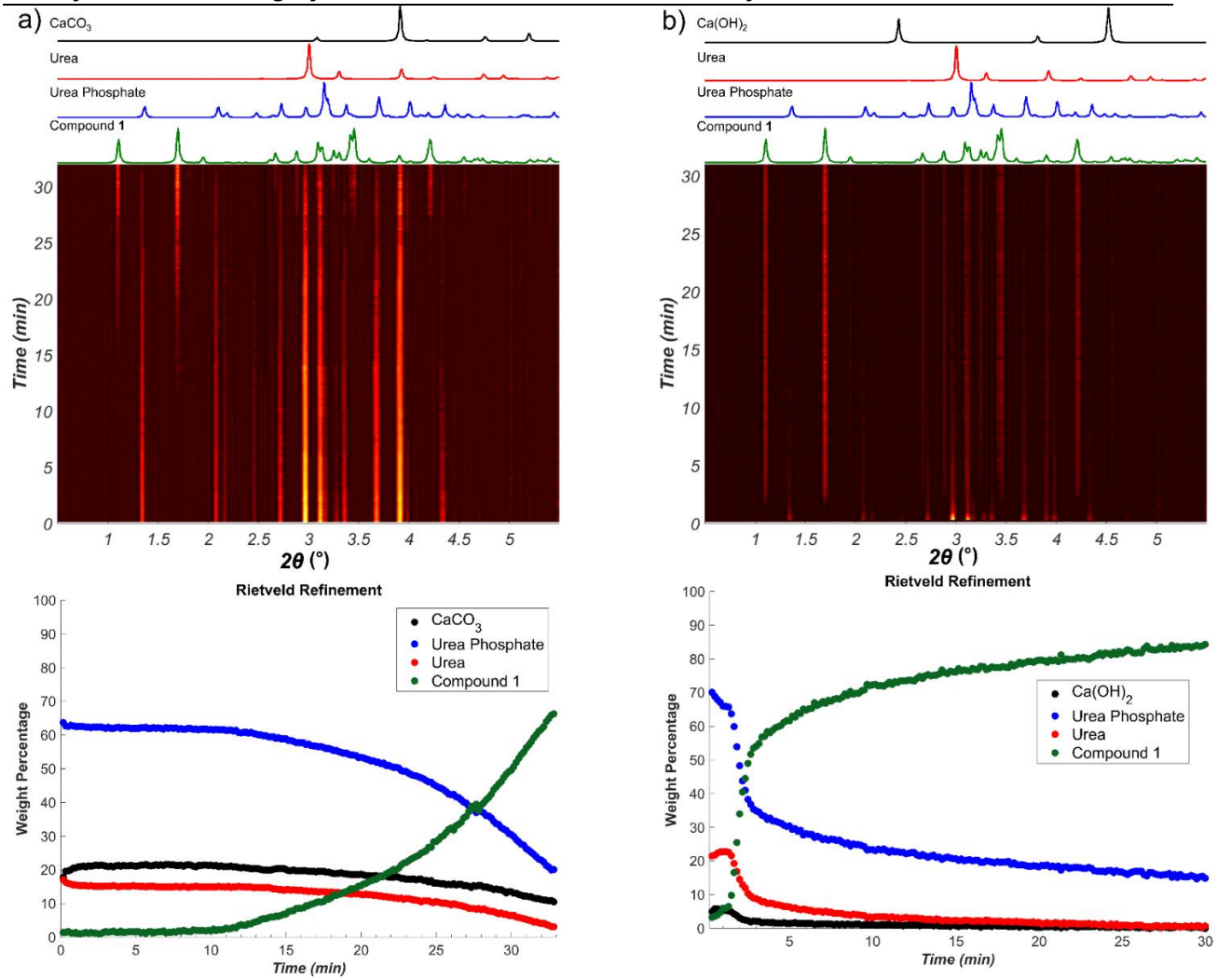

*Figure 83. Real-time PXRD monitoring of the formation of **1**: a) time-resolved XRPD patterns of the reaction using $CaCO_3$, with corresponding calculated patterns for reactants and product shown above the plot and the reaction profile obtained by sequential Rietveld refinement of the in situ PXRD data shown below; b) time-resolved XRPD patterns of the reaction using $Ca(OH)_2$, with corresponding calculated patterns for reactants and product shown above the plot and the reaction profile obtained by sequential Rietveld refinement of the in situ PXRD data shown below.*

Reaction profiles from *in situ* Raman spectroscopy (Figure 84a) reveal sigmoidal behaviour for the reaction involving $CaCO_3$ with 50% conversion achieved after ca. 10 minutes. In contrast, the reaction with $Ca(OH)_2$ proceeded much faster, with a very short induction period as seen from Rietveld analysis of *in situ* PXRD data. Such dramatic difference in reaction rates is even more notable considering that the commercially used $Ca(OH)_2$ contained ca. 13 % $CaCO_3$ by weight (9.6 mol%, as established by TGA) (see Appendix 4 SI-21&22). The two reactions also exhibited visually observable differences in rheology during the reaction, with the reaction involving $Ca(OH)_2$ proceeding in a moist paste, but the reaction with $CaCO_3$ consistently being a free-flowing powder (see Appendix 4 SI-1).

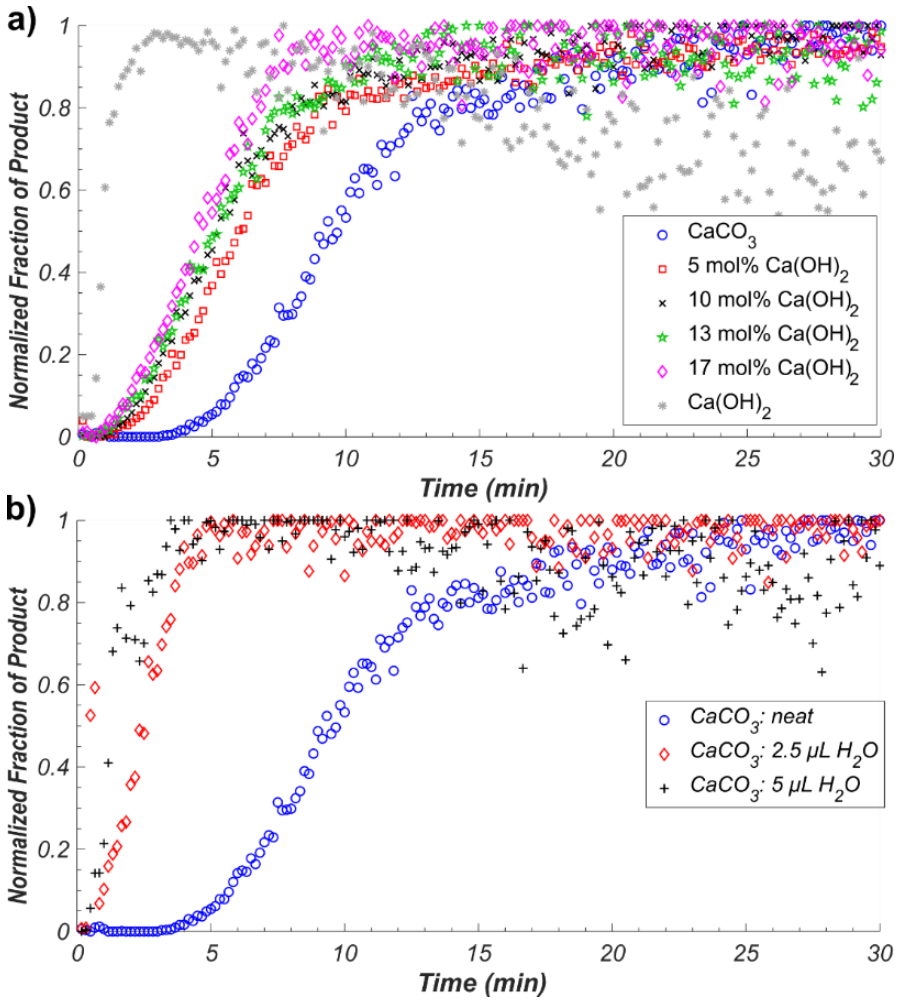

*Figure 84. a) Monitoring the relative rates of formation of **1** from $CaCO_3$ (blue) and $Ca(OH)_2$ (grey), as well as various mixtures. b) The addition of small volumes of water to the synthesis of **1** from $CaCO_3$, results in a significant increase in reaction rate as*

observed by in situ Raman spectroscopy. In each case the total weight of solid reactants was approximately 180 mg.

TGA of the calcium precursors revealed that $CaCO_3$ does not contain any moisture, and $Ca(OH)_2$ is estimated to contain less than 2% by weight of absorbed water. We therefore speculated that the progress of synthesis might be affected by the water that is formed by the neutralization reactions. As sigmoidal reaction kinetics are typically associated with autocatalysis,[19] wherein a reaction product facilitates conversion of remaining reactants, we envisaged a process in which the formation of water molecules creates a more mobile environment that could facilitate mechanochemical reactivity. Indeed, previous studies have noted that a liquid phase released from a hydrated starting material can enhance the formation of hydrogen-bonded co-crystals or coordination polymers.[20-25] However, there has not yet been a real-time, quantitative investigation of how a product formed in a chemical reaction, which involves the rearrangement of covalent bonds, could exhibit autocatalytic behaviour in mechanochemistry.

We explored this possibility by conducting further *in situ* Raman kinetic studies, but on reactions in the presence of small amounts of water added to reaction mixtures (2.5 µL water for η=0.014 µL/mg and 5 µL water for η = 0.029 µL/mg, where η corresponds to the ratio of added liquid volume to reactant weight) involving $CaCO_3$, urea, and urea phosphate. As anticipated, the addition of water resulted in a clear reaction acceleration and shortening of the induction period of the reaction (Figure 84b). Importantly, changing the amount of water had a significant effect on reaction kinetics, a test previously employed by the James group to evaluate autocatalytic behaviour, which confirmed autocatalysis by water generated in the reaction.[17] The herein observed catalytic effect is remarkable, as the amount of added water corresponds to very low η values: one to two orders of magnitude lower than those accessible in typical liquid-assisted grinding (LAG) reactions, where η is typically between 0.1-2 µL/mg, and reactivity enhancement is sometimes explained by physical presence of a liquid.[26-28] In order to further confirm that the observed sigmoidal kinetics is due to autocatalysis by water as a product of chemical reaction, rather than due to effects of nucleation and crystal growth of **1**,‡ we also performed reaction based on $CaCO_3$ reactant that were seeded with pre-synthesized **1**. The addition of different amounts of **1** to the reaction mixture was found to exhibit no

significant effect on the measured reaction kinetics, which is further consistent with the sigmoidal behaviour being a result of water-based autocatalysis (see Appendix 4).

The observed high sensitivity of mechanochemical reaction kinetics to deliberate additions of minute amounts of water is consistent with the proposed self-acceleration of reaction progress due to released water. This was further validated by probing the kinetics of reactions in which a fraction of the $CaCO_3$ reactant was replaced by an equivalent amount of $Ca(OH)_2$. Real-time monitoring by Raman spectroscopy of mechanochemical reactions with 5, 10, 13, and 17 mol% of $CaCO_3$ replaced by $Ca(OH)_2$ reveals immediate and significant improvement in reaction rate and shortening of the induction period (Figure 84a). The $Ca(OH)_2$ reactant is expected to generate twice the amount of water by-product compared to $CaCO_3$, effectively acting as solid source of catalytic amounts of water. Real-time monitoring of the reactions permitted us to plot the time required for 50% conversion with respect to water added as a liquid, or in the form of $Ca(OH)_2$, revealing a non-linear relationship consistent with autocatalysis (Figure 85a).

Autocatalytic behaviour was validated by analysing *in situ* data using an autocatalysis model for solid-state reactions, with respect to mol fraction of generated water (α):[29]

$$\frac{\mathrm{d}\alpha}{dt} = \mathrm{k}\alpha(1-\alpha) \qquad (1)$$

While the amount of water in the reaction is not readily measured by Raman spectroscopy, in the reaction of $CaCO_3$ it should be equivalent to the amount of product formed. In the α range from 0.2 to 0.8, when the molar fraction of the product in the reaction is between 20% and 80%, equation 1 yields a linear plot (Figure 85b), consistent with water-mediated autocatalysis.[30] The inability to obtain a linear fit during early and late phases of the reaction might be due to poor diffusion or mixing issues when the amount of product or reactants is low. It is remarkable that autocatalytic behavior can be observed at $\alpha \approx 0.2$, which would correspond to ca. 1.2 μL of water generated in the reaction, and an approximate η of 0.007 μL/mg. Such η value is nearly three orders of magnitude lower than in a typical LAG reaction and, considering that the water is generated directly in the reaction, indicates that the observed reaction enhancement is an example of chemical autocatalysis rather than liquid-assisted[26] mechanochemistry.

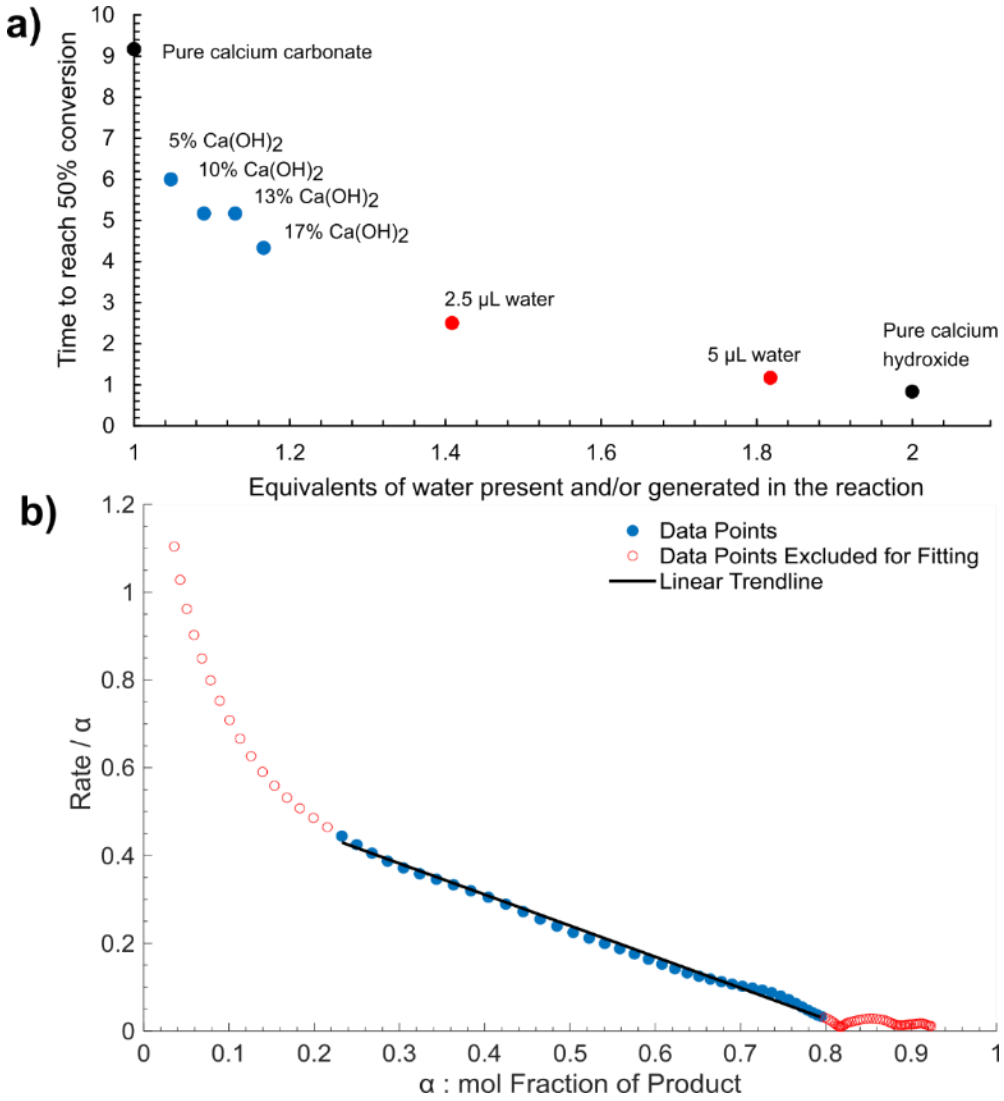

*Figure 85. a) The reaction rate measured as the time required to reach 50% conversion as a function of the total equivalents (relative to calcium) of water present and/or generated in the system. b) Reaction rate (dα/dt)/α vs. α, where α is the mol fraction of **1** as determined by in situ Raman spectroscopy for the synthesis using $CaCO_3$ reactant. Linear behaviour is observed between α = 0.2 and 0.8, consistent with autocatalysis due to a reaction product. Fitting parameters are reported in the Appendix 4 section 14.04.*

The herein presented autocatalytic behaviour is central for the ability to rapidly synthesize **1** without large amounts of water. The ability to accelerate synthesis by using water amounts that are minuscule even for LAG mechanochemistry is particularly important due to the high aqueous solubility of this material, which is beneficial for fertilizer use but hinders its preparation from solution. Once mechanochemically made, **1** exhibits properties highly desirable in a fertilizer. Thermal analysis reveals a high thermal stability for **1**, which releases urea at 124°C, a higher temperature compared to urea phosphate

which decomposes at 116 °C (see Appendix 4 SI-25&26). Moisture stability of **1** was compared to that of urea by dynamic vapour sorption (DVS) across the relative humidity (RH) range from 0-95%, at 25 °C. The measurements confirm the ability of **1** to interact with water more strongly, while maintaining a more modest water absorption profile compared to urea (Figure 86). For urea, increasing RH led to negligible water uptake until the deliquescence point at 74% RH, with further increases in humidity leading to continuous hygroscopic growth of the aqueous droplet. On decreasing RH, the droplet decreased in size, below 74% RH became supersaturated with respect to urea, and below 50% RH formed an effloresced particle. Co-crystal **1** exhibited a deliquescence phase transition at 65% RH, but no distinct efflorescence point, as evidenced by a continuous hysteresis down to low humidity values (<20% RH) values. The hysteresis and presence of absorbed water in **1** over a wide range of RH values suggests a continuous transition of the bound-to-free water, potentially due to strong hydrogen bonding to hydrophilic, polar groups of **1.**[31] While such behaviour is beneficial for fertilizer use, it also clearly illustrates the synthetic benefit of the herein demonstrated autocatalytic effect, as it enables access to **1** as a well-defined and dry (by TGA) solid, using only traces of water.

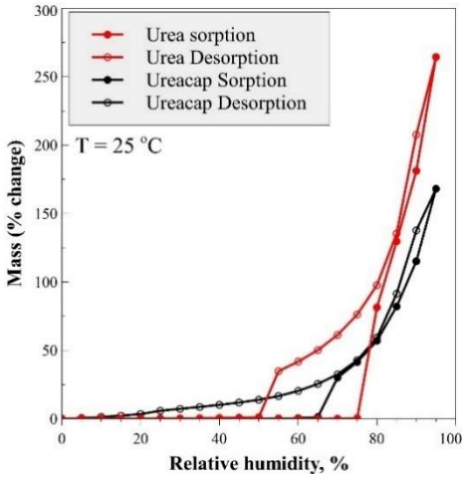

*Figure 86. Adsorption/desorption branches of RH on urea and **1**.*

8.04 Conclusion

In conclusion, we used *in situ* X-ray diffraction and spectroscopy to provide direct and quantitative evidence of chemical autocatalysis in a mechanochemical reaction. The presented results further our understanding of fundamental principles and mechanisms

of mechanochemistry, an area that has recently attracted significant interest.[32-42] While chemical autocatalysis is not the only potential reason for appearance of sigmoidal kinetics in a mechanochemical reaction,‡ this study provides direct evidence that such a model is relevant for mechanochemical reactions and, in principle, may be broadly applicable to water-forming acid-base milling reactions. The enhancement of mechanochemical reactions in liquid-assisted grinding can sometimes be explained by a purely physical effects of dissolution and having a liquid phase present.[26-28] Herein, however, reaction acceleration is observed due to water directly generated by the reaction, at amounts that are up to three orders of magnitude lower than in a typical liquid-assisted grinding system, resulting in an *in situ* observed autocatalytic reaction profile. These observations highlight the herein explored reaction as an example of chemical autocatalysis in the solid state, which enables reaction acceleration at amounts of water significantly smaller than in liquid-assisted mechanochemistry.

The efficient autocatalysis observed herein is also of practical value, as it enables the synthesis of a highly hygroscopic fertilizer co-crystal material using only minuscule amounts of water, even for standards of liquid-assisted mechanochemistry. This demonstrates how water-based autocatalysis can be used to greatly simplify the preparation of ionic co-crystals and other valuable material whose synthesis in solution is made cumbersome by high affinity to water and tendency to form supersaturated solutions.

8.05 Acknowledgements

We acknowledge support from DESY, and Form-Tech Scientific, Inc. T. F. acknowledges support of NSERC Discovery Grant (RGPIN-2017-06467), Discovery Accelerator (RGPAS 507837-17), and E. W. R. Steacie Memorial Fellowship (SMFSU 507347-17). J.B. and L.S. acknowledge support from USA National Science Foundation (NSF), Grant CHE 1710120.

8.06 References

1. Baltrusaitis, J.; *ACS Sustainable Chemistry & Engineering* **2017,** *5*, (11), 9527-9527.

2. Casali, L.; Mazzei, L.; Shemchuk, O.; Honer, K.; Grepioni, F.; Ciurli, S.; Braga, D.; Baltrusaitis, J.; *Chemical Communications* **2018,** *54*, (55), 7637-7640.

3. Finlay, K.; Patoine, A.; Donald, D.B.; Bogard, M.J.; Leavitt, P.R.; *Limnology and Oceanography* **2010,** *55*, (3), 1213-1230.

4. Honer, K.; Kalfaoglu, E.; Pico, C.; McCann, J.; Baltrusaitis, J.; *ACS Sustainable Chemistry & Engineering* **2017,** *5*, (10), 8546-8550.

5. Sandhu, B.; Sinha, A.S.; Desper, J.; Aakeröy, C.B.; *Chemical Communications* **2018,** *54*, (37), 4657-4660.

6. Bremner, J.M.; Douglas, L.A.; *Soil Science Society of America Journal* **1971,** *35*, (4), 575-578.

7. Fenn, L.B.; Matocha, J.E.; Wu, E.; *Soil Science Society of America Journal* **1981,** *45*, (5), 883-886.

8. Fenn, L.B.; Tatum, G.; Horst, G.; *Fertilizer research* **1990,** *21*, (3), 125-131.

9. Stumpe, J.M.; Vlek, P.L.G.; Lindsay, W.L.; *Soil Science Society of America Journal* **1984,** *48*, (4), 921-927.

10. Chen, J.P.; Isa, K.; *Journal of the Mass Spectrometry Society of Japan* **1998,** *46*, (4), 299-303.

11. Frazier, A.W.; Lehr, J.R.; Smith, J.P.; *Journal of Agricultural and Food Chemistry* **1967,** *15*, (2), 345-347.

12. James, S.L.; Adams, C.J.; Bolm, C.; Braga, D.; Collier, P.; Friščić, T.; Grepioni, F.; Harris, K.D.M.; Hyett, G.; Jones, W., et al.; *Chemical Society Reviews* **2012,** *41*, (1), 413-447.

13. Honer, K.; Pico, C.; Baltrusaitis, J.; *ACS Sustainable Chemistry & Engineering* **2018,** *6*, (4), 4680-4687.

14. Sharma, L.; Kiani, D.; Honer, K.; Baltrusaitis, J.; *ACS Sustainable Chemistry & Engineering* **2019,** *7*, (7), 6802-6812.

15. Gracin, D.; Štrukil, V.; Friščić, T.; Halasz, I.; Užarević, K.; *Angewandte Chemie International Edition* **2014,** *53*, (24), 6193-6197.

16. Halasz, I.; Kimber, S.A.J.; Beldon, P.J.; Belenguer, A.M.; Adams, F.; Honkimäki, V.; Nightingale, R.C.; Dinnebier, R.E.; Friščić, T.; *Nature Protocols* **2013,** *8*, 1718.

17. Hutchings, B.P.; Crawford, D.E.; Gao, L.; Hu, P.; James, S.L.; *Angewandte Chemie International Edition* **2017,** *56*, (48), 15252-15256.

18. Julien, P.A.; Malvestiti, I.; Friščić, T.; *Beilstein Journal of Organic Chemistry* **2017,** *13*, 2160-2168.

19. Plasson, R.; Brandenburg, A.; Jullien, L.; Bersini, H.; *The Journal of Physical Chemistry A* **2011,** *115*, (28), 8073-8085.

20. Tumanov, I.A.; Michalchuk, A.A.L.; Politov, A.A.; Boldyreva, E.V.; Boldyrev, V.V.; *CrystEngComm* **2017,** *19*, (21), 2830-2835.

21. Karki, S.; Friščić, T.; Jones, W.; Motherwell, W.D.S.; *Molecular Pharmaceutics* **2007,** *4*, (3), 347-354.

22. Užarević, K.; Štrukil, V.; Mottillo, C.; Julien, P.A.; Puškarić, A.; Friščić, T.; Halasz, I.; *Crystal Growth & Design* **2016,** *16*, (4), 2342-2347.

23. Fang, X.; Yao, M.; Guo, L.; Xu, Y.; Zhou, W.; Zhuo, M.; Shi, C.; Liu, L.; Wang, L.; Li, X., et al.; *ACS Sustainable Chemistry & Engineering* **2017,** *5*, (11), 10735-10743.

24. Lukin, S.; Stolar, T.; Tireli, M.; Blanco, M.V.; Babić, D.; Friščić, T.; Užarević, K.; Halasz, I.; *Chemistry – A European Journal* **2017,** *23*, (56), 13941-13949.

25. Kulla, H.; Greiser, S.; Benemann, S.; Rademann, K.; Emmerling, F.; *Molecules* **2016,** *21*, (7), 917.

26. Friščić, T.; Childs, S.L.; Rizvi, S.A.A.; Jones, W.; *CrystEngComm* **2009,** *11*, (3), 418-426.

27. Bowmaker, G.A.; *Chemical Communications* **2013,** *49*, (4), 334-348.

28. Hasa, D.; Jones, W.; *Advanced Drug Delivery Reviews* **2017,** *117*, 147-161.

29. Prout, E.G.; Tompkins, F.C.; *Transactions of the Faraday Society* **1944,** *40*, (0), 488-498.

30. Mata-Perez, F.; Perez-Benito, J.F.; *Journal of Chemical Education* **1987,** *64*, (11), 925.

31. Basu, S.; Shivhare, U.S.; Mujumdar, A.S.; *Drying Technology* **2006,** *24*, (8), 917-930.

32. Andersen, J.; Mack, J.; *Angewandte Chemie* **2018,** *130*, (40), 13246-13249.

33. Andersen, J.M.; Mack, J.; *Chemical Science* **2017,** *8*, (8), 5447-5453.

34. Michalchuk, A.A.L.; Tumanov, I.A.; Boldyreva, E.V.; *CrystEngComm* **2013,** *15*, (32), 6403-6412.

35. Kulla, H.; Fischer, F.; Benemann, S.; Rademann, K.; Emmerling, F.; *CrystEngComm* **2017,** *19*, (28), 3902-3907.

36. Bouvart, N.; Palix, R.-M.; Arkhipov, S.G.; Tumanov, I.A.; Michalchuk, A.A.L.; Boldyreva, E.V.; *CrystEngComm* **2018,** *20*, (13), 1797-1803.

37. Užarević, K.; Ferdelji, N.; Mrla, T.; Julien, P.A.; Halasz, B.; Friščić, T.; Halasz, I.; *Chemical Science* **2018,** *9*, (9), 2525-2532.

38. Michalchuk, A.A.L.; Tumanov, I.A.; Boldyreva, E.V.; *CrystEngComm* **2019,** *21*, (13), 2174-2179.

39. Kulla, H.; Michalchuk, A.A.L.; Emmerling, F.; *Chemical Communications* **2019,** *55*, (66), 9793-9796.

40. Kulla, H.; Haferkamp, S.; Akhmetova, I.; Röllig, M.; Maierhofer, C.; Rademann, K.; Emmerling, F.; *Angewandte Chemie International Edition* **2018,** *57*, (20), 5930-5933.

41. Colacino, E.; Carta, M.; Pia, G.; Porcheddu, A.; Ricci, P.C.; Delogu, F.; *ACS Omega* **2018,** *3*, (8), 9196-9209.

42. Stolle, A.; *Ball Milling Towards Green Synthesis: Applications, Projects, Challenges* **2014,** *7*, (31), 241.

9. Expanding the Toolbox: Monitoring the Mechanochemical Co-crystallization of Pharmaceuticals in Real-Time using Dual Fluorescence and Raman Spectroscopies

9.01 Preface

A principal advance in monitoring and understanding mechanochemical ball milling reactions in this Thesis is the development and application of *in situ* fluorescence emission spectroscopy. This chapter applies tandem fluorescence and Raman spectroscopies to better understand the co-crystallization and amorphization of indometacin, an active pharmaceutical ingredient (API) which is fluorescent in the solid state. This proof-of-principle work highlights the ability to use fluorescence emission and Raman spectroscopy to understand changes in the supramolecular solid-state environment induced by milling pharmaceutically relevant materials in real-time. This chapter is a manuscript being prepared for submission as Patrick A. Julien, Luzia S. Germann, Robin S. Stein, and Tomislav Friščić* aimed for *Angewandte Chemie International Edition* with modifications made to fit cohesively into this Thesis. All experimental work was conducted by P. A. Julien with L. S. Germann assisting with the processing of synchrotron diffraction data and R. S. Stein conducting solid-state NMR measurements. The manuscript was written by P. A. Julien and edited by T. Friščić.

9.02 Abstract

Screening for and synthesizing co-crystals of active pharmaceutical ingredients (APIs) *via* mechanochemical methods is an increasingly popular approach to enhance the physicochemical properties of solid APIs. In this work, we report the first use of *in situ* fluorescence spectroscopy to monitor mechanochemical ball-milling reactions, specifically the formation of the indometacin-saccharin co-crystal and the amorphization of indometacin. We combine real-time measurements by fluorescence and Raman spectroscopies to gain novel insight into mechanochemical reactions and monitor their

progress. This dual spectroscopic approach to *in situ* monitoring of mechanochemical reactions is a highly accessible means of studying the kinetics and mechanisms of transformations in the ball mill. It facilitates understanding mechanochemical reactions of compounds of pharmaceutical interest and advances organic chemistry in the ball mill.

9.03 Introduction

The desire to administer medications in tablet form has led to continuous and substantial interest in the solid-state properties of active pharmaceutical ingredients (APIs). Process-induced transformations are a critical concern throughout the pharmaceutical manufacturing process, as phase transformation between different solid forms of APIs and excipients can affect the bioavailability of drugs which can lead to issues in drug approval and delivery.[1, 2] Of particular concern are amorphous forms which can significantly modify the bioavailability of drugs and are generally unpredictable due to their metastable nature and ability to spontaneously recrystallize. Importantly, amorphous forms are difficult to measure and observe.[3] Methods for detecting amorphous solid forms of pharmaceuticals during multiple stages in pharmaceutical processing have garnered significant attention.[4] Ball milling is a an often encountered means of generating amorphous forms of APIs[5, 6] and other molecules,[7] with indometacin being one of the most studied APIs as it undergoes amorphization to a kinetically robust amorphous phase or polymorph interconversion depending on milling conditions.[8-10] The use of Raman spectroscopy to distinguish and quantify the amorphous form, the stable crystalline γ-form, and the metastable α-form of indometacin is well established in the literature.[11-15] Co-crystallization is a powerful approach towards stabilizing the solid forms of APIs and modulating the physicochemical properties of APIs such as solubility, bioavailability, and stability of the resultant solid-state form.[16,17] Similarly to amorphization, mechanochemistry has gained considerable popularity as a means to design, discover, and synthesize new solid forms of pharmaceutical solids, such as co-crystals.[18,19] However, little is known about the mechanisms which underlie mechanochemical transformations. To better study mechanochemical reactions of APIs, novel *in situ* techniques based on either synchrotron X-ray powder diffraction[20] (XRPD) or Raman spectroscopy[21] have recently been developed and applied to the

mechanochemical synthesis of co-crystals. Monitoring milling reactions using synchrotron XRPD studies has also recently been applied towards understanding amorphization and polymorphic transitions in solid-state carbohydrates.[22, 23]

Fluorescence spectroscopy has increasingly been applied in the characterization of pharmaceutical solids,[24-27] as it is non-destructive and can be highly sensitive to changes in solid-state arrangement of molecules. We have previously reported the first use of fluorescence to distinguish the solid forms (co-crystal, polymorph, solvate, and amorphous) of indometacin.[28] From an instrumental perspective, fluorescence spectroscopy is easily applied to monitoring mechanochemical reactions, as it can easily be conducted through transparent milling jars with suitable optical properties which enable the transmission of both the excitation and emission radiation wavelengths. Readily available and low cost ultraviolet excitation sources[29] and visible charge coupled device (CCD) detectors, enable rapid acquisition of the entire emission spectrum with high sensitivity and time resolution using simple and low cost setups.[30,31] These components can easily be integrated into existing real-time monitoring setups using Raman spectroscopy, and provide tandem *in situ* monitoring of milling reactions without the need for synchrotron radiation sources.

In order to demonstrate the applicability of the newly developed dual-spectroscopic approach to monitoring mechanochemical transformations in pharmaceutical solid-forms, we have chosen to explore both the amorphization of indometacin by neat grinding and the co-crystallization between indometacin and saccharin *via* liquid-assisted grinding (LAG) (Figure 87) as model systems. Both reactions exhibit characteristic changes in fluorescence emission and Raman spectra upon amorphization and co-crystallization. Importantly, the formation of the indometacin-saccharin co-crystal also exhibits a characteristic change in Raman shift,[32] which enables the simultaneous acquisition and correlation of Raman spectroscopy and fluorescence data.

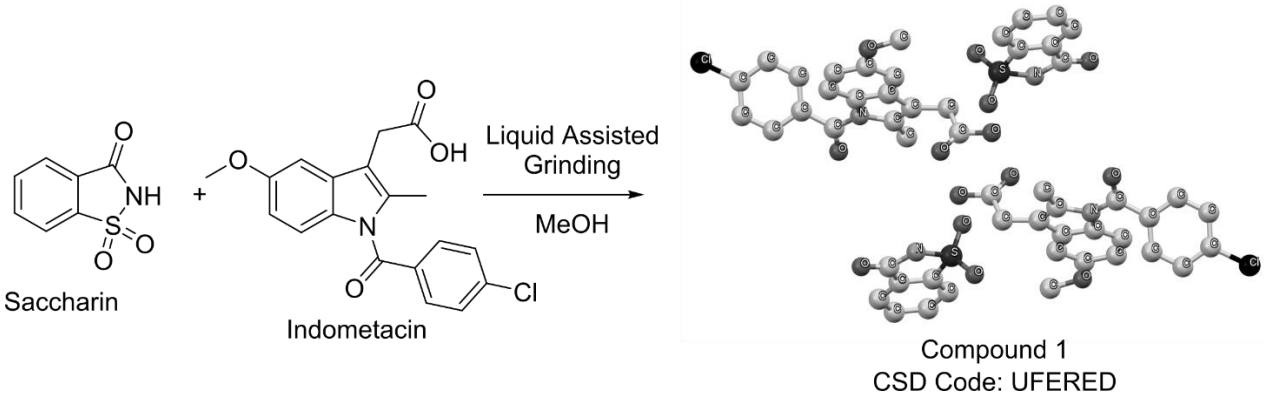

*Figure 87. Mechanochemical synthesis of indometacin-saccharin co-crystal (Compound **1**).*

9.04 Results and Discussion

(a) Design of the tandem reaction monitoring setup

The crystalline forms of both commercial starting materials and mechanochemically synthesized compound **1**, were verified by X-ray powder diffraction (Figure 88).

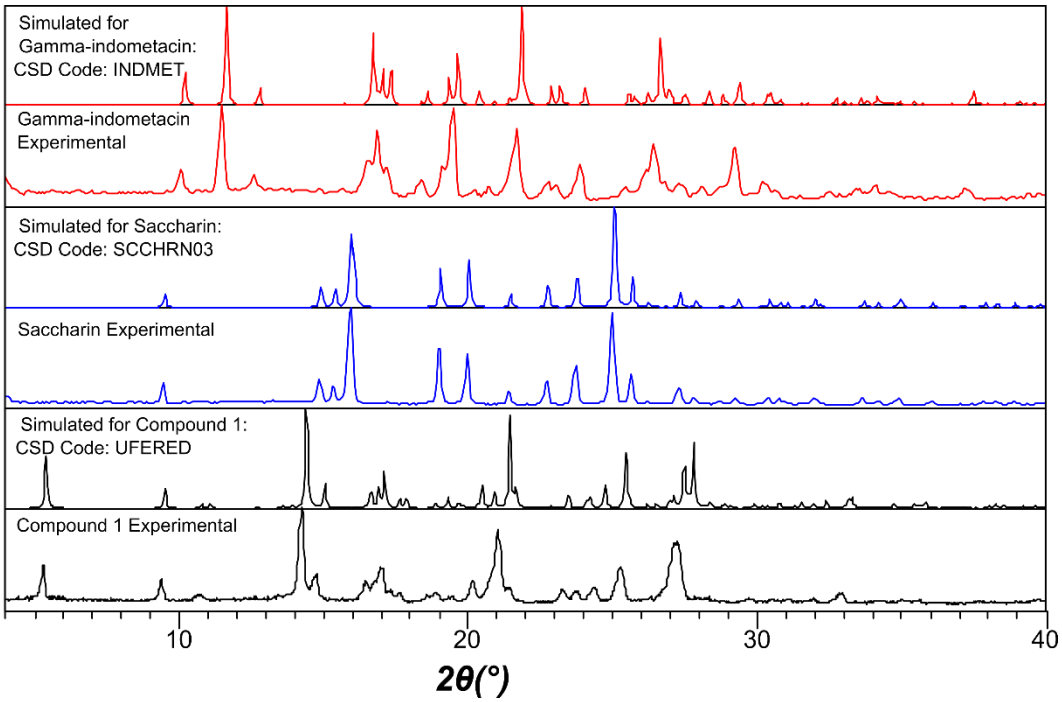

*Figure 88. X-ray powder diffraction patterns of commercial γ-form indometacin (red), saccharin (blue) and compound **1** (black) obtained from milling synthesis compared with their respective simulated diffraction patterns based on their reported crystal structures.*

In order to design a setup capable of efficiently measuring the fluorescence emission of indometacin, saccharin, and compound **1**, both excitation and emission spectra of all relevant compounds was measured. Samples were tightly packed into the wells of a poly-styrene 96-well plate in order to maintain a consistent surface area and amount of sample measured as much as possible, and both excitation and emission spectra were acquired using a well-plate reader (Figure 89). Excitation spectra demonstrate that a wavelength near 375-380nm is optimal for all compounds. The emission spectra demonstrate that the intensity of the emission from indometacin is considerably higher than that of saccharin, with the co-crystal exhibiting the strongest luminescence of the solid forms measured in this study. Solid saccharin is the most red-shifted of the three solid phases with a maximum emission slightly below 450nm, while solid γ-form indometacin has a maximum near 475nm. Upon co-crystallization the emission redshifts to a maximum emission near 510nm.

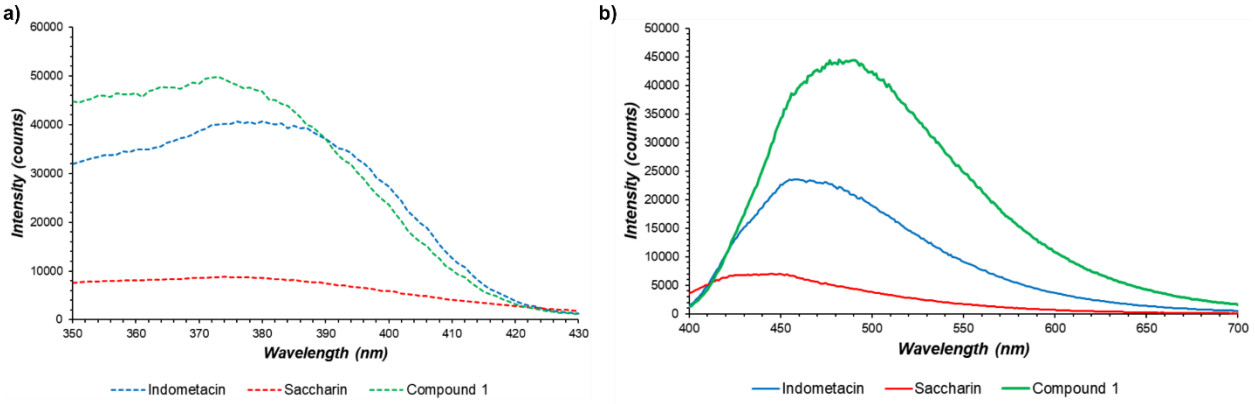

*Figure 89. a) Excitation spectra with emission monitored at 450nm of γ-form indometacin, saccharin, and compound **1**. b) Fluorescence emission spectra of indometacin, saccharin, and compound **1**, under excitation at 380nm. All spectra were recorded on a well-plate reader.*

Tandem real-time reaction monitoring using simultaneous Raman and fluorescence spectroscopies provides an opportunity to validate the *in situ* fluorescence measurements, analysis, and provide additional insights. Towards our goal of developing a tandem spectroscopic approach, the lack of fluorescence emission above 700nm of all the measured compounds suggested the use of Raman spectroscopy using a 785nm

excitation laser without any observed interference. The Raman spectra of indometacin, saccharin, and compound **1** are consistent with spectra reported in the literature[12, 13, 15] and suggest the reaction could be monitored with minimal interference from the transparent PMMA milling jars, by focusing on the region between 1500-1800 cm^{-1} (Figure 90).

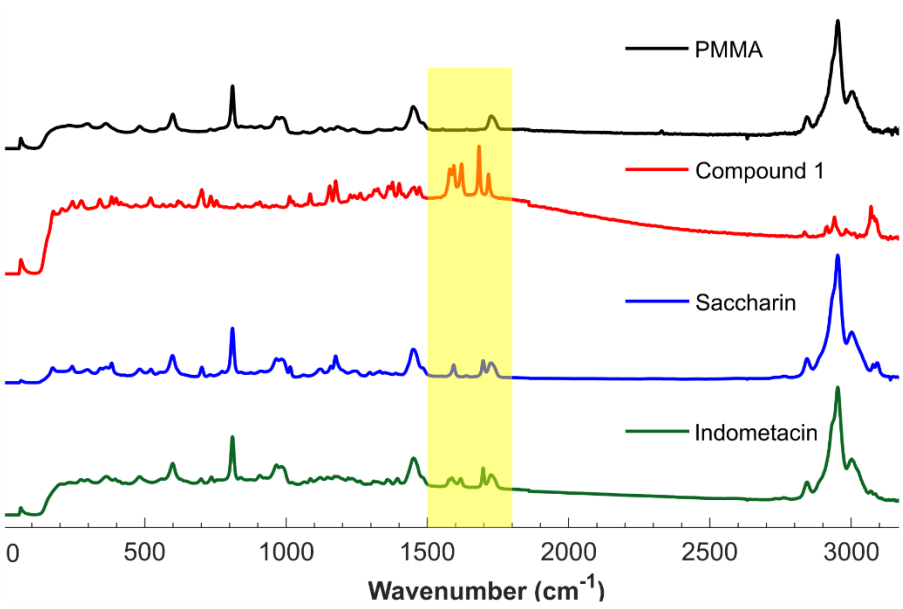

*Figure 90. Raman spectra for indometacin, saccharin, and compound **1** along with the Raman spectrum of the PMMA jar which can interfere with the sample signal. The highlighted region between 1500-1800 cm^{-1} was chosen due to strong sample signals and minimal interference from PMMA.*

The fluorescence equipment was integrated into our existing real-time Raman reaction monitoring setup as shown in Figure 91.[33] For real-time fluorescence measurements on this system, an excitation source of a 375nm laser was selected, along with a diverging lens to spread the excitation light onto a larger amount of sample through the optically transparent PMMA milling jars. The resulting fluorescence emission was collected *via* a fiber-optically-coupled spectrometer, before being analyzed using customized data processing routines previously applied to Raman spectroscopy data.[33]

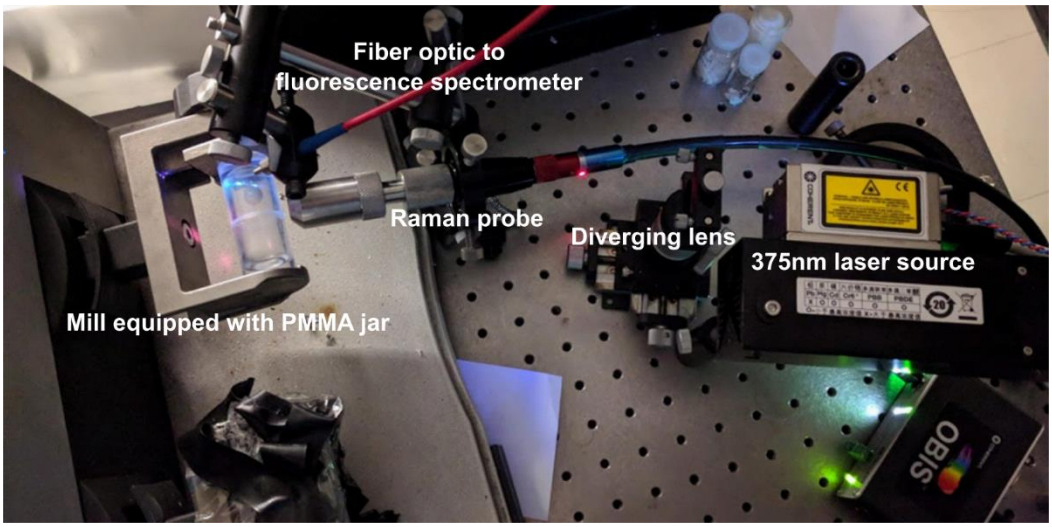

Figure 91. Labeled photograph of the developed setup for running tandem real-time monitoring of milling reactions using fluorescence emission and Raman spectroscopy.

(b) *In situ monitoring of the co-crystallization of indometacin and saccharin*

To better understand the formation of the indometacin-saccharin co-crystal *via* LAG we conducted *in situ* synchrotron X-ray powder diffraction studies at the Deutsches Elektronen-Synchrotron (DESY) Petra III P02.1 beamline following previously reported procedures,[20] which suggests that the formation of the co-crystal is rapid and proceeds without the presence of other potential crystalline intermediate phases, such as the reported methanol solvate of indometacin (CSD Code: BANMUZ)[34] as shown in Figure 92.

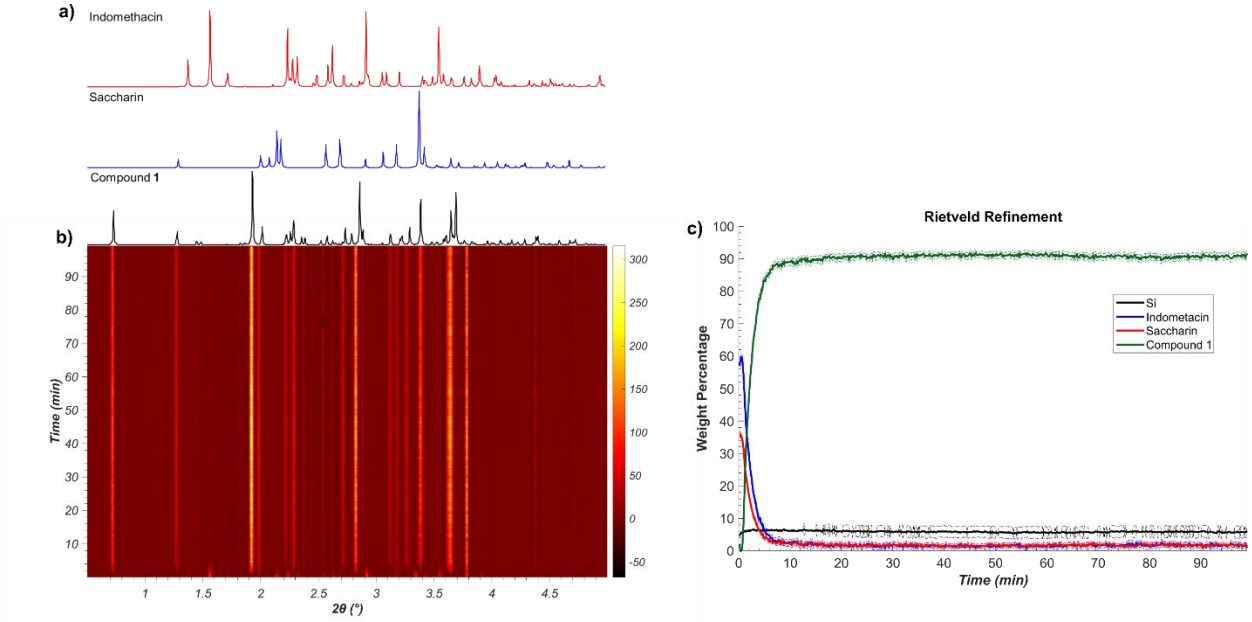

*Figure 92. (a) Simulated diffraction patterns for indometacin (CSD code: INDMET), saccharin (CSD code: SCCHRN02) and compound **1** (CSD code: UFERED). (b) Synchrotron X-ray powder diffraction patterns showing the mechanochemical formation of **1**. (c) Weight percentage of each phase as estimated by Rietveld refinement.*

Tandem monitoring of the LAG reaction of indometacin and saccharin with methanol using fluorescence spectroscopy (Figure 93b) and Raman spectroscopy (Figure 94b) both reveal quantitative conversion within 5 minutes. For the case of fluorescence spectroscopy, a rapid and significant increase in both emission intensity and a redshift of the signal are observed. Either of these changes can be used to estimate the reaction profile over time. Luminescence intensity can be measured at the maximum of the emission profile, and normalized relative to the highest intensity measured (Figure 93c). In order to compare of Raman and fluorescence data, we have applied the fitting procedure originally developed for *in situ* Raman spectroscopy to both the real-time Raman spectroscopy and fluorescence emission data. Each *in situ* spectrum can be modeled as a combination of the spectra of pure solid starting materials and product (Figure 93a, Figure 94a) *via* non-negative least squares (NNLS) procedure, as has previously been described for Raman data.[33] Subsequent normalization by setting the sum contribution of starting materials and product to 1.0 in each spectrum provides an estimate of the reaction profile (Figure 93d, Figure 94c).

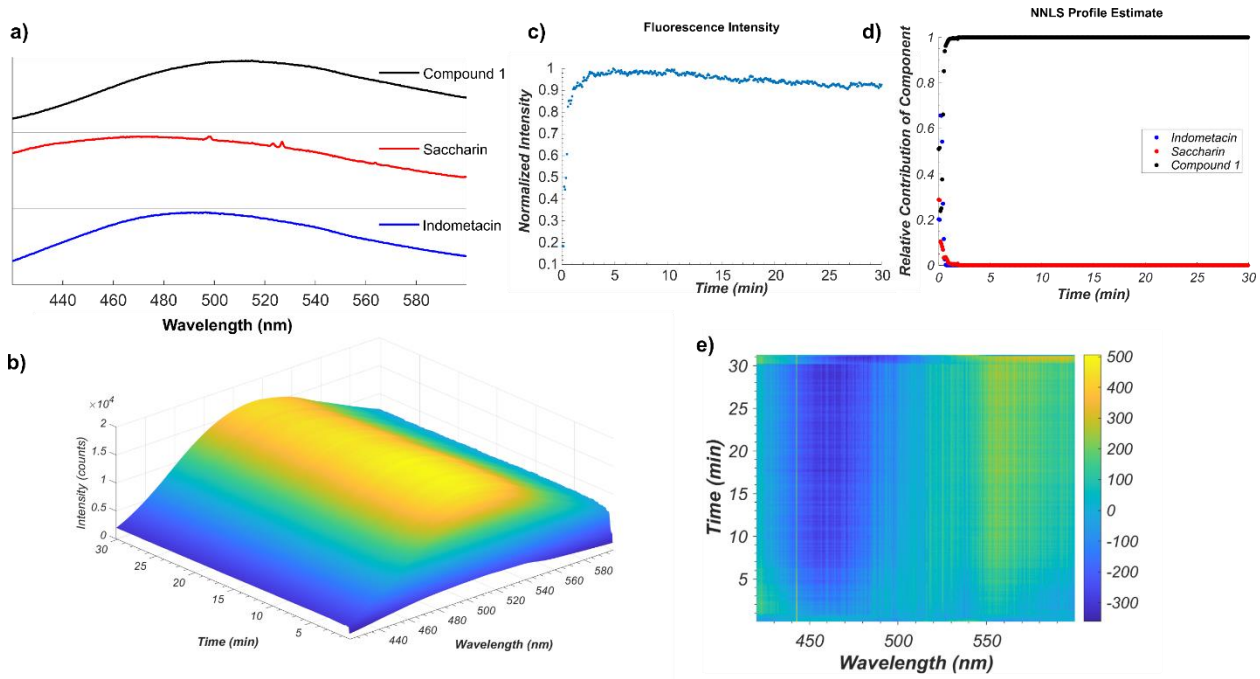

*Figure 93. (a) Fluorescence emission of indometacin, saccharin, and compound **1**. (b) Time resolved fluorescence emission acquired during the mechanochemical synthesis of compound **1**. (c) Normalization of the maximum fluorescence intensity throughout the data set. (d) Relative amounts of indometacin, saccharin, and **1** estimated using non-negative least squares fitting of the in situ dataset. (e) time-dependent residuals after NNLS fitting.*

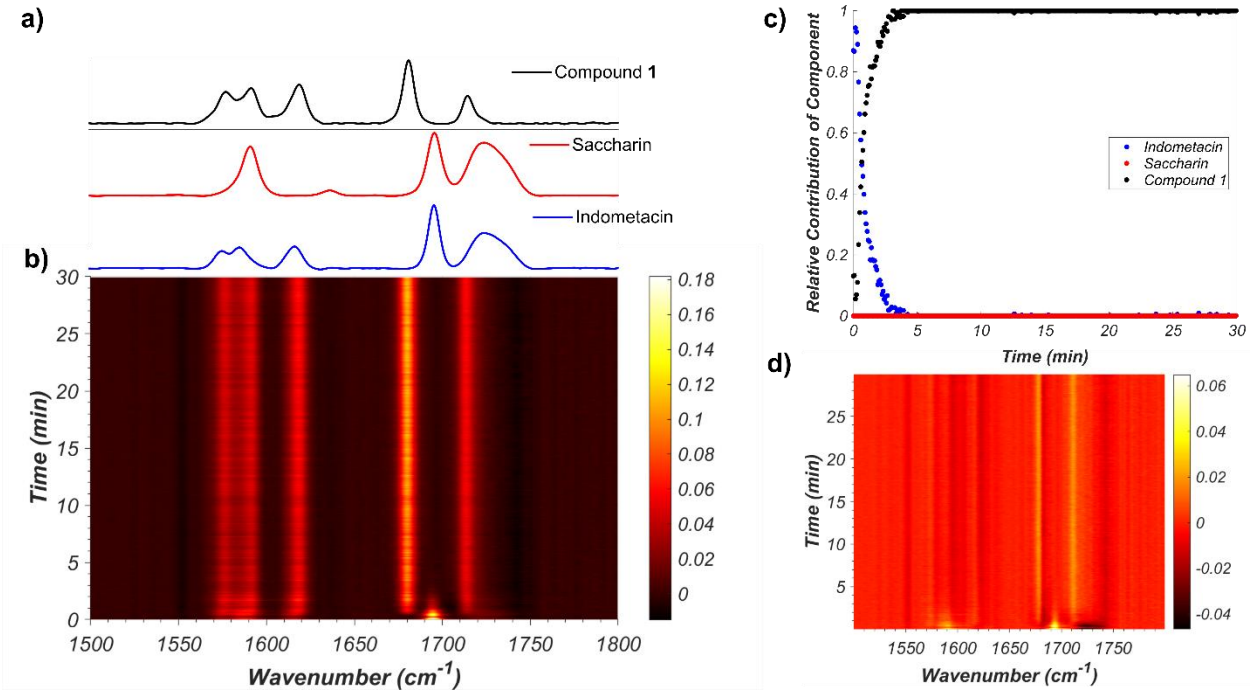

*Figure 94. (a) Raman spectra of indometacin, saccharin, and compound **1**. (b) Time resolved Raman spectra acquired during the mechanochemical synthesis of compound **1**. (c) Relative amounts of indometacin, saccharin, and **1** estimated using non-negative least squares fitting of the in situ dataset. (d) time-dependent residuals after NNLS fitting.*

Estimated reaction profiles from NNLS fitting for both spectroscopic techniques are in good agreement (Figure 95), with the profile of the fluorescence data set suggesting a more rapid conversion, which may in part be due to the broad shape and significant overlap of the fluorescence signal between indometacin and compound **1**. This overlap complicates the detection of low concentrations of indometacin or co-crystal in the presence of a large excess of the other. For both fluorescence and Raman data there is clear pattern within in the residuals (Figure 93e,Figure 94d), although for the case of fluorescence the intensity of the residuals is low (< 5%). Deviation in the model may be due to differences between the spectra of the pure components and *in situ* data set or it may be due to baseline effects and interference from PMMA, which may distort the shape of the profile. While this highlights the difficulty in analyzing real-time spectroscopic data for milling reactions, developing novel analysis methods is beyond the scope of the present work. Despite these concerns, the estimated profiles obtained enable a preliminary comparison of the estimated reaction profiles. Both NNLS fitting procedures

are in good agreement with each other, as well as with the change in fluorescence intensity, which was calculated by normalizing the maximum fluorescence intensity for each *in situ* measured spectrum. This suggests that monitoring the emission intensity is a simple way of utilizing fluorescence to monitor mechanochemical reactions, provided there are significant changes in emission intensity between products and starting materials. The ability to estimate reaction profiles utilizing unprocessed intensity changes is rare in real-time monitoring of milling reactions, as both X-ray diffraction methods and Raman spectroscopy utilize highly focused beams measuring only a small sample area, often below 1 square millimeter, and are thus highly susceptible to stochastic changes in intensity due to motions during milling.[35]

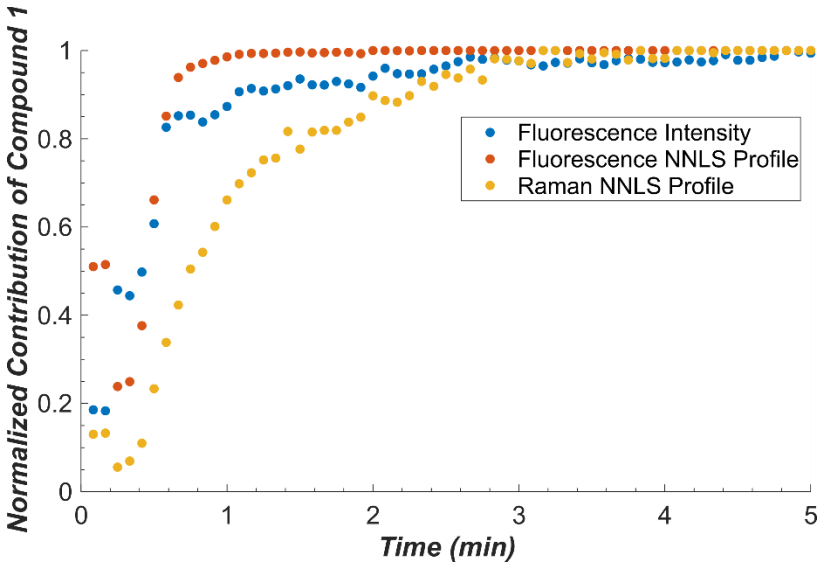

*Figure 95. Estimated formation of compound **1** via NNLS fitting of both Raman and fluorescence data sets.*

The formation of compound **1** was confirmed by XRPD and is consistent with the pattern simulated for the crystal structure reported in the literature (CSD code: UFERED) with no traces of starting material detected (Figure 88). Further verification was done by synthesizing compound **1** using an established literature procedure[36] and comparing the cross polarization magic angle spinning solid-state nuclear magnetic resonance (CP-MAS-SSNMR) of the ^{13}C nuclei, which proved to be identical to the previously reported spectroscopic data, as shown in Figure 96.

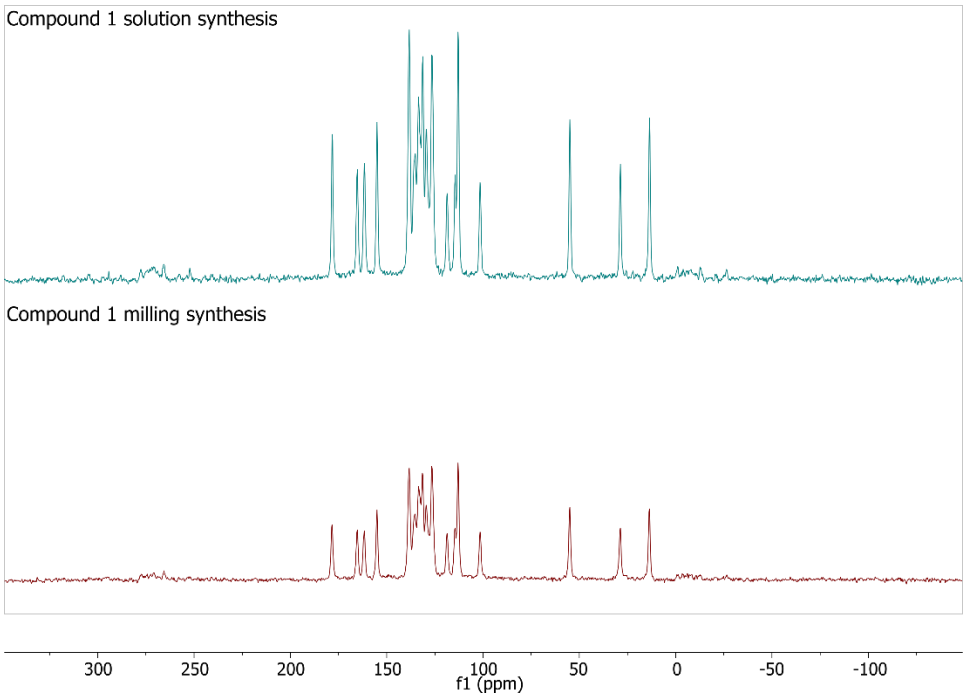

*Figure 96. ^{13}C CP-MAS-SSNMR of solution synthesized (top) compound **1** and that of the reaction mixture after monitoring of the milling reaction.*

(c) Milling amorphization of indometacin

Having explored the utility of the herein introduced dual spectroscopic approach for following the mechanochemical co-crystallization of indometacin, we subsequently monitored the amorphization behavior of indometacin under grinding conditions without any additives (i.e. neat grinding), which has previously been measured using *ex situ* X-ray powder diffraction[37] and *ex situ* Raman spectroscopy.[13, 14] To the best of our knowledge this is the first report of monitoring the amorphization of an API *via* milling in real-time using spectroscopic techniques. The use of *in situ* Raman spectroscopy to monitor the room temperature milling of γ-indometacin in a vibratory ball mill operating at 30 Hz reveals three distinct phases of indometacin, namely γ-form, α-form, and amorphous (Figure 97b), which were identified by comparison with samples synthesized by either precipitation from an ethanol/water mixture for α-form,[38] or quenching a melt of indometacin in liquid nitrogen to form amorphous indometacin.[39] Fitting of the measured *in situ* data set using the Raman spectra of these pure samples to estimate the relative composition of the reaction mixture revealed the emergence of an amorphous phase

within 10 minutes which exists in combination with γ-indometacin. After approximately 75 minutes, this mixture begins to partly convert to the α-form. The observed transformation is consistent with previous *ex situ* diffraction work for milling at 30°C, which suggested the milling process results in a 1:1 mixture of α and amorphous forms.[37] In this case the reaction proceeds faster, likely due to different milling conditions, as we are using a vibratory ball mill operating at 30 Hz in contrast to the previously reported centrifugal ball mill operating at ~4Hz. This partial transformation may be in part explained due to the glass transition of indometacin (T_g = 43 °C)[12] with temperatures for milling conditions similar to those employed in this work having previously been reported to reach 40°C.[33] Interpretation of the fluorescence data is considerably more challenging, as the α and amorphous forms of indometacin exhibit nearly identical fluorescence profiles (Figure 98a). The same NNLS fitting procedure utilized for the Raman spectra was applied to the *in situ* fluorescence emission (Figure 98b) using fluorescence spectra of the same pure samples utilized for the Raman measurements. The initial rapid amorphization of the γ-form is detected, however the emergence of the α-form from the amorphous form was not detected (Figure 98c) by NNLS fitting. This is likely due to the similarity of the fluorescence profiles of the α and amorphous forms as the emergence of the α-form is neither detected in the estimated profile, nor is it present in the residuals (Figure 98d). Monitoring the maximum emission intensity of each spectrum, however, does reveal a slight increase in emission intensity corresponding to the formation of the α-phase. This suggests a limited ability of the current setup to detect changes between α-form and amorphous indometacin.

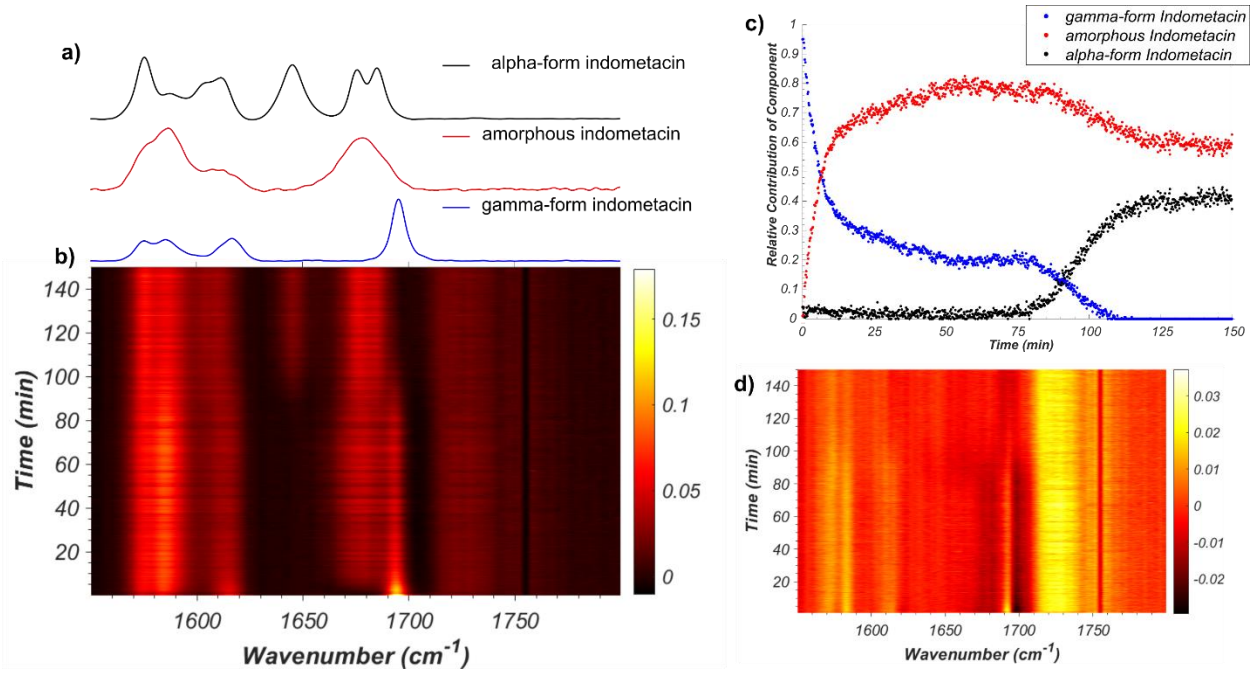

Figure 97. (a) Normalized Raman spectra of γ-form, α-form, and amorphous indometacin synthesized via solution protocols.[38, 39] (b) Time resolved Raman spectra acquired during the milling of γ-indometacin. (c) Relative amounts of γ-form, α-form, and amorphous indometacin estimated using non-negative least squares fitting of the in situ dataset. (d) time-dependent residuals after NNLS fitting.

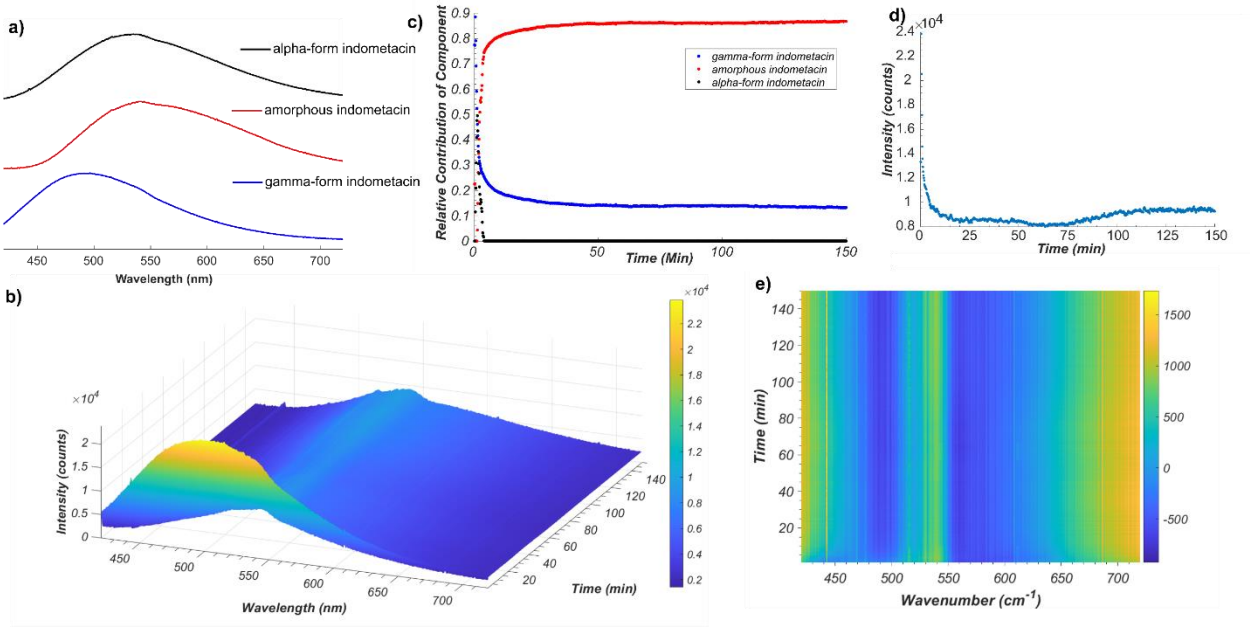

Figure 98. (a) Normalized fluorescence spectra of γ-form, α-form, and amorphous indometacin synthesized via solution protocols.[38,39] (b) Time resolved fluorescence emission acquired during the milling of indometacin. (c) Relative amounts of γ-form, α-form, and amorphous indometacin estimated using non-negative least squares fitting of the in situ dataset, which fails to detect the emergence of α-form indometacin. (d) Normalization of the maximum fluorescence intensity throughout the data set. (e) time-dependent residuals after NNLS fitting.

The solid indometacin sample was analyzed after milling using XRPD, revealing diffraction signals consistent with the reported α-phase, but with broad diffraction maxima and elevated baseline consistent with the presence of amorphous or nano-crystalline material (Figure 99). Comparison to a sample of solution synthesized α-indometacin *via* ^{13}C CP-MAS-SSNMR spectroscopy confirms that the indometacin obtained after milling is in the α-form. However, SSNMR spectroscopy does not reveal any amorphous content, suggesting the sample fully crystallized in the process of either preparing or spinning the SS-NMR sample. The apparent steady-state behaviour of the γ-form/amorphous and α-form/amorphous mixtures during milling is remarkable given the instability of the sample after milling has stopped, suggesting that prolonged neat grinding can produce mixtures of crystalline and amorphous phases which appear to converge towards a specific ratio. This behavior remains poorly understood and the herein tandem dual spectroscopic

approach provides a powerful and novel approach which does not rely on synchrotron radiation with which to examine mechanochemical amorphization reactions. This dual spectroscopic setup enables detailed fundamental studies into amorphization under milling conditions which are of practical importance due to the potential for the formation of amorphous phases during mechanical processing of pharmaceuticals and the desire to synthesize amorphous formulations of APIs to improve solubilities.[40]

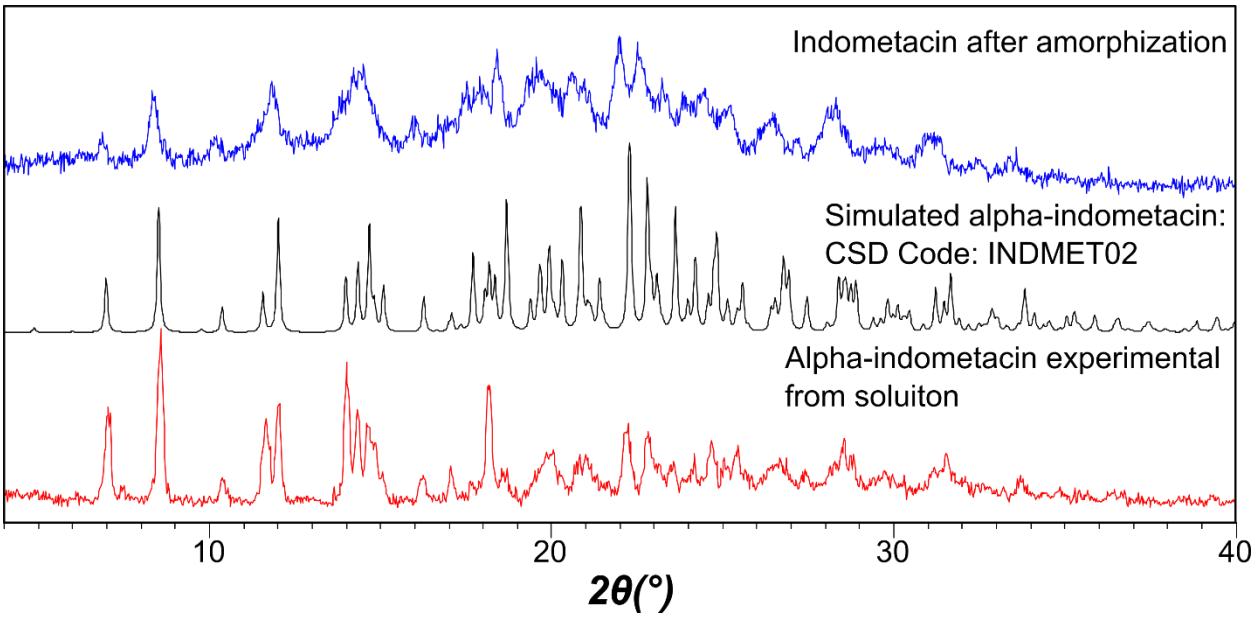

Figure 99. XRPD pattern of indometacin after milling (top) compared with the pattern simulated for the reported structure of α-form indometacin (middle) and α-form synthesized from solution (bottom). [38]

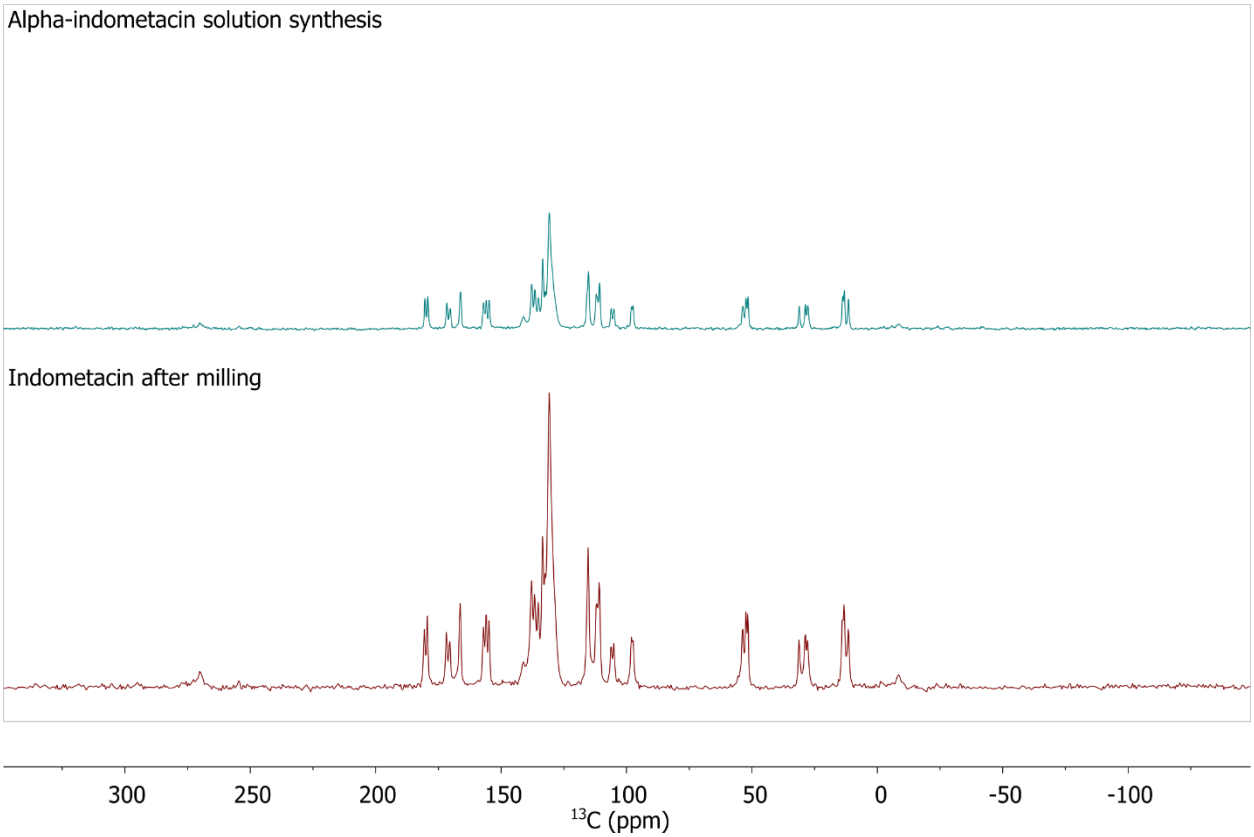

Figure 100. Comparison of ^{13}C CP-MAS-SSNMR spectra of solution synthesized α-indometacin (top)[38] and the indometacin sample after milling (bottom).

9.05 Conclusions

The utility of fluorescence spectroscopy in real-time monitoring of milling reactions has been demonstrated for the first time and compared with simultaneous Raman spectroscopy to yield the first dual spectroscopic approach for real-time monitoring of milling reactions. This cost-effective setup enables monitoring mechanochemical reactions of pharmaceutical materials, which are of particular relevance due to concerns over mechanical treatment in pharmaceutical manufacturing. In contrast to the previously applied *ex-situ* techniques, the high temporal frequency of data acquisition for *in-situ* techniques represents a significant advance in the field of mechanochemical reaction kinetics that enables the development of kinetic models which enhance understanding of mechanochemical reactions relevant to the solid forms of pharmaceuticals and other organic materials.

9.06 Experimental

All chemicals were purchased from Sigma Aldrich and used without further purification, including the purchased indometacin which was γ-form. All milling experiments were conducted using a RETSCH MM400 operating at 30 Hz using a ~15 mL PMMA milling jar and 3 g zirconia ball.

(a) Milling Syntheses

Compound **1** was prepared mechanochemically by milling 198 mg γ-indometacin (0.55 mmol) with 101 mg of saccharin (0.55 mmol) in the presence of 20 µL of methanol. Milling of γ-indometacin was conducted using 198 mg γ-indometacin (0.55 mmol).

(b) Solution syntheses

Amorphous indometacin was synthesized according to literature procedure[39] by heating 300 mg of γ-indometacin above 165°C and pouring the resulting melt into liquid nitrogen, forming an amorphous mass which was triturated into a powder using a mortar and pestle.

α-indometacin was synthesized using a modified literature procedure dissolving 300 mg of γ-indometacin in 5 mL of ethanol at 80°C before adding 10 mL of room temperature distilled water and filtering the resulting precipitate.

(c) Fluorescence, SS-NMR, and XRPD Characterization

Preliminary fluorescence measurements were performed in clear polystyrene 96-well microplates, with sample densely packed into each well, and loaded into a Biotek Synergy 2 multi-mode microplate reader. X-ray powder diffraction (XRPD) patterns were collected using a Bruker D2 Phaser powder diffractometer equipped with a Cu Kα (λ = 1.54060 Å) source, nickel filter and Lynxeye detector. ^{13}C Solid-state NMR spectra were collected using a Varian VNMRS 400 MHz NMR Spectrometer, with a magic angle spinning rate of 14kHz using a tancpx pulse sequence and calibrated with respect to glycine signal at 176.5 ppm.

(d) Real-time synchrotron diffraction measurements

In situ diffraction measurements were collected at the Deutsches Elektronen-Synchrotron (DESY) Petra III P02.1 beamline at an X-ray wavelength of 60 keV (λ ~ 0.207 Å) with a 1x 1 mm^2 collimated X-ray beam and a PerkinElmer 2D area detector operating at a time resolution of 10 seconds and a modified RETSCH MM400. All 2-D XRPD patterns were integrated using Dioptas.[41] Sequential Rietveld analysis was performed in TOPAS-Academic V5[3] using a silicon standard measured under identical experimental conditions. Datasets were subsequently corrected, truncated, and plotted using custom scripts in MATLAB R2018a with PMMA baseline subtraction performed using the Sonneveld and Visser algorithm.[42]

(e) *In situ* Raman measurements

All Raman spectra were collected RamanRxn1™ analyzer by Kaiser Optical Systems Inc. every 5 seconds using a 785 nm laser. Spectra were dark and intensity corrected using the Holograms® software package before being processed. Pure samples of starting materials and products were loaded on glass slides and measured. *In situ* datasets were subsequently imported into MATLAB2018a[43] and baseline corrected using the Sonneveld and Visser algorithm,[42] truncated to the limits shown in the data sets and normalized using vector normalization (L2 norm). Background subtraction of the PMMA milling jar was performed by performing a linear regression of a previously recorded PMMA spectrum to each *in situ* spectrum and subtracting the PMMA spectrum. After these corrections, the data was analyzed *via* NNLS, where in situ collected spectra were fitted as a sum of the normalized component spectra using a non-negative linear least squares algorithm (“lsqnonneg” in MATLAB) and profile estimates were normalized by setting the sum of all components in each spectrum to 1.0.[33]

(f) Real-time Fluorescence spectroscopy measurements

Fluorescence measurement were conducted using a Coherent OBIS 375nm LX 50 mW excitation source and fiber-optically coupled QE65000 spectrometer from Ocean Optics. Pure samples of starting materials and products were loaded on glass slides and measured. *In situ d*atasets were subsequently truncated to the limits shown in their respective figures and plotted using custom scripts in MATLAB R2018a.[43] NNLS profiles

were obtained in an identical manner as described for Raman spectra. Fluorescence intensity values were calculated by finding the maximum value of each *in situ* spectrum.

9.07 References

1. Hubert, S.; Briancon, S.; Hedoux, A.; Guinet, Y.; Paccou, L.; Fessi, H.; Puel, F.; *International Journal of Pharmaceutics* **2011,** *420*, (1), 76-83.
2. Zhang, G.G.Z.; Law, D.; Schmitt, E.A.; Qiu, Y.; *Advanced Drug Delivery Reviews* **2004,** *56*, (3), 371-390.
3. Hancock, B.C.; Zografi, G.; *Journal of Pharmaceutical Sciences* **1997,** *86*, (1), 1-12.
4. Yu, L.; *Advanced Drug Delivery Reviews* **2001,** *48*, (1), 27-42.
5. Willart, J.F.; Descamps, M.; *Molecular Pharmaceutics* **2008,** *5*, (6), 905-920.
6. Descamps, M.; Willart, J.F.; *Advanced Drug Delivery Reviews* **2016,** *100*, 51-66.
7. Caron, V.; Willart, J.-F.; Lefort, R.; Derollez, P.; Danède, F.; Descamps, M.; *Carbohydrate Research* **2011,** *346*, (16), 2622-2628.
8. Otsuka, M.; Matsumoto, T.; Kaneniwa, N.; *Chemical & Pharmaceutical Bulletin* **1986,** *34*, (4), 1784-1793.
9. Bahl, D.; Bogner, R.H.; *Pharmaceutical Research* **2006,** *23*, (10), 2317-2325.
10. Crowley, K.J.; Zografi, G.; *Journal of Pharmaceutical Sciences* **2002,** *91*, (2), 492-507.
11. Heinz, A.; Savolainen, M.; Rades, T.; Strachan, C.J.; *European Journal of Pharmaceutical Sciences* **2007,** *32*, (3), 182-192.
12. Hédoux, A.; Paccou, L.; Guinet, Y.; Willart, J.-F.; Descamps, M.; *European Journal of Pharmaceutical Sciences* **2009,** *38*, (2), 156-164.
13. Taylor, L.S.; Zografi, G.; *Pharmaceutical Research* **1998,** *15*, (5), 755-761.
14. Strachan, C.J.; Rades, T.; Gordon, K.C.; *Journal of Pharmacy and Pharmacology* **2007,** *59*, (2), 261-269.
15. Hédoux, A.; Guinet, Y.; Descamps, M.; *International Journal of Pharmaceutics* **2011,** *417*, (1), 17-31.
16. Schultheiss, N.; Newman, A.; *Crystal Growth & Design* **2009,** *9*, (6), 2950-2967.
17. Vishweshwar, P.; McMahon, J.A.; Bis, J.A.; Zaworotko, M.J.; *Journal of Pharmaceutical Sciences* **2006,** *95*, (3), 499-516.
18. Delori, A.; Friscic, T.; Jones, W.; *CrystEngComm* **2012,** *14*, (7), 2350-2362.
19. Friščić, T.; Jones, W.; *Crystal Growth & Design* **2009,** *9*, (3), 1621-1637.

20. Halasz, I.; Puškarić, A.; Kimber, S.A.J.; Beldon, P.J.; Belenguer, A.M.; Adams, F.; Honkimäki, V.; Dinnebier, R.E.; Patel, B.; Jones, W., et al.; *Angewandte Chemie International Edition* **2013,** *52*, (44), 11538-11541.

21. Gracin, D.; Štrukil, V.; Friščić, T.; Halasz, I.; Užarević, K.; *Angewandte Chemie* **2014,** *126*, (24), 6307-6311.

22. Bordet, P.; Bytchkov, A.; Descamps, M.; Dudognon, E.; Elkaïm, E.; Martinetto, P.; Pagnoux, W.; Poulain, A.; Willart, J.-F.; *Crystal Growth & Design* **2016,** *16*, (8), 4547-4558.

23. Martinetto, P.; Bordet, P.; Descamps, M.; Dudognon, E.; Pagnoux, W.; Willart, J.-F.; *Crystal Growth & Design* **2017,** *17*, (11), 6111-6122.

24. Alves, J.C.L.; Poppi, R.J.; *Analytica Chimica Acta* **2009,** *642*, (1), 212-216.

25. Moreira, A.B.; Dias, I.L.T.; Neto, G.O.; Zagatto, E.A.G.; Kubota, L.T.; *Analytica Chimica Acta* **2004,** *523*, (1), 49-52.

26. Moreira, A.B.; Oliveira, H.P.M.; Atvars, T.D.Z.; Dias, I.L.T.; Neto, G.O.; Zagatto, E.A.G.; Kubota, L.T.; *Analytica Chimica Acta* **2005,** *539*, (1), 257-261.

27. Warnecke, S.; Rinnan, Å.; Allesø, M.; Engelsen, S.B.; *Applied Spectroscopy* **2015,** *69*, (3), 323-331.

28. Frenette, M.; Cosa, G.; Friscic, T.; *CrystEngComm* **2013,** *15*, (25), 5100-5106.

29. Muramoto, Y.; Kimura, M.; Nouda, S.; *Semiconductor Science and Technology* **2014,** *29*, (8), 084004.

30. Neece, G.A., *Microspectrometers: an industry and instrumentation overview*; Optical Engineering + Applications SPIE: 2008; Vol. 7086.

31. *QE65000 Data Sheet*, Ocean Optics: 830 Douglas Ave, Dunedin, FL.

32. Basavoju, S.; Boström, D.; Velaga, S.P.; *Pharmaceutical Research* **2008,** *25*, (3), 530-541.

33. Julien, P.A.; Malvestiti, I.; Friščić, T.; *Beilstein Journal of Organic Chemistry* **2017,** *13*, 2160-2168.

34. J. G. Stowell, S.R.B., G. Zografi, M. Yoshioka; *CCDC 198477: Experimental Crystal Structure Determination, The Cambridge Structural Database* **2002**.

35. Friščić, T.; Halasz, I.; Beldon, P.J.; Belenguer, A.M.; Adams, F.; Kimber, S.A.J.; Honkimäki, V.; Dinnebier, R.E.; *Nature Chemistry* **2012,** *5*, 66.

36. Alhalaweh, A.; Sokolowski, A.; Rodríguez-Hornedo, N.; Velaga, S.P.; *Crystal Growth & Design* **2011,** *11*, (9), 3923-3929.

37. Otsuka, M.; Otsuka, K.; Kaneniwa, N.; *Drug Development and Industrial Pharmacy* **1994,** *20*, (9), 1649-1660.

38. Kaneniwa, N.; Otsuka, M.; Hayashi, T.; *Chem Pharm Bull (Tokyo)* **1985,** *33*, (8), 3447-3455.

39. Yoshioka, M.; Hancock, B.C.; Zografi, G.; *Journal of Pharmaceutical Sciences* **1994,** *83*, (12), 1700-1705.

40. Hancock, B.C.; Parks, M.; *Pharmaceutical Research* **2000,** *17*, (4), 397-404.

41. Prescher, C.; Prakapenka, V.B.; *High Pressure Research* **2015,** *35*, (3), 223-230.

42. Sonneveld, E.J.; Visser, J.W.; *Journal of Applied Crystallography* **1975,** *8*, (1), 1-7.

43. Press, W.H.; Teukolsky, S.A.; Vetterling, W.T.; Flannery, B.P.; *The art of scientific computing* **1992,** *2*, 1002.

10. Discussion and Conclusion

Mechanochemistry has only recently emerged as a versatile synthetic methodology for a wide variety of different materials, with notable advantages such as reducing or eliminating the need for solvent, minimizing the waste generated, and often accelerating reaction times giving improved yields, selectivity, and space-time yields. In addition, mechanochemistry has facilitated the discovery of new phases and intermediate structures not stable in solution. Given the increasing need for sustainable methods of chemical synthesis and the relative simplicity of running mechanochemical reactions, the prevalence of mechanochemical methods is likely to continue to increase. Despite increased attention, the fundamental behaviors of mechanochemical methods remain poorly understood relative to solution methods. The work in this Thesis focused on developing novel means for real-time monitoring of milling reactions by improving both existing setups and data processing.

A principal contribution of this Thesis is the expansion of methodologies for conducting and analyzing *in situ* monitoring of milling reactions. The use of fluorescence spectroscopy to monitor milling reactions has been pioneered in this Thesis and can provide considerable insight into fluorescent systems, especially those containing luminescent lanthanides. The development of sapphire milling jars has expanded the scope of mechanochemical reactions accessible for monitoring using the current *in situ* Raman spectroscopy and X-ray diffraction methodologies, by minimizing the background signal from the jar, which can obscure the sample signal. The combination of *in situ* milling measurements and variable temperature heating experiments represent a novel approach to decoupling friction based thermal effects from mechanical or mixing effects. These real-time approaches will hopefully improve the fundamental understanding of the role of temperature in milling processes.

The projects in this Thesis necessitated the development of novel data processing approaches. Although most of the data processing was consistent with approaches described in the literature, and implemented independently, the application of non-negative matrix factorization is a novel and highly efficient means of analyzing *in situ* data. Simultaneously estimating reaction components and profiles for milling reactions holds

considerable promise in providing reasonable estimates when spectra or diffraction patterns of pure compounds are very difficult to obtain and may be of use for real-time reaction monitoring beyond milling. Rapid advances in machine learning techniques such as NMF promise new avenues for analyzing *in situ* data. The numerous existing and emerging approaches to analyzing *in situ* data warrant comparison to facilitate the development of accessible and standardized approaches. While considerable progress towards a validated and user friendly software capable of analyzing real-time data has been made over the course of this Thesis, considerable research and implementation work remains.

A broad range of experimental systems, from co-crystals to metal organic frameworks, were explored in this Thesis to demonstrate the utility of the developed techniques for the increasingly diverse applications of milling in the context of synthetic chemistry. This generated numerous scientific contributions, including variable reaction kinetics in the reaction between benzil and *ortho*-phenylenediamine exhibiting linear and sigmoidal reaction profiles as a function of milling frequency (Chapter 4) which was later demonstrated to be largely due to thermal effects (Chapter 5). This work suggests that mechanochemical reaction profiles can be highly sensitive to relatively minor differences in temperature, and that higher mobility in the solid state can be achieved without large-scale melting. Novel mechanochemical syntheses of both Zn-MOF-74 (Chapter 6) and lanthanide organic frameworks (Chapter 7) based on terephthalic and trimesic acids were discovered from insoluble oxide and carbonate precursors, respectively. Monitoring these transformations revealed step-wise reaction profiles which provide insights into both the mechanism of formation and relative stability of various phases. These projects also guided the ongoing effort to explore BINOL based ligands as optically active and potentially chiral ligands for MOFs (Appendix 3), which have led to some promising porous frameworks outside of this Thesis. Monitoring the milling synthesis of the co-crystal of calcium-urea-phosphate (Chapter 8) provided the first direct evidence of water-mediated chemical autocatalysis in a mechanochemical reaction. Similarly, monitoring the co-crystallization, amorphization, and polymorphic transition of indometacin under milling conditions by Raman and fluorescence emission spectroscopies (Chapter 9) demonstrated the ability to identify intermediates, amorphous phases, and provides a

potential foundation for future kinetic studies of highly dynamic and unstable mixtures during mechanical processing.

Overall, the means for monitoring mechanochemical reactions remain limited in contrast to solution methods. However, given the infancy of the field of monitoring milling reactions, I believe this Thesis has expanded the scope and applicability of these techniques, although a pressing need for more techniques remains. Expanding the number and utility of real time monitoring of milling reactions provides a means of understanding what drives mechanochemical reactions. Moving beyond a “black box” approach to mechanochemistry where what happens inside of the milling vessel remains unknown, unlocks the ability to discover the driving forces behind milling reactions. This understanding will be critical for both developing highly efficient, cost-effective, and more environmentally friendly syntheses based on milling. Despite having only recently garnering significant attention by the research community, mechanochemical approaches have already revealed synthetic pathways and materials inaccessible by traditional solution methodologies often using real-time approaches, suggesting that improved monitoring of milling reactions may result in the discovery of novel chemistry. The work in this Thesis supports a currently emerging realization that fundamental behaviors observed in mechanochemical reactions are extremely diverse and perhaps unsurprisingly dependent on the reaction being studied. Real time approaches allow for the rapid determination of driving forces in a reaction, which is critical both in reaction optimization and scale up. Shining light on milling reactions is likely to improve our understanding of mechanochemistry and enable greener and more efficient chemistry. I believe the future of mechanochemistry is bright and I look forward to many more years monitoring its future.

11. Appendix 1: Supplementary Information for: The Effect of Milling Frequency on a Mechanochemical Organic Reaction Monitored by *In Situ* Raman Spectroscopy

Patrick A. Julien,[1] Ivani Malvestiti,[1,2] Tomislav Friščić[1,*]

Address: [1] Department of Chemistry, McGill University, Montreal, QC, Canada
[2]Departamento de Química, Universidade Federal de Pernambuco, PE, Brazil.

1. Selected Raman Spectra of Pure Components

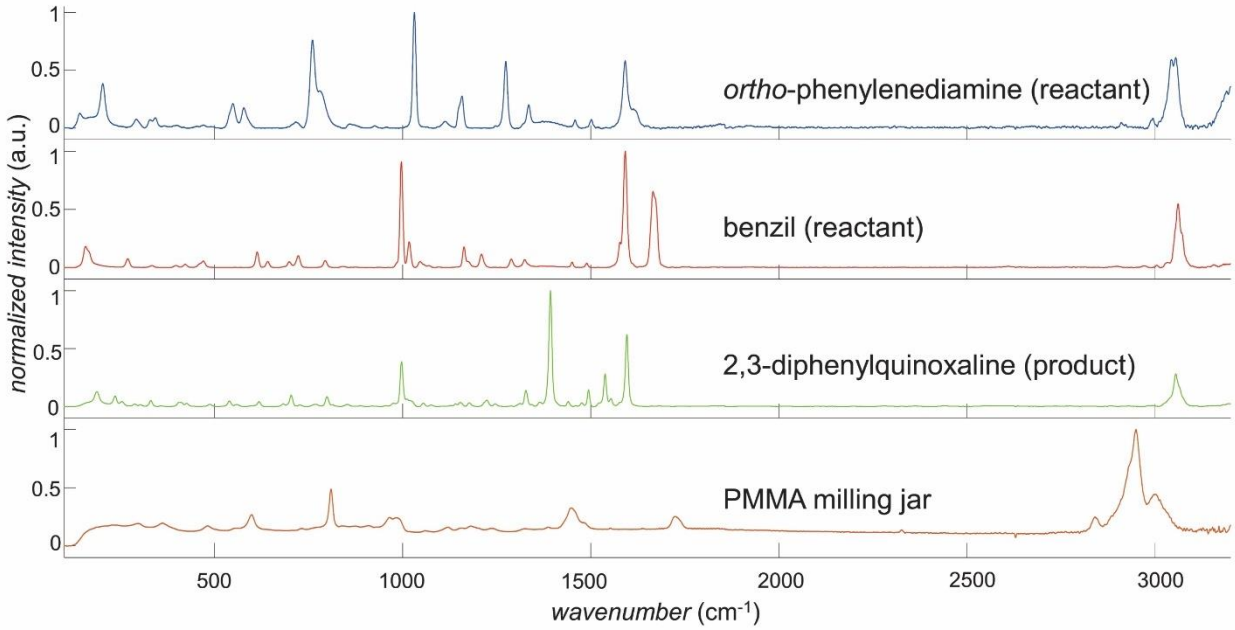

Figure S1. Relevant Raman Spectra (top to bottom): reactant *ortho*-phenylenediamine; reactant benzil; product 2,3-diphenylquinoxaline and an empty PMMA milling jar.

2. Experimental Setup

Figure S2. Picture of the experimental setup, showing a 15 mL volume PMMA jar mounted on a milling station of the Retsch MM400 mixer mill and the tip of the Raman spectroscopy probe.

3. Product Characterization

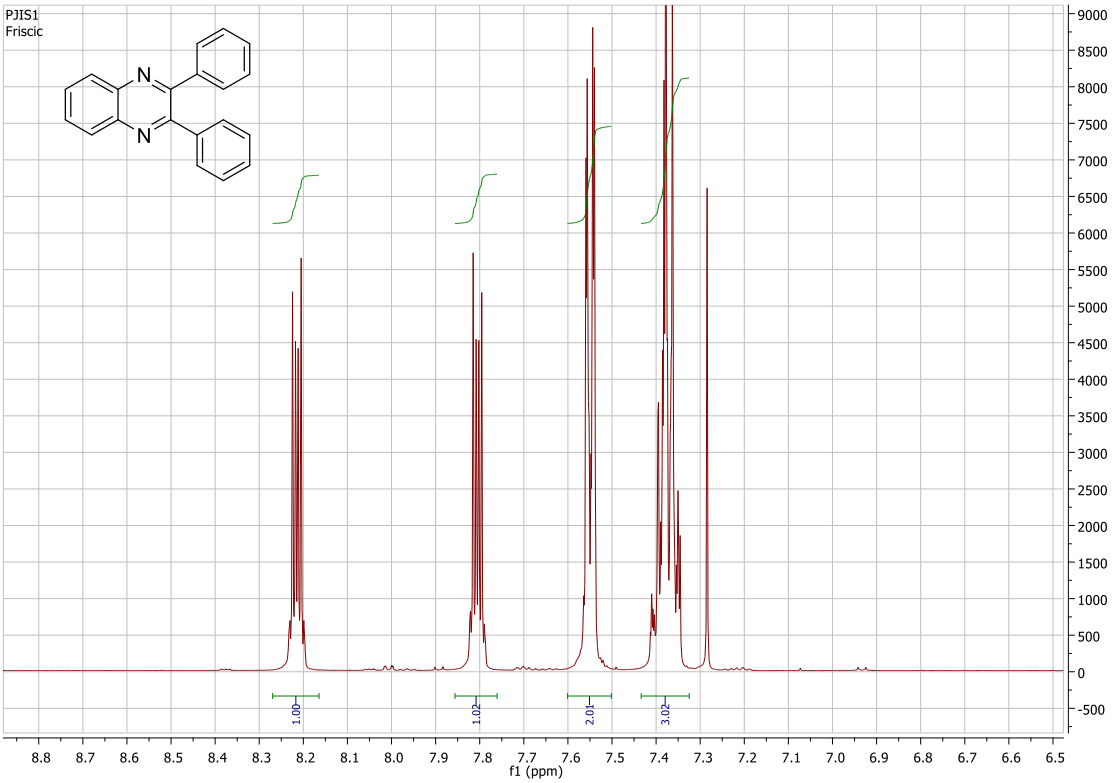

Figure S3. The ^{1}H NMR spectrum of the crude 2,3-diphenylquinoxaline product obtained by mechanochemical reaction conducted at 30 Hz (30 Hz, Exp. 1), recorded in $CDCl_3$. The spectrum reveals only trace impurities and matches the spectrum previously reported in the *Spectral Database for Organic Compounds (SDBS)*, SDBS No. 32951HSP-48-683.

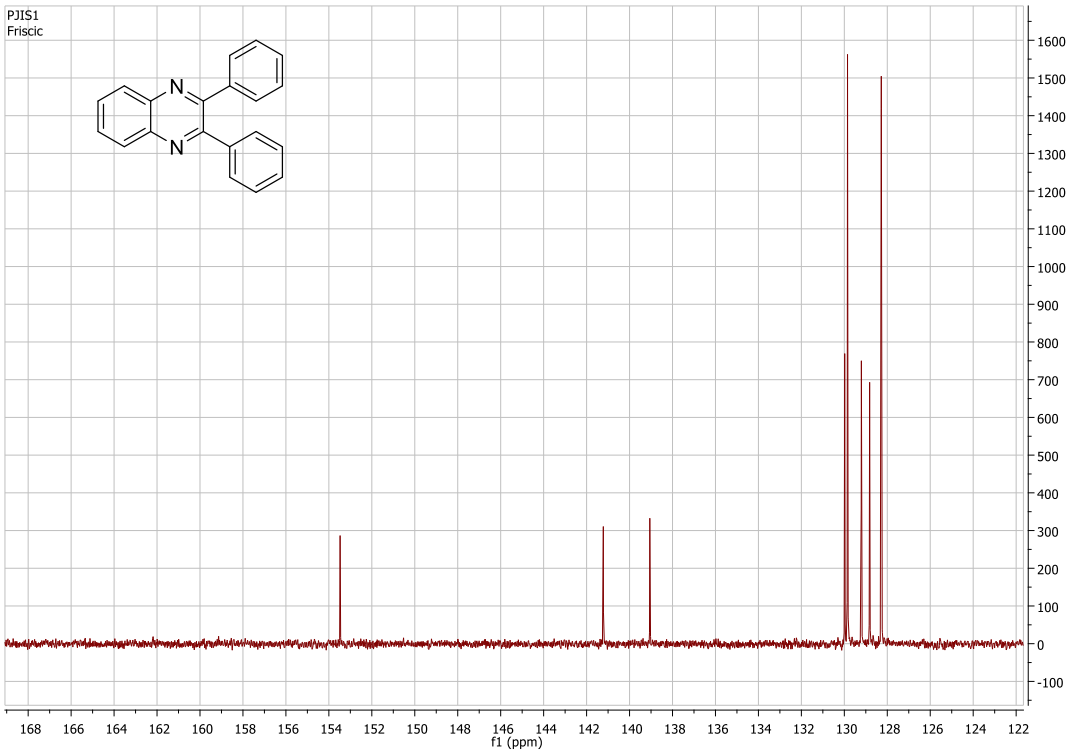

Figure S4. The ^{13}C NMR spectrum of the crude 2,3-diphenylquinoxaline product obtained by mechanochemical reaction conducted at 30 Hz (30 Hz, Exp. 1), recorded in $CDCl_3$. The spectrum reveals only trace impurities and matches the spectrum previously reported in the *Spectral Database for Organic Compounds (SDBS)*, SDBS No. 32951CDS-10-500.

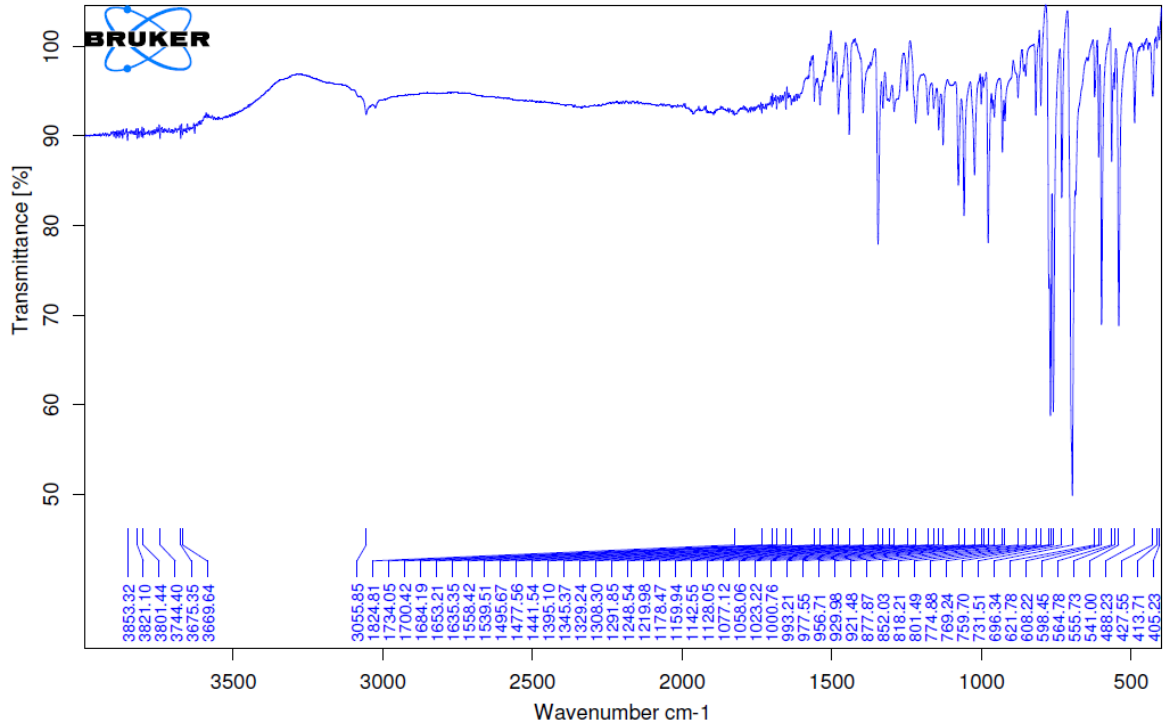

Figure S5. Fourier-transform infrared attenuated total reflectance (FTIR-ATR) spectrum of the crude 2,3-diphenylquinoxaline product obtained by mechanochemical reaction conducted at 30 Hz (30 Hz, Exp. 1). The spectrum matches the spectrum previously reported in the *Spectral Database for Organic Compounds (SDBS)*, SDBS No. 32951 IR-NIDA-74153.

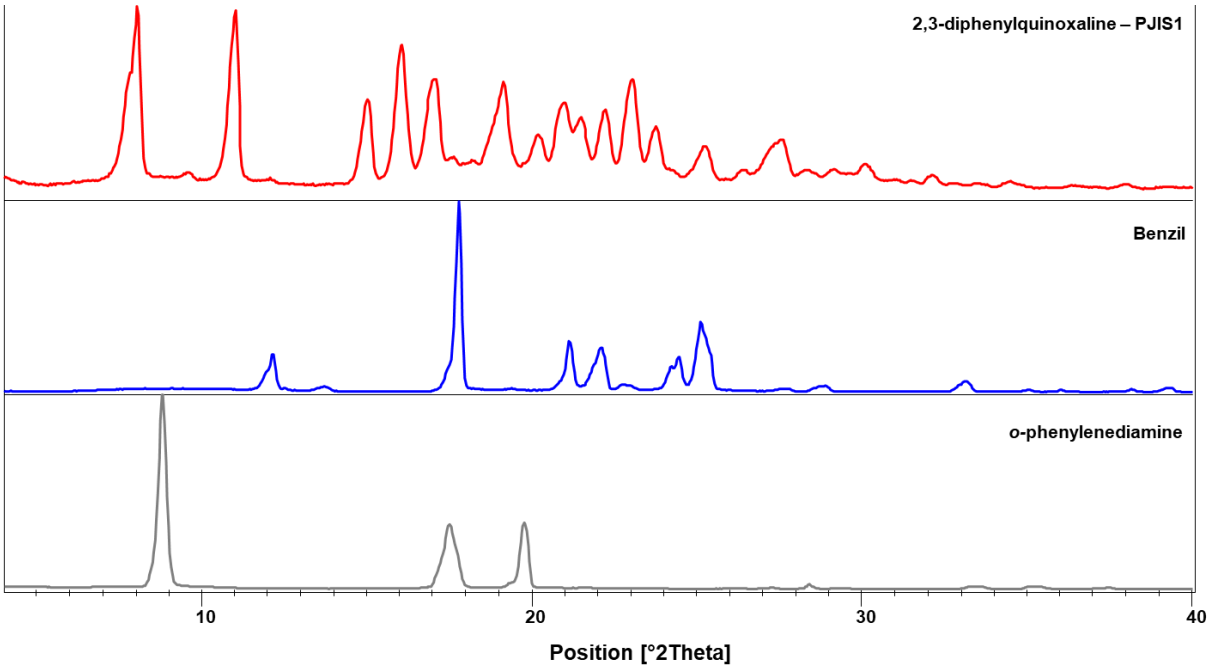

Figure S6. Example powder X-ray diffraction patterns for the mechanochemical synthesis of 2,3-diphenylquinoxaline (top to bottom): the crude product of the reaction conducted by ball milling at 30 Hz (30 Hz, Exp. 1); benzil reactant and reactant *ortho*-phenylenediamine.

Reaction Number	Frequency (Hz) and Experiment #	Conversion (%)
1	**30, Exp. 1**	**99+**
2	**30, Exp. 2**	**99+**
3	**30, Exp. 3**	**99+**
4	**27.5, Exp. 1**	**99+**
5	**27.5, Exp. 2**	**99+**
6	**27.5, Exp. 3**	**97.0**
7	**25, Exp. 1**	**99+**
8	**25, Exp. 2**	**98.0**
9	**25, Exp. 3**	**99+**
10	**22.5, Exp. 1**	**99+**
11	**22.5, Exp. 2**	**99+**
12	**22.5, Exp. 3**	**99+**
13	**20, Exp. 1**	**79.5**
14	**20, Exp. 2**	**74.5**
15	**20, Exp. 3**	**83.0**

Table S1. Reaction conversions, based on integration of 1H NMR spectra of crude milling products. If starting material could not be detected, conversion is listed as 99+%.

4) Spectroscopic Data and Fitting Plots for All Experiments

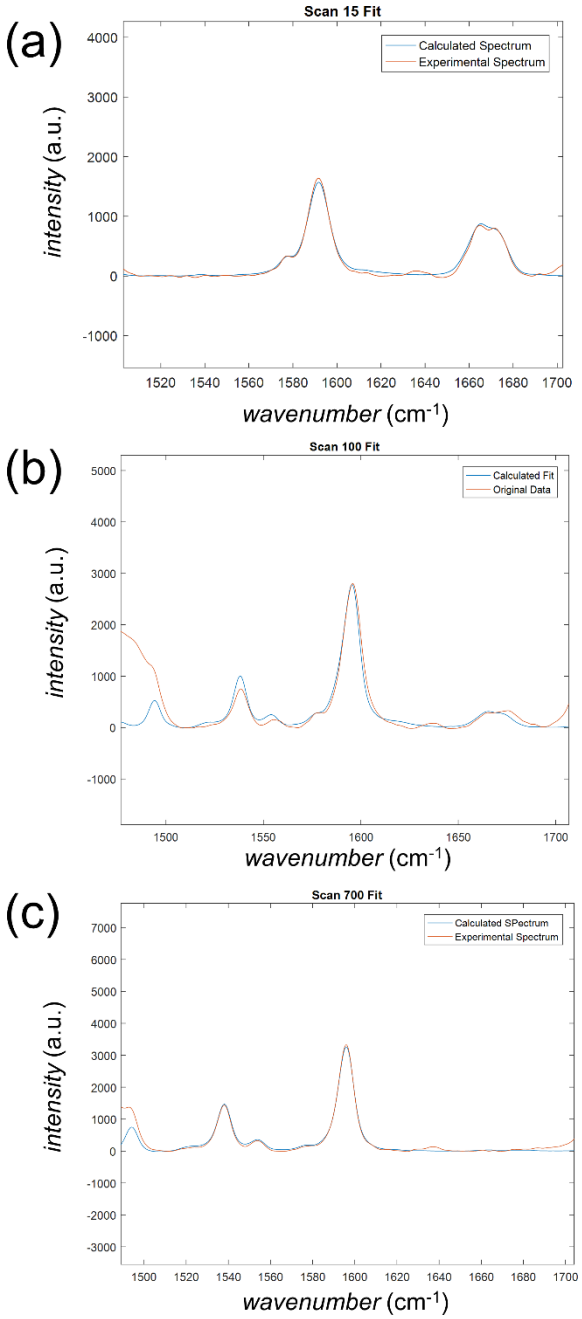

Figure S7. Comparison of experimental and calculated spectra for Experiment 1, 30 Hz (the complete dataset and residuals for this experiment are presented in the manuscript, main paper): (a) scan #15 (after 75 seconds milling); (b) scan #100 (after 500 seconds milling) and (c) scan #700 (after 3500 seconds milling).

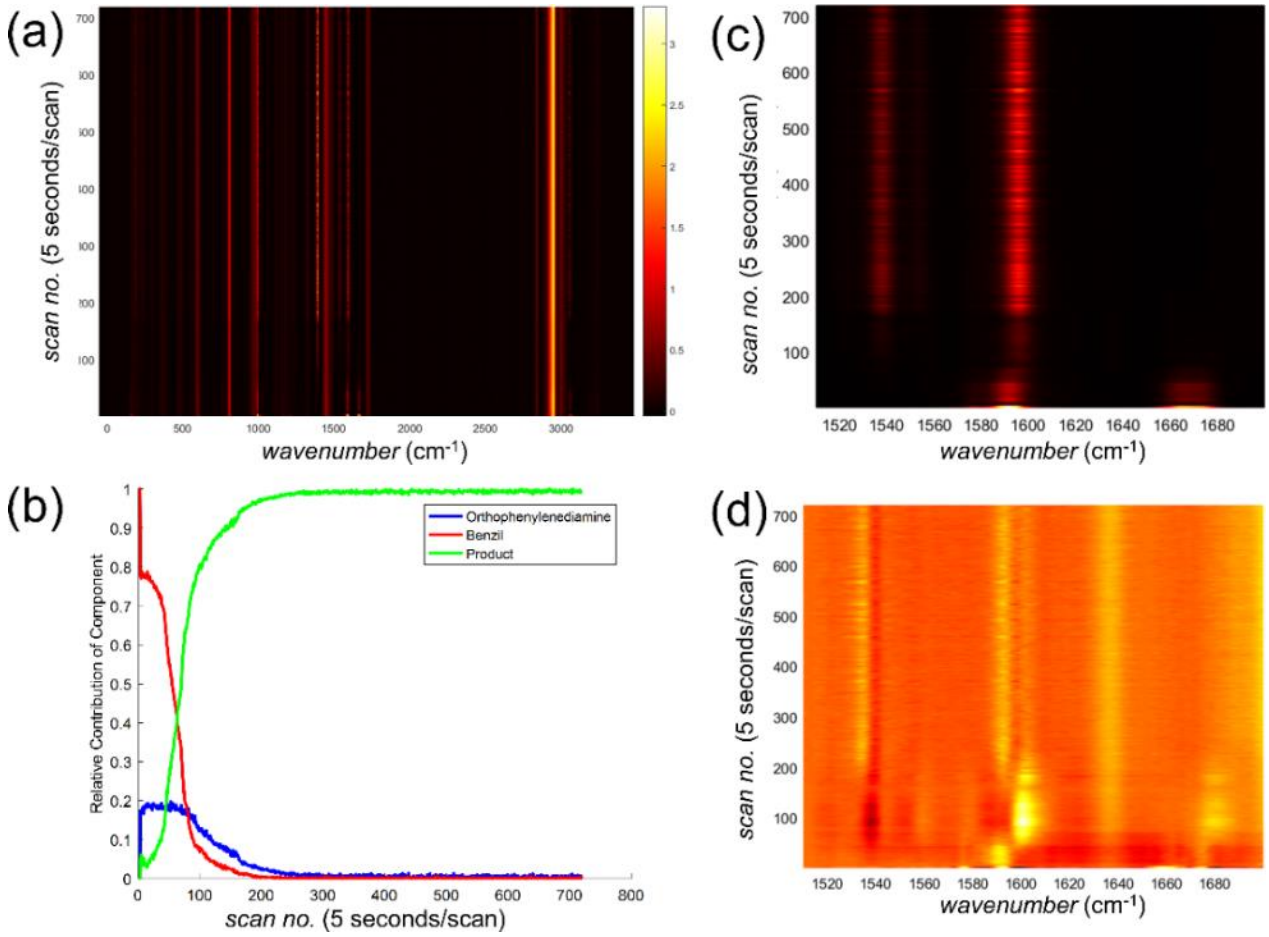

Figure S8. Data for Experiment 2, 30 Hz: (a) the entire time-resolved Raman spectrum for the second experiments conducted by milling at 30 Hz; (b) the associated time-dependent change in spectral contributions of the product (green) and the two reactants (red and blue); (c) section of the spectrum selected for least-squares fitting and (d) the final residual spectrum.

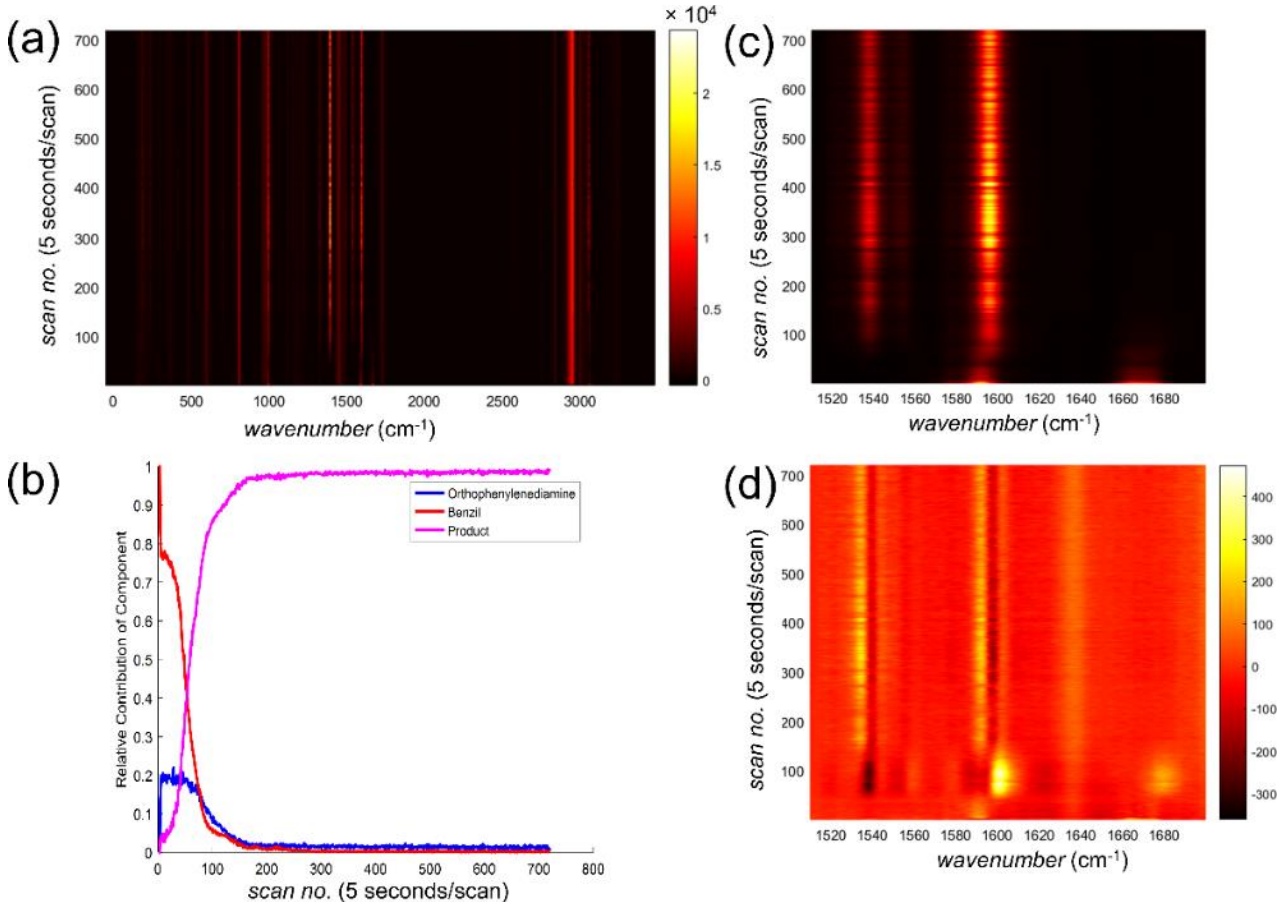

Figure S9. Data for Experiment 3, 30 Hz: (a) the entire time-resolved Raman spectrum for the third experiment conducted by milling at 30 Hz; (b) the associated time-dependent change in spectral contributions of the product (green) and the two reactants (red and blue); (c) section of the spectrum selected for least-squares fitting and (d) the final residual spectrum.

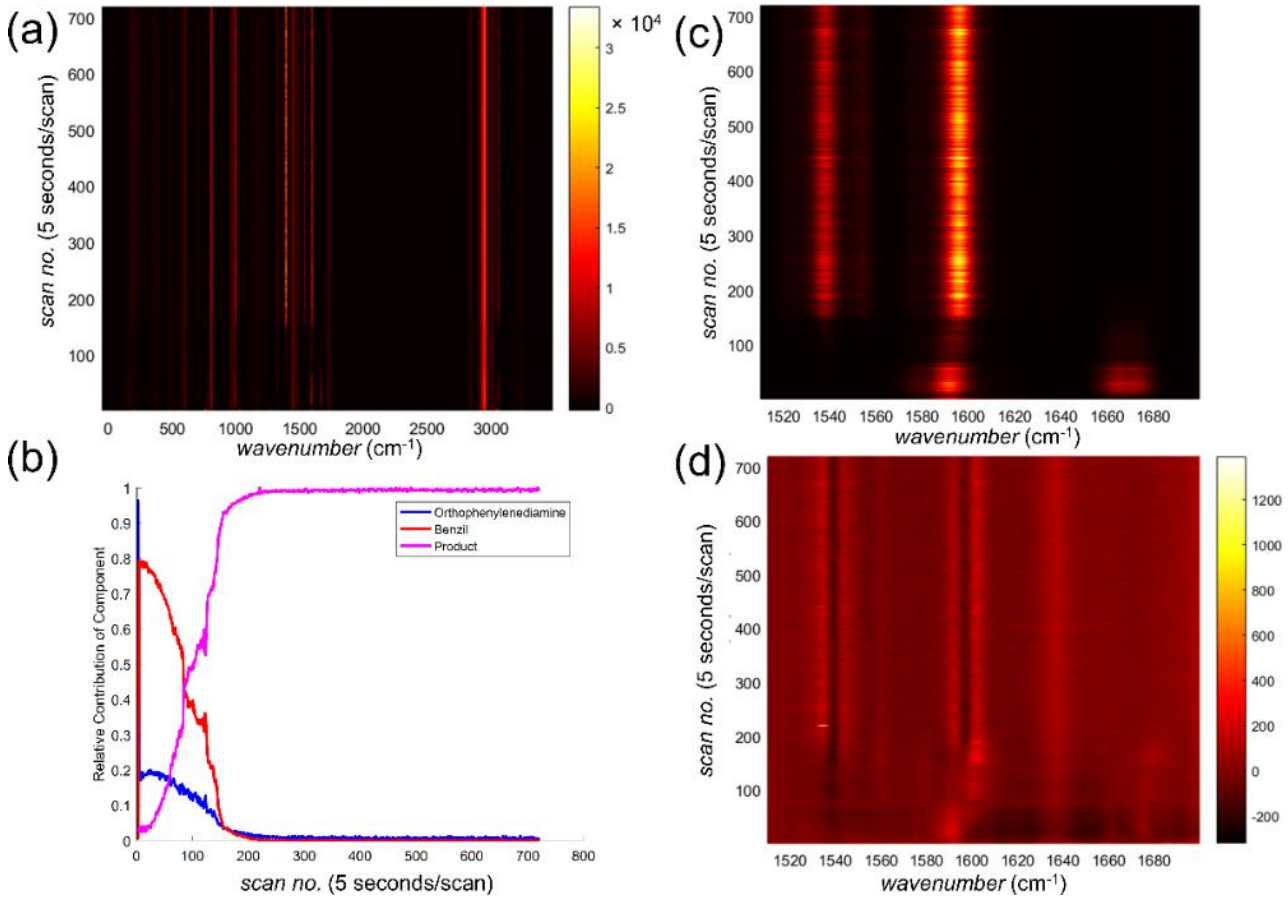

Figure S10. Data for Experiment 1, 27.5 Hz: (a) the entire time-resolved Raman spectrum for the first experiment conducted by milling at 27.5 Hz; (b) the associated time-dependent change in spectral contributions of the product (green) and the two reactants (red and blue); (c) section of the spectrum selected for least-squares fitting and (d) the final residual spectrum.

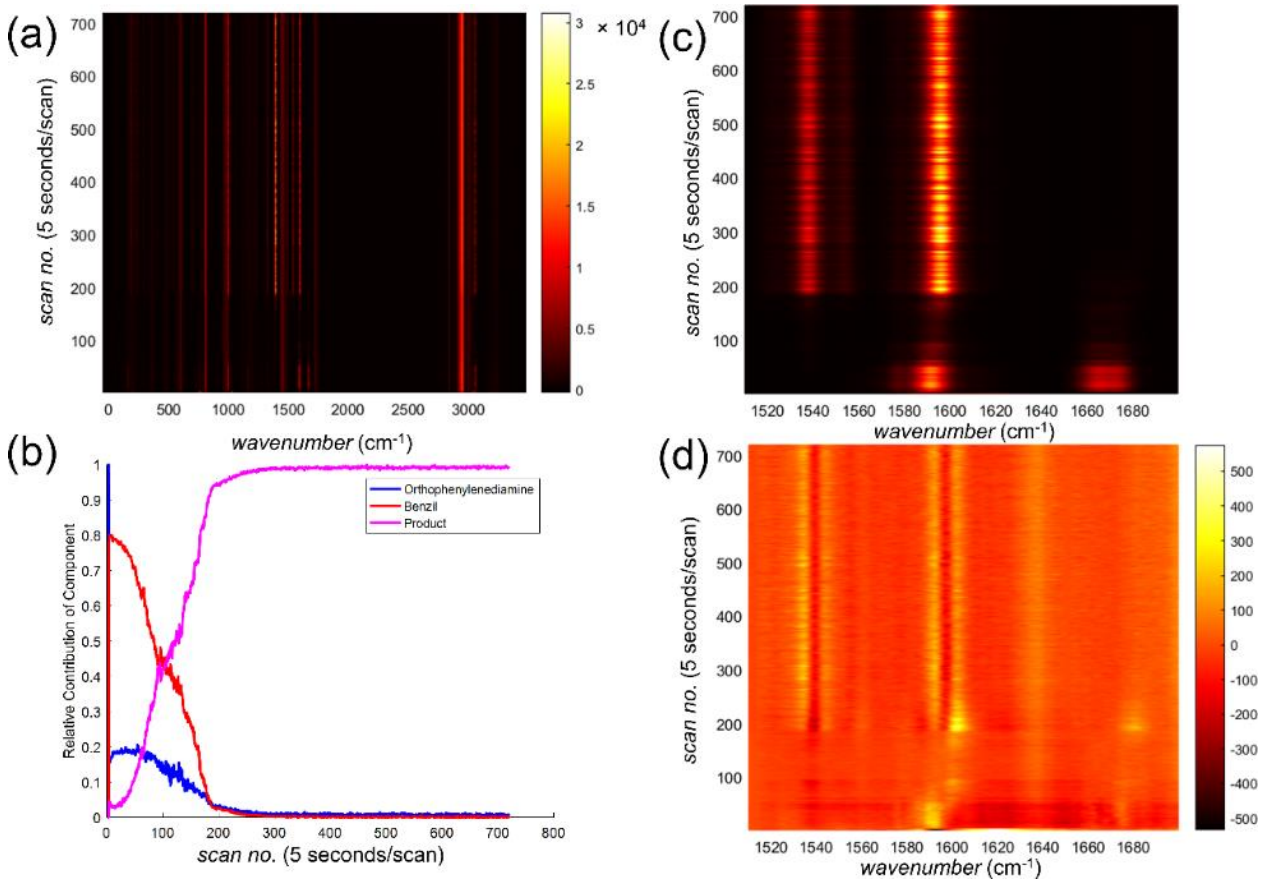

Figure S11. Data for Experiment 2, 27.5 Hz: (a) the entire time-resolved Raman spectrum for the second experiment conducted by milling at 27.5 Hz; (b) the associated time-dependent change in spectral contributions of the product (green) and the two reactants (red and blue); (c) section of the spectrum selected for least-squares fitting and (d) the final residual spectrum.

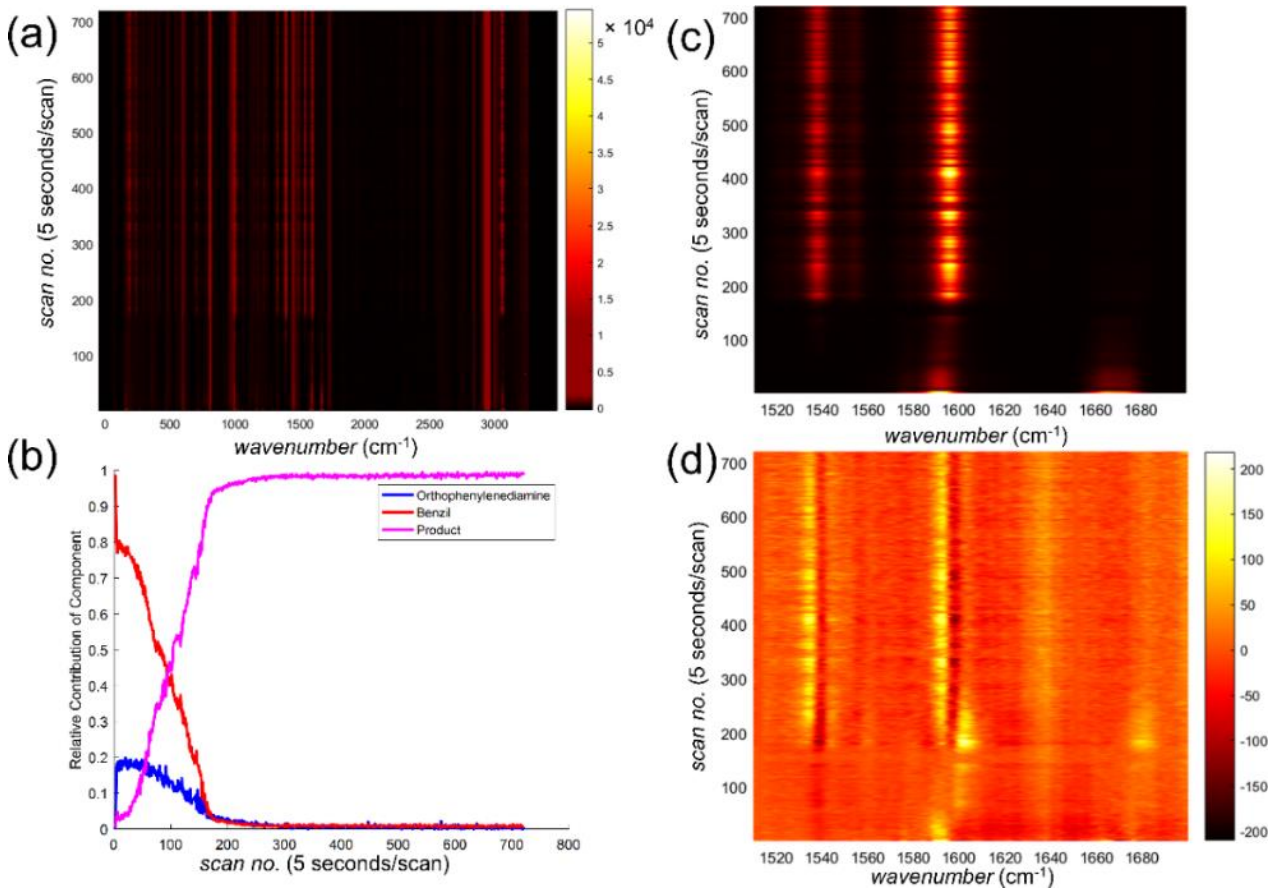

Figure S12. Data for Experiment 3, 27.5 Hz: (a) the entire time-resolved Raman spectrum for the third experiment conducted by milling at 27.5 Hz; (b) the associated time-dependent change in spectral contributions of the product (green) and the two reactants (red and blue); (c) section of the spectrum selected for least-squares fitting and (d) the final residual spectrum.

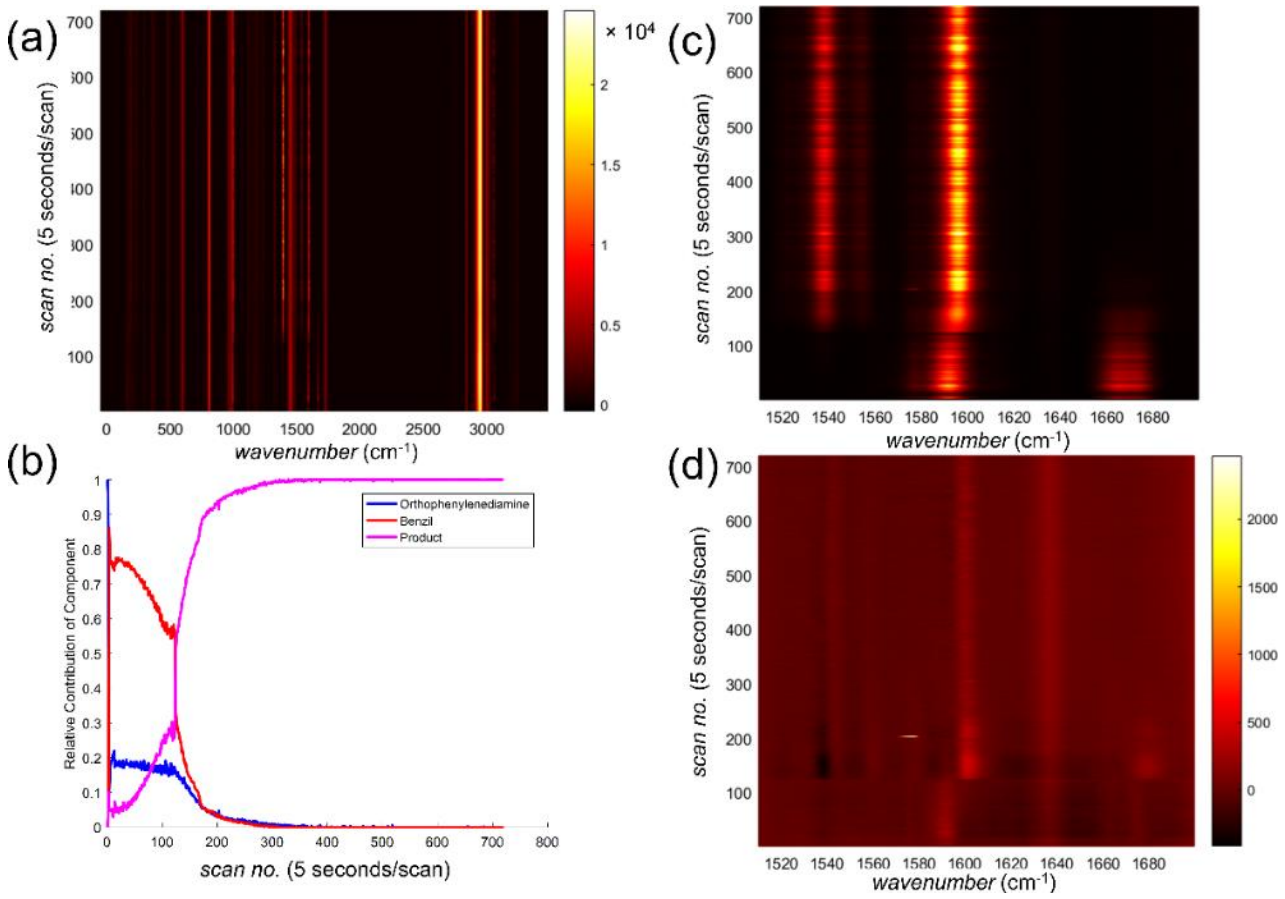

Figure S13. Data for Experiment 1, 25 Hz: (a) the entire time-resolved Raman spectrum for the first experiment conducted by milling at 25 Hz; (b) the associated time-dependent change in spectral contributions of the product (green) and the two reactants (red and blue); (c) section of the spectrum selected for least-squares fitting and (d) the final residual spectrum.

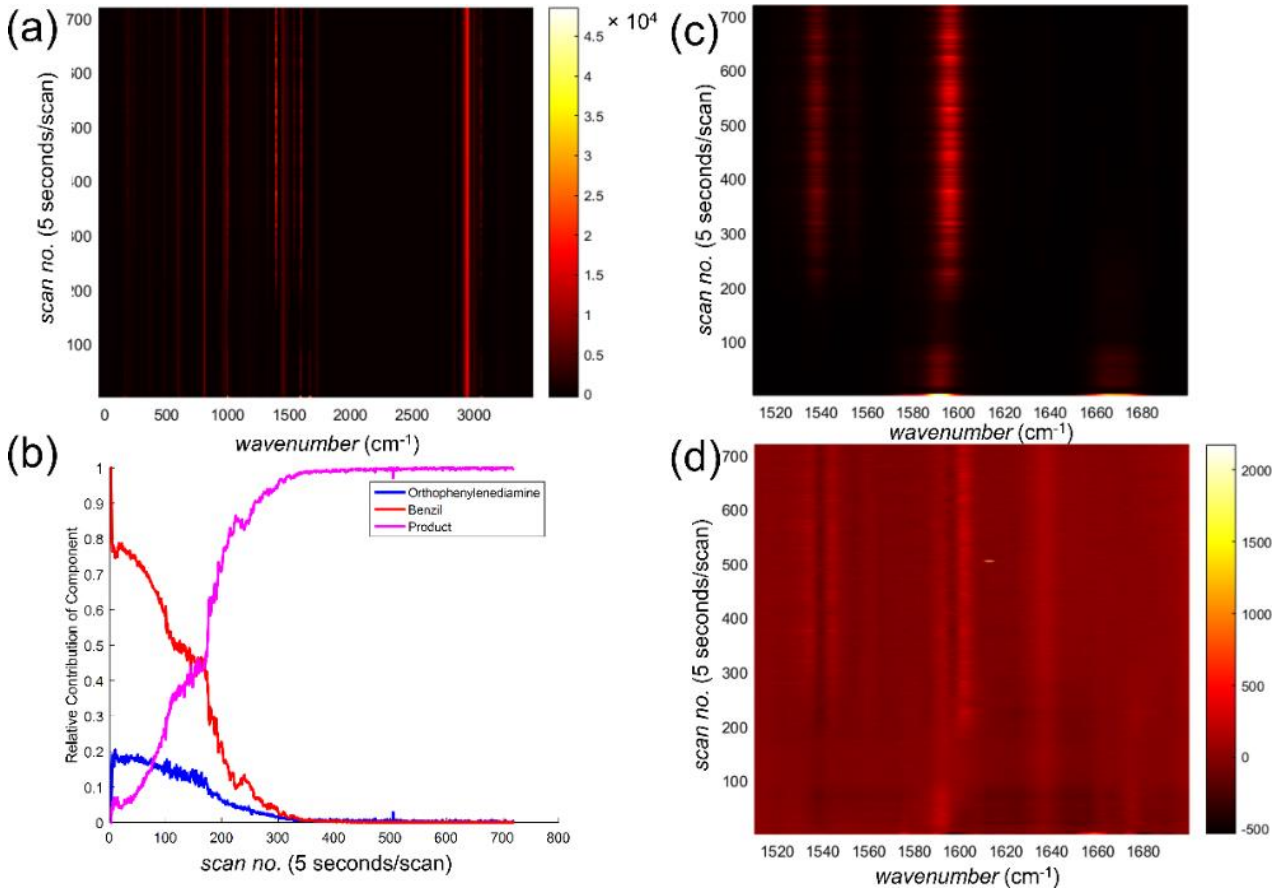

Figure S14. Data for Experiment 2, 25 Hz: (a) the entire time-resolved Raman spectrum for the second experiment conducted by milling at 25 Hz; (b) the associated time-dependent change in spectral contributions of the product (green) and the two reactants (red and blue); (c) section of the spectrum selected for least-squares fitting and (d) the final residual spectrum.

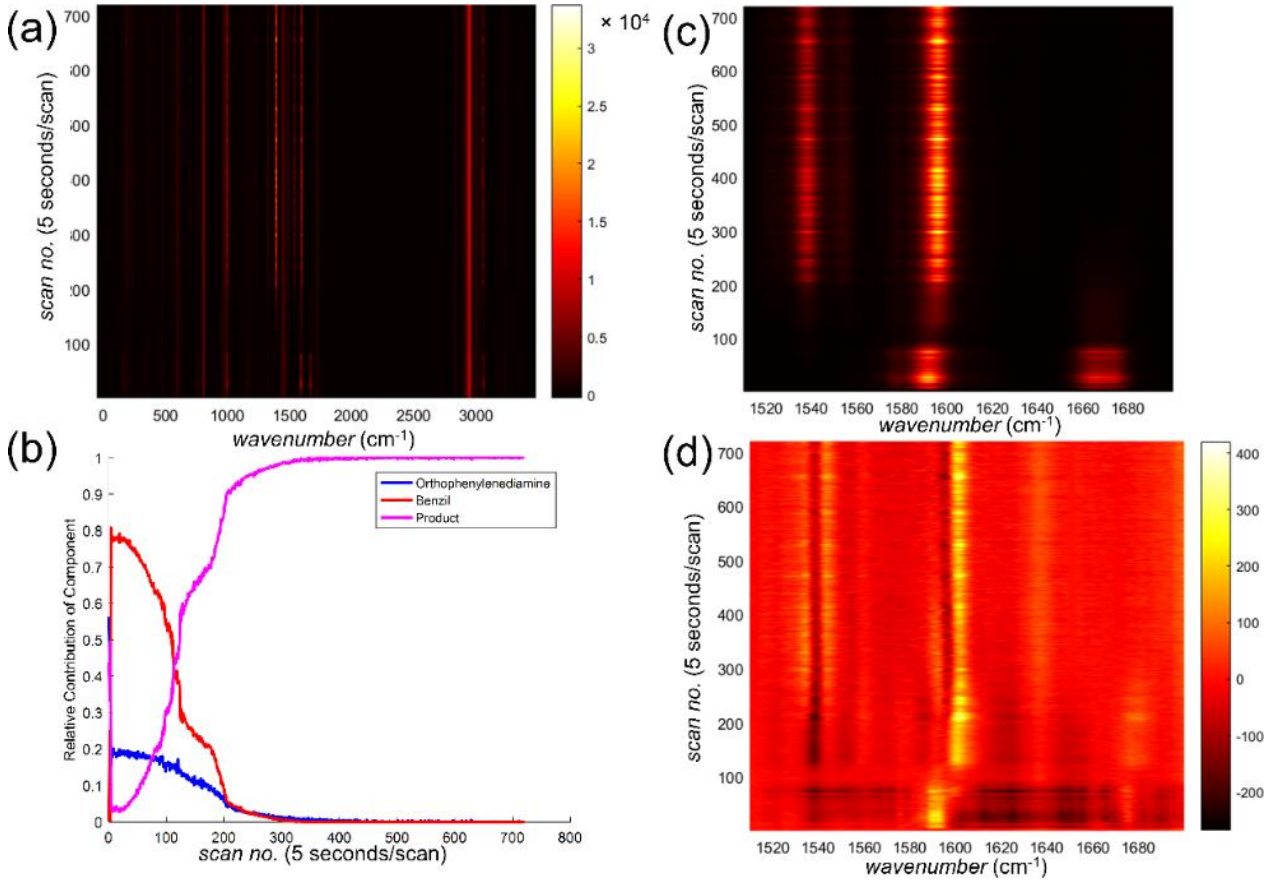

Figure S15. Data for Experiment 3, 25 Hz: (a) the entire time-resolved Raman spectrum for the third experiment conducted by milling at 25 Hz; (b) the associated time-dependent change in spectral contributions of the product (green) and the two reactants (red and blue); (c) section of the spectrum selected for least-squares fitting and (d) the final residual spectrum.

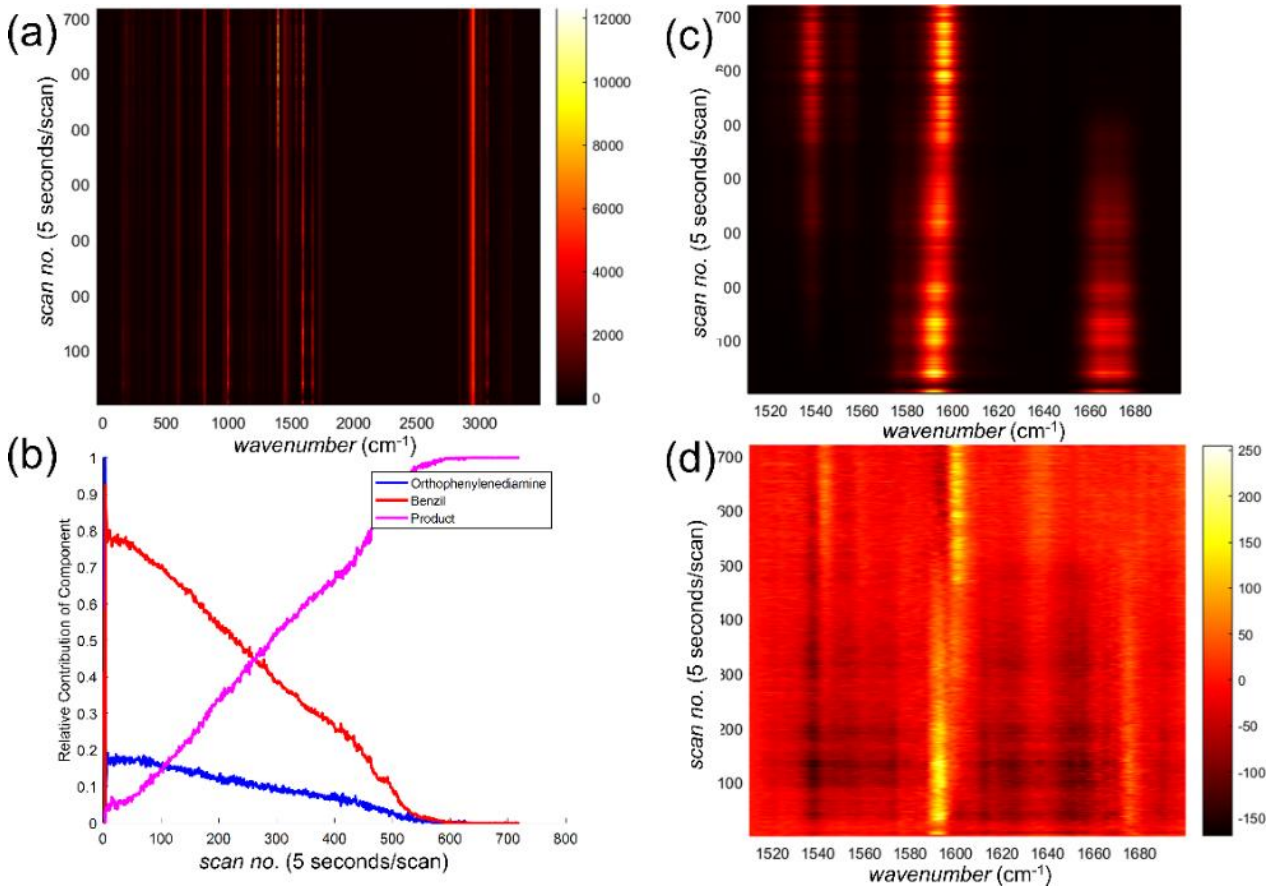

Figure S16. Data for Experiment 1, 22.5 Hz: (a) the entire time-resolved Raman spectrum for the first experiment conducted by milling at 22.5 Hz; (b) the associated time-dependent change in spectral contributions of the product (green) and the two reactants (red and blue); (c) section of the spectrum selected for least-squares fitting and (d) the final residual spectrum.

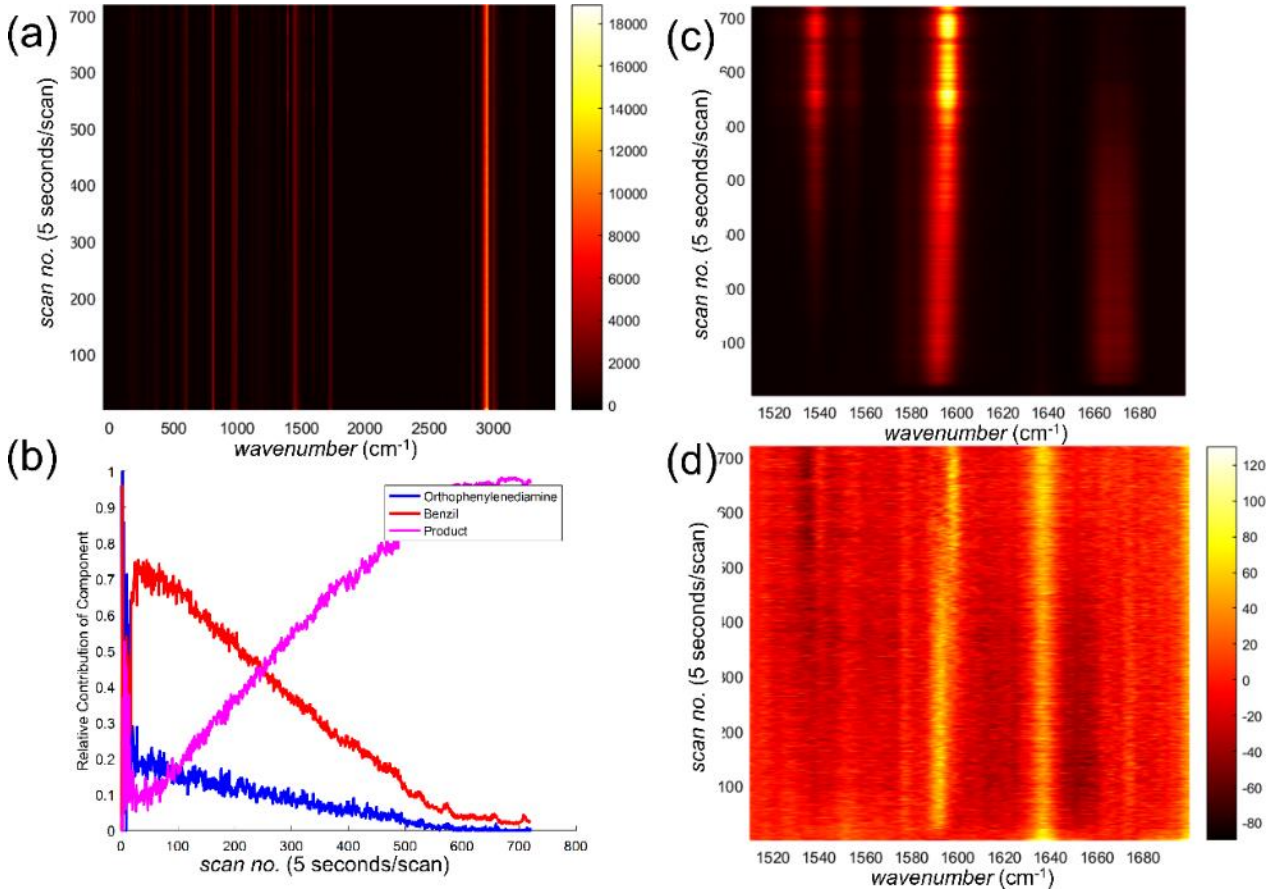

Figure S17. Data for Experiment 2, 22.5 Hz: (a) the entire time-resolved Raman spectrum for the second experiment conducted by milling at 22.5 Hz; (b) the associated time-dependent change in spectral contributions of the product (green) and the two reactants (red and blue); (c) section of the spectrum selected for least-squares fitting and (d) the final residual spectrum.

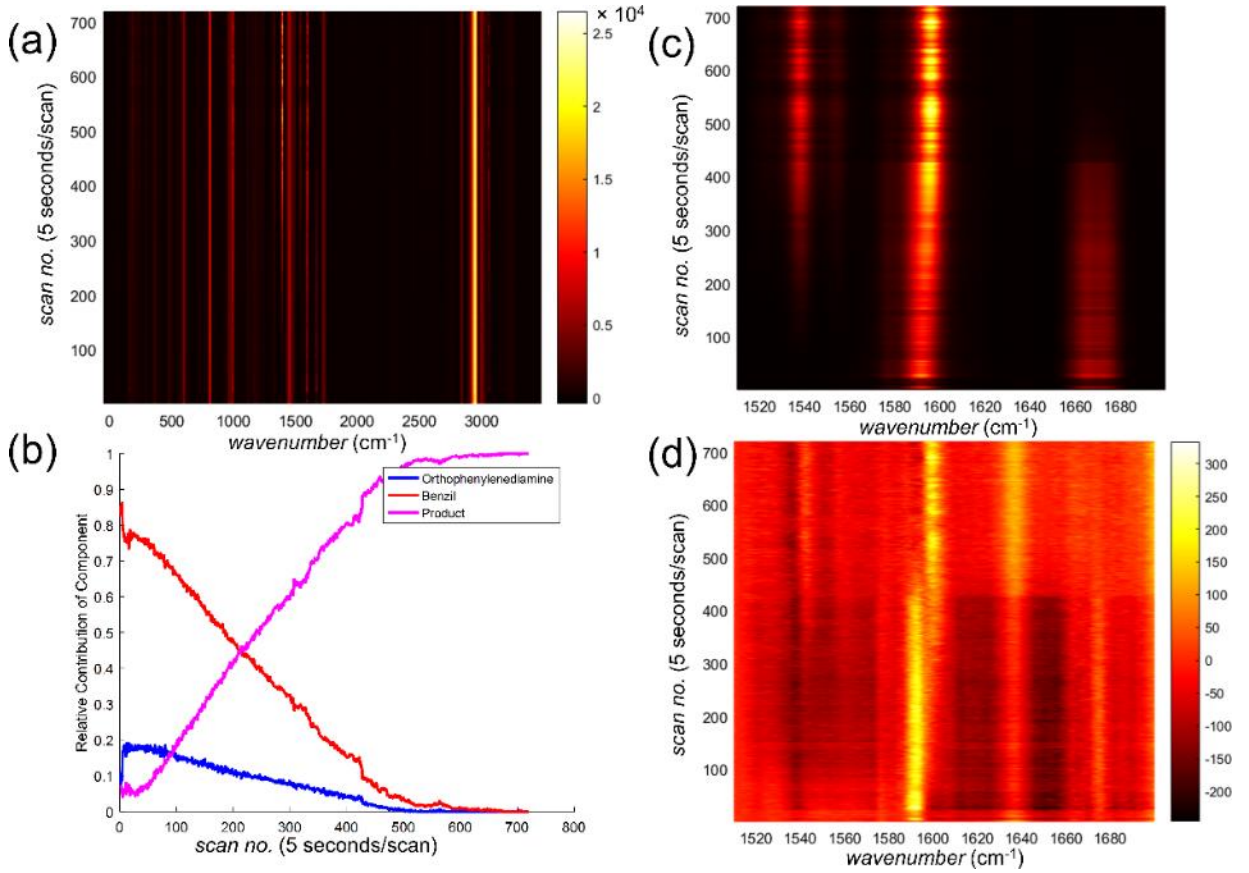

Figure S18. Data for Experiment 3, 22.5 Hz: (a) the entire time-resolved Raman spectrum for the third experiment conducted by milling at 22.5 Hz; (b) the associated time-dependent change in spectral contributions of the product (green) and the two reactants (red and blue); (c) section of the spectrum selected for least-squares fitting and (d) the final residual spectrum.

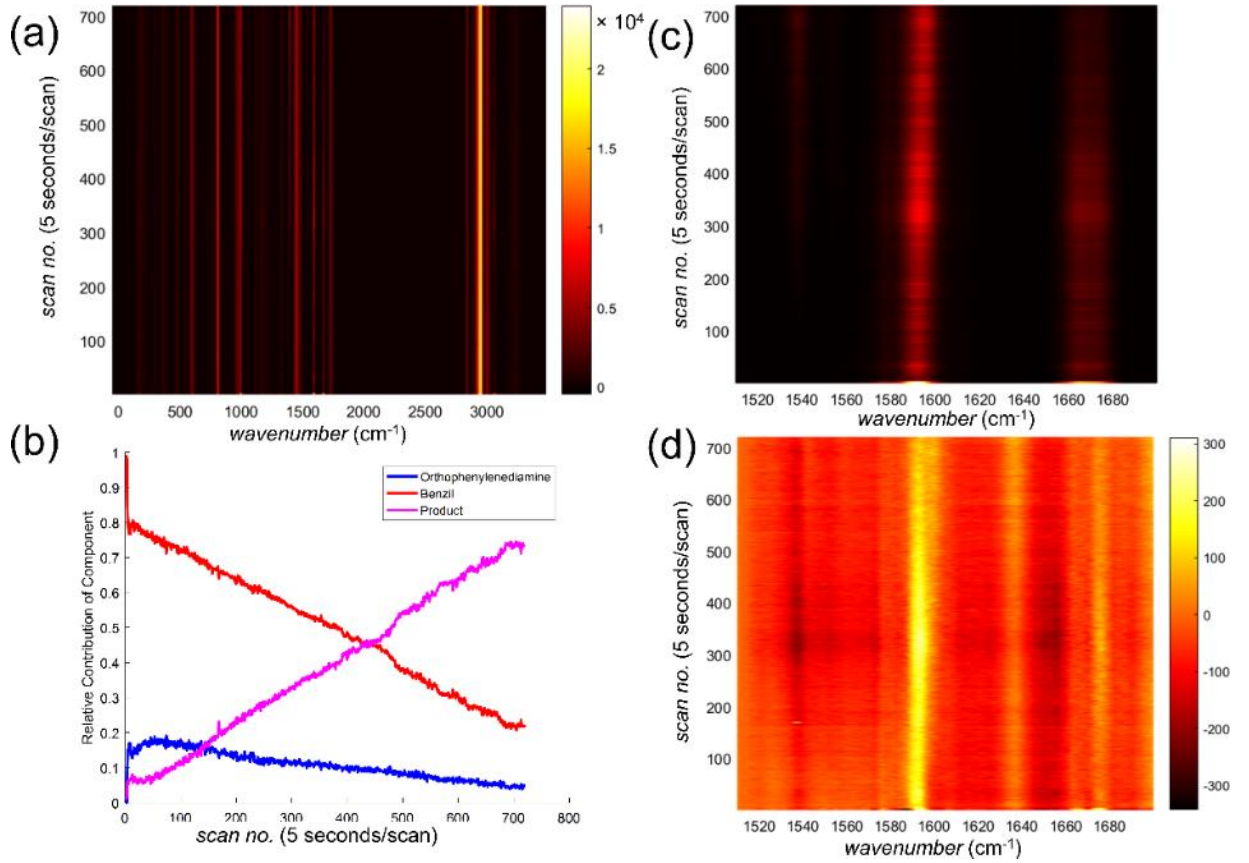

Figure S19. Data for Experiment 1, 20 Hz: (a) the entire time-resolved Raman spectrum for the first experiment conducted by milling at 20 Hz; (b) the associated time-dependent change in spectral contributions of the product (green) and the two reactants (red and blue); (c) section of the spectrum selected for least-squares fitting and (d) the final residual spectrum.

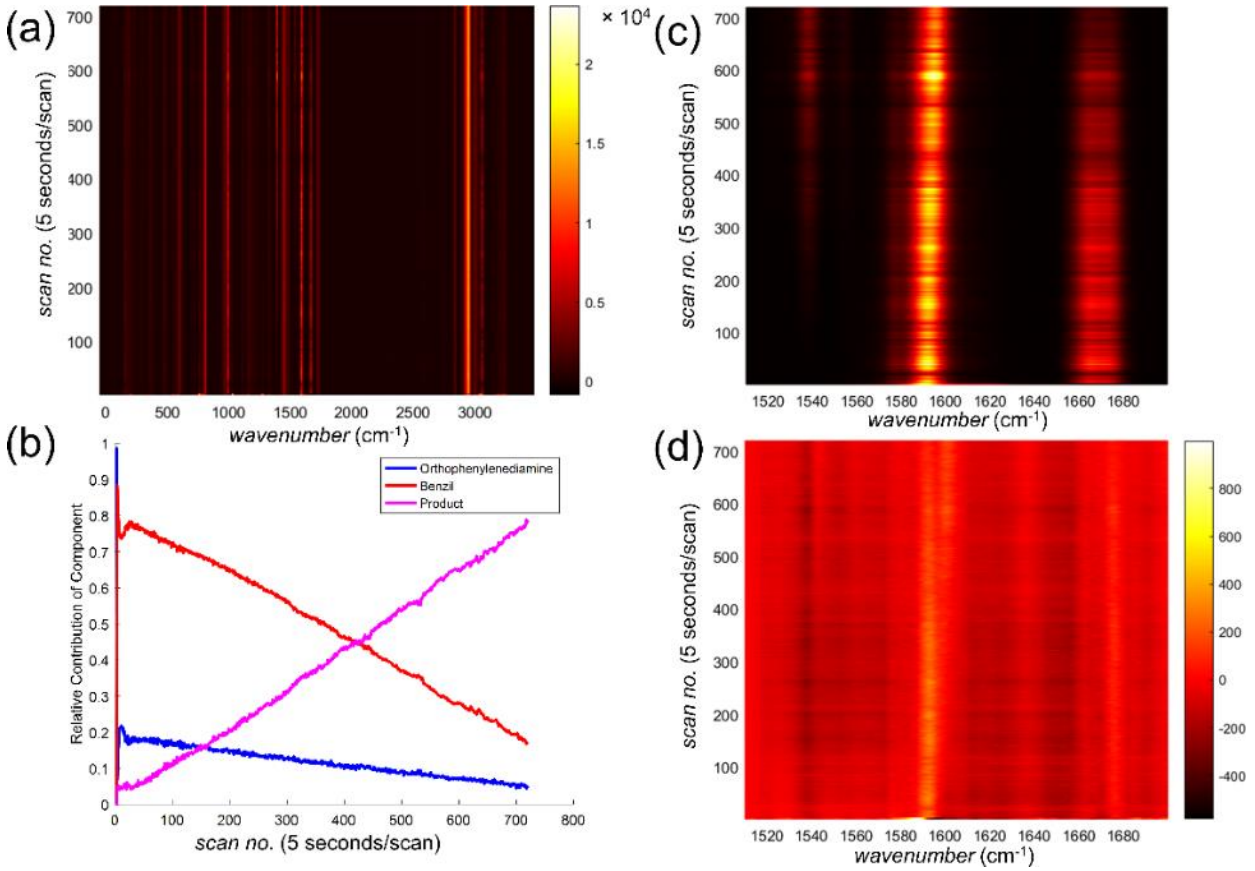

Figure S20. Data for Experiment 2, 20 Hz: (a) the entire time-resolved Raman spectrum for the second experiment conducted by milling at 20 Hz; (b) the associated time-dependent change in spectral contributions of the product (green) and the two reactants (red and blue); (c) section of the spectrum selected for least-squares fitting and (d) the final residual spectrum.

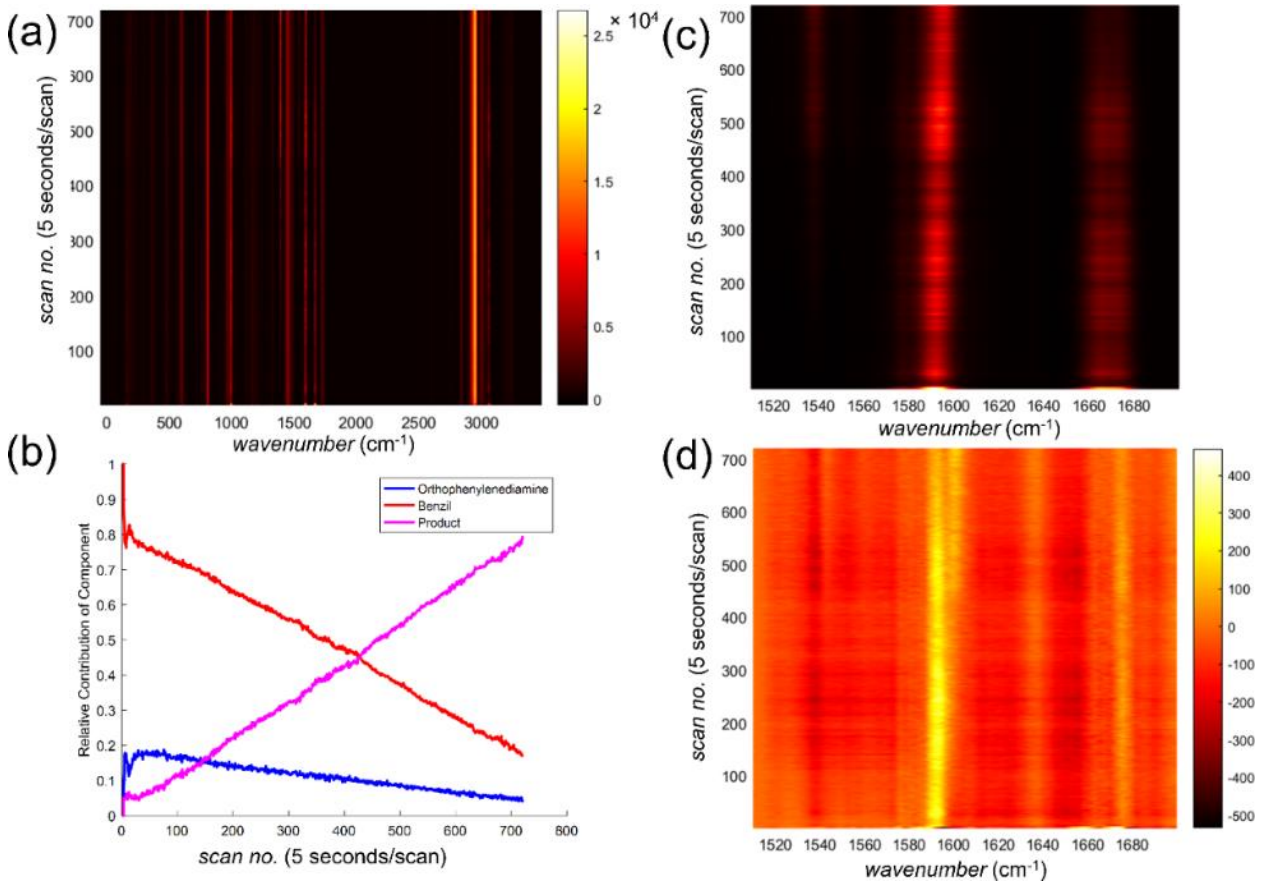

Figure S21. Data for Experiment 3, 20 Hz: (a) the entire time-resolved Raman spectrum for the third experiment conducted by milling at 20 Hz; (b) the associated time-dependent change in spectral contributions of the product (green) and the two reactants (red and blue); (c) section of the spectrum selected for least-squares fitting and (d) the final residual spectrum.

12. Appendix 2: Supplementary Information for: *In situ* monitoring and mechanism of the mechanochemical formation of a microporous MOF-74 framework

Patrick A. Julien, Krunoslav Užarević, Athanassios D. Katsenis, Simon A. J. Kimber, Timothy Wang, Omar K. Farha, Yuancheng Zhang, José Casaban, Luzia S. Germann, Martin Etter, Robert E. Dinnebier, Stuart L. James*, Ivan Halasz*, Tomislav Friščić*

12.01 Materials and methods

2,5-dihydroxyterephthalic acid (H_4**dhta**) was purchased from TCI America, ZnO was purchased from Sigma Aldrich, and dimethylformamide (DMF) was purchased from ACP Chemicals. All chemicals were used without further purification.

FTIR-ATR spectroscopy. Fourier-transform infrared attenuated total reflectance (FTIR-ATR) were recorded on Bruker Vertex 70 spectrometer with RockSolidT^M interferometer in the range of 4400-400 cm^{-1}, with 4 cm^{-1} step.

TGA and DSC experiments. Thermogravimetric analyses were performed on a Mettler-Toledo TGA DSC 1 Star^e system thermobalance using alumina crucibles under air stream with the heating rate of 10 °C min^{-1}. The results were processed with the Mettler STARe 9.01 software.

Powder X-ray diffraction (PXRD). Patterns used for *ex situ* qualitative analysis of the samples were collected on a Bruker D2 diffractometer, Cu*Kα* radiation, flat plate sample on a zero background in BraggBrentano geometry, tension 30kV, and current 10 mA. The patterns were collected in the angle region between 4° and 40° (2*θ*) with a step size of 0.05° and 0.65 s counting per step. Powder X-ray diffraction (PXRD) patterns for activated samples were recorded on a Rigaku ATXG diffractometer equipped with an 18 kW Cu rotating anode, MLO monochromator, and a high-count-rate scintillation detector (measurements made over a range of 3°<2θ<50° with a 4 °/min scanning speed).

Solid-state nuclear magnetic resonance (SSNMR). Spectra were acquired on a Varian VNMRS spectrometer operating at 100.53 MHz for ^{13}C and 399.76 MHz for ^{1}H using a 7.5 mm T3 CPMAS probe, or on a Bruker Avance III HD operating at 150.86 MHz for ^{13}C and 599.90 MHz for ^{1}H using a 4 mm double resonance MAS probe. The spectra were

calibrated with respect to glycine signal at 176.5 ppm. Assignment of Zn-MOF-74 solid-state NMR spectra was guided by recently published work on solid-state NMR spectroscopy of a MOF-74 material: Xu, J.; Terskikh, V. V.; Huang, Y. *J. Phys. Chem. Lett.* **2013**, *4*, 7.

For spectra acquired on a Varian VNMRS spectrometer, samples were spun at 5 kHz and cross-polarization at an rf field of about 50 kHz was performed for 1.5 ms. The SPINAL 64 decoupling rf field was about 50 kHz. The recycle delay was 2 s and between 100 and 900 scans were acquired of each sample, depending on its sensitivity. TOSS was used in CP sequences using 45 kHz ^{13}C pulses. In interrupted decoupling sequences, 11 µs ^{13}C 180^{o} pulses were used and decoupling was stopped for 100 µs.

For spectra acquired on a Bruker Avance III HD spectrometer, samples were spun at 12.5 kHz and Broad banded cross-polarization was achieved by applying a 2 ms long spin lock at an rf field of 75 kHz on ^{13}C while the ^{1}H spin lock was ramped between 61 and 82 kHz. Selective cross-polarization was achieved by applying the same rf fields with no ramp for 250 µs. The SPINAL 64 decoupling rf field was about 85 kHz. The recycle delay was 5 s and between 256 and 512 scans were acquired of each sample, depending on its sensitivity. In interrupted decoupling sequences, 6.6 µs ^{13}C 180° pulses were used and decoupling was stopped for 1.2 ms.

Ex situ monitoring by PXRD was performed on Bruker D2 diffractometer and by FTIR-ATR on a Bruker Vertex 70 spectrometer. For *ex situ* analyses, milling was stopped at designated time in order to take the samples for analyses. The analyses were performed immediately upon the sampling, during the following period of milling.

Activation of MOF-74 samples were performed on a Micromeritics SmartVacPrep (Micromeritics, Norcross, GA, USA) and N_2 isotherms were measured on a Micromeritics Tristar II (Micromeritics, Norcross, GA, USA). The powder samples of MOF-74 (≈100 mg) were extracted with methanol using a Soxhlet extractor for 36 h. The extracted samples were transferred into sorption tubes and outgassed on a SmartVacPrep under dynamic vacuum at 150°C for 12 h. Measurements were performed at 77 K, with the temperature held constant using liquid N_2 bath.

Scanning electron microscopy (SEM) images and energy- dispersive X-ray spectroscopy (EDS) mapping were recorded on a Hitachi SU8030 SEM.

12.02 Synthetic procedures

(a) Mechanosynthesis of Zn-MOF-74 using H_2O as the grinding liquid

220 mg (1.1 mmol) of H_4**dhta** and 180.7 mg of ZnO (2.2 mmol) were placed in separate halves of PMMA milling vessel. 250 μL of water was added on ZnO and the reaction mixture was milled for 45 minutes before no traces of ZnO were visible in the PXRD. Collected pale-yellow microcrystalline product was further analyzed by FTIR-ATR, SS NMR and thermal analysis.

(b) Mechanosynthesis of Zn-MOF-74 using DMF as the grinding liquid

All syntheses were performed (unless stated otherwise) in PMMA 10 mL jar, using one 3.5 g steel ball and Retsch MM400 mixer mill operating at 30 Hz. The mass of the reactants was adjusted to correspond the experiments from ESRF, with 220 mg (1.1 mmol) of H_4**dhta** and 180.7 mg of ZnO (2.2 mmol). Each reactant was placed to separate part of the milling vessel, followed by the addition of 250 μL of DMF to ZnO. Milling was stopped at designated times, to collect the PXRD data of the reaction mixture. Experiment was considered to be finished when no traces of ZnO were visible in the PXRD. For pure DMF liquid additive the reaction mixture was milled for more than 3 hours before the peaks corresponding to ZnO disappeared. The product was further analyzed by FTIR-ATR, SS NMR and thermal analysis.

(c) Mechanosynthesis of Zn-MOF-74 using DMF/water mixture as the grinding liquid.

220 mg (1.1 mmol) of H_4**dhta** and 180.7 mg of ZnO (2.2 mmol) were placed in separate halves of PMMA milling vessel. Mixture of 200 uL of DMF and 50 μL of water was added on ZnO and the reaction mixture was milled for 60 minutes before collecting the PXRD. No traces of ZnO were visible in the PXRD and the collected yellow-green microcrystalline product was further analyzed by FTIR-ATR, SS NMR and thermal analysis.

(d) Mechanochemical synthesis of the intermediate (2).

220 mg (1.1 mmol) of H_4DHTA and 126 mg of ZnO (1.54 mmol) were placed in separate halves of PMMA milling vessel. 270 µL of DMF was added on ZnO and the reaction mixture was milled for 35 minutes. Collected yellow microcrystalline product was further analyzed by FTIR-ATR, SS NMR and thermal analysis. **S.2.5 Mechanosynthesis of Zn-MOF-74 from the $Zn(H_2O)_2(H_2$dhta) polymer**

0.135 g of $[Zn(H_2DHTA)(H_2O)_2]_n$ was mixed with 36.8 mg of ZnO in 14 mL PMMA milling vessel, followed by addition of 100 µL of water to the mixture. Vessel was positioned in the Retsch MM400 mill and milled for 45 minutes using 3.5 g stainless steel ball (30 Hz). Pale yellow product was collected and analyzed.

(e) Scaled-up mechanosynthesis of Zn-MOF-74

1.1 g (5.5) mmol of H_4**dhta** was mixed with 903 mg (10.1 mmol) of ZnO in a 50 mL stainless steel vessel. 1000 µL of water were added to the solid mixture and the vessel was placed in Retsch PM100 planetary mill operating at 525 rpm, for 120 minutes (4 x 3.5 g balls). The obtained pale yellow product (2.7 g) was collected from the jar and analyzed by FTIR-ATR, SS NMR and thermal analysis.

12.03 *In situ* monitoring of dry milling of ZnO AND H_4dhta

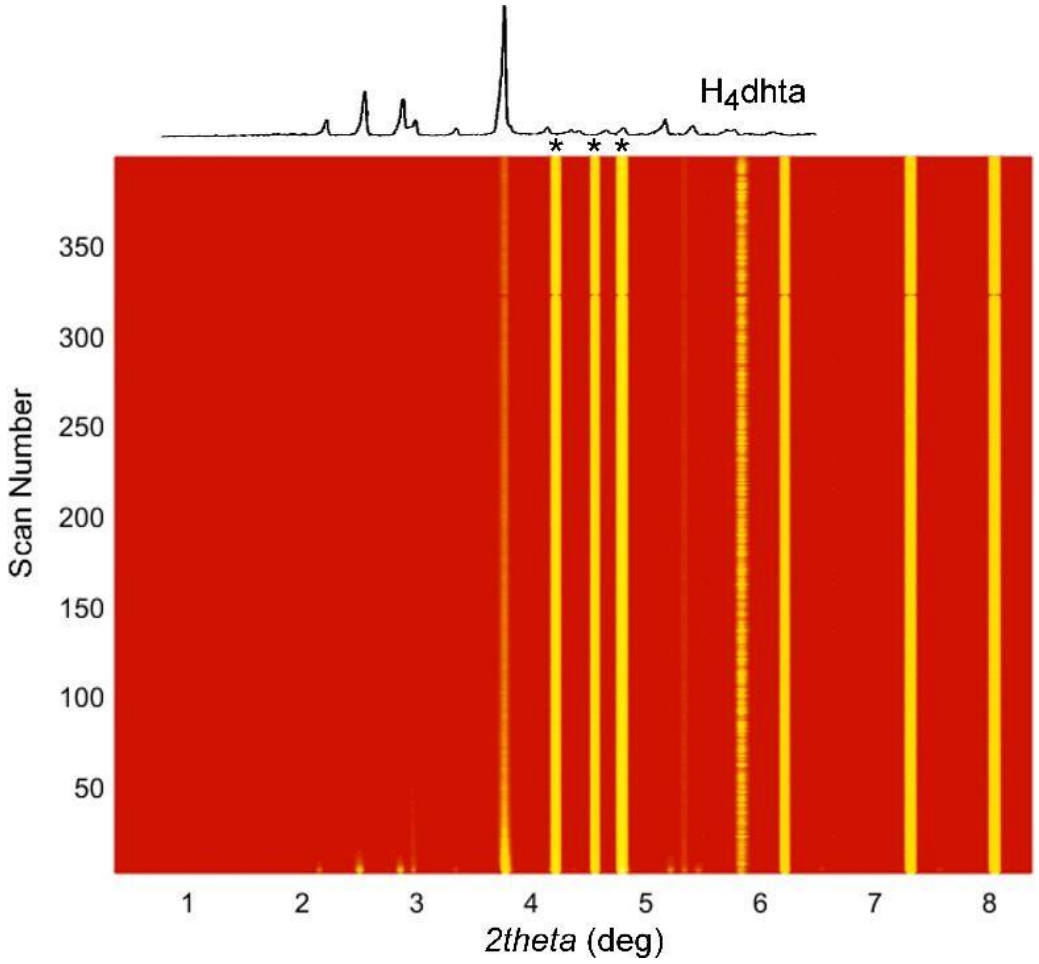

Figure S1. Time-resolved *in situ* X-ray powder diffractogram for the dry milling (30 Hz, 3.5 g steel ball) of ZnO and H_4**dhta** (stoichiometric ratio 2:1). The monitoring was performed at PETRA III beamline of DESY synchrotron with λ = 0.207 Å radiation (time-resolution of 10 seconds). Even after 70 minutes milling no evidence of chemical reaction was observed. Characteristic ZnO X-ray reflections are denoted with '*'.

12.04 Mechanochemical LAG with H_2O synthesis of Zn-MOF-74

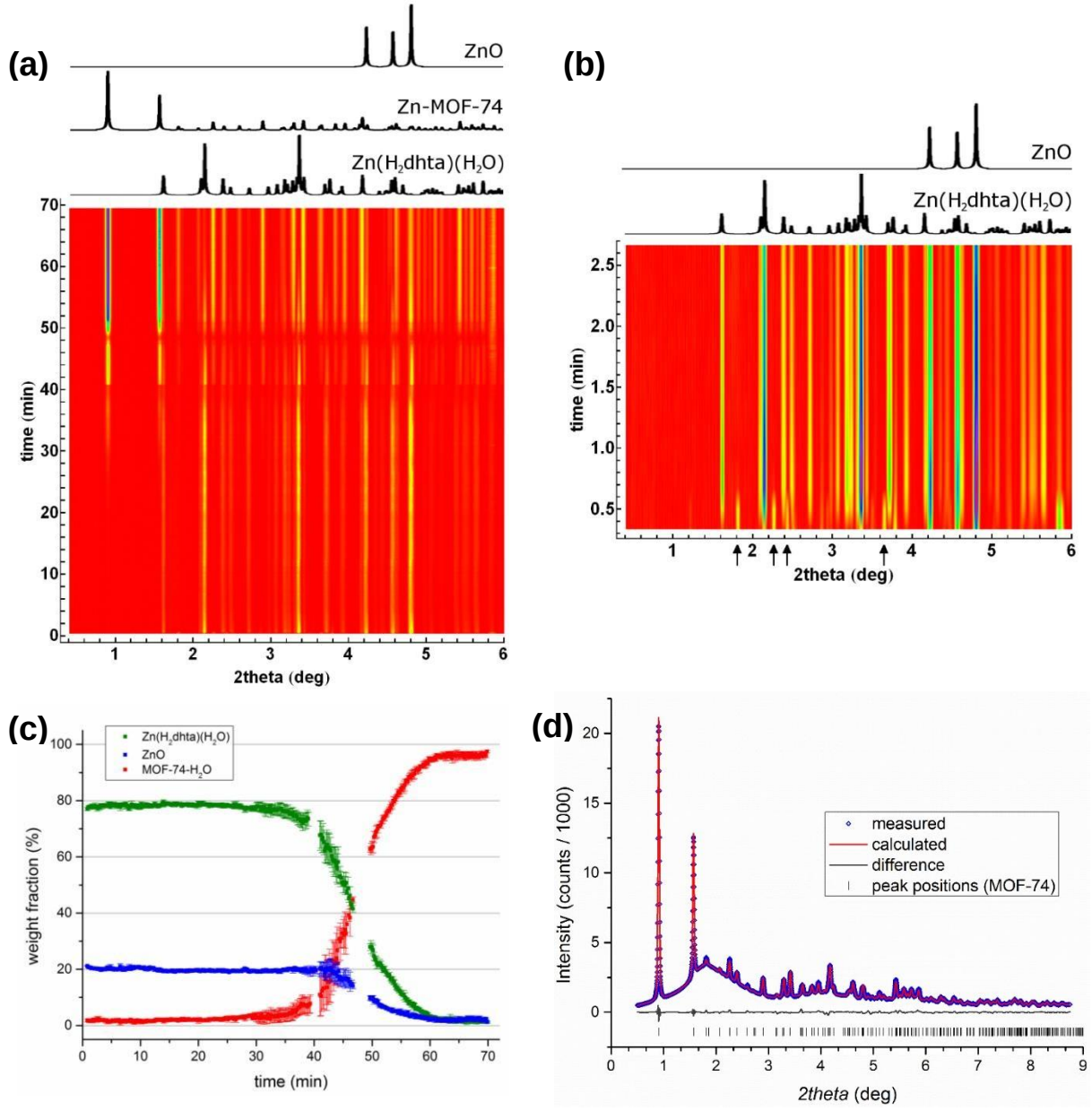

Figure S2. (a) Complete real-time *in situ* X-ray powder diffractogram for the reaction of ZnO and H_4**dhta** (stoichiometric ratio 2:1) in the presence of water, by using 3.5 g steel ball. The monitoring was performed at PETRA III beamline of DESY synchrotron with λ = 0.207 Å radiation; (b) real-time *in situ* X-ray powder diffractogram from(a), focusing on the first two minutes of the milling reaction, showing disappearance of H_4**dhta** in first 40 s of milling and rapid formation of $Zn(H_2O)_2(H_2$**dhta**). For clarity, X-ray reflections of H_4**dhta** are highlighted by arrows. (c) The Rietveld analysis of the same milling reaction,

illustrating the concomitant disappearance of X-ray reflections of ZnO and $Zn(H_2O)_2(H_2$**dhta**), starting at around 35 minutes into milling. The rates of disappearance of ZnO and $Zn(H_2O)_2(H_2$**dhta**) are similar, leading to simultaneous formation of the product Zn-MOF-74. (d) The Rietveld analysis of the final X-ray diffraction pattern confirms that the final product is Zn-MOF-74, without any observable traces of $Zn(H_2O)_2(H_2$**dhta**) or ZnO visible in the pattern.

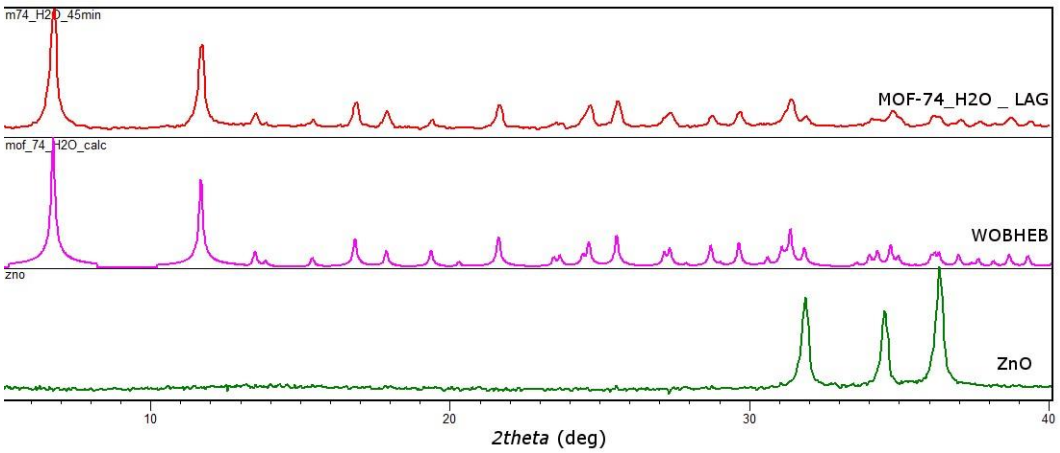

Figure S3. Comparison of PXRD patterns for Zn-MOF-74 (top, red) obtained after by LAG (30 Hz, 3.5 g steel ball) of a stoichiometric 1:2 mixture of H_4**dhta** and ZnO with water as a grinding liquid, compared to the calculated pattern for Zn-MOF-74 hydrate (CSD code WOBHEB, purple) and measured pattern for ZnO (green).

12.05 Ex situ Reaction monitoring

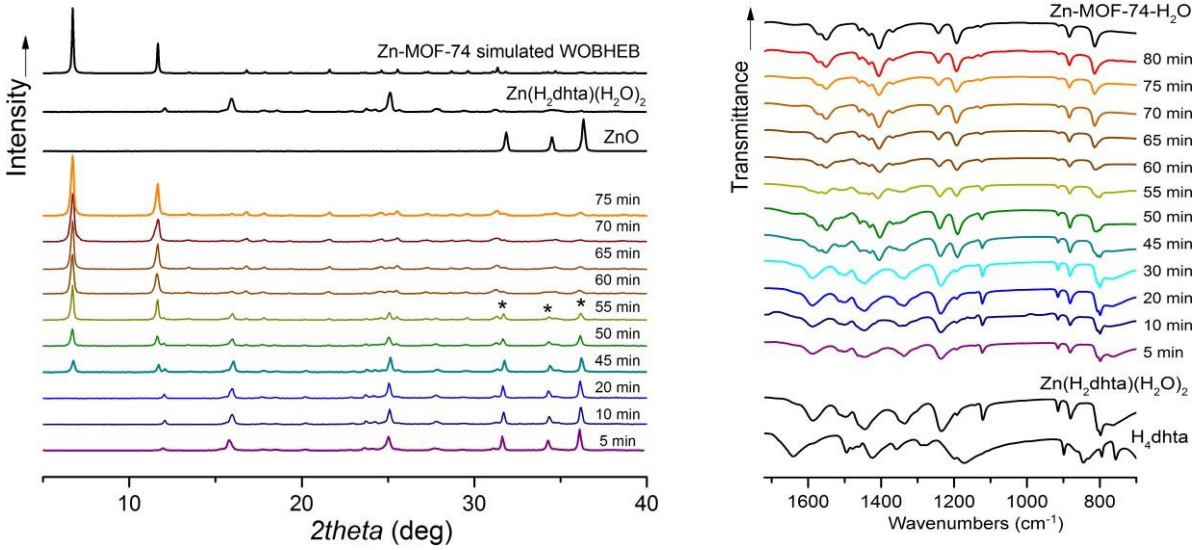

a) ex situ PXRD monitoring

b) *ex situ* FTIR-ATR monitoring

Figure S4. Results of combined *ex situ* time-resolved monitoring of the mechanochemical reaction (30Hz, 3.5 g stainless steel ball) between ZnO and H_4**dhta** (2:1 molar ratio) in the presence of water as the grinding liquid, using: (a) X-ray powder diffraction and (b) FTIR-ATR spectroscopy. Diffraction and spectroscopic analyses were performed at the same time, immediately upon sampe extraction. (a) PXRD monitoring shows the rapid appearance of the Zn(H_2**dhta**)(H_2O)$_2$ polymer, with no reflections of the H_4**dhta** reactant even in the first PXRD pattern, collected after 5 min milling. X-ray reflections characteristic for Zn-MOF-74 occur after ca. 45 min milling, when the reflections of ZnO and Zn(H_2O)$_2$(H_2**dhta**) begin to disappear. The reflections of both ZnO and Zn(H_2O)$_2$(H_2**dhta**) disappear at ca. 60 min milling, leaving Zn-MOF-74 as the sole product visible *via* PXRD; (b) the FTIR-ATR analyses of the same reaction also indicate complete disappearance of H_4**dhta** reactant after 5 minutes milling, with only observable absorption bands corresponding well to Zn(H_2**dhta**)(H_2O)$_2$ polymer (ZnO does not exhibit any notable absorption in this spectral region). The absorption bands of Zn(H_2**dhta**)(H_2O)$_2$ polymer start to diminish at ca. 45 min milling, when the absorption bands characteristic for Zn-MOF-74 also arise. There is no significant change in spectra

after ca. 70 min milling. The final spectrum matches shows no evidence of H_4**dhta** or Zn(H_2**dhta**)(H_2O)$_2$ polymer.

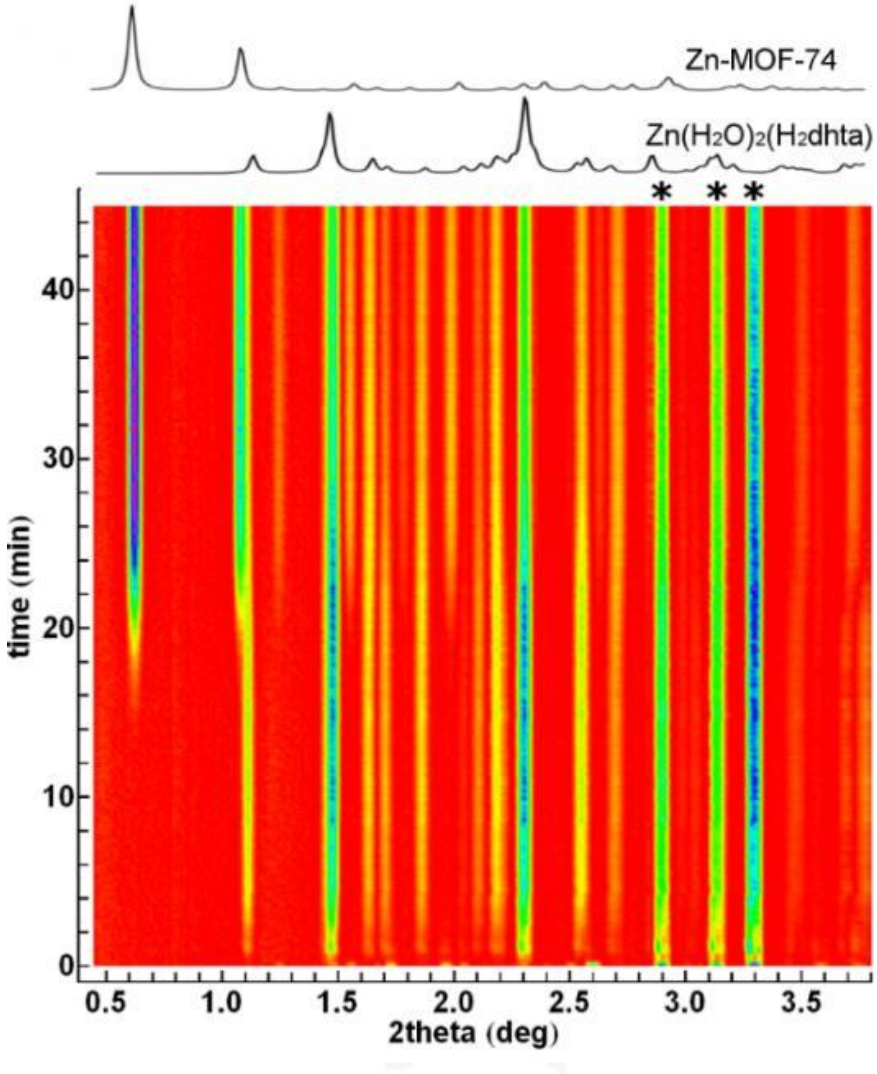

Figure S5. Time-resolved *in situ* X-ray powder diffractogram for the reaction of ZnO and H_4**dhta** (stoichiometric ratio 2:1) in the presence of water, using a 2.9 g stainless steel ball. The monitoring was performed at ESRF synchrotron with λ = 0.14 Å radiation. Final product is a mixture of Zn-MOF-74, Zn(H_2**dhta**)(H_2O)$_2$ and ZnO.

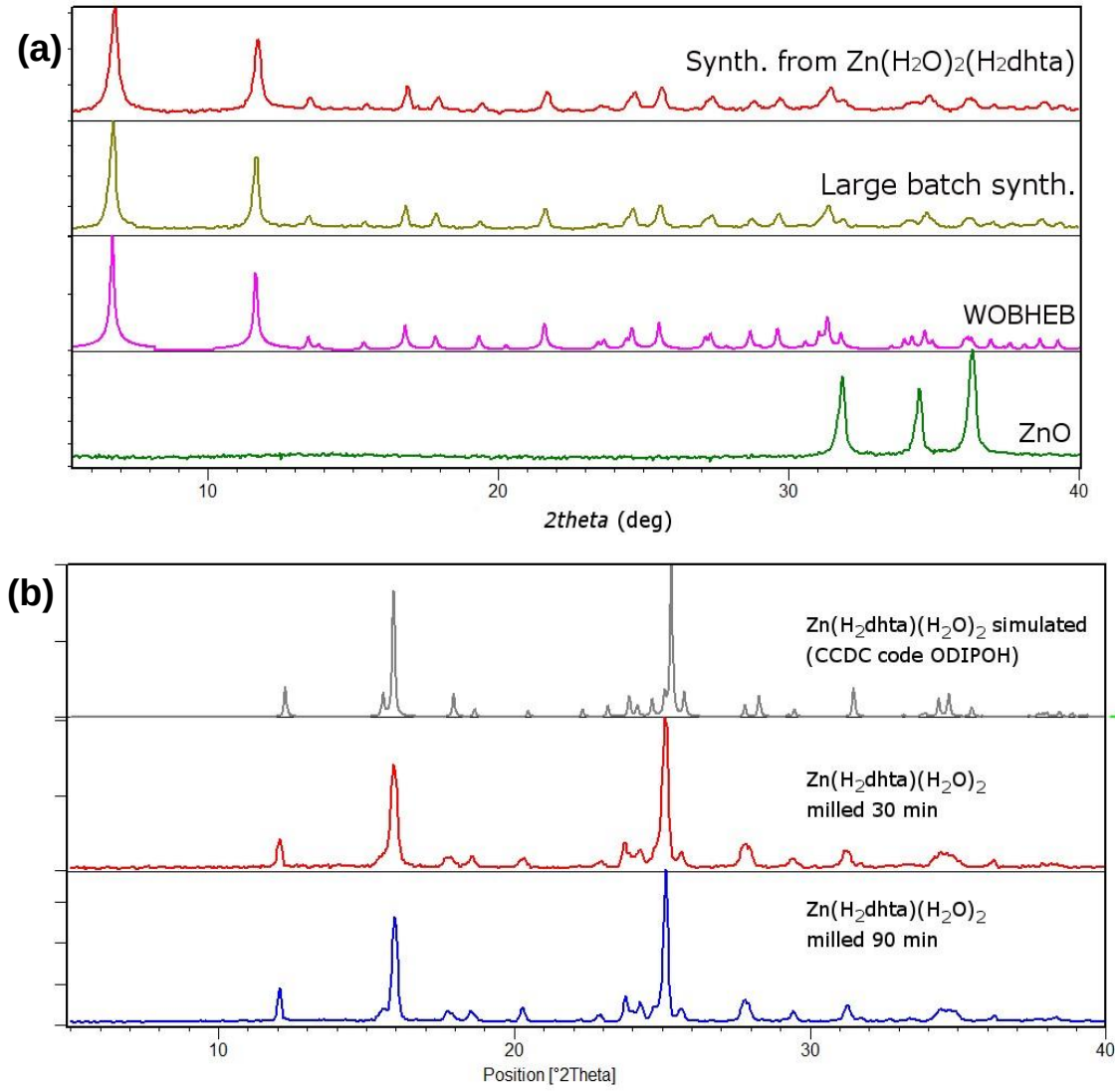

Figure S6. (a) Comparison of PXRD patterns for (top to bottom): (red) Zn-MOF-74 obtained by LAG (30 Hz, 3.5 g stainless steel ball) of an equimolar mixture of $Zn(H_2O)_2(H_2$**dhta**) polymer and ZnO, with H_2O as the grinding liquid; (olive) product of 5 mmol synthesis of Zn-MOF-74 in a planetary mill (525 rpm, 120 min, four stainless setel balls of 3.5 g); (magenta) calculated for the crystal structure of Zn-MOF-74 hydrate (CSD code WOBHEB) and (green) ZnO reactant. (b) Comparison of PXRD patterns for $Zn(H_2O)_2(H_2$**dhta**) polymer (top to bottom): (black) simulated for the known crystal structure (CSD code ODIPOH); (red) $Zn(H_2O)_2(H_2$**dhta**) after 30 min milling and (blue) $Zn(H_2O)_2(H_2$**dhta**) after 90 min milling.

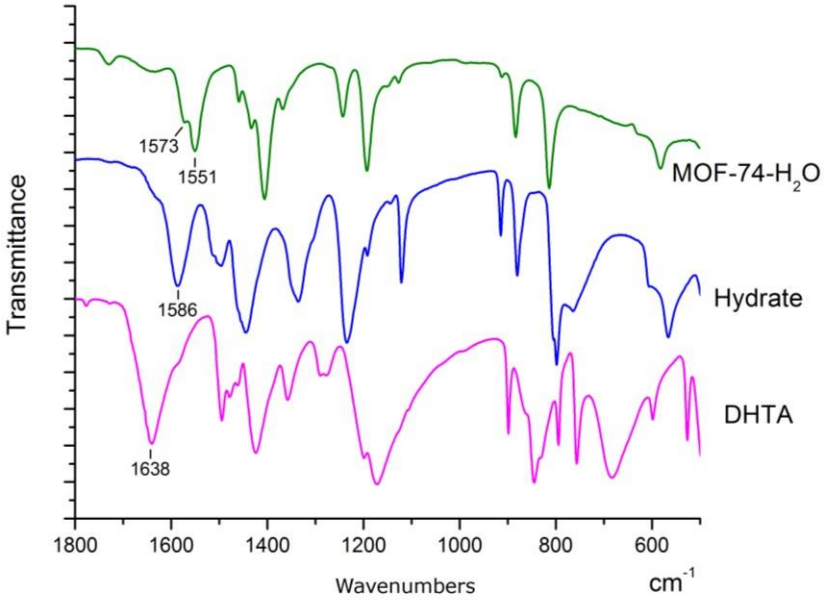

Figure S7. Comparison of FTIR-ATR spectra for the product and reactants of the mechanochemical synthesis of ZnMOF-74 using water as the milling liquid.

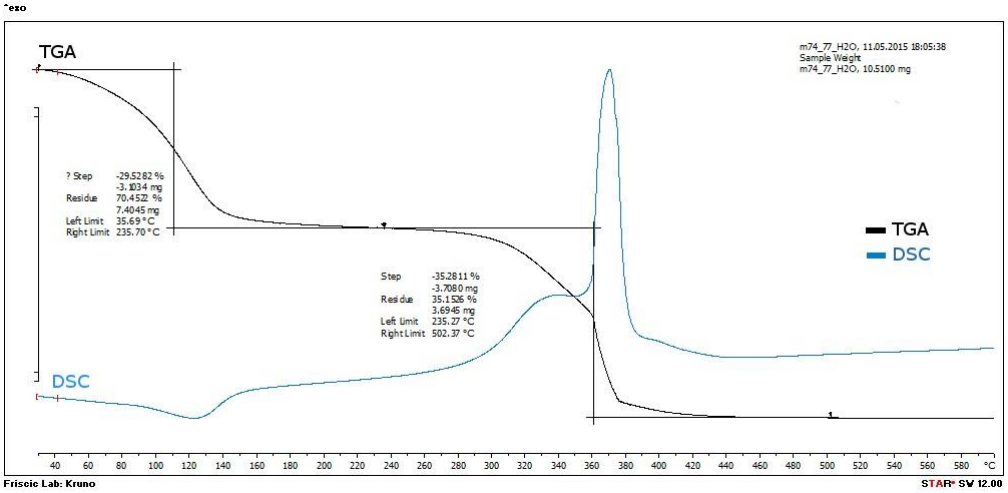

Figure S8. The combined TGA (black) and DSC (blue) thermograms (air, 30-600 °C, 10 °C/min) for the Zn-MOF-74 product made by milling (30 Hz, 3.5 g steel ball) of a 1:2 stoichiometric mixture of H_4**dhta** and ZnO, with H_2O as the milling liquid. The first step in TGA corresponds to loss of water included in MOF pores and coordinated to metal

centers. The final step in TGA thermogram, associated with two exothermic signals in the DSC thermogram, is attributed to the decomposition of Zn-MOF-74 framework and degradation of the organic ligand. The final product of thermal decomposition is ZnO, as confirmed by PXRD.

12.06 Mechanochemical LAG synthesis of Zn-MOF-74, DMF milling liquid

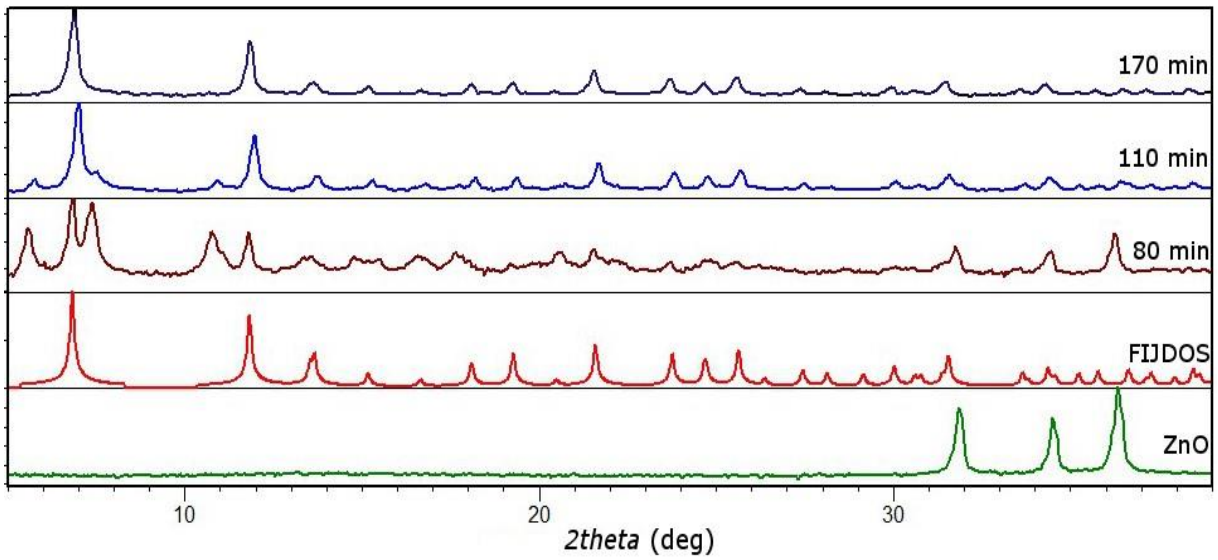

Figure S9. Time-resolved XRPD patterns for mechanochemical reaction of ZnO and H_4**dhta** (2:1 molar ratio), using DMF as the milling liquid. The pattern after 80 min milling reveals presence of **2**. Further milling leads to complete disappearance of **2** and ZnO, and formation of Zn-MOF-74 as the final product. Experimental XRPD patterns are compared to that simulated for the crystal structure of the DMF solvate of Zn-MOF-74 (CSD code FIJDOS, red) and that of ZnO reactant (green).

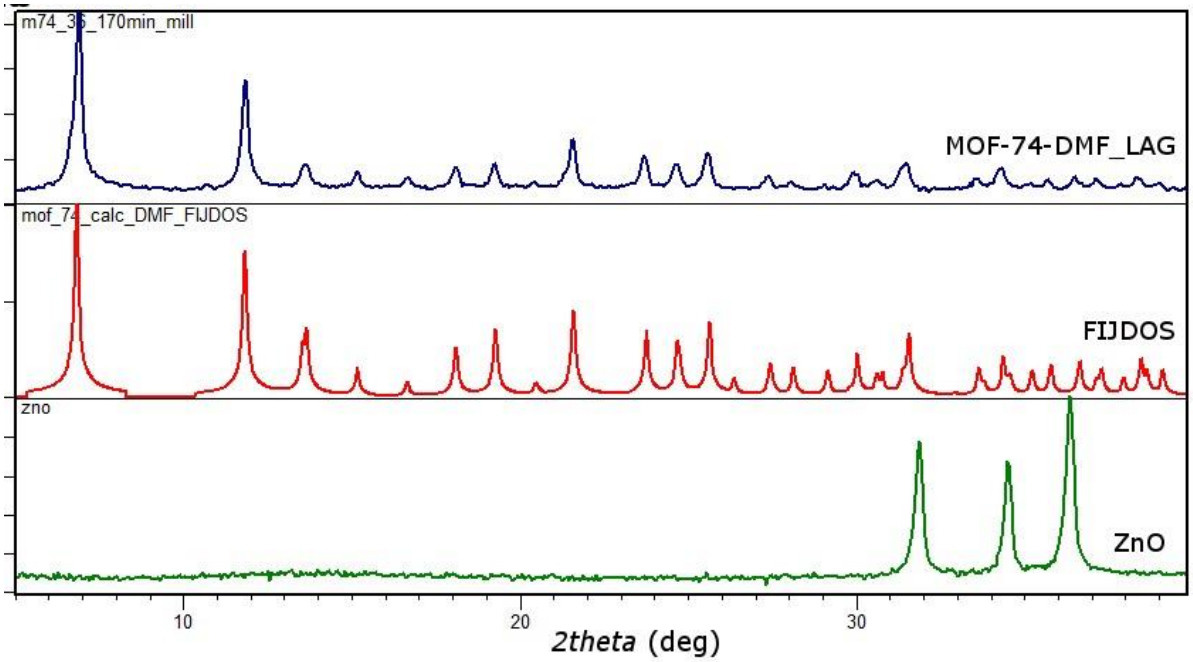

Figure S10. Comparison of XRPD patterns for (top-to-bottom): (blue) Zn-MOF-74 obtained after 170 min milling (30 Hz, 3.5 g steel ball) of a 1:2 stoichiometric mixture of H_4**dhta** and ZnO, using DMF as the milling liquid; (red) simulated PXRD pattern for the structure of the DMF solvate of Zn-MOF-74 (CSD code FIJDOS) and (green) ZnO reactant.

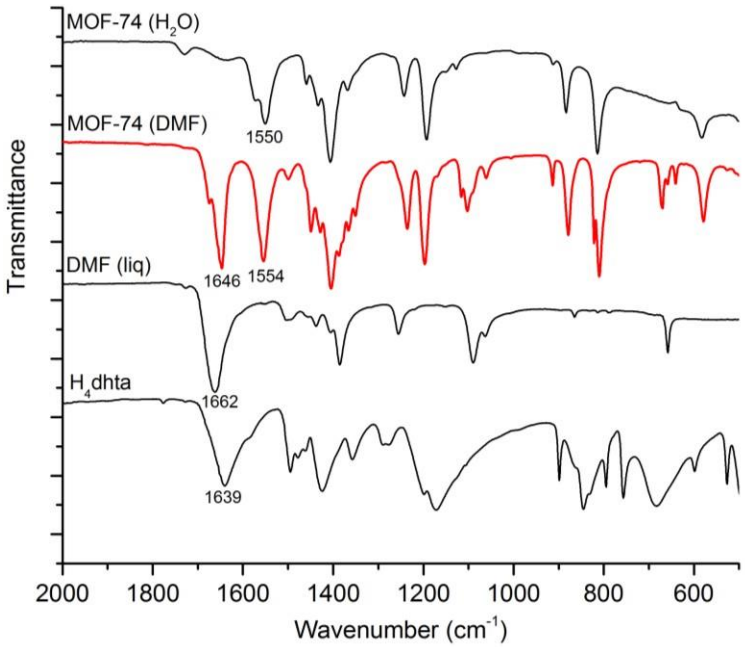

Figure S11. Comparison of FTIR-ATR spectra for (top-to-bottom): Zn-MOF-74 made by milling with water as the grinding liquid; Zn-MOF-74 made by milling (170 min, 30 Hz, 3.5 g steel ball) with DMF as the grinding liquid; liquid DMF and reactant H$_4$**dhta**. The FTIR-ATR spectrum of the product made by LAG with DMF closely resembles that of Zn-MOF-74 made by LAG with water, with additional absorption bands corresponding to DMF. No trace of starting H$_4$**dhta** is observable in the as-synthesized products.

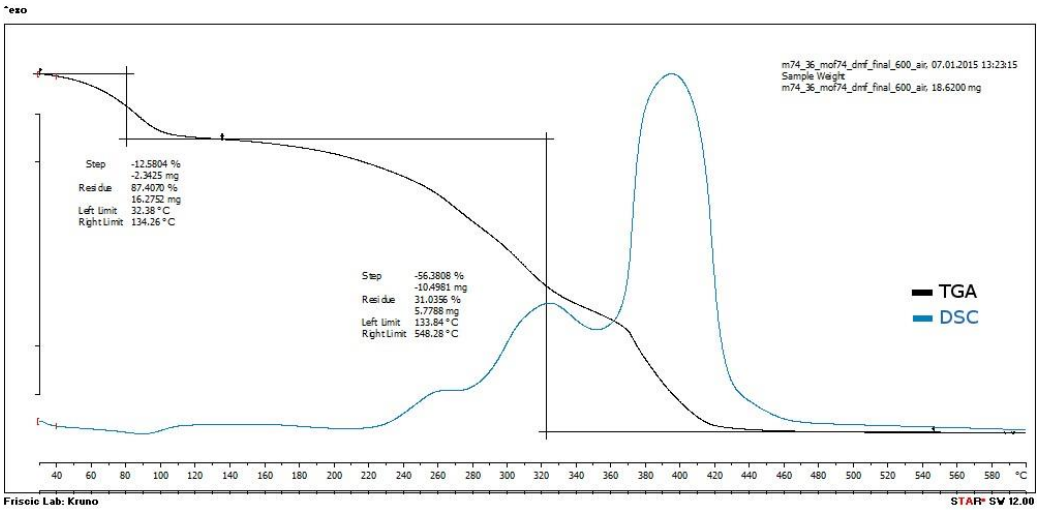

Figure S12. Combined TGA (black) and DSC (blue) thermograms (recorded in air, 30-600 °C, heating rate 10 °C/min) for the Zn-MOF-74 made by LAG using DMF as the grinding liquid. The first step in TGA corresponds to loss of solvent included in the MOF. The second step, which involves three exothermic signals in the DSC thermogram, is interpreted as the loss of coordinated DMF and complete decomposition of the MOF structure. The end product of thermal decomposition is ZnO (confirmed by PXRD).

12.07 Mechanosynthesis of Zn-MOF-74 using DMF/H_2O grinding liquid

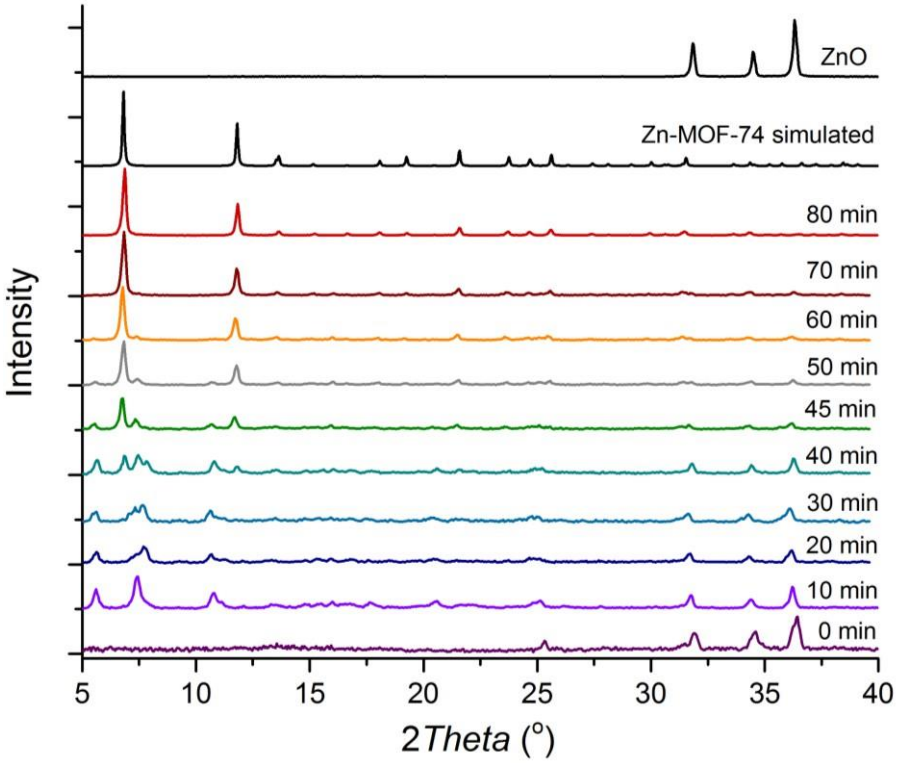

Figure S13. PXRD diffractograms for time-resolved *ex situ* analysis (Ni-filtered Cu*K*α radiation) of mechanochemical reaction of ZnO and H_4**dhta** (2:1 molar ratio) using a stainless steel ball of 3.5 grams and a DMF:H_2O mixture (4:1 v/v) as the grinding liquid. The pattern taken at 10 min shows presence of **2**, identical to that observed by *in situ* monitoring (Figure 2a in the manuscript). After 40 min, reflections of Zn-MOF-74 appear.

Characteristic reflections ZnO and **2** begin to disappear upon further milling to yield Zn-MOF-74 as the only observable phase. Formation of Zn-MOF-74 is supported by FTIR-ATR and SSNMR spectroscopy. For comparison, diffractograms (black) are also provided for Zn-MOF-74 DMF solvate (simulated, CSD code FIJDOS) and ZnO reactant.

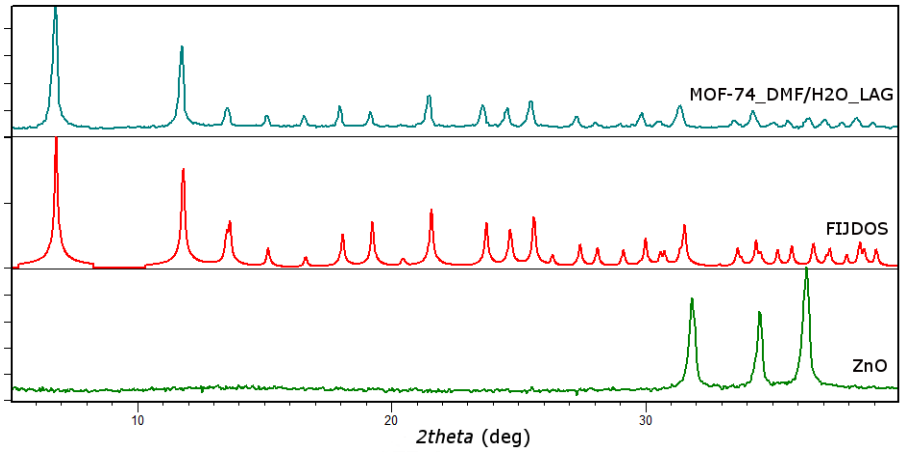

Figure S14. Comparison of PXRD patterns (top to bottom): Zn-MOF-74 (blue) made by 60 min non-interrupted milling (30 Hz, 3.5 g stainless steel ball) of a 1:2 stoichiometric mixture of H_4**dhta** and ZnO, with a mixture of DMF:H_2O (4:1 v/v) as the grinding liquid; calculated for the crystal structure of Zn-MOF-74 DMF solvate (CSD code FIJDOS, red) and ZnO reactant (green).

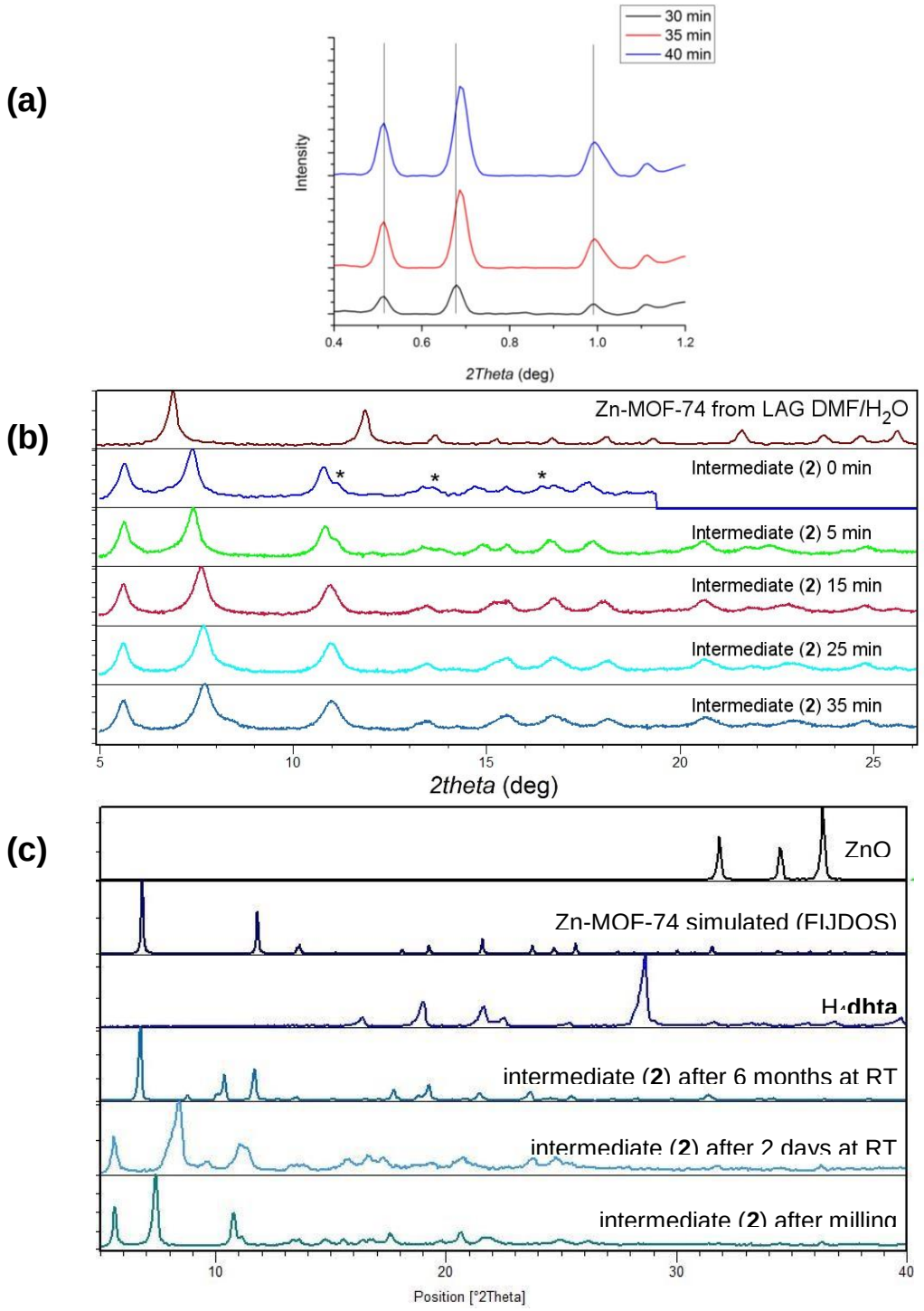

Figure S15. (a) Selected diffractograms from *in situ* PXRD monitoring of LAG of ZnO and H_4**dhta** (stoichiometric ratio 2:1) with a DMF:water mixture (4:1 v/v, η=0.625 μL/mg, λ=0.142 Å), using a 2.9 gram ball, illustrating changes to the PXRD pattern of **2** at 30 (black), 35 (red) and 40 minutes milling (blue), before Zn-MOF-74 formation. (b) XRPD data for **2** by 30 minutes of non-interrupted milling (30 Hz, 3.5 g steel ball)

of a 1:1.4 stoichiometric mixture of H_4**dhta** and ZnO in the presence of a DMF:H_2O (4:1 v/v) as a liquid additive, compared to the pattern simulated for Zn-MOF74 DMF solvate (CSD FIJDOS, red). Intermediate **2** is unstable upon standing in air, as seen by disappearance of reflections denoted with '*' and shift of the reflection at 2θ=7.40° to 7.6°. Attempts to wash the sample with DMF led to partial formation of Zn-MOF-74. (c) Changes to the XRPD pattern of **2** upon storage.

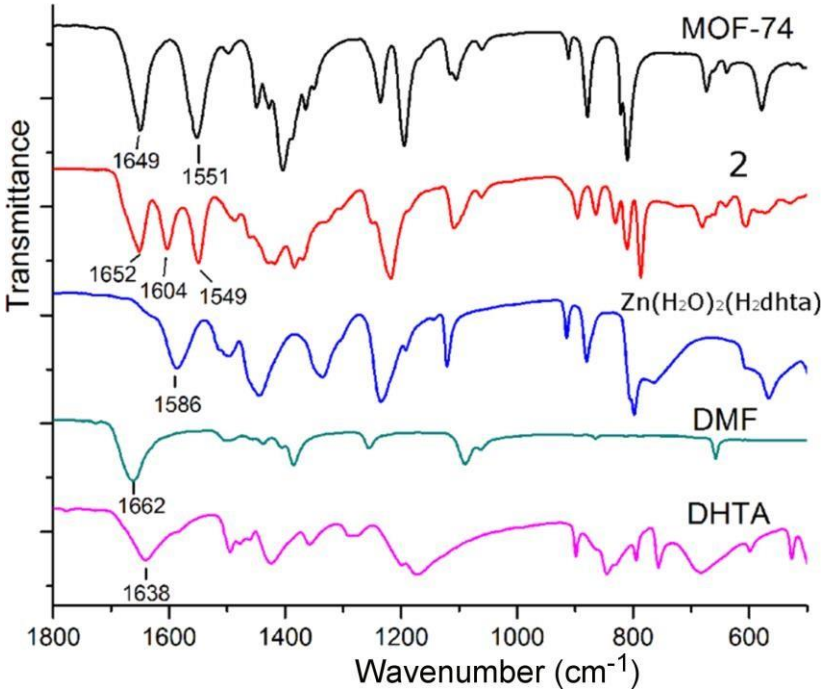

Figure S16. FTIR-ATR spectra of (top-to-bottom): Zn-MOF-74 made by LAG (DMF/water grinding liquid); intermediate phase **2**; $Zn(H_2O)_2(H_2$**dhta**) polymer; liquid DMF and H_4**dhta.**

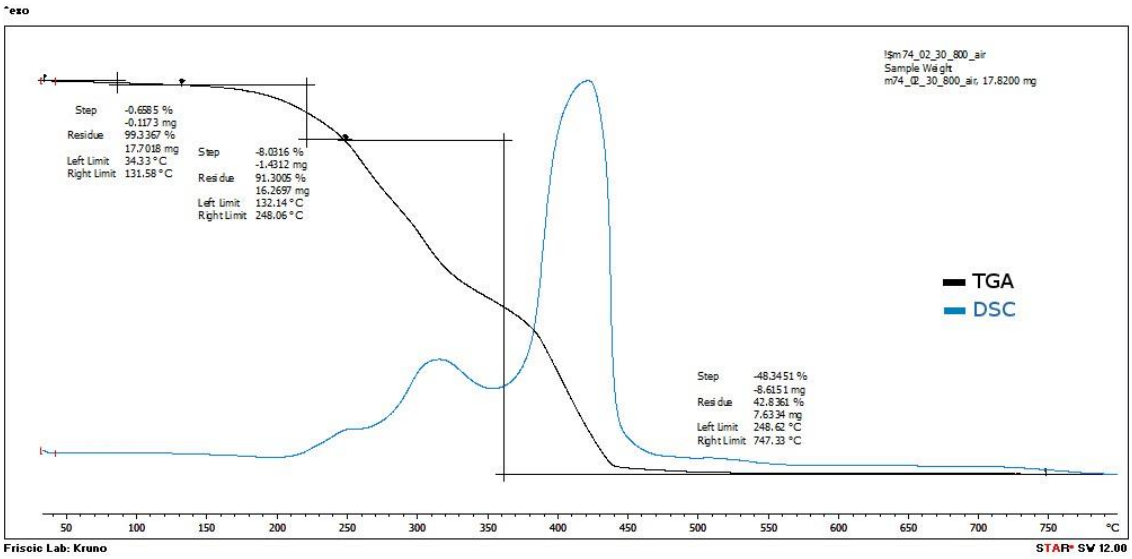

Figure S17. Combined TGA (black) and DSC (blue) thermograms (recorded in air, 30-600 °C, heating rate 10 °C/min) for heating of Zn-MOF-74 made by milling (30 Hz, 3.5 g steel ball) of H_4**dhta** and ZnO (1:2 stoichiometric ratio), in the presence of a DMF/H_2O mixture as the grinding liquid. The first step in TGA corresponds to egress of included solvent from the MOF material. The second step corresponds well to decomposition of MOF-74 material, and degradation of the organic ligand. The final product of thermal decomposition is ZnO (confirmed by PXRD).

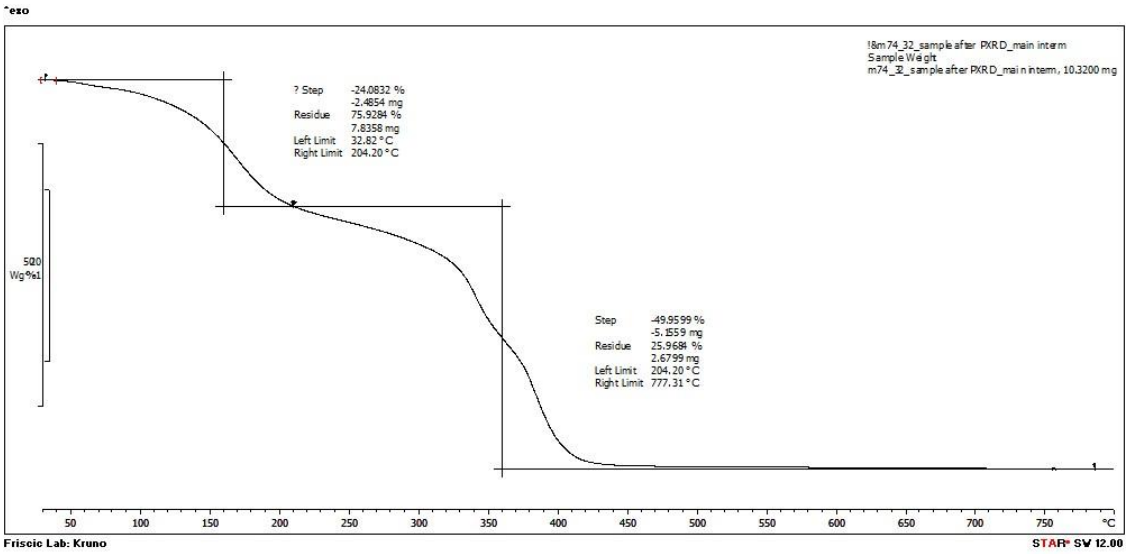

Figure S18. The TGA thermogram (recorded in air, 30-800 °C, heating rate 10 °C/min) of **2**, isolated after 30 min milling (30 Hz, 3.5 g steel ball) of a 1:1.4 stoichiometric mixture of H_4**dhta**:ZnO using a DMF/H_2O mixture as the grinding liquid. The first degradation step most likely corresponds to loss of included solvent molecules, and the final decomposition leads to formation of ZnO (confirmed by PXRD analysis).

12.08 Solid-state NMR spectroscopy

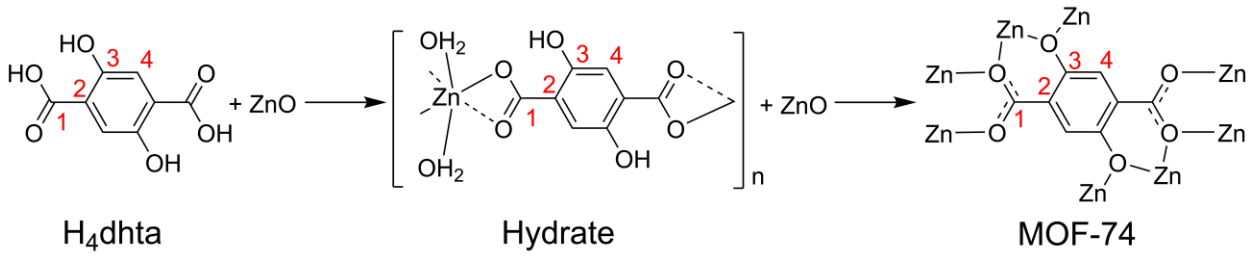

Scheme S1. Schematic representation of carbon atom numbering and connectivity of the organic **dhta**– based moiety in $Zn(H_2O)_2(H_2$**dhta**) coordination polymer and the MOF-74 product.

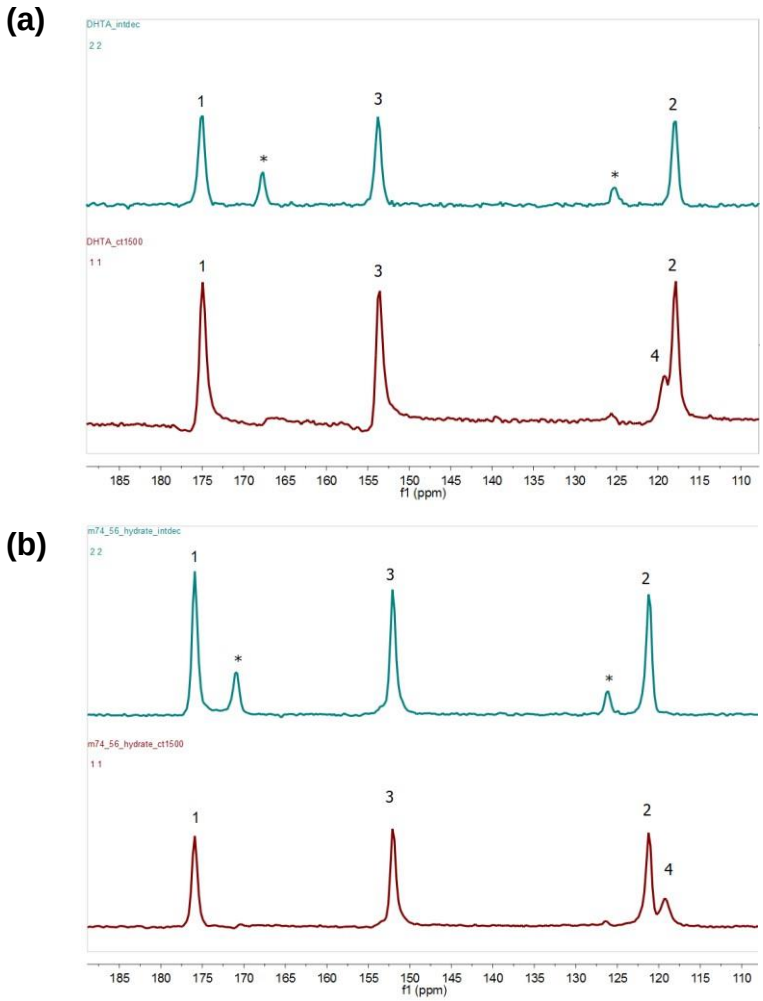

Figure S19. (a) Comparison of ^{13}C ssNMR CP-MAS spectra for H_4**dhta** collected on a Varian VNMRS spectrometer. The top spectrum is collected with interrupted decoupling to suppress and identify the C– H carbon atom, and the bottom spectrum using the TOSS technique to suppress and identify spinning sidebands. (b) Comparison of ^{13}C ssNMR CP-MAS spectra for $Zn(H_2O)_2(H_2$**dhta**). The top spectrum is collected with interrupted decoupling to suppress and identify the C–H carbon atom, and the bottom spectrum using the TOSS technique to suppress and identify spinning sidebands. Atom numbering is based on Scheme S1. Sidebands are denoted with '*'.

(a)

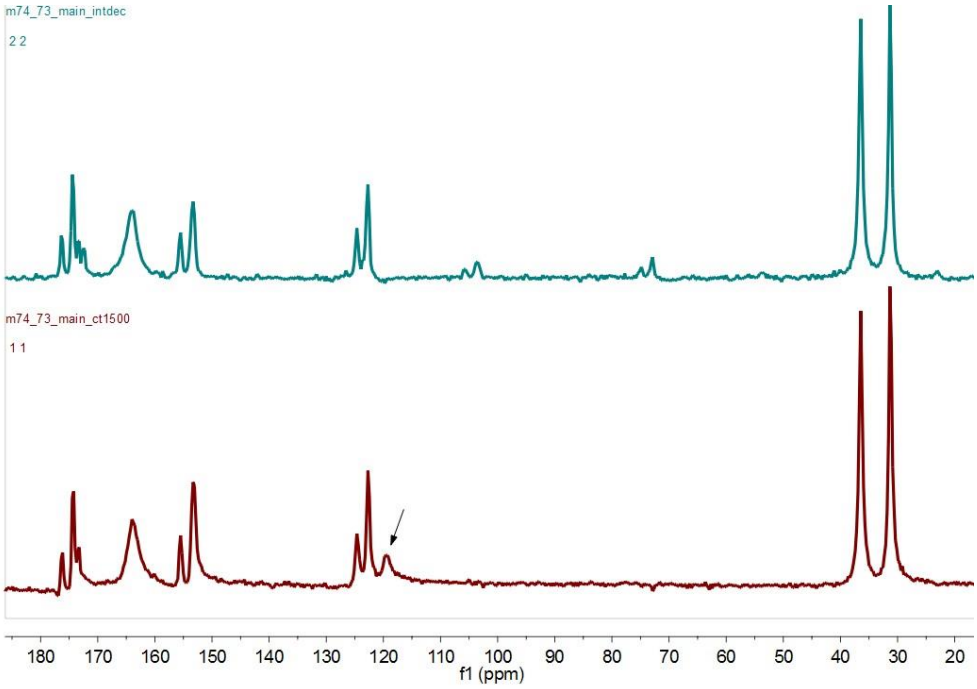
m74_73_main_intdec
2 2
m74_73_main_ct1500
1 1
180 170 160 150 140 130 120 110 100 90 80 70 60 50 40 30 20
f1 (ppm)

(b)

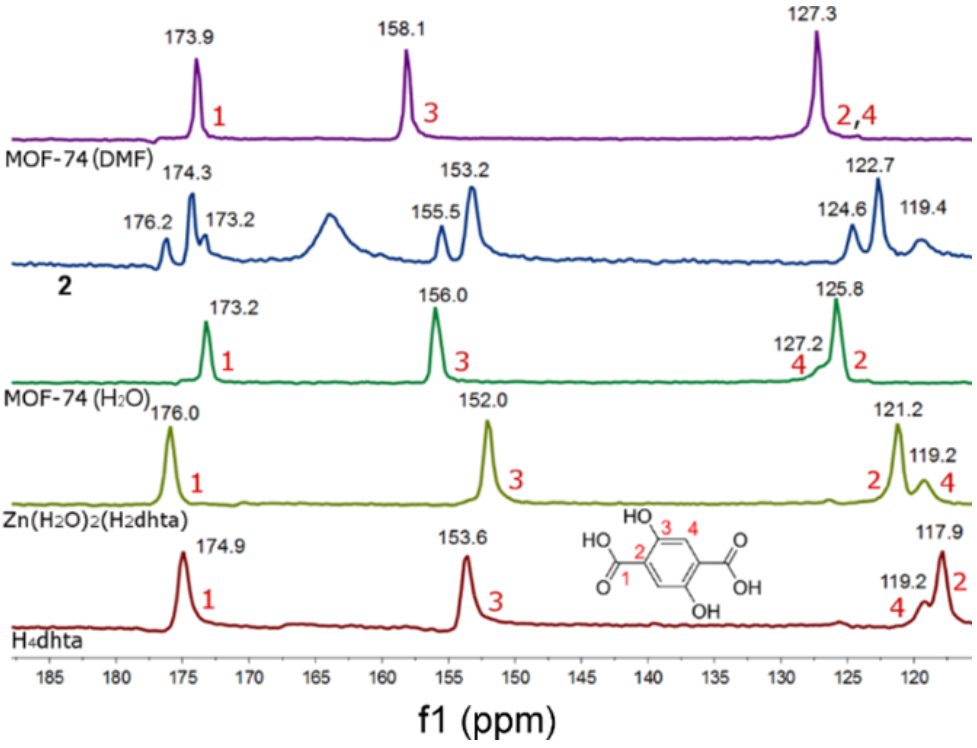
MOF-74 (DMF)
173.9
158.1
127.3
1
3
2,4
2
174.3
176.2
173.2
153.2
155.5
122.7
124.6
119.4
MOF-74 (H2O)
173.2
156.0
125.8
127.2
1
3
4
2
Zn(H2O)2(H2dhta)
176.0
152.0
121.2
119.2
1
3
2
4
H4dhta
174.9
153.6
117.9
119.2
1
3
4
2
HO
OH
OH
O
O
185 180 175 170 165 160 155 150 145 140 135 130 125 120
f1 (ppm)

Figure S20. (a) ^{13}C ssNMR CP-MAS spectra for **2** made by LAG using a DMF:water mixture as the grinding liquid, collected on a Varian VNMRS spectrometer. The top spectrum is collected with interrupted decoupling to suppress and identify C–H carbon atom signals (denoted with the arrow), and the bottom spectrum using the TOSS technique to suppress and identify spinning sidebands. (b) Comparison of ssNMR ^{13}C CP-MAS spectra of (top-to-bottom), collected on a Varian VNMRS spectrometer using the TOSS technique: Zn-MOF-74 made by LAG (DMF/water); compound **2**; Zn-MOF-74 made by LAG (H_2O); $Zn(H_2O)_2(H_2$**dhta**) and H_4**dhta**.

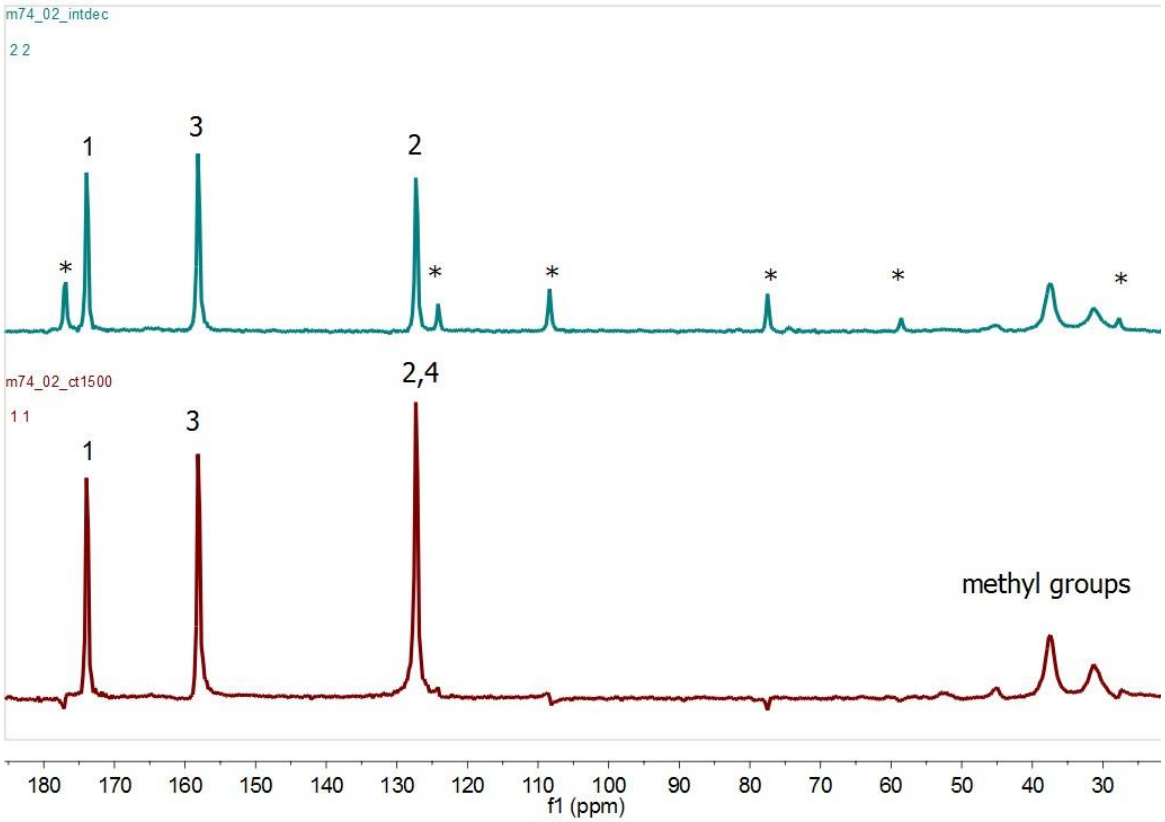

Figure S21. Comparison of ^{13}C ssNMR CP-MAS spectra for the Zn-MOF-74 (LAG DMF) product, collected on a Varian VNMRS spectrometer. The top spectrum is collected with interrupted decoupling to suppress and identify C–H carbon atom), and the bottom spectrum using the TOSS technique to suppress and identify spinning sidebands. Sidebands are denoted with '*'.

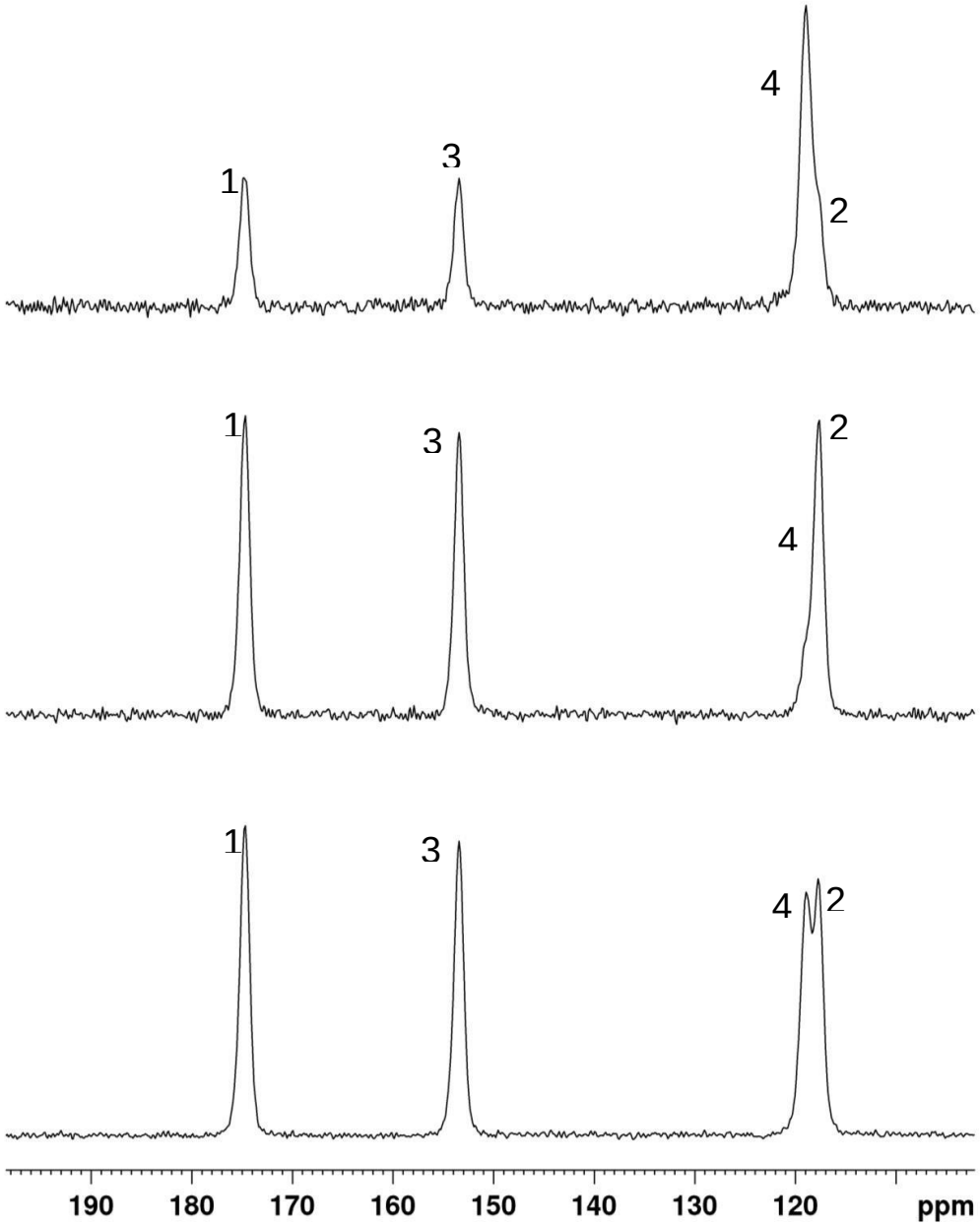

Figure S22. (Comparison of ^{13}C ssNMR CP-MAS spectra for H_4**dhta** collected on a Bruker Avance III HD spectrometer: (top) 250 μs cross-polarization time, leading to selective enhancement of the C-H group carbon atom signal; (middle) interrupted decoupling spectrum, with the signal belonging to the C-H group carbon atom supressed,

and (bottom) 2 ms cross-polarization time with signals of all carbon atoms being similar. Signal labels are based on Scheme S1.

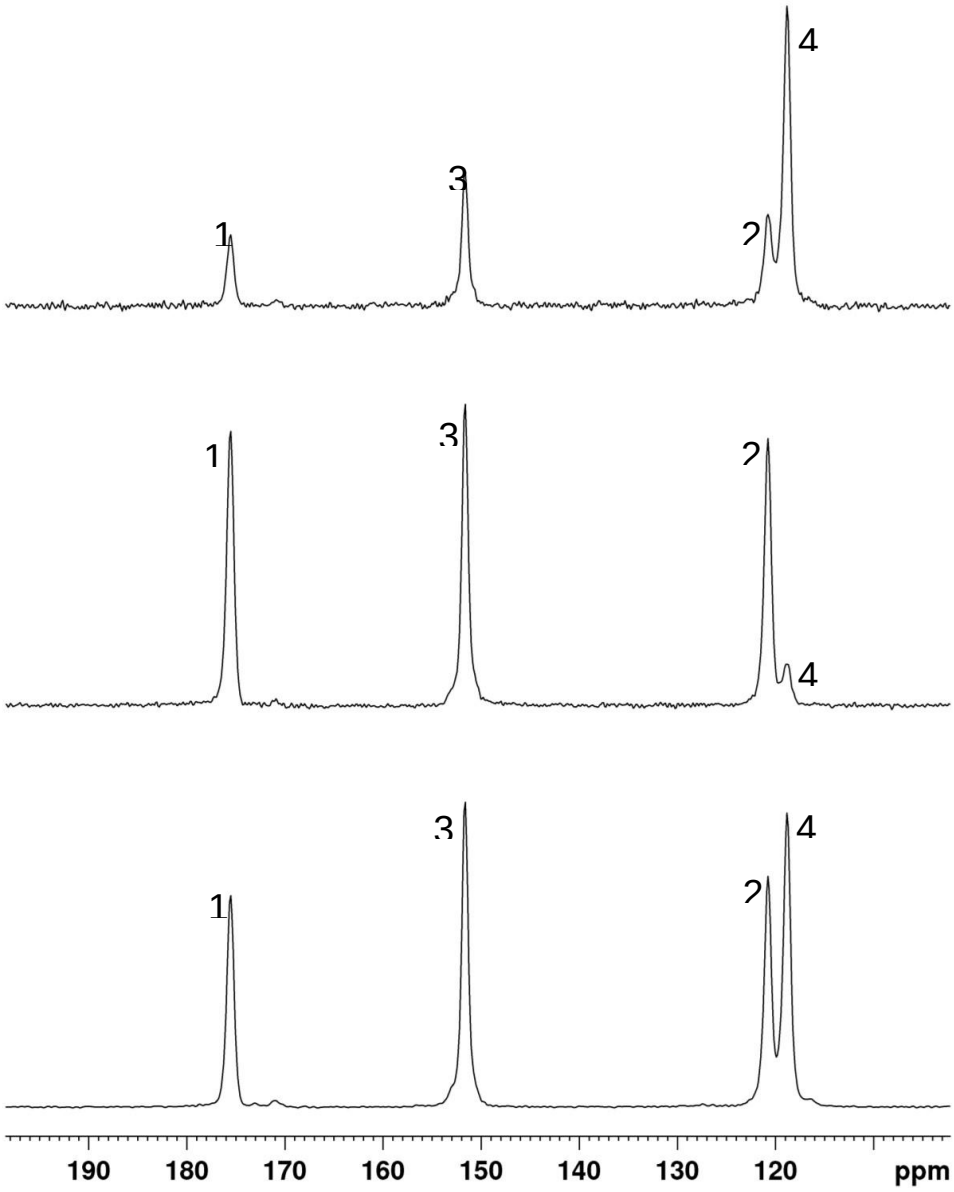

Figure S23. Comparison of ^{13}C ssNMR CP-MAS spectra for $Zn(H_2O)_2(H_2$**dhta**) collected on a Bruker Avance III HD spectrometer: (top) 250 μs cross-polarization time, leading to selective enhancement of the C-H group carbon atom signal; (middle) interrupted decoupling spectrum, with the signal belonging to the CH group carbon atom supressed, and (bottom) 2 ms cross-polarization time with signals of all carbon atoms being similar. Signal labels are based on Scheme S1.

12.09 Scanning electron microscopy (SEM) and porosity measurements

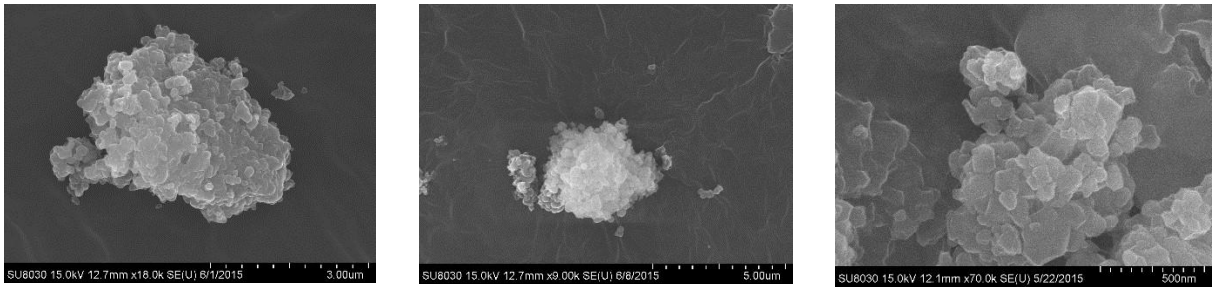

Zn-MOF-74 (LAG H_2O) Zn-MOF-74 (LAG DMF/H_2O) Zn-MOF-74 (LAG DMF)

Figure S24. SEM micrographs of the microcrystalline Zn-MOF-74 samples prepared by different LAG procedures.

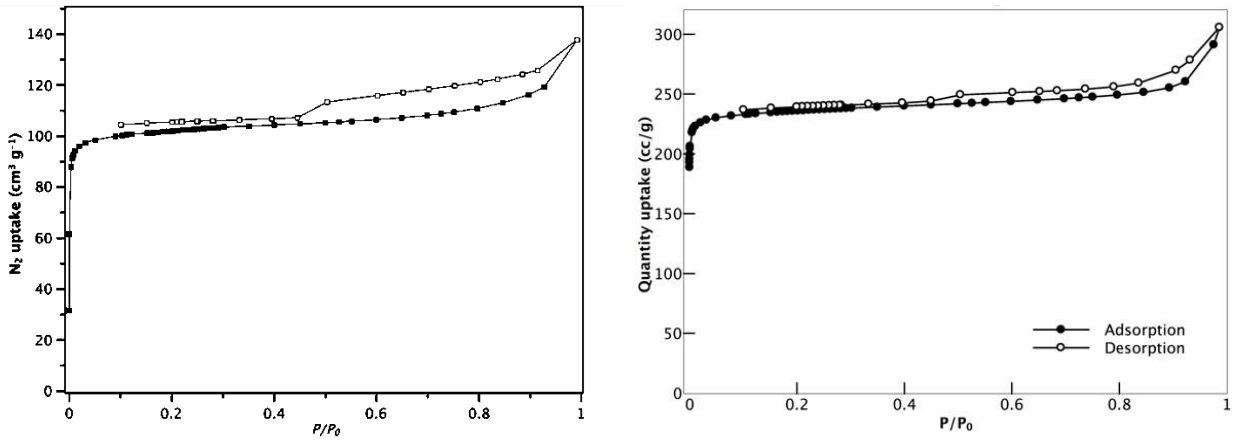

Figure S25. Isotherm curves for Zn-MOF-74 prepared by LAG with water.

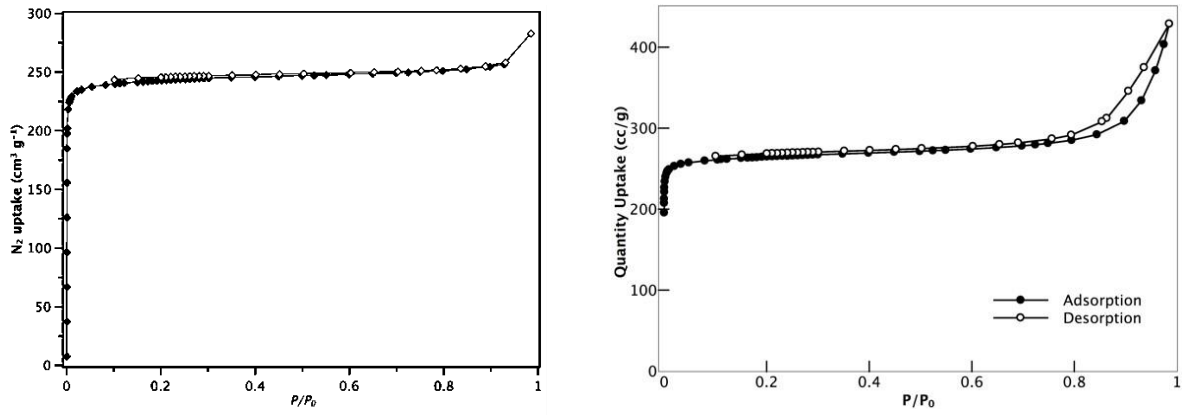

Figure S26. Isotherm curves for Zn-MOF-74 samples prepared by LAG with DMF/water mixture.

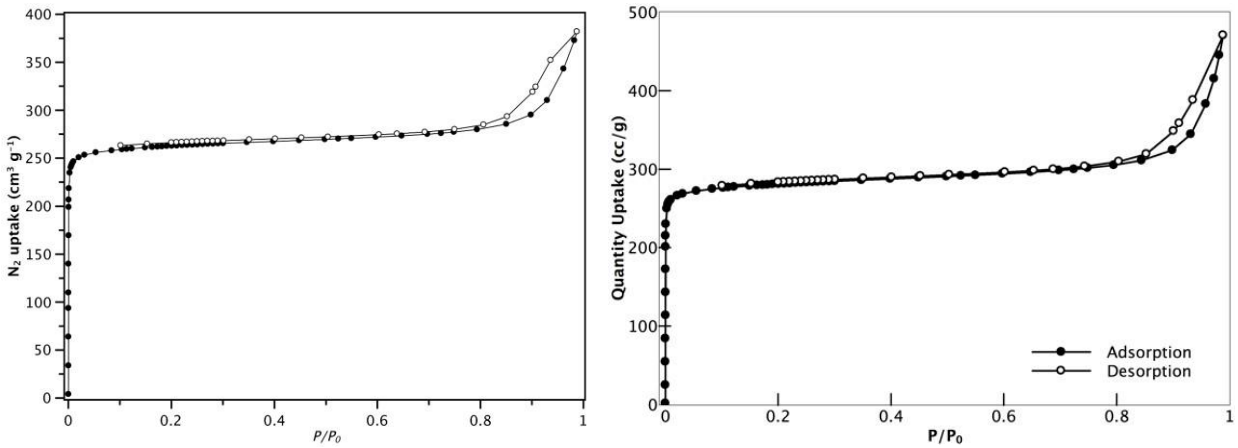

Figure S27. Isotherm curves for Zn-MOF-74 samples prepared by LAG with DMF.

13. Appendix 3. Investigation of BINOL-3,3′-dicarboxylate as a ligand for the formation of extended coordination-based structures

13.01 Preface

The work in this appendix deviates somewhat from the primary theme of this Thesis in that it does not center around the monitoring mechanochemical reactions. Having developed the mechanochemical syntheses of reported MOFs, we wished to extend our experience from synthesizing known frameworks to the development of novel frameworks. BINOL-dicarboxylates were explored with the ultimate goal of assembling chiral, porous, fluorescent materials. This chapter describes the resulting synthesis of several fluorescent coordination polymers, which provided the basis for on-going investigations into the synthesis of novel fluorescent, porous, and potentially chiral metal organic frameworks. This chapter is published as: Patrick A. Julien, Jan-Constantin Christopherson, Hatem M. Titi, Robin D. Rogers, Tomislav Friščić. *Supramolecular Chemistry,* 2018, **30**, 488-503. All reported compounds were synthesized and characterized by P. A. Julien. Crystallographic data collection was performed by P. A. Julien and Hatem Titi. Crystallographic structure determination and subsequent analysis was performed by Hatem Titi and T. Friščić.

13.02 Abstract

We provide a structural study of the ability of BINOL-3,3′-dicarboxylate, an inexpensive and readily accessible 1,1′-binaphthol-based ligand, to form extended self-assembled coordination polymers and frameworks in combination with divalent zinc and copper ions. While the structural diversity of herein described materials illustrates the untapped potential of the BINOL-3,3′-dicarboxylate in forming coordination polymer structures, we also provide the first example of an open two-dimensional framework established using this ligand as the only anionic, metal-bridging constituent.

13.03 Introduction

Metal-organic frameworks (MOFs) have emerged as promising materials for a wide variety of applications such as gas storage and separations, sensors, or solid heterogeneous catalysts, due to their open channels, uniform catalytic sites, and the ability to incorporate functionalized and or chiral organic linkers[1]. The often highly crystalline nature of these materials can be used to provide important structural insights about complex guest molecules and enables the development of design strategies for better catalytic activity and selectivity[2]. In the context of developing MOFs based on chiral linkers, a particularly valuable unit is the 1,1′-binaphthol (BINOL) fragment. Originally developed as a ligand for the synthesis of chiral catalysts in the form of discrete coordination complexes or organic molecules,[3,4] the BINOL unit has been utilized by several groups in generating extended coordination structures, such as one-dimensional (1-D) coordination polymers, two-dimensional (2-D) and three-dimensional (3-D) frameworks, as well as cage-like structures[5–10]. Specifically, a search of the Cambridge Structural Database (CSD)[11] revealed 177 extended coordination-based structures involving a non-constrained 2,2′-binaphthyl unit. In case of BINOL-based ligands, such extended structures have typically been enabled through the introduction of functionalities capable of coordinating to metal ions in the 4,4′- or 6,6′-positions of the BINOL core. **Error! Reference source not found.**(a) depicts some of the more popular B INOL-based ligands[5–10], based on a CSD search, that have been developed for such purposes.

The BINOL-based building blocks are particularly interesting in generating catalytically-active coordination polymers and MOFs, due to the ability to combine their axial chirality, described by the angle χ between the 1,1′-connected planes of naphthalene rings, with luminescent properties and the ability to exploit the hydroxyl moieties in the 2,2′-positions for attaching acidic catalysts, in the form of Lewis acids or phosphoric acid. [3, 4, 12] Prominent examples of this strategy include lanthanide BINOL-phosphonates[13] utilized for cyanosilylation of aldehydes and ring opening of *meso*-carboxylic anhydrides, a pyridine-functionalized BINOL and cadmium coordination polymer,[14] and an isoreticular

series of BINOL-based frameworks,[15] which both catalyse the addition of diethylzinc to aldehydes forming secondary alcohols in high enantiomeric excess.

Here, we address the capacity of 1,1′-bi-2-naphthol-3,3′-dicarboxylic acid (**H_4bna**, **Error! Reference source not found.**(b)) for the formation of extended coordination structures based on zinc(II) and copper(II) ions. Our study is focused on **H_4bna** as a building block for extended coordination-based structures, due to the presence of carboxylic acid moieties in the 3,3′-positions, and because it is readily accessible, which is related to the ease and low cost of synthesis. Consequently, **H_4bna** can be considered a simple, readily available alternative to more complex or costly BINOL derivatives, with carboxylate groups placed in positions that can both give rise to extended structures, and potentially even be exploited as steric bulk for achieving high enantioselectivity in diverse reactions. The selection of zinc and copper as preferred metal centres in the herein described investigation of extended coordination structures based on **H_4bna** is based on the search of CSD that demonstrated that these metal ions, which are highly popular in the synthesis of MOFs, are significantly less explored compared to cadmium(II) and manganese(II) ions.

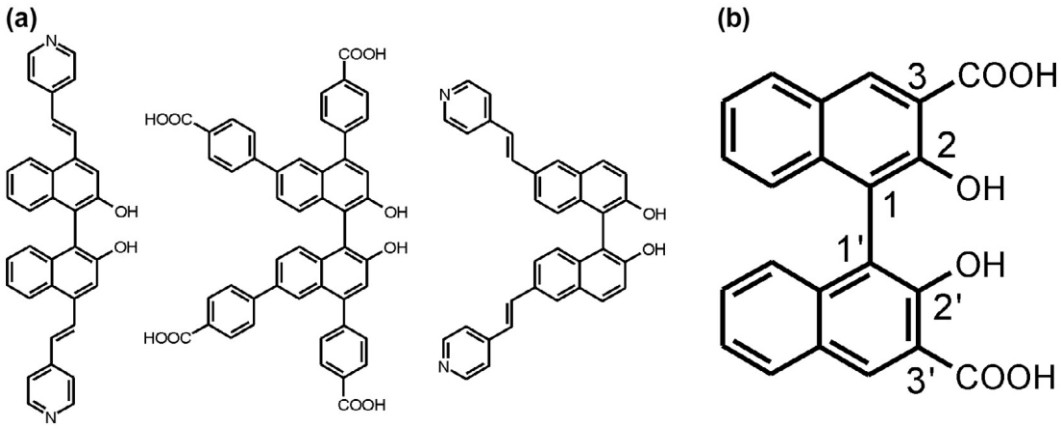

*Figure 101. Commonly used functionalized BINOL-based molecular components and (b) a partially numbered schematic of a molecule of **H_4bna**.*

In particular, our CSD survey revealed a total 177 crystal structures based on the 1,1′-binaphthyl fragment, of which 21 structures involve carboxylate ligands derived from **H_4bna**. These encompass a total of eight structures of Cd^{2+} (CSD codes AMIMUE,

ARESIZ, ARESOF, IXADIU, PICJUI, PICKAP, REKZEN and REKZIR),[16–20] five structures involving Mn^{2+} (CSD codes: HAKFOQ, HAKFOQ01, HAKFOQ02, QOHQOV and QOHQUB),[21–23] two structures for each of the metal ions Zn^{2+} (CSD codes: ARESUL and DUPRAI) (*17*), In^{3+} (CSD codes: VUXHEC and VUXHIG)[24] and Cu^{2+} (CSD codes: ZIRJUH and ZIRKAO) as well as one structure for each of the metal ions Co^{2+} (CSD code CIJPIW)[22] and Ni^{2+} (CSD code CIJPAO)[22]. With our interest to demonstrate the ability of **H_4bna**-based ligands to act as the principal building blocks of framework structures, we further explored this structural data-set for systems, in which the **H_4bna**-derived ligand is the only anionic and metal-bridging component. Overall, there are only 14 such structures, which are all derived from the anionic **H_2bna^{2-}** unit, obtained by deprotonation of the two carboxylic acid moieties of **H_4bna**. Of these structures, we were surprised to find that the majority are based on Cd^{2+} (four structures) and Mn^{2+} (five structures), whereas Zn^{2+} and Cu^{2+}, i.e. the metal ions that are highly popular in the design of MOFs, are represented with only one and two structures, respectively. Consequently, we decided to further explore the formation of coordination compounds of **H_4bna** using zinc- and copper-based metal nodes.

13.04 Experimental section

All chemicals were purchased from Sigma Aldrich and used without further purification. All solvents were ACS reagent grade, purchased from ACP Chemicals Inc. Fourier-transform infrared attenuated total reflectance (FTIR-ATR) spectra were collected on a Bruker Vertex 70 equipped with a PLATINUM diamond ATR unit. Nuclear magnetic resonance (NMR) spectra were collected on a Bruker 500 MHz AVIIIHD 500 spectrometer in d_6-DMSO purchased from Cambridge Isotope Laboratories. Racemic **H_4bna** was synthesised according to the literature procedure from 3-hydroxy-2-naphthoic acid,[25] and verified against literature reported infrared, ^{1}H- and ^{13}C-NMR spectra.[26] Thermogravimetric analysis (TGA) was performed using a TGA5500 (TA instruments Ltd, Delaware, USA) thermobalance. All measurements were done under air atmosphere, in which the samples (*ca*. 1–3 mg) were heated to 500 or 600 °C, at a heating rate of 10 °C min^{-1}.

Fluorescence spectra were measured on a Biotek Synergy 2 multi-mode microplate reader using clear polystyrene 96-well microplates. Fluorescence images were acquired on a HORIBA Jovin Yvon Dynamyc microscope equipped with a Lumenera INFINITY 3 CCD Camera and an X-Cite® Series 120Q excitation source by Excelitas Technologies. Microscope images were collected on a Leica DM2500 equipped with a Lumenera INFINITY 1 CCD Camera.

Powder X-ray diffraction (PXRD) data was collected on a Bruker D8 Advance equipped with a Lynxeye linear position sensitive detector (Bruker AXS, Madison, WI), using Ni-filtered Cu*K*α radiation. Due to the small amount of each sample available, neat samples were smeared directly onto the silicon wafer of a proprietary low-background sample holder.

(a) Synthesis of compounds 1–5 Compounds 1a and 1b in a mixture

4-aminopyridine (6 mg, 0.07 mmol) and **H_4bna** (25 mg, 0.07 mmol) were dissolved in 4 mL of *N,N*dimethylformamide (DMF), and zinc(II) nitrate hexahydrate (20 mg, 0.07 mmol) was dissolved in 1 mL distiled water. These solutions were mixed together in a test tube and heated at 50 °C for two days. Upon cooling to room temperature, the reaction mixture yielded colourless crystals (17 mg). Inspection of the crystals using a microscope revealed that the sample is a mixture of two types of crystals (Figure S1), of which one set (**1a**) rapidly cracks and becomes opaque, forming a material that is crystalline to PXRD and emits a green fluorescence under ultraviolet (UV) light. The other type of crystals (**1b**) was stable in air, emitting a blue fluorescence. Manual separation provided approximately 2 mg of **1b**.

(b) Compound 1b

The selective formation of compound **1b** was achieved by dissolving 4-aminopyridine (6 mg, 0.07 mmol) and **H_4bna** (25 mg, 0.07 mmol) in 2 mL of DMF, while an equimolar amount of zinc(II) nitrate hexahydrate (20 mg, 0.07 mmol) was dissolved in 2 mL distilled water. The solutions were mixed together in a test tube and heated at 55 °C for two days. Upon cooling to room temperature, filtration of the reaction mixture yielded colourless

crystals (4.2 mg) in a yield of 9.4%. TGA of the crystals in air gave a residue of 12.3%, consistent with expected ZnO residue of 12.8% (Figure S3).

(c) Compound 2

H_4bna (27 mg, 0.072 mmol) was dissolved in 4 mL of DMF, and copper(II) nitrate trihydrate (17 mg, 0.072 mmol) was dissolved in 1 mL of distiled water. The solutions were mixed together in a test tube and pyridine (6 µL, 0.075 mmol) added. The respective stoichiometric ratios of **H_4bna**, the copper(II) source and pyridine in the reaction mixture were 1:1:1. The tube was mixed and heated to 50 °C for two days and allowed to cool to room temperature, yielding blue block crystals along with a green powder (see Figure S4). In two separate experiments, the weight of the crystals after separation from the powdered material was 10 mg (18% yield) and 19 mg (35% yield). After manual separation from the powder, TGA of the crystals in air gave a residue of 12.1% (Figure S5). The difference from the residue of 10.5% calculated for degradation of **2** to CuO is most likely due to incomplete separation of crystals from the powder by-product.

(d) Compound 3

Copper(II) nitrate trihydrate (10 mg, 0.042 mmol) and **H_4bna** (31 mg, 0.084 mmol) were dissolved in 4 mL DMF and 1 mL distiled water, respectively. These solutions were mixed together in a test tube and 7 µL of pyridine (0.085 mmol) was added. The respective stoichiometric ratios of **H_4bna**, the copper(II) source and pyridine in the reaction mixture were 1:2:2. The solution was heated to 50 °C for two days and subsequently allowed to cool to room temperature, yielding blue crystals (**3**) along with a green powdered product (see Figure S6). After manual separation from the powder, the weight of the crystals was 3 mg (11% yield). TGA of the crystals in air gave a residue of 11.5%, consistent with a residue of 11.8% calculated for decomposition of **3** into CuO (Figure S7).

(e) Compound 4

4-aminopyridine (15 mg, 0.162 mmol) and **H_4bna** (60 mg, 0.162 mmol) were dissolved in 4 mL DMF, and zinc(II) nitrate hexahydrate (24 mg, 0.081 mmol) was dissolved in 1

mL distiled water. These solutions were mixed together in a test tube and heated to 100 °C for two days, yielding 10 mg of colourless crystals (**4**, 11% yield, Figure S8). TGA of the crystals in air gave a residue of 7.4%, consistent with expected ZnO residue of 7.1% (Figure S9).

(f) Compound 5

This material was serendipitously obtained in the form of several single crystals upon attempting to obtain a mixed-ligand metal-organic material involving *N*,*N′-bis*(4-pyridyl) pyromellitic diimide and **H$_4$bna** ligands. Specifically, *N*,*N′bis*(4-pyridyl)pyromellitic diimide (26 mg, 0.070 mmol) and **H$_4$bna** (26 mg, 0.070 mmol) were dissolved in 4 mL of N,N-dimethylformamide, while copper(II) nitrate trihydrate (17 mg, 0.070 mmol) was dissolved in 1 mL of distilled water. These solutions were mixed together in a test tube, heated to 100 °C for two days, yielding upon cooling a purple powder and several blue crystals of **5** (Figure S10). X-ray powder diffraction of the purple precipitate did not show the presence of **5** and we suspect that 4-aminopyridine is a result of the thermal hydrolysis of *N*,*N′-bis*(4pyridyl)pyromellitic diimide under the reaction conditions. Attempts to reproduce the synthesis of **5** have so far not been successful.

The formation of coordination complexes with **H$_4$bna** could be discerned using FTIR-ATR spectroscopy, notably by the disappearance of the absorption band of the reactant **H$_4$bna** at *ca.* 1450 cm^{-1}, which is tentatively assigned to symmetrical stretching of the carboxylic acid group (**Error! Reference source not found.**).[27]

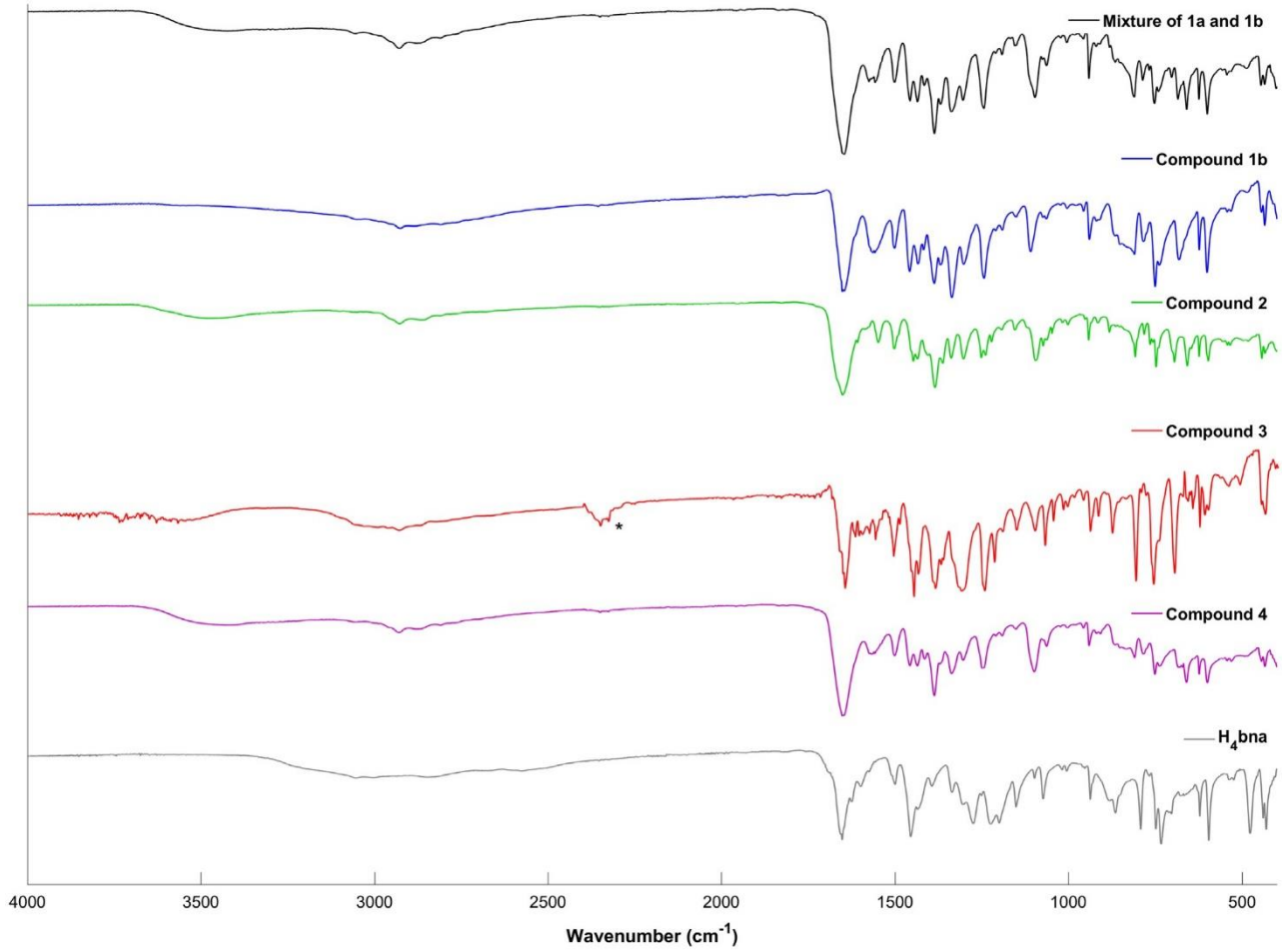

*Figure 102. Comparison of FTIR-ATR spectra for (top to bottom): compounds **1a** and **1b** in a mixture, compound **1b** only, compound **2**, compound **3**, compound **4** and the reactant **H_4bna**. the signal of atmospheric co_2 signal in the spectrum of **3** is designated with the symbol '*'.*

(g) Single crystal X-ray diffraction and structure solution

Single crystal X-ray diffraction data for all compounds were collected on a Bruker D8 Advance diffractometer (Bruker-AXS, Madison, WI, USA) with a Photon 100 CMOS area detector and an IμS microfocus X-ray source (Bruker AXS). X-ray diffraction experiments on single crystals of compounds **1a**, **3**, **4**, and **5** were conducted using Mo*K*α radiation, while Cu*K*α radiation was used for compounds **1b** and **2**. Single crystals were often found to readily lose solvent upon exposure to air, and were coated with Paratone oil (Hampton Research, Aliso Viejo, CA, USA) during X-ray single crystal data collection. All structures were determined at room temperature, except for compound **5** that was cooled to 100 K under a cold stream of nitrogen using an Oxford Cryostream cryostat (Oxford

Cryosystems, Oxford, UK). Unit cell determination, data collection, data reduction, and correction for absorption were all conducted using the Apex2 software suite (Bruker AXS). Crystal structures were solved by an iterative dual space approach as implemented in SHELXT.[28] Non-hydrogen atoms were located from the difference map and refined anisotropically. Hydrogen atoms bonded to carbon atoms were placed in calculated positions. All hydrogen atom coordinates and thermal parameters were constrained to ride on the carrier atoms. Anomalous thermal ellipsoids for some of the DMF molecules were found in all structures, possibly due to unresolvable disorder. In compounds **1** and **3** the disordered DMF molecules were successfully modelled, as was the disordered pyridine ligand coordinated to the copper(II) centre in compound **3**. An overview of crystallographic data for all compounds is provided in Table 1, and full crystallographic structure data has been deposited with the Cambridge Crystallographic Data Centre under CCDC deposition numbers 1583059 (**1a**), 1811878 (**1b**), 1583060 (**2**), 1583061 (**3**), 1583062 (**4**) and 1583063 (**5**).

13.05 Results and discussion

(a) Coordination polymers with Zn^{2+}

Compounds **1a** and **1b** were observed to form concomitantly from reaction of equimolar amounts of zinc nitrate, **H_4bna** and 4-aminopyridine in a 4:1 mixture of DMF and water as solvent. Crystals of the two compounds could readily be distinguished under ultraviolet (UV) light using a microscope (Figure S1). Upon short exposure to air, however, crystals of **1a** rapidly became opaque and crumbled into a powder emitting a green fluorescence (**Error! Reference source not found.**(a) and (b)), which largely l imited their analysis to single crystal X-ray diffraction. In contrast, crystals of **1b** were stable in air for extended periods of time and could be manually separated.

The PXRD pattern of the reaction product recorded immediately after separation from the mother liquor matched well to a combination of diffraction patterns calculated for the herein reported structures of **1a** and **1b** (**Error! Reference source not found.**). TGA of t he crude reaction product was consistent with the presence of **1a** and **1b** (Figure S2).

13. Appendix 3. Investigation of BINOL-3,3′-dicarboxylate as a ligand for the formation of extended coordination-based structures

Single crystal X-ray structure analysis of **1a** revealed a 1-D coordination polymer structure, with the composition Zn(**H_2bna**)$(DMF)_2$·2DMF. The structure consists of parallel coordination polymer chains that run in the crystallographic *b*-direction, parallel to the crystallographic 2_1 screw axis.

Table 2. General and crystallographic data for herein structurally characterised compounds.

Compound	**1a**	**1b**	**2**	**3**	**4**	**5**
Formula	$C_{65}H_{73}N_7O_{19}Zn_2$	$C_{59}H_{63}N_5O_{19}Zn_2$	$C_{114}H_{111}Cu_3N_{12}O_{27}$	$C_{70}H_{59}Cu_2N_6O_{15}$	$C_{60}H_{52}N_6O_{14}Zn$	$C_{57}H_{45}CuN_6O_{13}$
M_r	1387.04	1276.88	2271.76	1351.31	1146.44	1085.53
radiation	mo*K*α	cu*K*α	cu*K*α	mo*K*α	mo*K*α	mo*K*α
T (K)	298(2)	298(2)	298(2)	298(2)	298(2)	100(2)
crystal system	monoclinic	orthorhombic	trigonal	orthorhombic	monoclinic	monoclinic
Space group	$P2_1$	$Pca2_1$	$P3_221$	$C222_1$	$C2/c$	$P2_1/c$
a (Å)	9.0750(10)	12.1236(4)	8.9898(5)	12.129(6)	20.724(3)	13.189(3)
b (Å)	17.626(2)	24.1890(8)	8.9898(5)	13.152(6)	11.1436(14)	18.059(4)
c (Å)	11.6970(14)	21.3972(7)	39.636(2)	20.570(9)	24.187(4)	11.436(2)
α (°)	90	90	90	90	90	90
β (°)	102.484(4)	90	90	90	91.031(6)	102.319(5)
γ (°)	90	90	120	90	90	90
V (Å^3)	1826.8(4)	6274.9(4)	2774.1(3)	3282(3)	5584.8(14)	2661.1(9)
Z	1	4	1	2	4	2
ρ_c (g cm^{-3})	1.261	1.352	1.360	1.368	1.364	1.355
μ (mm^{-1})	0.726	1.566	1.334	0.720	0.512	0.481
F(000)	724.0	2656.0	1182.0	1398.0	2384.0	1124.0
2*θ*-range for data collection (°)	6.52–63.002	8.26–139.35	6.69–130.414	4.98–53.002	5.132–52.82	4.844–48.59
reflections collected	57,876	54,251	26,360	24,793	18,022	58,972
independent reflections	11,977	11,437	3133	3405	5686	4300
Data/restraints/parameters	11,977/792/516	11,437/718/782	3133/37/243	3405/342/262	5686/31/368	4300/30/375
S	1.041	1.024	1.060	1.068	1.010	1.348
R_1 and wR_2 for $I \geq 2\sigma_I$	0.044, 0.106	0.058, 0.136	0.051, 0.153	0.068, 0.154	0.081, 0.180	0.069, 0.183
R_1 and wR_2 for $I \geq 2\sigma_I$	0.070, 0.117	0.098, 0.155	0.052, 0.154	0.097, 0.168	0.166, 0.220	0.100, 0.194
largest diff. peak/hole (e Å^{-3})	0.47/−0.23	0.90/−0.45	1.19/−0.48	0.62/−0.43	0.61/−0.50	1.14/−0.42
Flack parameter	0.026(3)	0.28(4)	0.024(7)	0.041(13)	–	–

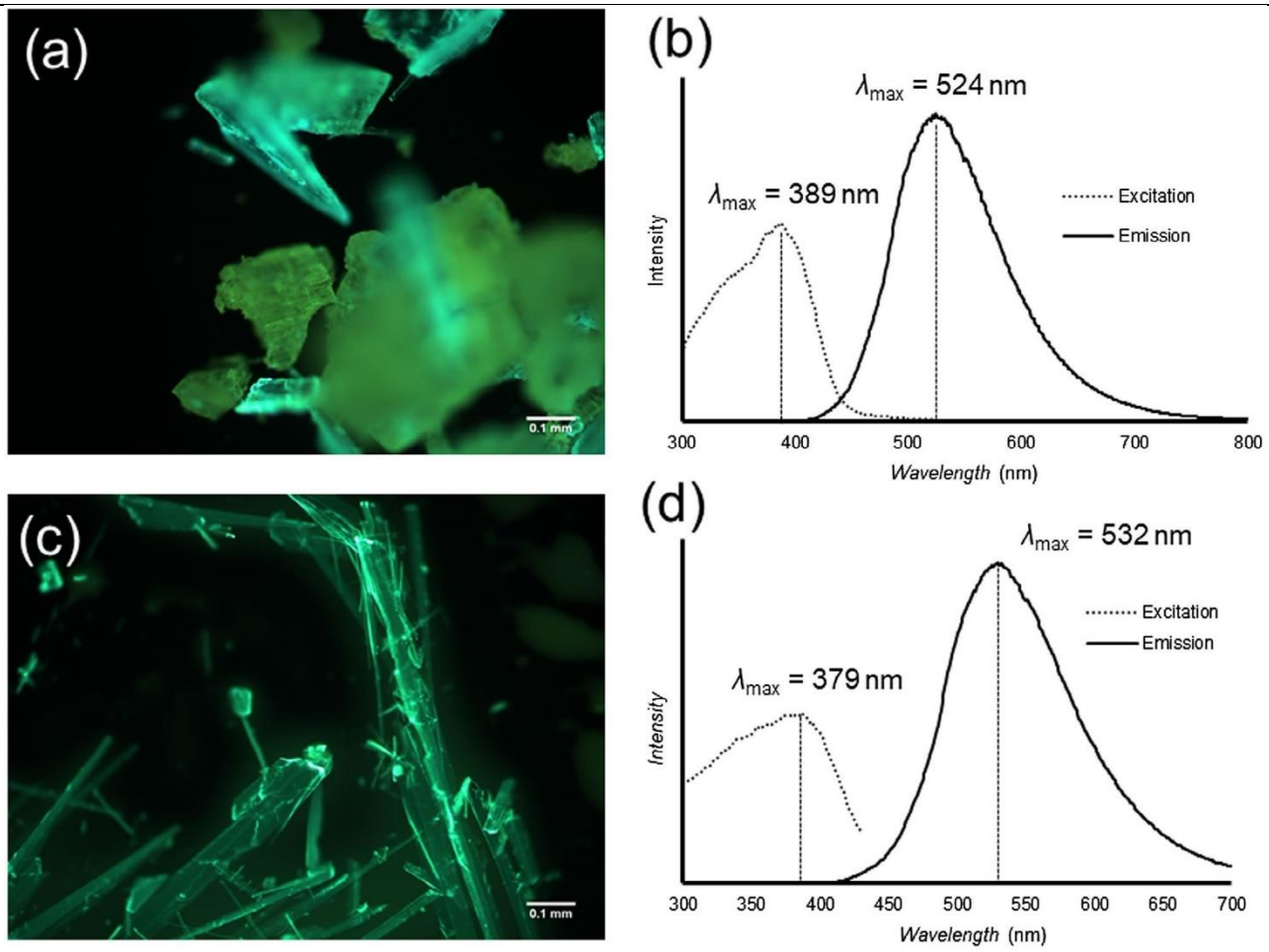

*Figure 103. Fluorescence emission of the products from the synthesis of compounds **1a** and **1b**. (a) Optical microscopy images recorded under ultraviolet (UV) light for crude reaction mixture containing **1a** and **1b** after short exposure to air and (b) corresponding fluorescence emission (solid line) and excitation (dotted line) spectra. (c) Separately prepared crystals of **1b** and (d) corresponding fluorescence emission (solid line) and excitation (dotted line) spectra. Fluorescence emission spectra were recorded upon excitation with 384 nm radiation, while excitation spectra were measured at 550 nm.*

Each coordination polymer chain in **1a** consists of tetrahedrally-coordinated zinc ions that are bridged by **H_2bna^{2-}** ligands (**Error! Reference source not found.**(a)). Specifically, each z inc ion is coordinated by two oxygen atoms belonging to two DMF molecules (Zn–O distances 1.970(2) and 2.038(3) Å), and two symmetrically inequivalent carboxylate moieties from adjacent **H_2bna^{2-}** ligands, with Zn–O distances of 1.952(2) and 1.994(2) Å. At the same time, the second oxygen atom of the latter carboxylate group forms a short contact to the Zn^{2+} ion, at a distance of 2.528(3) Å. Besides the DMF molecules that are directly coordinated to metal ions, the crystal structure of **1a** also contains two crystallographically distinct DMF molecules that occupy channels formed between parallel chains of Zn(**H_2bna**) $(DMF)_2$ (**Error! Reference**

source not found.(b)). These guest molecules are situated in planes parallel to the (1 0 1) family of crystallographic planes and are found in the immediate vicinity of the coordinated DMF molecules. As a result, the structure of **1a** can be interpreted as consisting of alternating layers occupied largely by the of metal-organic Zn(**H_2bna**) polymer chains and layers occupied mostly by coordinated and non-coordinated DMF molecules (**Error! Reference source not found.**(c)).

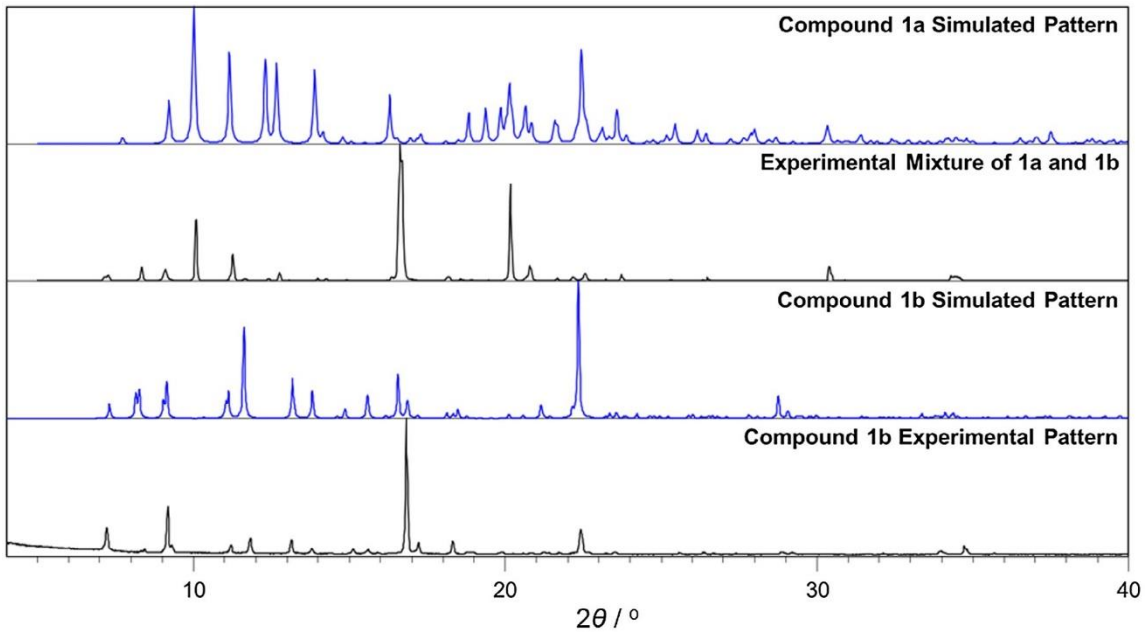

*Figure 104. Comparison of PXRD patterns for the synthesis of compounds **1a** and **1b** (top-to-bottom): simulated for herein reported structure of **1a**; recorded for a mixture of **1a** and **1b** crystals obtained using a 4:1 mixture of DMF and water as solvent; simulated for herein reported structure of **1b** and recorded for a sample of **1b** crystals synthesised from a 1:1 mixture of DMF and water as a solvent. The experimental diffractograms are likely to exhibit preferred orientation effects, as they have been recorded on a small sample of gently crushed crystals, from which the single crystal for crystal structure determination was also obtained.*

Crystallographic analysis by single crystal X-ray diffraction reveals that **1b**, while also a 1-D coordination polymer, is structurally very different from **1a**. In contrast to structurally uniform tetrahedral zinc atoms found in **1a**, each polymer chain of **1b** consists of alternating chemically and crystallographically inequivalent zinc atoms coordinated in octahedral or trigonal bipyramidal fashion, bridged by **H_2bna^{2-}** ligands (**Error! Reference source not found.**). The c oordination environments of the two types of zinc nodes are profoundly different. The coordination environment of the octahedral zinc nodes consists of two oxygen atoms from

carboxylate groups of **H_2bna^{2-}** units acting as monodentate ligands, two oxygen atoms of two DMF molecules and two oxygen atoms

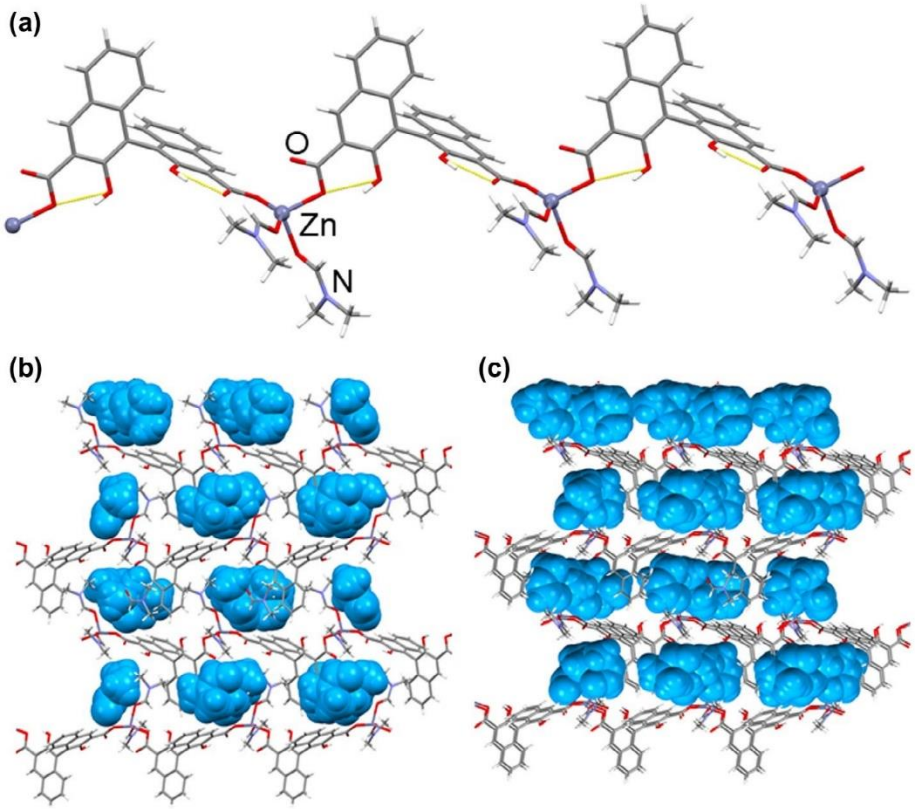

*Figure 105. Different views of the crystal structure of **1**: (a) a single chain of Zn(**H_2bna**)$(DMF)_2$ with O–H···O hydrogen bonds and the short carboxylate O···Zn shown using dotted yellow lines; (b) view of the crystal structure parallel to the crystallographic b-axis, with guest DMF molecules shown using a space-filling model and (c) identical view of the structure as in (b), but with both coordinated and non-coordinated guest DMF molecules shown using a space-filling model, illustrating the formation of metal-organic and DMF occupied layers.*

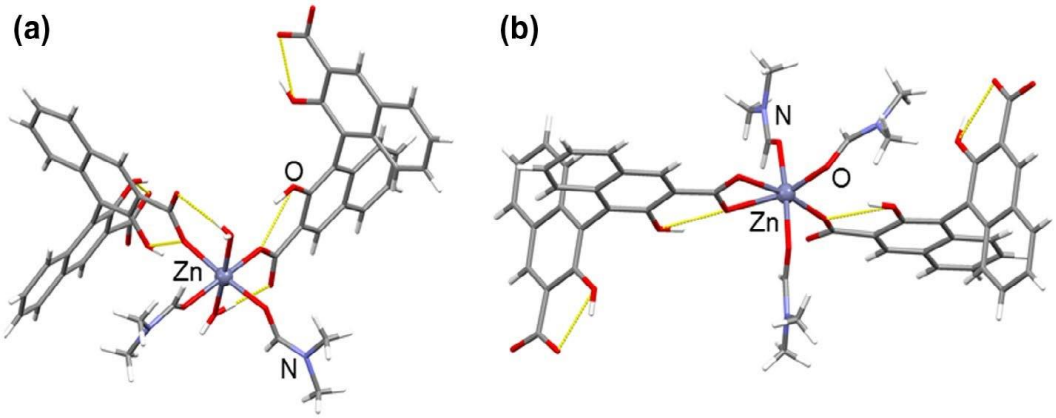

*Figure 106. Fragments of a coordination polymer chain in **1b**, illustrating: (a) an octahedrally-coordinated and (b) a trigonal bipyramidal zinc node. Zinc atoms are shown in ball-and-stick mode, and hydrogen bonds as yellow dotted lines.*

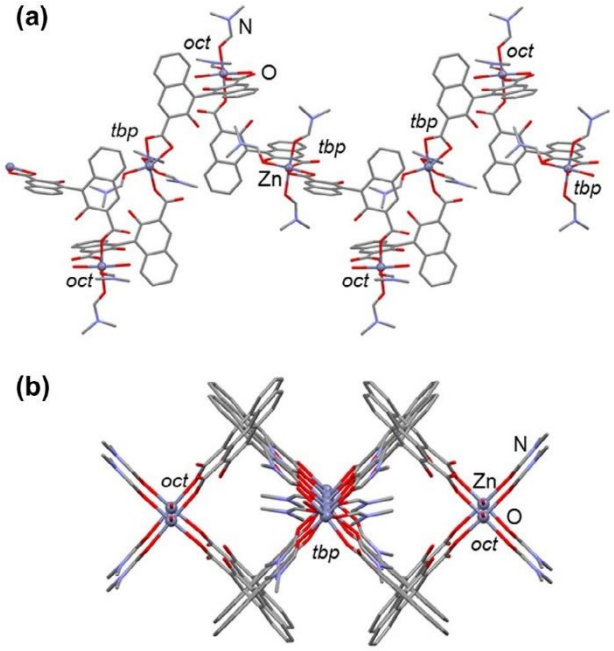

*Figure 107. A single coordination polymer chain of **1b**, viewed: (a) side-on and (b) parallel to the crystallographic c-axis, with octahedral (oct) and trigonal bipyramidal (tbp) nodes indicated. For clarity, hydrogen atoms have been omitted.*

belonging to coordinated water molecules. The water molecule ligands adopt a mutually *trans*-arrangement, while the two oxygen atoms of the **H_2bna^{2-}** ligands, as well as the two coordinated DMF molecules are mutually *cis*-oriented. The zinc nodes adopting a distorted trigonal-bipyramidal arrangement of ligands are coordinated by oxygen atoms of three DMF molecules in the equatorial plane, whereas the axial positions are occupied by two carboxylate groups of **H_2bna^{2-}** moieties. One of the carboxylate groups binds to the zinc atom through a single oxygen atom, with a Zn–O distance of 2.041(5) Å, while the other one binds to the metal ion through both oxygen atoms, with Zn–O bond lengths of 2.185(5) and 2.230(5) Å. Due to the presence of two differently coordinated metal centres, the formula of **1b** is best given as $Zn(DMF)_3Zn(DMF)_2(H_2O)_2(\mathbf{H_2bna})_2$.

The coordination polymer chains of **1b** (**Error! Reference source not found.**(a)) p ropagate along the 2_1-screw axis and adopt a helical form, in which the five-coordinate zinc nodes are situated within the helix, and the octahedral ones are on the periphery (**Error! Reference source not found.**(b)). The adjacent chains are associated into layers p arallel to the crystallographic *ac*-plane through O–H···O hydrogen bonds, in which the

donors are water molecules coordinated to octahedral zinc atoms of one chain, while the acceptors are oxygen atoms of DMF molecules and carboxylate ligands coordinated to five-coordinate zinc atoms in the neighbouring chains.

As compound **1b** contains additional water ligands, whereas **1a** is a DMF solvate, we explored the coordination polymer synthesis in reaction media containing a larger fraction of water. This exploration led to a selective synthesis of crystals of **1b** by using a 1:1 (*v*/*v*) mixture of DMF and water as the solvent. The separately prepared sample of **1b** consisted of needle-like crystals that were characterised by fluorescence emission spectroscopy (**Error! Reference source not found.**(c) and (d)), PXRD (**Error! Reference source not found.**) and (TGA, Figure S3). The solid-state fluorescence profile of **1b**, obtained upon excitation with 384 nm radiation, is characterised by an emission maximum at a wavelength of 532 nm (**Error! Reference source not found.**(c) and (d)).

The structures of **1a** and **1b** are significantly different from that of the previously published structure(*29*) of the hydrated Zn(**H$_2$bna**) polymer, Zn(**H$_2$bna**)(H$_2$O)$_2$, which was obtained by hydrothermal reaction at 130 °C of zinc(II) acetate, **H$_4$bna** and NaOH in respective stoichiometric ratios 4:1:2. The structure of Zn(**H$_2$bna**)(H$_2$O)$_2$ consists of dimeric ring-shaped Zn$_2$(**H$_2$bna**)$_2$ units that are further assembled into 1-D chains through 8-membered rings formed by two carboxylate groups and two Zn^{2+} ions adopting a trigonal bipyramidal coordination (**Error! Reference source not found.**, CSD code DUPRAI).

An important intramolecular feature of the **H$_2$bna^{2-}** ligand is the angle between naphthalene moieties (χ), which affects the relative positions of metal-binding carboxylate moieties in the 3- and 3′-positions of the ligand

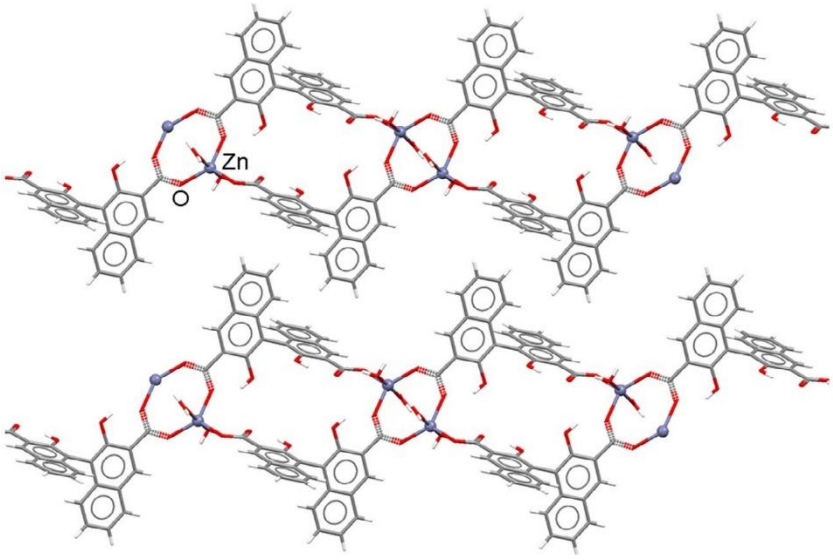

*Figure 108. View of the crystal structure of the previously published coordination polymer Zn(**H₂bna**)(H₂O)₂ (CSD code DUPRAI), demonstrating the formation of 1-D chains.*

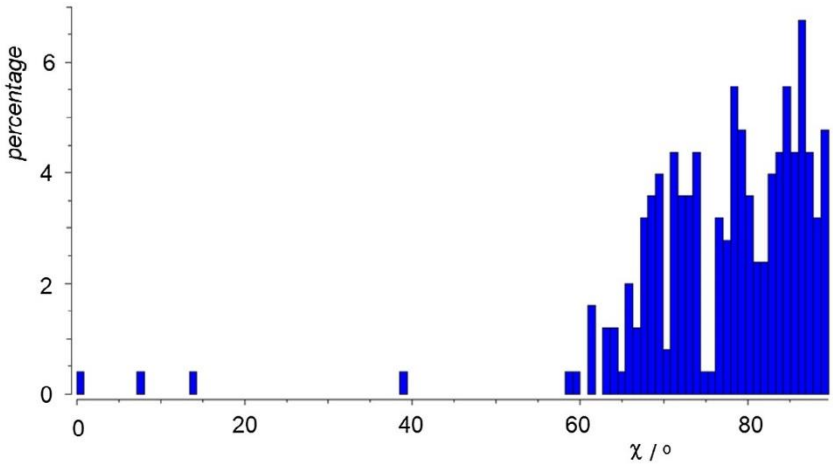

Figure 109. Distribution of the χ-angle for the 177 crystal structures of coordination polymers involving 1,1'-binaphthyl-based ligands found in the CSD[11].

and, therefore, may have a significant impact on the overall geometry of the resulting extended metal-organic structure. For **1a** and Zn(**H₂bna**)(H₂O)₂ the respective *χ* angles are almost identical: 82.0° and 80.9°. Compound **1b** contains two crystallographically inequivalent **H₂bna²⁻** units with slightly larger *χ* angles of 83.2° and 85.9°. Based on our survey of the CSD, both of these values are comparable to those found in structures of

coordination polymers involving 1,1′-binaphthyl-based ligands (**Error! Reference source not found.**).[11]

However, maybe the most important salient difference between herein reported **1a**, **1b** and previously described Zn(**H₂bna**)(H_2O)$_2$ is the fact that, despite using a racemic sample of **H₄bna**, both **1a** and **1b** crystallize in the non-centrosymmetric space groups $P2_1$ and $Pca2_1$. In contrast, Zn(**H₂bna**)(H_2O)$_2$ adopts the centrosymmetric space group $P2_1/c$. As the syntheses of **1a** and **1b** are conducted at a low temperature of 50°C and below, the interconversion of BINOL-based ligand enantiomers is not likely. This observation hints at the possibility that the mostly DMF-based environment favours the formation of a conglomerate, i.e. a mixture of equal amounts of left- and right-handed non-centrosymmetric coordination polymer structures, whereas a predominantly aqueous environment favours the formation of a centrosymmetric, racemic structure.[30]

(b) Coordination polymers with Cu^{2+}

Attempts to synthesise a coordination polymer of Cu^{2+} under reaction conditions analogous to those used for the formation of **1a** and **1b** have so far not been successful,

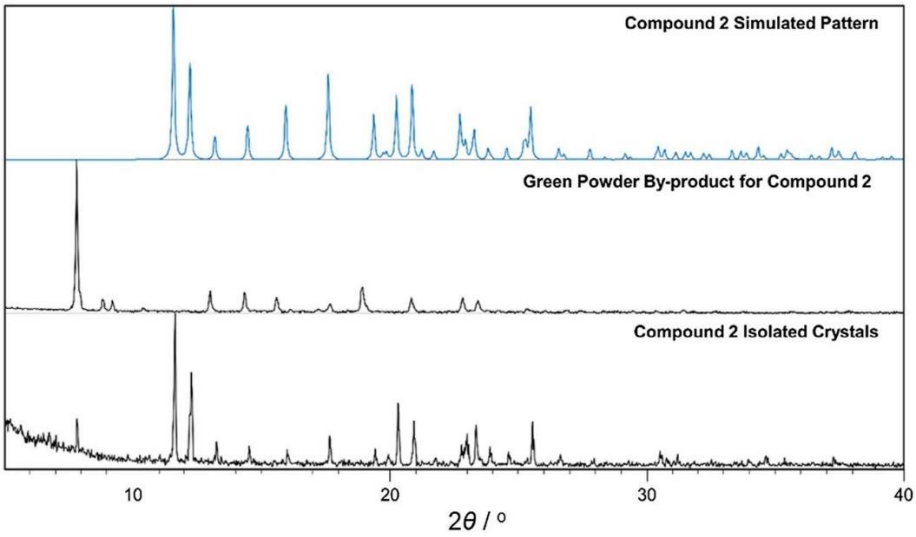

*Figure 110. Comparison of PXRD patterns for the synthesis of compound **2** (top to bottom): simulated pattern for herein reported structure of **2**; measured for the green powder by-product and measured for manually separated crystals of **2**. the diffractograms reveal the persistence of a small amount of the powder by-product in the manually separated sample of **2**.*

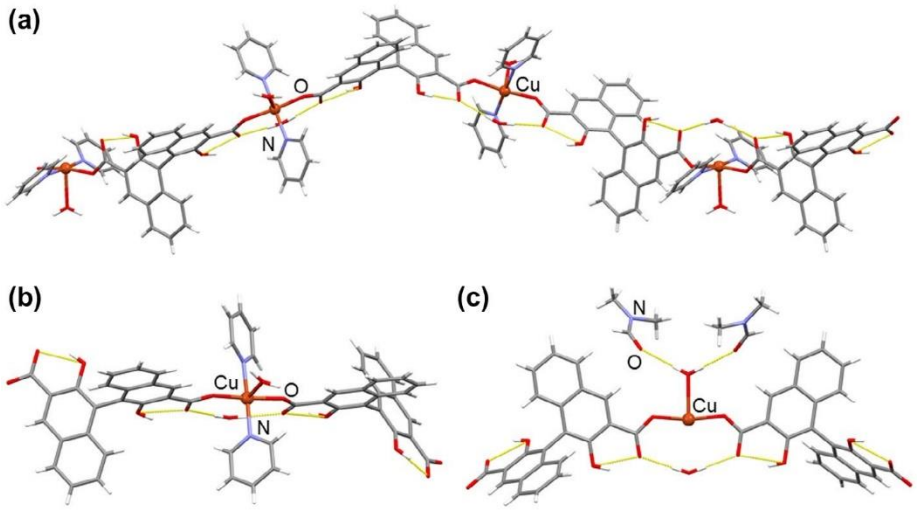

*Figure 111. Different view of the crystal structure of **2**: (a) a single chain of the coordination polymer [Cu(**H₂bna**)(pyridine)₂(H₂O)](H₂O)], with DMF molecules hydrogen bonded to the coordinated water molecules omitted for clarity; (b) the local environment of the copper(II) ion and (c) view of the $R_2^2(10)$ hydrogen- and coordination-bonded ring in the structure of **2**, with hydrogen bonds shown using dotted yellow lines.*

with reaction mixtures yielding no crystalline product. Consequently, we attempted the synthesis of coordination polymers in the presence of pyridine as a base. This procedure was explored under different reaction conditions, and crystalline materials were obtained when using a either 1:1 or a 1:2 stoichiometric ratio of precursors $Cu(NO_3)_2 \cdot 3H_2O$ and **H₄bna**. In particular, reaction of the two precursors in a 1:1 stoichiometric ratio led to blue crystals of compound **2** that were characterised by single crystal X-ray diffraction, along with a green powder as a by-product (Figure S4). The single crystals were established to be a solvated coordination polymer of composition [Cu(**H₂bna**)(pyridine)₂(H₂O)](H₂O)·2DMF whose structure at a temperature of 150 K was also reported by Tanaka and co-workers (CSD code ZIRJUH).[31] The green powder that also formed in the reaction has not yet been characterised but, according to PXRD analysis, is also crystalline (**Error! Reference source not found.**).

The herein determined structure of **2** at room temperature structure shows no major differences from the earlier report, consisting of 1-D coordination- and hydrogen-bonded chains of composition [Cu(**H₂bna**)(pyridine)₂(H₂O)](H₂O)·2DMF (**Error! Reference s ource not found.**(a)). The Cu^{2+} ions in each chain adopt a square pyramidal coordination

geometry, formed by two *trans*-arranged oxygen donor atoms from two different **H_2bna^{2-}** carboxylate ions (Cu–O distance 1.931(3) Å) and two nitrogen atoms of pyridine ligands (Cu–N distance 2.035(4) Å) in the equatorial positions. The apical coordination site of each Cu^{2+} ions is occupied by an oxygen atom of a coordinated water molecule at the Cu–O separation of 2.409(3) Å (**Error! Reference source not found.**(b)), to which two DMF molecules are attached through symmetry equivalent O–H···O hydrogen bonds (O···O distance 2.994(8) Å). Importantly, another water molecule is anchored opposite to the apical coordination site of the copper(II) ion *via* two symmetry equivalent O–H···O hydrogen bonds (O···O distance 2.806(7) Å) to carboxylate oxygen atoms that are not involved in Cu–O bonding, but are involved in the intramolecular S(6) O–H···O hydrogen-bonded rings[32] of the **H_2bna^{2-}** ligand (O···O distance 2.555(4) Å). This makes each Cu^{2+} ion a member of a planar ring encompassing a total of 10 atoms, and two O–H···O hydrogen bonds. Following the graph-set notation developed by Etter, this corresponds to a $R_2^2(10)$ ring motif (**Error! Reference source not found.**(c)) .[33] Overall, the coordination- and hydrogen-bonded chains in **2** adopt a helical shape, and run parallel to the threefold screw axis of the crystal structure, with a repeat distance of 39.6 Å.

Crystals of compound **3**, also blue in colour (Figure S6), were obtained under nominally identical reaction conditions as those that led to the formation of **2**, but using a respective 1:2 stoichiometric ratio of $Cu(NO_3)_2 \cdot 3H_2O$ and **H_4bna**. The crystals were obtained in a mixture with a powder that has not yet been structurally characterised but exhibited a different PXRD pattern from the crystals (**Error! Reference source not found.**).

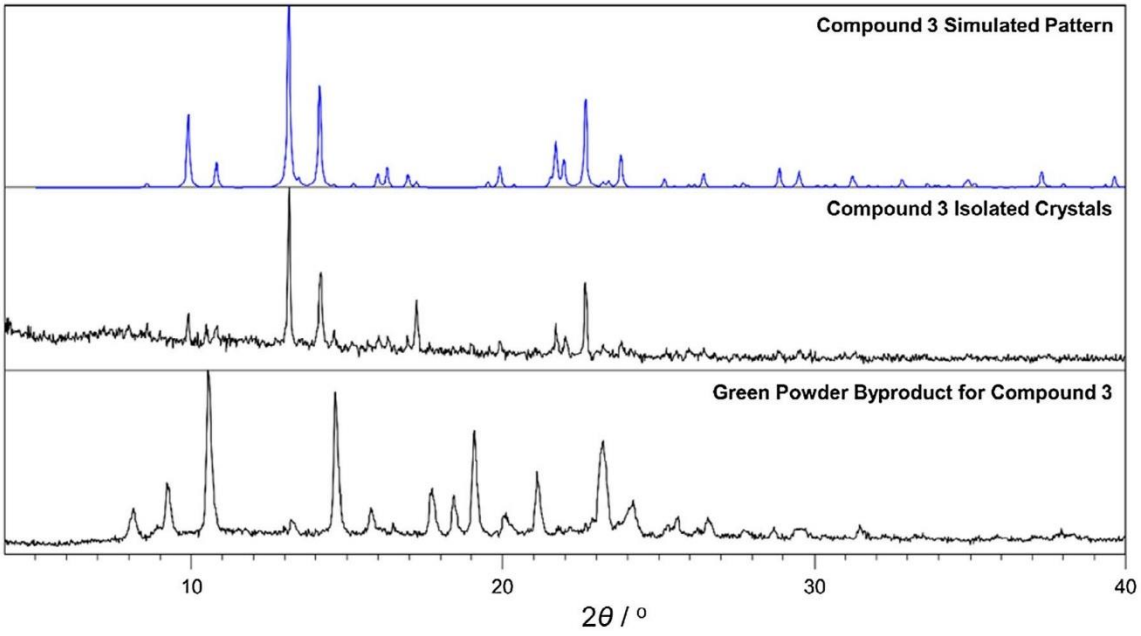

*Figure 112. Comparison of PXRD patterns for the synthesis of compound **3** (top to bottom): simulated pattern for herein reported structure of **3**; measured for manually separated crystals of **3** and measured for the green powder by-product of the reaction. The diffractograms reveal the persistence of a small amount of the powder by-product in the manually separated sample of **3**.*

Crystal structure analysis by single X-ray diffraction revealed that **3** should formally be considered a partially desolvated analogue of **2**, with the composition [Cu(**H$_2$bna**)(pyridine)$_2$(DMF)](H$_2$O). Like in **2**, the copper(II) ions in **3** are again positioned on a crystallographic mirror plane, adopting a square pyramidal coordination geometry, in which the equatorial plane is defined by a *trans*-arranged N_2O_2 set of donor atoms belonging to two symmetry equivalent carboxylate (Cu–O distance 1.956(5) Å) and two symmetry equivalent pyridine moieties (Cu–N distance 2.018(7) Å). However, the apical coordination position on each Cu^{2+} ion in **3** is occupied not by a water molecule, but by an oxygen atom of a DMF ligand disordered over the crystallographic mirror plane, with a Cu–O distance of 2.252(9) Å length (**Error! Reference source not found.**(a)). The c oordination- and hydrogen-bonded $R_2^2(10)$ ring motif observed in **2** is also retained in **3** (**Error! Reference source not found.**(b)), with a water molecule held to the metal-o rganic structure *via* two symmetrically equivalent O–H···O hydrogen bonds (O···O distance of

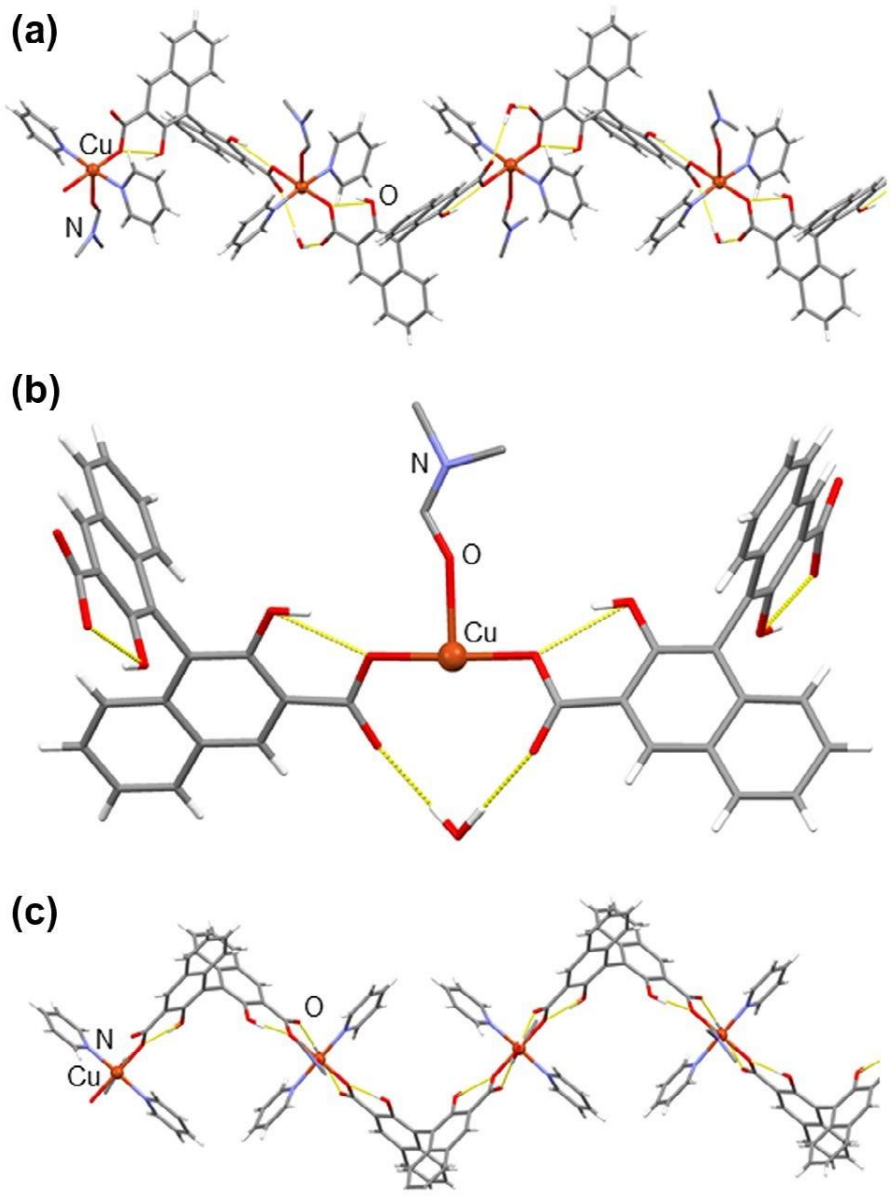

*Figure 113. Different view of the crystal structure of **3**: (a) a single chain of the supramolecular coordination polymer [Cu(**H₂bna**)(pyridine)₂(DMF)](H₂O); (b) view of the $R_2^2(10)$ hydrogen- and coordination-bonded ring in the structure of **2**, with hydrogen bonds shown using dotted yellow lines and (c) a different perspective of the [Cu(**H₂bna**)(pyridine)₂(DMF)](H₂O) supramolecular chain, illustrating its zigzag geometry.*

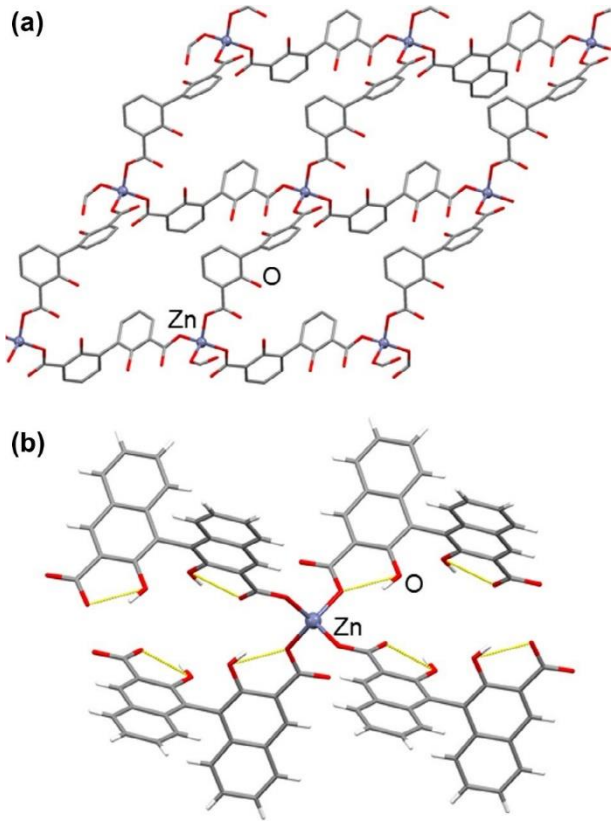

*Figure 114. Views of the crystal structure of compound **4**: (a) a view of a single sql-topology sheet of the anionic coordination polymer [Zn(**H₂bna**)₂]²⁻, with hydrogen atoms, apyH+ counterions, DMF guest molecules and terminal benzene moieties of each **H₂bna²⁻** ligand omitted for clarity and (b) the local coordination environment of a single Zn²⁺ ion in the structure of **4**.*

2.93(2) Å), but with significant structural differences: it is no longer planar, and the carboxylate oxygen atoms involved in the hydrogen bonds are no longer the same ones that are involved in the *intra*molecular *S*(6) hydrogen-bonded motifs in **H₂bna²⁻**. These structural differences also mean that the 3-hydroxy moieties of the **H₂bna²⁻** ligand are now placed on the same side of the $R_2^2(10)$ ring motif as the apical coordination site of the copper(II) ion.

This, combined with a χ angle of 84.3°, significantly different than the 73.3° angle observed in **2**, provides the coordination polymer chains in **3** with a zigzag-shaped topology with a repeat distance of 20.6 Å (**Error! Reference source not found.**(c)), n otably different from the helical geometry observed for the polymer chains in **2**. Similar to

1a and **1b**, both coordination polymers **2** and **3** crystallized in non-centrosymmetric groups $P3_221$ and $C222_1$, respectively, despite the use of racemic **H_4bna** as the reactant.

(c) Open anionic frameworks based on Zn^{2+} and on Cu^{2+}

Next, we addressed the formation of coordination complexes involving anions derived from **H_4bna** in the presence of 4-aminopyridine as a stronger base. Reaction of $Zn(NO_3)_2{\cdot}6H_2O$ with two equivalents of **H_4bna** and 4-aminopyridine in a mixture of DMF and water gave, after heating at 100 °C, colourless crystals of **4** (Figure S8). Single crystal X-ray diffraction revealed that **4** consisted of open square-grid (*sql*) topology anionic sheets with composition $[Zn(\mathbf{H_2bna})_2]^{2-}$ (Figure 13(a)).

The structure represents the first example of a 2-D coordination framework structure established solely by a **H_4bna**-based ligand. The $[Zn(\mathbf{H_2bna})_2]^{2-}$ sheets are based on zinc ions tetrahedrally coordinated by four oxygen atoms belonging to four symmetrically equivalent **H_2bna^{2-}** ligands (**Error! Reference source not found.**(b)), each with a χ angle of 88.1°. Cavities of each *sql*-$[Zn(\mathbf{H_2bna})_2]^{2-}$ sheet are occupied by protonated 4-aminopyridinium cations ($apyH^+$) and DMF molecules, resulting in a material with an overall formula $(apyH)_2[Zn(\mathbf{H_2bna})_2]{\cdot}2DMF$. PXRD analysis of the bulk product matched the diffraction pattern simulated for the structure of **4** established by single crystal X-ray diffraction (**Error! Reference source not found.**). The $apyH^+$ counterions in the structure of **4** are anchored to the cavities in the $[Zn(\mathbf{H_2bna})_2]^{2-}$ frameworks through

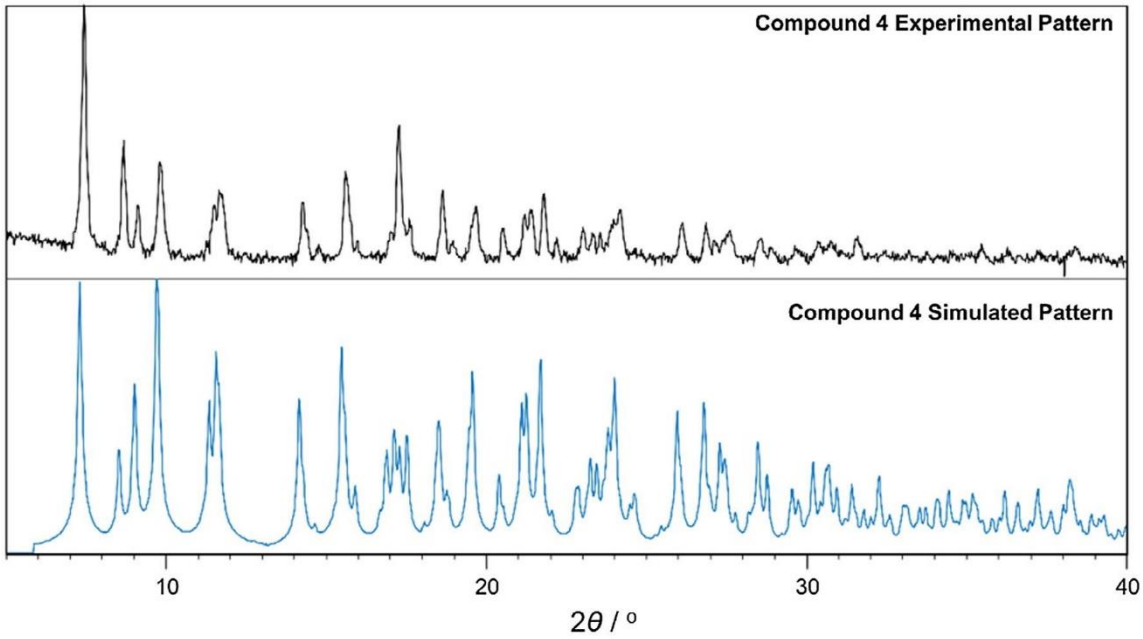

*Figure 115. Comparison of PXRD patterns for the synthesis of compound **4**: (top) measured for crystals of **4** and (bottom) to bottom): simulated for herein reported crystal structure of **4**.*

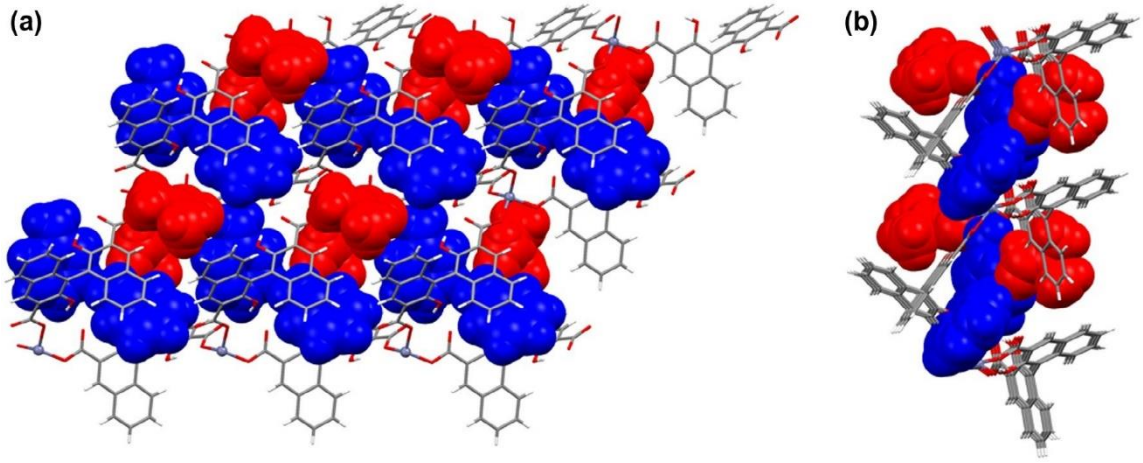

*Figure 116. View of guest apyH+ cations (shown in blue) and DMF molecules (red) in a single sheet of **4**: (a) top-down and (b) side view of the coordination polymer sheet.*

three N–H···O hydrogen bonds. Specifically, the N–H group from the protonated pyridinium moiety is acting as a bifurcated hydrogen bond donor, with N···O distances to the metal-organic acceptor atoms of 2.861(7) and 3.010(7) Å, while one N–H group from the 4-amino substituent forms a single N–H···O hydrogen bond of 2.958(6) Å length to the $[Zn(\mathbf{H_2bna})_2]^{2-}$ framework. The second N–H moiety of the 4-amino substituent is

attached to a neighbouring neutral DMF guest molecule *via* a N–H···O hydrogen bond of 2.884(9) Å length (**Error! Reference source not found.**). The reasons for the formation o f the anionic 2-D *sql*-[Zn(**H₂bna**)₂]$^{2-}$ framework in **4**, as opposed to neutral 1-D chains observed in **1** or neutral 1-D tapes in the previously reported Zn(**H₂bna**)(H₂O)₂ are unclear. On one hand, it is possible that the presence 4-aminopyridine played a critical role, by enabling more efficient deprotonation of **H₄bna**, therefore increasing the concentration of **H₂bna^{2-}**, and providing apyH^{+} cations that may be acting as templates for the formation of an open framework structure. On the other hand, the higher temperature employed in the synthesis of **4** might also play a role in leading to a structure of higher dimensionality, as was observed previously by the Rao group for metal oxalate framework structures.[34]

Similar to compounds **1a** and **1b**, compound **4** also exhibits noticeable green fluorescence on exposure to ultraviolet light. The emission is red-shifted compared to **1b**, with an emission maximum measured at 554 nm upon excitation with 384 nm radiation (**Error! Reference source not found.**).

*Figure 117. Fluorescence of compound **4** upon exposure to ultraviolet light: (a) optical microscopy image of a samples of **4** and (b) fluorescence emission (solid line) and excitation (dotted line) spectra. the fluorescence emission spectrum was recorded upon excitation with 384 nm radiation, while the excitation spectrum was measured at 550 nm.*

Compound **5** is a copper(II) analogue of **4**, with composition (apyH)₂[Cu(**H₂bna**)₂]·2DMF. The compound was serendipitously obtained in the form of crystals (Figure S6) in an attempt to obtain a mixed-ligand framework by elevated

temperature reaction of copper(II) nitrate, **H_4bna** and the extended *bis*-N-(4-pyridyl)amide ligand in a mixture of water and DMF. Despite similarity in compositions, the structure of **4** is very different from **5**, as it is composed of anionic linear 1-D chains with a formula $[Cu(\mathbf{H_2bna})_2]^{2-}$. The chains are based on cyclic dimeric units of composition $Cu_2(\mathbf{H_2bna})_2$, which are associated into a 1-D structure by sharing a metal ion with a square-planar coordination geometry (Cu–O distances: 1.934(3) and 1.956(3) Å) (**Error! Reference s ource not found.**(a)). The interplanar χ angle for the $\mathbf{H_2bna^{2-}}$ ligands in each chain is 82.5°. The chains are further connected by N–H···O hydrogen bonds to $apyH^+$ cations, which results in the formation of two-dimensional supramolecular hydrogen- and coordination-bonded sheets that lie parallel to the (011) family of crystallographic planes (**Error! Reference source not found.**(b) and (c)).

*Figure 118. Views of the crystal structure of **5**: (a) single coordination polymer chain of $[Cu(\mathbf{H_2bna})_2]^{2-}$, with guest $apyH^+$ cations and DMF molecules omitted for clarity; (b) a top-down view and (c) an edge-on view of the supramolecular hydrogen- and coordination-bonded sheets in the structure of **5**, with $apyH^+$ cations and DMF molecules shown using a space-filling model.*

The hydrogen-bonding preferences of the apyH$^+$ cations in **5** are similar to those seen in compound **4**: the N–H group of the protonated pyridinium group and one N–H group of the 4-amino substituent are engaged in the formation of N–H···O hydrogen bonds to the oxygen atoms of the polymeric metal-organic anions (N···O distances 2.846(6) and 3.079(7) Å, respectively), whereas the second N–H group of the 4-amino moiety is involved in an N–H···O hydrogen bond (N···O distance 2.792(9) Å) with a guest DMF molecule.

13.06 Conclusions

In summary, we have described five new extended coordination structures generated by using the racemic version of the BINOL-based ligand **H$_4$bna** in combination with Zn^{2+} and Cu^{2+}. All of the herein observed self-assembly motifs are mutually different, and also significantly different from those in previously reported coordination polymers of the same ligand. The presented structures of compounds **1a**, **1b** and **4** also demonstrate the ability of zinc ions to adopt a wide range of coordination geometries in combination with **H$_4$bna**-derived anions, including a tetrahedral, an octahedral and a trigonal bipyramidal one. The observed structural diversity illustrates the yet untapped potential of the **H$_4$bna**-based ligands, specifically the anionic **H$_2$bna^{2-}**, for the assembly of structures with different dimensionality and symmetry properties. Each of the zinc-based supramolecular architectures also exhibits characteristic solid-state fluorescence, indicating that a clear understanding of and control over structural diversity of these types of materials should open routes to new solids with controllable luminescence.

We believe that the crystal structure of herein reported compound **4**, (apyH)$_2$[Zn(**H$_2$bna**)$_2$]·2DMF, is of particular relevance, as it represents the first example of a 2-D framework based only on the readily available BINOL-type ligand **H$_2$bna^{2-}**. We are currently continuing the systematic study of coordination polymers and frameworks of **H$_4$nba** derived ligands, focusing on zinc, copper, and nickel, as well as enantiopure versions of the ligand.

13.07 Supplementary Information

All supplementary information, namely, characterization data for compound **1-5**, and figures references labeled with S are contained in Appendix 3.

13.08 Acknowledgements

We are grateful to Dr. Davin Tan, Nanyang Technological University, Singapore, and Dr. Steven P. Kelley, University of Missouri, for their assistance in acquiring X-ray diffraction data. We acknowledge NSERC Discovery Grant (RGPIN-2017-06467) and E. W. R. Steacie Memorial Fellowship (SMSFU 507347-17) for funding. P.A.J. is grateful for the financial support of an NSERC post-graduate doctoral scholarship (PGS-D).

This work was supported by the NSERC Discovery [grant number RGPIN-2017-06467] and E. W. R. Steacie Memorial Fellowship [grant number SMSFU 507347-17] and financially supported by the NSERC Post-Graduate Doctoral Scholarship (PGS-D).

13.09 References

1. Kuppler, R.J.; Timmons, D.J.; Fang, Q.-R.; Li, J.-R.; Makal, T.A.; Young, M.D.; Yuan, D.; Zhao, D.; Zhuang, W.; Zhou, H.-C. *Coord. Chem. Rev.* **2009,** *253,* 3042–3066.
2. Wang, C.; Zheng, M.; Lin, W. *J. Phys. Chem. Lett.* **2011,** *2,* 1701–1709.
3. Brunel, J.M. *Chem. Rev.* **2005,** *105,* 857–898.
4. Chen, Y.; Yekta, S.; Yudin, A.K. *Chem. Rev.* **2003,** *103,* 3155– 3212.
5. Wu, C.-D.; Zhang, L.; Lin, W. *Inorg. Chem.* **2006,** *45,* 7278–7285.
6. Wanderley, M.M.; Wang, C.; Wu, C.-D.; Lin, W. *J. Am. Chem. Soc.* **2012,** *134,* 9050–9053.
7. Ma, L.; Lin, W. *Angew. Chem. Int. Ed.* **2009,** *48,* 3637–3640.
8. Ma, L.; Wu, C.-D.; Wanderley, M.M.; Lin, W. *Angew. Chem. Int. Ed.* **2010,** *49,* 8244–8248.
9. Wu, C.-D.; Lin, W. *Angew. Chem. Int. Ed.* **2005,** *44,* 1958–1961.
10. Wu, C.-D.; Lin, W. *Dalton Trans.* **2006,** 4563–4569.
11. Cambridge Structural Database, version 5.38, May 2017 update.
12. Wang, Z.; Cohen, S.M. *Chem. Soc. Rev.* **2009,** *38,* 1315–1329.

13. Evans, O.R.; Ngo, H.L.; Lin, W. *J. Am. Chem. Soc.* **2001,** *123,* (42)**,** 10395–10396.
14. Wu, C.-D.; Hu, A.; Zhang, L.; Lin, W. *J. Am. Chem. Soc.* **2005,** *127,* 8940–8941.
15. Ma, L.; Falkowski, J.M.; Abney, C.; Lin, W. *Nat. Chem.* **2010,** *2,* 838–846.
16. Yang, J.-H.; Li, W.; Zheng, S.-L.; Huang, Z.-L.; Chen, X.-M. *Austr. J. Chem.* **2003,** *56,* 1175–1178.
17. Zheng, S.-L.; Yang, J.H.; Yu, X.-L.; Chen, X.-M.; Wong, W.-T. *Inorg. Chem.* **2004,** *43,* 830–838.
18. Ren, H.-W.; Liu, Z.-D.; Qu, Y.; Tan, M.-Y.; Zhu, H.-L. *Acta Crystallogr.* **2004,** *E60***,** m948–m949.
19. Li, L.J.; Wang, L.Z.; Yang, X.Y.; Wang, G.Y.; Tian, Ch; Du, J.L. *Russ. J. Coord. Chem.* **2013,** *39, 2*39–244.
20. Zhang, L.-Y.; Zhang, J.-P.; Lin, Y.-Y.; Chen, X.-M. *Cryst. Growth Des.* **2006,** *6,* 1684–1689.
21. Tanaka, K.; Kikumoto, Y.; Shiro, M. *Polymers* **2011,** *3,* 1866– 1874.
22. Huang, W.-Y.; Chen, Z.-L.; Wang, K.; Zhou, X.; Liang, F.-P. *Transition Met. Chem.* **2012,** *37,* 291–296.
23. Gao, Q.; Jiang, F.-L.; Wu, M.-Y.; Huang, Y.-G.; Wei, W.; Hong, M.-C. *Cryst. Growth Des.* **2010,** *10,* 184–190.
24. Gao, Q.; Jiang, F.-L.; Wu, M.-Y.; Huang, Y.-G.; Chen, L.; Wei, W.; Hong, M.-C. *J. Solid State Chem.* **2009,** *182,* 1499–1505.
25. Cram, D.J.; Helgeson, R.C.; Peacock, S.C.; Kaplan, L.J.; Domeier, L.A.; Moreau, P.; Koga, K.; Mayer, J.M.; Chao, Y. *J. Org. Chem.* **1978,** *43,* 1930–1946.
26. Someshwar, N.; Ramanathan, C.R. *Tetrahedron: Asymmetry* **2015,** *26* (20)*,* 1209–1213.
27. Max, J.-J.; Chapados, C. *J. Phys. Chem. A* **2004,** *108,* 3324–3337.
28. Sheldrick, G. *Acta Crystallogr. C* **2015,** *71,* 3–8.
29. Zhang, L.-Y. *Acta Crystallogr.* **2010,** *E66,* m23.
30. Huang, K.-S.; Britton, D.; Etter, M.C.; Byrn, S.R. *J. Mat. Chem.* **1997,** *7,* 713–720.
31. Tanaka, K.; Kikumoto, Y.; Hota, N.; Takahashi, H. *New J. Chem.* **2014,** *38,* 880–883.

32. Glusker, J.P. *Topics Curr. Chem.* **1998,** *198,* 1–56.

33. Etter, M.C. *J. Phys. Chem.* **1991,** *95,* 4601–4610.

34. Dan, M.; Rao, C.N.R. *Angew. Chem. Int. Ed.* **2006,** *45,* 281– 285.

13.10 Supplementary Information for: Investigation of BINOL-3,3′-dicarboxylate as a ligand for the formation of extended coordination-based structures

1. Characterization of a mixture of Compounds **1a** and **1b**

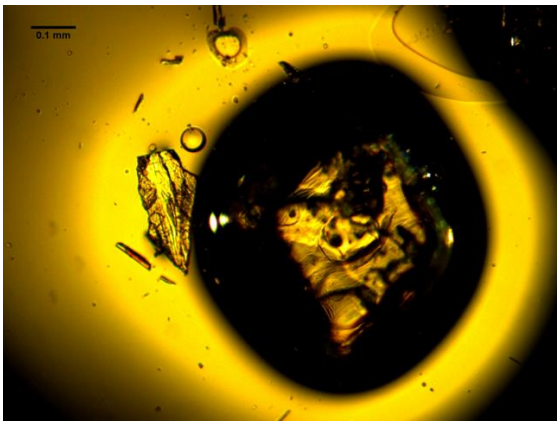

Figure S1. Example of a microscopy image of the mixture of compounds **1a** and **1b**, illustrating that the as-prepared sample consists of large blocks and smaller needles.

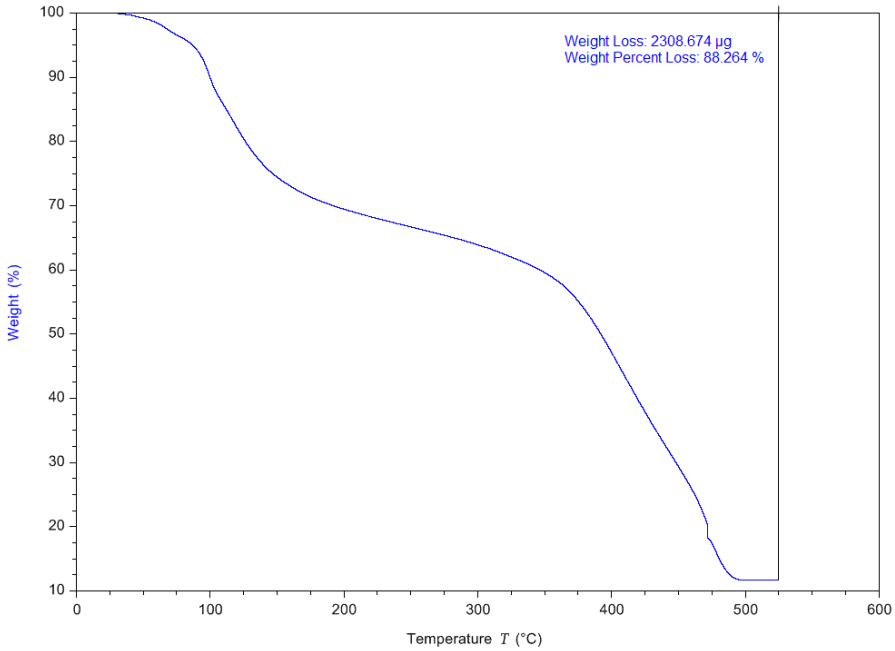

Figure S2. Thermogravimetric analysis curve for the mixture of compounds **1a** and **1b**, recorded in air. The residue after complete oxidation of the material is 11.7% by weight.

2. Characterization of Compound **1b**

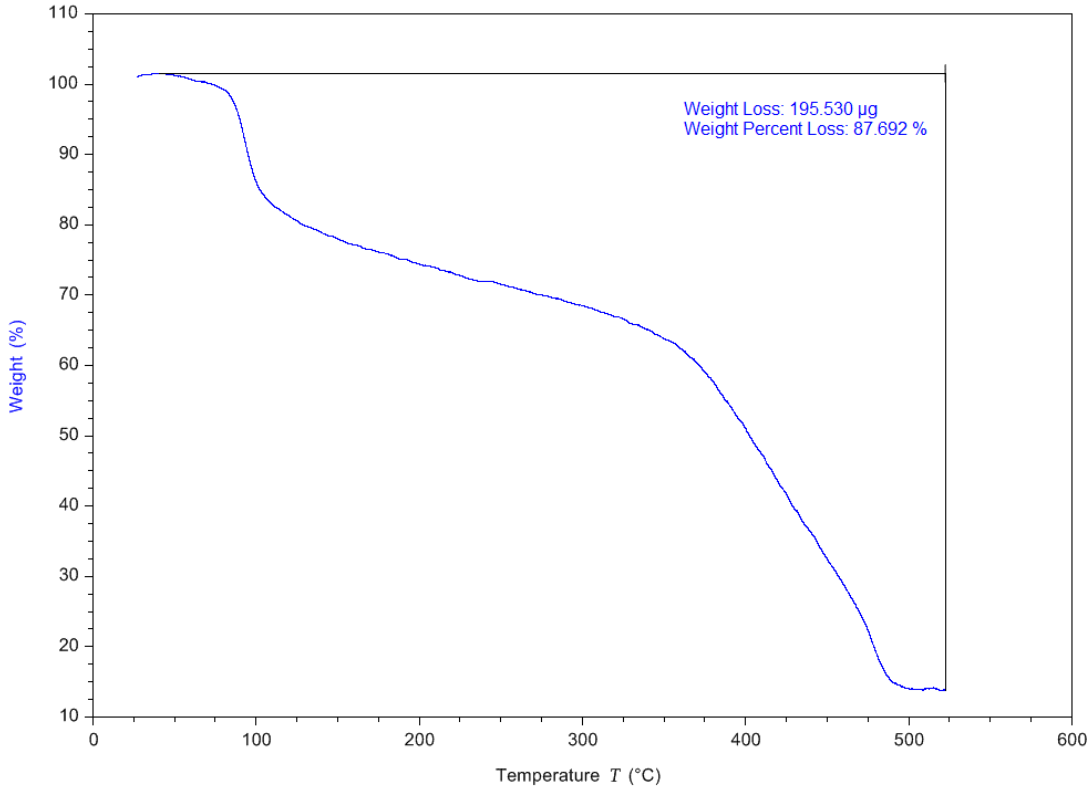

Figure S3. Thermogravimetric analysis curve for compound **1b**, recorded in air. The residue after complete oxidation of the material is 12.3% by weight, which compares well to the expected ZnO residue of 12.8%.

3. Characterization of Compound **2**

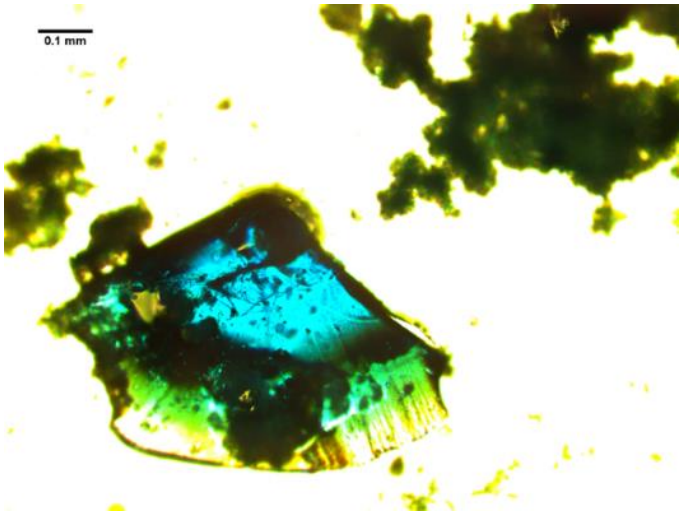

Figure S4. Microscopy image of crystals of Compound **2** (blue) along with a polycrystalline green byproduct.

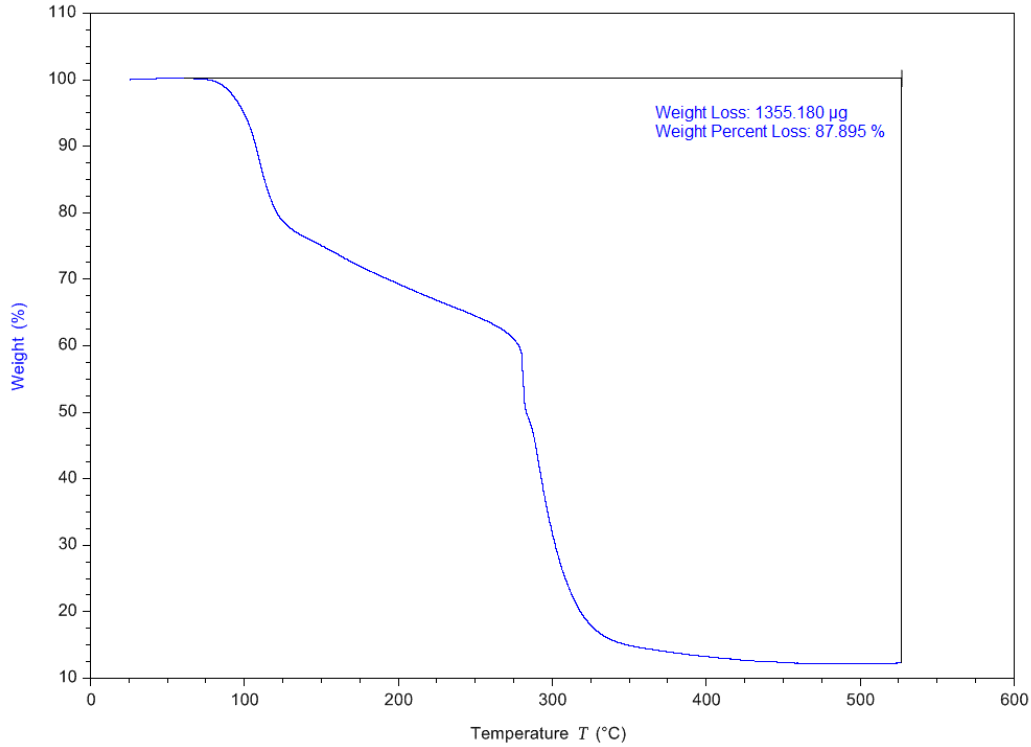

Figure S5. Thermogravimetric analysis curve for compound **2**, recorded in air. The residue after the experiment is 12.1%, which is different from 10.5% expected for **2**. The difference is explained by presence of impurity phases that could not be completely separated, that are also evident in the powder X-ray diffraction pattern of the bulk material (Figure 9 in manuscript).

4. Characterization of Compound **3**

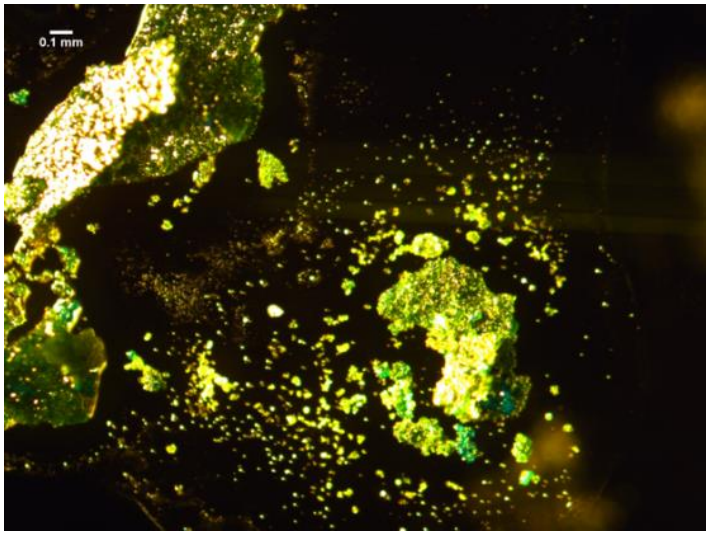

Figure S6. Microscopy image of crystals of compound **3** (blue), along with the polycrystalline green byproduct.

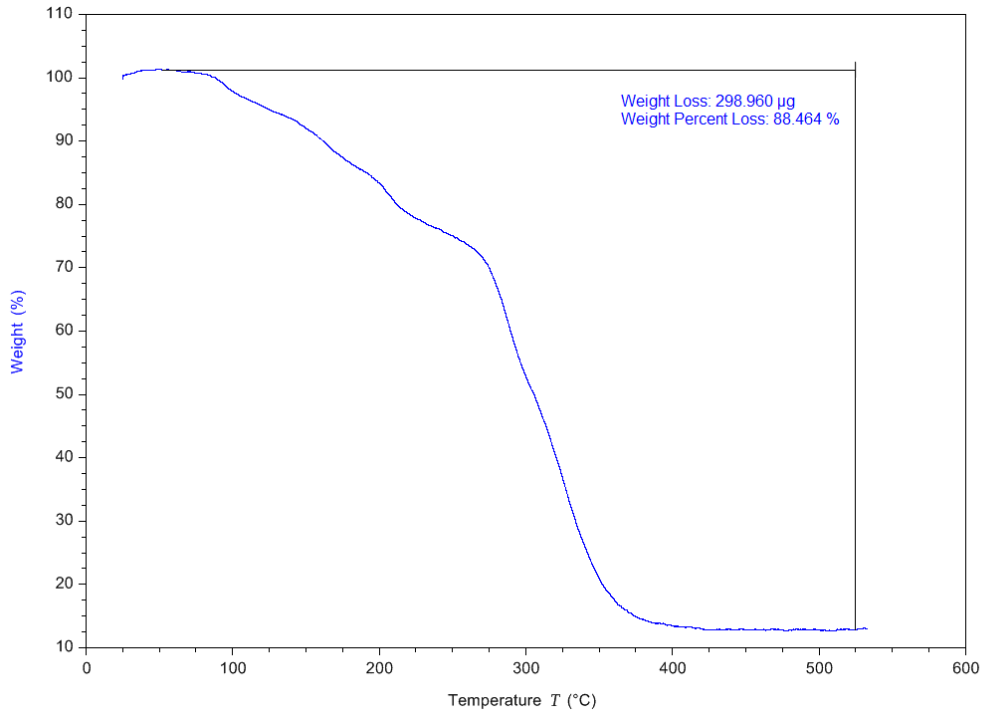

Figure S7. Thermogravimetric analysis of compound **3**, recorded in air. The final residue of 11.5% agrees well with the 11.8% expected for **3**.

5. Characterization of Compound **4**

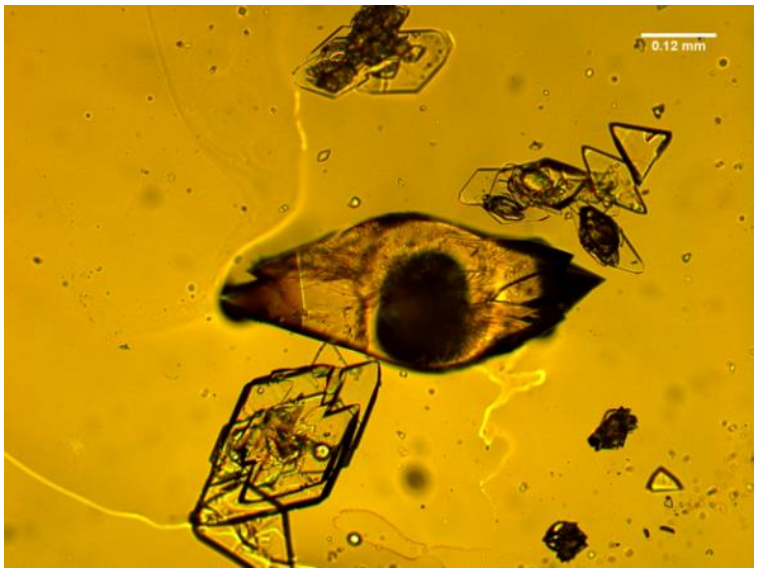

Figure S8. Example microscopy image of crystals of Compound **4**.

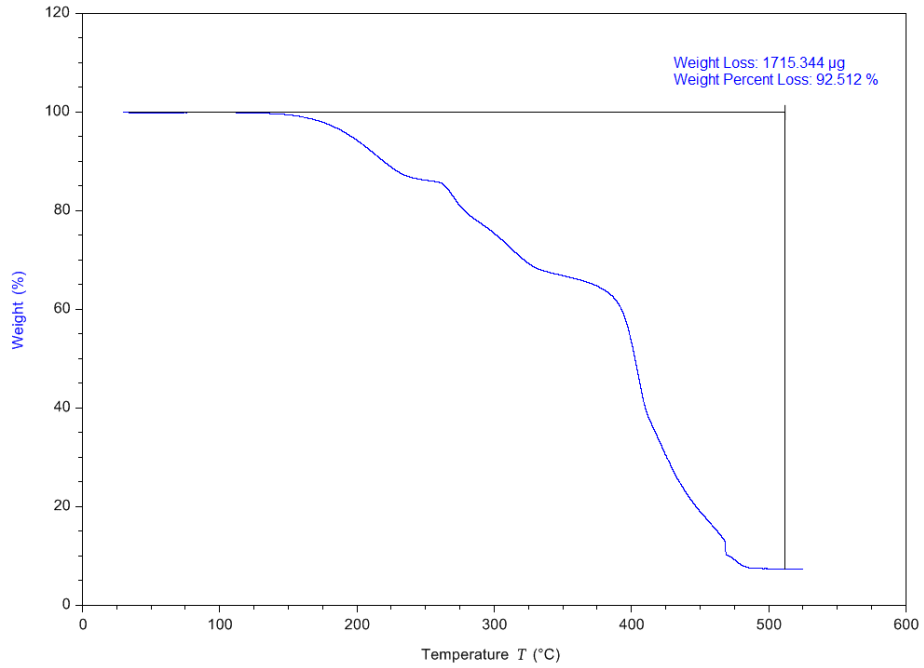

Figure S9. Thermogravimetric analysis curve of compound **4**, recorded in air. The final residue of 7.5% is consistent with 7.1% expected for **4**.

6. Characterization of Compound **5.**

Figure S10. Example microscopy image of crystals of compound **5**. The central crystal was used in crystal structure determination.

14. Appendix 4 : Supplementary information for *in situ* monitoring of mechanochemical synthesis of calcium urea phosphate fertilizer co-crystal reveals highly effective water-based autocatalysis

14.01 Experimental Procedures

(a) Materials and Methods

Materials: All reagents were used as purchased without further purification. Calcium hydroxide and carbonate were purchased from ACP Chemicals (Montreal, QC) as ACS grade reagents. Urea (USP grade) and urea phosphate (98%) were purchased from Sigma Aldrich.

FTIR-ATR spectroscopy: Fourier-transform infrared attenuated total reflectance (FTIR-ATR) were recorded on Bruker Vertex 70 spectrometer with RockSolid interferometer in the range of 3500-400 cm^{-1}.

X-ray powder diffraction (XRPD): Patterns used for *ex situ* qualitative analysis of the samples were collected on a Bruker D2 diffractometer, Ni-filtered Cu-*Kα* radiation, flat plate sample on a zero background sample holder in Bragg-Brentano geometry, tension 30kV, and current 10 mA.

***In situ* Raman Spectroscopy:** Reactions were conducted in an approximately 10 mL sapphire milling jar, using a 2 g zirconia ball and a Retsch® MM400 mixer mill running at 30 Hz. These were monitored using a RamanRxn1™ analyzer by Kaiser Optical Systems Inc. every 10 seconds using a 785 nm laser. Spectra were dark and intensity corrected using the Holograms® software package before being processed. All data was processed using MATLAB in accordance with previously published procedures[1].

***In situ* X-ray powder diffraction (XRPD):** Reactions were conducted in a 15 mL polymethylmethacrylate (PMMA) milling jar, using two 1.3 g stainless steel ball in a modified Retsch® MM400 mixer mill running at 30 Hz. Reaction monitoring was performed at the high-resolution powder diffraction beamline PETRA III (P02.1) beamline

at DESY using an unfocused and collimated X-ray beam with the size of ca. 1x 1 mm^2 and a time resolution of 10 seconds. The beamline is equipped with a PerkinElmer 2D area detector. The wavelength was determined with the NIST NSR 660a (LaB_6) standard using two different detector positions, λ = 0.207 Å (59.9 keV). All 2D XRPD patterns were integrated using Dioptas[2]. Sequential Rietveld analysis was performed in TOPAS-Academic V5[3]. A silicon standard was measured under identical experimental conditions as the *in situ* monitoring experiments and was used to describe the instrumental profile function (IPF). The IPF was modelled with a modified Thompson-Cox-Hasting pseudo-Voight function using $\left|Z/\cos^2(\theta)\right|^{0.5}$ for the Gaussian and $X\ tan(\theta)+Y\cos(\theta)$ for the Lorentzian profile as implemented in TOPAS (for further information see [3]).

The background of each powder pattern was modelled with a Pawley pseudo-phase (*Pmmm*, *a* = 40 Å, *b* = *c* = 0.1 Å, crystallite size with a Lorentzian crystallite size of 1.5). All XRPD pattern were analyzed from 0.5 to 5 ° 2*θ*. The known crystal structures calcite (Open Crystal Structure Database number 1010928), urea (CSD code UREAXX01), urea phosphate (CSD code CRBAMP01), and compound **1** (CSD code URECAP) were taken from the corresponding databases. The lattice parameters and crystallite size of each phase were refined from the powder pattern, where the phase was most prominent and fixed afterwards. During the sequential Rietveld refinement only the scale factor of each phase was freely refined.[4]

TGA and DSC experiments: Thermogravimetric analyses were performed on a Mettler-Toledo TGA DSC 1 Stare system thermobalance using alumina crucibles under air stream with the heating rate of 10 °C min^{-1}. The results were processed with the Mettler STARe 9.01 software.

Dynamic Vapor Sorption Experiments: The DVS Intrinsic dynamic vapor sorption (DVS) apparatus (Surface Measurement Systems, USA), equipped with an SMS ultrabalance with a mass resolution of ±0.1µg, was used to obtain ramping and equilibrium water vapor sorption isotherms. Approximately 5 mg of powder samples was placed in the apparatus using aluminum pans and initially dried over 600 min with a

stream of dry nitrogen to establish a dry mass at 25 °C. The dry mass was calculated after the end of the first drying stage (0% RH). The sorption cycle experiments were performed from 0% relative humidity (RH) to 95% RH in a step of 5% RH in a pre-programmed sequence before decreasing to 0% RH in a reverse order. The instrument maintained a constant target RH until the moisture content change per minute (*dm/dt*) was <0.002% per minute over a 10 min period.

The relative humidity (RH) here is defined as where P_o is the saturated vapor pressure of water at 298 K and 1 atm and *P* is the actual water pressure at the same temperature and pressure, e.g.

$$RH = \frac{P}{P_o} * \ 100\ (\%)$$

(b) Synthesis

Calcium Carbonate Reactions: For all reactions containing only calcium carbonate as the calcium source, 40 mg of urea (0.67mmol), 106 mg of urea phosphate (0.67mmol), and 34 mg calcium carbonate (0.34mmol) were combined in the milling vessel along with the milling ball(s). For liquid additions, 2.5 or 5 microliters of distilled water were added using a micropipette. For the reactions in with premade **1**, either 3mg or 6mg of **1** was added to the reaction mixture before milling.

Calcium Hydroxide Reactions: For all reactions containing only calcium hydroxide as the calcium source, 42 mg of urea (0.7 mmol), 111 mg of urea phosphate (0.7 mmol), and 26 mg calcium hydroxide (0.35 mmol) were combined in the milling vessel along with the milling ball(s).

Mixed Reactions: Reactions containing both calcium hydroxide and calcium carbonate were run with 40 mg of urea (0.67mmol), and 106 mg of urea phosphate (0.67mmol) with the following amounts of calcium carbonate and hydroxide:

mol% $Ca(OH)_2$ to $CaCO_3$	**5**	**10**	**13**	**17**
mg of $CaCO_3$	31.6	30	28.3	26.6
mg $Ca(OH)_2$	1.17	2.2	3.14	3.94

14.02 Reaction rheology

Figure SI-1. Visual difference in reaction rheology between the synthesis of calcium urea phosphate from calcium hydroxide (left) and calcium carbonate (right). The calcium hydroxide reaction proceeds more as a wet paste, in contrast to the solid powder present in the reaction of calcium carbonate. The rheology of the product after full conversion is similar between calcium carbonate and calcium hydroxide.

14.03 Comparison of Raman signal in PMMA vs. sapphire milling jars

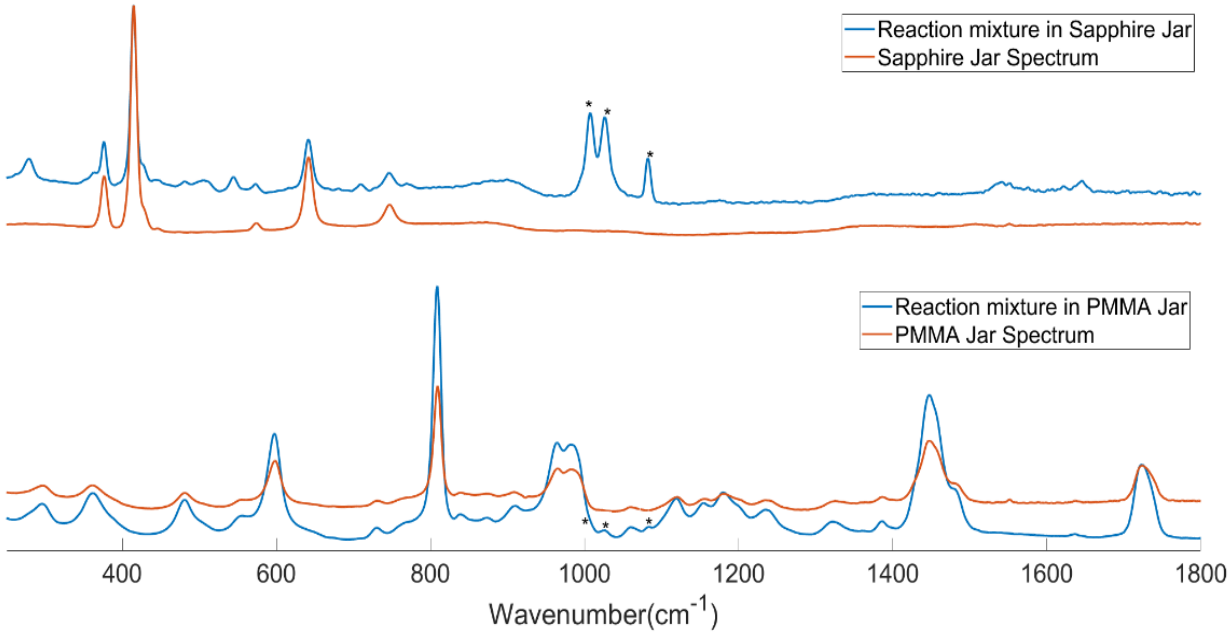

Figure SI-2. Normalized *in situ* Raman spectra for the reaction of calcium carbonate with urea and urea phosphate in sapphire (top) and PMMA (bottom) jars. * denote the most prominent peaks of the starting materials of the reaction.

14.04 Kinetic Analysis of reaction of $CaCO_3$ with urea and urea phosphate

a. Data Trendline

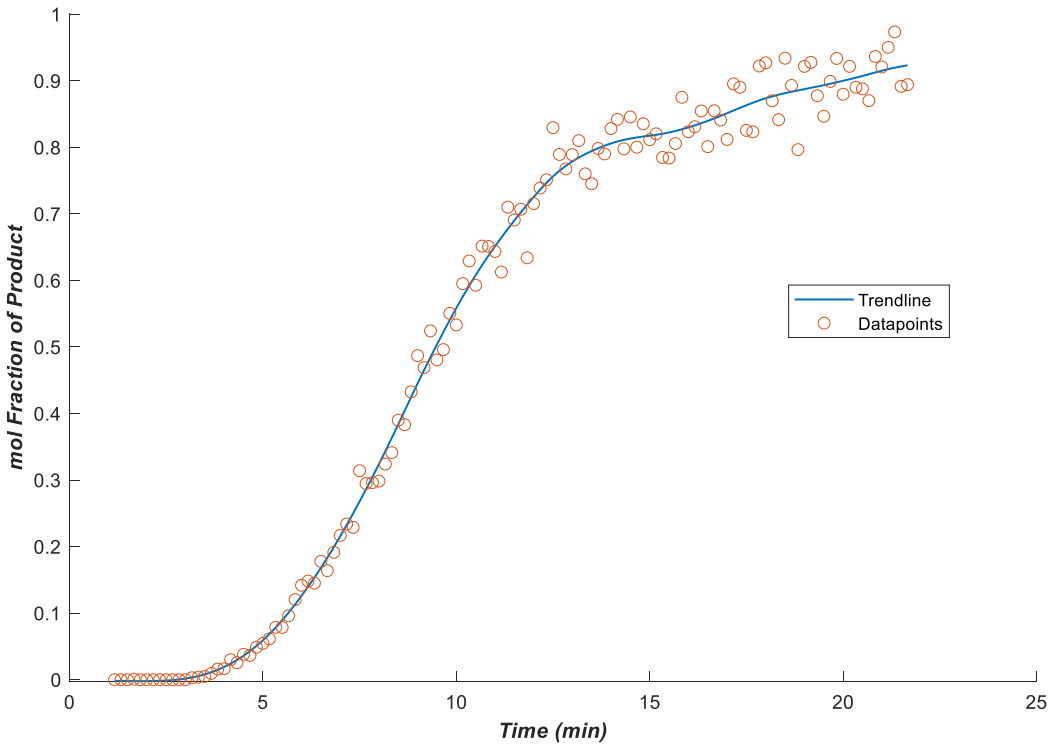

Figure SI-3. mol fraction of calcium-urea-phosphate in the reaction of calcium carbonate, urea, and urea phosphate from *in situ* Raman spectroscopy. Trendline generated *via* smoothing spline fitting in the curve fitting toolbox of MATLAB.

Fitting results and Parameters for Smoothing Spline fit:

Smoothing spline:

f(x) = piecewise polynomial computed from p

Smoothing parameter, p:	0.39472418
Sum of Squares Due to Error:	0.08659

14. Appendix 4 : Supplementary information for in situ monitoring of mechanochemical synthesis of calcium urea phosphate fertilizer co-crystal reveals highly effective water-based autocatalysis

R-square:	0.9943
Adjusted R-square:	0.9938
RMSE:	0.02771

(a) Reaction Rate: Derivative of mol fraction trendline

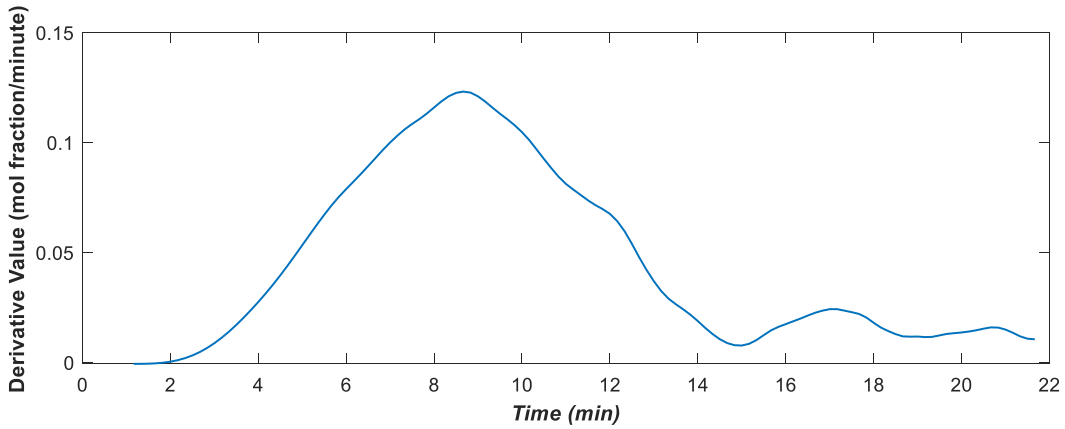

Figure SI-4. Computed derivative (using MATLAB *differentiate* function) of the trendline of the mol fraction of product, with parabolic shape characteristic of autocatalytic reactions.

Fitting results and Parameters for Reaction rate (dα/dt)/α vs. α, where α is the mol fraction of 1 as determined by *in situ* Raman spectroscopy for the synthesis using $CaCO_3$ reactant:

Linear model Poly1:

f(x) = p1*x + p2

Coefficients (with 95% confidence bounds):

p1 = -0.7183 (-0.7385, -0.698)

p2 = 0.6006 (0.589, 0.6121)

Goodness of fit:

Sum of Squares Due to Error:	0.006319
R-square:	0.9923
Adjusted R-square:	0.9921
RMSE:	0.01257

14.05 XRPD Data

(a) Starting Materials

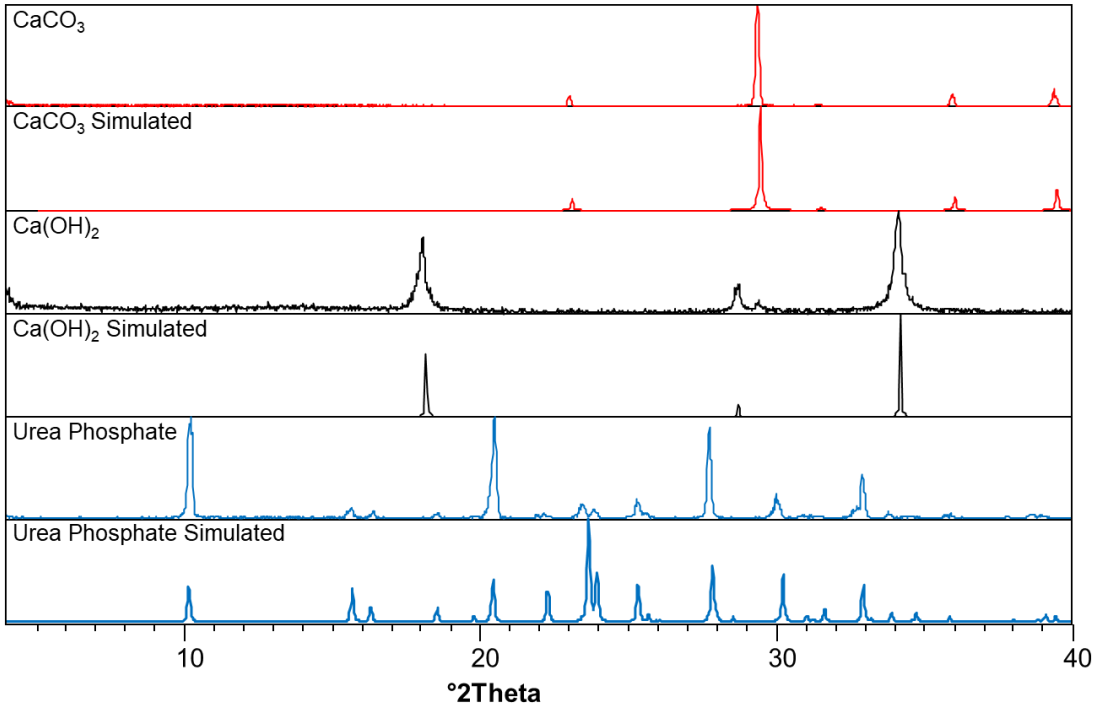

Figure SI-5. Measured and calculated XRPD patterns of the reactants used. A small amount of calcium carbonate can be observed in calcium hydroxide pattern.

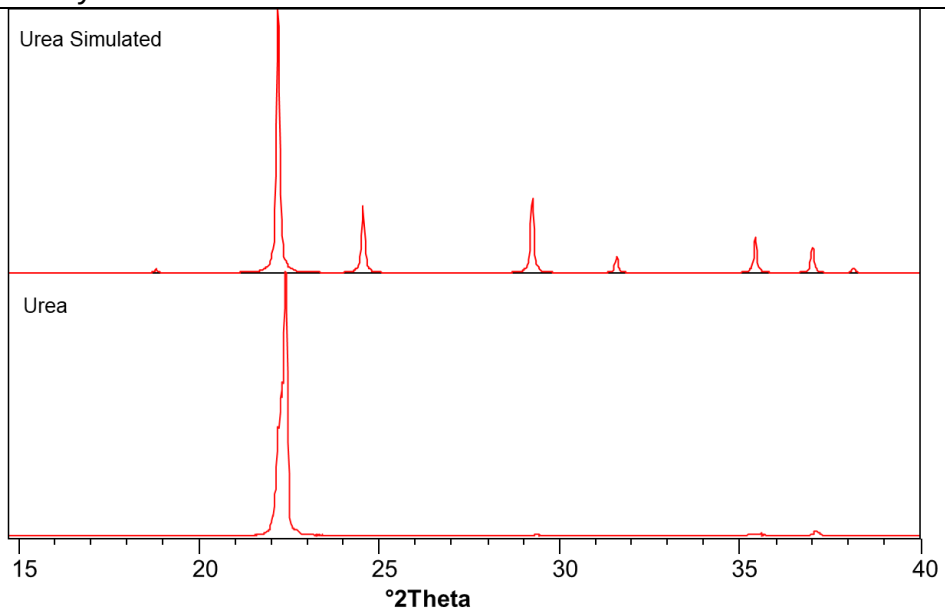

Figure SI-6. Simulated (top) and measured (bottom) XRPD patterns of urea. A very strong preferred orientation effect is observed in the sample.

(b) Products

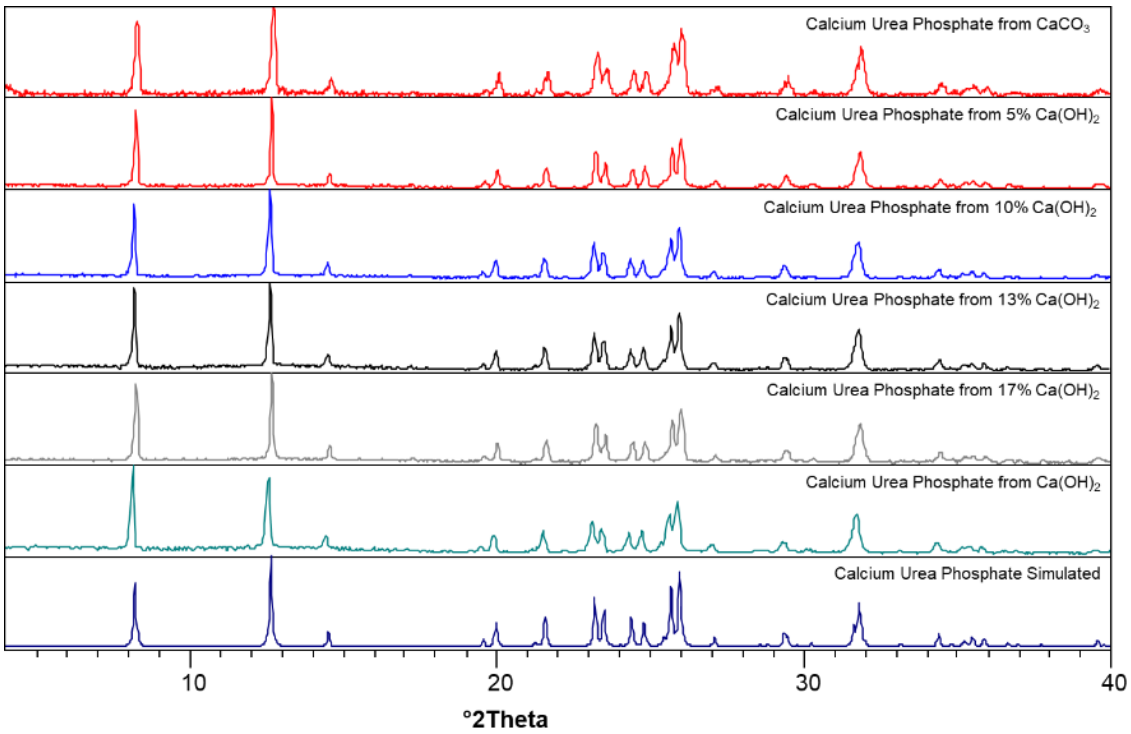

Figure SI-7. XRPD patterns of the reaction products. All products match the simulated XRPD pattern of **1** (calcium urea phosphate, CSD code URECAP) at the bottom.

14.06 Infrared Spectroscopy Data

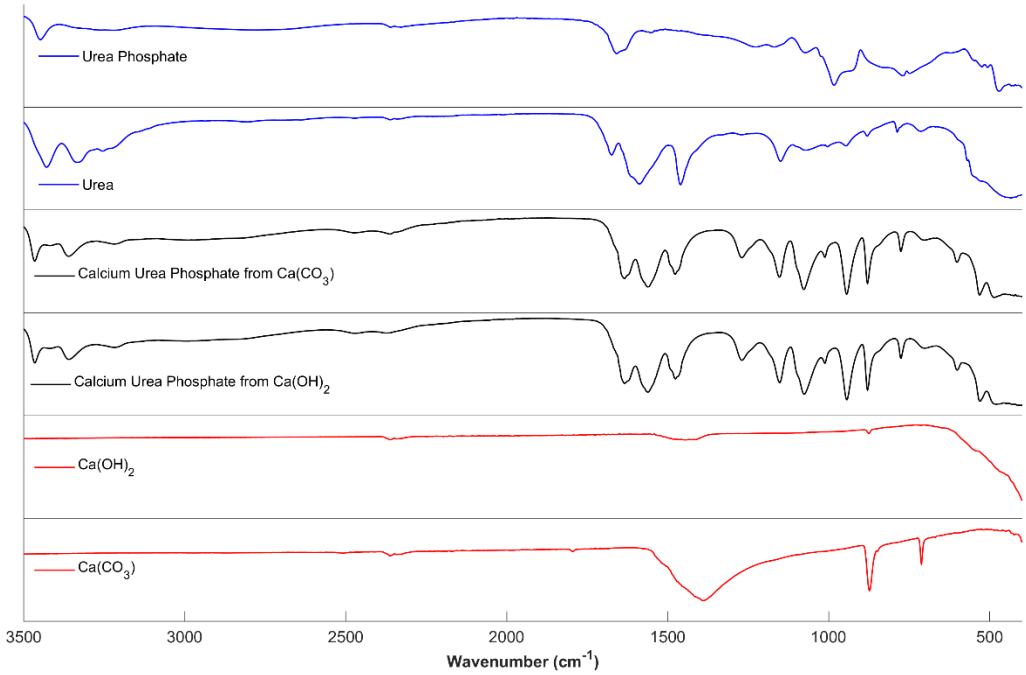

Figure SI-8. Comparison FTIR spectra of both calcium sources (red), urea and urea phosphate (red), and **1** (calcium urea phosphate) synthesized from both calcium hydroxide and calcium carbonate (black).

14.07 *In situ* Raman Datasets

Reactions with $Ca(OH)_2$ reactant

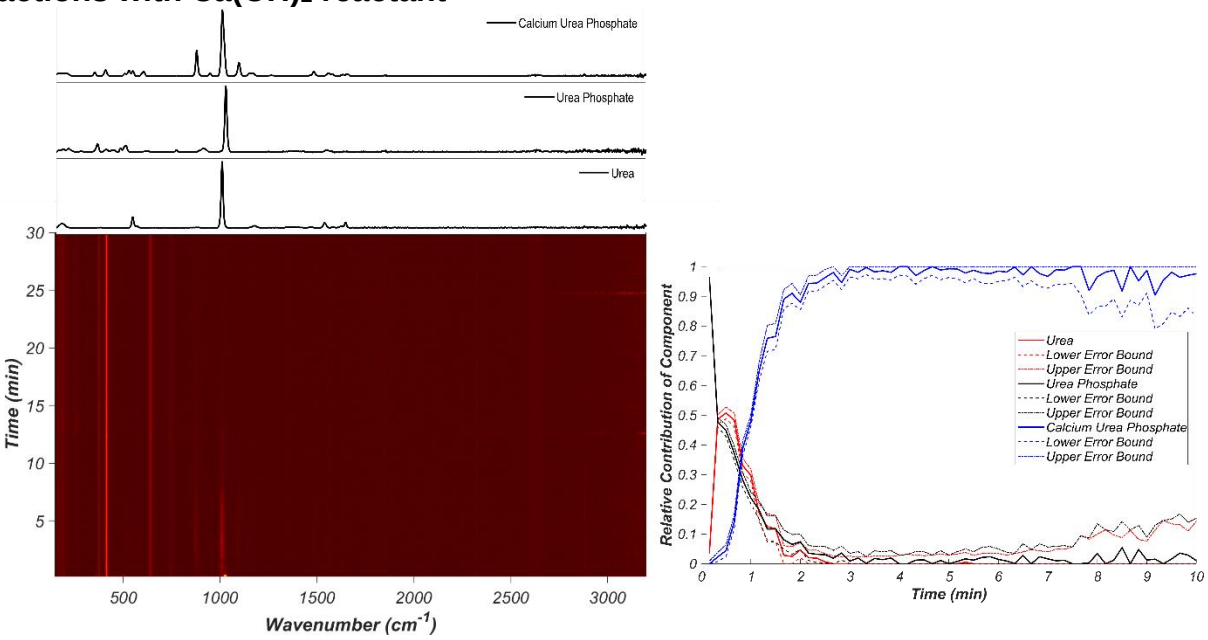

Figure SI-9. (Bottom Left) *In situ* Raman spectra for the synthesis of **1** (calcium urea phosphate) from calcium hydroxide. Calcium hydroxide is not visible due to poor intensity of the signal, so the data was fit with the Raman spectra urea and urea phosphate reactants, and calcium urea phosphate product (top left). (Bottom Right) Non-negative least squares fitting profiles, error bounds correspond to two times the standard deviation of the residual.

14.08 Datasets for reactions with $CaCO_3$ and $Ca(OH)_2$ reactants

(a) Reaction of 5 mol% $Ca(OH)_2$ and 95 mol% $CaCO_3$

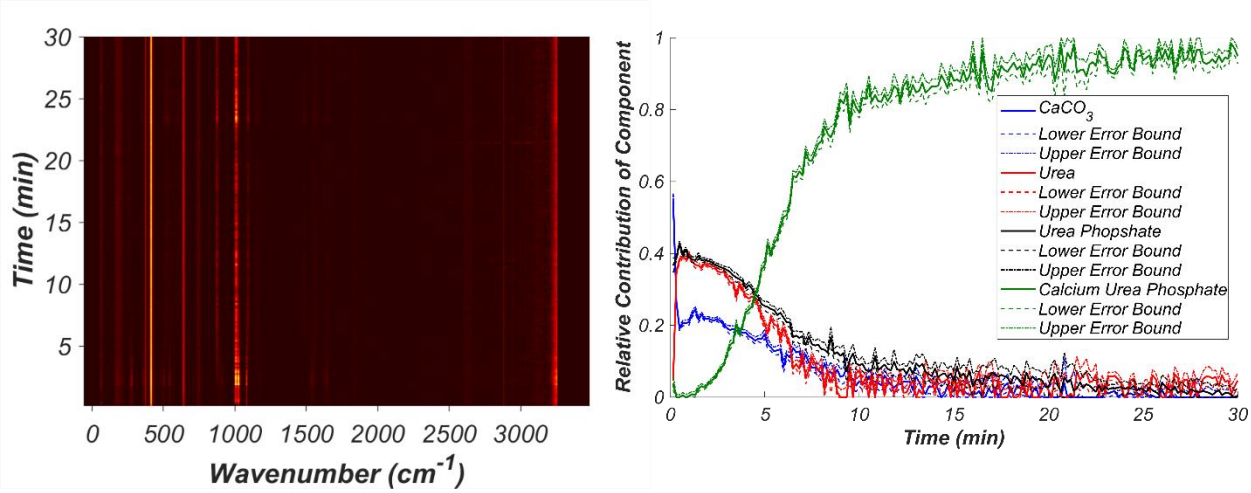

Figure SI-10. (Left) *In situ* Raman spectra for the synthesis of **1** (calcium urea phosphate) from calcium carbonate with the addition of 5 mol% $Ca(OH)_2$. (Right) Non-negative least squares fitting profiles, with errors corresponding to two times the standard deviation of the residual.

(b) Reaction of 10 mol% $Ca(OH)_2$ and 90 mol% $CaCO_3$

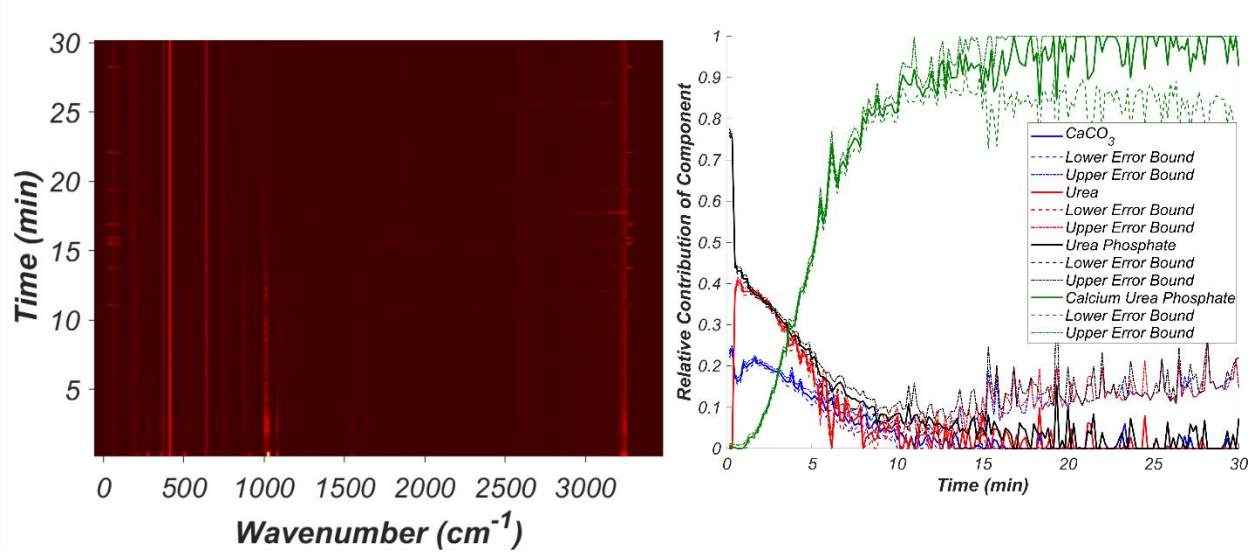

Figure SI-11. (Left) *In situ* Raman spectra for the synthesis of **1** (calcium urea phosphate) from calcium carbonate with the addition of 10 mol% $Ca(OH)_2$. (Right) Non-negative least squares fitting profiles, with errors corresponding to two times the standard deviation of the residual.

(c) Reaction of 13 mol% $Ca(OH)_2$ and 87 mol% $CaCO_3$

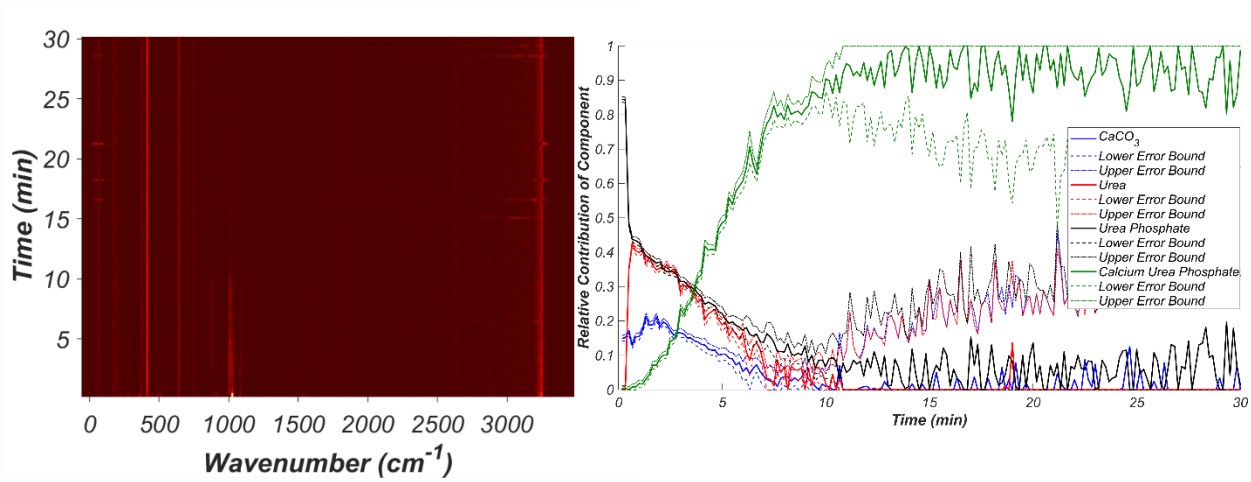

Figure SI-12. (Left) *In situ* Raman spectra for the synthesis of **1** (calcium urea phosphate) from calcium carbonate with the addition of 13 mol% $Ca(OH)_2$. (Right) Non-negative least squares fitting profiles, with errors corresponding to two times the standard deviation of the residual.

(d) Reaction of 17 mol% $Ca(OH)_2$ and 83 mol% $CaCO_3$

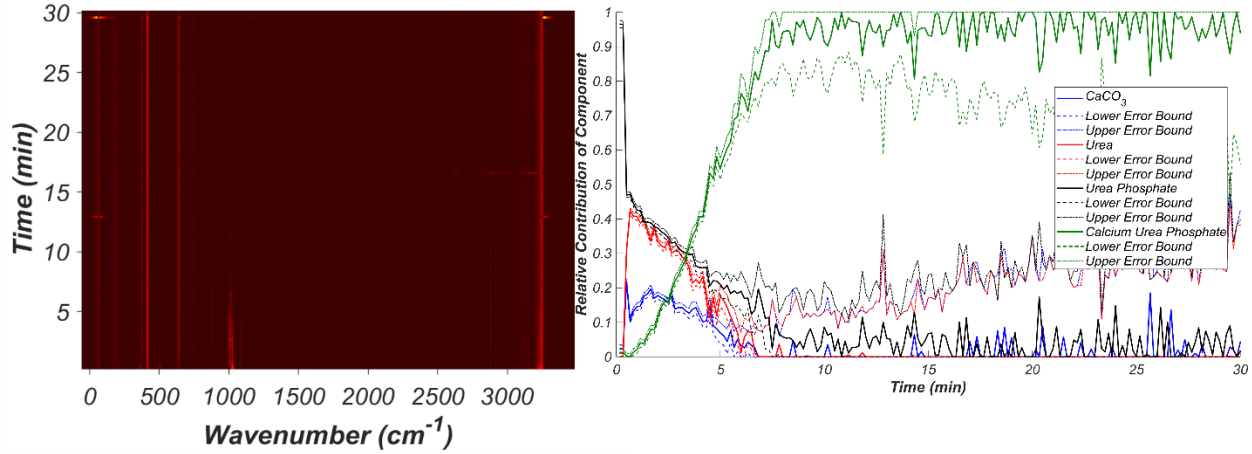

Figure SI-13. (Left) *In situ* Raman spectra for the synthesis of **1** (calcium urea phosphate) from calcium carbonate with the addition of 17 mol% $Ca(OH)_2$. (Right) Non-negative least squares fitting profiles, with errors corresponding to two times the standard deviation of the residual.

14.09 Datasets for reactions with deliberate addition of water

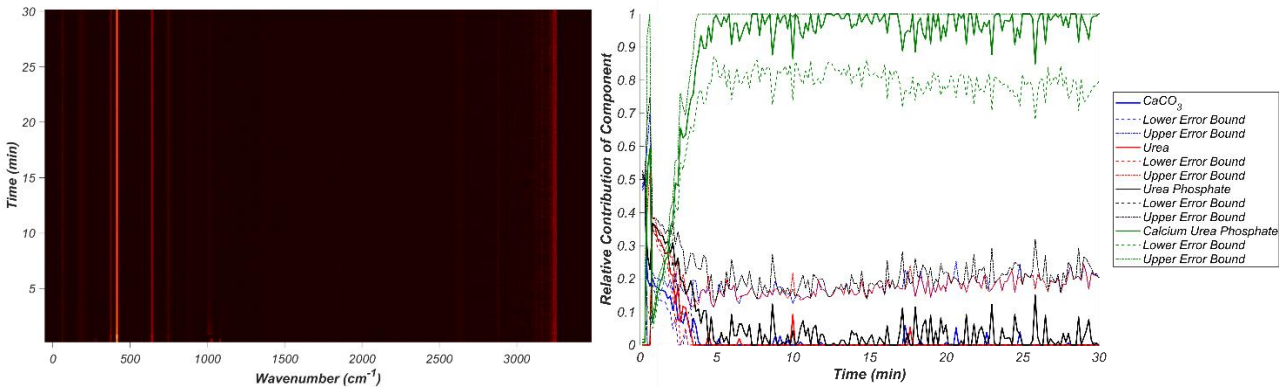

Figure SI-14. (Left) *In situ* Raman spectra for the synthesis of **1** (calcium urea phosphate) from calcium carbonate with the addition of 2.5 µL of water. (Right) Non-negative least squares fitting profiles, with errors corresponding to two times the standard deviation of the residual.

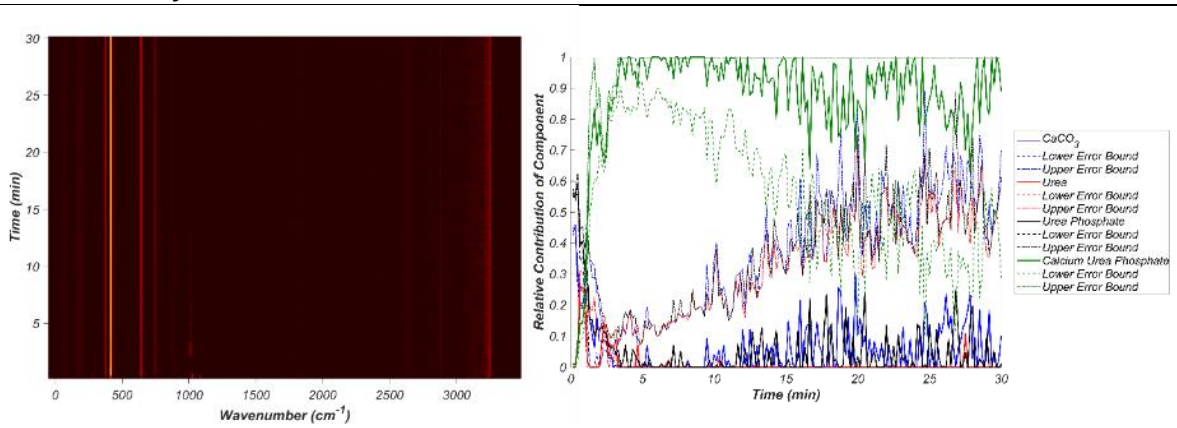

Figure SI-15. (Left) *In situ* Raman spectra for the synthesis of **1** (calcium urea phosphate) from calcium carbonate with the addition of 5 µL of water. (Right) Non-negative least squares fitting profiles, with errors corresponding to two times the standard deviation of the residual.

14.10 Datasets for Reactions in the Presence of Pre-made Compound 1

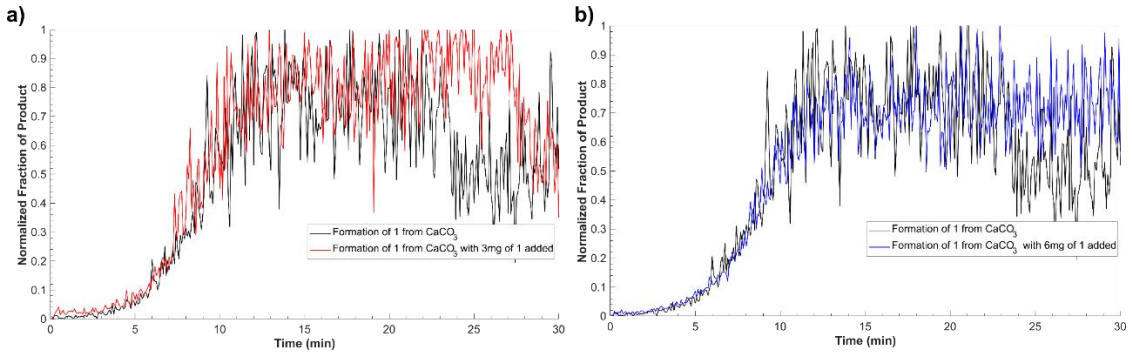

Figure SI-16. Comparison of the kinetics of formation of compound **1** from $CaCO_3$ *via in situ* Raman spectroscopy (black, trace), with the kinetics for the same reaction conducted with the addition of either 3 mg (a, red trace) or 6 mg (b, blue trace) of pre-synthesized **1**. The lack of any significant change in reaction profile suggests that the observed autocatalytic effects are not due to nucleation of **1**. Datasets for these reactions are found in the subsequent figures.

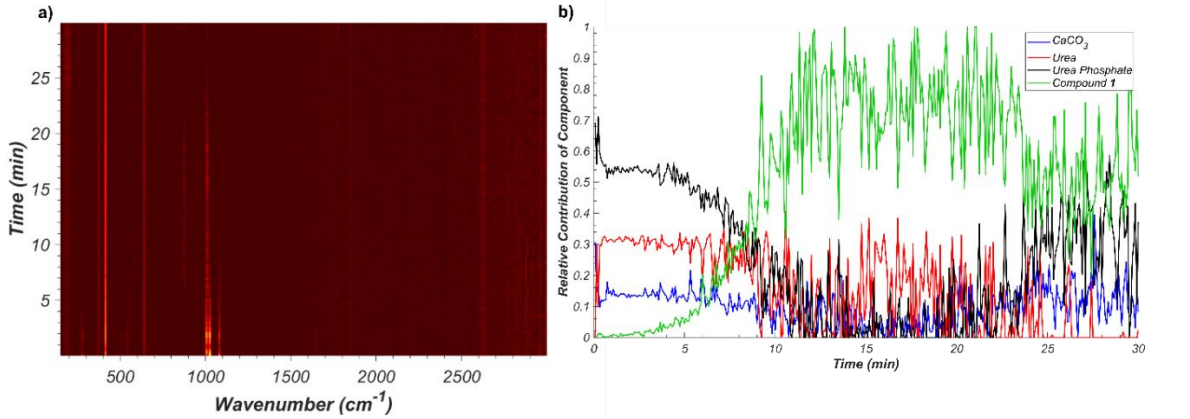

Figure SI-17. a) *In situ* Raman spectra for the synthesis of **1** (calcium urea phosphate) from calcium carbonate. b) Non-negative least squares fitting profiles estimated for the dataset.

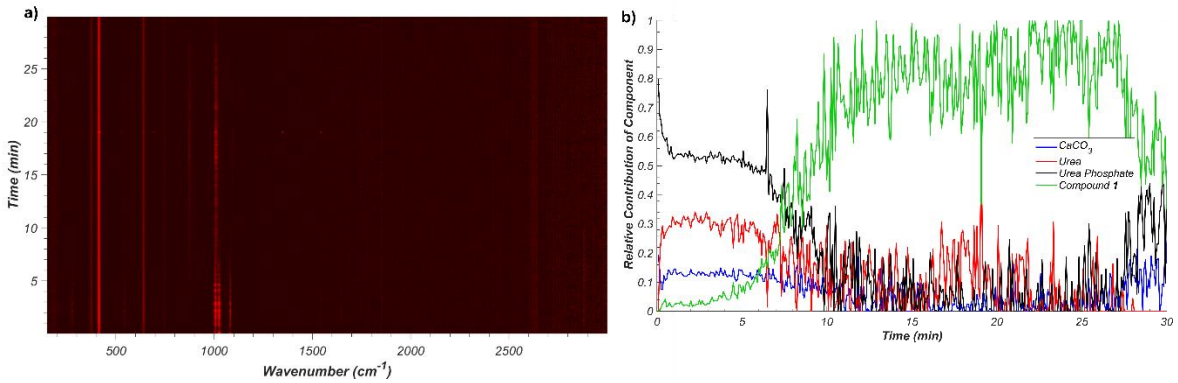

Figure SI-18. a) *In situ* Raman spectra for the synthesis of **1** (calcium urea phosphate) from calcium carbonate with the addition of 3 mg of pre-synthesized compound **1**. b) Non-negative least squares fitting profiles estimated for the dataset.

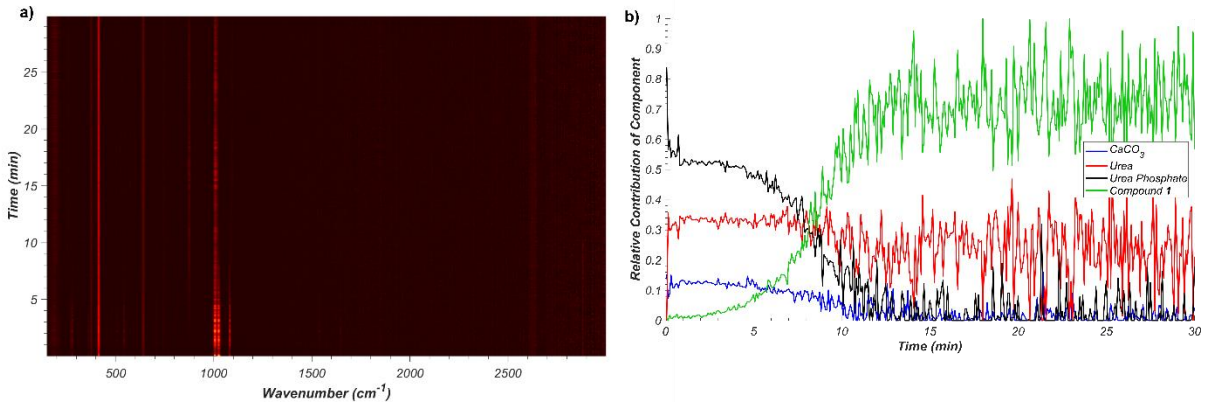

Figure SI-19. a) *In situ* Raman spectra for the synthesis of **1** (calcium urea phosphate) from calcium carbonate with the addition of 6mg of pre-synthesized compound **1**. b) Non-negative least squares fitting profiles estimated for the dataset.

14.11 XRPD Patterns of starting materials

(a) XRPD patterns of reactants

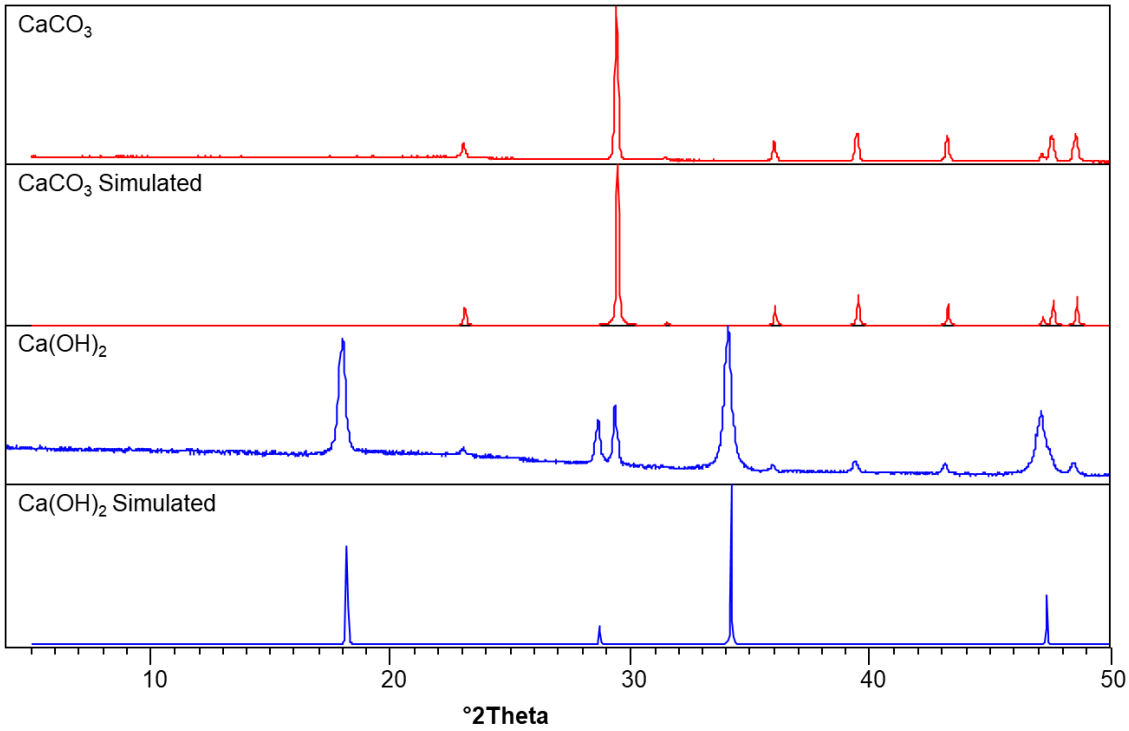

Figure SI-20. Comparison of measured and calculated XRPD patterns of the reaction starting materials used for the *in situ* XRPD measurements. The calcium carbonate phase appears to be pure while the calcium hydroxide phase contains calcium carbonate.

14.12 TGA/DSC Data

(a) Calcium Carbonate

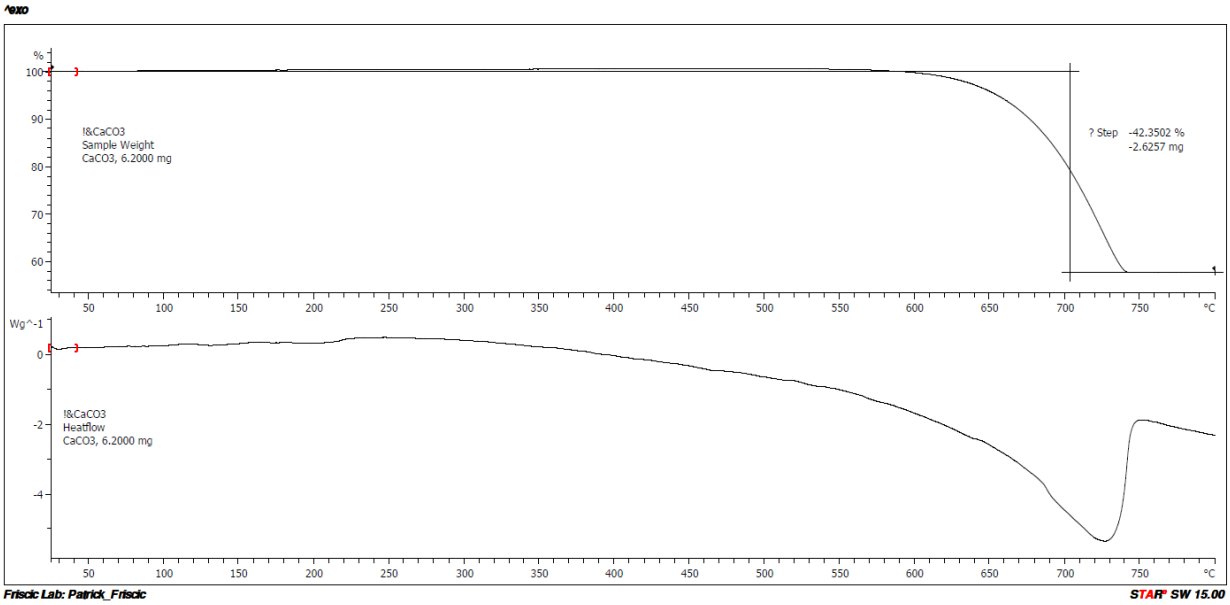

Figure SI-21. TGA(top)/DSC(bottom) curves for calcium carbonate.

(b) Calcium Hydroxide

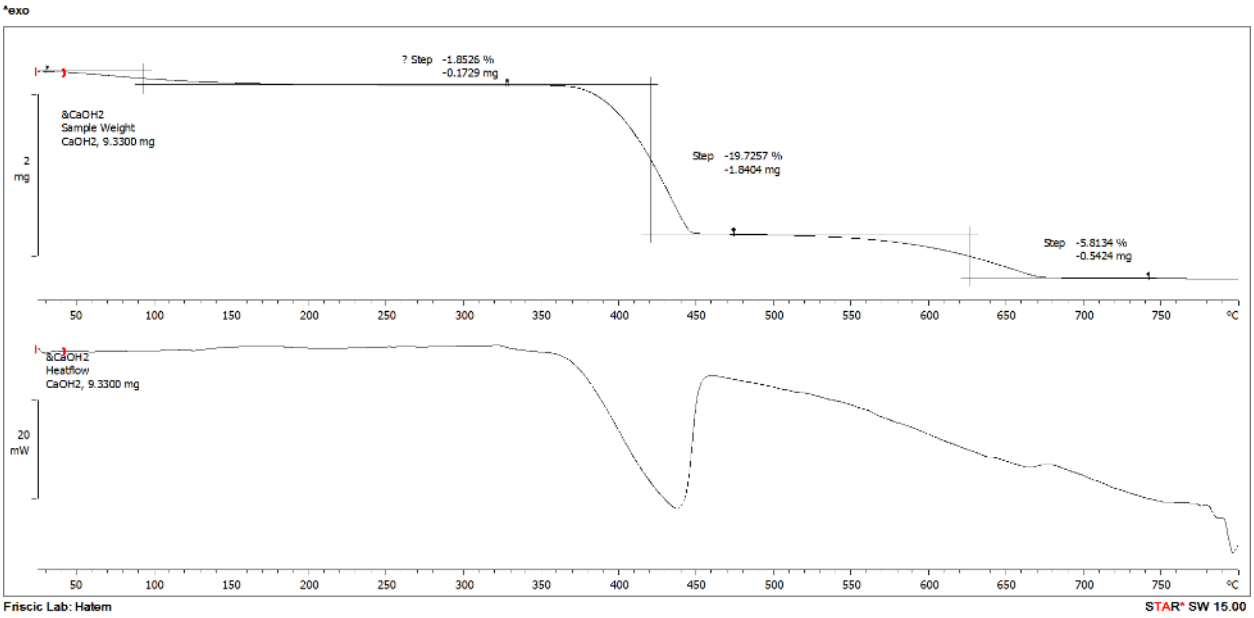

Figure SI-22. TGA(top)/DSC(bottom) curves for calcium hydroxide, showing small water loss less than 2%.

(c) Urea

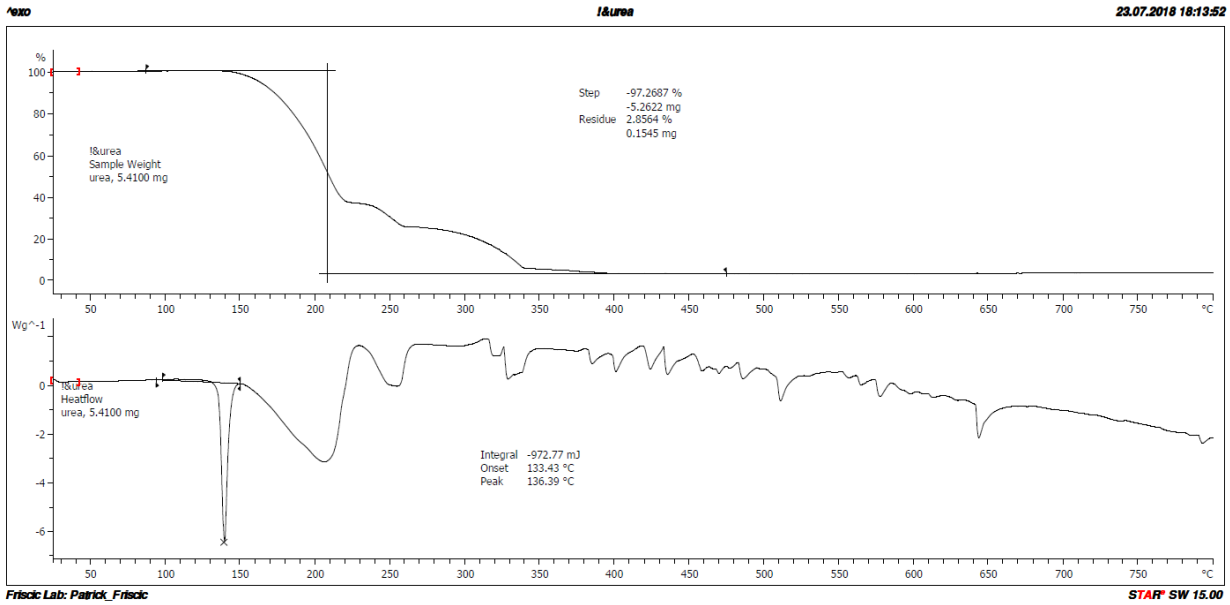

Figure SI-23. TGA(top)/DSC(bottom) curves for urea. Melting near 136 °C precedes decomposition beginning near 150 °C.

(d) Urea Phosphate

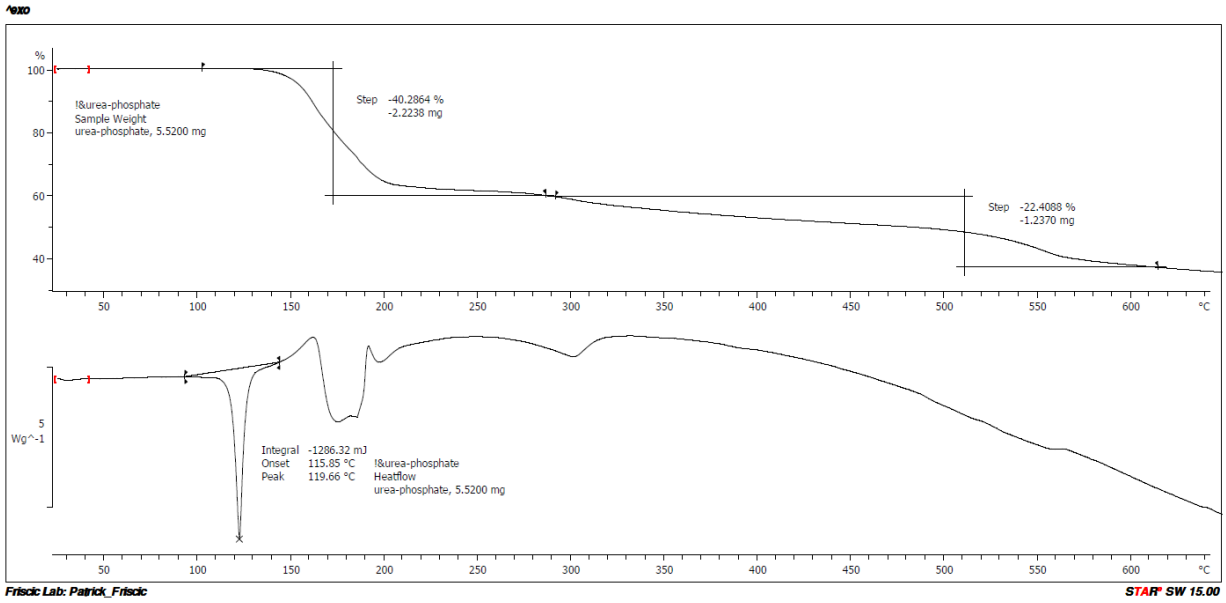

Figure SI-24. TGA(top)/DSC(bottom) curves for urea phosphate. Melting near 120 °C precedes decomposition beginning near 140 °C.

(e) Compound 1 (Calcium Urea Phosphate)

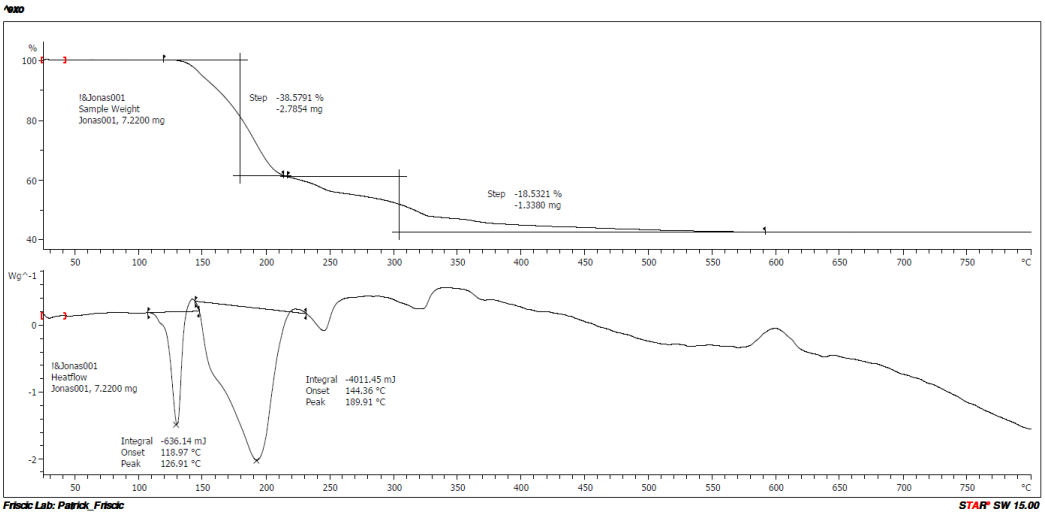

Figure SI-25. TGA(top)/DSC(bottom) curves for **1** (calcium urea phosphate), as synthesized from $Ca(CO_3)$. Melting near 125 °C precedes decomposition beginning near 150 °C.

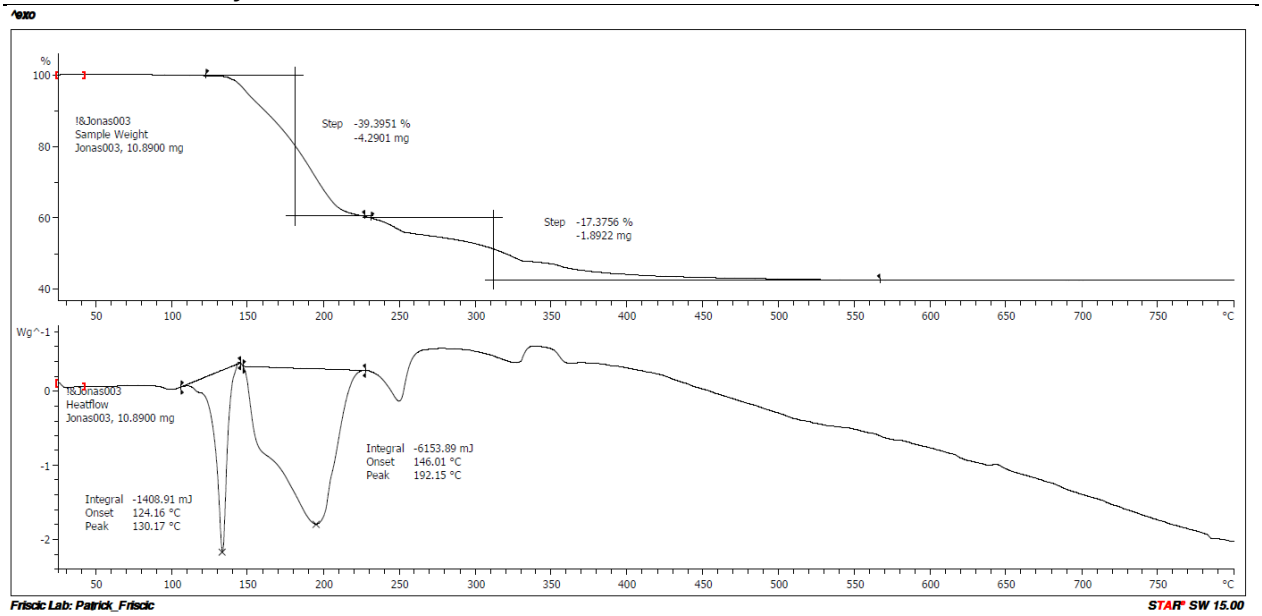

Figure SI-26. TGA(top)/DSC(bottom) curves for **1** (calcium urea phosphate), as synthesized from $Ca(OH)_2$. Melting near 128 °C precedes decomposition beginning near 150 °C.

14.13 References

1. P. A. Julien, I. Malvestiti and T. Friščić, *Beilstein J. Org. Chem.*, 2017, **13**, 2160-2168.

2. C. Prescher and V. B. Prakapenka, *High Press. Res.*, 2015, **35**, 223-230.

3. a) A. Coelho, Topas Academic Version 5, Coelho Software, Brisbane, 2012

   b) R. A. Young, *Introduction to the Rietveld method*, Oxford University Press, 1993.

4. H. M. Rietveld, *J. Appl. Crystallogr.*, 1969, **2**, 65-71.